JPL Document D-34923

Terrestrial Planet Finder Coronagraph

Science and Technology
Definition Team (STDT)
Report

Editors:

**Marie Levine, Stuart Shaklan
and James Kasting (Penn State University)**

June 12, 2006

Approvals
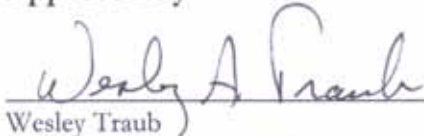
Released by

_____   June 12 2006

Marie Levine
TPF-C Systems Manager

Approved by

_____   12 June 2006.

Wesley Traub
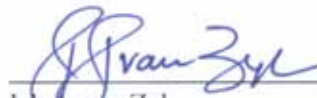TPF Project Scientist, JPL

_____   12 June 2006

Daniel Coulter
TPF Project Manager, JPL

_____   12 June 2006

Michael Devirian
Navigator Program Manager, JPL

_____   12 June 2006

Jakob van Zyl
Director for Astronomy & Physics, JPL

_____   16 June 2006

Zlatan Tsvetanov
TPF Program Scientist, NASA HQ

_____   June 16, 2006

Lia LaPiana
TPF Program Executive, NASA HQ

Goals for the Terrestrial Planet Finder Coronagraph Mission

The question "are we alone?" has its roots deep in human consciousness, and its answer could revolutionize our world view. Starting with Galileo's invention of the telescope 400 years ago, which he used to prove the existence of other worlds, and continuing through a century of astonishing discoveries—galaxies, stars, planets, and distant oceans—science has given us a dramatically clearer picture of the universe and our place within it. Today, we finally have tools within reach to seek life beyond Earth, and to answer this age-old question. The *Terrestrial Planet Finder-Coronagraph (TPF-C)* mission is a giant step towards that goal.

Over the last decade, extrasolar planets have been discovered around nearly 200 nearby stars. Most of these planetary systems are quite different from our own—with Jupiter-sized planets orbiting close to their parent stars—mainly because radial velocity measurements are most sensitive to such planets. New observing techniques, such as coronagraphy and nulling interferometry, are needed to detect smaller, Earth-like planets by their own light and to characterize them as possible harbors for life.

Characterization of a terrestrial-sized planet at its most fundamental level means learning about its mass, diameter, temperature, and atmospheric and surface composition. The presence of liquid water is considered a prerequisite for life, and several gases (O_2, O_3, CH_4, N_2O) are considered possible indicators of life. Establishing the presence of any of these compounds in a planet's atmosphere or on its surface requires spectroscopic measurements of the planet's emitted and reflected light in both the visible/near-IR and the thermal infrared. The *TPF-C* mission described in this report is the first of two NASA missions that will obtain these required data. The second is *TPF-I/Darwin*, a NASA/ESA nulling interferometer that is described elsewhere.

In addition to detecting and characterizing Earth-like planets, *TPF-C* will characterize many Jupiter-like giant planets and circumstellar dust disks. Such planetary system constituents provide clues to the course of planet formation, and may affect the habitability of co-existing terrestrial planets by influencing their bombardment histories.

These observations must be carried out in space. Ground-based telescopes cannot do the job, for two reasons. First, ground-based telescopes must observe through the turbulence of the atmosphere. Although some of the resulting blurring can be compensated by adaptive optics, it appears infeasible to see a planet as faint as Earth, even for telescopes as large as 100 m in diameter. Second, Earth's atmosphere contains significant concentrations of the very biogenic gases that one would wish to measure. Separating out the absorption features of an extrasolar planet's atmosphere from those of Earth's atmosphere appears to be an intractable problem, given the small number of photons from the observed planet and the resulting limited spectral resolution.

Technology progress necessary for *TPF-C* has been dramatic in recent years. At least a dozen new types of coronagraphs have been invented that might enable us to see an Earth close to a vastly brighter star. Methods for canceling the halo of starlight scattered within the telescope have also been demonstrated, thereby dramatically relaxing the requirements for optical surface quality. In both areas, laboratory tests are currently getting close to achieving flight-quality performance. The telescope mirror itself needs to be relatively large (8m×3.5m), but it is still within reach of current

fabrication capabilities. Alternative coronagraph designs described in this report might allow the mission to be accomplished with a smaller mirror.

A large visible-wavelength space telescope of the quality needed to detect habitable Earth-sized planets would also have important applications to other areas of astrophysics. In particular, it would profoundly advance the science of extragalactic observations, out to the very edge of the universe. Topics of literally cosmic importance could be addressed, including the expansion rate of the universe, dark energy, dark matter, and the formation of the first stars after the Big Bang. With its planned wide-field camera, *TPF-C* could conduct many of its deep-space observations in parallel with the search and characterization of Earth-like planets. In addition, the mission would provide dedicated time for separate pointed observations in a program that would be open to the general astronomical community.

In summary, *TPF-C* is one of the most scientifically compelling endeavors that the human race can envision today. The technology needed to accomplish the mission is either available already or well within reach. Pursuing this mission would give NASA a leading role in developing science and technology, and will be inspirational to people everywhere.

A Very Brief History

With enlightened foresight, in 1985 NASA organized a Planetary Astronomy Committee, to "provide advice on … initiating the search for and characterization of other planetary systems". In the same year the Space Science Board of the National Research Council of the National Academy organized the Committee on Planetary and Lunar Exploration to "extend its exploration strategy to planetary systems outside the Solar System".

In 1988 NASA organized a Science Working Group to "formulate a strategy for the discovery and study of other planetary systems". The first extrasolar planets were discovered only a few years later (1995). Soon thereafter NASA established the first Terrestrial Planet Finder (*TPF*) Science Working Group, which reported in 1999 that *TPF* "will revolutionize humanity's understanding of the origin and evolution of planetary systems", and produced a schematic design of a thermal-infrared *TPF* Interferometer (*TPF-I*) to accomplish that task.

In 2000 NASA funded an academic-industry competition to devise additional concepts for finding and characterizing Earth-like planets, resulting in dozens of new ideas, among which the leading one was the *TPF* Coronagraph (*TPF-C*). In parallel, in 2000, the second *TPF* SWG was established to develop an initial Science Requirements Document.

In 2005 NASA chartered the Science and Technology Definition Team (STDT) to work with the *TPF-C* Project scientists and engineers, and deliver a mature Science Requirements Document for *TPF-C*, a narrative on *TPF-C*'s potential for general astrophysics observations, a Design Reference Mission, an assessment of design concepts and operational scenarios, recommendations on technology developments needed, a recommended end-to-end science program, assistance in communicating with the astronomical community, and a report summarizing their work. This is that report.

The STDT met in plenary session six times throughout 2005 and early 2006, held scores of telephone meetings, and exchanged many hundreds of emails. The STDT built on the foundation of two major studies that had just been completed: the Science Requirements Document of the *TPF-C* SWG (2004); and the Flight Baseline-1 engineering feasibility study of the *TPF-C* Project Office at JPL and GSFC (2005). The STDT also incorporated the results of five major competitively-awarded Instrument Concept Studies (2006). In addition, the STDT devoted a very substantial effort to the research and writing of the Science Requirements Document and Design Reference Mission sections of this report.

This STDT report contains all of the scientific and engineering material requested in the STDT's Charter (February 2005), delivered on schedule (June 2006). We plan to publish soon five (5) companion Volumes which provide the detailed information behind the STDT Report. The Volumes are: 1) Design Reference Mission Studies, 2) Flight Baseline 1 Design Information and Performance Assessment, 3) Instrument Concept Study Reports, 4) TPF-C Technology Plan and 5) Publications. The STDT wishes it could have delivered even more, however, drastic funding cuts imposed in mid-2005 and early 2006 precluded the development of two additional parts of the study that had been chartered: a section of advice on the conduct of the end-to-end science program (not provided because the Phase-A start has been delayed indefinitely); and a section on a second iteration of the engineering study, Flight Baseline-2 (not provided because the engineering staff was no longer funded). We regret these losses, but we expect that they will be made up in the future. With these caveats, we believe that the present study is more than fully responsive to the STDT's Charter, and we are pleased to be able to present this study to NASA and the community at large.

Authors

STDT Members
J. Roger Angel, University of Arizona
Michael E. Brown, California Institute of Technology
Robert A. Brown, Space Telescope Science Institute
Christopher Burrows, Metajiva
Mark Clampin, NASA Goddard Space Flight Center
Alan Dressler, Carnegie Observatories
Henry C. Ferguson, Space Telescope Science Institute
Heidi B. Hammel, Space Science Institute
Sara R. Heap, NASA Goddard Space Flight Center
Scott D. Horner, Lockheed-Martin
Garth D. Illingworth, University of California, Santa Cruz
N. Jeremy Kasdin, Princeton University
James Kasting, Penn State University (Co-Chair)
Mark J. Kuchner, NASA Goddard Space Flight Center
Douglas Lin, University of California, Santa Cruz
Mark S. Marley, NASA Ames Research Center
Victoria Meadows, Spitzer Science Center
Martin C. Noecker, Ball Aerospace & Technology Corp.
Ben R. Oppenheimer, American Museum of Natural History
Sara Seager, Carnegie Institution of Washington
Michael Shao, NASA Jet Propulsion Laboratory
Karl R. Stapelfeldt, NASA Jet Propulsion Laboratory
Wesley A. Traub, NASA Jet Propulsion Laboratory (Co-Chair)
John T. Trauger, NASA Jet Propulsion Laboratory

NASA Jet Propulsion Laboratory
James Alexander
Kunjithapatham Balasubramanian
Virginia Ford
Sarah Hunyadi
Marie Levine (TPF-C Systems Manager)
Douglas Lisman
Stuart Shaklan (TPF-C Architect)

NASA Goddard Space Flight Center
Charles Bowers
David Content

Industry Contractors
Terry Cafferty (TC Technology)
Joe Pitman (Lockheed-Martin)
Erin Sabatke (Ball Aerospace)

Acknowledgements

Table of Contents

List of Figures

List of Tables

Executive Summary

The Terrestrial Planet Finder (*TPF-C*) is a deep space mission designed to detect and characterize Earth-like planets around nearby stars. *TPF-C* will be able to search for signs of life on these planets. *TPF-C* will use spectroscopy to measure basic properties including the presence of water or oxygen in the atmosphere, powerful signatures in the search for habitable worlds. This capability to characterize planets is what allows *TPF-C* to transcend other astronomy projects and become an historical endeavor on a par with the voyages of the great navigators.

Overall Scientific Goals

The scientific goals of the *TPF-C* mission—to discover and study Earth-sized planets around neighboring stars—are ambitious, exciting and profound, addressing some of the most important questions humankind can ask about its place in the universe. Scientists have found a variety of giant planets, and are poised to find smaller planets, more and more like the Earth. *TPF-C* will be our first chance to detect large numbers of Earth-sized planets nearby, see them directly, measure their colors, study their atmospheres, and look for evidence of life there. These goals make *TPF-C* a special project in the history of astronomy, one capable of firing human imagination and revolutionizing the way we think about ourselves and the universe.

The existence of planets around other stars, an unsupported scientific hypothesis until the mid-1990s, is no longer in doubt. Nearly 200 extrasolar planets have been discovered around other main sequence stars, most of these using the ground-based radial velocity (RV or Doppler) technique. Most of these planets found by the RV method are Jupiter-sized or larger, but several may be as small as Neptune, and the smallest one is only 7.5 Earth masses. A new planet found by gravitational microlensing may be even smaller, about 5.5 Earth masses.

The next frontier for planet-finding is to look for rocky, terrestrial-type planets around other stars. NASA's upcoming *Kepler* mission[*] and ESA's *Eddington* mission[†] will do this for more than a hundred thousand very distant stars, while the *Space Interferometry Mission[‡] (SIM PlanetQuest)* searches around nearby stars. Both Kepler and *SIM* have the capability to detect at least a few Earth-size planets if they are common. Ongoing ground-based searches may also reveal Earth-mass planets around very low-mass stars. *TPF-C*, however, is being designed to search for and characterize Earth-sized planets (and smaller) around nearby stars. These stars span a wide range of masses both smaller and larger than the Sun.

How well *TPF-C* will be able to characterize the planets it discovers depends on the design of both the telescope and the spectrograph. The baseline design has a wavelength range of 0.5-1.1 μm and a spectral resolving power, $\lambda/\Delta\lambda$, of 70. For an Earth twin (planet and star exactly like our Earth and Sun) seen at 10 pc distance, these capabilities would enable *TPF-C* to measure absorption bands of water vapor, oxygen, and possibly ozone. The presence of water vapor is an indicator of potential habitability, as liquid water is considered to be a prerequisite for life as we know it. Oxygen and ozone are potential indicators of life itself, because on Earth they come mainly via photosynthesis. There may be planets on which O_2 and O_3 can build up abiotically, but for most planets within the

---

[*] http://www.kepler.arc.nasa.gov/
[†] http://smsc.cnes.fr/COROT/index.htm
[‡] http://sim.jpl.nasa.gov

liquid water habitable zone, these gases are considered to be reliable bioindicators. Hence, *TPF-C* is the first mission with the potential to provide compelling evidence of life on extrasolar planets. We may not answer this question definitively with *TPF-C*, but subsequent missions, specifically *TPF-I* and *Life Finder*, will probe even more deeply into this age-old question that encompasses science, philosophy, and issues of human identity and destiny.

***TPF-C* can also study giant planets and dust disks — the entire *planetary system architecture* — at the same time that it looks for Earth-like planets, supporting our studies of the potential habitability of any Earth-like planet.** If our own Solar System is a guide (it still is, by what we know today), planets like Earth are found in planetary *systems* that include other small rocky planets, *e.g.*, Venus and Mars, along with gas giants like Jupiter and Saturn, and ice giants like Uranus and Neptune. The larger planets are of interest in their own right, but they may also be crucially connected to the habitability of the Earth-like planets. In our own Solar System, for example, Jupiter helps shield Earth from collisions with comets, but also perturbs some asteroids into Earth-crossing orbits. Thus understanding the potential habitability of an Earth-like planet requires study of the entire *planetary system architecture*. Fortunately, these studies can be done at the same time as terrestrial planet-finding observations that they support.

TPF-C will also study the dust clouds around stars, to learn about the process of planetary formation. Some observations of very young stars will be included, though these stars are not favorable for the terrestrial planet search program. Planetary systems themselves do not occur in isolation around stars. Collisions between small bodies (asteroids) within the system, and vaporization of icy planetesimals (comets) from farther out both create dust that orbits the star along with the planets. This dust reflects starlight, giving rise to the *zodiacal light* in our own Solar System and to *exozodiacal light* in other planetary systems. The planets in a given system must be observed against these backgrounds of the "zodi" and the "exozodi." The exozodiacal light in a given system must be measured and "removed" in order to see the planets. However, it is also known that the dust distribution can be perturbed by the gravitational influence of planets; thus the exozodi light may be a powerful tool for finding and studying the planets in a system. For these reasons, the study of exozodiacal dust clouds is an integral part of the *TPF-C* mission. Mapping out the exozodiacal light can be carried out simultaneously with the search for terrestrial planets.

In addition to its primary goal of searching for terrestrial planets and the dusty systems that accompany them, *TPF-C* will make substantial contributions in other areas of general astrophysics. The telescope will be very large, smooth, and stable, and so will exceed the performance of *HST* in several respects, including collecting area, angular resolution, and PSF stability. To take advantage of this large telescope, a separate instrument—a wide-field camera—is planned, in addition to the coronagraph. This instrument would channel light along a different optical path, and hence could perform its tasks either in parallel with planet-finding activities or by using the telescope in pointed mode. The science that could be performed in parallel includes imaging of distant galaxies, similar to the *Hubble* Deep Fields but with even greater depth and clarity. Such deep fields could be obtained during the extended time intervals, one day to several weeks, required for planetary detection and characterization. Pointed observations will yield key constraints on theories of Dark Energy, through precise measurements of the *Hubble* constant and the distance vs. redshift relation. Observations of collections of stars in the Milky-Way and nearby galaxy will probe the "fossil record" of star formation, using stars too faint to detect with *HST* or *JWST*.

The science portion of this report (Chapter 1) is organized around a set of detailed science objectives for each part of the mission. These objectives are summarized below. They are explained in more detail in Section 1.3.

Detailed Science Objectives

Terrestrial Planet Science

Objective 1: Directly detect terrestrial planets within the habitable zones around nearby stars or, alternatively, show that they are not present.

Objective 2: Measure orbital parameters and brightnesses for any terrestrial planets that are discovered.

Objective 3: Distinguish among planets, and between planets and other objects, through measurements of planet color.

Objective 4: Characterize at least some terrestrial planets spectroscopically, searching for absorption caused by O_2, O_3, H_2O, and possibly CO_2 and CH_4. It is highly desirable to measure Rayleigh scattering and photosynthetic pigments; such information may provide evidence of habitability and even of life itself.

Giant Planets and Planetary System Architecture Science

Objective 5: Directly detect giant planets of Jupiter's size and albedo at a minimum of 5 AU around solar type stars, and to determine orbits for such giant planets when possible, given the finite lifetime of the *TPF-C* mission.

Objective 6: Obtain photometry for the majority of detected giant planets, to an accuracy of 10% in at least three broad spectral bands, and in additional bands for the brightest or well-placed giants.

Objective 7: Characterize some detected giant planets spectroscopically, searching for the absorption features of CH_4 and H_2O.

Disk Science and Planet Formation Science

Objective 8: Measure the location, density, and extent of dust particles around nearby stars for the purpose of comparing to, and understanding, the asteroid and Kuiper belts in the Solar System.

Objective 9: Characterize disk-planet interactions with the goal of understanding how substructures within dusty debris disks can be used to infer the presence of planets.

Objective 10: Study the time evolution of circumstellar disks, from early protoplanetary stages through mature main sequence debris disks.

General Astrophysical Science

Objective 11: Constrain the nature of Dark Energy via precise measurements of the Hubble constant and the angular-diameter vs. redshift relation.

Objective 12: Use the fossil record of ancient stars in the Milky Way and nearby galaxies to measure the time between the Big Bang and the first major episodes of star formation.

Objective 13: Determine what sources of energy reionized the universe and study how galaxies form within dark-matter halos, through a program of low-resolution spectroscopy of large statistical samples, gathered in parallel with the *TPF-C* planet search program.

Objective 14: Carry out a diverse General-Observer program in the tradition of the *Hubble, Chandra, Spitzer,* and *James Webb Space Telescope* observatories.

From these science objectives, Level 1 science requirements have been derived; these are described in Section 1.4. The Level 1 requirements are the basic contract by which the performance of the mission is to be evaluated, before and after launch.

Basic Telescope Concept

The technical challenges for such a mission are great. *TPF-C* will detect planets by isolating their faint light from the glare of their host stars, using advanced coronagraphic techniques. The *Hubble Space Telescope (HST)* can also make coronagraphic observations but at a sensitivity which is far from the level required for terrestrial planet discovery. At the visible and near-IR wavelengths where *TPF-C* will operate, an Earth-like planet at an Earth-like distance from its star is roughly 10^{10} times dimmer than the star. Isolating the planet's light requires exceptionally efficient starlight suppression — eliminating nearly all the light of the star without suppressing the light of its planets. This also requires a very large-aperture telescope, both to gather enough light from the faint planets and to achieve the needed angular resolution.

In order to examine a statistically significant sample of nearby stars, *TPF-C* must be able to look at stars out to a distance of at least 10 parsecs, or about 32 light years. At that distance the host star and an Earth-like planet orbiting 1 AU away from it would be separated by an angle θ less than 0.1 arcsecond, or 100 mas (milliarcsec). *TPF-C* is designed to reach closer separations, $\theta \cong 60$ mas at $\lambda = 0.5\ \mu$m. This inner limit is called the inner working angle (IWA). A judicious engineering choice for the baseline design of *TPF-C* limits the IWA to $\theta = 4\lambda/D$; this suggests that the diameter of the telescope should be at least $D \cong 8$ m. However, present launch vehicles cannot accommodate a monolithic 8 m *circular* telescope, nor is any such capability under development. Consequently, the baseline design for the *TPF-C* primary mirror is an 8×3.5 m *ellipse*, a shape and size that could be launched with present rockets.

The present baseline mission is limited by light-gathering power (photon statistics) as well as spatial resolution. Alternative and more powerful starlight suppression systems are being studied (see below) that could conceivably operate at $\theta = 2\lambda/D$, and provide starlight suppression with nearly a 100% throughput. These might allow equivalent science to be undertaken with smaller aperture, or might allow a richer science program with the baseline 8×3.5 m aperture. However, these alternative approaches are currently less mature than the $4\lambda/D$ systems of the baseline design, for which detailed engineering analyses have been performed. The baseline design for the telescope and starlight suppression system is currently the only well-studied approach.

Design Reference Mission

The traditional purpose of a Design Reference Mission (DRM) is to provide benchmarks of scientific output, to be used for comparing different observatory designs. The DRM comprises several kinds of observations or scientific studies, which are chosen to represent all the principal kinds of activities over the mission lifetime.

Early work on the DRM for *TPF-C* also followed this path. A key figure of merit was completeness, defined as the fraction of all possible habitable zone (HZ) orbits that are examined for the presence of a planet at least once during the mission. We can also say the probability of a false negative result for a given star (a planet does exist in the HZ but is never found) is one minus the completeness. Mission models chiefly focused on the integration time needed to reach a given planet sensitivity for each star in the catalog, the number of visits needed to achieve a certain completeness, and how many stars can be scrutinized at that level. One could compare different telescope and coronagraph architectures based on how many stars they could examine. These early studies said between 35 and 50 stars could be searched for planets, using 2 years out of a 5-year mission lifetime. Another year was reserved for characterization (mainly spectra) and 2 years for general astrophysics.

Recently, the STDT changed the focus of the requirements: from completeness goals on each star to the expected value of the total number of planets found and characterized. A mission aimed at completeness will emphasize the scrutiny of the last few unexamined orbits (hiding places for a planet) around each star. This will allocate a lot of observing time to stars already shown to have a low probability of hosting a terrestrial planet. But a mission aimed instead at the total number of discovered planets will spend its next hour(s) on the star most likely to yield a planet. Thus, over the mission, more stars will be observed, but with lower average completeness per star.

Teams at STScI and JPL expanded their mission studies to include Monte Carlo simulations incorporating a novel scheduling tool: an "auction" of observing time based on each star's "completeness rate" — estimated probability of yielding a planet per unit time, with the benefit of knowledge from prior observations. Mission studies showed a promising harvest of planets — typically 30+ planets found, assuming every star has at least one terrestrial planet in the HZ.

But a set of one-time planet detections cannot be called a successful mission; *TPF-C* must also characterize its planets. When examining the consequences of that mission requirement, the two teams uncovered new constraints, mainly arising from the types, scheduling, and total time of follow-up observations.

We have made substantial progress in understanding how the final scientific output depends on observatory requirements and mission scheduling. Now we understand that *TPF-C*, more than any previous space astronomy mission, relies on just-in-time contingent scheduling of observations to achieve its greatest scientific harvest. This is mainly because many of the exo-planets we find will be a surprise, and then their orbital motions limit the times when we can see them again. We will have some prior knowledge about which local stars have terrestrial planets — mostly heavier planets, found by *SIM*. *Kepler* can only give us an estimate of the *fraction* of local stars with terrestrial planets, based on a sample of distant stars. Smaller or more distant terrestrial planets will be undetected or poorly known before *TPF-C*. Our Monte Carlo studies show that when we detect a planet for the first time, we may have as little as two weeks to wait before its orbital motion makes it unobservable

again — too faint, or too close in angle to the star. This means we must be quick to schedule a follow-up observation. There are several reasons why follow-up observations are vital:

- Differentiating between planets and background confusion sources
- Low-resolution color measurements, to categorize the type of planet
- Orbit determination, to distinguish small inner planets from large outer planets, and to help characterize their habitability.
- Higher-resolution spectroscopy, to search for atmospheric signatures of water, oxygen, and other molecules.

The same Monte Carlo studies suggest that once a planet disappears, due to either brightness or angular separation, it can be very difficult to find again. We must use our best chances, right after the first detection, to constrain the possible orbits and thus the range of times it might reappear. This "recovery" of the planet after its first disappearance plays an important role in characterization.

The recent mission studies (see Section 2), incorporating these impacts, now tell us that the FB1 system may not be adequate for the new science requirements the STDT has just adopted. This gap between capabilities and requirements is understandable, given the history. There has been no design team available to trade off different ways of relieving the gap. But it appears that modest changes to the FB1 engineering requirements may be sufficient to close this gap. This analysis will have to wait for rejuvenated funding.

Some additional work (see Section 2.2) has been focused on how to "front-load" the observing schedule with stars which are known to harbor planets, either from *SIM* astrometric detections of small rocky planets or from giant planet detections (by any method) which suggest the possible existence of small rocky planets. Some stars may yield tentative detections by *SIM* that can be confirmed and strengthened by *TPF-C* detection and characterization. This is a very useful additional guideline in the design of a mission observing schedule.

Flight Baseline Design (FB1)

The current design for the *TPF* Coronagraph, Flight Baseline 1 or FB1, operates in visible wavelengths from 0.5 µm to 1.1 µm with an effective inner working angle (IWA) of 65.5 mas or $4\lambda/D$, an outer working angle (OWA) of 500 mas, a scattered light level equal to 10^{-10} of the stellar peak brightness ($\Delta mag_i = 25$), and stability or knowledge of that scattered light to about 6% ($\Delta mag_s = 28$). The mission will operate in an L2 orbit over a 5 year life cycle.

The observatory design requires a high precision optical system in order to provide a stable, high-quality wavefront to the coronagraph. The starlight suppression system (SSS) is a stellar coronagraph designed to eliminate diffracted light and control scattered light, in order to reduce the background light in the instrument to a level that is less than 10^{-10} of the incident light. For FB1, diffracted light is removed with a Lyot-type coronagraph from the region in the image plane where planets might be found. Other approaches, such as the shaped-pupil coronagraph, are currently under consideration and might be viable options for further design implementations of *TPF-C*.

In FB1, scattered light is controlled using a coarse deformable mirror (DM) and a pair of fine DMs. The coarse DM compensates for large wavefront deviations left in the telescope due to gravity re-

lease and launch stresses. The fine DMs have a 1 micron stroke and high actuator density; as a pair they can control both amplitude and phase wavefront distortions up to a spatial frequency limit determined by the actuator density.

The telescope has an 8 × 3.5 m elliptical primary mirror with a system effective focal length of 14 m. The field of regard is only 5 arcsec, and the field over which aberrations must be corrected is further reduced through the use of fine steering and deformable mirrors inside the coronagraph. The distance between the primary and secondary is 12 m at the vertex and the focus is close to the middle of the primary aperture.

The observatory needs to reject both thermal and jitter perturbations at an extreme level. Thermal stability is accomplished with large deployable concentric conic-shaped v-groove layers which shed the solar heat input and isolate the payload from changing sun angles during observational maneuvers; and with a thermal enclosure around the payload that actively controls temperatures in the back end of the telescope. Jitter stability is provided through a two-stage passive isolation system which offers the required vibration reduction from the reaction wheel disturbances. Alternatively, an active, non-contact isolation and pointing system capable of providing significant performance margin is being considered.

This FB1 design is the second in a series of 3 to 4 design iterations expected to be completed prior to entering Phase A. Each cycle will lead to a progressively more detailed design while continuously investigating options to improve and optimize performance. For FB1 the design reflects updated science requirements with a $4\lambda/D$ inner working angle, impacting the size of the primary and the design of the occulting mask. The FB1 analyses investigated the thermal and jitter impact on the contrast stability requirements, assessed contributors to the static and dynamic error budgets and scoped out requirements for the active thermal control system. In subsequent design cycles, the engineering team will incorporate models from the Instrument Concept Studies, improve the contrast capability of the starlight suppression system, add fidelity to the active thermal control system and optimize the system performance of the end-to-end observatory.

TPF-C Performance Drivers

The performance requirements for *TPF-C* begin with adequate suppression of starlight. An ordinary telescope allows starlight to spread across the angular width of the entire planetary system, overwhelming the faint signal of the planet (typically ten billion times fainter than the star). We know by analysis and experiment that *TPF-C's* advanced coronagraph features—pupil and field masks to suppress diffraction, and deformable mirrors to suppress starlight scattered by wavefront errors—can successfully control both types of stray starlight from $4\lambda/D$ to almost $50\lambda/D$. The goal of 10^{-10} suppression in this region is at the heart of the "static error budget". It is important that the number 10^{-10} is chosen only partly to keep the background photon rate small and integration times low.

The observation strategy is the principal reason to aim for 10^{-10} suppression. The residual starlight contributes a speckle background which can vary by 100% in the width of the point spread function ($\sim\lambda/D$). To distinguish these speckles from true planets, we compare two images of the planetary system taken with a different "roll" orientation—rotation around the optical axis. This pair of images is called an observation. Through the roll maneuver, speckles are expected to stay fixed on the telescope and thus on the focal plane, while the planet stays fixed on the sky and moves on the focal

plane, rotating around the star image. During an observation, the speckle brightness pattern must be stable to much less than the expected planet brightness, so that the image subtraction will unambiguously distinguish speckles from planets.

This requires a new performance budget governing all sources of variation in the speckle brightness pattern. An important consequence of establishing this "dynamic error budget" is the fact that it places the most stringent constraints on the static error budget. The brighter a speckle is at the start of an observation, the smaller a thermal or mechanical disturbance it takes to change the speckle's brightness by 2×10^{-11} (or whatever 1-σ planet sensitivity floor we might choose).

These two error budgets have been drawn up and are described in Section 3.2. Most of these requirements have been shown to be feasible, either in the laboratory or by detailed analyses of the FB1 concept, summarized below.

FB1 Performance Assessment

The major result of our FB1 modeling work is that the environmental perturbations during operation appear to be controlled sufficiently— both thermally and dynamically— to ensure that the image plane contrast remains stable to the required levels. The current sunshade isolates the telescope and payload adequately. Active vibration control easily isolates the payload from reaction wheel vibrations. Passive vibration isolation control could be effective, but it would require more tuning and would provide less margin. Vibrations from mechanisms in the instruments and starlight suppression system have yet to be included, but selective damping seems feasible and promising. The next cycle will include these.

An important feature of this area is that the commercial thermal and dynamic analysis software have limitations that are becoming well understood, and the team has implemented patches where appropriate to produce credible results. For longer term production mode use, better integrated modeling tools are being developed. These will provide parallel code architectures for much improved analysis cycle time, efficient inter-operability between the multi-physics analyses (thermal, structural, dynamics, controls and optics) and numerical algorithms required for high accuracy solutions.

Our analysis and modeling have shown that the baseline wavefront control system with realistic optical specifications cannot provide truly broad-band contrast suppression. We have learned how to modify the dual-DM wave front controller to perform better over a broad band while relaxing wave front and reflectivity uniformity requirements. The new design also reduces the number of optical components in the system. These changes will be incorporated in the next design cycle.

The baseline primary mirror concept is a thin monolithic ULE face sheet fused to lightweight ULE honeycomb core cells and mounted on 3 rigid supports. This has the potential to meet all operational requirements, but more consideration of fabrication, ground handling and testing accommodations is needed. The FB1 launch loads are too severe around the mounting points, for example. This complex assembly will need further development to address the full range of difficulties it will face. Furthermore, the FB1 observatory mass margin is too low for the capability of the chosen EELV launch vehicle. FB1 was not focused on mass optimization but significant improvements have already been identified and will be applied to the next cycle.

Within FB1 the active thermal control system was simplified to include only heaters (with no feedback) as locally applied power within the thermal enclosure. FB1 was purposely focused only on meeting those requirements of the active control system, rather than including detailed features which are not yet well understood. The goal was to use FB1 to understand how difficult and challenging the active control system will be before addressing how it should be implemented. FB1 sensitivity analyses defined the heater location, power levels and cycles required for maintaining the thermal stability of the observatory. This information will be used in the next cycle to design a higher fidelity representation of the active thermal control system.

Conclusions from the FB1 design and analysis cycle, along with open trades for possible design alternatives, will guide the next design cycle toward better performance and deeper detail. The team and community have gained significant knowledge through this exercise and will continue to do so as they await the start of the next design iteration, FB2.

Instrument Reports

In February 2005, NASA HQ solicited proposals for several instrument concept studies (ICS) for *TPF-C*, as part of the ROSES 2005 NRA. In June 2005, five groups were selected to conduct concept studies of a variety of instruments that might be built for *TPF-C*. The selected proposals were:

PIAA-AHA, an instrument for starlight suppression, planet detection, and spectroscopy, using two novel techniques.	Angel, Guyon
Visible Nuller, instrument for starlight suppression and planet detection	Shao
Mag30Cam, a wide-field camera for general astrophysics	Brown
CorECam, a simple coronagraph camera with color filters	Clampin
CorSpec, an integral field spectrometer for spectroscopic study of planets in the coronagraph	Heap

The reports of these five teams are summarized briefly below and at greater length in Section 4.1.3.

PIAA/AHA Alternative Coronagraph

This is an instrument with integrated star suppression system for imaging and spectroscopy of terrestrial exoplanets. It combines the PIAA (Phase-Induced Amplitude Apodization) method to reach an inner working distance of $2\lambda/D$, (see below) with AHA (Anti-Halo Apodization). AHA is a new interferometric technique to sense the phase and amplitude of the residual starlight halo, and to suppress it by destructive interference with explicitly created anti-halo speckles. The two methods in conjunction promise not only the improved inner working distance, but much higher sensitivity by covering a 360 degree field without the losses in resolution and flux inherent in the baseline Lyot system. The instrument also incorporates dichroic mirrors to allow simultaneous full spectral coverage from 0.5–1.5 microns. The combined effect of increased throughput, resolution, field cover and bandwidth is more than an order of magnitude reduction in integration time compared to the baseline design. This combined with closer inner working angle allows for a much richer observing program.

It should be noted that if this approach is adopted for *TPF-C*, the *HST-JWST* paradigm in which instrument teams are selected independent of the telescope is no longer applicable. This is because the science imaging and spectroscopy and the star suppression and wavefront correction systems are necessarily completely integrated, with the same imaging arrays providing the science, wavefront and speckle nulling data. A silver lining of the extended *TPF* delay is the time it opens up for development of the powerful PIAA and AHA technologies to the technology readiness level needed for a Phase A selection.

Visible Nuller

The visible nuller (VN) together with the post coronagraph calibration interferometer is being studied because it provides potential gains in several areas. The nuller has the potential to have an inner working angle of $2\lambda/D$, significantly expanding the number of potential targets. The detection of oxygen in the atmosphere of an Earth-like exo-planet is a key goal and a nulling coronagraph at $2\lambda/D$ has ~7 times more potential targets than one at $4\lambda/D$. The post coronagraph calibration interferometer (PCCI) is an equally important, perhaps even more important development. The PCCI relaxes the required wavefront stability of the telescope by about a factor of 1000, from a few picometers per hour to a few picometers per 3~4 seconds. The PCCI has two functions:

- to measure the wavefront with very high accuracy and high photon efficiency, to ~30 picometer in ~2 minutes for a ~5 mag star; this is needed to set the deformable mirror to create the 10^{-10} dark hole, and
- to measure the post coronagraph speckle pattern to 3~10% so that the ~10^{-10} residual speckle pattern can be subtracted in post processing to ~ 10^{-11}, in order for a 10^{-10} planet to be detected with a SNR of 5~10.

The PCCI is being used in a number of ground and space coronagraphic instruments: a nulling coronagraph on a sounding rocket to launch in 2007; the Gemini Planet Imager, the first of the second generation instruments for the Gemini telescope; and the Planet Formation Imager, an extreme AO coronagraph for the Thirty Meter Telescope (TMT).

Wide-Field Camera

A wide-field camera (WFC) enriches the science return from *TPF-C*. Even a field of view (FOV) of only 10 sq. arcmin would be mostly unaffected by scattered light from stars in the coronagraph. It would obtain parallel images of the deep cosmos at no cost of observing time. In pointed mode, it would extend *Hubble*-type imaging to 24 times greater sensitivity and 3 times better resolution. A 50 sq. arcmin FOV in a wedge shape extending to 10 arcmin off axis would produce a parallel survey of 10 sq. deg of sky to below 30th magnitude, which is 1000 times more cosmic volume than the various *Hubble* deep fields and more sensitivity than any of them. A WFC with an FOV of 10-100 sq. arcmin for the wavelength range 400–1700 nm is compatible with the baseline design for *TPF-C*. Its scientific potential would be unrivaled by any currently planned telescope. on the ground or in space. A WFC is a low-risk, high-benefit option for *TPF-C*. It would effectively double the mission value at marginal costs. Recognizing the scientific benefits of such a camera, the STDT has incorporated it into the minimum, baseline, and desired mission requirements.

CorECam

The CorECam instrument concept study addressed the requirements and science program for *TPF-C*'s primary camera. CorECam provides a simple interface to the Starlight Suppression System (SSS) provided by the *TPF-C* Project, and comprises camera modules providing a visible and near-infrared (NIR) camera focal plane imaging. In its primary operating mode, CorECam will conduct the core science program of *TPF-C*, detecting terrestrial planets at visible wavelengths. CorECam additionally provides the imaging capabilities to characterize terrestrial planets, and conduct an extended science program focused on investigating the nature of the exo-solar systems in which terrestrial planets are detected. In order to evaluate the performance of CorECam, we developed a comprehensive, end-to-end model using OSCAR modeling software, which provided a number of key conclusions on the robustness of the *TPF-C* baseline design, and allowed investigation of alternative techniques for wavefront sensing and control. The CorECam team recommends photon counting detectors be baselined for imaging with *TPF-C*, since they provide mitigation against the background radiation environment, improve sensitivity, and facilitate alternative WFSC approaches.

CorSpec

The coronagraphic spectrograph (CorSpec) team explored an instrument concept that would fulfill all four scientific objectives of *TPF-C* by

(1)   Spectrally characterizing the atmospheres of detected planets;
(2)   Directly detecting terrestrial planets in the habitable zone around nearby stars;
(3)   Studying all constituents of a planetary system including terrestrial and giant planets, gas and dust around sun-like stars of different ages and metallicities; and
(4)   Enabling simultaneous, high-spatial-resolution, coronagraphic spectroscopy of AGN's, super-novae, and other objects requiring high-contrast spectroscopy.

The instrument concept consists of a set of four integral field spectrographs (IFS), each covering a spectral band ~22% wide, and together covering the full spectral range of *TPF-C*. Each IFS has a 134 x 134 microlens array to obtain a R~70 spectrum of each Nyquist-sampled image element in the coronagraphic field, and each uses a photon-counting charge-multiplication CCD to record the ~18,000 spectra.

The concept assumes that the *TPF-C*'s starlight suppression system is similarly composed of four independent units, each optimized for a given spectral band, and that each unit is capable of suppressing the starlight to an acceptable level over a passband 22% wide. Members of the CorSpec team have developed a preliminary concept design of the starlight suppression system.

Alternative Mission Designs

Several concepts with the potential to improve performance and simplify the design have been proposed. These include changing the telescope from the present Richey-Chretien design to a three-mirror astigmat (TMA), actuating the primary mirror, and two alternative starlight suppression concepts (captured in the VN and PIAA/AHA studies and their reports). It may also be possible to employ aluminum coatings on the primary and secondary mirror to enable UV astrometry with the general astrophysics instrument (GAI).

The baseline telescope is a Richey-Chretien design with a small diffraction-limited field of view. The field is adequate for planet detection over several arcseconds; it was not designed for wide-field imaging. A TMA, on the other hand, can be designed for a field ~ 10 arcmin in diameter, sufficient for the GAI. It may also have the advantage of relaxing the positional stability tolerances on the optics. It may, however, require a radical repackaging of the starlight suppression system (SSS).

A major issue confronting the baseline design is the manufacture and on-orbit gravity release of the primary mirror, which may be as large as several microns. The baseline design includes a coarse deformable mirror (DM) to compensate the sag. But the sag is problematic for the GAI, which does not have its own wavefront control system. An alternative approach under consideration is an actuated primary mirror instead of the coarse DM. Actuation could take the form of a small number of force actuators to correct a few large-scale modes, enough to bring the residual wavefront error within the dynamic range of the fine DMs in the SSS. A more radical approach would be to build the primary as a ~ 1 cm thick meniscus connected via ~ 10^4 position actuators to a lightweight welded ULE structural support. The telescope wavefront would be corrected against deformation of the support by the primary mirror actuators, eliminating the baseline arrangement of coarse and fine deformable mirrors, conjugated to the primary. This approach would require significant technology development. Suitable piezo actuators could be developed from the current DM concepts or from existing commercial actuators with 50 pm readout and 10 micron stroke. Further study is required to understand and develop solutions for athermalizing and reducing the mass of the actuators, and for the transition from the launch to operational environment. In addition, concepts are needed to reduce the mass of the cables across the 8 m aperture.

The baseline mission design starlight SSS carries both a Lyot coronagraph and a shaped pupil coronagraph. The Lyot coronagraph uses an eighth-order mask that, like the shaped pupil, is very effective at rejecting thermally-induced changes to low-order aberrations in the system. The baseline carries several masks optimized for discovery and characterization for different stellar classes. However, none of the masks are useful at inner working angles much below $4\lambda/D$.

Alternative SSS concepts have already been mentioned: the PIAA and visible nuller. Each also has an associated concept for wavefront sensing and control which might be applicable to Lyot and shaped pupil systems.

Verification Approach

Because of its large size and extreme stability requirements, *TPF-C* poses significant challenges for pre-launch verification. To date, planning for Integration and Test (I&T) has concentrated on the Optical Telescope Assembly (OTA). It is considered to be the most challenging task because testing to the required precision may be beyond the capability of facilities that we expect to be available. Specifically, it may not be possible to test end-to-end performance of *TPF-C* on the ground because its extraordinary performance requirements will only be achieved in zero-gravity and in an extremely stable thermally environment. The baseline solution is to devise an approach that combines test and analysis in ground-based testing to verify on-orbit performance requirements. Component requirements will be verified directly by testing to the highest level of assembly possible, and additional tests will be performed to verify the analytical models of each component. These component models will be assembled to form the verified system model, in a manner parallel to the hardware assembly and verification process. The extent to which requirements will be inferred by analysis rather than by

direct measurements will be driven by considerations of cost and risk that have yet to be addressed. As a minimum, we know that for the baseline primary mirror our ability to relieve gravity sag and to duplicate on-orbit thermal and vibration environments will most likely fall far short of what is necessary to directly verify the flight requirements; for this reason, analytical methods will be required to infer flight performance from ground test data. The final system test will therefore be limited to verifying alignment workmanship and to correlating system model parameters, by overdriving the input thermal and jitter environment.

During the FB1 cycle, integration and test plans were sketched out for the primary mirror assembly: the necessity of extreme, nanometric precision, when combined with the mirror's very large size (8.5×3m) and flexibility, poses major challenges. Plans call for figuring and final measurement of the primary mirror to be performed on the best zero-G mount possible, however, this is not necessarily compatible with flight mounting schemes. On the high fidelity zero-G mount, the mirror will be subjected to mechanical and thermal loads while its optical performance is measured with an interferometer at the center of curvature. These measurements are as faithful as can be achieved on the ground to the on-orbit performance of the mirror— they will be used as inputs to the integrated structural-thermal-optical model. After the mirror is integrated with its flight support to the Aft Metering Structure (AMS) and the Payload Support Structure (PSS), a different gravity unloading scheme will have to be used. It is assumed that this setup will not be as effective as the high fidelity zero-G mount used before. Thermal and dynamic loading will be applied in order to observe their effect on the assembled sub-system with its the flight mount. These data will be used to correlate model parameters, and the model will then be exercised in a simulated flight environment to analytically predict on-orbit performance. These analytical results will then be compared to the requirements for verification.

The alternative and most definitive verification approach is of the complete *TPF-C* spacecraft system prior to launch. An off-axis collimator would be used to illuminate the full aperture with a scene of a star and planet at 10^{-10} contrast, and the ultimate proof would be to see an image showing the planet obtained by using all the internal wavefront control and star suppression systems working as on orbit.

A test like this of the baseline design would not be possible, because of uncorrectable gravity bending of the primary in the spacecraft configuration. But it would in principle be possible for the alternative primary described above, with high authority position actuators. The stroke of the actuators would be matched to the bending of the integrated reference structure, so the primary figure could be corrected under 1 g load as well as in space. Local quilting of the facesheet would be small and of high frequency, and would not spoil such a test. The collimator would need to have a clear aperture and be off-axis, like the primary, but its optical quality need not be significantly better than that of the primary. The spacecraft star suppression system would take care of the residual collimator wavefront errors along with those of the primary.

As noted above, such a test would be successful only if the vibration and thermal environment were adequately controlled. The test facility would have to be designed from the ground up with these requirements in mind. We recommend that a feasibility study for the complete test facility be included when *TPF* funding again becomes available.

Key Technologies, Development Plan & Progress to Date

Planet detection, characterization, and verification are the core drivers of the *TPF-C* technology efforts, particularly in the early phase. In order to mitigate this technical risk, *TPF-C* has developed a detailed technology plan which lays out the scope, depth and inter-relatedness of activities that will enable the project to demonstrate sufficient technology maturation to enter into Phase A. Specifically, there are four milestones which require testbed demonstrations of critical starlight suppression technologies as well as validated testbed models and error budgets. These milestones are not intended to be all inclusive, but rather serve as benchmarks of progress. Testing of Milestone 1 for demonstration of narrowband starlight suppression at 1×10^{-9} contrast has been completed, and testing of Milestone 2 has begun for demonstration of broadband starlight suppression. Milestone 3a and 3b will validate starlight suppression models and will demonstrate flight system performance.

The challenge is to control diffracted light over a broad spectral range while mitigating the effects of internal and external errors. Technology development is organized into six areas that address aspects of this challenge. They are:

1. Fabrication of a pathfinder demonstration mirror that establishes the state-of-the-art in fabrication of large, off-axis, low-scatter mirrors;
2. Development of a starlight suppression testbed which tests various masks, deformable mirrors for wavefront correction, wavefront sensing and control approaches and starlight suppression algorithms;
3. Investigation, analysis and fabrication of more advanced masks and stops;
4. Development of modeling tools that will represent the extreme precision needed to model the test beds and the flight system so that feasibility for the mission can be understood;
5. Development of testbeds to investigate alternative architectures for starlight suppression;
6. Precision materials properties measurements.

Technology Demonstration Mirror (TDM)

The requirements for the *TPF* coronagraph primary mirror allocates error for the surface quality in terms of spatial frequency, and the Technology Demonstration Mirror (TDM) was defined to study the ability to fabricate a mirror which meets the lower spatial frequency requirements. The TDM is a 1.8 meter diameter mirror composed of six outer core segments and one inner hexagonal core segment. Each segment is composed of a honeycomb core with a thin front and back facesheet. Fabrication of the TDM using low temperature slumping and fusing techniques will demonstrate whether state-of-the-art technology can meet the special frequency requirements. The effort will also provide methodologies to measure the performance of the mirror and to interpret the measured data for requirements verification. Owing to funding cuts, the TDM effort has been put on hold with 2 of the core segments completed.

Trade studies have resulted in the selection of light-weighted, fuse-bonded ULE as the substrate material. The ULE boules being used have tight requirements on coefficient of thermal expansion (CTE) and have been selected to meet them. Calibration standards to measure the CTE of the selected boules were re-measured to verify calibration and that the CTE requirements were met.

Coating the mirror will be a challenge because coating uniformity requirements are tight. Non-uniform coatings will cause amplitude errors that will interfere with the starlight suppression requirement. In addition, polarization effects of the candidate coatings are being studies to understand

the polarization effect on starlight suppression, as well as to develop concepts for mitigation of the induced polarization of the light.

High Contrast Imaging Testbed

The heart of the coronagraph system is the starlight suppression system that includes wavefront sensing and control components, as well as various masks and stop elements. The High Contrast Imaging Testbed (HCIT) enables the exploration of starlight suppression methods and hardware in a flight-like environment within which various concepts for masks and stops designs, wavefront sensing approaches, and control algorithms are being investigated. The testbed layout is flexible so that alternate concepts can be tried and guest investigator testing is available. The testbed is installed in a vacuum chamber and has been measured to have milli-Kelvin thermal stability and Angstrom wavefront stability. A series of increasingly mature and robust deformable mirrors have been developed, fabricated, calibrated and installed to demonstrate precise wavefront control.

Current narrow band performance has reached an average contrast of $<1x10^{-9}$ throughout both the outer working angle of $4\lambda/D$ to $10\lambda/D$ and the inner working angle of $4\lambda/D$ to $5\lambda/D$ using laser light at 785nm as specified in the technology Milestone 1 definition. Moving torwards the goals of technology Milestone 2, current broad band contrast has reached an average contrast of about $1x10^{-8}$ over the same areas at 785±10 nm. Following that, the testbed is scheduled to explore alternate mask options and broad band wavelength performance improvements.

Mask and Stops

Developing mask and stop forms, researching candidate mask materials and their related influences, modeling light propagation and sensitivity to form errors are areas of research supporting the contrast goal of 10^{-10} required to detect and characterize Earth-like planets.

The technology has developed models of polarized light propagation through masks that include electromagnetic field effects and wave band performance. Such models are used to guide mask fabrication sensitivities requirements. Modeling and assessing sensitivity has led to development of a promising new mask form called an 8th order mask. Two types of 8th order masks have been built to demonstrate this mask form, using High Energy Beam Sensitive (HEBS) glass and a deposited aluminum binary representation. These masks are scheduled for testing in the HCIT.

Materials research has focused on careful measurement of material properties and influences on the mask performance. This research is expected to lead to mask solutions that increase the bandwidth of performance and polarization tolerance of future masks.

The *TPF* Coronagraph will rely heavily on modeling and analyses throughout its mission lifecycle, thus developing models, validating them, and implementing them are a key task for the project. Current modeling activities can be separated into 3 broad areas: predictions of on-orbit performance, analytical tool development in support of specific Coronagraph needs, and verification and validation of the analyses.

Development of on-orbit performance models includes modeling the thermal and dynamic responses of the observatory during operation in space and will be covered in Section 3.0 describing the observatory design. These models are tied to optical performance models that represent the propagation of the wavefront through the perturbed surfaces, including diffraction, polarization,

mask and stop effects and optimization algorithms for the deformable mirrors. Broad band wavelength effects are being added.

Modeling and Simulation

In Modeling process verification and validation will be performed on the HCIT and future testbeds that are envisioned as the mission progresses. Optical performance modeling is being carried on the HCIT to verify contrast sensitivity to various error contributors, with the goal of validating a testbed error budget which parallels the flight system error budget.

Also under development is a fully integrated modeling tool that simulates under a single computational code the thermal, mechanical, control and optical performance of the flight system. This tool has structural evaluation, embedded thermal radiation and conduction capabilities, a NASTRAN native input format for the model description, scalability to very large problems with very efficient numerics, seamless interface to optical analysis codes, and eventually end-to-end sensitivity and optimization abilities. This tool has been used to run simple trade studies for the *TPF-C* modeling team.

Alternative Starlight Suppression Testbed

Three additional methods of starlight suppression are being supported by *TPF-C*. A testbed has been developed at Princeton University to design, analyze, fabricate and test pupil plane masks. A testbed has been developed as a joint effort of NOAO and University of Hawaii to build and study a pupil re-mapping concept. Finally, a testbed has been developed at JPL, using visible light and interferometric techniques to create a null over a star, enabling imaging of orbiting planets.

Precision Material Properties Measurements

A critical step in predicting *TPF-C* system performance is to use material data of the highest accuracy and precision. The JPL Dilatometer laboratory is a state-of-the art facility which measures thermal strains from room temperature to $20^{\circ}K$ at an accuracy of about 2 ppb. Active thermal control allows the samples to maintain a stability of $5 \text{ m}^{\circ}K$ for as long as necessary, allowing the measurement of thermal relaxation, a form of dimensional instability and material nonlinearity. Such capability is required to measure variations in CTE distributions in ULE or nonlinear behavior of Zerodur.

The JPL tribometer is also being designed to study the physics and material properties of sub-Coulombic friction as a function of temperature, pre-load and interface materials. This is an immature field which is critical for the representation of deployment mechanisms along the optical path.

Conclusions

When it eventually flies, *TPF-C* will be one of the most scientifically exciting missions ever launched by NASA. A positive indication of extraterrestrial life, or even the detection of a habitable planet similar to Earth, would alter the way in which humans look at themselves and at the universe. Most of the technology required to perform this mission already exists. The parts that do not, especially the coronagraphic techniques required to achieve 10^{-10} starlight suppression at close distances to the star, can likely be developed over the next year or two, given a modest amount of funding. We hope that this report will help provide the motivation to finish off these development tasks and to get the *TPF-C* mission itself restarted in as short a time as possible.

Blank Page

Blank Page

1.0 TPF-C Science Requirements

1.1 Introduction

The search for planets has flourished since the initial planet discoveries in the past decade. The discovery of pulsar planets in 1991 (Wolszscan and Frail, 1992) was soon followed by the discovery of planets around main sequence stars in 1995 (Mayor and Queloz, 1995). At present, more than 155 extrasolar planets have been identified (see http://www.exoplanet.eu; also http://exoplanets.org). Most of these planets orbit main sequence stars, although one planet has been identified around a white dwarf (Sigurdsson et al., 2003). By far the majority of these planets have been detected by the radial velocity method (*e.g.,* Marcy and Butler, 1998), in which the back-and-forth reflex motion of the star is determined spectroscopically by measuring the Doppler shift of multiple spectral lines. This method is most sensitive to massive planets located in short-period orbits close to their parent stars. As time progresses, such planets are being found farther and farther away from their parent stars. Several Neptune-mass bodies (~15 Earth masses) close to their host stars have now been discovered (*e.g.,* Butler et al., 2004). The smallest planet detected by radial velocity is a ~7.5 Earth-mass object orbiting the M star GJ 876 (Rivera et al., 2005). An even smaller (~5.5 Earth-mass) planet has been reported recently from a gravitational microlensing survey (Beaulieu et al., 2006), although the mass of the planet (and lensing star) is only inferred statistically.

Interest is now beginning to shift to the next frontier—that of detecting and characterizing Earth-sized planets around other stars. Such planets are too small to be found around sun-like stars using the radial velocity method, as the velocity change induced by the planet's motion is well below the velocities of convective cells on the star's surface. Hence, a variety of other space-based astronomical techniques are being explored. NASA's *Kepler* mission, currently scheduled for launch in 2008, will attempt to find Earth-sized planets by looking for transits. *Kepler* will monitor ~100,000 fairly distant stars simultaneously for 5 years, looking for a periodic drop in light intensity of the order of 0.01 percent. ESA's *Corot* mission works on this same principle but is somewhat less ambitious. *Kepler* and *Corot* will measure the size distribution of low-mass planets. After *Kepler* and *Corot*, NASA's proposed *SIM* mission will attempt to find planets that are Earth-sized or slightly larger, by performing accurate, space-based astrometry. *SIM* should be able to look for planets that are 3-4 Earth masses around a substantial number of nearby stars and may be able to find 0.5 Earth-mass planets around the very closest stars. *SIM* will characterize the mass distribution of low-mass planets.

NASA's twin *Terrestrial Planet Finder* missions represent the next step beyond *Kepler* and *SIM* and will be capable of direct imaging. *TPF-C*, the topic of this document, is a visible/near-IR coronagraph that will search for Earth-sized planets by looking for starlight scattered from the planets' atmosphere and surface. The difficult part of this mission is observing a planet near its parent star, which is roughly 10^{10} times brighter at these wavelengths. This requires extremely efficient suppression of the star's own light. This document describes how this difficult feat may be accomplished. *TPF-I*, which is currently scheduled to fly roughly 5 years after *TPF-C*, is an interferometer that will operate in the thermal infrared. Such an instrument can observe the planet's own emitted radiation. *TPF-I* is currently envisioned as a set of four free-flying spacecraft, each with its own mirror. The beams from each mirror would be combined coherently at a fifth spacecraft to perform nulling interferometry. Again, the radiation from the star would be suppressed, allowing the much dimmer planet(s) to be seen around it.

An exciting new feature of both *TPF* missions compared to *Kepler* and *SIM* is the capability of performing spectroscopy. The light (or infrared radiation) from the observed planet will be broken down into different wavelength bins to form a spectrum. That spectrum should contain absorption bands that may provide information concerning the composition of the planet's atmosphere and the nature of the planet's surface. Of particular interest are features that indicate whether the planet might be habitable, or perhaps even inhabited by life. For example, both *TPF-C* and *TPF-I* should be able to look for H_2O absorption bands. Liquid water is essential to life as we know it, and so its presence in the gas phase is probably a prerequisite for planetary habitability. In addition, *TPF-C* is sensitive to O_2, while *TPF-I* is highly sensitive to its photochemical byproduct, O_3. Most of Earth's oxygen was produced by photosynthetic organisms, so the presence of O_2 or O_3 in a planet's atmosphere would be strongly suggestive of life. There are, of course, caveats that must be added to this statement, some of which are mentioned below. The important point, though, is that the two *TPF* missions, especially when considered together, may provide the first real data bearing on the existence of extraterrestrial life. Hence, these missions should be of great interest to astrobiologists, as well as astronomers and planetary scientists. It is exciting that telescope/spacecraft technology has advanced far enough to make such missions possible.

In addition to its primary mission of searching for, and characterizing, terrestrial planets, *TPF-C* should also be capable of advancing astronomical knowledge in several related areas. In particular, *TPF-C* will be useful for studying planetary system architectures (including giant planets) and for studying circumstellar and protoplanetary disks. *TPF-C* will also have capabilities that may be useful for studying non-planetary astrophysics. These auxiliary science areas are considered to be an integral part of the *TPF-C* mission, and each is accorded its own discussion in the document that follows.

1.2 Definition of Scientific Terms

Prior to discussing the scientific requirements of *TPF-C*, the scientific terms used herein must be precisely defined. Some of these terms are still under debate among scientists. The definitions used here are for the purposes of clearly specifying the scientific needs of *TPF-C*. They are not meant to be interpreted as a contribution to these debates, rather as a cogent set of terms from which the requirements can be accurately described. However, an attempt has been made to make these definitions fit with current understanding of the science as much as is possible.

1.2.1 Planet

A planet is an object that is gravitationally bound and supported from gravitational collapse by either electron degeneracy pressure or Coulomb pressure, that is in orbit about a star, and that, during its entire history, never sustains any nuclear fusion reactions in its core. Reliance on theoretical models indicates that such objects are less massive than approximately 13 times the mass of Jupiter (M_J) for objects with metallicities close to that of the Sun. Objects with masses between 13 and 75 M_J (known as brown dwarfs) fuse deuterium for a portion of their youth (Sudarsky et al., 2003, and references therein). Objects with masses above 75 M_J are known as stars. A lower mass limit to the class of objects called planets has not been convincingly determined.

1.2.2 Terrestrial Planet

A terrestrial planet is a planet which is primarily supported from gravitational collapse through Coulomb pressure, and which has a surface defined by the radial extent of the liquid or solid interior. Terrestrial planets are often referred to as "rocky planets." A gaseous atmos-

phere may exist above the surface, but this is not a defining feature of a terrestrial planet. Theory suggests that most terrestrial planets will have masses less than about 10 times Earth's mass ($M_{\oplus}$), as planets larger than this are likely to capture gas during accretion and develop into giant planets. Terrestrial planets that undergo final accretion after their protostellar nebula has dissipated may, however, achieve larger masses while still remaining "rocky."

1.2.3 Habitable Planet
A habitable planet is a terrestrial planet on whose surface liquid water can exist in steady state. This definition presumes that extraterrestrial life, like Earth life, requires liquid water for its existence. Both the liquid water, and any life that depends on it, must be at the planet's surface in order to be detected remotely. This, in turn, requires the existence of an atmosphere with a surface pressure substantially above the triple point pressure of water, 6.1 mbar, and a mean surface temperature somewhere between 0°C and 374°C (the critical point for water). Planets habitable by Earth-like life must have surface temperatures below ~120°C. For the purposes of the mission, the lower-mass limit for a habitable planet is set at 1/3 $M_{\oplus}$. Objects smaller than this are unlikely to hold onto their atmospheres effectively and are therefore lower priority targets for *TPF-C*.

Caveat: Some planets (or moons) that do not have liquid water at their surfaces may indeed be habitable, or even inhabited. Jupiter's moon Europa is widely believed to have an ocean of liquid water, or a water-ammonia mixture, beneath its icy surface, in which life could conceivably be present. However, if life is present on Europa, it is *not* detectable from Earth, and it would certainly not be detectable from a planet orbiting a distant star. Mars is another planet where subsurface life is possible. Indeed, measurements of CH_4 in Mars' atmosphere (Mumma et al., 2003; Formisano et al., 2004; Krasnopolsky and Owen, 2004) suggest to some researchers that life may be present. The quantities of gas detected, however, are extremely small, and are best detected at very high spectral resolutions (R $\cong$ 50,000 for the ground-based measurements) and sensitivities that are unlikely to be accessible to *TPF-C*. Remote detection of subsurface life on extrasolar planets is possible in theory, but it will not be considered here.

1.2.4 Habitable Zone and Continuously Habitable Zone
The habitable zone, or HZ, is the region around a star in which a planet may maintain liquid water on its surface. Its boundaries are defined empirically in Section 1.3.1.1.1, based on the observation that Venus appears to have lost its water some time ago and that Mars appears to have had surface water early in its history. **The continuously habitable zone, or CHZ, is the region that remains habitable over some finite period of time as a star ages.** All main sequence stars brighten with time, and so the HZ moves outward with time. For our own Solar System, the CHZ is usually defined over the entire solar lifetime, ~4.6 billion years (Hart, 1978).

Caveat: These definitions do *not* preclude the possibility that other planetary bodies (or moons) may support liquid water, and even life, beneath their surfaces. Such life is probably not detectable remotely, however, and thus is not something that can be searched for by *TPF*.

1.2.5 Potentially Habitable Planet
A potentially habitable planet is one whose orbit lies within the habitable zone. This includes planets that have high eccentricities, but whose semi-major axis is within the habitable zone. In this document, the habitable zone boundaries are defined generously, so as not to exclude any possibly

habitable planets. But this definition implies that some planets within the habitable zone may not actually be habitable.

1.2.6 Earth-like Planet
An Earth-like planet is a habitable planet of approximately one Earth mass.

1.2.7 Earth Twin/Solar System Twin
An Earth twin is a planet of exactly one Earth mass and one Earth radius with Earth's albedo and atmospheric composition. A Solar System twin is a system of 9 planets orbiting a G2V star, *i.e.*, a star like the Sun that is identical in every respect to our own Solar System.

1.2.8 Eta_Earth ($\eta_\oplus$)
(Eta_sub_Earth) **Eta_Earth is the fraction of stars that have at least one potentially habitable planet (PHP).** In other words, it is the fraction of stars that have at least one planet within their habitable zone. For this document, this is interpreted to mean the fraction of *observed* stars that have at least one PHP, as it is used to estimate an expectation value for the number of potentially habitable planets, N_{PHP}, that will be found throughout the duration of the mission.

1.2.9 Direct Detection
Direct detection is the detection of a planet by separating the light emitted or reflected by the surface or atmosphere of a planet from that of the star it orbits. The words "direct" and "directly," when used in reference to "detection," are specifically meant to distinguish between the *TPF-C* mission and the vast majority of work in exoplanetary science to date, which has relied on precise measurements of nearby stars to reveal the existence of planets. We also use direct detection to include *recording* as much information about the planet light as is technically feasible. More generally, direct detection refers to the ability to distinguish the light emergent from a particular celestial object from that of any other. In the case of *TPF-C*, the primary issue is that for every 10^{10} photons that arrive from a nearby star, only one is expected from an accompanying Earth-like planet. Detecting these few photons from the planet requires extraordinarily precise instrumentation.

1.2.10 Giant Planet
Giant planets are those with masses substantially greater than terrestrial planets but less than brown dwarfs, e.g., 0.03 M_J < M < 13 M_J (~10 $M_\oplus$ < M < ~4000 $M_\oplus$). Our Solar System retains two types of giant planets (Figure 1.2-1); other types are seen in extrasolar planetary systems. Jupiter and Saturn are *gas giants*, characterized by an extended thick atmosphere composed primarily of hydrogen, with bulk masses of M_J and 0.3 M_J respectively. Their interiors are thought to contain a substantial fraction of metallic hydrogen surrounding a rocky core. Their visible "surfaces" are usually defined to be the cloud-top level at a pressure of roughly 1 bar, typically ammonia clouds for Jupiter and Saturn. Giant planets younger or more massive than Jupiter will show bright water clouds instead of ammonia clouds. Giants that are even warmer (or young) will be cloud free. *Ice giants*, represented locally by Uranus and Neptune at 0.046 and 0.054 M_J, respectively, (14 and 17 $M_\oplus$) have hydrogen/helium envelopes like gas giants. However, their interiors contain a thick mantle of briny ices, likely water, that surround a rocky core. Their visible cloud-tops (the "surface") are composed of methane clouds. The term "*Hot Jupiter*" refers to a planet with mass comparable to or greater than Jupiter (but less than the deuterium-burning limit of ~13 M_J) that is located close to its primary star (*e.g.*, within 3 AU). similarly, a "*Hot Neptune*" will have very different spectral properties

than an ice giant in our solar system. Observing giant planets with a variety of temperatures will elucidate important processes in giant planet atmospheres and the evolution of these planets over time.
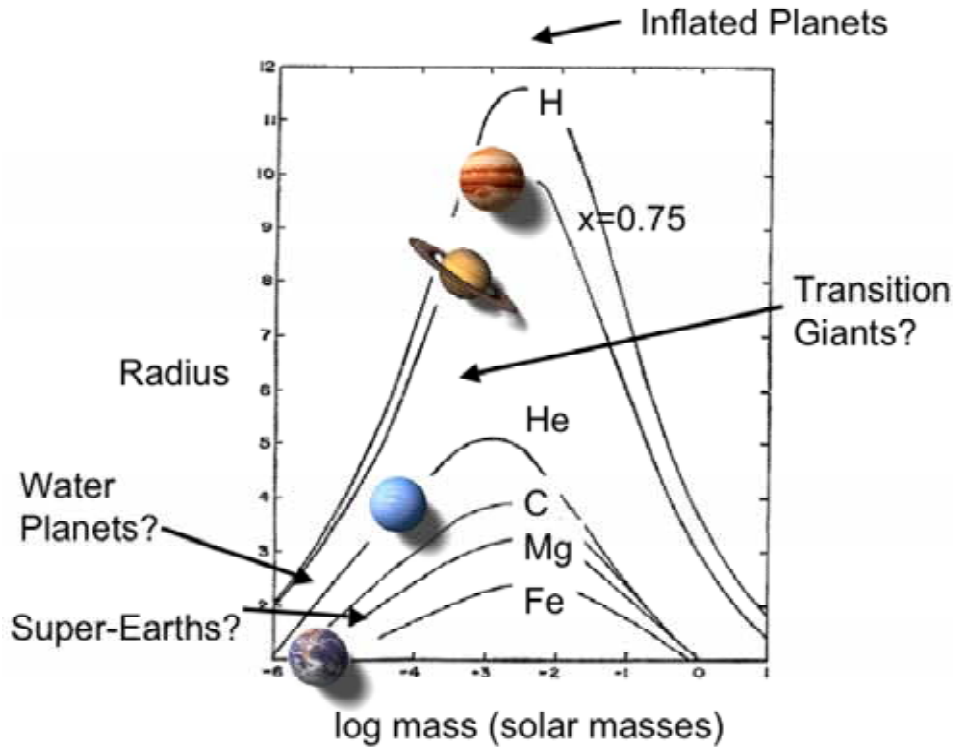
Figure 1.2-1. Planetary radius (in units of 10^4 km) as a function of planet mass for zero-temperature homogeneous spheres of various composition (Zapolsky & Salpeter 1969). The masses and radii of Jupiter, Saturn, Uranus, and Neptune are shown.

1.2.11 Planetary System Architecture
Planetary system architecture refers to the location and masses of the various components of a planetary system, including planets, small bodies, and dust. The presence and properties of giants in a planetary system alters the formation and dynamical evolution of all planets, including any terrestrial planets, residing around their common host star. A systematic determination of giant planet dynamical properties, including orbital eccentricity and inclination, would permit identification of locations of enhanced formation and islands of stability, not only of giant planets but also terrestrial planets in multiple planet systems.

1.2.12 Exozodiacal Dust
Exozodiacal dust is the extrasolar analog of zodiacal dust. Zodiacal dust is the Solar System cloud of 10-100 μm diameter silicate grains (*e.g.* Grun et al., 1985) produced by collisions among asteroids and by the outgassing of comets. This sparse disk of zodiacal dust is the most luminous component of the solar system after the sun. Zodiacal dust can be seen by the naked eye at a dark site as a triangle of light along the ecliptic plane.

1.2.13 The "Zodi" Unit
The unit "zodi" is defined to mean an exozodiacal cloud with the same surface density and scattering properties (*i.e.* analogous to) the solar system zodiacal cloud. The zodi is not a unit of surface brightness or flux because the surface brightness of an exozodiacal cloud changes de-

pending on the luminosity of the central star. For different numbers of zodi, we provide the corresponding surface brightness for different realizations (orientation, *etc.*) of exozodiacal clouds in Appendix 1. B, using ZODIPIC, an IDL code that evaluates the zodi for any given star and disk orientation.(Publicly available online at http://eud.gsfc.nasa.gov/Marc.Kuchner/home.html.).

1.2.14 Pericenter Shift

Pericenter shift refers to a disk asymmetry that occurs when the disk contains a planet on an eccentric orbit, and the orbits of the debris particles acquire a forced eccentricity in response to secular planetary perturbations. For example, the solar zodiacal cloud contains a pericenter shift of approximately 0.01 AU in response to Jupiter's eccentricity of 0.048. The offset scales as the eccentricity of the perturbing planet's orbit. When an asymmetric exozodiacal cloud with pericenter shift is imaged through a coronagraph, the coronagraph may accentuate the disk asymmetry, producing an image with an apparent peak near the inner working angle that can easily be as bright as an Earth-like planet. In order not to confuse a pericenter shift with an extrasolar Earth-like planet, *TPF-C* should be able to operate under the assumption that exozodiacal clouds commonly have 0.07 AU of pericenter shift, the amount the solar zodiacal cloud would have if Jupiter had an eccentricity of 0.35, the median for exoplanets.

1.2.15 Protoplanetary, Debris, and Exozodiacal Disks

Circumstellar disks are the host environments of planet formation, and signposts of asteroid and comet populations in mature planetary systems. In wavelength-integrated light, disks can be many orders of magnitude brighter than individual extrasolar planets. Disks are often classified into the following categories:

Young stellar object ("protoplanetary") disks are disks of gas and dust with radii of several hundred astronomical units, and masses of 0.001–0.01 M$_\odot$. They are often found around pre-main sequence stars. While the mass of these disks is mostly molecular hydrogen gas, their opacity is dominated by dust grains. They are highly optically thick in scattered light: $\tau \sim 10^2$–10^4. These disks have sufficient mass to form a solar system like our own, and are considered analogous to the early solar nebula. They are often referred to as protoplanetary disks even if the presence of a forming planet within the disk has not been established observationally. Their central objects are either T Tauri stars or Herbig Ae stars, the pre-main sequence analogs to solar-type and 2-3 M (sun stars respectively. The nearest significant young stellar object populations are located at distances of 120–140 pc; the host stars range in brightness from V= 6–16, and the disk angular radii range from 0.3-3.0 arcsec. Due to their high optical depths, these disks can be relatively bright in scattered light. Imaging at contrasts of $\sim 10^6$ would enable significant advances over results from *HST*, and should be straightforward for *TPF-C.*

Debris disks are dusty products of collisions between remnant planetesimals. One out of every seven main sequence stars possesses an infrared excess indicating the presence of circumstellar dust. Given that the timescales for removal of dust particles via radiation pressure and P-R drag are much less than these stellar ages, the dust particles cannot be residual material from the protoplanetary disk. Instead, ongoing dust production from asteroid collisions and cometary passages is required. Debris disks are highly tenuous and optically thin; the brightest example, β Pictoris, contains only a few lunar masses of dust. Little or no gas is found in debris disks, but studies of the gas component are nevertheless important to understanding the dust production and transport mechanisms. The dust in debris disks is usually quite cold, with > 90 % of such systems show-

ing detectable infrared excesses only at wavelengths longer than 30 microns. This corresponds to dust in the region 10 to 100 AU from the central star, analogous to the Kuiper Belt region of our own solar system. Perhaps two hundred debris disks are known from infrared photometry to date, but only 10 relatively high optical depth systems have resolved images at any wavelength. The host stars are located over the distance range 3–100 pc, the host star brightness ranges from V= 0–12, and the disk angular sizes range from ~0.3 to 150 arcsec.

Exozodiacal Dust Disks are tenuous disks of dust, analogous to our solar system's zodiacal dust cloud. Exozodiacal dust disks are interesting in their own right as signposts of planets and asteroids, and not just noise for terrestrial planet detection. See Sections 1.2.12 and 1.3.3.

1.2.16 Parallel Observations
Parallel observations are those that are made in parallel with planet-searching/characterization. Such observations include studies of exozodiacal dust clouds (under disk science) and deep-field studies of galaxies and quasars (under general astrophysics).

1.2.17 Pointed Observations
Pointed observations refer to science investigations that are carried out separately from planet-searching/characterization, looking at targets that are *not* included in the normal *TPF-C* target star list. Examples include observations of dust disks around very young stars and astrophysical observations of non-stellar objects.

1.3 Science Objectives
A list of *TPF-C* science objectives, stated in general terms, was given in the Executive Summary. These objectives are repeated and elaborated on in the subsections that follow. They are *not* meant to directly drive mission design. Specific science requirements and goals are given in Section 1.3.5.

1.3.1 Terrestrial Planet Science

1.3.1.1 Detecting Potentially Habitable Planets

> **Objective 1: To directly detect terrestrial planets that exist within the habitable zones around nearby stars or, alternatively, to show that they are not present**

Fulfilling Objective 1 is a primary goal of the *TPF-C* mission. Deciding how best to do this requires making assumptions about a number of different parameters. These include the location of the habitable zone around each star, the types of stars to be included in the search, and the size range of planets for which to look. The following three subsections present the information used to support values adopted in this SRD. The last subsection discusses the difficult question of how big the telescope needs to be in order to have a reasonable chance of finding a potentially habitable planet.

1.3.1.1.1 Habitable Zone Location and Width

<u>Summary</u>
In order to search for planets within the habitable zone (HZ), one needs to define the HZ around different star types. The HZ limits used in this SRD are 0.75 AU for the inner edge and 1.8 AU for the outer edge, scaled by the square root of stellar luminosity.

Discussion

These HZ boundaries are empirical limits based on observations of Venus and Mars. Venus' semi-major axis is 0.72 AU. Radar maps of Venus' surface suggest that liquid water has not been present there for at least the last 1 billion years (Solomon and Head, 1991). The Sun was ~8% dimmer back at that time, according to standard solar evolution models (*e.g.*, Gough, 1981). Thus, the solar flux at Venus' orbit then was equal to that at a distance of 0.72 AU $(1/0.92)^{1/2} \cong 0.75$ AU today. The outer edge of the HZ is based on the observation that Mars, which orbits at 1.52 AU, looks as if it may well have been habitable at or before 3.8 billion years ago (Pollack, 1979; Pollack et al., 1987). The Sun is thought to have been ~75 % as bright at that time. Hence, the solar flux hitting Mars back then was equivalent to that at a distance of 1.52 AU $(1/0.75)^{1/2} = 1.8$ AU.

The empirical HZ values adopted for this SRD can also be justified theoretically. The inner edge of the HZ is thought to be set by loss of surface water (Rasool and DeBergh, 1969; Ingersoll, 1969; Kasting, 1988). Photodissociation of stratospheric H_2O by stellar UV radiation, followed by escape of hydrogen to space, causes an ocean to be lost with a geologically short period of time—tens to hundreds of millions of years. The outer edge of the HZ is determined by condensation of CO_2. CO_2 is a greenhouse gas that keeps the planet warm enough for liquid water. If a planet is too far from its parent star, CO_2 begins to condense out of the gas phase into CO_2 ice and the temperature-stabilizing CO_2 feedback cycle (Walker et al., 1981) disappears.

Although 1-D climate models have been used to calculate the HZ boundaries (Kasting, 1988, 1991) they are incapable of accurately simulating the effects of clouds (H_2O or CO_2) on the planetary radiation budget and hence are not reliable. They do, however, serve to illustrate the importance of various climatic feedback processes. For example, the CO_2 weathering feedback is the reason why the HZ is now considered to be relatively wide (Kasting et al. 1993), rather than narrow (Hart, 1978, 1979). The CO_2 weathering feedback is a strong negative feedback in the inorganic carbon cycle, or carbonate-silicate cycle. CO_2 is produced by volcanism and is lost by weathering of silicate rocks on land, followed by deposition of carbonate sediments in the oceans. As a planet's surface temperature decreases, the silicate weathering slows down, and this allows CO_2–a major greenhouse gas—to accumulate in the planet's atmosphere. Planets near the outer edge of the HZ can thus compensate for the low incident stellar flux by developing a large greenhouse effect.

The 0.75 AU and 1.8 AU HZ boundaries apply to planets orbiting a Sun-like star. The Sun is a 4.5 billion-year-old G2V star with an effective temperature of ~5700 K. The HZ around more or less massive (*i.e.*, more or less luminous) stars are shifted by a factor of $(L/L_\odot)^{0.5}$. The approximate location of the HZ around different main sequence stars is illustrated in Figure 1.3-1. For illustration, the boundaries shown in the diagram are the zero-age-main-sequence (ZAMS) values, based on theoretical "runaway" and "maximum" greenhouse limits from Kasting et al. (1993). An additional complication is that the HZ moves outwards, at different rates for different types of stars, as the stars age. Also, see Kasting et al. (1993) for additional correction factors to this $(L/L_\odot)^{0.5}$ scaling for different star types, based on their effective temperatures. These correction factors can shift the HZ boundaries inward (outward) by up to 10 percent for stars that are hotter (cooler) than the Sun.
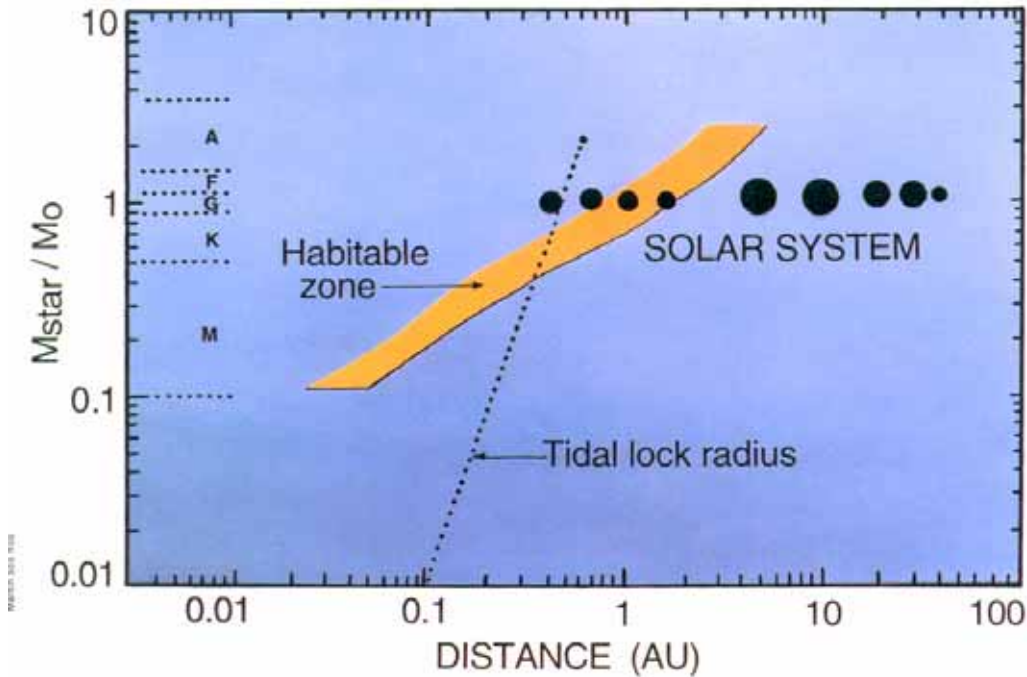
Figure 1.3-1. The instantaneous habitable zone around different stars at the time when they first entered the main sequence. The dotted curve shows the distance at which a planet's rotation would become locked within 4.5 Gyr. The nine planets in our own Solar System are shown as well. (Modified from Kasting et al. 1993).

1.3.1.1.2 Types of Stars to be Searched

<u>Summary</u>
Stars of type F, G and K are of greatest physical interest because they are expected to be the most suitable for finding Earth analogues, based on our solar-system-centric viewpoint of stellar lifetimes and radiation environments. Designed to be most capable of finding planets around these stars, *TPF-C* is not well-suited to surveying earlier (*i.e.*, more massive) or later (*i.e.*, less massive) star types.

<u>Discussion</u>
A *TPF-C* design to survey G-type stars specifies a contrast ratio and angular separation capability. This precludes massive bright stars or low-mass faint stars from being studied by *TPF-C*. Massive stars that are very bright, 'A' stars for example, have HZs that lie far away from the star. Because the massive stars are so luminous, the planet-star contrast ratio is exceedingly small (for a planet with an Earth-like albedo). So, even though the HZ angular separation for massive stars may be favorable for *TPF-C*, the planet-star contrast is too low. This precludes seeing Earth-sized planets at the inner edge of the HZ around stars earlier than about F0. For low-mass stars, M stars in particular, a different problem arises. Their HZs lie close to the star; hence, the contrast ratio of a habitable planet is favorable, but the angular separation of the planet from the star is typically very small. Only a few M stars may be accessible to *TPF-C*, given an inner working angle of roughly 60 mas. (A free-flying *TPF-I* with a variable baseline may be able to observe more such late-type stars.) See the *TPF-C* Design Reference Mission and/or http://sco.stsci.edu/*TPF*_top100/ for potential lists of stars accessible to *TPF-C*.

Stars of all types are of interest for planet finding, and indeed many arguments have been presented arguing for and against life on planets around F stars and M stars, for example in Turnbull (2005), Turnbull and Tarter (2003), Kasting et al. (1993), and Segura et al. (2003).

1.3.1.1.3 Terrestrial Planet Mass Distribution

<u>Summary</u>

The mass distribution of terrestrial planets is unknown. Therefore, the SRD (see Section 1.3.5) recommends simply assuming a delta function mass distribution at 1 $M_\oplus$ in designing the mission and in planning search strategies. The typical arguments for the terrestrial planet mass distribution are inconclusive.

<u>Discussion</u>

The inner Solar System contains two relatively large terrestrial planets (Earth at 1 $M_\oplus$ and Venus at 0.82 $M_\oplus$) and two small ones (Mars at 0.11 $M_\oplus$ and Mercury at 0.055 $M_\oplus$). Extrapolating this observed mass distribution reliably to other planetary systems is essentially impossible. One can also examine the radial velocity planet mass distribution. Radial velocity measurements of over 155 extrasolar giant planets suggest that the number of planets dN between mass M and $M+dM$ follows a power law distribution with $dN/dM \propto M^{-1.0}$ (Marcy et al., 2005). Here, $N(M)$ is the number of planets with mass $> M$. Integration of this power law from a smaller mass M_1 to a larger mass M_2 yields the result that the number of planets with masses in this range is proportional to $\log(M_2/M_1)$. If this were true for terrestrial planets as well, then there should be as many planets at 10 $M_\oplus$ (or 0.1 $M_\oplus$) as at 1 $M_\oplus$. In this case, *TPF-C* would find predominantly heavier planets because these would be the easiest to detect. There are, however, good reasons *not* to follow such an extrapolation. The giant planet mass distribution function is only good up to ~3 M_J. Above this range, the power law is closer to $dN/dM \propto M^{-2.0}$ (G. Marcy, private comm., 2005). In this regime, the number of planets between mass M_1 and M_2 is $\propto (1/M_1 - 1/M_2)$, implying that that there should be ten times as many planets at 1 $M_\oplus$ as at 10 $M_\oplus$—a completely different conclusion from the one just drawn. There are simply not enough observational data to construct a reliable terrestrial planet mass distribution.

The potential of a planet to hold onto its atmosphere and to support life clearly does depend on its mass; thus, it is still useful to speculate on the lower and upper mass limits for a planet to remain habitable. A reasonable lower limit on the mass of a habitable planet is ~1/3 $M_\oplus$. Planets much smaller than this are unlikely to be habitable, for two reasons. First, small planets have a good chance of losing their atmospheres over time. Mars, which has half Earth's radius, one fourth of Earth's surface area, and one ninth of Earth's mass, *does* seem to have lost most of its atmosphere over the course of its history, much of it by way of sputtering by solar wind particles (Kass and Yung, 1995; Jakosky and Phillips, 2001). Second, small planets like Mars cool off more quickly than do large planets, leaving them without sufficient internal energy to drive volcanism or plate tectonics. Earth system models show that volcanism and/or plate tectonics is essential to long-term climate stability because it provides a mechanism for recycling carbonate rocks back into gaseous CO_2 (Walker et al., 1981; Kasting, 1993). Earth itself would likely not have remained habitable for billions of years were it not for the recycling of CO_2 by plate tectonics. The lower limit on planetary size to maintain such activity for 4 billion years or more is not well known. Observationally, Mars appears to have lost most of its volcanism (and its initially warm climate) within the first 1 billion years of its

history (Pollack, 1979; Carr, 1989). Placing the lower limit for planetary habitability at ~3 Mars masses is a reasonable assumption.

The upper limit on terrestrial and habitable planets is undetermined. Conventional arguments state that a planet much larger than ~10 $M_\oplus$ should capture significant amounts of gas from its nebular disk followed by runaway growth into a giant planet (*e.g.*, Pollack et al., 1986). Alternatively, a planetary core that accretes gas after its nascent disk has dissipated, or forms in a hot region of the disk, can be predominantly rocky even up to 20 to 60 $M_\oplus$ (Rafikov, 2004). Planetary habitability is not necessarily much affected by large mass. Large planets would presumably have hotter interiors than does Earth and, hence, greater volcanic activity. As long as a planet is big enough to have volcanism, the basic factors affecting the evolution of its climate and atmosphere are expected to be more or less the same.

1.3.1.1.4 Planetary Albedo/Contrast

Summary
Detecting Earth-sized planets close to their parent stars requires that the *TPF-C* telescope be able to achieve high contrast. As discussed below, the required contrast ratio, *C*, is ~1.15×10^{-10} for an Earth-like planet orbiting a Sun-like star at quadrature (*i.e.*, half illuminated). For the inner and outer edge of the habitable zone, *C* is 1.78 times larger and 3.24 times smaller, respectively.

Discussion
If one assumes that a planet scatters light like a Lambertian sphere, *i.e.*, equally in all directions, then it should be dimmer than its parent star by a factor (Sobolev, 1975)

$$C(\alpha) = \frac{2}{3} A(r/a)^2 \left[\frac{\sin(\alpha) + (\pi - \alpha)\cos(\alpha)}{\pi} \right]$$

(1.1)

Here, *A* is the planet's Bond (bolometric) albedo, *r* is its radius, *a* is its orbital distance (assumed constant for simplicity), and α is the phase angle of the planet defined as the planet-star-observer angle. $C(\alpha)$ is wavelength-dependent, so technically *A* needs to be defined for the wavelength range of interest (the spherical albedo). At quadrature ($\alpha = \pi/2$), $C = (2/3)A(r/a)^2/\pi$. For an Earth-like planet orbiting a Sun-like star, $A \cong 0.3$ (Goody and Yung, 1989, p. 1; Goode et al., 2001), $r = 6371$ km, and $a = 1.5 \times 10^8$ km, so the contrast ratio *C* is ~1.15×10^{-10}. In reality, Earth is not a Lambertian scatterer, so this value is only approximate.

From Eq.(3.1), one can see that the contrast ratio will be better (worse) for planets that are bigger (smaller) than Earth. If one neglects the possible variation with mass in a planet's density, a minimum-mass potentially habitable planet of 1/3 $M_\oplus$ would have a contrast ratio that is worse than that of Earth by a factor of $(1/3)^{2/3} \cong 0.5$. A ten-$M_\oplus$ planet would have a contrast ratio $10^{2/3} \cong 4.6$ times higher than Earth. Contrast ratios at the outer edge of the HZ, 1.8 AU, are worse than 1-AU values by a factor of $1/(1.8)^2 \cong 0.3$.

1.3.1.1.5 Zodiacal and Exo-zodiacal Backgrounds

Summary
TPF-C must be able to achieve Objective 1 under the assumption that all exoplanetary systems have an unknown quantity of exozodiacal dust of up to 3 zodis with an unknown pericenter shift of up to 0.07 AU. *TPF-C* must also be designed to take into account the local zodiacal background—a relatively smooth background of 22–23 magnitudes per square arcsecond that varies slowly around the sky. The inclusion of exozodiacal dust is essential because the exozodi could complicate planet searching in two ways: First, it is potentially substantially brighter than the local zodiacal cloud. Second, it likely has structure, both radial and azimuthal, on the scale of the resolution of *TPF-C*.

Discussion
Although its optical depth is only $\sim 10^{-7}$, a patch of the solar zodiacal cloud only 0.3 AU across has roughly the same surface area as an Earth-sized planet. Our zodiacal cloud is comparable to a single 10–100 km diameter asteroid ground to dust, so it is easy to imagine that similar and even brighter clouds may be common in other planetary systems and that exozodiacal dust may often dominate the scattered light from the habitable zones of nearby stars. This challenge for *TPF* was discussed at length at a dedicated meeting at NASA Ames in 1997 (Backman et al., 1997); the results of that meeting inform this document.

Figure 1.3-2 shows simulated 0.5-μm images of the solar system as viewed by *TPF-C* from a distance of 10 pc. To show how the zodiacal cloud dominates the scattered light, the direct starlight has been completely removed, revealing only light scattered from the Earth and the solar zodiacal cloud. The left panel shows the scene with no masks or stops in place; the starlight is magically removed without these aids. This view reveals the central concentration of the zodiacal light. The right panel shows the same view with an eighth-order mask and matched Lyot stop in place. In this view, the central light from the dust is blocked, showing the Earth's light on the right side of the mask, forming an image comparable in brightness to the limb of the zodiacal cloud. Even when the image mask helps block the zodiacal light, this light still dominates the images.

Coronagraph schemes each provide different rejection of exozodiacal background (See, *e.g.*, Guyon, 2003). For example, coronagraph designs that block the pupil plane with pupil plane masks and Lyot stops are intrinsically more sensitive to diffuse sources, like dust clouds, compared to point sources, like planets. The planet/disk contrast decreases with the size of the final PSF; it is highest for the pupil-mapping scheme, and lowest for the apodized pupil.

As defined in this subsection, the zodi represents today's zodiacal cloud only. Measurements of He concentrations in sea floor sediments suggest that the concentration of dust in the solar system has varied over factor of ~5 during the last 100 million years, from roughly 0.4 to 2 zodis except for rare peaks tied to individual collisional cascades (Farley et al., 2001). These measurements are probably accurate to ~50%, based on differences in measurements from detectors located around the Earth. *TPF-C* must tolerate a 3-zodi background based on the range of dust fluxes identified in this study. Are exozodiacal clouds expected to be similar to the Solar System zodiacal cloud? The answer is "yes" for the following reasons: An exozodiacal cloud is expected to flow from a cloud of small bodies with a very different distribution than the small bodies in our solar system. A saving grace is that the secular decay in semimajor axis, *a*, due to Poynting-Robertson drag, *da/dt*, is roughly in-

versely proportional to the distance from the star (Wyatt & Whipple 1950); thus, continuity dictates that a steady state cloud that is not collisional approaches a uniform face-on optical depth interior to the source of the particles. Sometimes it makes sense to use an approximation for the zodi—for example, in an observing simulation limited by computer time. In this circumstance, it is common to use a 23 magnitude per square arcsecond uniform background for a solar type star. This is not recommended here, because the zodi brightness should scale with the star's brightness (*i.e.*, absolute magnitude). Using a constant zodi background will therefore confuse the target star choice. A second reason for not adopting a uniform zodi background is that the zodi brightness scales with disk inclination. A limitation to the zodi usage proposed here (Appendix 1.B) is that dust clouds that are >100 times denser than our zodiacal cloud may be collisionally depleted in their centers; hence, the utility of the solar-system analogy begins to fail at ~100 zodis. Therefore, in the range of 1–100 zodis we adopt as our model a cloud with uniform optical depth and infinite radial extent.
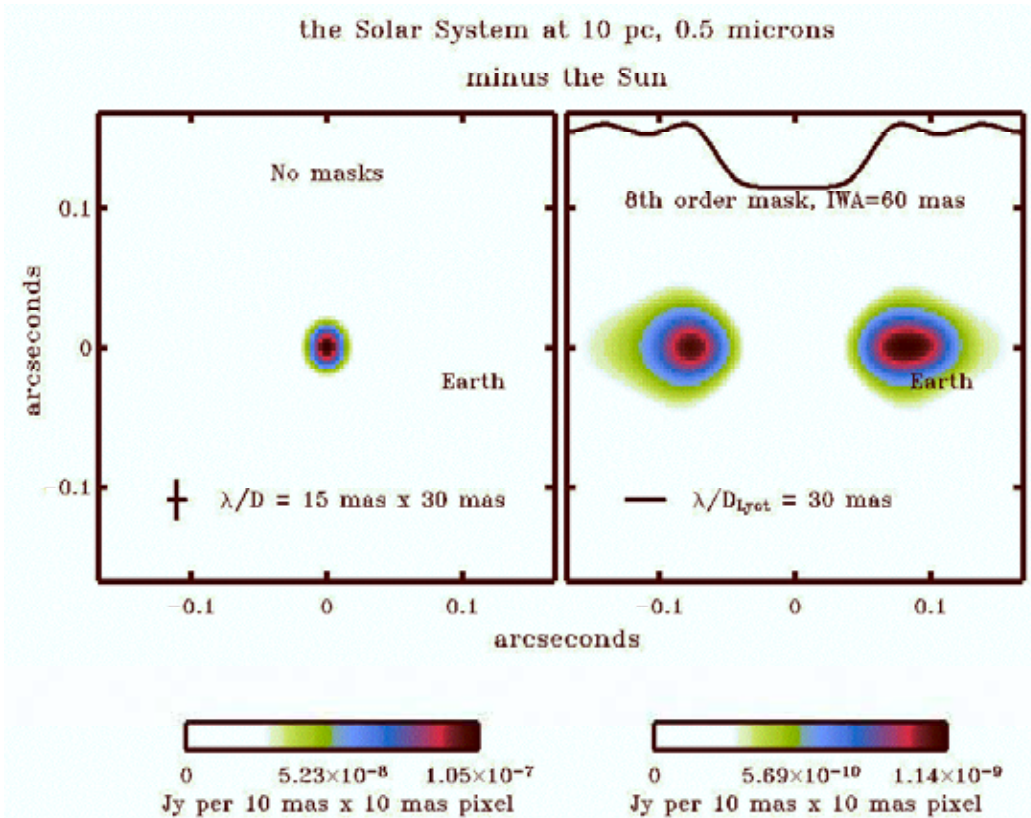
Figure 1.3-2. The solar system, viewed by *TPF-C* from 10 pc away, at λ=0.5 μm: (left) with no masks, but the direct starlight magically removed, and (right) with an eighth-order mask and matched Lyot stop. Zodiacal dust dominates the images.

The pericenter shift is important because a coronagraph may accentuate the disk asymmetry, producing an image with an apparent peak near the inner working angle that can easily be as bright as an exoearth. Although only one debris disk—the solar system—clearly shows resonant trapping of dust by a planet, several known debris disks (HR 4796, Fomalhaut, Vega) show large-scale asymmetries that may reflect secular perturbations from an extrasolar planet on an eccentric orbit. In an optically-thin disk, the main secular effect caused by a planet on an eccentric orbit is a translation in the center of light from the disk along the direction away from the pericenter of the planet's orbit, an effect called pericenter shift. When an exozodiacal cloud with pericenter shift is imaged through a corona-

graph the coronagraph may accentuate this asymmetry, producing an image with an apparent peak near the inner working angle that can easily be as bright as an exoearth. Fortunately, this translation and the resulting surface brightness peak are stationary on time scales of tens of thousands of years, so re-observation of a system and spectroscopic measurements should allow one to distinguish this dust cloud feature from a real orbiting planet.

the Solar System at 10 pc, 0.5 microns

minus the Sun and the Earth, with 0.1 AU pericenter shift
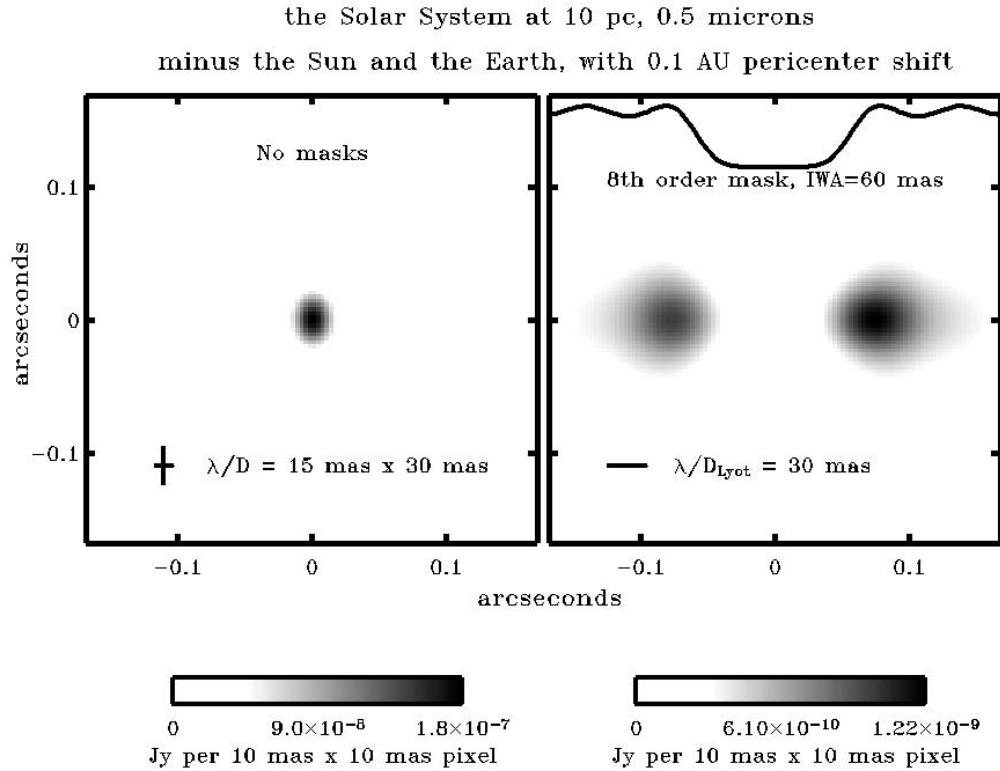
Figure 1.3-3. The effect of pericenter shift. The same system as in Figure 1.3-2, but with no Earth and with 0.1 AU of pericenter shift in the zodiacal cloud, creating a brightness asymmetry that mimics a terrestrial planet.

1.3.1.1.6 Number of Stars to Search

<u>Summary</u>

The number of stars *TPF-C* should search depends on $\eta_\oplus$, the assumed frequency of Earth-like planets, and the required completeness per star. Here $\eta_\oplus$ is defined as the fraction of observed stars that have at least one potentially habitable planet (see Section 1.2.8). Estimates for the value of $\eta_\oplus$ are highly uncertain because no terrestrial-mass planets around main sequence stars have been detected. Even though the true value of $\eta_\oplus$ is not yet known, one must assume something about its value in order to decide how many stars *TPF-C* should observe. Assuming $\eta_\oplus = 0.1$ is reasonable and conservative, based on the arguments below.

<u>Discussion</u>

The only empirical data that bear on the value of $\eta_\oplus$ come from ground-based planet searches, mostly from radial velocity (RV) data. According to these data, the fraction of single stars for which

planetary companions have already been found is ~0.07 (Marcy et al., 2005). The detected planets, ~155 total (as of 6/16/05), were mostly found using RV and are within 5 AU of their parent stars. The RV technique is clearly biased towards finding large planets that are close their parent stars and that have short orbital periods. Extrapolation of the RV data based on residual stellar motions (indicating companions for which only part of an orbit has been seen) suggests that ~12% of stars have giant planets within 20 AU (*ibid.*). The difference between these two fractions (0.12−0.07 = 0.05) represents the fraction of stars that have giant planets between 5 AU and 20 AU and, hence, may resemble our Solar System. If these planetary systems do indeed contain terrestrial planets, then a conservative estimate for $\eta_\oplus$ is 0.05. More realistically, many of the observed stars that do not exhibit measurable residual motions may still have sub-Jupiter-sized giant planets at large distances, along with terrestrial planets at small distances. So, the real value of $\eta_\oplus$ could be as high as 0.8–0.9. The only stars that almost certainly *do not* have habitable planets are those for which a giant planet has been found orbiting near or inside the HZ.

If planets are distributed randomly around nearby stars, a conservative estimate of the expectation value for the number of potentially habitable planets that will be found is $N_{PHP} = \eta_\oplus N_{stars}$, where N_{stars} is the number of stars searched. (N_{PHP} could be greater than this if some stars have more than one potentially habitable planet.) This estimate assumes a 100% complete search of each star's entire habitable zone. A minimal requirement for *TPF-C* is that the expectation value for the number of potentially habitable planets found should be greater than one. If one stipulates that N_{PHP} should be 3, then N_{stars} would need to be ~30. For a search that was 90% complete, N_{stars} would need to be $30/0.9 \cong 33$ in order to have an expectation value of 3 potentially habitable planets found.

A star sample size of ~30 would also provide a strong upper bound on $\eta_\oplus$ should planets not be found. If a 100% complete search of 30 stars revealed no planets, the odds that $\eta_\oplus \geq 0.1$ would be $0.9^{30} \cong 0.04$. Hence, one could say with >95% certainty that $\eta_\oplus \leq 0.1$. This does *not* imply that the mission should only search for planets around the closest 30 stars. Exactly the same expectation value for N_{PHP} and nearly the same upper limit on $\eta_\oplus$ could be derived by surveying half the habitable zone around 60 stars. The actual mission should be designed to search for planets as efficiently as possible by targeting stars for which the chances of finding potentially habitable planets are the highest.

Maximizing the probability of finding potentially habitable planets is a sensible way to optimize the *TPF-C* mission; however, it should not be the only consideration. In practice, any such optimization process will entail making assumptions about planetary orbital distances, eccentricities, albedos, phase functions, and most importantly planetary size distributions. None of these factors can be accurately known in advance of the mission; hence, no search strategy can be truly "optimal". Given this constraint, it makes sense to also ensure that *TPF-C* will be able to find potentially habitable planets in systems with which we are familiar, *i.e.*, in our own Solar System. It would be a grave mistake, for example, to design a system that was capable of finding 10-$M_\oplus$ planets, but was incapable of finding Earth. After all, there may be no terrestrial planets larger than Earth. So, regardless of the desire to maximize the number of potentially habitable planets located, *TPF-C* must also be capable of finding terrestrial planets like the ones in our own Solar System.

1.3.1.2 Characterizing Planetary Orbits

> **Objective 2: To measure orbital parameters for any terrestrial planets that are discovered**

1.3.1.2.1 Determination of Planetary Orbits

<u>Summary</u>
Determination of planetary orbits is an integral part of identifying potentially habitable planets. Indeed, one cannot know for sure whether a planet resides in the habitable zone of its parent star without having at least a crude determination of its orbit. A more distant planet, viewed from a position somewhat behind the star, may appear to be close to it based on a single observation. Hence, multiple observations of each planet-harboring star will be required. The number of visits needed in order to determine a planet's orbit depends on the measurement error, which is something that is not yet known at this stage of mission planning.

<u>Discussion</u>
Estimating the planetary orbit is important for at least three reasons: (1) The planetary distance from the star regulates the planetary temperature and therefore determines habitability. (2) The dynamical structure of a planetary system, which comprises the size, shape, and alignment of the orbits, can be interpreted in terms of the formative and evolutionary history of the system. (3) Predicting the future observability of a planet, which is critical for efficiently scheduling *TPF-C*, demands an estimate of the orbit.

The theory of the photometric orbit is the union of the theory of the Keplerian revolution with the theory of planetary photometry:

$$\Delta mag = -2.5 \, \log \frac{A_{\text{eff}} \Phi(\beta)}{\pi r^2} \qquad (1)$$

where Δmag is the ratio of the planetary flux to the stellar flux, expressed as a stellar magnitude; A_{eff} is the effective area, defined as the area of the planetary disk times the geometric albedo; $\Phi(\beta)$ is the phase function; and r is the distance between the planet and star. Therefore, aside from the phase function, a solution for the photometric orbit comprises seven parameters, six dynamical and one photometric. The dynamical parameters are (1) semimajor axis, (2) eccentricity, (3-5) three Euler angles to orient the orbit in space, and (6) the mean anomaly at some specific time. The photometric parameter is (7) A_{eff}.

For Earth-like planets, the constant factor in Kepler's Third Law, relating the orbital period and the semimajor axis, involves only the stellar mass, which can be estimated from the spectral type of the star.

Logically, the unknown phase function introduces additional parameters, which future analysis of actual data may require for good fits. For now, however, a reasonable first step in the analysis phase of the *TPF-C* project is to assume the Lambertian phase function in both the preparation of Monte Carlo planets and in the analysis of datasets based on computer "observations" of those planets.

This assumption effectively removes phase-functional parameters from consideration in the orbital solution, with little or no compromise to the validity of the analysis of the requirement for estimating the orbit. (The practical implications of assuming the Lambertian phase function could be explored by using alternative phase functions to prepare the Monte Carlo planets, while retaining the Lambertian phase function in the orbital solutions.)

Solving for the photometric orbit from a direct-imaging data set is a new research problem. Each data point is a seven-vector comprising the two-dimensional position relative to the star and the uncertainties (x, δx, y, δy), the relative brightness and its uncertainty (Δmag, $\delta\Delta mag$), and the time (t). A solution of the photometric orbit is a minimum of χ_r^2 in the seven-dimensional space of the theoretical parameters, where the reduced χ^2 statistic is defined as:

$$\chi_r^2 \equiv \frac{\sum_{k=1}^{N}\left[\left(\frac{X(t_k)-x_k}{\delta x_k}\right)^2 + \left(\frac{Y(t_k)-y_k}{\delta y_k}\right)^2 + \left(\frac{\Delta MAG(t_k)-\Delta mag_k}{\delta\Delta mag_k}\right)^2\right]}{N-7} \qquad (2)$$

,

where N is the number of data points. A *unique* solution is a *global* minimum of χ_r^2.

Three measurements are sufficient for an orbital solution, which may or may not be useful. It is precisely this question that must be addressed by Monte Carlo studies: how many data points, of what quality, are needed to obtain a useful orbital solution for a given planet (or a faction of possible planets) detected for a given *TPF-C* target star. Meanwhile, before such an analysis has been completed, it is still possible to make some basic statements about the situation:

1. Using the technique of "Monte Carlo projection" introduced by Brown (2004, *ApJ* 610:1079–1092), it is possible to obtain probabilistic predictions of future detectability even when the data set does not support an accurate orbital solution. This technique may be helpful recovering planets based on observations at the first epoch of detectability, which will never cover a complete orbit.

2. Monte Carlo projection can also be used to determine the probability that a given data set is compatible with a habitable-zone orbit, even when the data set does not support an accurate orbital solution.

3. As illustrated in Figure 1.3-4, observational access to the photometric orbit is limited. A proper analysis may find that the inner working angle, limiting sensitivity, and astrometric accuracy of *TPF-C* must be improved to enable a useful orbital solution with sufficient probability.

4. Assuming photon-limited astrometry, and specifying that the coordinates x and y lie in the directions of the long and short dimensions of the elliptical primary mirror, respectively,

$$\delta x = 0.5\frac{FWHM_{thin}}{SNR}d \text{ and } \delta y = 0.5\frac{FWHM_{fat}}{SNR}d$$

where SNR is the signal-to-noise ratio, d is the stellar distance, and $FWHM$ is the full width at half maximum of the point-spread function. Thus, astrometric accuracy can be improved by both nar-

rowing the point-spread function—by increasing the mirror size or reducing or eliminating a Lyot pupil mask, for example—or by achieving high SNR, by longer integration times.
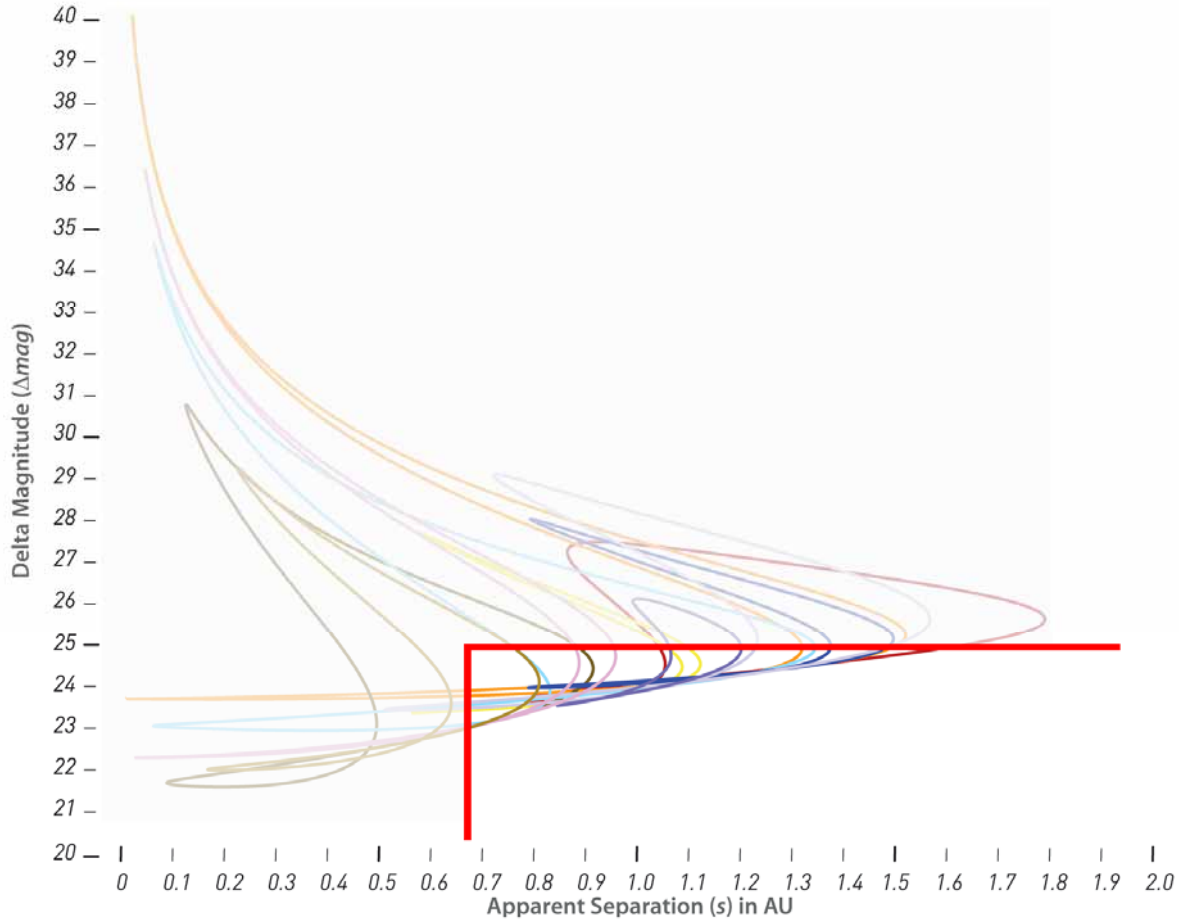
Figure 1.3-4. Limited access to the photoastrometric orbit for the purposes of determining the orbit and predicting future observability. The curves depict the variations in separation and delta magnitude over one orbital period for ten randomly selected habitable-zone planets around a Sun-like star. Each curve is suppressed where the planet is not detectable, which is for separations smaller than the inner working distance (vertical red line) and for delta magnitudes greater than the limiting sensitivity (horizontal red line). (This plot assumes a limiting delta magnitude of 25, and a value of the product of the distance to the star and the angular size of the central field obscuration equal to 0.68 AU.) For exposures of the same depth as the searching observations, only the unsuppressed portions of the curves can be detected and contribute data points for the orbital solution and estimations of future observability.

1.3.1.2.2 Orbital Phase Space

Summary
In order to model *TPF-C*'s detection potential it is necessary to make assumptions about orbital eccentricities and semi-major axes. Uniform distributions of eccentricities < 0.1 and uniform spacing of the logarithm of the semi-major axis are adopted for this SRD.

Discussion
A reasonable assumption is that most planets reside in planetary systems. There is little or no reason to base *TPF* search strategies on the orbital characteristics of observed extrasolar giant planets, many of which are highly eccentric, as this distribution is heavily biased by selection effects.

A better basis for estimation of eccentricities is provided by the two most massive terrestrial planets, Venus and Earth. Located in or near the habitable zone in our own Solar System, both planets have eccentricities < 0.1, and they retain these low eccentricities over time scales comparable to the lifetime of the solar system (Laskar, 1994). Mars also has an eccentricity < 0.1, but its value may occasionally increase to ~0.2 as a consequence of gravitational perturbations by Jupiter and the other planets (*ibid.*). However, Mars is smaller than the lower mass limit adopted here (0.3 $M_\oplus$) for a habitable planet. The SRD adopts the reasonable assumption that potentially habitable planets have eccentricities < 0.1.

Planetary semi-major axes are consistent with geometric spacing in our own Solar System and in systems with multiple giant exoplanets (Kuchner, 2004). The reason for this is likely related to considerations of dynamical stability. Planets tend to space themselves geometrically in orbital distance (*e.g.*, Gladman, 1993), meaning that the ratio of orbital periods of adjacent planets is comparable. For example, for the solar system planets this ratio is between 1.6 and 2.5 (neglecting only the pair Mars-Jupiter). The stability requirement can also be given in terms of orbital spacing. A given system is stable if the planets are spaced by more than a given number of Hill radii, where $R_{HILL} = a (M/3M_*)^{1/3}$ (Chambers et al., 1996). Here, a represents a planet's orbital distance, M is the planet's mass, and M_* is the stellar mass. If planetary spacing, da, depends on R_{HILL}, which in turn scales linearly with a, then da/a is constant (or at least independent of a), implying logarithmic (or geometric) spacing.

1.3.1.3 Characterizing Planets by Their Color

> **Objective 3: To distinguish among planets, and between planets and other objects, through measurements of planet color**

Summary
Measurements of planet brightness in several broad wavelength bands, at a spectral resolution of roughly 4, are useful to estimate a planet's nature. The ratio of these values to the star's intrinsic brightness in the same bands provides information about the wavelength dependence of the planet's albedo. With observations in at least 3 such bands, the planet's color can be determined and compared with other planets.

Discussion

Once the existence of a planet has been established, a zeroth-order estimate of its nature can be obtained from its semi-major axis and its brightness in the detection wavelength band. The planet brightness can be expressed as a planet-star contrast or "delta-magnitude" with respect to its parent star. The absolute planet brightness is derived from the *TPF-C* measured planet-star contrast together with a ground-based stellar brightness measurement. One can make a zeroth-order classification of the planet as a gas giant or terrestrial planet, based purely on its intrinsic brightness. At a given orbital radius, a gas giant planet should be brighter simply because it is bigger.

To get a better estimate of the planet's nature, the next step will be to measure its brightness in several broad wavelength bands, at a resolution of roughly 4. Assuming observations in at least 3 such bands, the planet can be placed on a color-color diagram. Filters that match particular absorption bands, such as methane, would provide an even finer level of characterization.

Figure 1.3-5 illustrates the utility of color. The planets in our Solar System cluster in distinct areas of the diagram, according to their types. The rocky planets with little or no atmosphere (Mercury, Moon, Mars) cluster together in the "red-red" corner of the diagram, and the most methane-rich gas giants (Uranus, Neptune) cluster on the opposite "blue-blue" corner of the diagram. In between these extremes, the less methane-rich gas giants (Jupiter, Saturn) and Titan cluster. Finally, Earth and Venus each occupy distinct positions, owing to their flat spectra with a blue up-turn and down-turn, respectively. One may anticipate that extrasolar planets exhibiting varied surface and atmospheric composition, geologic histories, and cloud types will populate other regions of such a diagram.
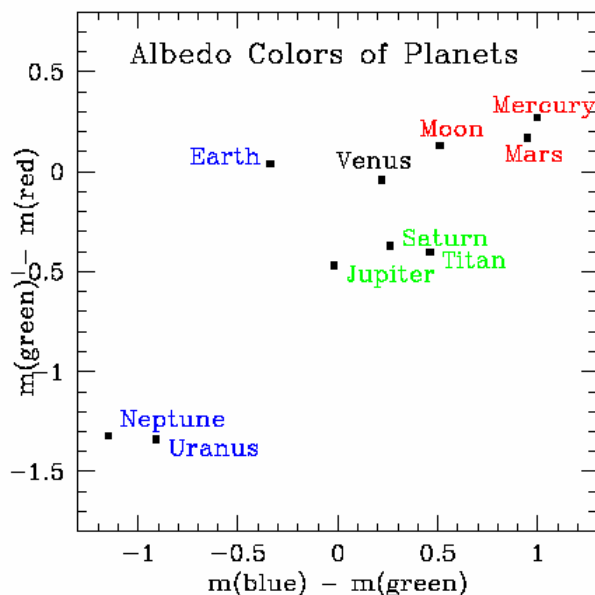
Figure 1.3-5. Color-color diagram for Solar System objects. (Courtesy of W. Traub)

Great care must be taken when interpreting color, however, because multiple physical processes might produce similar colors. A Venus with different particle size clouds, for example, might have a similar color to an object like Earth's moon with somewhat different fractions of maria and highlands terrain. Experience gained from higher resolution spectral characterization of the most acces-

sible planets will ultimately determine the utility of color for reliably characterizing planets. Certainly color will be useful for recognizing new classes of objects and for setting priorities for planning observations. In the most favorable case, if solar system trends are found to generally hold, color might be indicative of albedo, and hence allow one to estimate planetary radius and mass for objects below the *SIM* detection threshold.

1.3.1.4 Characterizing Planets by Spectroscopy

> **Objective 4: To characterize at least some terrestrial planets spectroscopically, searching for absorption caused by O_2, O_3, H_2O, and possibly CO_2 and CH_4. It would also be highly desirable to measure Rayleigh scattering and photosynthetic pigments. Such information may provide evidence of habitability and even of life itself.**

1.3.1.4.1 Spectral Range

<u>Summary</u>
TPF-C is designed as a planet characterization mission, as well as a planet detection mission. For stars not too different from the Sun, planet detection is accomplished most easily at wavelengths in or just beyond the visible, 0.5-0.8 μm, where the photon flux is highest and where silicon-based CCDs are most sensitive. Given sufficient spectral resolution ($R \equiv \lambda/\Delta\lambda > 70$), this wavelength range would permit the detection of O_2, H_2O, and possibly O_3 on a planet like present Earth (DesMarais et al., 2002; Figs. 1 and 2). Extended wavelength coverage to 1.1 microns, or even 1.7 microns, would be desirable.

<u>Discussion</u>
The strongest O_2 band is the A band at 0.76 μm. O_2 is considered an excellent biomarker gas, at least for planets orbiting within the liquid water HZ (Owen, 1980; Sagan et al., 1993). Possible "false positives" for life, *i.e.*, mechanisms for producing high abiotic O_2 concentrations, have been identified for planets orbiting outside the HZ (Kasting, 1997; DesMarais et al., 2002). Specifically, runaway greenhouse planets like early Venus or frozen planets somewhat larger than Mars might build up high atmospheric O_2 concentrations abiotically. However, knowledge of the planet's orbit, combined with other spectroscopic indicators, could be used to decide whether the presence of O_2 is evidence for life. Models of phase-dependent terrestrial planet spectra currently under development suggest that there may be optimal phases at which to observe specific spectral features (*e.g.*, O_3; V. Meadows, in preparation).

Although data over a spectral range of 0.5–0.8 microns would provide useful information about a planet like the modern Earth, being confined to this wavelength region would greatly limit the ability of *TPF-C* to characterize other types of terrestrial planets. For example, Venus and Mars are both relatively featureless at visible wavelengths but show well-defined absorption features in the near-infrared (a). In particular, CO_2 has bands at 1.05, 1.2, and 1.6 μm that should be detectable at a spectral resolution R = 70, especially for planets with dense CO_2 atmospheres (b). Identifying CO_2 in a planet's atmosphere would provide strong confirmation that it was a terrestrial (rocky) planet. Giant planets lack appreciable CO_2 because equilibrium chemistry generally favors CH_4 in their cool, reducing observable atmospheres, and CO at depth.
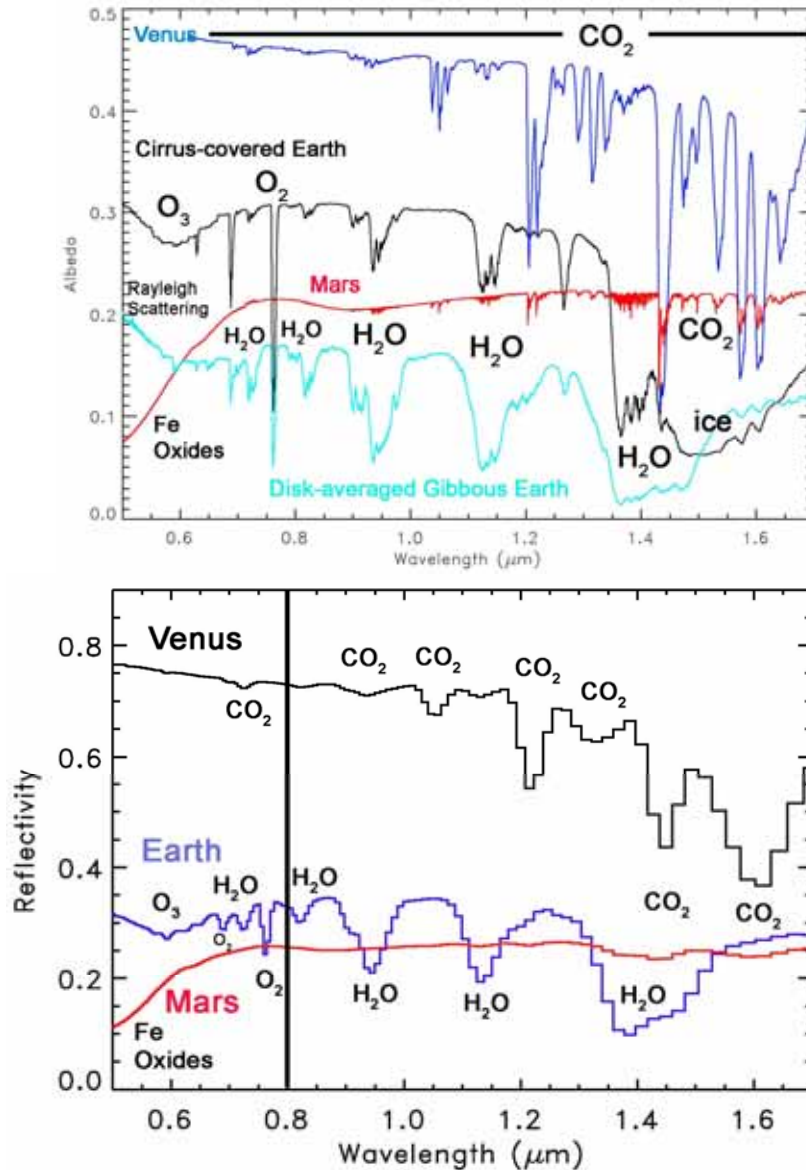
Figure 1.3-6. Spectra of Venus, Earth, and Mars. a) Full-resolution synthetic disk-averaged albedo spectra (from Meadows, 2006). Synthetic Earth spectra are shown for both uniform high cirrus cloud cover, and as a fit to Earthshine observations of the gibbous Earth. The Venus spectrum was approximated to a disk average and has been multiplied by 0.6 to fit the plot. The Mars and Earth spectra are disk-averages of 3-D spatially- and spectrally-resolved Virtual Planetary Laboratory models of the Earth and Mars (Tinetti et al., 2005, 2006). For the observed Earth, which was ocean-dominated with relatively little cloud cover, the Rayleigh scattering (0.45-0.6 µm) is pronounced, but the ozone is less apparent. The ozone absorption is much more pronounced for the Earth with cloud cover, increasing the difficulty of identifying the Rayleigh scattering component. b) Degraded albedo spectra (R = 70) of the Venus, Earth (gibbous phase), and Mars spectra shown in panel 'a'

Extended wavelength coverage would also be useful in characterizing a planet like the early Earth. Geologists are fairly certain that O_2 and O_3 were virtually absent from Earth's atmosphere prior to ~2.3 billion years ago, despite the fact that life had originated by 3.5 billion years ago or earlier (Holland, 1994; Farquhar et al., 2000). Hence, a *TPF*-type mission launched by aliens from some extrasolar planet at some arbitrary time during the last 4.5 billion years would stand a good chance of missing the fact that Earth was inhabited, if that mission searched only in the visible. A mission that searched out to ~1.1 μm, however, would likely have picked up the signal of CH_4 at 1.0 μm (Figure 1.3-6a,b). (CH_4 has absorption bands at even shorter wavelengths, but these are weaker and would be difficult to distinguish from overlapping H_2O bands.) Computer models of an anoxic Archean Earth (2.5-3.8 billion years ago) predict that the atmosphere may have contained as much as 0.1-1 percent CH_4, most of which was produced by biological activity (Pavlov et al., 2000, 2001; Catling et al., 2001; Kharecha et al., 2005). Seeing such a signature would not necessarily prove that life was present, as CH_4 can also be produced abiotically by such processes as serpentinization of ultramafic rocks (Berndt et al., 1996; Kelley et al., 2001; Kasting and Catling, 2003). However, even if CH_4 is not a reliable bioindicator, seeing it in a planet's atmosphere would provide an indication of atmospheric redox state and would likely promote further observation to determine whether the signal was indeed biological in origin.

It may be possible, around some stars at least, to look even further into the near infrared. A mission that was capable of taking spectra out to 1.7 μm would be capable of looking for the signal of CO_2 at 1.6 μm. This might be useful in characterizing certain early-Earth type planets, as the shorter wavelength CO_2 bands may be unobservable because of their weaker band strengths and/or overlap with H_2O and CH_4 bands (a). Although the 1.6-μm CO_2 band is not observable at R=70 on a planet like modern Earth (b), it might well be observable on planets farther out in the HZs of their parent stars. As discussed earlier (Section 1.3.1.1.1), such planets are expected to build up dense (0.1–10 bar) CO_2 atmospheres as a consequence of the negative feedback provided by the carbonate-silicate cycle. This information would be particularly useful for planets on which CH_4 was also detected, as CH_4 is often considered as being characteristic of giant planets.

1.3.1.4.2 Spectral Resolution

<u>Summary</u>
A high enough spectral resolution is needed to resolve absorption features of interest to *TPF-C*. A minimum spectral resolution of 70 over the entire *TPF-C* bandpass is required. This minimum number is set by the O_2 feature in Earth's spectrum, as well as to enable *TPF-C* to search for absorption bands of unspecified gases or surface minerals.

<u>Discussion</u>
The reflectivity spectrum of the Earth, for many different abundances of its main detectable atmospheric constituents, was studied by Des Marais et al (2002). In that paper the appearance of spectral bands of H_2O, CO_2, O_3, CH_4, N_2O, and O_2 was calculated. The effect of clouds on these spectra was also estimated. In particular, the location and full-width at half-maximum of each major spectral band was tabulated, along with the strength of each band as a function of atmospheric mixing ratio. From this tabulation, one can obtain first-order estimates of the width and depth of each spectral band, for any value of mixing ratio, all assuming an Earth-like atmosphere. See 1.4.1 for a reproduction of the table.
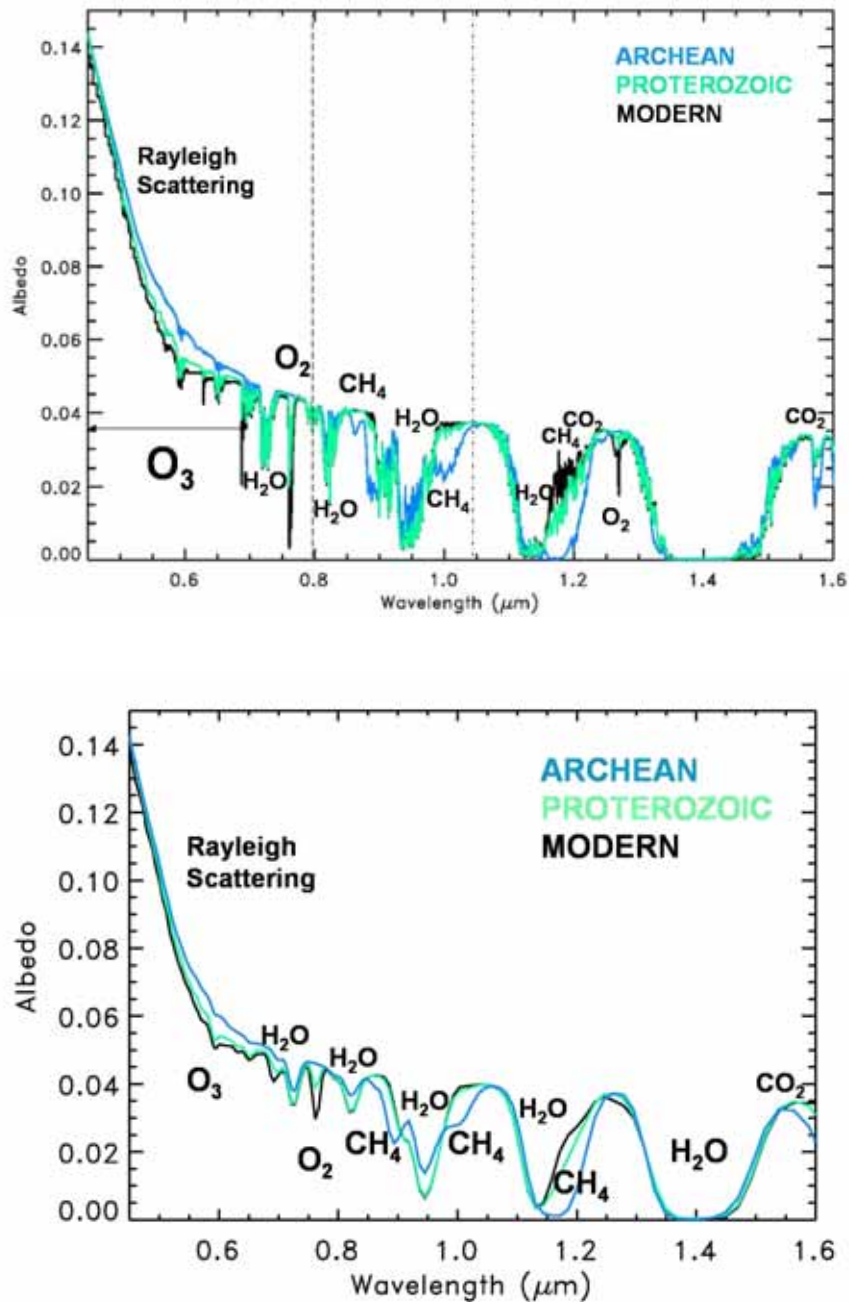
Figure 1.3-7. a) Synthetic spectra of hypothetical Earth atmospheres at various times during the planet's history (from Meadows 2006). Modern—335 ppmv CO$_2$, 1.6 ppmv CH$_4$; Proterozoic (1.5 Gyr ago)—335 ppmv CO$_2$, 100 ppmv CH$_4$; Archean (3.0 Gyr ago)—2000 ppmv CO$_2$, 1000 ppmv CH$_4$. Model atmospheres and spectra calculated using techniques described in detail in Segura et al. (2003). b) Same spectra, degraded to R = 70 resolution.

Other factors besides spectral resolution are important for *TPF-C* to be able to identify spectral features. In addition to knowing the width and wavelength location of a given feature, one also needs to specify the likely depth of each feature, or alternatively the depth that one would like to be able to detect. Here one needs to consider the likely effect of clouds, which will make spectral lines less

deep that in a clear atmosphere, and also the effects of mixing ratios and pressure, both of which are roughly equally important for saturated lines.

For each case posed, the count rate in each detection channel can be estimated and the integration times determined. One will need to make sure that reference continuum levels can be measured in a given spectrum. One should also consider the effects of spectral confusion, if the noise is too great or the spectral resolution not adequate to distinguish features, or if we encounter a planet with a completely unexpected spectral signature.

1.3.2 Giant Planets and Planetary System Architecture Science

The central science of the "Giant Planets and Planetary System Architecture" theme is: *to understand the range of planets and planetary architectures in other systems.* The architecture of each stellar system reflects the planetary formation process and influences the evolution of all the planets within the system, including those within the habitable zone. An understanding of system architecture leads to a more complete understanding of how an evolving planetary system becomes habitable.

The presence, distribution, and atmospheric composition of giant planets within a planetary system provide information on the formation of that system. Giant planet atmospheres may provide the most accessible record of the abundance and distribution of key volatile species—particularly water—in remote systems. Furthermore, the planets in a planetary system are coupled like masses on a string; the presence of a planet (especially a giant planet) on an eccentric orbit anywhere in a system can cause an otherwise habitable-looking terrestrial planet to have eccentricity variations that would take it far from the habitable zone every 10,000 to 100,000 years. Thus, a terrestrial planet discovered by *TPF-C* can be most thoroughly assessed for habitability if the other planets in the planetary system are identified and characterized.

From a planetary architecture perspective, the properties of a planet that are of greatest interest are: mass, radius, effective temperature, orbit, and atmospheric composition. Mass and radius provide information on bulk composition. Effective temperature traces both evolutionary history and atmospheric energy balance; understanding the latter requires knowledge of the planet's orbital parameters. Atmospheric composition yields clues to the origin and evolution of the planet. In our Solar System, the non-noble gas atmospheric composition of solar system giants (Figure 1.3-8) provides a fingerprint of early planetary formation processes, a starting point for discussions of the origin and volatile enrichment of giant planet atmospheres. By comparing atmospheric composition as a function of mass and orbital distance among different stellar systems, an entirely new framework for understanding the origin of giant planets can be constructed. In turn, the chemical and dynamical environment of any terrestrial planets in the habitable zone will be elucidated.

Giant planets influence the position and spacing of the terrestrial planets, as well as the material available to build them, by regulating the transport of volatiles within a planetary system. Interactions of small, organic-rich planetesimals with migrating giant planets are thought to play a significant role in delivering comets and perhaps asteroids into the inner solar system, and thus in establishing the prebiotic inventories of planetary objects, including Earth (e.g. Pierazzo & Chyba, 1999). The most volatile-rich meteorites, carbonaceous chondrites, are known to contain several types of amino acids; comets appear to contain up to ten times more organics than carbonaceous chondrites.

Objects larger than few kilometers in diameter are the most important contributors of extraterrestrial material to Earth (Anders, 1989). In the past, their usefulness in delivering complex organic molecules to a planetary surface was thought to be weakened by the extreme thermodynamic conditions occurring during an impact event. However, theoretical and laboratory studies have recently suggested that non-negligible fractions of complex organics can survive the shock events associated with large impacts, and secondary organics have been synthesized in strong shock events in the laboratory (Peterson et al., 1997; Blank et al. 2001). The atmospheric compositions of the detected giant planets yield clues to the magnitude of the bombardment flux in the inner stellar system of *TPF-C* target stars. Determination of the orbital state (semimajor axis, eccentricity, and orbital plane) of extrasolar giant planets could also have significant implications for the habitability of terrestrial planets with that system.
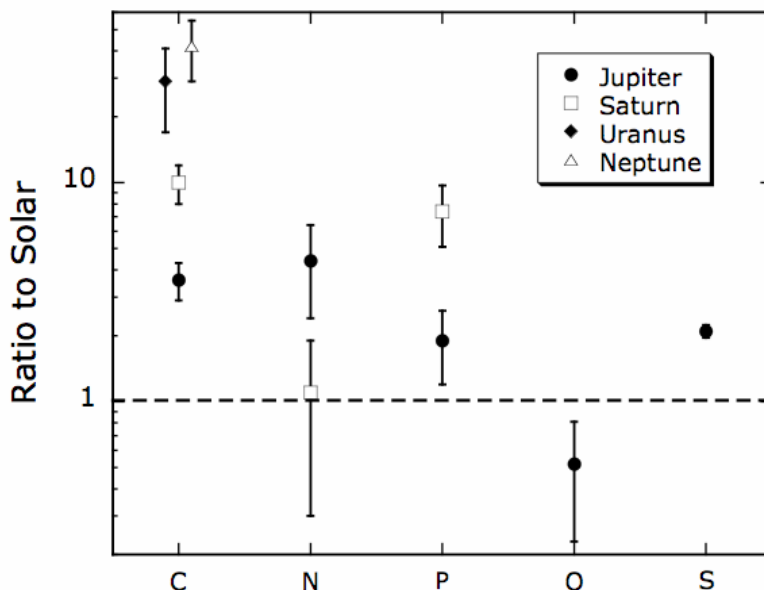
Figure 1.3-8. Compositional variation of giant planets in our Solar System. The measured atmospheric composition of solar system giant planets (neglecting the noble gases), expressed as a ratio to solar abundance (Lodders 2003), provides a fingerprint of the giant planet formation process. For example, the near-uniform enrichment of volatiles in Jupiter's atmosphere has been interpreted (Owen *et al.* 1999) as evidence that planetesimals bombarded the atmosphere over time (*e.g.*, Atreya *et al.* 2003). Such planetesimals could also have delivered volatiles to the Solar System's habitable zone.

Finally, giant planets that formed in or migrated into the habitable zone, though not themselves habitable, may have moons. Thus, giants in the HZ may offer a habitable abode even while they disrupt the formation of a terrestrial planet. similarly, if a water-rich world like the ice giant Neptune resided at 3 AU (as is seen elsewhere), would it be habitable? By studying ice giants and how they are placed in other systems, a different definition of "habitable environment" might emerge.

High-precision radial velocity methods on the ground, and *SIM* in space, may measure or place useful limits on the mass and orbital parameters for most massive planets detectable by *TPF-C*. Nevertheless, *TPF-C* working alone-or in synergy with other spacecraft-will be able to place limits on the radii, albedos, and effective temperatures of detected planets and, in particular, probe their atmos-

pheric composition. Only by characterizing all of these aspects of detected giants will *TPF-C* be able to address issues such as those raised above.

1.3.2.1 Detecting Giant Planets and Solar System Twins

> **Objective 5: To directly detect giant planets of Jupiter's size and albedo at a minimum of 5 AU around solar type stars, and determine orbits for such giant planets when possible, given the finite lifetime of the *TPF-C* mission**

Summary

In our Solar System—the only known habitable planetary system to date—Jupiter was the primary mass driver for planet formation and evolution. The presence of a Jupiter-like planet is therefore important to understanding terrestrial planet formation and the origin of the exozodiacal dust. Jupiter's (mass-scaled) location at 5 $(M_\star/M_\odot)^2$ AU thus sets an absolute lower boundary for the outer working angle (OWA) of the telescope. An outer working angle of 10 $(M_\star/M_\odot)^{1/2}$ AU for giant planet detection is desired to permit an assessment of systems with architectures similar to our Solar System (*e.g.*, to detect Saturn-like planets).
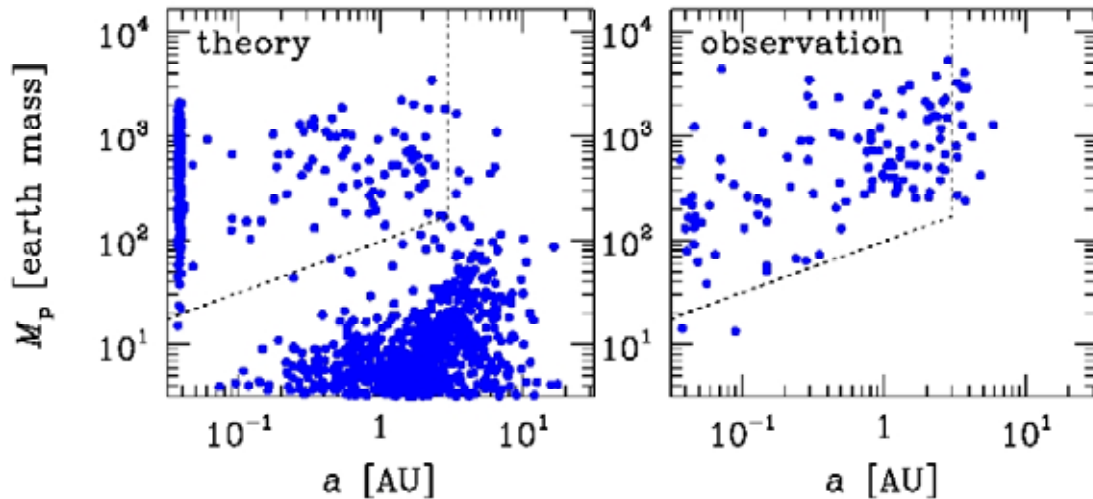
Figure 1.3-9. Model evolutionary scenarios compared with observed extrasolar planets. By comparing architectures of other stellar systems with theory, new insights can be gained into the planetary formation process. *TPF-C* should have the capability of detecting a Jupiter twin out to an Outer Working Angle of 10 AU in systems harboring an Earth twin (diagram courtesy D. Lin).

Discussion

Conventional sequential-formation scenarios for planets also call for a larger OWA than that required to study terrestrial planets in the HZ. In such theories formation of solid cores with several $M_\oplus$ is followed by the accretion of gas. A critical demarcation point in these scenarios is the location where the Keplerian velocity of planetesimals around the host star is a substantial fraction ($\sim 1/3$) of the escape velocity from the surface of a few-$M_\oplus$ core. For ice giant formation in our Solar System, this demarcation point apparently delineated an outer boundary at around 10 AU, and simulations also limit the ice-giant formation domain to be of order 10 $(M_\star/M_\odot)^{1/2}$ AU, independent of host star metallicity and disk-depletion time scales (Figure 1.3-9). Other factors (*e.g.*, planetary migration, planetesimal scattering, internal dynamical instability, external stellar perturbation) influence the

outer boundary, but only at a fractional level. Thus, for planetary systems like our own, it is desirable to set the upper limit for the outer working angle to this criterion of 10 $(M_\star/M_\odot)^{1/2}$ AU.

1.3.2.1.1 Direct Detection of Giant Planets

<u>Summary</u>
Giant planets are interesting in their own right, so the *TPF-C* camera filter sets should include search filters optimized for detecting and characterizing giant planets. The *TPF-C* capability for giant planets is important because for many primary stars *TPF-C* could be the major facility for finding giant planets with semi-major axes at 5 to 10 AU, or giant planets substantially less massive than Jupiter.

<u>Discussion</u>
TPF-C giant planet detection space is complementary to ground-based planet searches, even though many giant planets visible to *TPF-C* will already have been detected by other means. For example, early-type stars and giant planets substantially less massive than Jupiter at 5 to 10 AU from their star are outside of the current radial velocity (RV) survey planet detection range. RV detections also require long observational baselines at radii greater than 5 AU, although some massive planets may show at least linear acceleration trends before *TPF-C* launches. Ground-based extreme AO (Gemini, VLTI) may also detect Jupiters at 20 AU (Figure 1.3-10). But challenges increase for ExAO as orbital distances decrease (see Section 1.3.4 for further discussion about ground-based capabilities).
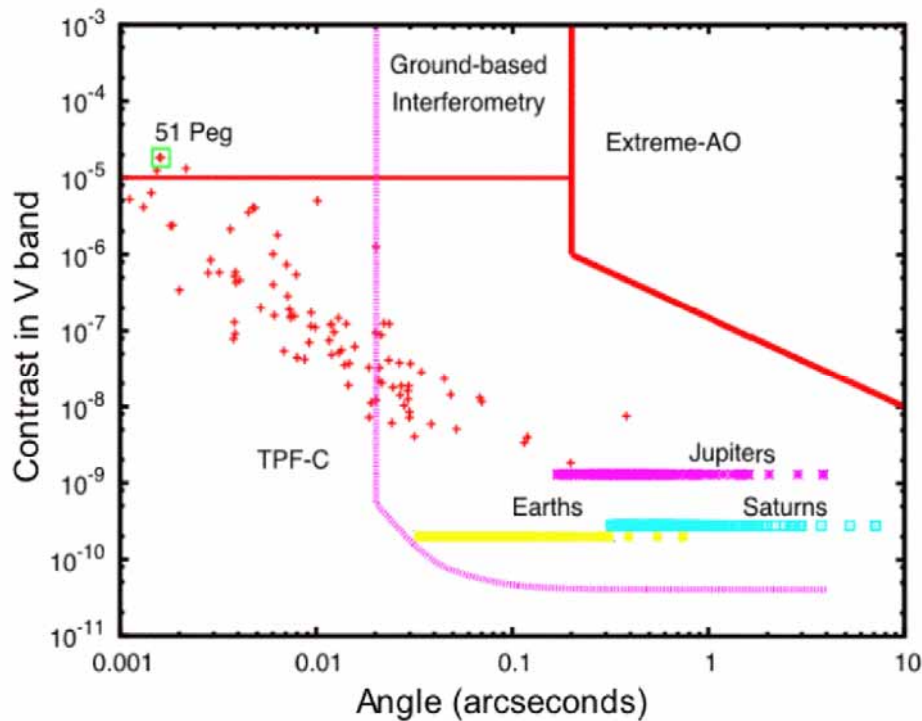
Figure 1.3-10. Parameter space uniquely accessible to *TPF-C*. The purple curve shows the expected contrast of *TPF-C* as a function of angular separation from a target star. Crosses indicate known precise-Doppler planets. The red lines indicate the parameter space potentially accessible from the ground via interferometry and extreme AO on existing telescopes.

TPF-C giant planet detection space will be complementary to *SIM*. Because of their large astrometric signal, giants in large orbits will be readily detected by *SIM* even though the observational baseline will be much less than an orbital period. For stars at greater than 6 pc distance, a Neptune-mass planet at 10 AU could escape *SIM* detection and yet, depending on its composition (and thus radius and albedo), still be detectable by *TPF-C*. Also, should *TPF-C* survey a set of stars at greater distances in order to bring the 5–10 AU region within the OWA, this extended set of stars would likely not have been surveyed by *SIM*; this would also be true should *TPF-C* survey young, more distant stars. Furthermore, some *TPF-C* survey targets will not be in the *SIM* sample.

1.3.2.1.2 Giant Planet Orbit Determination

Summary

The orbits of giant planets must be determined in order to know their eccentricities and semi-major axes. These parameters are important for understanding the giant planets' gravitational perturbations on the planetary system. The semi-major axis prescribes the incident radiation on the planet, which is key for interpreting giant planet colors and spectra. Orbital properties are needed to understand multiple planet systems and interactions.

Orbit determination is a highly nonlinear problem that will need to be supplemented by any information available from radial velocity and from *SIM* astrometry. (Note that *TPF-C* is aided greatly by the maximum *SIM* time baseline, so launch of *SIM* 5-10 years before *TPF-C* would be ideal.) In general, the distant giant planets detected by *TPF-C* will make significantly less than a complete orbit during the lifetime of *TPF-C*; hence, the accuracy of the giant planet orbit determination will be a direct function of astrometric accuracy of *TPF-C*. Orbital degeneracies may remain even after the *TPF-C* nominal mission. Astrometric measurements of giant planet positions should be a high priority in an extended mission.

Discussion

In general, astrometric accuracy is approximately equal to the PSF width divided by the signal-to-noise of the point source. All giant-planet orbital determinations will ultimately be limited by finite astrometric accuracy; thus, *TPF-C* must achieve a high level of astrometric accuracy. This requirement includes, but is not limited to, any effects from an uncertain position of the center star, any field distortions, and any pixel size uncertainties.

Combining the decade-long astrometric data from *SIM* and *TPF-C* with accurate (m/s) radial velocity surveys over a similar time span, the masses of gas giants can be determined with sufficient accuracy to infer their mass-period distribution. This distribution provides vital information on the onset, rate, and termination of planetesimal coagulation and gas accretion. According to current conventional theoretical models, gas giants can form interior to the snow line only in relatively massive disks. But around disks with modest masses, gas giants can form rapidly near the snow line and migrate inward during their active accretion phase. Gas-giant growth is terminated by the formation of gaps, and giant migration may eventually lead to the observed logarithmic semi-major axis distribution. The early emergence of the gas giants also promotes the accumulation of planetesimals, the emergence of critical-mass cores, and the formation of additional gas giants just beyond the outer edge of the gap.

Many stars with known planets bear signs of additional planets. The determination of the multiplicity, masses, semi-major axes and dynamical properties of gas giants in multiple-planet systems can provide valuable constrains on (1) the planet-formation efficiency and time scale, and (2) the origin of planetary dynamical diversity, such as their semi-major axis and eccentricity distributions.

It will be particularly fruitful to search for gas or ice giants around stars with relatively short-period planets. The kinematic distribution of such systems (semi-major axes, eccentricities, and inclinations) can be used to isolate the dominant processes which lead to planetary dynamical diversity. Ideally, three astrometric points are sufficient to determine the 6 parameters that define a planetary orbit (assuming the mass of the central star is known). In the realistic limit of finite astrometric accuracy, meaningful constraints on the planet orbit are only obtained when the planet is seen at a number of positions widely spaced compared to the astrometric accuracy over a time significant compared to the orbital period.

1.3.2.1.3 Studies of Known Giant Planets: Orbits, Radii, and Masses

<u>Summary</u>
Many extrasolar giant planets discovered by ground-based radial velocity surveys or by *SIM* will be accessible to *TPF-C* (Figure 1.3-10). Ideally, *TPF-C* should study many of these planets for orbital properties and to constrain their radii. The planet radius can be determined for moderate-mass, old giant planets by using *TPF-C* and *TPF-I* data. A planet's radius is key for extracting many of its properties, including albedo and thermal emission. Together with mass (as determined by radial velocity surveys or by *SIM*), knowledge of the planet's radius yields insight into bulk planetary composition, providing new data for planetary origins studies. A measured radius is equally important for recognizing new kinds of planets such as super Earths and ocean planets (e.g., Kuchner 2003; see Figure 1.3-2). Some fraction of *TPF-C* time should be devoted to targeting known giant and intermediate-mass planets at favorable positions in their orbits to facilitate determinations of mass (with *SIM*) and radius (with *TPF-I*).

<u>Discussion</u>
TPF-C can help to determine orbits or masses for known radial velocity planets. For the radial velocity planets, for which only M sin(i) is known, *TPF-C* orbit determinations will provide the inclination and thus the actual planet mass. *SIM* will determine the masses and orbits of many of these planets. However, *TPF-C* detection of planets measured by *SIM* breaks degeneracies in the *SIM* astrometry, and thus allows lower and/or more accurate masses to be determined.

TPF-C can be used to estimate planet radius. Visible-light-only measurements of planet flux from *TPF-C* give the product of planetary albedo and area. Model-based estimates of the albedo (perhaps informed by the observed phase function for very bright planets) will allow some limits to be placed on the planetary radius. Mid-infrared measurements of planet thermal emission from *TPF-I* will constrain the combination of planetary temperature and area. Since the planet's atmospheric temperature depends upon the absorbed incident radiation and any internal luminosity, a combination of the visible and mid-IR measurements allows the planetary radius and albedo to, in principle, be derived if the internal luminosity is known or is small.

Radius is important because giant planets are born hot with large radii, and they contract and cool as they age (*e.g.*, Baraffe et al. 2003; Burrows et al. 2003). An accurate radius provides a window into a

planet's gross composition, evolutionary history, and the presence of any large unaccounted-for interior energy source. The well-studied extrasolar giant planet HD209458b, for which the radius has been determined from transit data, provides an example. The derived value of 1.42 Jupiter radii (Cody and Sasselov 2002) indicates that the planet is composed predominantly of H and He. Yet theoretical evolutionary calculations without an added interior energy source disagree with the observed radius by 20–30%.

For some giant planets, however, radius will be challenging to extract since an internal luminosity must be assumed. For young or massive planets the internal heat flux dominates the atmospheric energy budget over absorbed incident radiation. For example, nearly half of Jupiter's current thermal emission is intrinsic luminosity. As a planet ages, the contribution of the incident flux becomes relatively more important, with intrinsic luminosity paying a lesser role. As main sequence stellar (and hence planet) ages are typically not known to high accuracy, and as the planet mass will not be perfectly known, model-based estimates of the internal luminosity will in some cases be uncertain to 50% or more. Furthermore, internal processes (such as He differentiation, as seen on Saturn) can substantially affect the internal luminosity. Thus, radii derived by the combination of *TPF-C* and *TPF-I* for massive or young giant planets will generally have an appreciable (up to 30% (Marley et al. 2006)) uncertainty and have limited utility for constraining bulk planetary composition. For planets older or less massive than Jupiter, the radius uncertainty will be dominated by photometric errors rather than internal luminosity, and is thus expected to be relatively small, and hence useful.

1.3.2.2 Colors of Giant Planets

> **Objective 6: To obtain photometry for the majority of detected giant planets, to an accuracy of 10% in at least three broad spectral bands, and in additional bands for the brightest or well-placed giants**

Summary
As discussed in Section 1.3.1.3, colors can provide some information about giant planets. Colors are especially sensitive to clouds, as clouds control the amount of scattering in the red, and hence determine the continuum brightness. Colors may be particularly useful for distinguishing ice giants that are very dark in the red due to strong methane absorption (Neptune/Uranus) from gas giants have much higher red flux (Jupiter/Saturn). As discussed in Section 1.3.1.3, the limitations of the color observations are mitigated by spectroscopic observations. The accuracy limit is required to allow meaningful comparisons to TPF-I data, enabling the determination of albedo and radius.

1.3.2.3 Spectroscopy of Giant Planets

> **Objective 7: To characterize some detected giant planets spectroscopically, searching for the absorption features of CH_4 and H_2O**

Summary
TPF-C offers a unique opportunity to spectroscopically characterize a wide variety of planets, including those with no solar system analogs in terms of size and mass. Twenty-five of the known precise-Doppler planets are within reach of *TPF-C* spectroscopy, providing a ready-made target list for spectroscopy even before any new planets are discovered.

Discussion

Low-resolution spectra can elucidate the structures and compositions of extrasolar planet atmospheres, even for planets without measured masses or radii. Model spectra for generic planets of a variety of masses and ages have been computed at a range of wavelengths (*e.g.*, Marley et al. 1999; Burrows et al. 2003; Burrows et al. 2004). Low-resolution spectroscopy can provide a first estimates of planetary size, surface gravity, and temperature by detecting molecular species (*e.g.*, signatures of H_2O, CH_4, alkali metals, and Rayleigh scattering). Giant planet spectra are highly sensitive to clouds (Marley et al. 1999). Metallicity and photochemistry also play a role in determining spectral shape. Different spectroscopic features are present at different temperatures; for example, the hottest planets will likely show alkali metals, cooler planets will contain H_2O vapor features, while on planets as cold as Jupiter almost all water has condensed into clouds, leaving CH_4 and NH_3. Measurements of atmospheric composition as a function of orbital radius (obtainable with low resolution spectra, at least for methane and water) can elucidate the radial variation of composition, and hence degree of volatile enrichment.

As an illustration, Figure 1.3-11 shows optical spectra of Solar System giants with their prominent methane absorption lines. Even the low resolution expected of *TPF-C* permits discrimination between gas giants (Jupiter, Saturn) and the colder ice giants (Uranus, Neptune). Thus, clouds indicate the first-order temperature structure of a planet's atmosphere. The strong CH_4 bands present on all four solar system giants are likely to be weaker on terrestrial planets, where those species have been photodissociated, and their H escaped to space.
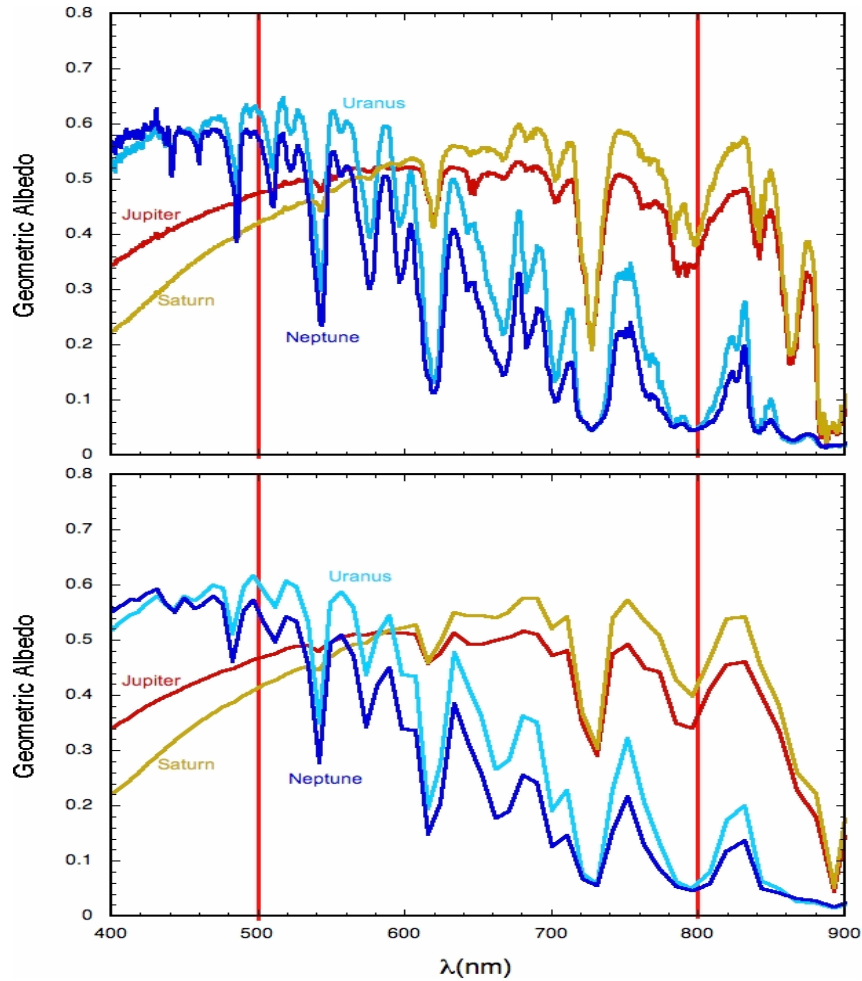
Figure 1.3-11. Spectra of the local giant planets.
Top: Ground-based spectra adapted from Karkoschka (1994). Bottom: Same spectra degraded to the minimum spectral resolution of 70. The difference between ice giants (blue) and gas giants can be easily discerned, as can the dominant methane absorption features at 619, 727, 790, and 890 nm. However, R=70 resolution results in significant loss of structure that is diagnostic of detailed atmospheric chemistry.

However, sometimes physical parameters (including the presence and composition of clouds, the mixing ratios of the atomic and molecular species, and atmospheric structure) can be degenerate at visible wavelengths. Modest extension of the wavelength range to beyond the 0.889-μm methane band would be extremely useful for interpreting the spectra of colder planets. Optimal coverage for more massive planets would be greatly enhanced by pushing the wavelength coverage out to 1.7 μm (Figure 1.3-12).
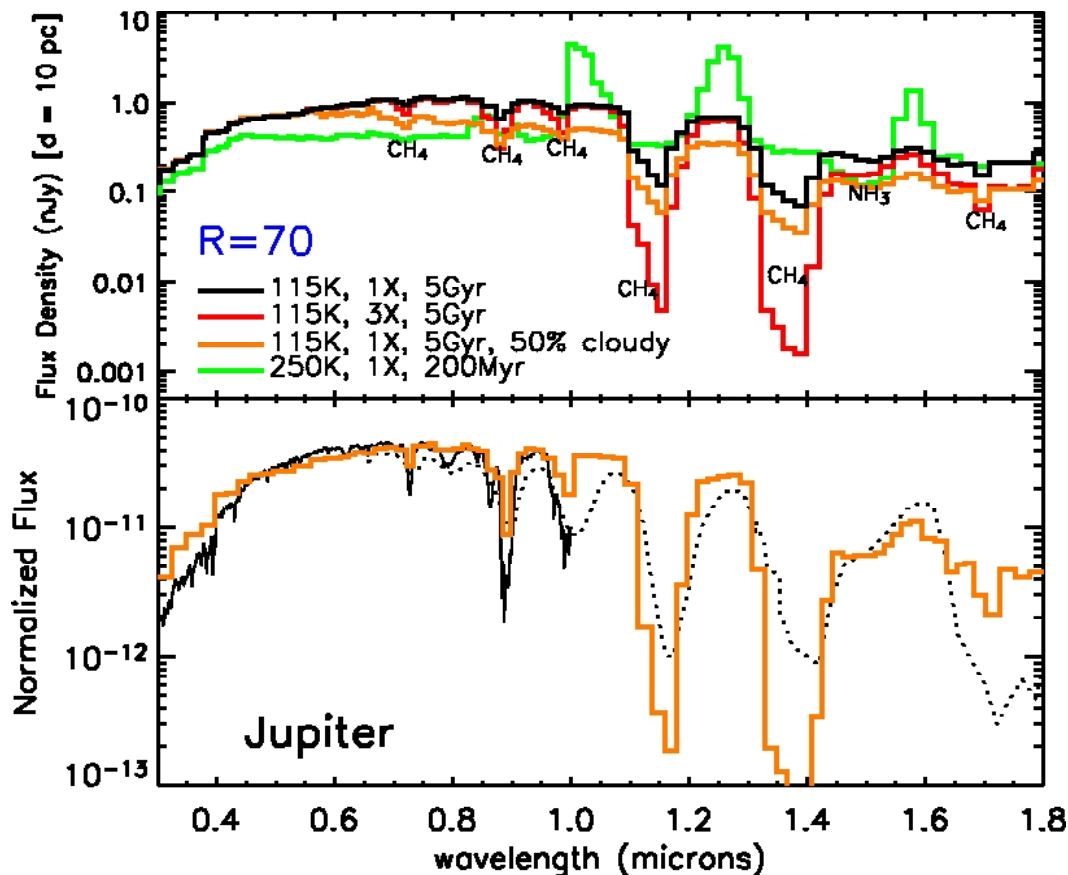
Figure 1.3-12. Model Spectra of Giant Planets.

Figure 1.3-12 demonstrates the advantages of pushing beyond 1 μm for planet characterization. Top: Four giant planet models are shown, each at 5 AU and with Jupiter's mass. At Jupiter's age, wavelengths longward of 1 μm provide the best discriminator between a Jupiter "twin" (black) and models with higher metallicity (red) or less fractional cloud cover (orange). A younger Jupiter (green) would be warmer, showing thermal emission and ammonia absorption. In general, the near-IR offers: significantly enhanced sensitivity to methane since the absorption bands are stronger; greater wavelength coverage to characterize Mie scattering by clouds; and sensitivity to thermal emission in warmer planets. Bottom: the model spectrum of a Jupiter "twin" (orange in this panel; black in the upper panel) is compared with an actual Jupiter spectrum shortward of 1 μm (Karkoschka 1994); the dash line longward of 1 μm is from Clark and McCord (1979) scaled to match the short-wavelength spectra at 1 μm. Models courtesy Jonathan Fortney and Mark Marley.

1.3.3 Circumstellar Disks and Planet Formation Science

TPF-C is likely to find significantly more dust disks around nearby stars than it will Earth-like planets. This section discusses requirements for *TPF-C* that will allow it to perform groundbreaking disk science. Since disks around young stars are considered the site of planet formation, this chapter also touches on planet-formation issues that *TPF-C* can potentially address. Disks as an astrophysical noise source are discussed in Section 1.3.1.1.5.

1.3.3.1 Survey of Dusty Debris around Solar-type Stars

> **Objective 8.** **To measure the location, density, and extent of dust particles around nearby stars, in order to develop a comparative understanding of asteroid and Kuiper belts.**

Along with giant planets and terrestrial planets, small bodies (asteroids and comets) form the third major component of a planetary system. The location and density of small body populations can affect terrestrial planet habitability by determining the frequency of climate-altering impact events. To fully understand the long-term habitability of a terrestrial planet, knowledge of any surrounding small body population is needed. Do all planetary systems contain asteroid and Kuiper Belts? Can asteroid belts form at any orbital semi-major axis location, intermixed between any combination of terrestrial and giant planets, or are they preferentially found at the inner edge of the "snow line" between the terrestrial and giant planet zones? What is the relative frequency of cold debris disks and exozodiacal dust disks over the optical depth range 1-100 zodis? Do the properties of debris disks and exozodiacal dust disks depend on the host star age or spectral type? To address these key issues in comparative planetology, imaging of exozodiacal dust disks and Kuiper Belts is needed across a broad sample of solar-type stars.

For the region corresponding to the inner solar system (orbital radii of 0.7–5 AU), *TPF-C*'s terrestrial planet detection survey will simultaneously accomplish a sensitive survey for exozodiacal dust down below an optical depth of 1 zodi. To provide a uniform survey of exozodiacal dust, first-epoch planet search imaging should be completed around all the survey targets, even if the target is quickly determined to have a dust inventory that is too high for terrestrial planet finding. Imaging in a single optical band will be sufficient and should be carried out early in the mission so as to maximize the time available for follow-up studies of dust orbital motion.

Imaging of dust at orbital distances beyond 10 AU (extrasolar Kuiper Belts) will be made difficult by the finite outer working angle of *TPF-C*'s coronagraphic dark hole (currently sized at 1 arcsec at λ = 0.7 μm). Disk studies can be carried out beyond this radius, but will probably be limited to 100 zodi optical depths or brighter if the coronagraphic camera provides a continuous imaging field of view from the outer edge of the dark hole to radii of ~10 arcsec. Studies of the inner regions of extended nearby debris disks such τ Ceti, Fomalhaut, Vega, and β Leo require a field of view at least this large. In addition, studies of dust populations in the Kuiper Belt region could be accomplished at highest sensitivity by observing a more distant stellar sample (d~ 50 pc), for which the Kuiper debris disk would largely fall within the coronagraphic dark hole. This can be left as a candidate General Observer project.

1.3.3.2 Characterizing Disk-Planet Interactions

> **Objective 9.** **To characterize disk-planet interactions and to understand how substructures within dusty debris can be used to infer the presence of planets.**

Disks provide a continuous medium of test particles that are responsive to the gravity of any accompanying planets. Planets can sweep out central holes and radial gaps in disks; inclined planets can induce midplane warps (seen in the disk of β Pic); eccentric planets can induce an eccentricity in

an otherwise circular disk (seen in the Fomalhaut ring); and dust particles can become trapped in mean-motion resonances with planets, leading to asymmetric or clumpy dust density distributions (possibly seen in the disk of ε Eri). The theory of such interactions is steadily improving and provides hope that observed disk properties may eventually be inverted
to indirectly measure the mass and orbital properties of extrasolar planets. A solid theoretical understanding of these effects is crucial, as asymmetries in the distribution of exozodiacal dust can mimic the signal of an extrasolar terrestrial planet, potentially confusing *TPF-C*'s primary mission.
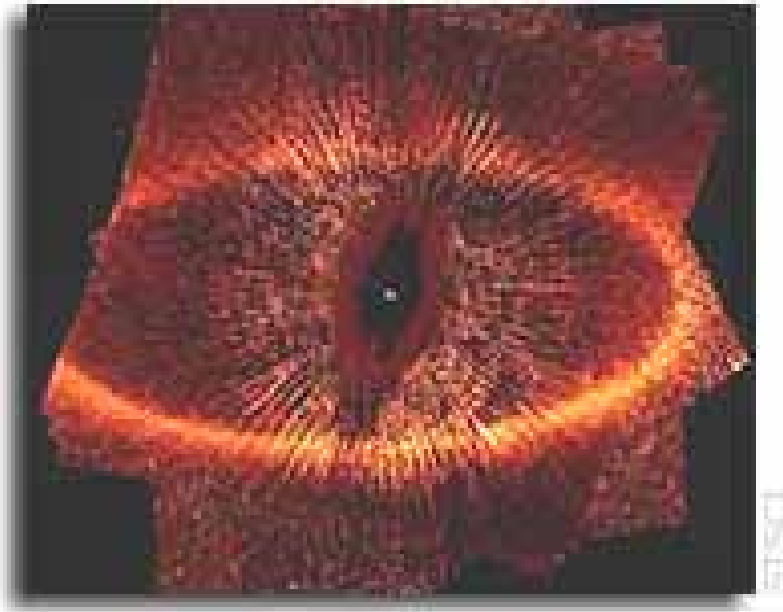
Figure 1.3-13. *HST*/**ACS scattered light image of the dust debris ring around Fomalhaut. (Kalas et al. 2005). The ring center is clearly displaced from the stellar position, indicating that the ring is intrinsically eccentric. Apsidal alignment of the ring particle orbits can only be maintained through the perturbations of an unseen interior planet on an eccentric orbit. This is the most clear-cut example to date of debris disk structures pointing toward an unseen planetary perturber.**

The key missing piece in our understanding of disk-planet interactions is the simultaneous direct detection of a planet and a perturbed disk structure in the same extrasolar system. Early in its mission, *TPF-C* should conduct an imaging search for dust structures around a significant number of stars already known to possess extrasolar planets, and for which the planetary ephemerides are well-known. Such a dataset would calibrate the dynamical models, validating their predictive power for indirect detections of planets that would be otherwise go unrecognized in *TPF-C* datasets.

Planets orbiting at semi-major axes beyond roughly 10 AU have orbits too long to permit detection via radial-velocity or astrometric techniques within a human lifetime, and they will be too faint for *TPF* to detect in reflected light. But these coldest planets may tell critical chapters of the planet formation story. New models of planet-disk interactions (Type III migration) suggest that planets can easily migrate out to the outermost parts of protoplanetary disks (Masset and Papaloizou, 2003). Is this mechanism the dominant migration mechanism? Or do planets mostly migrate inwards, as the existence of 51 Pegasi-type planets suggests? The outermost planets can excite inner planets by dynamically coupling them to passing stars (Zakamska and Tremaine, 2004). Could this mechanism explain the large eccentricities of the observed precise-Doppler planets? The recent announcement

of a massive planet candidate found ~50 AU from a young brown dwarf in the TW Hydrae association (Chauvin et al., 2004) is an existence proof that objects up to 5 Jupiter masses can exist in this region.

The only way to detect these most distant planets around stars of solar age and mass may be to study the structures of debris disks. Resolved images of extrasolar debris disks reveal resonant structures that probably indicate the presence of planets buried in the dust. Recent advances in debris disk dynamics (*e.g.*, Kuchner and Holman, 2003) allow detected structures to be used to infer the mass and eccentricity of a perturbing planet as small as ~10 Earth masses. A direct imaging detection of a Neptune analog, at a contrast of 3×10^{-12}, would be impossible for *TPF-C*. However, given a sufficient amount of Kuiper Belt dust, the existence of such a planet could easily be inferred from its gravitational effects on the surrounding disk. The same technique might enable the detection of Mars-mass planets by their effects on inner exozodiacal disks. Multi-epoch imaging will be particularly important in such cases, where the orbital periods will be only 1-2 years, and where dust asymmetries should have mean motions commensurate with the period of the perturbing object.

The requirements for studies of disk/planet interactions are continuous disk imaging from the IWA to radii of 10 arcsec (as in Figure 1.3-14), and a sufficiently large sample of disk structures imaged in systems with known planets so that the dynamical models can be validated for broad application to *TPF-C* data.
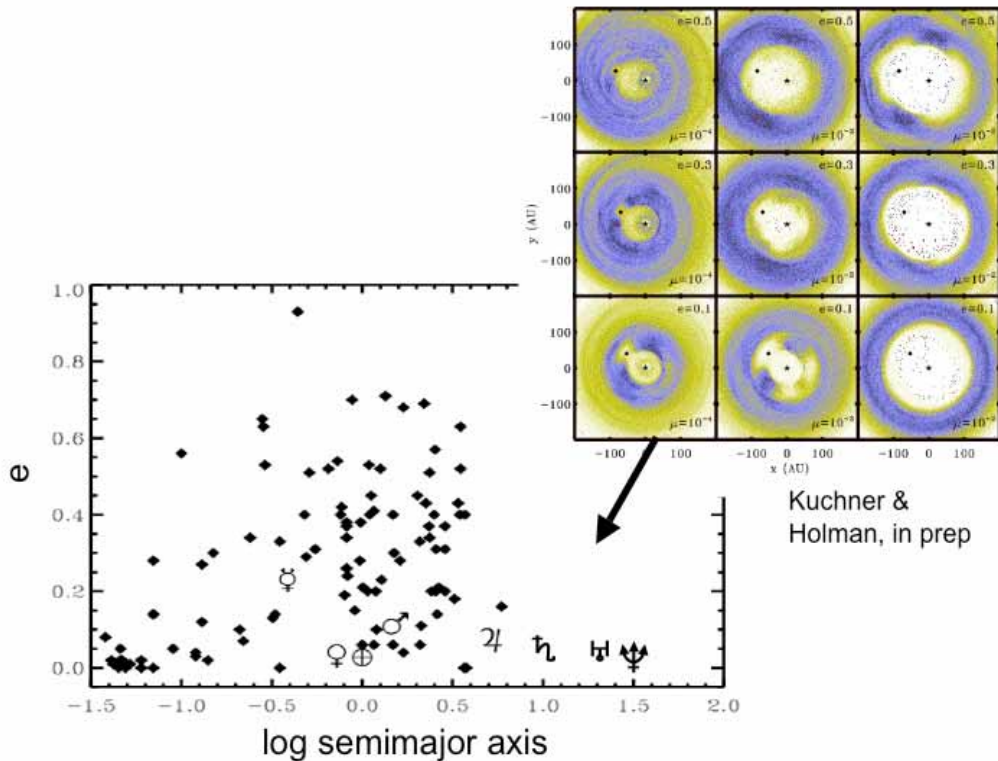
Figure 1.3-14 Orbital eccentricities and semimajor axes of known extrasolar planets detected by the precise-Doppler method (see http://exoplanets.org) and models of collisionless dust disks containing planets of various masses and eccentricities (inset). Observing these structures with *TPF* can fill in the gap at > 10 AU, where the planets are too faint to detect directly, and orbital periods are too long for indirect methods, like the Precise Doppler method.

1.3.3.3 Disk Evolution and Planet Formation

> **Objective 10. To understand the time evolution of circumstellar disk properties, from early protoplanetary stages through mature main sequence debris disks**

Planet formation takes place within the circumstellar disks of young stars. The evolutionary path from a dusty primordial disk toward terrestrial planets is believed to follow a sequence of dust sedimentation to the disk mid-plane, dust grain growth, the build-up of solid planetesimals, the run-away growth of planetary cores, and a final phase of accretion and dynamical clearing of the system. While this scenario has a sound theoretical foundation, most of it remains to be confirmed by direct observation. These events appear to take place quickly (within the first 10 MYrs of a star's life), within a disk approximately 100 AU in radius, and (for the nearest known systems) on sub-arcsecond angular scales. The youngest debris disks are particularly important targets for study, as they form the evolutionary link between massive primordial disks and remnant debris disks. The distances of young disks (typically 150 pc) render their host stars as faint as V magnitude 17. To enable studies of disk evolution, *TPF-C* must be able to guide on sources as faint as this for coronagraphic observations.

The structural evolution of circumstellar disks can be traced with high spatial resolution, high contrast imaging. Direct measurements of disk vertical thickness as a function of radius can indicate the progress of dust settling. As an optically thick disk flattens, it becomes fainter: measurements of the radial surface brightness profile can thus indirectly probe the radial variation of disk thickness. When protoplanets form, they are expected to clear their feeding zone, and open central holes or radial gaps in the continuous disk. They may also induce broader disk perturbations and asymmetries like those discussed in the previous section. *TPF-C* can resolve these structures with a typical spatial resolution of 2 AU, and nominal inner working angle of 8 AU. Since young disks are expected to be relatively bright (contrasts of about 10^{-6}), they should be accessible at a more aggressive inner working angle of $2 \lambda/D$ if suitable coronagraphic masks are provided.

The growth of dust grains is a key part of the story of planet formation. At visual wavelengths, grain properties can be diagnosed from the wavelength dependence of the opacity, the scattering phase function, and the strength of the polarization induced by scattering. Small grains preferentially scatter in the blue, strongly forward scatter, and produce a strong polarization signature. As grains grow beyond several microns in size, their opacity loses its wavelength dependence across visible wavelengths, their phase function becomes isotropic, and the induced polarization becomes much weaker. If the scattering geometry is understood, high resolution imaging with *TPF-C* can provide direct measurements of these dust properties. Constraints on dust grain sizes are crucial for understanding if a disk is dominated by primordial material or grains released by shattering planetesimal collisions, and thus for classifying a disk's evolutionary state. Polarimetric imaging capable of detecting 1% polarization at the 5 sigma level would be a desirable added capability for *TPF-C*. Polarization discontinuities in dust disks may help distinguish clumpy disk structure from the light of an embedded planet.

At visible wavelengths, circumstellar disks primarily appear in scattered stellar continuum light. However, a few notable gas spectral features are also accessible. Very young stars possess collimated jets, fed by disk accretion, that emit strongly in the lines of H alpha 656 nm, [S II] 671 nm, and [O I] 631 nm. *TPF-C* studies of these jets will resolve their collimation region, illuminating the magnetic

field structure that permeates the entire disk. Gas within a disk itself will also be accessible to imaging with *TPF-C*: resonant Na I 588 nm emission has been mapped in the disk of beta Pictoris (Olofsson et al., 2001), revealing a significant gas component that still strongly affects the spatial distribution of dust particles. The observatory design should provide for narrowband imaging studies in these various lines, at spectral resolutions of 70 or better.

1.3.4 Comparison with Ground-Based Capabilities

1.3.4.1 Competing Ground-Based Facilities for Direct Detection and Spectroscopy of Extrasolar Giant Planets

Planned extremely-large-aperture ground-based telescopes probably cannot perform spectroscopy of giant planets like those found in a planetary system like our Solar System. The aggressively optimistic study of Dekany et al. (2005) demonstrates this point vividly. Dekany et al. (2005) modeled the performance of a 30-m ground-based telescope assuming: the optimum combination of wave-front sensing and science detection simultaneously in the same wavelength band (H = 1.6 μm); and use of an efficient servo system and a ultra-fast ultra-large deformable mirror (100 times as many elements as any used today, sampling the atmosphere 100 times faster than any current AO system). They found that under these assumptions, a Jupiter analog around a solar-type star at 10 pc would be 30 times fainter than the background speckles. Even if such a theoretically perfect ground-based system could be built and 97% of the background speckles subtracted, strong telluric water absorption bands in the near IR would prevent this idealized telescope from measuring the most interesting extrasolar planet absorption features.

1.3.4.2 Competing Ground- and Space-Based Facilities for Circumstellar Disk Studies

More precise measurements of the exozodiacal dust levels around nearby stars probably require removing the bulk of the starlight from the photometric signal, as a coronagraph or nulling interferometer do. The Keck Interferometer (KI) and the Large Binocular Telescope Interferometer (LBTI) are designed to perform this task and to survey nearby main sequence stars for exozodiacal dust. The nominal performance goal for the KI nuller is 10 zodis, and the nominal performance goal for the LBTI is 3 zodis. These tools will likely have the power to dramatically redirect *TPF* efforts, if they discover that, for example, all G type stars have 30 zodi disks.

Ground-based nulling interferometry is new technology, and both the KI and LBTI experiments presently lag years behind their original timetables. The information garnered from these experiments will be statistical; these interferometers cannot survey all the *TPF*- target stars, since they are located in the northern hemisphere, and even a survey of all the accessible *TPF-C* target stars would probably represent an impractical use of telescope time because of the faintness of many of the stars. And, most saliently, a feature of the Keck Interferometer and the LBTI not captured by Figure 1.3-15 is that these mid-infrared interferometers are much more sensitive to exozodiacal dust around intrinsically more luminous stars. LBTI and the Keck Interferometer may tell us little about the dust environments of the K stars in the *TPF-C* survey. At a given mid-IR flux, an F star has a much larger habitable zone angular size than a K star. But IR bright K main sequence stars are rare---a flux-limited interferometer survey will contain few K stars, and the typical K star interferometer targets will be fainter than typical F star interferometer targets. Consequently, the Keck Interferometer and LBTI exozodiacal dust surveys will probably not be as sensitive to circumstellar dust around

K stars; they will provide only poor statistical information about this class of targets, not much better than Spitzer photometry. The later spectral types may have the same statistical distribution of exozodiacal clouds as the F and G stars in the *TPF-C* sample, or they may not; these types will have a different age distribution which may be reflected in their zodi distribution.

Currently, we can only reason by extrapolating and by making analogies with the solar system. Bryden et al. (2005) point out that debris disks with $L_{dust}/L_\star \geq 10^{-3}$ are rare around old FGK stars, and that the disk frequency in this population increases from 2±2% for $L_{dust}/L_\star \geq 10^{-4}$ to 12±5% for $L_{dust}/L_\star \geq 10^{-5}$. Figure 1.3-15 shows this trend compared to the projected sensitivities of the Keck interferometer and the LBTI for solar-type stars. Figure 1.3-15 also depicts the likely range in dust concentration in our own solar system over the last hundred million years.
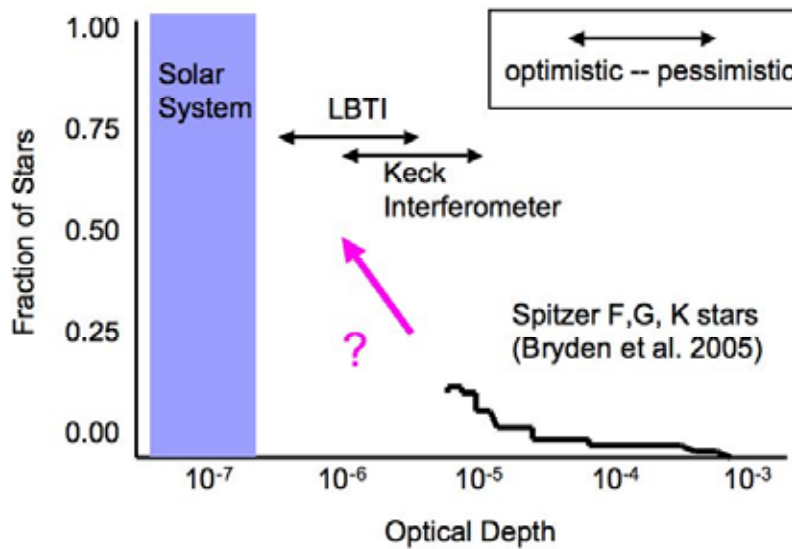
Figure 1.3-15 Our present knowledge of the prevalence of exozodiacal clouds around sun-like stars.

1.3.5 General Astrophysics Objectives and Requirements

For the purpose of this document, general astrophysics includes all of astrophysics apart from the search and characterization of planets or disks around nearby stars.

General astrophysics is broad, the questions are changing, and the questions that motivate general astrophysics on *TPF-C* also motivate the development of other missions and ground-based facilities. Because general astrophysics is not the primary driver for *TPF-C*, the goals in this area are constrained by what is realizable without compromising the planet search and characterization. The objectives outlined below may exceed what can be accomplished with parallel-mode observing and only 25% of the primary "pointed" time. In contrast to the primary mission, it is acceptable that for general astrophysics more can be accomplished with the facility than resources will allow. Progress in astrophysics will require a large, diffraction-limited optical space telescope, whether or not it is optimized for finding terrestrial planets.

While the terrestrial planet search will require a highly optimized mission that will need to be carefully planned before launch, the remaining parts of the mission need not be as carefully scripted. Scientific peer review after launch may be the optimal means to achieve an appropriate balance between general astrophysics, planet characterization, and general research on planetary and protoplanetary systems.

The science programs described in the next three subsections have been chosen because they are scientifically compelling and are likely to require *TPF-C* capabilities. The fourth subsection lists other programs that may be suitable for a General-Observer program.

1.3.5.1 Cosmology, Dark Energy, and Dark Matter

Objective 11: To constrain the nature of Dark Energy via precise measurements of the Hubble constant and the angular-diameter vs. redshift relation.
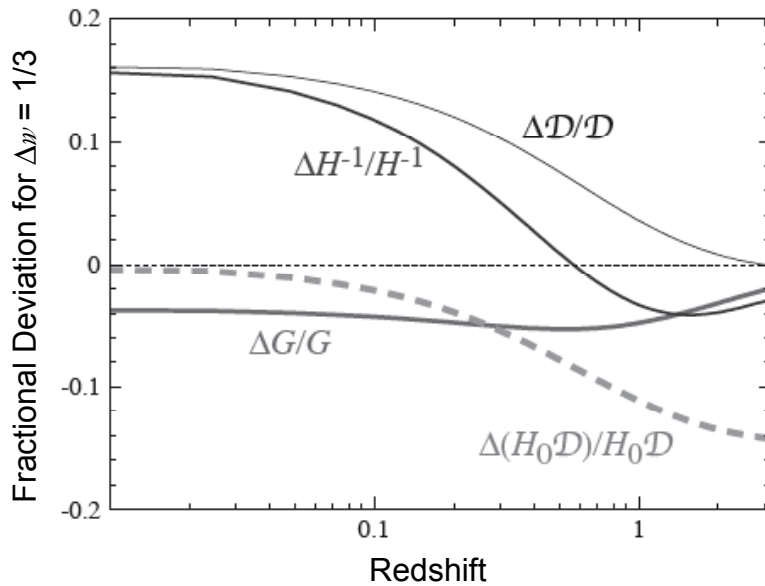
Figure 1.3-16. This figure shows the deviation in four dark-energy observables as a function of redshift between two models: one with *w* = -1 and the other with *w* = -2/3. *Other cosmological parameters have been adjusted to leave the CMB fluctuations unchanged.* *H* is the Hubble parameter, *D* is the co-moving angular-diameter distance, $H_0 D$ is a relative distance (e.g. from comparing the apparent magnitudes of high-z supernovae to a local sample), and *G* is the growth rate of density fluctuations from self gravity. Fixing the CMB observables changes the perspective on where the largest deviations from the fiducial ΛCDM model occur. Given that the CMB is a high-redshift probe, the largest effect on distances and growth is seen as z $\rightarrow$ 0. In fact, the single most useful measurement that would complement the CMB distance measure is a Hubble constant measurement that is accurate to the percent level. From Hu (2005).

Recent observations have improved our knowledge of the cosmological parameters greatly, but have also demonstrated that we understand very little about the underlying fabric of the universe. Roughly 73% of the energy density of the universe appears to be in the form of "dark energy," which is causing the expansion of the universe to accelerate. We do not know what dark energy is, how it relates to the known forms of energy, or to dark matter (which represents 23% of the mass-energy density of the universe and is also poorly understood). Dark energy is often characterized by

its equation of state $p = w\rho c^2$, where p is pressure, ρ is density, c is the speed of light, and w is a parameter which may be a constant or a function of time or expansion factor. The cosmological constant has a present-day $w_0 = -1$ and $w' = 0$. Concepts for measuring w_0 and w' have been widely discussed and debated. Constraining w_0 to better than ± 0.1 and w' to better than ± 0.2 appears achievable using high-redshift Type Ia supernovae. However, complementary approaches are essential to overcome systematic errors in any one technique. It is important that the complementary techniques achieve comparable levels of precision. *TPF-C* has the potential to do so with two distinct observing programs.

1.3.5.1.1 The Hubble Constant

Viable dark energy models must reproduce the fluctuations in the microwave background. With the CMB fluctuations held fixed, Hu (2005) argues that to measure the equation of state of the dark energy, the best complement to current and future CMB measurements is a measurement of the Hubble constant that is accurate at the few percent level. *SIM*'s measurements of distances to Galactic stars and to the LMC should significantly improve the local calibration of the distance scale. Further improvements in H_0 accuracy will require measurements of more nearby host galaxies of Type Ia SNe and/or observations of primary distance indicators for galaxies distant enough to be moving with the Hubble flow. With its higher resolution and greater sensitivity, *TPF-C* will be able to detect Cepheids at 2.5 times the distance of *Hubble*. This will enable accurate distance measurements to more than 10 times the number of galaxies, providing a better calibration of the absolute magnitude of Type Ia SNe, and providing better control of systematics such as dependence on metallicity and reddening and providing Cepheid distances for galaxies in the Hubble flow. Combining 2% uncertainties in H_0 with *Planck*'s cosmic microwave background measurements should yield a precision of ± 0.04 of in w from these observations alone.

This program requires pointed observations with a relatively wide field of view. The high spatial resolution afforded by *TPF-C* is essential for overcoming crowding in the Cepheid measurements. Absolute calibration will require careful attention.

Table 1.3-1. Major terms in the H_0 error budget (From Freedman et al. 2001). *SIM* observations will address the LMC zero point. *TPF-C* observations will address the other terms.

TABLE 14

OVERALL SYSTEMATIC ERRORS AFFECTING ALL METHODS

Source of Uncertainty	Description	Error (%)
LMC zero point	Error on mean from Cepheids, TRGB, SN 1987A, red clump, eclipsing binaries	± 5
WFPC2 zero point	Tie-in to Galactic star clusters	± 3.5
Reddening	Limits from NICMOS photometry	± 1
Metallicity	Optical, NICMOS, theoretical constraints	± 4
Bias in Cepheid PL	Short-end period cutoff	± 1
Crowding	Artificial star experiments	$+5, -0$
Bulk flows on scales $> 10,000$ km s^{-1}	Limits from SN Ia, CMB	± 5

NOTE.—Adopted final value of H_0: $H_0 = 72 \pm 3$ (random) ± 7 (systematic) km s^{-1} Mpc^{-1}.

1.3.5.1.2 Gravitational Lensing

With detailed modeling, the distribution of gravitational arc radii as a function of redshift in clusters of galaxies provides a measurement of the angular-diameter distance vs. redshift relation and an independent, purely geometrical, measurement of the effect of dark energy. The *Planck* mission is expected to detect roughly one cluster per square degree via the Sunyaev-Zeldovich (S-Z) effect, and the Atacama Large Millimeter Array and the South Pole Telescope will add to that sample. By 2010, studies of this large, relatively unbiased, sample of clusters will be a major focus of observational cosmology.

Pointed observations with *TPF-C* will provide the deepest, highest resolution observations of gravitationally lensed arcs and arclets in these clusters. Dalal et al. (2005) have noted that noise due to intervening large-scale structure, combined with uncertainties in the mass profiles of the lensing clusters, limit the usefulness of a single cluster. *TPF-C* will be able to observe a substantial sample of clusters with a modest investment of observing time. A photometric and spectroscopic grism survey of 50 clusters would yield hundreds of arc and arclet positions and redshifts as well as positions and redshifts for thousands of foreground galaxies. Combined with X-ray and velocity-dispersion constraints on the cluster mass profile, it may well be possible to achieve constraints on dark energy that are competitive with (and completely independent of) other proposed techniques.
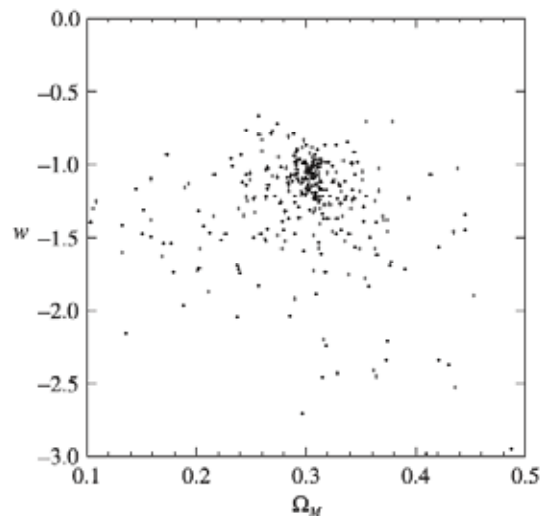
Figure 1.3-17. From Dalal et al. (2005). Cosmological parametersderived from fitting sets of 50 strongly lensed sources between redshifts z_{src} = 0.8 and 5, generated by ray-tracing through N-body simulations with full light cone tiling. Each point corresponds to a realization of the intervening planes and lensed images. An input cosmology of Ω_M=0.3, *w* = -1 was used to generate the lensed images. In this simulation, constraints on the mass and mass profile of the cluster came from lensing alone. Constraints could be significantly stronger when information on the cluster shape and density profile from X-ray, S-Z and velocity dispersion measurements are included. With a sufficiently large cluster sample, this technique will be a powerful additional probe of Dark Energy.

The same observations will yield valuable constraints on the nature of dark matter. N-body simulations and analytical models suggest that dark-matter halos should have a nearly universal density profile, characterized by two power-law slopes and a scale radius. The ratio of the scale radius to the virial radius is expected to vary with halo mass, and to show a distribution of values at fixed halo mass. The values of the parameters that describe halo profiles depend on the small-scale power

spectrum and hence the nature of dark matter (e.g. whether it is warm or self-interacting). Measurements via gravitational lensing of the mass-density profiles of a large sample of S-Z selected clusters will thus constrain the nature of dark matter.

Measurements of strong lensing by individual galaxies will also provide important constraints on the nature of dark matter. The spectrum of density fluctuations in CDM has sufficient power on small scales that dark matter halos in galaxies are expected to be lumpy. This lumpiness has been invoked to explain "flux anomalies" in several well-known gravitational lens systems. However, the extent to which the flux anomalies support CDM is hotly debated. With follow-up of large optical and radio surveys, we expect roughly 600 lens systems will be known by 2015, of which 10% will be useful for substructure tests. *TPF-C* will provide precise positions and fluxes of the components of the lensed images, grism redshifts for some of them, and will reveal faint additional images below the current limits of detection. Combined, this data set will allow a critical test of the substructure predicted by CDM theory on galactic scales.

This program requires pointed observations with a relatively wide field of view. The high spatial resolution afforded by *TPF-C* is essential for overcoming crowding in the Cepheid measurements. Absolute calibration will require careful attention. This program would benefit from both an optical and a near-infrared channel, because the Cepheid amplitudes are higher at shorter wavelengths, but their period-luminosity relation has smaller scatter in the near infrared.

1.3.5.1.3 Supernova Cosmology

A wide-field parallel camera would allow a supernova search in parallel with the planet search. If the camera is equipped with a grism, the supernova redshift, type, and phase in its light curve can be determined from a single observation. The estimated occurrence rate of SNe Ia at interesting redshifts is 1 per 60 arcmin^2 per 45-day period. The Mag30Cam proposal estimate is a sample of 450 SNe over 5 years. While not as ambitious as SNAP and other JDEM concepts, this survey would be extremely important if JDEM is not primarily a supernova-search mission.

1.3.5.2 The Fossil Record of Galaxy Formation

> **Objective 12: To use the fossil record of ancient stars in the Milky Way and nearby galaxies to measure the time between the Big Bang and the first major episodes of star formation**

Observations of very distant galaxies represent a major focus of present research with the *Hubble* and *Spitzer* observatories, and are at the core of the *James Webb Space Telescope (JWST)* mission. These observations will give us tremendous insight into the first billion years of galaxy evolution, showing where and when the first stars began to form. However, the observations do not tell us where the first (or even second or third) generations of stars ended up.

Detailed studies of stellar populations in nearby galaxies (including the Milky Way and its satellites) are the natural complement to observations of high-redshift galaxies. Observations of Milky-Way globular clusters and resolved stellar populations in nearby galaxies are currently among the most challenging for *HST* and represent a significant fraction of the observing time. *TPF-C* will expand the accessible volume for such studies by more than an order of magnitude, allowing study of a range of galaxy types with different star-formation histories SF(t).

1.3.5.2.1 Milky-Way Globular Clusters

SIM will improve distance measurements to globular clusters and the absolute calibration of the main sequence. Nevertheless, it is hard to predict the magnitude of the remaining uncertainties in absolute ages of the oldest stars in the Milky Way. Current theoretical models do not match the exact morphology of the main-sequence and sub-giant branches of globular clusters, suggesting problems with the theoretical treatment of element diffusion, semi-convection, and/or model atmospheres. The white-dwarf cooling curve provides an age estimate that is sensitive to different physics than the main-sequence turnoff. Regardless of theoretical advances in the next decade, this is a crucial test of stellar evolution theory: the results for ages derived this way must agree with the results for ages derived from main-sequence fitting.

To date only one cluster (M4) has been measured, with heroic effort, with *HST* and a second more metal-poor cluster (NGC 6397) has just been observed but no results are as yet available. *TPF-C* can do the measurement with a few hours observing time out to ~7 kpc, which brings 32 globular clusters (and the Galactic bulge) within reach. Uncertainties in this technique are currently dominated by sampling statistics, bolometric corrections, distance uncertainties, and uncertainties in the chemical composition of the outer layers of the white dwarfs. *TPF-C* will reduce these uncertainties enough that ages to an absolute accuracy of better than 0.5 Gyr may be possible. With improved age accuracy, a comparison of the relative ages of the globular clusters will provide new and detailed insight into the star-formation history of the Milky Way within its first few billion years. This should help reveal whether globular clusters formed before or after reionization, and whether they primarily formed in situ or were accreted over time from other galaxies.

All stars with masses greater than the mass of the Sun that formed in the early stages of the Universe have since evolved into some sort of remnant (black hole, neutron star, white dwarf). The white dwarf population in a globular cluster has evolved from stars with initial masses up to about 8 times that of the Sun. A careful analysis of the luminosity distribution of cluster white dwarfs can yield the initial mass distribution of their progenitors. Dynamical studies of globular clusters, which will greatly benefit from *TPF-C* astrometry, will yield valuable constraints on the neutron star and black-hole populations. Together, these observations will provide perhaps our best handle on the mass-function of this early generation of stars, which played a crucial role in the early chemical evolution of our galaxy.

This program requires pointed observations a wide-field camera with broad-band filters.

1.3.5.2.2 Star-Formation Histories beyond the Local Group

With *HST* it is possible, with major investments of observing time, to measure the main-sequence turnoff (MSTO) in any galaxy in the Local Group. This provides the gold-standard for estimating ages and metallicities. However, there are only two giant galaxies in the Local Group (the Milky Way and M31). All the rest are subluminous relative to the characteristic luminosity of galaxies (L*). There are no giant ellipticals in the Local group. *TPF-C* will allow measurements of the MSTO in galaxies to a distance of 4 Mpc, a volume that includes more than 200 galaxies, including several L* galaxies of various types in the Ursa Major and Sculptor groups. Measurements of a suitable statistical sample will indicate whether or not galaxies started forming stars simultaneously and will test our inferences from observations of high-redshift galaxies. These observations constrain the star-

formation histories in the outer disks, outer bulges, and halos of galaxies, because even *TPF-C* will be limited by crowding in the inner regions.

Hierarchical CDM models suggest that the accretion of dwarf galaxies onto giant galaxies could be a way of building the stellar halos of galaxies. The Sagittarius dwarf and the M31 tidal stream are examples that this process continues to the present, although it is unclear whether it is the dominant mechanism for creating halos. Horizontal-branch stars in halos can be detected to 10 Mpc, and the red-giant branch can be detected to 100 Mpc, enabling characterization of the spatial distribution and metallicities of halo stars in thousands of galaxies. Model predictions for these statistical distributions can only be tested by observations of a sufficiently large statistical sample of galaxies, which is not feasible with *HST*, but can be done with a few hundred hours of *TPF-C* observing time.

These investigations require pointed observations with a relatively large-field camera.
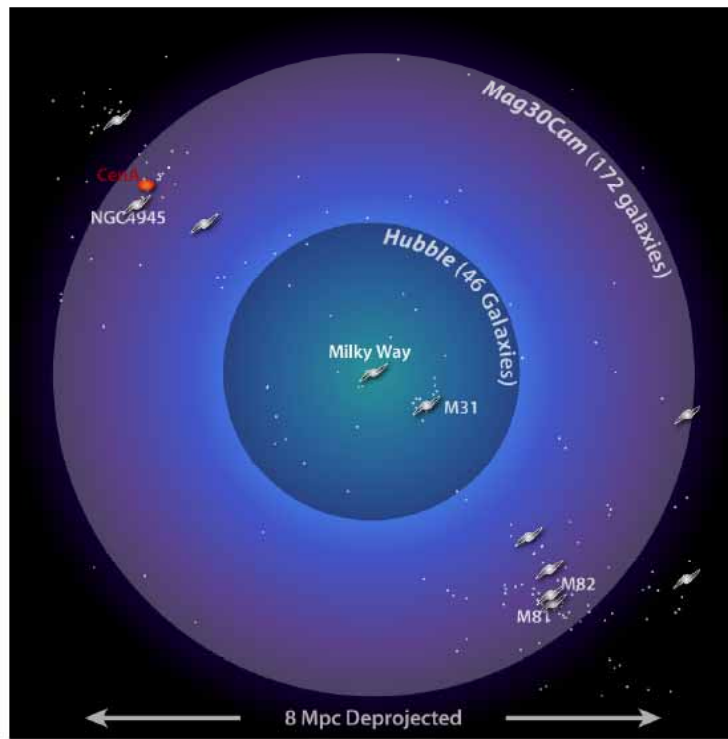
Figure 1.3-18. For stellar population studies, *TPF-C* can reach a 12Gyr main-sequence turnoff out to 4 Mpc in 200 hours of exposure time per field in V and I bands. (From Wide Field Camera Instrument Concept Study.)

1.3.5.3 Galaxies, Dark Halos, and Reionization

Objective 13: To determine what sources of energy reionized the universe and to better understand how galaxies form within dark-matter halos, through a program of low-resolution spectroscopy of large statistical samples, gathered in parallel with the TPF-C planet search program.

While the current hierarchical paradigm of galaxy formation is spectacularly successful at reproducing the clustering properties of galaxies on large scales, there are potentially serious failures on small scales: discrepancies in the predicted galaxy luminosity function (particularly the relative numbers of dwarf and giant galaxies), difficulties in reproducing the number of massive old galaxies at high redshift and the number of strong sub-mm sources, difficulties in explaining the entropy of gas in clusters of galaxies, and difficulties in explaining the properties of damped Ly-α absorbers along the line of sight to distant quasars. It is clear that the theory of galaxy formation is still incomplete and it seems likely that surprises will continue to emerge as our observations improve.

TPF-C will resolve substructure in galaxies, measure the clustering properties of distant galaxies as a function of size, stellar populations and morphology, and constrain the topology and time-sequence of reionization. While these topics will be addressed in part by *HST* and *JWST*, detailed study is likely to await *TPF-C*'s greater sensitivity, better spatial resolution, and larger field of view. Because these are primarily statistical studies of field galaxies, the observations can be done in parallel with the planet search, provided the scattered background in the parallel camera field of view is sufficiently low and uniform.

1.3.5.3.1 The Evolution of Galaxy Internal Structure

TPF-C will provide a resolution of better than 100 pc for galaxies at any redshift. Neither Webb nor JDEM will approach these resolutions. Very large (20–30 m) ground-based telescopes with adaptive optics (AO) may achieve similar resolution over small fields in the infrared ($\lambda > 1$ μm). However, *TPF-C*'s gain over Hubble and ground-based AO is not just resolution: for typical L* galaxies at redshift z > 3, studies of resolved structures are limited primarily by S/N, even in the Hubble Ultra-Deep Field. (L* is the luminosity typical of the Milky Way galaxy and M31.) Even with vast improvements expected in AO, the giant ground-based telescopes planned for the next decade will suffer the same problem due to the high near-IR sky background. *TPF-C* will thus be unique in providing the most detailed view of the internal structures of distant galaxies, and will do this for samples of order 10^6 galaxies in narrow slices of redshift. With this resolution and sensitivity, the study of galaxy evolution enters a new realm. Instead of modeling the global properties of barely resolved objects, star-formation histories can be constrained for many independent regions of individual galaxies. By this time, hydrodynamical simulations will be making believable, testable predictions for the internal structures of galaxies. Viewing galaxies with this resolution over a wide range of lookback times, we may finally be able to determine whether galaxies form from the inside out, the outside in, or primarily through mergers. With large statistical samples, it will be possible to determine whether star-formation occurs primarily in disks (punctuated by merger events), or primarily during the merger events themselves.
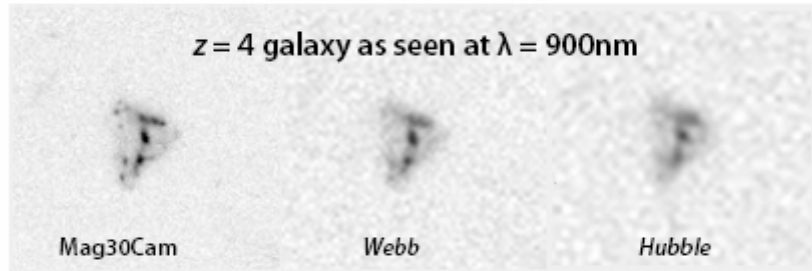
Figure 1.3-19. *TPF-C*'s Improved Resolution and S/N Compared with Webb and Hubble. The simulated object is an L* galaxy at z = 4 observed in a broadband filter centered at ~900 nm.

1.3.5.3.2 Reionization

Reionization was the last major phase transition for most of the baryonic matter in the universe. Polarization of the microwave background measured by *WMAP* suggests that substantial ionization had begun as early as $z \sim$ z ~ 11 (Page et al. 2006). Luminosity functions of Ly-α galaxies show that the neutral fraction was already ≤30% at $z \sim$ 6.5 (Malhotra & Rhoads, 2004), and spectra of $z > 6$ quasars show opaque Gunn-Peterson troughs (Becker et al. 2001), indicating that reionization was not fully complete before $z \sim$ 6.2. At $z \sim$ 6, the Ly-α line is at 850 nm, where *TPF-C* will offer greater sensitivity and resolution than *Webb*. This will allow a direct census of galaxy and quasar populations at $5.5 < z < 7$ down to unprecedented flux levels. An optical grism survey could accurately determine the luminosity function and spatial distribution of galaxies and active galactic nuclei at redshifts up to $z \sim$ 7, providing a census of possible ionizing photons. Redshifts up to $z \sim 12$ could be probed with a near-infrared channel. (If the sources remain insufficient to account for the ionization—as some current studies suggest—more exotic explanations, such as decaying particles, may be required.) A census from 65 independent lines of sight near high-latitude *TPF-C* target stars would be particularly valuable if galaxies are highly clustered and reionization is inhomogeneous. The Gunn-Peterson trough optical depth can be measured for sources brighter than 24th magnitude (and constrained on average through a stacking analysis of fainter sources). Ly-α transmission is strongly suppressed in a neutral IGM, so we should see a sharp decline in the number beyond the redshift of reionization. The spatial distribution and topology of the Ly-α emitters in a neutral IGM can be used to find the central "overlap phase" of reionization. Prior to overlap, the detectable Ly-α galaxies should be found in isolated clumps, each corresponding to one ionized bubble in the IGM. The size of these bubbles is expected to be a few arcmin—easily detected with *TPF-C*.

1.3.5.3.3 Galaxies and Dark-Matter Halos

In contemporary theories of galaxy formation, galaxies form at peaks in the underlying dark-matter density field, and reside in virialized dark-matter halos either as the central galaxy or as satellites orbiting within a larger halo. The observed properties of galaxies, such as color, morphology, or luminosity, depend on the mass and assembly history of their dark-matter halos. The environmental dependence of galaxy properties arises from their correlation with halo mass as well as the correlation of halo mass with collapse history and with the larger-scale density field.

Clustering measurements of galaxies are essential for making the connection between observations and hierarchical models. The models robustly predict the number-density of halos above a fixed mass threshold and the correlation function of those halos. Measuring the correlation function of

galaxies thus establishes the mass scale for the dark-matter halos in which they reside. The comparison of the number-density of galaxies to the number density of halos indicates how many galaxies on average occupy each halo.

Clustering studies require large samples and large volumes. A grism survey with *TPF-C* could yield redshifts for more than 10^6 galaxies, with well-determined colors and morphologies from the accompanying broad-band imaging. Tracing the Halo Occupation Distribution (Berlind & Weinberg 2002) vs. redshift will test the paradigm that galaxies form at dark-matter density peaks, and allow us to trace the origin of Hubble sequence back to the underlying dark-matter physics. *TPF-C* will complement efforts from the ground and *JWST* by providing the best measurements of position, luminosity function, and morphology and evolution of satellite galaxies orbiting within dark-matter halos at redshifts $z > 1$.

1.3.5.4 General-Observer Program

Objective 14: To enable a diverse General-Observer program in the tradition of the Hubble, Chandra, Spitzer, and James Webb Space Observatories

The success of all the Great Observatories has depended critically on having a General-Observer Program, administered by peer review, that has access to a significant fraction of the available observing time. *TPF-C* should be no different. A few examples of programs that might be carried out in this manner are given below.

Examples of Possible General-Observer Programs:

(1) Measurements of the mass spectrum of bodies in the outer solar system (e.g. the Kuiper belt).
(2) Obtaining precise distances to millisecond pulsars to improve tests of general relativity and better constrain the properties of nuclear material.
(3) Micro-lensing parallax measurements to measure the mass function of isolated black holes and neutron stars in and towards the Galactic bulge.
(4) Coronagraphic observations of galaxies responsible for the damped Lyman-alpha lines in the spectra of quasars.
(5) Parallax distances to 30% precision for white dwarfs and brown dwarfs out to distances of 10 kpc.
(6) Proper-motion measurements of stars in the Galactic halo to search for the effects of CMD substructure on stellar orbits.
(7) High-resolution observations of star-forming regions to explore the physics of star-formation and interactions between young stars and their environment.

1.4 Specific Science Requirements

Following is a list of specific science requirements for the *TPF-C* mission. Baseline mission requirements are listed first, followed by minimum mission requirements and goals for an even more capable, desired mission. These requirements are derived from the scientific objectives listed above and the accompanying explanatory text. They will ultimately form the basis for the Level 1 requirements

for the *TPF-C* mission once the mission planning reaches that stage. A brief explanation for how these requirements were derived is given below.

1.4.1 Baseline Mission Requirements

(1) *TPF-C* shall be able to detect an Earth twin in a Solar System twin at a distance of 10 pc.

(2) *TPF-C* shall be able to detect a Jupiter twin at quadrature in this same system.

(3) **TPF-C* shall be able to find ~30 potentially habitable planets if all target stars have one such planet. Equivalently, *TPF-C* shall have an excellent chance (95%) of detecting at least one planet that is potentially habitable, assuming that ten percent or more of all target stars have such a planet ($\eta_\oplus = 0.1$). The following assumptions are to be made in estimating these numbers:

    1. Planetay semimajor axes uniformly distributed in log space
    2. Planetary mass distribution: delta function at 1 $M_\oplus$
    3. Planetary eccentricities randomly distributed between 0 and 0.1
    4. Exozodi = 3×local zodi (as viewed from various observing angles)
    5. Lambertian phase function
    6. Planet visible spherical albedo = 0.3 (geometric albedo = 0.2)
    7. Habitable zone 0.75 to 1.8 AU scaled by the stellar luminosity
    8. Target detection should be completed within three years of mission lifetime

(4) **For at least 50 percent of detected planets whose *angular* separation at discovery lies within the projected habitable zone of their parent star, *TPF-C* shall measure the actual semi-major axes to within 10 percent. *TPF-C* shall also measure their orbital eccentricities to an absolute accuracy of ±0.3.

(5) *TPF-C* shall be able to detect photons within the spectral range from 0.5 μm to 1.1 μm.

(6) *TPF-C* shall be able to measure the absolute brightness of the Earth twin planet in Requirement (1) in at least one bandpass to within 10%.

(7) For the Earth and Jupiter twins in Requirements (1, 2), *TPF-C* shall be able to measure the relative brightness in at least three broad spectral bands to a relative accuracy of 10% or better.

(8) *TPF-C* shall be able to detect O_2 and H_2O in the atmosphere of the Earth twin planet specified in Requirement (1). Relevant absorption bands and required resolutions are listed in 1.4.1. *TPF-C* shall also be able to detect CH_4 in the atmosphere of a Jupiter twin in this same system. Detection is defined as the ability to measure the equivalent width of a spectral band to within 20% accuracy.

(9) *TPF-C* shall have a minimum spectral resolution of 70 over the entire bandpass specified in requirement (5) to allow the mission to search for absorption bands of unspecified gases or surface minerals.

General astrophysics requirement:

(10) To support general astrophysics, *TPF-C* shall have a camera with a field of view of at least 10 square arcminutes, capable of operating in parallel to the planet search, and capable of zodiacal-light-limited broad-band imaging over the *TPF-C* spectral range. The calibration shall provide 1% absolute photometric accuracy. The guiding system shall allow diffraction-limited observations with this camera over more than 99% of the sky.

Disk science requirements:

(11) *TPF-C* shall be able to guide on stars as faint as $V_{AB} = 16$.

(12) *TPF-C* shall be able to detect disk emission lines of Na I, H α, [S II], and K I.

(13) *TPF-C* shall be capable of optical imaging at inner working angles of $2\lambda/D$ (or half the normal inner working angle) at contrast levels of 10^{-6}.

(14) Further details on requirements (3) and (4) are given in Section 4.4 below.

1.4.2 Minimum Mission Requirements

(1) *TPF-C* shall be able to detect an Earth twin in a Solar System twin at a distance of 8 pc.

(2) *TPF-C* shall be able to detect a Jupiter twin at quadrature in this same system.

(3) *TPF-C* shall be able to find ~14 potentially habitable planets if all target stars have one such planet. Equivalently, *TPF-C* shall have an excellent chance (95%) of detecting at least one planet that is potentially habitable, assuming that twenty percent or more of all target stars have such a planet ($\eta_\oplus = 0.2$). The assumptions to be made in estimating this number are the same as in the baseline mission.

(4) Same as for the baseline mission, but for a system at 8 pc.

(5) The spectral range for the minimum mission is 0.5–0.85 μm.

(6) Same as for the baseline mission.

(7) Same as for the baseline mission, but for a system at 8 pc.

(8) *TPF-C* shall be able to measure those absorption bands listed in the baseline mission that fall within the minimum mission spectral range.

(9) Spectral resolution of 70 over the entire bandpass is *not* required for the minimum mission.

(10-13) Same as for the baseline mission

1.4.3 Desired Mission Requirements

(1, 3, 6) Same as for the baseline mission

(2) *TPF-C* shall also be able to detect a Saturn twin at quadrature in a Solar System twin at a distance of 10 pc.

(4) Same as for the baseline mission, except that planetary eccentricities shall be measured to an absolute accuracy of ±0.1.

(5) The desired spectral range is 0.4 μm to 1.7 μm.

(7) Measurements of brightness in more than 3 bandpasses are highly desirable for bright or well placed planets.

(8) In addition to O_2 and H_2O, *TPF-C* shall be able to detect O_3 for the Earth twin in Requirement (1) and CH_4 for a planet like the early Earth. It shall also be able to detect CO_2 in the atmosphere of a Venus twin orbiting in a Solar System twin at a distance of 5 pc.

(9) Same as for the baseline mission, but over the extended spectral range.

General astrophysics requirement:

(10) To support general astrophysics, *TPF-C* shall have a camera capable of surveying 10 square degrees to a point-source limiting magnitude V = 30 (10 σ) while operating in parallel with the planet search. This camera shall be capable of zodiacal-light-limited broad-band imaging over the *TPF-C* spectral range. The calibration shall provide 1% absolute photometric accuracy. The guiding system shall allow diffraction-limited observations with this camera over more than 99% of the sky.

Disk science desired requirements:

(11-13) Same as for the baseline mission.

(14) *TPF-C* shall be capable of continuous imaging coverage extending from the central star to radii of 10 arcsec. This is a requirement on the detector imaging field of view, not on the outer working angle of the high contrast dark hole.

(15) *TPF-C* shall have a coronagraphic dark hole outer working angle of 2 arcsec at at least one wavelength.

(16) *TPF-C* shall have polarimetric imaging capability.

1.4.4 Rationale behind these Requirements

Requirements (1)– (4) determine the necessary size of the telescope mirror, the efficacy of the starlight suppression system, and the general capabilities of the spacecraft itself. Requirement 1 sets a constraint on the coronagraph inner working angle and contrast. It may be superceded by Requirement (3), but it ensures that *TPF-C* can find an Earth twin, if it exists, regardless of other assumptions made in the mission modeling. Requirement 2, detecting a Jupiter twin at quadrature, determines a minimum outer working angle for the coronagraph. The minimum outer working angle is doubled for the desired mission by requiring that it detect a Saturn twin at quadrature. Surveying extrasolar planetary systems to the equivalent distance of Saturn is highly desired because it would provide much more information about planetary system architecture. Saturn is the natural outer limit for such a search because its contrast ratio to the star is similar ($\sim 10^{-10}$) to that of Earth.

Requirements (3) and (4)) are the most general and should have the most significant impact on mission design, as they impose constraints on the complete spacecraft system. Demonstrating that these requirements can be met requires detailed modeling of the entire mission sequence, as is done in the Design Reference Mission that follows in the present report. Such modeling necessarily involves making assumptions about parameters, *e.g.*, the mass distribution of terrestrial planets, which are not well known. But Requirement (1) ensures that *TPF-C* will still be able to detect an Earth.

The minimum mission is also designed to have a 95% chance of finding at least one potentially habitable planet (requirement 3), but in this case it has been assumed that data from other missions (*e.g.*, *Kepler*) has shown that $\eta_\oplus$ is at least 0.2, as opposed to the baseline assumption of $\eta_\oplus = 0.1$. If stars are randomly distributed in space, then the distance to which the telescope must be able to observe is reduced by a factor of $2^{1/3} \cong 1.25$. Hence, the distance to which an Earth twin must be detectable is reduced from 10 pc to 8 pc (requirement 1). Because the actual value of $\eta_\oplus$ is not known, descoping to the level of the minimum mission is extremely risky and is not to be considered unless *Kepler* (or some other mission) demonstrates that terrestrial planets are reasonably abundant. Given the delay in the *TPF-C* mission, such information may become available prior to the design phase for *TPF-C*.

Requirement (4) begins the process of planetary characterization by constraining the orbits of detected planets. Both this requirement and requirement (3) came under intense discussion near the end of the activities of the present Science and Technology Definition Team. Results of modeling studies performed for the Design Reference Mission, described later in this report, show that satisfying requirement (4) for all detected planets would be difficult or impossible for the FB1 mission design. As written, this requirement is applied to 50 percent of detected planets whose angular separation at discovery lies within the projected habitable zone of their parent star. In reality, these detected planets may include giant planets in orbits well beyond 1.8 AU that simply appear to be close to the parent star because of the angle at which they are being viewed.

Scientifically, one would like to know the orbits of *all* detected planets. The parameter of greatest physical interest is the planet's semi-major axis. This must be known in order to determine whether or not the planet resides within the habitable zone, in a time-averaged sense. (See Section 3.1.2.1.) Hence, requirement (3) cannot be fully satisfied without having this information. The semi-major axis can be derived from a planet's period, using Kepler's 3rd law; however, guaranteeing that a particular planet will be observed enough times during the course of the mission in order to do this is not an easy task. The planet's eccentricity is somewhat less important, as the large heat capacity of the ocean would moderate surface temperatures on a planet like Earth. Planets with high eccentricities may not be suitable for land-based life, as a consequence of high seasonal surface temperature variations. Measuring a planet's eccentricity accurately is considered difficult, and so the baseline requirement is not very strict. Measuring the eccentricity more accurately is reserved for the desired mission.

An alternative form of requirements (1)– (4) that may remove some of the ambiguities identified above is given in Appendix 1.D. These alternative requirements have *not* been discussed in detail by the committee; hence, they should be viewed cautiously. They are included here so as to provide guidance to the next group that works on designing this mission.

In requirement (5), the baseline spectral range, 0.5–1.1 μm, is the region where CCD detectors are most sensitive. Their sensitivity falls off dramatically between 1.0 and 1.1 μm, so the ability to characterize a planet may not be uniform over this entire wavelength range. The minimum mission spectral range of 0.5–0.85 μm is the region where solar-type stars are brightest and planets are easiest to detect. Reducing the wavelength coverage may relax requirements on various parts of the telescope optical system. The desired spectral range, 0.4–1.7 μm, allows for an increased chance of measuring Rayleigh scattering at the short end and for detecting spectral features of various atmospheric gases (especially CH_4 and CO_2) at the long end. The desired mission would thus provide much improved characterization capability for both terrestrial and giant planets.

Requirement (6) expresses the desire to obtain absolute photometry of the observed planets. The true radius, albedo, and effective temperature of detected terrestrial planets will eventually be determined by equating the emitted flux measured by *TPF-I* to the difference between the incident flux and the reflected stellar flux measured by *TPF-C*. While the effective temperature is proportional to only the fourth root of this quantity, the radius goes as the square root and the albedo is linearly dependent. Planetary spectra are typically highly wavelength dependent, so achieving a reliable estimate of the planetary albedo requires an absolute measurement of the reflected flux over one bandpass, combined with knowledge of the relative brightness of different bandpasses (Requirement 7). Ideally this quantity would be measured at several phase angles to properly account for the angular dependence of scattering.

Color determination (Requirement 7) does not require absolute photometry, but it requires accurate relative photometry in different spectral bands. This requirement is not expected to be difficult to satisfy and is therefore applied uniformly to the baseline, minimum, and desired missions.

Requirement (8) places detailed constraints on the spectral resolution required to search for different trace gases that we might expect to find on terrestrial and jovian planets. *Detecting O_2 and H_2O for Earth is considered essential.* The H_2O band at 0.94 μm is much easier to detect than other H_2O bands

at shorter wavelengths, according to the outcome of design studies for the CorSpec instrument (this report). That is why this particular band has been chosen. The spectral resolution requirement is different for different spectral bands, so the spectrograph resolution may vary with wavelength. Detection of CO_2 requires that *TPF-C* have good sensitivity to wavelengths beyond 1.0 μm and, hence, is reserved for the desired mission. Detection of O_3 is considered difficult as well due to the extreme broadness of the absorption feature at 0.6 μm, and so is reserved for the desired mission.

Requirement (9) specifies that the spectral resolution should be 70 over the entire wavelength range. This would enable the mission to detect spectral features and identify spectral continuum regions that are not anticipated based on the planets in our own Solar System. It is listed here as a baseline requirement because it is considered so desirable for planetary characterization that it would be relaxed only under great pressure. It might, however, preclude certain telescope/instrument designs for which the spectral resolution varies with wavelength. This requirement should be revisited should it pose an insuperable problem for the coronagraph design.

Requirement (10) ensures that the mission will include a wide-field camera of some sort that would be capable of doing more general astrophysical observations in parallel with the search for planets. Pointed observations with this instrument are also envisioned, but this capability is intentionally *not* allowed to drive the design of the mission. The difference between the baseline requirement and the desired mission requirement is that the baseline version specifies only the field of view of the camera, whereas the desired mission requirement specifies a total sky area that must be surveyed . This latter requirement was moved from the baseline to the desired mission only after the final instrument reports came in. The GA report indicates that carrying out a successful sky survey of this magnitude may require alterations to the FB1 2-mirror design for the front end of the telescope. The sky survey requirement also assumes that the telescope main mirror is elliptical, and hence will need to be cycled through at least 3 different roll positions. Such role maneuvers may not be needed if the final telescope design is spherical. The sky survey requirement further assumes that $\eta_\oplus$ is low, so that most of the mission will be spent in search mode, rather than in planet characterization. If $\eta_\oplus$ turns out to be high, then much of the mission time may be spent in planet characterization. The mission will then be a huge success, but this could result in a smaller total area of sky being surveyed for background objects.

Requirement (10) for the minimum mission is the same as for the baseline design. *TPF-C will include a capable wide-field camera for doing general astrophysics.* The only question is how that capability will be exercised.

Requirements (11)– (13) in the baseline mission are included specifically to enable the study of protoplanetary disks around young stars that might not otherwise be observed by *TPF-C*. Requirement (11) ensures that *TPF-C* can point at a star that may be largely obscured by dust. Requirement (12) ensures the capability of detecting spectral features of interest to disk science. Requirement (13) ensures that *TPF-C* will be able to image disks around distant stars for which the required inner working angle is less than the baseline value. This is considered possible because the contrast ratio between such disks and their parent stars ($\sim 10^{-6}$) is much less than the constrast ratio for terrestrial planets.

The desired mission contains 3 additional disk science requirements. Requirement (14) expresses a desire that the telescope have continuous imaging capability from close to the star out to 10 arcsecs.

Requirement (15) extends the outer working angle of the coronagraph out to 2 arcsec. Requirement (16) expresses a desire to look at disks in polarized light. All 3 of these requirements may impose constraints on the design of the telescope/coronagraph and, hence, are listed as desired features to be added if possible.

Table 1.4-1 below points to sections of the Science Requirements Document (SRD) that support the Requirements listed in the previous section.

Table 1.4-1 Science Requirements Index

Science Requirement	Supporting Section of the SRD
1 Detect an Earth twin at 10 pc	1.3.1.1.6
2 Detect a Jupiter twin at 10 pc (at quadrature)	1.3.2.1
3 Find 30 potentially habitable planets ($\eta_\oplus = 1$)	1.3.1.1.6
Specific assumptions	
Planetary spacing	1.3.1.2.2
Planetary mass distribution	1.3.1.1.3
Planetary eccentricities	1.3.1.2.2
Exozodi background	1.3.1.1.5
Lambertian phase function	1.3.1.1.4
Planetary albedo	1.3.1.1.4
Habitable zone boundaries	1.3.1.1.1
Target detection time	See Design Reference Mission (Section 2.0)
4 Measure semimajor axes and eccentricities	1.3.1.1.1
5 Detect photons from 0.5-1.1 μm	1.3.1.4.1
6 Measure the absolute brightness of the Earth twin	1.4.4
7 Measure the color of the Earth and Jupiter twins	1.3.1.3
8 Detect O_2 and H_2O for the Earth twin	1.3.1.4
Detect CH_4 for the Jupiter twin	1.3.2.3
9 Minimum spectral resolution of 70	1.4.4
10 General astrophysics camera field of view	1.3.5
Disk science requirements	
11 Guiding on faint stars	1.3.3.3
12 Detecting emission lines of Na, H, S, and K	1.3.3.3
13 Working at 2λ/D at lower contrast ratios	1.3.3.3
Desired mission requirements	
14 Continuous imaging out to 10 arcsec	1.3.3.3, 1.3.3.2
15 Dark hole outer working angle of 2 arcsec	1.3.3.1
16 Polarimetric imaging capability	1.3.3.3

Appendix 1.A TPF Spectral Lines (Desmarais et al., 2002)

TABLE 1.   MOLECULAR SPECIES AND SPECTRAL BANDS USED IN THIS STUDY

Band	Species	σ (cm^{-1}) Minimum	Maximum	Average	Resolution	λ (μm) Minimum	Maximum	Average
1	H_2O	200	300	250	2	33.33	50.00	40.00
2	H_2O	300	400	350	4	25	33.33	28.57
3	H_2O	400	576	488	3	17.36	25	20.49
4	H_2O	1,356	1,500	1,428	10	6.67	7.37	7.00
5	CO_2	587	750	668	4	13.33	17.04	14.96
6	CO_2	930	990	960	16	10.75	10.10	10.42
7	CO_2	1,046	1,102	1,074	19	9.56	9.07	9.31
8	O_3	1,005	1,067	1,036	17	9.37	9.95	9.65
9	CH_4	1,257	1,356	1,306	13	7.37	7.96	7.65
10	CH_4	1,150	1,356	1,253	6	7.37	8.70	7.98
11	Cont.	804	986	895	5	10.14	12.44	11.17
12	Cont.	1,082	1,226	1,154	8	8.16	9.24	8.67
13	H_2O	5,080	5,580	5,330	11	1.79	1.97	1.88
14	H_2O	6,740	7,480	7,110	10	1.34	1.48	1.41
15	H_2O	8,580	9,050	8,815	19	1.10	1.17	1.13
16	H_2O	10,320	10,930	10,625	17	0.91	0.97	0.94
17	H_2O	12,000	12,350	12,175	35	0.81	0.83	0.82
18	H_2O	13,630	14,000	13,815	37	0.71	0.73	0.72
19	CO_2	4,780	5,080	4,930	16	1.97	2.09	2.03
20	CO_2	6,020	6,570	6,295	11	1.52	1.66	1.59
21	CO_2	8,120	8,360	8,240	34	1.20	1.23	1.21
22	CO_2	9,410	9,650	9,530	40	1.04	1.06	1.05
23	O_2	7,840	7,950	7,895	72	1.26	1.28	1.27
24	O_2	13,010	13,200	13,105	69	0.76	0.77	0.76
25	O_2	14,380	14,650	14,515	54	0.68	0.70	0.69
26	O_3	15,250	19,000	17,125	5	0.53	0.66	0.58
27	O_3	30,000	32,000	31,000	16	0.31	0.33	0.32
28	CH_4	4,040	4,570	4,305	8	2.19	2.48	2.32
29	CH_4	5,610	6,190	5,900	10	1.62	1.78	1.69
30	CH_4	9,790	10,280	10,035	20	0.97	1.02	1.00
31	CH_4	11,040	11,390	11,215	32	0.88	0.91	0.89
32	CH_4	12,420	12,850	12,635	29	0.78	0.81	0.79
33	CH_4	13,660	13,900	13,780	57	0.72	0.73	0.73

Two IR continuum (Cont.) bands (11 and 12) are also given, where in a cloud-free atmosphere, emission from the surface might be seen. Columns 3–5 give the nominally optimum wavenumber values (minimum, maximum, and average) for each band. Column 6 gives the corresponding spectral resolution. Columns 7–9 give the same information in terms of wavelength.

TABLE 2. CURVE-OF-GROWTH VALUES FOR EACH MOLECULAR BAND ARE LISTED HERE, FIRST FOR THE THERMAL EMISSION IR REGION, AND SECOND FOR THE VISIBLE, NEAR-IR, AND UV REGIONS

Thermal

Gas, concentration	Curve-of-growth value at given wavenumber			
H_2O	250 cm^{-1}	350 cm^{-1}	488 cm^{-1}	1,428 cm^{-1}
1 ppm	0.090	0.043	0.072	0.048
10 ppm	0.213	0.124	0.025	0.161
100 ppm	0.341	0.279	0.068	0.427
1,000 ppm	0.377	0.416	0.153	0.747
10,000 ppm	0.339	0.436	0.226	0.850
CO_2	668 cm^{-1}	960 cm^{-1}	1,074 cm^{-1}	
100 ppm	0.470	0.029	0.037	
350 ppm	0.520	0.037	0.050	
1,000 ppm	0.548	0.054	0.075	
10,000 ppm	0.549	0.153	0.207	
O_3	1,036 cm^{-1}	710 cm^{-1}		
1 ppm	0.382	0.141		
3 ppm	0.406	0.154		
6 ppm	0.405	0.162		
N_2O	592 cm^{-1}	1,174 cm^{-1}	1,290 cm^{-1}	
100 ppb	0.014	0.008	0.050	
310 ppb	0.031	0.023	0.095	
1,000 ppb	0.063	0.063	0.160	
CH_4	1,306 cm^{-1}			
0.5 ppm	0.056			
1.6 ppm	0.091			
5.0 ppm	0.137			
100 ppm	0.300			
1,000 ppm	0.330			
10,000 ppm	0.262			

Visible/near-IR/UV

Gas, concentration	Curve-of-growth value at given wavenumber					
H_2O	5,330 cm^{-1}	7,110 cm^{-1}	8,815 cm^{-1}	10,625 cm^{-1}	12,175 cm^{-1}	13,815 cm^{-1}
10 ppm	0.236	0.178	0.041	0.025	0.003	0.003
100 ppm	0.586	0.485	0.172	0.124	0.025	0.024
1,000 ppm	0.901	0.830	0.500	0.401	0.118	0.130
10,000 ppm	0.990	0.988	0.885	0.795	0.379	0.441
CO_2	4,930 cm^{-1}	6,295 cm^{-1}	8,240 cm^{-1}	9,530 cm^{-1}		
100 ppm	0.170	0.007	0.170	0.0002		
350 ppm	0.309	0.030	0.309	0.0006		
1,000 ppm	0.443	0.065	0.443	0.001		
1%	0.667	0.260	0.667	0.011		
10%	0.714	0.566	0.714	0.062		
CH_4	4,305 cm^{-1}	5,900 cm^{-1}	10,035 cm^{-1}	11,215 cm^{-1}	12,635 cm^{-1}	13,780 cm^{-1}
0.5 ppm	0.005	0.003	0.063	0.001	0.0009	0.002
1.6 ppm	0.009	0.012	0.011	0.002	0.0009	0.002
5.0 ppm	0.111	0.039	0.025	0.004	0.0009	0.003
100 ppm	0.462	0.298	0.039	0.060	0.010	0.010
1,000 ppm	0.587	0.630	0.315	0.417	0.032	0.073
10,000 ppm	0.627	0.814	0.881	0.818	0.267	0.455
O_2	7,895 cm^{-1}	13,105 cm^{-1}	14,515 cm^{-1}			
1%	0.023	0.150	0.025			
10%	0.104	0.388	0.088			
21%	0.153	0.474	0.124			
50%	0.230	0.565	0.181			
O_3	17,125 cm^{-1}	31,000 cm^{-1}				
1 ppm	0.048	0.305				
3 ppm	0.112	0.531				
7 ppm	0.195	0.692				

For each species and abundance level, the average depth of each important spectral feature is listed, with the central wavenumber of the corresponding band noted at the top of each column. Refer to Table 1 for bandwidths and corresponding wavelength values. Entries range from weak lines (e.g., 0.029, or 2.9% average depth) to strong lines (e.g., 0.474, or 47.4% average depth). The values given are appropriate for an Earth-like temperature structure and mixing ratio profile for each species. For O_3 the mixing ratio values refer to the peak abundance in the stratosphere.

Appendix 1.B Zodi brightness table and ZODIPIC description

ZODIPIC is a computer code that performs an iterative calculation of the cloud surface brightness to distribute computing power evenly in logarithmic intervals of circumstellar radius, thereby providing an accurate calculation of the total zodiacal cloud flux. The ZODIPIC model contains several levels of detail beyond a simple face-on cloud of isotropic scatters. Some of this detail is probably not relevant to *TPF*. Figure 1.B-1 compares a few different zodiacal cloud models at 0.5 microns, each computed by ZODIPIC. The first model (black line) is a simple, circularly-symmetric face-on cloud with isotropic scattering. Each subsequent model adds one new detail—first a non-zero inclination, then a realistic scattering phase function, then a pericenter shift. The information in this figure appears in Table 1.B-1. These details amount to at most, corrections of 1 magnitude---in the absence of a coronagraph. However, in the presence of a coronagraph, the central peaking of the zodiacal brightness and the pericenter shift can make a big difference, as discussed in Section 1.3.1.1.5.
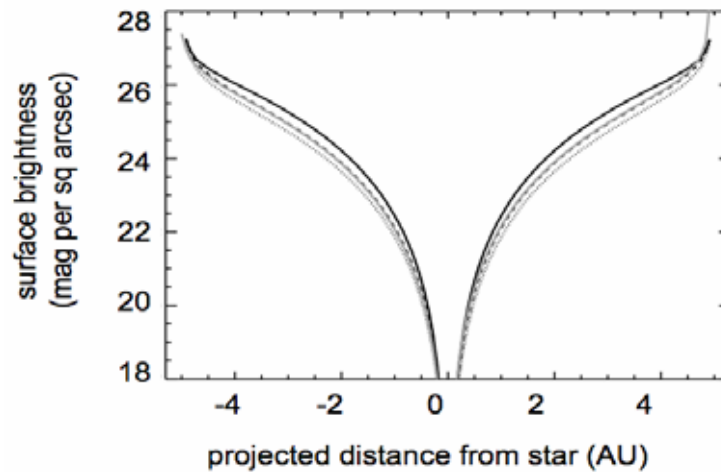
Figure 1.B-1. Four Exozodiacal Cloud Models from ZODIPIC with Increasing Complexity: face-on, isotropic scattering (black line), same model, 60 degrees from face-on, major axis (dotted line), same as previous, with forward scattering phase function from Hong (1985) (dashed line), same as previous with 0.07 AU pericenter shift (grey line).

Table 1.B-1 contains the surface brightness at 0.5 microns for four exoodical cloud models computed by ZODIPIC. These models are discussed in Section 1.3.1.1.5. The model in the fourth column of this table is the one that should be used as the standard 1-zodi exozodiacal background. For higher exozodiacal backgrounds, multiply by the desired zodi background. The physical basis used in ZODIPIC, and hence the data in the table, are not valid over 100 zodis.

Table 1.B-1 Various 1-zodi models. Surface brightness in magnitudes per square arcsecond at λ = 0.5 μm, at a range of distances from the star. Models are for a solar twin (Kelsall et. al. 1998) in various cases. (1) face-on disk, isotropic scattering, outer radius at 5 AU, albedo =0.2; (2) same disk seen at the median inclination, 60° from face-on; (3) the resulting disk profile using a Hong phase function (forward-scattering) instead of isotropic scattering; (4) the resulting disk assuming 0.07 AU pericenter shift (7× the solar system value).

R (AU)	face-on	+60° incl	+Hong	+Pericenter
-4.92	27.224912	27.125381	27.268370	26.973110
-4.84	26.946017	26.776519	26.936202	26.728681
-4.76	26.756849	26.519609	26.692447	26.569458
-4.68	26.634985	26.351643	26.533004	26.459467
-4.60	26.548928	26.235510	26.422412	26.358045
-4.52	26.467940	26.128134	26.319718	26.264177
-4.44	26.382423	26.010033	26.207425	26.175056
-4.36	26.322455	25.936437	26.136098	26.091286
-4.28	26.254425	25.848631	26.052002	26.011151
-4.20	26.189449	25.765095	25.971523	25.944446
-4.12	26.131180	25.696107	25.904309	25.869314
-4.04	26.068342	25.617798	25.828727	25.803569
-3.96	26.010976	25.550756	25.764030	25.739994
-3.88	25.952312	25.483624	25.698356	25.674421
-3.80	25.893164	25.415693	25.631832	25.602720
-3.72	25.831361	25.342177	25.560462	25.538173
-3.64	25.770354	25.274703	25.494197	25.472730
-3.56	25.709964	25.206930	25.427684	25.406667
-3.48	25.648100	25.138799	25.360645	25.339747
-3.40	25.585504	25.069974	25.292882	25.272159
-3.32	25.522429	25.001545	25.226024	25.207986
-3.24	25.458684	24.934562	25.159587	25.137923
-3.16	25.393005	24.864034	25.089888	25.068192
-3.08	25.324826	24.790786	25.017688	24.996104
-3.00	25.255621	24.717020	24.944623	24.923141
-2.92	25.184237	24.641834	24.870291	24.852158
-2.84	25.112778	24.567650	24.797267	24.776117
-2.76	25.038099	24.489410	24.719593	24.698558
-2.68	24.961549	24.409545	24.640388	24.619885
-2.60	24.883486	24.329455	24.560891	24.538545
-2.52	24.803642	24.246340	24.478355	24.455290
-2.44	24.720431	24.161483	24.394397	24.369695
-2.36	24.635995	24.073736	24.307399	24.281129
-2.28	24.546382	23.981604	24.215806	24.190787
-2.20	24.455221	23.889072	24.124293	24.098751
-2.12	24.359801	23.792446	24.028048	24.001812
-2.04	24.260369	23.691059	23.927157	23.900415

R (AU)	face-on	+60° incl	+Hong	+Pericenter
-1.96	24.157998	23.587604	23.824653	23.796181
-1.88	24.050586	23.478242	23.715818	23.687165
-1.80	23.940436	23.366755	23.605419	23.574654
-1.72	23.822328	23.247552	23.486634	23.456282
-1.64	23.703298	23.126753	23.366939	23.333074
-1.56	23.575666	22.999336	23.240145	23.202434
-1.48	23.440528	22.863152	23.104868	23.067044
-1.40	23.298883	22.720744	22.963639	22.925412
-1.32	23.147050	22.567989	22.812039	22.773425
-1.24	22.988493	22.409534	22.654866	22.614119
-1.16	22.815569	22.237193	22.483752	22.439423
-1.08	22.632758	22.054059	22.302032	22.255876
-1.00	22.435848	21.856647	22.105982	22.055910
-0.92	22.229401	21.648691	21.900427	21.838270
-0.84	22.000663	21.420758	21.674783	21.606300
-0.76	21.742494	21.163424	21.420713	21.344482
-0.68	21.468400	20.893439	21.149920	21.069577
-0.60	21.150440	20.578417	20.838874	20.748250
-0.52	20.786928	20.219298	20.484774	20.381071
-0.44	20.362577	19.801986	20.074374	19.953311
-0.36	19.853172	19.304806	19.586902	19.442006
-0.28	19.216163	18.690374	18.987069	18.807787
-0.20	18.365318	17.888244	18.208083	17.975083
-0.12	17.082689	16.729225	17.087139	16.845899
-0.040	15.085110	14.940984	15.419003	14.699244
0.040	15.085110	14.940984	15.419003	14.951688
0.12	17.082689	16.729225	17.087139	17.359124
0.20	18.365318	17.888244	18.208083	18.405519
0.28	19.216163	18.690374	18.987069	19.143326
0.36	19.853172	19.304806	19.586902	19.715984
0.44	20.362577	19.801986	20.074374	20.184044
0.52	20.786928	20.219298	20.484774	20.579870
0.60	21.150440	20.578417	20.838874	20.922849
0.68	21.468400	20.893439	21.149920	21.224955
0.76	21.742494	21.163424	21.420713	21.485849
0.84	22.000663	21.420758	21.674783	21.734253
0.92	22.229401	21.648691	21.900427	21.956679
1.00	22.435848	21.856647	22.105982	22.165089
1.08	22.632758	22.054059	22.302032	22.353614
1.16	22.815569	22.237193	22.483752	22.530423
1.24	22.988493	22.409534	22.654866	22.697727
1.32	23.147050	22.567989	22.812039	22.853983
1.40	23.298883	22.720744	22.963639	23.001252
1.48	23.440528	22.863152	23.104868	23.141010
1.56	23.575666	22.999336	23.240145	23.273948

R (AU)	face-on	+60° incl	+Hong	+Pericenter
1.64	23.703298	23.126753	23.366939	23.401024
1.72	23.822328	23.247552	23.486634	23.521887
1.80	23.940436	23.366755	23.605419	23.637824
1.88	24.050586	23.478242	23.715818	23.745848
1.96	24.157998	23.587604	23.824653	23.852786
2.04	24.260369	23.691059	23.927157	23.954339
2.12	24.359801	23.792446	24.028048	24.053744
2.20	24.455221	23.889072	24.124293	24.149469
2.28	24.546382	23.981604	24.215806	24.240649
2.36	24.635995	24.073736	24.307399	24.330569
2.44	24.720431	24.161483	24.394397	24.417428
2.52	24.803642	24.246340	24.478355	24.502366
2.60	24.883486	24.329455	24.560891	24.584357
2.68	24.961549	24.409545	24.640388	24.664195
2.76	25.038099	24.489410	24.719593	24.741210
2.84	25.112778	24.567650	24.797267	24.817875
2.92	25.184237	24.641834	24.870291	24.893027
3.00	25.255621	24.717020	24.944623	24.966797
3.08	25.324826	24.790786	25.017688	25.036928
3.16	25.393005	24.864034	25.089888	25.108536
3.24	25.458684	24.934562	25.159587	25.178684
3.32	25.522429	25.001545	25.226024	25.248295
3.40	25.585504	25.069974	25.292882	25.316249
3.48	25.648100	25.138799	25.360645	25.383709
3.56	25.709964	25.206930	25.427684	25.450328
3.64	25.770354	25.274703	25.494197	25.516568
3.72	25.831361	25.342177	25.560462	25.583184
3.80	25.893164	25.415693	25.631832	25.648914
3.88	25.952312	25.483624	25.698356	25.722476
3.96	26.010976	25.550756	25.764030	25.788713
4.04	26.068342	25.617798	25.828727	25.854252
4.12	26.131180	25.696107	25.904309	25.932500
4.20	26.189449	25.765095	25.971523	25.999977
4.28	26.254425	25.848631	26.052002	26.082460
4.36	26.322455	25.936437	26.136098	26.168732
4.44	26.382423	26.010033	26.207425	26.260934
4.52	26.467940	26.128134	26.319718	26.359742
4.60	26.548928	26.235510	26.422412	26.495057
4.68	26.634985	26.351643	26.533004	26.616612
4.76	26.756849	26.519609	26.692447	26.845079
4.84	26.946017	26.776519	26.936202	27.151113
4.92	27.224912	27.125381	27.268370	28.287927

Appendix 1.C References

Anders, E. Pre-biotic organic matter from comets and asteroids. *Nature* **342**, 255 (1989).

Backman, D. E. Caroff, L. J., Sandford, S. A. & Wooden, D. H. 1998, Exozodiacal Dust Workshop: Conference Proceedings

Beaulieu, J.-P.et.al. Discovery of a cool planet of 5.5 Earth masses through gravitational microlensing. *Nature* **439**, 437-440 (2006).

Becker, R. H. et al., Evidence for Reionization at z~6: Detection of a Gunn-Peterson Trough in a z=6.28 Quasar, *Ap. J.*, **122**, 2850-2857 (2001)

Berlind, A. A. and Weinberg, D. H., The Halo Occupation Distribution:Toward an Empirical Determination of the Relation between Galaxies and Mass, *Ap. J.,* **575**, 587 (2002).

Berndt, M.E., Allen, D.E., and Seyfried, W.E. Reduction of CO_2 during serpentinization of olivine at 300°C and 500 bar. *Geology* **24**, 351-354 (1996).

Blank, J. G., Miller, G. H., Ahrens, M.J., and Winans R. E. Experimental shock chemistry of aqueous amino acid solutions and the cometary delivery of prebiotic compounds. *Origins Life Evol. Biosph.* **31**, 15-51 (2001).

Brandeker, A. Liseau, R., Olofsson, G. & Fridlund, M. et al. 2004, *Astron. Astrophys.*, **418**, 681

Bryden G. et al. 2005, astro-ph/0509199

Burrows, A., Sudarsky, D., and Hubbard, W.B., A theory for the radius of the transiting giant planet HD 209458b, *Ap. J.* **594**, 545-551 (2003).

Burrows, A., Sudarsky, D., and Hubeny, I., Spectra and diagnostics for the direct detection of wide-separation extrasolar giant planets, *Ap. J.* **609**, 407-416 (2004).

Butler P., Vogt S., Marcy G., Fischer D., Wright J., Henry G., Laughlin G. & Lissauer J. A Neptune-Mass Planet Orbiting the Nearby M Dwarf GJ 436, *Ap. J. Lett.* **617**, 580 (2004).

Carr, M.H. Recharge of the early atmosphere of Mars by impact-induced release of CO_2. *Icarus* **79**, 311-327 (1989).

Catling, D.C., Zahnle, K.J., and McKay, C.P. Biogenic methane, hydrogen escape, and the irreversible oxidation of early Earth. *Science* **293**, 839-843 (2001).

Chambers, J. E., Wetherill, G. W., and Boss, A. P. The stability of multi-planet systems. *Icarus* **119**, 261-268 (1996).

Chauvin, G., Lagrange, A.-M., Dumas, C., Zuckerman, B., Mouillet, D., Song, I., Beuzit, J.-L., and Lowrance, P., *Astron. Astrophys.* **425**, L29 (2004).

Chiang E. I. & Goldreich, P. 1997, *Ap. J.*, **490**, 368

Clark, R. N. and McCord, T. B. Jupiter and Saturn - near-infrared spectral albedos. *Icarus* **40** 180-188 (1979).

Dalal, N., Hennawi, J. F., and Bode, P. Noise in Strong Lensing Cosmography, *Ap.J.*, **622**, 99-105.

Dekany, R. et al. 2005, submitted to PASP.

Dermott, S.F., Jayaraman, S., Xu, Y. L., Gustafson, B.Å.S. and Liou, J.-C. 1994, *Nature* **369**, 719

Des Marais, D.J. *et al.* Remote sensing of planetary properties and biosignatures on extrasolar terrestrial planets. *Astrobiology* **2**, 153-181 (2002).

Dole, S.H. *Habitable Planets for Man.* Blaisdell Publishing, New York, 158 pp (1964).

Farley, K.A.,Extraterrestrial helium in seafloor sediments: identification, characteristics, and accretion rate over geologic time, in Peucker-Ehrinbrink, B., and Schmitz, B., eds., *Accretion of Extraterrestrial Matter Throughout Earth's History*, Kluwer, New York, p. 179-204 (2001).

Farquhar, J., Bao, H., and Thiemans, M. Atmospheric influence of Earth's earliest sulfur cycle. *Science* **289**, 756-758 (2000).

Forget, F. and Pierrehumbert, R.T. Warming early Mars with carbon dioxide clouds that scatter infrared radiation. *Science* **278**, 1273-1276 (1997).

Formisano, V., Atreya, S., Encrenaz, T., Ignatiev, N., and Giuranna, M. Detection of methane in the atmosphere of Mars. *Science* **306**, 1758-1761 (2004).

Freedman, W. L., et al., Final Results from the Hubble Space Telescope Key Project to Measure the Hubble Constant,*Ap. J.* **553**, 47-72 (2001).

Gladman, B. Dynamics of systems of two close planets. *Icarus* **106**, 247-263 (1993).

Goode, P.R. *et al.* Earthshine observations of the Earth's reflectance. *Geophys. Res. Lett.* **28**, 1671-1674 (2001).

Goody, R.M. and Yung, Y.L. *Atmospheric Radiation: Theoretical Basis.* Oxford University Press, New York (1989).

Gough, D.O. Solar interior structure and luminosity variations. *Solar Phys.* **74**, 21-34 (1981).

Grun, E., Zook, H. A., Fechtig, H. & Giese, R. H., *Icarus* **62**, 244 (1985).

Guyon, O. Phase-induced amplitude apodization of telescope pupils for extrasolar terrestrial planet imaging. *Astron. Astrophys.* **404**, 379-387 (2003).

Hart, M.H. Habitable zones around main sequence stars. *Icarus* **37**, 351-357 (1979).

Hart, M.H. The evolution of the atmosphere of the Earth. *Icarus* **33**, 23-39 (1978).

Holland, H. D. Early Proterozoic atmospheric change. In *Early Life on Earth*, S. Bengtsson, ed., p. 237-244, New York, Columbia Univ. Press (1994).

Hong, S. S., *Astron. Astrophys.* **146**, 67 (1985).

Hu, W. Dark Energy Probes in the Light of the CMB. In *Observing Dark Energy*, S. Wolff and T. Lauer, eds, ASP Conference Series 339, 215-234 (2005).

Ingersoll, A.P. The runaway greenhouse: A history of water on Venus. *J. Atmos. Sci.* **26**, 1191-1198 (1969).

Jakosky, B.M. and Phillips, R.J. Mars' volatile and climate history. *Nature* **412**, 237-244 (2001).

Joshi, M. Climate model studies of synchronously rotating planets. *Astrobiology* **3**, 415-427 (2003).

Joshi, M.M., Haberle, R.M., and Reynolds, R.T. Simulations of the atmospheres of synchronously rotating terrestrial planets orbiting M dwarfs: Conditions for atmospheric collapse and the implications for habitability. *Icarus* **129**, 450-465 (1997).

Kalas, P., Graham, J.A., and Clampin, M. *Nature* **435**, 1067 (2005).

Karkoschka, E. Spectrophotometry of the jovian planets and Titan at 300- to 1000-nm wavelength: the methane spectrum. *Icarus* **111**, 174-192 (1994).

Kass, D.M. and Yung, Y.L. Loss of atmosphere from Mars due to Solar Wind-Induced Sputtering. *Science* **268**, 697-699 (1995).

Kasting, J.F. and Catling, D. Evolution of a habitable planet. *Ann. Rev. Astron. Astrophys.* **41**, 429-463 (2003).

Kasting, J.F. CO_2 condensation and the climate of early Mars. *Icarus* **94**, 1-13 (1991).

Kasting, J.F. Earth's early atmosphere. *Science* **259**, 920-926 (1993).

Kasting, J.F. Habitable zones around low mass stars and the search for extraterrestrial life. *Origins of Life* **27**, 291-307 (1997).

Kasting, J.F., Whitmire, D.P., and Reynolds, R.T. Habitable zones around main sequence stars. *Icarus* **101**, 108-128 (1993).

Kelley, D. S.et. al. A serpentinite-hosted ecosystem: the Lost City hydrothermal vent field. *Science* **307**, 1428-1434 (2005).

Kelley, D. S.et. al. An off-axis hydrothermal vent field near the Mid-Atlantic Ridge at 30ºN. *Nature* **412**, 145-149 (2001).

Kelsall, T. et al., The COBE Diffuse Infrared Background Experiment Search for the Cosmic Infrared Background. II. Model of the Interplanetary Dust Cloud, *Ap. J.* **508**, 44 (1998).

Kharecha, P. K., Kasting, J. F., and Siefert, J. L. A coupled atmosphere-ecosystem model of the early Archean Earth, *Geobiology* **3**, 53-76 (2005).

Krasnopolsky, V.A., Maillard, J.P., and Owen, T.C. Detection of methane in the martian atmosphere: evidence for life? *Icarus* **172**, 537-547 (2004).

Kuchner, M. A minimum-mass extrasolar nebula, *Ap. J.*, **612**, 1147-1151 (2004).

Kuchner M. J. & Holman, M. J., *Ap. J.* **588**, 1110 (2003)

Laskar, J. Large-scale chaos in the solar system. *Astron. Astrophys.* **287**, L9-L12 (1994).

Lodders, K. Solar System Abundances and Condensation Temperatures of the Elements, Circumstellar Debris Disks and Planet Formation

Lovelock, J.E. A physical basis for life detection experiments. *Nature* **207**, 568-570 (1965).

Lunine, J.I. *Astrobiology: A Multidisciplinary Approach.* Pearson/Addison-Wesley, San Francisco (2005).

Malhotra, S., and Rhoads, J.E. Luminosity Functions of Ly Emitters at Redshitfs z=6.5 and z=5.7: Evidence against Reionization at z<=6.5, *Ap. J.* **617**, 5 (2004)

Marcy, G. W. and Butler, R. P. Detection of extrasolar giant planets, *Ann. Rev. Astron. Astrophys.* **36**, 57-97 (1998).

Marcy, G., Butler, R. P., Fischer, D., Vogt, S., Wright, J. T., Tinney, C. G., and Jones, H. R. A., Observed properties of exoplanets: masses, orbits, and metallicities, *Prog. Theoret. Phys. Supp.* **158**, 1-19 (2005).

Marley, M., Fortney, J., Seager, S., and Barman, T. (2006) Atmospheres of Extrasolar Giant Planets, in Protostars and Planets V, in press.

Marley, M. S., Gelino, C., Stephens, D., Lunine, J.I., & Freedman, R. (1999) Reflected Spectra and Albedos of Extrasolar Giant Planets. I. Clear and Cloudy Atmospheres., *The Astrophysical Journal*, Volume **513**, Issue 2, pp. 879-893.

Masset, F. S., and Papaloizou, J. C. B., Runaway migration and the formation of hot Jupiters, *Ap J .***588**, 494 (2003).

Mayor, M. and Queloz, D. A Jupiter-mass companion to a solar-type star. *Nature* **378**, 355 (1995).

Meadows, V.S., "Modeling the Diversity of Extrasolar Terrestrial Planets", in Direct Imaging of Exoplanets: Science and Techniques, Proceedings of IAU Coll. 200, C. Aime and F. Vakili, eds. Cambridge University Press, 2006, 10pp, submitted.

Mischna, M.M., Kasting, J.F., Pavlov, A.A., and Freedman, R. Influence of carbon dioxide clouds on early martian climate. *Icarus* **145**, 546-554 (2000).

Mojzsis, S.J. *et al.* Evidence for life on Earth before 3,800 million years ago. *Nature* **384**, 55-59 (1996).

Mumma, M. J., Novak, R. E., DiSanti, M. A., and and Bonev, B. P. A sensitive search for methane on Mars (abstract). 35th Annual DPS Meeting, Monterey, CA (2003).

Olofsson, G., Liseau, R., and Brandeker, A., *Ap. J.* **563** L770 (2001).

Owen, T. Papagiannis, M. D. In *Strategies for Search for Life in the Universe.* Dordrecht, Reidel (1980).

Page, L., et al, Three Year Wilkinson Microwave Anisotropy Probe (WMAP) Observations: Polarization Analysis, A*stro-Ph*, **0603450** (2006).

Pavlov, A. A., Kasting, J. F., and Brown, L. L. UV-shielding of NH_3 and O_2 by organic hazes in the Archean atmosphere. *J. Geophys. Res.* **106**, 23,267-23,287 (2001).

Pavlov, A. A., Kasting, J. F., Brown, L. L., Rages, K. A., and Freedman, R. Greenhouse warming by CH_4 in the atmosphere of early Earth. *J. Geophys. Res.* **105**, 11,981-11,990 (2000).

Peale, S.J. Rotational histories of the natural satellites. In Burns, J.A. (ed.) *Planetary Satellites.* University of Arizona Press, Tucson, AZ (1977).

Peterson, E., Horz, F., and Chang, S. Modification of amino acids at shock pressures of 3.5 to 32 Gpa. *Geochimica et Cosmochimica Acta* **61**, 3937-3950 (1997).

Pierazzo, E. and Chyba, C. F. Amino acid survival in large cometary impacts. *Meteoritics & Planetary Science* **34**, 909-918 (1999).

Pollack, J. B., Hubickyj, O., Bodenheimer, P., Lissauer, J. J., and Greenzweig, Y., *Icarus* **124**, 62-85 (1996).

Pollack, J. B., Kasting, J. F., Richardson, S. M., and Poliakoff, K. The case for a wet, warm climate on early Mars. *Icarus* **71**, 203-224 (1987).

Pollack, J.B. Climatic change on the terrestrial planets. *Icarus* **37**, 479-553 (1979).

Rafikov, R. R., Fast accretion of small planetesimals by protoplanetary cores, *Astron. J.* **128**, 1348-1363, (2004).

Rasool, S.I. and DeBergh, C. The runaway greenhouse and the accumulation of CO_2 in the Venus atmosphere. *Nature* **226**, 1037-1039 (1970).

Rivera, E. J., Lissauer, J. J., Butler, R. P., Marcy, G. W., Vogt, S. S., Fischer, D. A., Brown, T. M., and Laughlin, G., A ~7.5 Earth-mass planet orbiting the nearby star, GJ 876, *Ap. J.* **634,** 625-640 (2005).

Rosing, M.T. ^{13}C-depleted carbon microparticles in >3700-Ma sea-floor sedimentary rocks from West Greenland. *Science* **283**, 674-676 (1999).

Sagan, C., Thompson, W.R., Carlson, R., Gurnett, D., and Hord, C. A search for life on Earth from the Galileo spacecraft. *Nature* **365**, 715-721 (1993).

Segura, A. *et al.* Ozone concentrations and ultraviolet fluxes on Earth-like planets around other stars. *Astrobiol.* **3**, 689-708 (2003).

Segura, A., J. F. Kasting, V. Meadows, M. Cohen, J. Scalo, D. Crisp, R. A. H. Butler, and G. Tinetti, Biosignatures from Earth-like planets around M stars. *Astrobiol.* **5**, 706-725 (2005).

Sigurdsson S., Richer H., Hansen B., Stairs I & Thorsett S. A young white dwarf companion to pulsar B1620-26: evidence for early planet formation, *Science* **301**, 193 (2003).

Sobolev, V.V. *Light Scattering in Planetary Atmospheres.* Pergamon, Oxford (1975).

Solomon, S.C. and Head, J.W. Fundamental issues in the geology and geophysics of Venus. Science **252**, 252-260 (1991).

Sudarsky, D., Burrows, A. and Hubeny, I., Theoretical spectra and atmospheres of extrasolar giant planets, *Ap. J.* **588**, 1121-1148 (2003).

Tinetti, G., V. Meadows, D. Crisp, W. Fong, H. Snively, Disk-averaged synthetic spectra of Mars, *Astrobiology* **5**(4), 461-482, (2005)

Tinetti, G., V. Meadows, D. Crisp, W. Fong, E. Fishbein, T. Velusamy, M. Turnbull Detectability of planetary characteristics in disk-averaged spectra I: the Earth model", *Astrobiology* **6**, 34-47 (2006).

Walker, J.C.G., Hays, P.B., and Kasting, J.F. A negative feedback mechanism for the long-term stabilization of Earth's surface temperature. *J. Geophys. Res.* **86**, 9776-9782 (1981).

Wolszczan A. and Frail D. A Planetary System around the millisecond pulsar PSR1257+12, *Nature* **255**, 145 (1992).

Wyatt, M. C., Dermott, S. F., Telesco, C. M., Fisher, R. S., Grogan, K., Holmes, E. K., & Piña, R. K. 1999, *Ap. J.* **527**, 918

Wyatt, M. C., Dermott, S. F., Telesco, C. M., Fisher, R. S., Grogan, K., Holmes, E. K., & Piña, R. K. 1999, *Ap. J.* **527**, 918

Wyatt, S. P., & Whipple, F. L., *Ap .J* **111**, 134 (1950).

Zakamska, N. L. and Tremaine, S., Excitation and propagation of eccentricity disturbances in planetary systems, *Astron. J.* **128**, 869 (2004).

Zapolsky, H.S. & Salpeter, E. E. The mass-radius relation for cold spheres of low mass. *Ap. J.* **158**, 809-813 (1969).

Appendix 1.D Alternative Form of Mission Requirements

In working through the Design Reference Mission for *TPF-C*, R. Brown proposed an alternative formulation for requirements 1-4 (Section 1.4.4). These requirements have not been discussed in detail by the STDT, but they may go at least part way towards removing the ambiguities noted in Section 1.4.4.

I.   *TPF-C* must have an excellent chance (>95%) of detecting 30 planets in three years of continuous searching operations, under the following assumptions:

A1. The area of the planetary disk is pi times the square of the Earth radius.

A2. The geometric albedo is 0.2.

A3. The phase function is Lambertian

A4. The semimajor axis is a random variable drawn from a probability distribution that is uniform over the range 0.75 to 1.8 AU and zero otherwise.

A5. The orbital eccentricity is a random variable drawn from a probability distribution that is uniform over the range 0 to 0.1 and zero otherwise.

A6. The pole of the orbit is a random variable uniformly distributed on the celestial sphere.

A7. Every star has one such planet initially located in its orbit at a random mean anomaly.

A8. The total background surface brightness due to zodiacal lights is four times 23rd magnitude per sq. arcsec.

II.   *TPF-C* must have an excellent chance (>U%) of differentiating between background confusion sources and a random detected planet (satisfying assumptions A1-6), before the chance of the planet becoming unobservable (undetectable or unviewable according to solar avoidance) is greater than V%.

III.   *TPF-C* must have an excellent chance (>W%) of determining the orbit of a detected planet (satisfying assumptions A1-6) to an accuracy sufficient to determine whether or not the orbit is or is consistent with A4-5 at a confidence level of X%.

IV.   *TPF-C* must have an excellent chance (>Y%) of predicting the observability of a detected planet (satisfying assumptions A1-6) at a time more than 6 months in advance with a success probability greater than Z%.

Percentages U, V, W, X, Y, and Z remain to be specified.

Appendix 1.E. The Previous Science Requirements for TPF (2004)

1.E.1 Historical Context

The second Science Working Group (SWG) for Terrestrial Planet Finder (*TPF*) was competitively selected and chartered by NASA Headquarters in fall 2002. The TPF-SWG met approximately quarterly for two years until it was dissolved in fall 2004. The TPF-SWG studied the scientific foundations of both the interferometer and coronagraph versions of TPF. Based on the 2002 industry studies of multiple options for TPF, the 2002 DesMarais report on *TPF* science in the visible and infrared, the January 2004 Presidental Vision statement, and the SWG's informal findings, in spring 2004 NASA decided to pursue the two leading types of TPF, the coronagraph and interferometer.

The final study product of the TPF-SWG was a single Science Requirements Document (SRD) for the combined TPF-C and TPF-I missions. This document, the first SRD for TPF, is published here for the first time. This SRD was the basis on which subsequent committees were formed in late 2004 to study the dual missions. The coronagraph committee, the present STDT, used the first SRD as the starting point for its own second SRD, this one specifically focusing on the coronagraph, as presented in the initial sections of the present Report. The first SRD was also the basis on which the *TPF* Project engineers and scientists designed the first version of a coronagraphic telescope system, the design known as Flight Baseline 1 (FB-1), which is presented in detail in other sections of the present volume.

In this Appendix we present the first SRD. Its content was developed during extensive discussions among the full SWG. A subcommittee of the SWG (members Jonathan Lunine, Sara Seager and Wesley Traub) tracked these discussions and iteratively produced a distilled executive summary published herein, all of which was approved in detail by the full SWG.

The reader will notice that there is much in common between the first and second SRDs. The main exception is that the first SRD focused on maximizing the *expected completeness* in a search for Earth-like planets, whereas the second SRD focuses on maximizing the *expected number of detections* of Earth-like planets.

The members of the second TPF-SWG (2002-2004) are listed below.

Dana Backman, Franklin and Marshall College
Charles Beichman, Jet Propulsion Laboratory
Robert Brown, Space Telescope Science Institute
Chris Burrows, Metajiva Corp.
William Danchi, Goddard Space Flight Center
Malcolm Fridlund, European Space Agency
Eric Gaidos, University of Hawaii
Phillip Hinz, University of Arizona
Kenneth Johnston, United States Naval Observatory
Marc Kuchner, Harvard-Smithsonian Center for Astrophysics
Douglas Lin, University of California, Santa Cruz
Jonathan Lunine, University of Arizona

Victoria Meadows, Jet Propulsion Laboratory
Gary Melnick, Harvard-Smithsonian Center for Astrophysics
Bertrand Mennesson, Jet Propulsion Laboratory
David Miller, Massachusetts Institute of Technology
Martin (Charley) Noecker, Ball Aerospace Corp
Sara Seager, Carnegie Institution of Washington
Eugene Serabyn, Jet Propulsion Laboratory
William Sparks, Space Telescope Science Institute
David Spergel, Princeton University
Wesley Traub, Harvard-Smithsonian Center for Astrophysics
John Trauger, Jet Propulsion Laboratory
Ted von Hippel, University of Texas
Neville Woolf, University of Arizona

1.E.2 *TPF* 2004 Science Requirements

Goals of TPF. The goals of the Terrestrial Planet Finder (*TPF*) mission are to detect directly and characterize Earth-like planets around nearby stars. The direct detection goal implies that *TPF* must separate planet light from starlight. The characterization goal implies that *TPF* must determine the type of planet, its gross physical properties and its main atmospheric constituents, allowing an assessment of the likelihood that life or habitable conditions exist there.

We estimate the number of planets *TPF* should find using simple and reasonable assumptions. *These goals and assumptions lead to the following requirements.*

Minimum and Full Missions. To allow a range of technical solutions and fiscal constraints, the initial planning must include a scientifically minimum mission, and the scientifically preferred, full mission.

Terrestrial Planet Definition. Considering the radii and albedos or effective temperatures of solar system planets, *TPF* must be able to detect terrestrial planets different from our own, down to a minimum terrestrial planet defined as having 1/2 Earth surface area, Earth albedo or the equivalent equilibrium effective temperature, and at visible wavelengths the phase function of a Lambertian sphere.

Orbit Phase Space. The distribution of orbital elements of terrestrial type planets is presently unknown, but observations suggest that giant planet orbits are distributed roughly equally in semi-major axis, and in eccentricity up to those of the solar system planets and larger. Therefore *TPF* must be designed to search for planets drawn from uniform probability distributions in semi-major axis over the range 0.7 to 1.5 AU and in eccentricity over the range 0 to 0.35, with the orbit pole uniformly distributed over the celestial sphere with random orbit phase.

Types of Stars. On astrophysical grounds, Earth-like planets should be found around stars that are roughly similar to the sun. Therefore *TPF* target stars should include main sequence F, G, and K stars that are at least 1 Gyr old.

Number of Stars to Search. We require the minimum mission to search at least 35 *core stars*, and the full mission to search at least 165 stars (35 core stars plus 130 *additional stars*).

Extended Number of Stars. We desire to search as many stars as possible, beyond the required core and additional star groups. We anticipate that any mission capable of satisfying the requirements will also be capable of searching many more stars if the requirements are relaxed. Therefore we desire that the mission search an *extended group of stars* defined as those systems *of any type* in which all or part of the continuously habitable zone (see below) can be searched.

Search Completeness. Search completeness is defined as that fraction of planets in the orbital phase space that could be found within instrumental and mission constraints. We require each core stars to be searched at the 90% completeness level for both the minimum and full *TPF* missions. For the additional stars in the full mission, the required 90% completeness is integrated over the additional stars.

Expected Number of "Earths". To obtain a statistically significant number of planets over as wide a range of assumptions as possible, within limits of time and instrumentation, *TPF* must search both deep and wide. Since *TPF* will be the first mission designed to directly detect terrestrial planets, the frequency of terrestrial planets will probably not be known until *TPF* measures it. For the Sun, this number is 3. For a typical nearby star, based on current knowledge of giant planets as well as theory, the best current estimate of this number is of order 0.1. For the minimum *TPF* and full *TPF* missions the number of stars and completeness requirements lead to an expectation value for the number of detections of, respectively, 3 and 15 terrestrial planets.

Habitable Zone. *TPF* should search the most likely range as well as the complete range of temperatures within which life may be possible on a terrestrial type planet. In the Solar System, the most likely zone is near the present Earth, and the full zone is the range between Venus and Mars. The habitable zone (HZ) is defined as the range of semi-major axes from 0.7 to 1.5 AU scaled by the square root of stellar luminosity. The minimum terrestrial planet must be detectable at the outer edge of the HZ. The continuously habitable zone (CHZ) is defined similarly, from 0.9 to 1.1 AU.

Spectral Range. The required spectral range of *TPF* is 0.5 to 0.8 micron in the visible and 6.5 to 13 microns in the infrared. The desired ranges are 0.5 to 1.05 micron and 6.5 to 17 microns.

Color. Colors distinguish planets from other objects. *TPF* must use color to characterize the type of planet and to measure its gross properties, including effective temperature at mid-IR wavelengths. Reference colors and relative magnitudes are those of Venus, Earth, Mars, and Jupiter. *TPF* must measure planet color in 3 or more bands (wavelengths and bandwidth

TBD), to an accuracy of 10%, for any detected planet. We require that the ratio of color-characterized planets to all detected planets have an expectation value of at least 50%.

Spectrum. *TPF* must use the spectrum of a planet to characterize its surface and atmosphere. The spectrum of the present Earth, scaled for semi-major axis and star luminosity, must be used as a reference. The required spectral resolution is 70 in the visible and 20 in the infrared. *TPF* must measure O_2, H_2O, and O_3 in the visible and H_2O and O_3 in the infrared. In this context, a measurement of a species is defined as the determination of the equivalent width of a spectral feature of that species to 20% accuracy. We desire to *TPF* measure Rayleigh scattering, photosynthetic pigments, CO_2, and CH_4 in the visible and CO_2 as well as CH_4 in the infrared. The desired spectral resolutions are 2 times the required values.

Characterization Completeness. It will be difficult to obtain spectra of the fainter or less well positioned planets. We require that the ratio of spectrally-characterized planets to all detected planets have an expectation value of at least 50%.

Giant Planets. The occurrence and properties of giant planets may determine the environments of terrestrial planets. We require the *TPF* field of view and sensitivity must be sufficient to detect a giant planet with the radius and geometric albedo or effective temperature of Jupiter at 5 AU (scaled by the square root of stellar luminosity) around at least 50% of its target stars. A signal-to-noise ratio of at least 5 is required.

Exozodiacal Dust. Determining and understanding the properties of the zodiacal cloud is essential to understanding the formation, evolution, and habitability of planetary systems. *TPF* must be able to detect planets in the presence of zodiacal clouds at levels up to 10 times the brightness of the zodiacal cloud in the solar system. As a goal, *TPF* should be able to determine the spatial and spectral distribution of zodiacal clouds with at least 0.1 times the brightness of the solar system zodiacal cloud.

Visitations. Multiple visits per star may be required to achieve completeness or to study a planet along its orbit, to determine its orbit, distinguish it from background objects, and validate a measurement. Therefore *TPF* must make enough visits to meet the completeness and other requirements.

Minimum Mission Scope Summary. The minimum *TPF* must be able to detect planets with half the area of the Earth, and the Earth's geometric albedo, searching the entire HZ of the core-group stars with 90% completeness per star. Flux ratios must be measured in 3 broad wavelength bands, to 10% accuracy, for at least 50% of the detected terrestrial planets. The spectrum must be measured—for at least 50% of the detected terrestrial planets—to give the equivalent widths of O_2, H_2O, and O_3 in the visible or H_2O, and O_3 in the infrared to an accuracy of 20%.

Full Mission Scope Summary. The full *TPF* must be able to detect planets with half the area of the Earth, with Earth's geometric albedo, searching the entire HZ of the 35 core-group stars plus the aggregated HZs of at least 130 additional stars with 90% completeness for both groups. Flux ratio must be measured in 3 broad wavelength bands to 10% accuracy for at least 50% of the detected terrestrial planets. The spectrum must be measured—for at

least 50% of the detected terrestrial planets—to give the equivalent widths of O_2, H_2O, and O_3 in the visible or H_2O, and O_3 in the infrared to an accuracy of 20%. Further, we desire that the mission search an *extended group of stars* defined as those systems *of any type* in which all or part of the CHZ can be searched.

Other constraints: Other than those specified above or in the table which follows, no other properties (e.g. metallicity or variability) of stars should be used to impose requirements on the *TPF* mission. "True wisdom is to know what is best worth doing *and* to do what is best worth doing" (Edward Porter Humphrey).

Table 1.E-0-1 Summary of Previous *TPF* Science Requirements (2004)

Key Parameter	Minimum TPF	Full TPF
Star types	F through K	F through K
Habitable Zone	0.7 to 1.5 AU scaled $L^{0.5}$	0.7 to 1.5 AU scaled $L^{0.5}$
Orbit Phase space	semi-major axis: uniform inclination: uniform eccentricity: 0-0.35	semi-major axis: uniform inclination: uniform eccentricity: 0-0.35
Number of stars to be searched	35 core stars	165 additional stars
Completeness per core star	90%	90%
Completeness per set of additional stars	N/A	90% integrated over the ensemble
Minimum planet area	1/2 Earth area	1/2 Earth area
Geometric albedo	Earth	Earth
Flux ratio	at least 3 broad wavelength bands;	at least 3 broad wavelength bands
Spectral range	0.5-0.8 [0.5-1.05]μm; 6.5-13 [6.5-17] μm	0.5-0.8 [0.5-1.05]μm 6.5-13 [6.5-17] μm
Characterization completeness	50%	50%
$\eta_\oplus$	0.1	0.1
Expected number of planets given above requirements	3	15
Giant planets	Jupiter brightness at 5 AU, 50% of stars	Jupiter brightness at 5 AU, 50% of stars
Maximum tolerable mean exo-zodi	10 zodi	10 zodi

2.0 Design Reference Mission

2.1 Introduction

The STDT has conducted a variety of theoretical studies of the *TPF-C* mission, which have been reported in publications or distributed as technical reports. These documents include two "design reference missions" (DRMs). Table 2.1-1 provides a bibliography. The unpublished documents form a volume of the STDT report.

To date, the four purposes of *TPF-C* mission studies have been:
(1) To explore the range of parameters for which the current design concept can robustly perform its intended research. We want to understand the correct scale of the mission.
(2) To identify systematic effects that may shape or constrain the science of *TPF-C*. We want to know what selection effects need to be compensated, calibrated, or further investigated to reduce risk or alleviate concern.
(3) To reveal the essential character of science operations for *TPF-C*. We want to develop the mission taking ground operations and the scientific process fully into account.
(4) To develop the relationships between the science programs of TPF-C and other missions, particularly the *Space Interferometry Mission* (*SIM*). We want to fully exploit the synergism inherent in complementary data sets.

This overview of mission studies for *TPF-C* includes key concepts, major findings, and issues left unresolved in spring 2006, at the time of the final report of the STDT.

Table 2.1-1 Bibliography of mission studies for *TPF-C*

	Short Reference	*Long Reference*	*Appendix*
1	Brown 2004a	Brown, R. A. 2004, "Obscurational completeness," ApJ 607:1003–1013.	
2	Brown 2004b	Brown, R. A. 2004, "New information from radial velocity data sets," ApJ 610: 1079–1092.	
3	Brown 2005	Brown, R. A. 2005, "Single-visit photometric and obscurational completeness," ApJ 624, 1010–1024.	
4	Kasdin 2006	N. J. Kasdin & I. Braems, "Linear and Bayesian Planet Detection Algorithms for the Terrestrial Planet Finder," ApJ 646 (Aug 2006)	
5	Brown 2006a	Brown, R. A. 2006, "Expectations for the early TPF-C mission," in IAUC 200, Direct Imaging of Exoplanets: Science and Techniques, eds. C. Aime & F. Vakili, (Cambridge: Cambridge Univ. Press), in press.	MS-1
6	Hunyadi et al. 2006a	Hunyadi, S. L., Shaklan, S. B. & Brown, R. A. 2006, "Single-visit completeness optimization," ApJ submitted.	MS-2
7	Hunyadi et al. 2006b	Hunyadi, S. L., Shaklan, S. B. & Brown, R. A. 2006, "Program completeness," ApJ in preparation.	MS-3
8	Brown 2006b	Brown, R. A. 2006, "Differentiating extrasolar planets	MS-4

		from background confusion by apparent motion," technical report.	
9	Brown 2006c	Brown, R. A. 2006, "Chasing Earth-like planets," in the STScI 2005 Annual Report, pp. 24-26.	MS-5
10	Brown 2006d	Brown, R. A., 2006, "On orbit determination with *TPF-C*," technical report.	MS-6
11	Brown 2006e	Brown, R. A. 2006, "Design reference mission for *TPF-C,"* briefing to STDT, March 14, 2006.	MS-7
12	Heap 2006	Heap, S. 2006, "*SIM–TPF-C* synergy," technical report	MS-8
13	DRM2	Heap, S., and Lindler, D. 2006, "A Design Reference Mission for *TPF-C*," technical report.	MS-9
14	DRM1	Brown, R. A., Hunyadi, S. L., & Shaklan, S. B. 2006, "A DRM for *TPF-C,"* technical report.	MS-10

2.2 Key concepts

The scientific requirements of *TPF-C* are sharply focused, well defined, and governed by the simple geometry and physics of planetary motion and photometry. They are therefore subject to quantitative assessment. Searching for planets is remarkably predictable: from a limited set parameters and assumptions, we can estimate the outcome of a searching observation, a series of observations, or even the results of the entire mission. Concepts at the heart of these abilities include *search completeness, signal-to-noise ratio, observational simulations, models,* and *algorithms.*

Search completeness (*C*) is the primary metric for evaluating planet searches. It is defined as the fraction of possible planets that are discoverable by a given instrument and observing protocol. Completenesses add. For example, the total completeness of two searches is equal to the completeness of the first search plus the completeness of the second search as computed for the planets that were obscured or too faint to be detectable by the first search. The *actual* number planets detected by a searching observation—zero or one, assuming the star has either zero or one planet—is a Bernoulli random variable with probability—and expectation value—equal to *C* times η, where η is the occurrence probability of planets. For any star, *C* can be estimated by Monte Carlo techniques, using models of the instrument, the planets of interest, and the observing protocols (Brown 2005).

In the mission studies to date, the signal-to-noise ratio (*SNR*) is built on five concepts.

- The *detection threshold* (SNR_0) is the value of the photon-statistical *SNR* that defines "detection." Typically, it is $SNR_0 = 5$ or 10, computed for a point source. Kasdin & Braems (2006) also includes in his *SNR* formulation a parameter for the probability of missed detection; this serves an equivalent purpose.
- The *limiting delta magnitude* (Δmag_0), which is 2.5 times the $\log_{10}$ of the maximum practical star-planet brightness ratio for detection. Larger Δmag_0 means a fainter planet can be detected.
- The *systematic* or *maximum limiting delta magnitude* ($\Delta mag_{0,max}$), which is set by the optical stability of the instrument (Brown 2005). The limiting delta magnitude Δmag_0 cannot

be more favorable than $\Delta mag_{0,max}$. For terrestrial planet studies, typically we must choose $\Delta mag_{0,max}$ = 25 or 26 magnitudes, (i.e. a planet sensitivity of 0.4-1.0×10^{-10} of stellar brightness).

- The *unit time for searching* (*T*) is the time required to achieve SNR_0 for a source with a specified Δmag_0.

- The *time calculator* comprises the algorithms for computing *SNR* as a function of *T* (or vice versa), given the *V*-magnitude of the star, Δmag_0, the level of zodiacal light, instrumental parameters, and the observational protocol (e.g., the number of roll angles sampled)..

Two types of observational simulation have been performed to evaluate the scientific gain achievable with *TPF-C*. These simulations are built around the Flight Baseline 1 (FB-1) design documented in Chapters 3-5 of this report. The first type comprises simulations to estimate the number of planets detected, verified, and/or characterized—during a set time period, typically one or more years. Such simulations have used *productivity* or *discovery rate* (C/T) to rank-order the target list, then have estimated the yield of planets by totaling the search completeness for the top-ranked stars that are observable in the time period. Unoptimized simulations set $\Delta mag_0 = \Delta mag_{0,max}$ for all stars, whereas optimized simulations remove less productive exposure time from some stars and give it to stars below the unoptimized cutoff rank. This optimization procedure increases total completeness (Hunyadi et al. 2006).

The ability to perform spectroscopy and photometry on the found planet set is a function $\Delta mag_{0,max}$ and the wavelength-dependent inner working angle, IWA. Spectroscopy and photometry require more sensitivity and access to longer wavelengths than detection. Thus planets that can be detected above the noise floor are not necessarily characterizable to the required levels, and over the required bandpass. How the limiting delta magnitude is handled—in particular the tradeoff between control and knowledge of the scattered light near a planet—is of critical importance in determining the mission scale.

The second type of observational simulation comprises studies of selection biases and operational issues using the *detected* or *found subset of planets*. The ability to perform such simulations is a byproduct of studies that estimate completeness. For each star, the Monte Carlo simulations for completeness create random samples of possible detected planets, including knowledge of their orbits and physical characteristics. The properties of the ensemble of possibly detected planets can be studied in detail by computing the future position and brightness of each planet in the sample, as needed.

Observational simulations require models to represent the stars, planets, instrument, and aspects of the observing program—in short, all the assumptions that logically intersect and engage in the *TPF-C* mission. The plasticity of this modeling framework means that the simulations can be readily updated with new information, to incorporate changes to the *TPF-C* design or revisions to the science requirements. In this light, a suite of mission studies or a DRM can be understood as a model in itself—a model of models. DRM1 and DRM2—and indeed, Table 1 as a whole—are examples.

In addition to parametric models, observational simulations require algorithms to compute needed data items, including C, T for both searching and spectroscopy, availability due to the solar-avoidance restriction, ability to disambiguate candidate planets (test for common proper motion), and orbit determination.

Table 2.2-1 lists the parametric models and algorithms related to the bibliography in Table 2.1-1. Future studies will expand and enrich the collection of models and algorithms.

Table 2.2-1. Models and algorithms defined or referenced by DRM1 and/or DRM2

	Model	*References*
1	Stellar qualification	DRM1, DRM2
2	Planets of interest	DRM1, DRM2
3	Instrumental performance	DRM1, DRM2
4	Strategic unknowns	DRM1, DRM2
5	Observational protocols	DRM1, DRM2
6	Rules and restrictions	DRM1
	Algorithm	*References*
1	Completeness	DRM1, DRM2
2	Searching exposure time	MS-3, DRM2, Kasdin 2006
3	Searching exposure time optimization	DRM1, MS-2
4	Spectroscopic exposure time	DRM2
5	Availability	DRM1, MS-4, DRM2
6	Recoverability	DRM1, MS-7(29), Brown 2004b
7	Ability to disambiguate	DRM1, MS-4
8	Orbit determination	MS-6, Brown 2004b

2.3 Studies to date

Three groups—at STScI, JPL, and GSFC—have assembled tool sets for investigating and evaluating the *TPF-C* science mission based on the foregoing concepts. In terms of code, these tool sets are largely independent, and they have been cross-validated to a significant degree. However, the variation of parameters used has been considerable, and the quantities computed have often been different and difficult to compare. Indeed, the science requirements and FB1 had not been finalized during the mission studies. Despite a patchwork of results, we nevertheless have general agreement on the basic logic, concepts, and framework for *TPF-C* mission studies. This is a durable advantage for the future, out of the STDT era.

We now summarize results pertaining to the first purpose of mission studies, to determine the true scale of the *TPF-C* mission. In this context, "scale" combines aperture size (inner working distance, astrometric accuracy), effective area (light gathering power), $\Delta mag_{0,max}$ (limiting sensitivity), and mission duration. There is considerable interdependence among these factors.

All studies conclude that the scale of the FB1 design is right for *detecting* about three Earth-like planets in the habitable zones of nearby stars in a three year observing program, assuming a 10% occurrence rate of such planets. This result is compatible with the planet finding science requirement. However, the result is borderline, not robust. For that reason, this conclusion— and the assumptions on which it is based—should be closely reviewed, both scientifically and technically. Furthermore, because of the following issues, additional mission studies are needed to find a scale of TPF-C that is robustly adequate. The studies also show that the assumed limiting delta magnitude, $\Delta\mathrm{mag}_{0,max}$=26.75, has a serious impact on the ability to meet multi-band photometry and spectroscopy requirements.

A. *The target list of qualified, productive stars for FB1 is thin.* For example, on the most inclusive ranked list, comprising 136 stars (http://sco.stsci.edu/starvault/index.php), the values of C/T for low-ranking stars are typically 50 times lower than those of high-ranking stars, and the values of T are typically 10 times longer. If a good star is removed for any scientific or technical reason, then a bad star must replace it. The impact goes straight to the bottom line, reducing the estimated number of planets found during the mission.

B. *FB1 may not be robust against the strategic unknowns—exozodiacal light, background confusion, and η.* If real exozodi brightness levels are consistent with current upper limits, the values of T will be larger, reducing the yield of planets from the mission. It may be possible to safely ignore background or manage the problem spectroscopically, but we are not yet confident this can be done. The alternative is using the test of common proper motion, which doesn't work for a considerable fraction of stars (Brown 2006b). Upcoming missions e.g. *Kepler* and *COROT* may resolve the issue of η.

C. *A realistic decision-making process for science operations has not yet been developed and tested by simulations.* A tenth of typical planets discovered with FB1 become undetectable in a couple of weeks, either fading with orbital phase or moving inside the IWA. Also, because typical values of T are denominated in days, scheduling decisions must be made quickly and accurately, based on relatively little—and likely ambiguous—information. Inefficiencies will waste time and lose planets.

D. *It difficult to determine orbits or recover planets after the discovery epoch.* After the initial detection, the best time to see the planet again ("recover" it) is immediately. Once it has disappeared, due to brightness or angle, the time to its next appearance is long and very uncertain; and its next appearance may be brief. This problem is worst for higher luminosity stars, where the detectable fraction of the photometric orbit is small and the orbital periods are long (Brown 2006d). If time is wasted on failed recovery attempts, or if high-yield, high-luminosity stars are replaced with low-yield, low luminosity stars to improve orbit determination, the number of planets found during the mission will be reduced.

Increasing the scale of *TPF-C* would ameliorate each of the issues. The true scale of *TPF-C* will be known when these concerns have been retired. Currently available mission modeling tools are adequate to address these questions.

Regarding systematic effects, the problems with planetary recovery, orbit determination, and disambiguation of background confusion by common proper motion have been mentioned. In addition, some selection biases have been identified, but their scientific impacts are not yet known (Brown 2006e p. 35). For example, the completeness for smaller (normalized) semimajor axis is poor for low luminosity stars, and poor for larger semimajor axis for high luminosity stars. We are also concerned about how best to combine technical performance (C/T) with scientific priorities (e.g., metallicity) in the prioritization target stars, to minimize undesirable selection effects.

We are certain that the science operations of *TPF-C* will be radically different from those of a general purpose observatory, like *Hubble*. For exoplanetary research, time—and timing—are of the essence. The observing schedule will be a just-on-time delivery, to take into account the most recent results. Adroitly managing the resource of time through hardware, software, and procedures will be the margin of success for this mission.

A great lesson of *TPF-C* mission studies to date is the power and versatility of observational simulations. Today, they are the accepted basis for evaluating the ability of a mission design to meet the science requirements, and for understanding its scientific strengths and weaknesses.

With respect to *SIM-TPF* synergy, *SIM* will detect planets of interest and measure their orbits well before the *TPF-C* mission. Almost all the planets discovered will be more massive than Earth and many will have contrast and separation amenable to characterization. Thus *TPF-C* will, in the early days of the mission, benefit from *SIM* measurements and characterize planets in known orbits with known masses. *SIM* will also discover more massive planets close to their stars, perhaps indicating low-priority targets not likely to harbor terrestrial planets in the habitable zone.

3.0 *TPF-C* Design Performance Assessment

3.1 Introduction

This section presents the performance assessment of a conceptual *TPF* Coronagraph design that meets the contrast requirements as of January 2005. This is a remarkable conclusion: realistic models predict that the largest telescope ever sent to space, with a monolithic glass mirror, will be able to prepare a starlight wavefront of such exquisite perfection and stability that it can be suppressed by a factor 10^{10}, allowing earth-sized planets to be detected and characterized around more than 30 nearby stars. Our models are still of intermediate fidelity: they embody a very detailed thermal-optical-mechanical design, with realistic material properties and disturbance couplings, but they are still not as accurate as we can expect to achieve in a few years. Even so, they persuasively support a conclusion that was viewed as ridiculously beyond reason less than 10 years ago.

In the last six months, science/mission modeling has significantly advanced, and now clearly outlines a rigorous path from our new formulation of the science requirements (Section 1) to the engineering requirements that support them (Section 3.2). As one might expect, with this new understanding, the FB1 requirements no longer seem quite adequate for the science we are aiming to achieve. However, the gaps are small, and probably require only a modest change in the engineering requirements and design. This reassessment has not been done yet, and should be among the first tasks when *TPF-C* is reinvigorated in coming years.

We had planned to conduct 3 to 4 design cycles in pre-Phase A, each of which would include a greater level of design detail and fidelity. **Flight Baseline 1 (FB1)** described herein is the second of these design iterations. The first cycle, named the **Minimum Mission Design** concept, was completed in 2004 and addressed the minimum science requirements established in 2004 (Appendix 1.E). It attempted to develop, model and analyze a system that could produce contrast adequate to find and characterize planets around 35 nearby stars, with an inner working angle of $3\lambda/D$. The telescope was designed with a 6 m × 3.5 m primary mirror, and the spacecraft included a full conic sun-shade. The Minimum Mission Design cycle established the integrated modeling approach that enabled the team to study observatory environmental perturbations and their effect on the wave front and contrast. The modeling process successfully tied structural, jitter and thermal models to optical performance models. The study calculated contrast performance, related the performance to an operational scenario that predicted the ability to find planets and to explore star habitable zones completely. The Minimum Mission Design, modeling and analysis is fully documented in a report that was completed 22 April 2004 (Levine and White, 2004). Several papers were also published describing the results: Ford et al. (2004), White et al. (2004), Kissil et al. (2004), and Shaklan et al. (2004). The cycle used simple beam models in non-critical areas, and simplified optical analyses, but was successful in demonstrating that a feasible observatory design incorporating a coronagraph system similar to the one represented in the High Contrast Imaging Testbed (HCIT) was thermally and dynamically stable enough to allow detection of earth-sized planets.

In the FB1 cycle, the system tolerances are relaxed by adopting a $4\lambda/D$ inner working angle, an 8 m × 3.5 m primary mirror, and an 8th order occulting mask, while maintaining the 2003 Science Requirements. Several observatory weaknesses discovered during the Minimum Mis-

sion Design analysis cycle were corrected. These included smoothing the sunshade vanes from a set of flat panels into continuous conic shapes, and stiffening the base of the secondary tower. Also, fidelity and detail were improved for thermal and structural models of the secondary mirror assembly, the secondary tower the multi-layer sun shade and its mounting to the spacecraft, and the primary mirror in its thermal enclosure. The model now incorporates radiatively-coupled thermal control of the primary mirror with an "oven" enclosure behind the mirror. Also included are heat loads from electronics, transferred by heat pipes to a passive radiator; and placeholder instruments, with the detectors co-located in a cold zone and cooled using heat pipes and another cold radiator. For the FB1 analysis, key analyses were the system thermal sensitivities, to understand the requirements for an active thermal control system. This work was completed in September 2005, and is described in an interim report (Ford ed. 2005) and several published papers (Blaurock et al, (2005), Kissil et al. (2005), Mouroulis and Shaklan (2005), Shaklan et al. (2005), Smith et al. (2005)).

The goal for the next design cycle, Flight Baseline 2 (FB2), is to increase the fidelity of the flight system still further and to update the science requirements as specified in Section 1 of this document. Significant expected improvements are:

- Incorporating the instruments defined in the Instrument Concept Studies (ICS) as described in Section 4.1.3,
- Defining and analyzing the active thermal control system required to maintain thermal stability of the observatory and
- Providing improvements to the starlight suppression systems to produce a deeper contrast.

Furthermore, several open design trades and alternate concepts identified in FB1 will be evaluated, and the results possibly incorporated into the FB2 design. These alternate concepts are described in Section 4. We envision a fourth and final design iteration to optimize the performance of the integrated end-to-end flight system. FB2 will also be responsive to the new science requirements presented here in Section 1, whereas FB1 was designed to respond to the previous Science Requirement Document (SRD) developed by the *TPF* Science Working Group (2001-03) (see Appendix 1.E). The first SRD focused on completeness requirements as a way of expressing the thoroughness and breadth of the planet search. The current SRD focuses instead on the expected number of planets found. The latter philosophy is more optimistic, maximizing the total number of discoveries rather than "draining the lake" around each star, to find planets or prove they are absent. The current SRD also calls for an expanded bandwidth of 0.5-1.1 μm. Furthermore, recent modeling of the mission planning process and scientific harvest has shown some new areas to emphasize in the engineering requirements (see bibliographic records in Table 2.2-1). While this change in emphasis and understanding impacts the <u>mission design</u> (Section 2), it is expected to have only a modest effect on the <u>observatory system design</u>. The engineering features highlighted and validated for FB1 should still be largely applicable for FB2.

The two main objectives of the FB1 design and analysis presented herein are to verify that the system meets the contrast requirements, thus demonstrating the existence proof of the mission, and to investigate the sensitivity of the performance to various design options such as vibration isolation and active thermal control. We will first present the derived top-level

engineering performance and design requirements needed to achieve a contrast of 7.5×10^{-11} at $4\lambda/D$. We will describe the overall mission concept and operational scenarios, followed by the optical layout for the telescope and coronagraph instrument, and then the mechanical and thermal design for the overall observatory and spacecraft systems. The baseline design is sufficiently detailed to capture the principal performance drivers, such as the conical "V-groove" sunshade architecture that provides adequate thermal stability, and the stowed configuration for shroud clearance Minute details of various sub-assemblies such as the deployment hinge/latch components are not yet included.

For FB1, it is not intended that the instruments or the starlight suppression system be optimized yet. At this stage of mission maturity, it is more important to provide an inclusive system model that captures many components and explores their interrelated effects, to improve our understanding about how to improve the starlight suppression system in the future.

The detailed FB1 starlight suppression system is modeled with many possibly desirable features, such as two complete separate polarization paths, locations for image-plane and pupil-plane masks, filter wheels, and multiple deformable mirrors, and includes Michelson interferometers to adjust both phase and amplitude profiles for each wavefront.

In parallel, the technology development teams have fabricated, measured, and characterized properties of masks that have been included in the optical performance model. Wavelength-dependent effects have been tested in the HCIT. A polarization-splitting Calcite crystal has been added to the HCIT to enable the study of polarization effects. Reflective and transmissive coatings have been modeled and measured. This knowledge has been incorporated in the models that represent the FB1 telescope and starlight suppression system performance, resulting in a much better representation of how the system will actually perform.

We present analyses of the impact of various noise sources and disturbances in the static error budgets. Furthermore, an integrated modeling approach has been implemented to analyze the end-to-end performance of the coronagraph contrast and wavefront errors (WFE) with thermal and jitter disturbances; those results are shown herein. We plan to extend this analysis to actual science simulations of planet signal extraction, but this is not included in this report. Finally, we propose a verification approach that outlines a method by which the system will be integrated and tested prior to launch.

REFERENCES

C. Blaurock, K. Liu, L. Dewell, and J. Alexander, Passive isolator design for jitter reduction in the Terrestrial Planet Finder Coronagraph, Proc. SPIE **5867**, 58670Y (2005)

V. Ford, D. Lisman, S. Shaklan, J. Trauger, T. Ho, D. Hoppe, and A. Lowman, The Terrestrial Planet Finder coronagraph: technology and mission design studies, Proc. SPIE **5487**, 1274 (2004)

V. Ford, ed., TPF Coronagrpah Flight Baseline 1 Design Interim Status Report, August 18, 2005, Jet Propulsion Laboratory, California Institute of Technology, Pasadena California.
http://planetquest.jpl.nasa.gov/documents/TPFC-FB1_Report.pdf

A. Kissil, E. Kwack, T. Ho, A. Liu and C. Blaurock, Structural modeling for the Terrestrial Planet Finder mission, Proc. SPIE **5528**, 10 (2004)

A. Kissil, E. Kwack, T. Ho, P. Dumont, S. Irish, and T Weng, Integrated modeling applied to the Terrestrial Planet Finder mission, Proc. SPIE **5867**, 586710 (2005)

M. Levine, and M. White, Terrestrial Planet Finder Coronagraph Minimum Mission Baseline Design and Analysis report, JPL D-28535, April 22, 2004. Jet Propulsion Laboratory, California Institute of Technology, Pasadena CA

P. Mouroulis and S. Shaklan, Optical design of the Terrestrial Planet Finder Coronagraph starlight suppression system, Proc. SPIE **5874**, 58740J (2005)

S. Shaklan, L. Marchen, F. Shao, R. Peters, T. Ho and B. Holmes, Metrology system for the Terrestrial Planet Finder Coronagraph, Proc. SPIE **5528**, 22 (2004)

S. Shaklan, L. Marchen, J. Green, and O. Lay, The Terrestrial Planet Finder Coronagraph dynamics error budget, Proc. SPIE **5905**, 59050D (2005)

A.. Smith, C. Blaurock, M. Krim, M. Levine, A. Liu, A. Martino, R. Ohl, and J. Pitman, Integration and verification of the Terrestrial Planet Finder coronagraphic observatory , Proc. SPIE **5905**, 59051C (2005)

M. White, S. Shaklan, P. Lisman, T. Ho, et al., Design and performance of the Terrestrial Planet Finder coronagraph, Proc. SPIE **5487**, 1234 (2004)

3.2 Science Derived Requirements

Flow Down

The science requirements are flowed down to observatory and instrument requirements using both analysis and the DRM Monte-Carlo models described in Section 2. Table 3.2-2 highlights the high-level instrument performance requirements, where known. To date, the focus of the DRM studies has been on planet detection. We are still in the process of studying the requirements for orbital parameter determination and spectral characterization.

The planet-to-star brightness ratio is described using stellar-magnitude differences. Contrast and Δmag are related by

$$\Delta\text{mag} = -2.5 \log_{10}(\text{contrast}) \tag{1}$$

For example, if contrast $= 10^{-10}$ then Δmag=25; and every factor 2.51 decrease in contrast will increase Δmag by 1.

Table 3.2-1 defines some specific brightness ratios used in the requirements of Table 3.2-2.

Table 3.2-1 Definition of Δmag used in Requirements

Symbol	Meaning
Δmag_p	Planet-star contrast
Δmag_i	Instrument contrast[a]
Δmag_s	Instrument contrast stability[b]

   [a] per-pixel ratio of scattered starlight at planet
       position vs. star central brightness
   [b] time variations during one observation

Also in Section 2 we introduced "completeness", the degree to which the observations have examined all possible orbits in the habitable zone for planets of a given size. Each observation achieves some single-visit completeness by itself, and the combination of several observations of that star, perhaps separated by several months, can achieve a "program completeness" which is higher. For example, if no such planets have been found with observations giving "program completeness" of 95%, then only 5% of all possible orbits meeting the definition of the habitable zone could hold a planet that has evaded detection. This is a false negative result, because the mission has falsely determined that there is no planet present. Thus the completeness and the false negative probability sum to 1.

Table 3.2-2. Mission Science and Instrument Requirements

Baseline Mission Requirements	Instrument Requirements
(1) TPF-C shall be able to detect an Earth twin in a Solar System twin at a distance of 10 pc.	Such a planet will appear as far as 100 mas from the star at quadrature. Thus we require the inner working angle **IWA < 100 mas**. The planet-star contrast is $\Delta mag_p = 24.84$ at quadrature assuming a geometric albedos of 0.2. We require the scattered light in the science focal plane to be calibrated to $\Delta mag_i > 26.6$; this provides SNR =5 for detection.
(2) TPF-C shall also detect a Jupiter twin at quadrature in this same system.	In a face-on orbit, a Jupiter twin in this system will appear ~0.5 arcsec from the star. This sets the minimum acceptable outer working angle OWA > 500 mas. The planet/star contrast ratio is relaxed to that of req. (1).
(3) TPF-C shall have an excellent chance (95%) of detecting at least one planet that is potentially habitable, assuming that ten percent or more of all target stars have such a planet ($\eta_\oplus = 0.10$). Equivalently, TPF-C shall find ~30 potentially habitable planets if all target stars have one such planet.	Mission modeling (see Section 2) of a telescope with an effective **IWA = 65.5 mas**, with an instrument contrast of 10^{-10} (**$\Delta mag_i > 25$**) and instrument contrast stability of 1.3×10^{-11} (**$\Delta mag_s = 27.24$**), is capable of meeting this requirement. This **Δmag_s** stability is a factor of 5 below the minimum planet flux ratio 6.3×10^{-11} (**$\Delta mag_p = 25.5$**). In addition, the instrument throughput, bandpass, collecting

	area, and observational overhead should be consistent with the parameters in Table 3.2-3. Note: this is one point design that meets these few requirements. It is possible to trade IWA and sensitivity to meet the science requirements. For example, if the stability is improved to $\Delta mag_s = 28.24$, the IWA can be relaxed to 74 mas.
(4) (a) If a planet resembling the Earth twin in requirement 1 is found, TPF-C shall measure its orbital period to within 10 percent. When combined with an estimate of the star's mass, this will provide an estimate of the semi-major axis of the planet's orbit, through Kepler's 3rd law. (b) TPF-C shall measure the eccentricity of the Earth twin planet's orbit to an absolute accuracy of ± 0.3.	We have not yet modeled this requirement and do not know if the IWA and limiting Δmag, and other requirements are sufficient to meet this science requirement.
(5) The telescope on TPF-C shall be able to detect photons within the spectral range from 0.5 μm to 1.1 μm.	The baseline starlight suppression system is expected to meet this requirement, though it will only meet the first three requirements in a single 110 nm bandpass at a time. Some alternate concepts may allow simultaneous observations over the full spectral range.
(6) TPF-C shall measure the absolute, wide-band brightness of a detected planet across the spectral range defined in requirement (5) to within 10%. Where this is not possible due to wavelength-dependent working angle constraints, the brightness must be measured over the entire wavelength range in which the planet is detectable.	This requirement calls for SNR = 10 vs. SNR=5 for requirement (3). This requirement pushes the stability another 0.75 mag deeper, to **$\Delta mag_s = 28$**.
(7) For the Earth twin in Requirement 1 and for a Jupiter twin in this same system, TPF-C shall measure the apparent brightness in at least three broad spectral bands to a relative accuracy of 10% or better. Measurements in additional bandpasses are highly desirable for bright or well placed planets.	This requirement is satisfied automatically if requirements (3) and (6) are satisfied. The Earth twin and Jupiter twin are brighter than the faintest planet observed to meet requirement (3), and the instrument is designed to detect in 110 nm-wide bands to a sensitivity of 10%.
(8) TPF-C shall detect O_2 at 0.76 mm and H_2O at 0.82 mm for the Earth twin planet specified in requirement (1). Required resolutions are listed in Appendix 1.B. TPF-C shall also be able to detect CH_4 at 0.73, 0.79, 0.89, and 1.00 mm for a Jupiter twin in this same system. Detection is defined as the ability to measure the equivalent width of a spectral band to within 20 % accuracy.	The instrument will be designed to accommodate the required spectral resolution. We have not yet studied the flow-down of this requirement to instrument contrast stability.

(9) TPF-C shall have a minimum spectral resolution of 70 over the entire bandpass specified in requirement (5) to allow the mission to search for absorption bands of unspecified gases or surface minerals.	The instrument will be designed to accommodate the required spectral resolution at each wavelength in the range 0.5μm to 1.0 μm.
(10) TPF-C shall have a camera with a field of view of at least 10 square arcminutes, capable of operating in parallel to the planet search, and capable of zodiacal-light-limited broad-band imaging over the TPF-C spectral range.	The telescope should be diffraction-limited on axis and over some field of regard assuming the General Astrophysics Instrument does not have a deformable mirror and has limited field-correction capability.
Minimum Mission Requirements	
(1) TPF-C shall detect an Earth twin in a Solar System twin at a distance of 8 pc if such a planet exists.	This increases the IWA to 125 mas.
(2) TPF-C shall also be able to detect a Jupiter twin in this same system if it exists.	This increases the OWA to 625 mas.
(3) TPF-C shall have an excellent chance (95%) of detecting at least one planet that is potentially habitable, assuming that twenty percent or more of all target stars have such a planet ($\eta_\oplus = 0.2$). Equivalently, TPF-C shall find ~14 potentially habitable planets if all target stars have one such planet. The assumptions to be made in estimating this number are the same as in the baseline mission.	Our DRM studies showed that this requirement was met with IWA = 110 mas and Δmag_s = 25.5, and telescope long dimension = 4.75 m (still assuming the same throughput as in Table 3.2-3). It is possible to trade IWA and instrument sensitivity to arrive at another point design that also meets the requirements.
(4) Same as for the baseline mission, but for a system at 8 pc.	Unknown impact.
(5) The spectral range for the minimum mission is 0.5–0.85 μm.	Simplifies coating design.
(6) For the minimum mission the brightness may be measured only in the detection bandpass.	Same instrument contrast stability as in (6) above.
(7) Same as for the baseline mission, but for a system at 8 pc.	Not a driving requirement.
(8) Same as for the baseline mission.	No change from (8) above.
(9) Spectral resolution is only as required for spectral line detection as specified in requirement (8).	No additional drivers for spectrometer; may simplify the design.
(10) TPF-C shall have a camera with a field of view of at least 10 square arcminutes, capable of operating in parallel to the planet search, and capable of zodiacal-light-limited broad-band imaging over the TPF-C spectral range.	The telescope should be diffraction-limited on axis and over some FOR assuming the GAI does not have a DM and has limited field-correction capability.
Desired Mission Requirements	
(1, 3, 4a, 6, 7, 9) Same as for the baseline mission	No additional drivers

(2) TPF-C shall also be able to detect a Saturn twin at quadrature in a Solar System twin at a distance of 10 pc.	Pushes outer working angle to 1 arcsec.
(4b) TPF-C shall measure the eccentricity of the Earth twin planet's orbit to an absolute accuracy of ±0.1.	Unknown impact.
(5) The desired spectral range is 0.4 μm to 1.7 μm.	Beam splitters for polarization or for Michelson devices would be impractical, due to difficulty in meeting coating requirements over this range.
(8) TPF-C shall be able to detect O_3 at 0.6 μm for the Earth twin in Requirement 1. It shall also be able to detect CO_2 at 1.05, 1.21, and 1.59 μm for a Venus twin orbiting in a Solar System twin at a distance of 5 pc.	Unknown impact.

In summary, we find sufficient performance for meeting all the baseline requirements except (4) with a *TPF-C* point design that achieves: **IWA = 65.5 mas**, OWA = **500 mas,** instrument contrast **$\Delta mag_i = 25$**, and instrument contrast stability of knowledge to **$\Delta mag_s = 28$**. This level of instrument stability enables SNR = 10 detection of planets as faint as **$\Delta mag_p = 25.5$.** We have not yet evaluated performance against the astrometry requirement (4), so we cannot say whether the engineering requirements will be significantly changed. The DRM model that led us to these requirements assumed the aperture dimensions, throughput, observational overhead, and noise sources given in Table 3.2-3.

Table 3.2-3. Instrument Parameters

Symbol	Value	Quantity
D	8 m	long axis of the telescope mirror
d	3.5 m	short axis of the telescope mirror
N	96	DM elements per axis
λ	550 nm	central wavelength
$\Delta\lambda$	110 nm	bandpass
t_o	0.4734	optical throughput
t_m	0.675	mask throughput
t_{Ly}	0.34	Lyot throughput
t_b	7200 sec	overhead for telescope slew maneuvers
n_x	28.6	noise pixels
Ω_x	1.18×10^{-15} steradian	solid angle of pixel critically sampling at central wavelength
μ	0.001/sec/pixel	dark count rate
ζ	5.00×10^{-11}	uniform contrast level in detection zone
R	2 e$^-$/pixel	read noise

The FB1 design and error budget were set up before the program completeness could be fully evaluated by the DRM models. At the time, we estimated that the speckle stability re-

quirement would be $\mathbf{\Delta mag_s = 26.75.}$ This is sufficient for SNR = 3 detection of planets to $\mathbf{\Delta mag_p = 25.5}$ but is not sufficient for the 10% photometry requirement (7) on the faintest planets in the sample. In future work we will revisit the tighter stability requirements and reevaluate performance margin.

The telescope is designed for an inner working angle of 4 * λ/D, which is an Inner Working Angle (IWA) = 57 mas at the center of the shortest operating band λ=550 nm. This is currently implemented with a linear field occulter, as shown in Figure 1.2-1. Considering this together with the roll rotations needed for each observation (see Sect 3.3.2.3), The effective IWA, however, is somewhat larger (65.5 mas) due to the elliptical shape of the aperture and the need to difference images at 30 deg. rotations (see Sect 3.3.3.1.6). We chose IWA =4λ/D rather than a more aggressive angle because, as will be described in Sect 3.2.2, the instrument stability requirements tighten very quickly for designs with smaller IWA.

Table 3.2-4 Top-level Engineering Requirements

Quantity	Baseline mission	Minimum mission	Desired mission	Drivers
Inner working angle (IWA)	65.5 mas	110 mas	65.5 mas	(3) planet counts
Outer working angle (OWA)	500 mas	625 mas	1 arcsec	(2) Jupiters
Instrument contrast Δmag_i	25	25	25	Stability
Instr. contrast stability Δmag_s	28	25.5	28	(6) 10% photometry
Wavelength range	0.5-1.1μm	0.5-0.85μm	0.4-1.7μm	(5)
Spectral resolution (min/max)	70/70	3/70	70/140?	(8) spectral lines

The TPF-C pointing control system is designed to operate on stars as faint as V=20. The spectrometer design (see e.g. Section 4.1.3.1.) has sufficient bandwidth and resolution to measure the Sodium, H-alpha, Sulfer, and Potassium features. While the baseline coronagraph 8th order mask does not work at 2 λ /D, a 4th or second order mask, or possibly an alternative coronagraph system (e.g. pupil remapping) could be selected using a filter-wheel approach or flip-in mirror. These would enable reduced contrast imaging at 2λ /D to meet the final disk imaging requirement. Models show that the system will meet 1e-6 contrast at 2λ/D using the same thermal and dynamic control systems designed for 1e-10 contrast at 4λ/D.

Let us assume that somehow we arrange for the N×N-actuator DM to span exactly the major and minor diameters of the pupil; that is, there are N actuators across D=8m in x, and also across d=3.5m in y. For this purpose we have chosen anamorphic optics — cylindrical mirrors — to give different magnifications in x and y, and thus circularize the pupil (see Sect. 3.3.3.2). Then the outer working angle is Nλ /2d = 1.55 arcsec, which meets the desired mission requirement (2) to detect a Jupiter at 10 AU in a planetary system at 10 pc.

The instrument outlined in Table 3.2-3 is capable of observing 30 habitable zones in 3 years of elapsed time using only 1 year of integration and overhead time. The remaining two years may be used for 1) spectroscopy and other photometric measurements; 2) orbital determination; 3) disambiguation observations if the current program is not sufficient; 4) non-coronagraph science.

3.3 Flight Baseline 1

Flight Baseline 1 is the name for a particular observatory design which was adopted for the first round of detailed analysis. It represented the best design choices and knowledge at that time, for the science requirements that were current at that time. Nominally the design choices were "frozen" in January 2005, similar to a configuration freeze for flight hardware; but this "freeze" was only to maintain a well-defined and consistent concept for the brief FB1 modeling effort, and avoid the frustration of building analytical models of a rapidly evolving design. And in fact, some features were refined or changed after this time, by a deliberate process involving all participants. As a separate activity, the team persisted with concept development and design changes, often substantial ones, and incorporated them as features of the emergent FB2 design.

This section presents the FB1 design concept and the results of analysis of FB1 are given in Section 3.4. Changes suggested or recommended for FB2 are described in Section 4.

3.3.1 System Architecture

TPF-C combines an advanced coronagraph optical system with thermal, structural, and control systems that provide the benign disturbance environment needed for such precise coronagraphy. These systems are highly interdependent, as is typical of modern missions such as SIM and JWST. This is reflected in the complexity of system models that are under development to answer high-level questions about system performance. It will also seriously challenge the development of plans for integration and test of the observatory, and testbeds to support it. The system architecture should be developed with all of these concerns in mind.

This section gives an overview of the fundamental architecture of the observatory; later sections give more details of the FB1 design as an implementation of this architecture.

3.3.1.1 Optical Configuration

The Terrestrial Planet Finder Coronagraph (*TPF-C*) is a high-precision optical system designed to directly detect the starlight reflected from planets orbiting nearby stars. To achieve this challenging goal, the optical system provides a stable, high-quality wave front to the coronagraph. The starlight suppression system (SSS) is a stellar coronagraph designed to eliminate diffracted light and control scattered light, resulting in an instrument background level that is $< 10^{-10}$ of the incident starlight. In this section, we describe the design and functionality of the optical systems.

There are several ways to remove diffracted light from the region in the image plane where planets might be found. For *TPF-C*, we provide accommodations for band-limited Lyot coronagraphs (Kuchner & Traub, 2002) and shaped-pupil masks (Kasdin et al, 2002). Band-limited Lyot coronagraphs use a band-limited mask (e.g., 0.5*(1-cos)) and a hard-edged Lyot stop to block all diffraction. Shaped pupil coronagraphs are binary masks placed in a pupil plane that shape the diffracted light into a finite-size core surrounded by a low (10^{-10}), broad halo. Both are under study; the *TPF-C* High Contrast Testbed has achieved scattered light levels of 10^{-9} using a band-limited Lyot mask (Trauger et al., 2004).

Scattered light is controlled using a coarse deformable mirror (DM) and a pair of fine DMs. The coarse DM compensates for large wave front deviations in the telescope caused e.g. by gravity release and launch stress. The fine DMs have ~ 1 micron stroke and high actuator density (Trauger et al, 2004). With one fine DM, the wave front phase can be controlled across the image plane, or alternatively the wave front phase and amplitude can be controlled for half of the image plane. With a pair of DMs both amplitude and phase are controlled up to the spatial frequency response limits of the mirrors.

The SSS includes polarizing beam splitters (PBS) and separate polarization channels to accommodate polarization aberrations and coronagraph mask polarization-dependent phase and amplitude effects. Without the PBSs, the two polarizations of starlight behave as separate scalar fields in the system, but with some significant discrepancies in their wavefronts and in their amplitude and phase response to polarization-dependent optics. If they were not separated, the the scattered light control system would be forced to find a compromise setting that does not meet the instrument contrast requirements (Balasubramanian et al, 2005). A separate coronagraph and DM pair is provided for each polarization channel.

The present design of the SSS represents a compromise between functionality and performance. In the future, as technology improves, we will be able to simplify the SSS by choosing between the Lyot and pupil plane coronagraphs, potentially accommodating coarse and fine control in one DM, or use actuators on the primary mirror to eliminate the need for a coarse DM. Larger DMs may obviate the anamorphic reducer, and sequential DMs can eliminate the Michelson beamsplitters while improving broad band performance (Shaklan & Green, 2005). Ultimately, new mask and coating technology may eliminate the PBSs. For now all these functions are present to ensure a coronagraph capable of delivering high contrast over the required field, albeit at the expense of throughput.

3.3.1.1.1 Telescope

The telescope is described in more detail in the paper by Howard et al (2005) and in Section 3.3.3.1. It is a 140 m focal length system with a 8 x 3.5 m elliptical aperture primary. The field of regard is only 5 arcsec, but the field over which aberrations must be corrected is further reduced through the use of fine steering and deformable mirrors inside the coronagraph. The distance between primary and secondary is 12 m at the vertex, as shown in Figure 3.3-1. Light from the secondary is folded to run parallel to the rear of the primary mirror. The focus is close to the middle of the primary aperture. A second fold mirror sends the light in the direction of the long axis of the elliptical primary. These two small folds are rotated about orthogonal axes to minimize polarization variation.
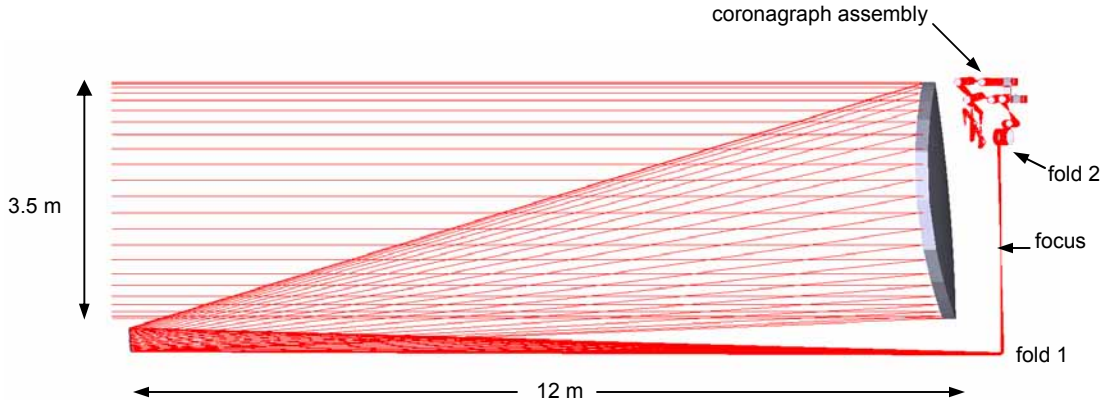
Figure 3.3-1. Telescope and Coronagraph Assembly

3.3.1.1.2 Starlight Suppression System

The starlight suppression system is essentially an expanded Lyot coronagraph, with four distinct and accessible pupil locations. One of these is occupied by the Lyot mask, one more occupied by a pair of fine DMs, another one is made available for implementing shaped pupil masks, and the last one is reserved for a second, "coarse" DM, compensating for gross errors induced by gravitational sag and release or launch stress.

In order to reduce polarization-dependent wave front and amplitude errors (Balasubramanian et al, 2005) the beam is split into two orthogonal polarization paths using a polarizing beamsplitter. This split is early in the path so that the system comprises two independent coronagraphs, one for each polarization. Anamorphic optics provide circular beam cross section onto the coarse DM and beyond. Two fine DMs per polarization path are used in a Michelson arrangement for amplitude and phase correction. All these subsystems are described in greater detail in Section 3.3.3.2. A functional block diagram is shown in Figure 3.3-2.
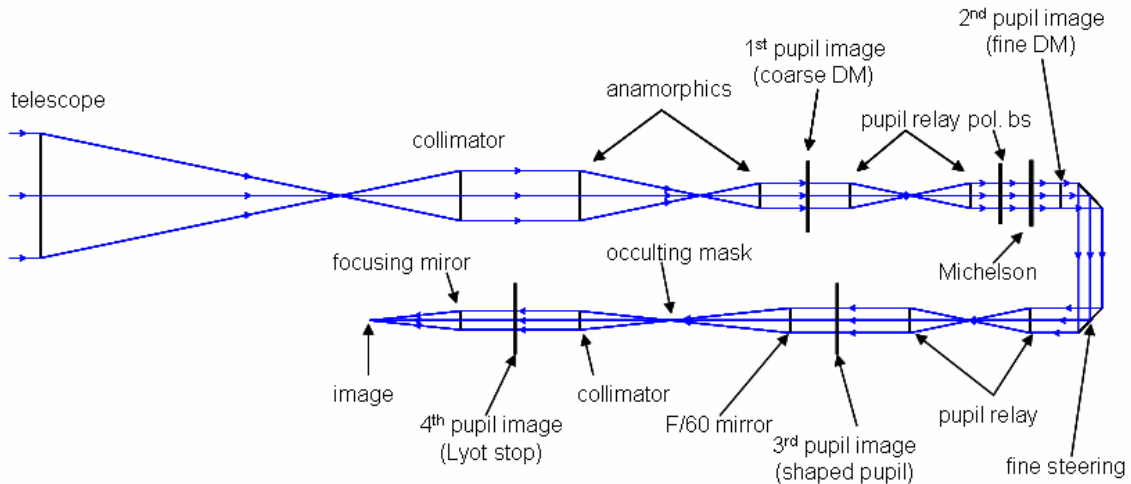
Figure 3.3-2. Functional Block Diagram of the Starlight Suppression System

A second schematic (Figure 3.3-3) shows in some more detail the most critical optical elements, various pupil relays, and pupil and intermediate image positions. It is to be noted that all powered elements are used only in a collimating or focusing mode, with aberrations corrected everywhere along the optical train at the level of ~0.0001λ along the axis. Actually, this error arises from the telescope and simply carries through the final image since all powered mirrors within the SSS are off-axis parabolas, which have no nominal wave front error at the correct focus. The minimum field of view of the system makes it unnecessary to use more complicated optics. The fine steering mirrors will nominally center the image of the star, while the DMs will correct the residual small aberration at that point.

```
                    Primary telescope
                           ↓
                   Anamorphic reducer
                           ↓
                       Coarse DM
                           ↓
                  Polarizing beamsplitter
                    ↓               ↓
              Michelson         Michelson
             (2 fine DMs)      (2 fine DMs)
                    ↓               ↓
              Pupil mask        Pupil mask
              (optional)        (optional)
                    ↓               ↓
            Field occulter    Field occulter
                    ↓               ↓
               Lyot mask        Lyot mask
                    ↓               ↓
              Final image       Final image
```
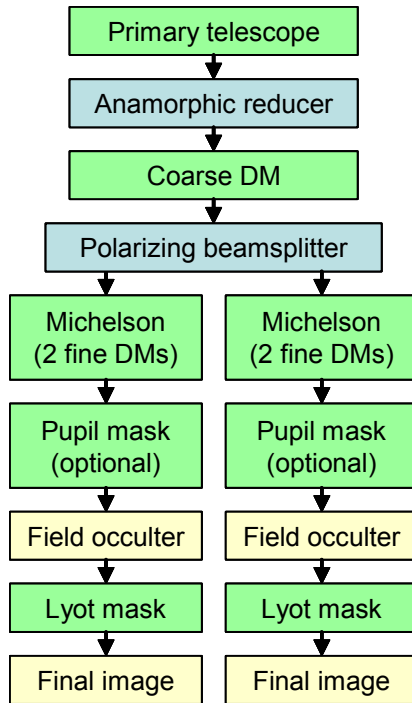
Figure 3.3-3. Schematic of the Starlight Suppression System showing the pupil locations, intermediate foci, and collimated spaces as well as the most critical optical elements.

Figure 3.3-4 shows typical masks for a Lyot coronagraph implementation. The entrance pupil is an 8×3.5m ellipse defined by the primary mirror. (Other mirror shapes have been considered and are among the trades discussed in Section 4.) After many stages of conditioning the starlight beam, it arrives at the occulting mask, which blocks the central peak and some of the side lobes of the star image. The beam emerging from this mask is recollimated and brought to another pupil image, called the "Lyot plane"; most of the starlight side lobes which have evaded the occulting mask form bright regions in the Lyot plane. The Lyot mask blocks these regions, admitting only the planet light. The Lyot planet is then brought to an image plane which shows a point-like planet image and some residual starlight.
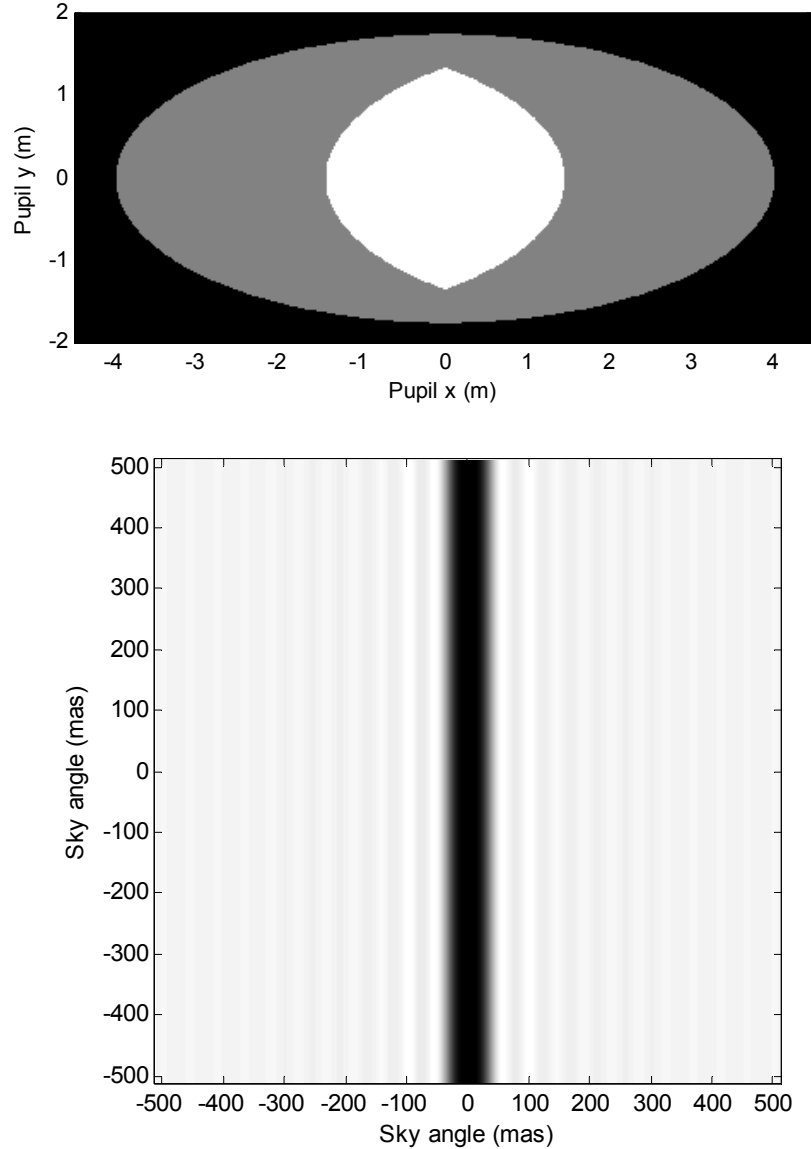
Figure 3.3-4. Lyot coronagraph masks. Top: Original 8×3.5m elliptical pupil mask (gray) and typical Lyot pupil mask (white). Bottom: Linear 8th-order occulting mask, which blocks most of the starlight

REFERENCES

K. Balasubramanian, D. Hoppe, P. Z. Mouroulis, L. Marchen, and S. Shaklan: "Polarization compensating protective coatings for *TPF-C*oronagraph optics to control contrast degrading cross polarization leakage", to appear in Proc. SPIE **5905** (2005).

J. M. Howard, P. Z. Mouroulis, A. K. Thompson, A. M. Smith, D. A. Content, T. Y. Ho, C. E. Jackson, R. G. Ohl, and S. B. Shaklan: "Optical design considerations for the Terrestrial Planet Finder-Coronagraph mission: optical telescope assembly", SPIE Proc. **5874**.

N. J. Kasdin, R. Vanderbei, D. Spergle, and M. Glittman, "Optimal shaped pupil corona-graphs for extrasolar planet finding," Proc. SPIE **4860**, 240-250 (2002)

M. J. Kuchner and W. A. Traub: "A coronagraph with a band-limited mask for finding ter-restrial planets," ApJ 570, 2002

S. B. Shaklan and J. J. Green, "Reflectivity and Optical Surface Height Requirements in a Broad Band Coronagraph I: Contrast Floor Due to Controllable Spatial Frequencies," sub-mitted to Appl. Opt. (2006).

J. T. Trauger, C. Burrows, B. Gordon, J. J. Green, A. E. Lowman, D. Moody, A. F. Niessner, F. Shi, D. Wilson, "Coronagraph contrast demonstrations with the High Contrast Imaging Testbed," Proc. SPIE **5487**, 1330 (2004)

3.3.1.2 Mechanical Configuration

The *TPF* Coronagraph mechanical configuration is designed around a given optical prescrip-tion, a thermal design, the required components and structural considerations. The *TPF-C* FB1 baseline design is composed by 2 main elements: the Spacecraft and the Science Pay-load. The element features are described below and and shown schematically in Figure 3.3-5 to illustrate the relationship between the components:

- Spacecraft:
  - Sunshade:
    - Large deployable conic shaped v-groove layers which insulate the payload from the changing sun angles during the observational sce-narios
    - Maximizes the opportunity to view target stars multiple times during one year so that planets will have time to orbit into a favorable posi-tion out from behind the star.
    - Structurally attached to the spacecraft through deployable arms and booms
    - Any dynamic snaps or warping of the sunshade structures will be fil-tered through the spacecraft before reaching the sensitive payload.
  - Other spacecraft components:
    - Dynamic isolation – either passively or active isolation. Both options were analyzed.
    - Also: thruster clusters, orbit maintenance fuel tanks, communica-tions antennas, and reaction wheels, solar panels and solar sail
- Science Payload:
  - Telescope:
    - Primary, Secondary, Tertiary mirror assemblies and supporting struc-tures
    - Laser metrology monitoring relative position of primary mirror to secondary mirror
    - Thermal control heaters, and related electronics
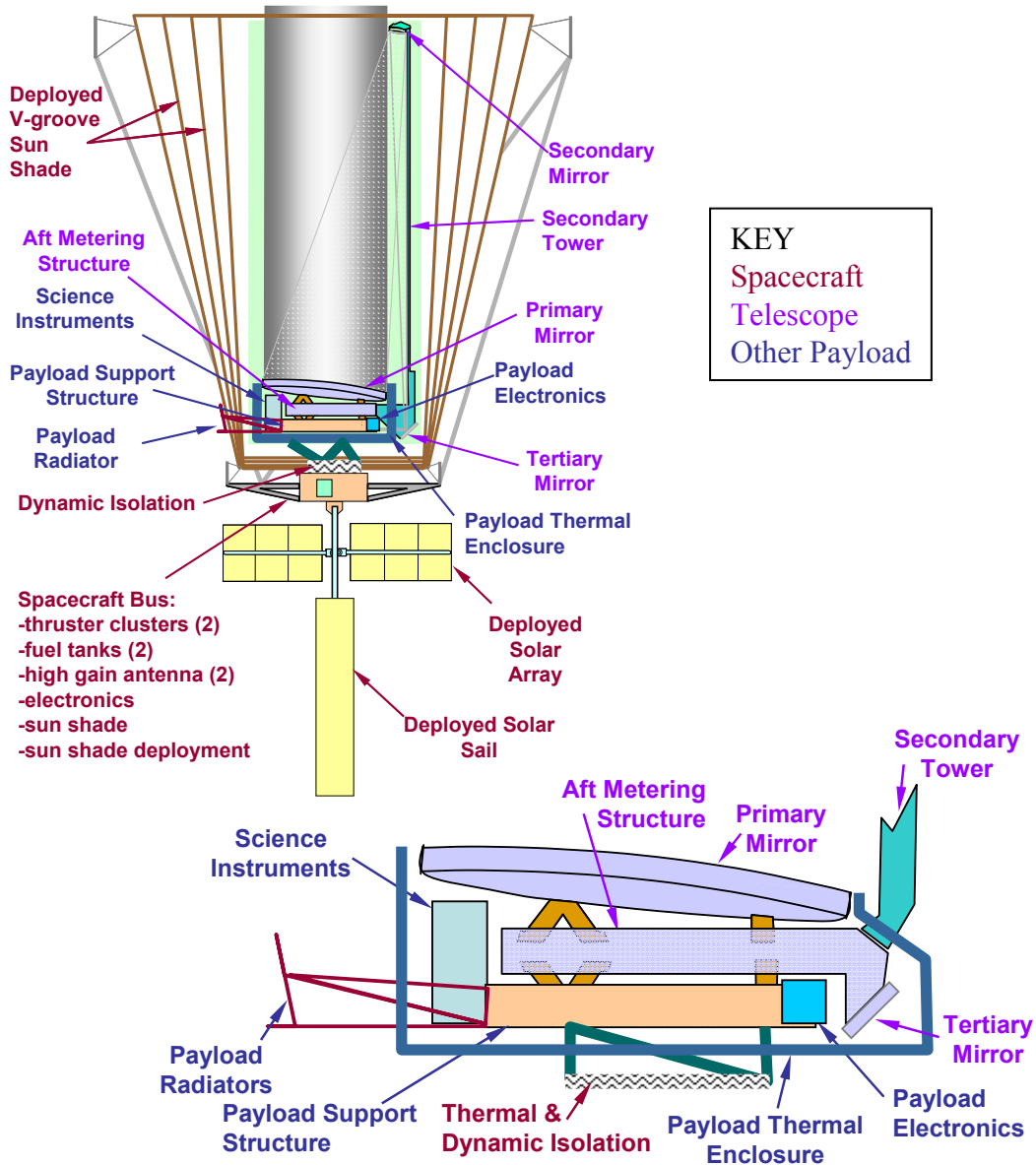
Figure 3.3-5. Schematic of the *TPF-C* Elements

- Other Payload:
  - Structure mounting payload to spacecraft
  - Starlight Suppression System
  - Science Instruments
  - Thermal control hardware: isothermal enclosure, heat pipes, radiators, and associated electronics
  - Electronics

The current telescope configuration consists of an off axis elliptical primary mirror measuring 8m x 3.5m and a secondary mirror 12 m from the primary mirror. The primary mirror is kinematically mounted on 3 flexured bipods on the backside of the mirror attached to a

strong-back structure, the Aft Metering Structure (AMS). The secondary mirror assembly is attached atop a folding tower on thermal isolators. The tower folds along 3 hinge lines to stow for launch. Each hinge will be locked out after the tower deploys as the locking mechanisms will then join the main structure together. Behind the secondary mirror is a fine positioning actuated hexapod. The tower assembly attaches to a bracket that kinematically interfaces to the AMS through 3 thermal isolating bipods. Both the primary and secondary mirrors are enclosed in separate thermal enclosures. The AMS is kinematically attached to the telescope support structure (TSS). The TSS supports the coronagraph instrument and primary mirror thermal enclosure. It is also acts as the telescope interface to the spacecraft and supports the telescope assembly during launch. See Figure 3.3-6 for details of the telescope assembly configuration and Figure 3.3-7 for the secondary tower stowing sequence.
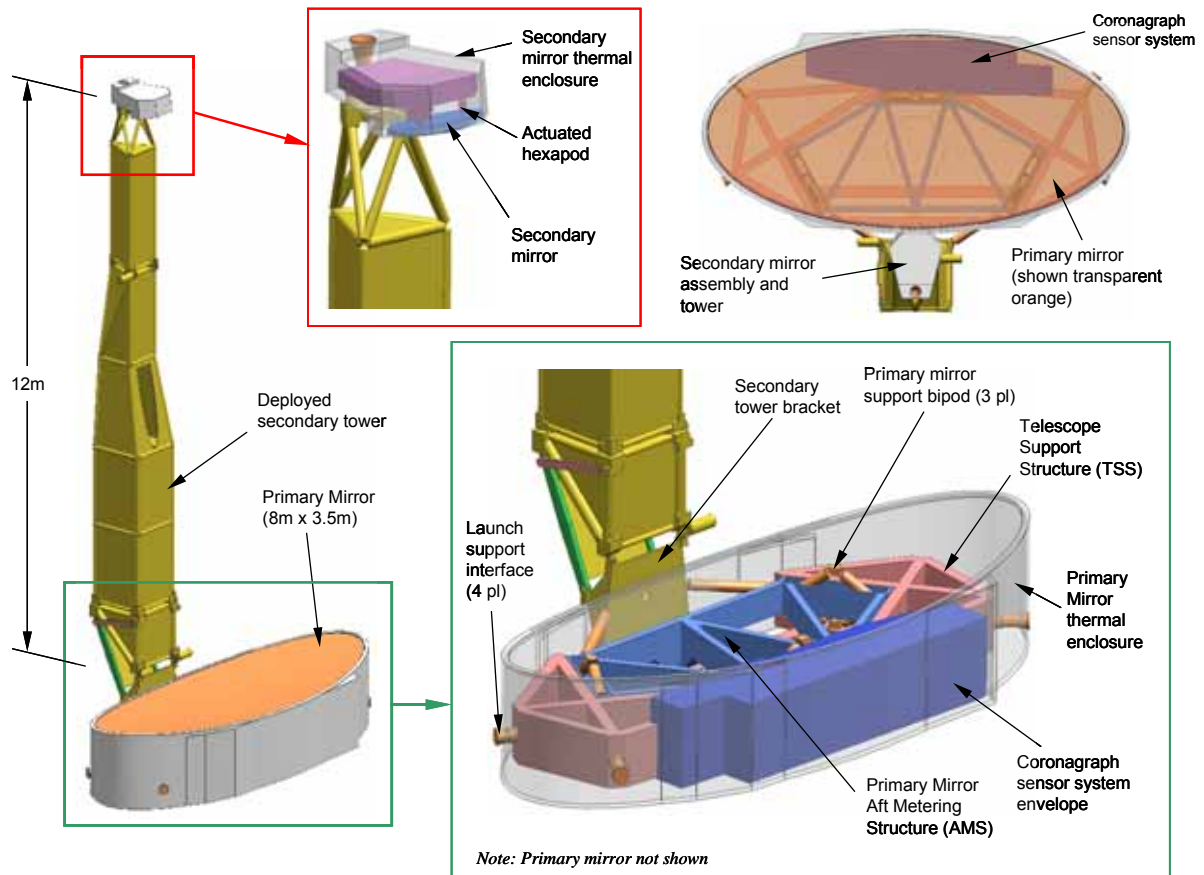
Figure 3.3-6. Deployed telescope assembly
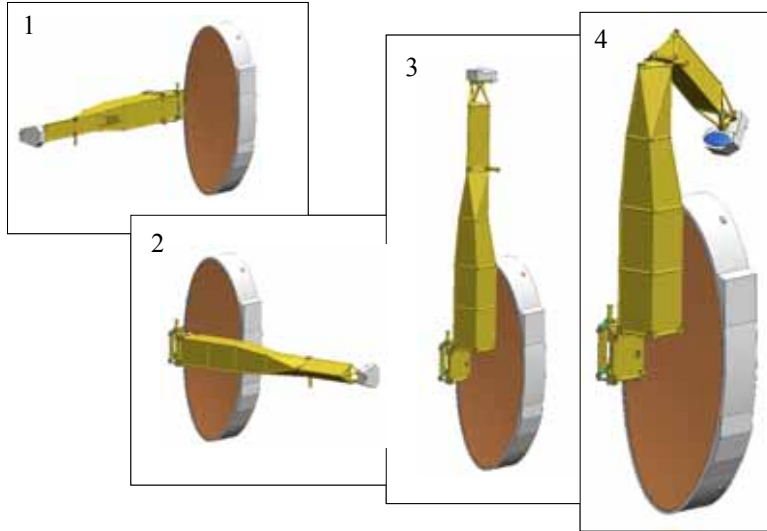
Figure 3.3-7. Secondary tower stowing sequence

The spacecraft configuration consists of the spacecraft/launch support structure, solar arrays, solar sail, propulsion system, v-groove thermal shade system and reaction wheel assembly. A unique feature of the spacecraft configuration is that there is no conventional spacecraft bus. Instead, part of the launch support structure is carried during flight operations that also support typical spacecraft equipment (i.e., electronic boxes, solar arrays, etc). The launch support structure that flies with the telescope during operation has a stowed and deployed configuration. During flight, the sides of the launch support structure folds open to allow the v-groove thermal shade to deploy. Other deployable spacecraft structures include the solar arrays and solar sail. See Figure 3.3-8and Figure 3.3-9 for details of the stowed and deployed spacecraft assembly configuration.
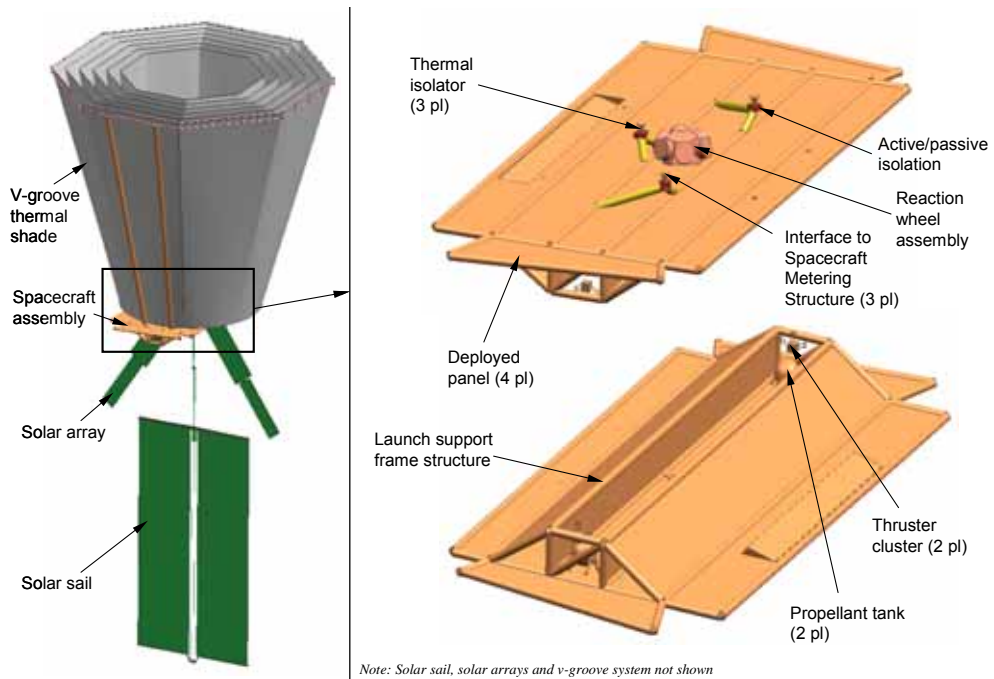
Figure 3.3-8. Deployed spacecraft assembly
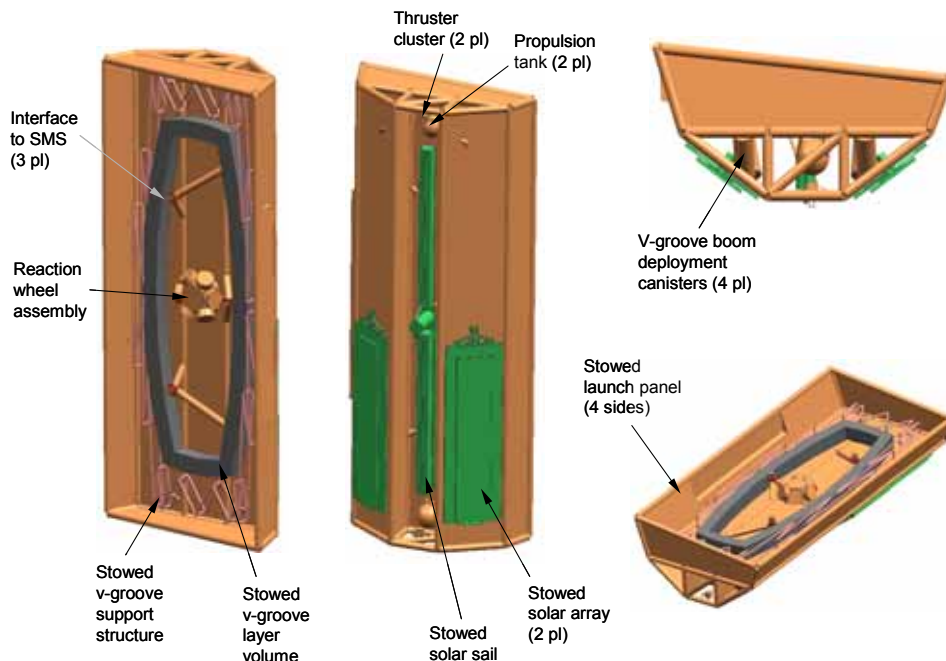
Figure 3.3-9. Stowed spacecraft assembly

The spacecraft and telescope assemblies are connected together at a single interface that will provide vibration isolation between the two assemblies either actively or passively. The interface will be locked for launch and separated for flight.

The flight system must be stowed for launch. Figure 3.3-10 shows the stowed flight system. A separable launch support truss is attached to the spacecraft to provide additional stiffness, stability and support due to the vertical orientation of the system during launch. Additional separable support struts are attached from the TSS and secondary tower to the spacecraft and launch support truss to support the telescope assembly.
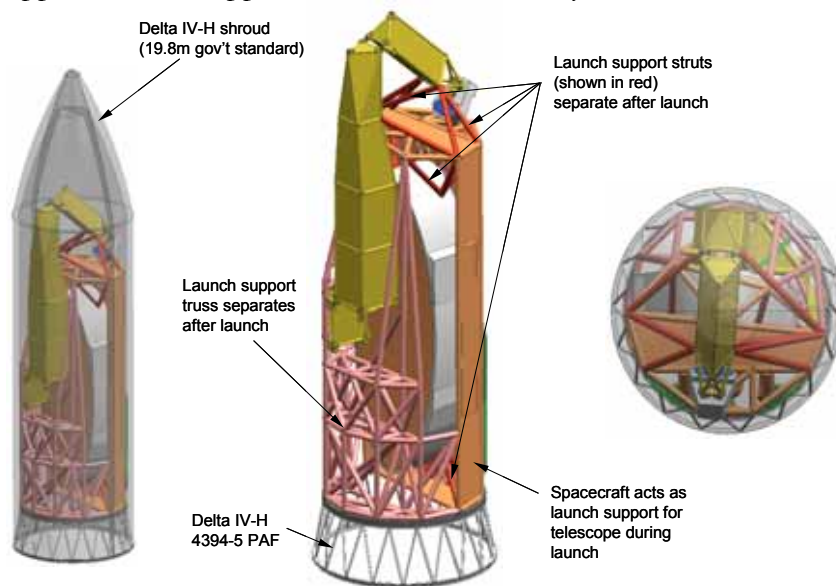
Figure 3.3-10. Stowed flight system

The stowed to deployed launch sequence is shown in Figure 3.3-11, and Figure 3.3-12 shows the flight system layout and overall dimensions.
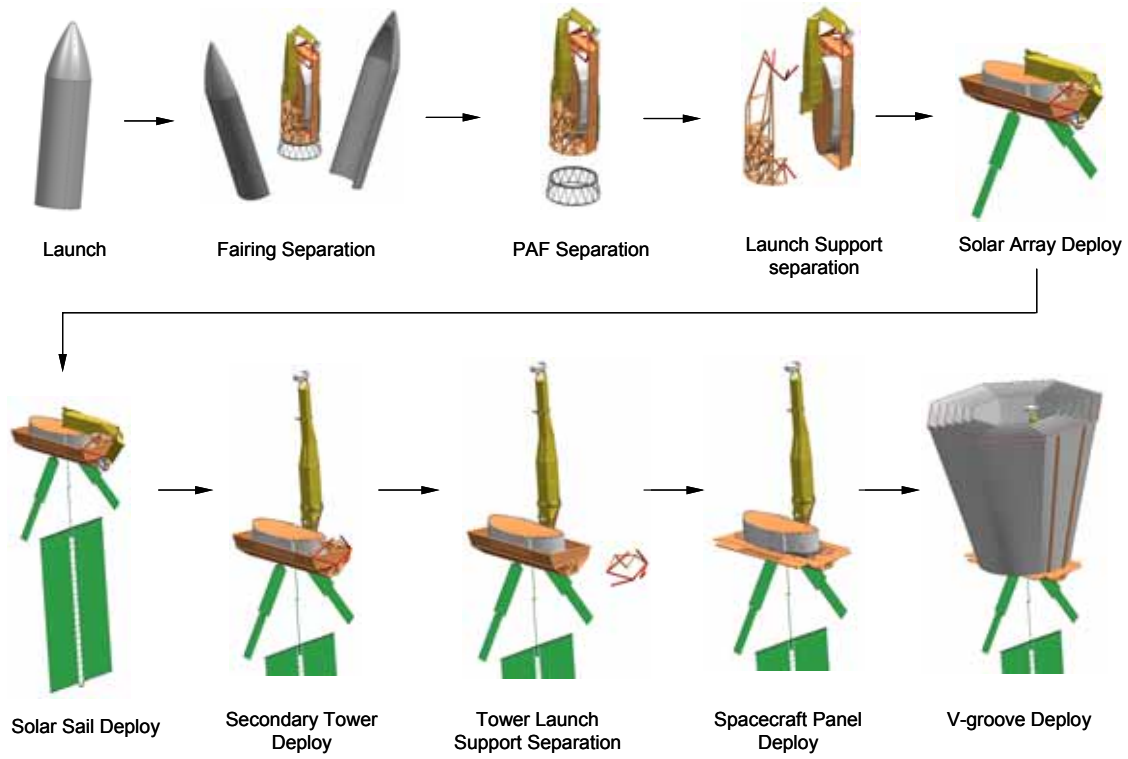
Figure 3.3-11. Deployment sequence
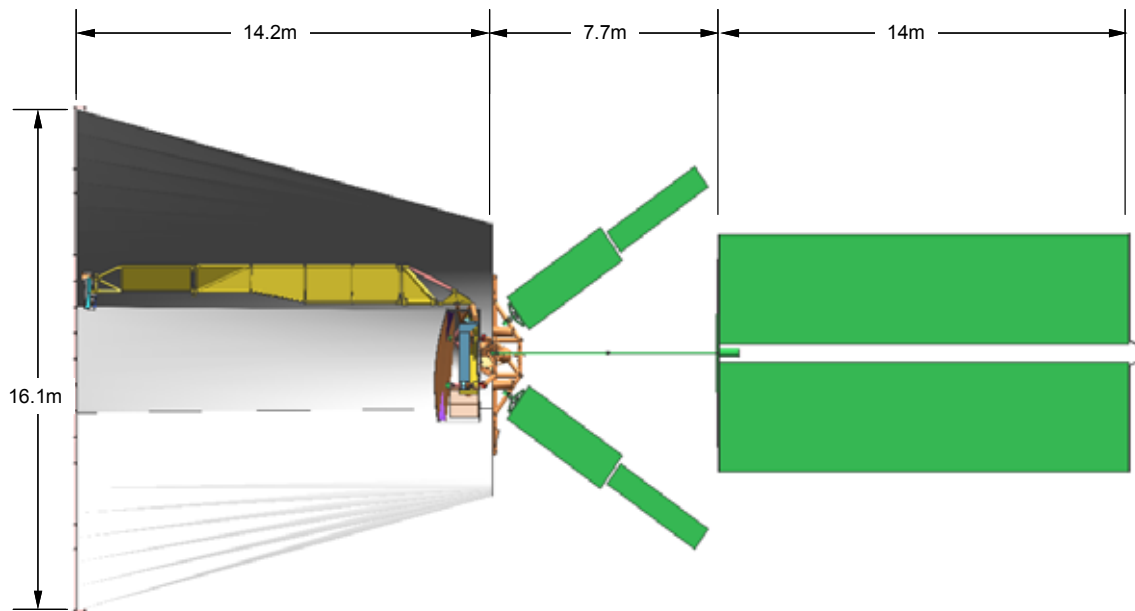
Figure 3.3-12. Deployed flight system cross section

Astro Aerospace of NGST has been studying the deployment and feasibility of the sunshade that is the primary passive method of thermal control for the system. The design they have developed consists of a 250-inch diameter, 505-inch long tube of plastic film surrounded by 5 concentric cones also fabricated from plastic film (Mylar or VDA Kapton). Each cone from inner to outer has an increasing cone angle. The largest cone flares out to 518 inches diameter, all the cones are the same length as the center cylinder. The proposed deployment and support structure consists of four 12-inch O.D. telescopic tube assemblies that act as the legs connected to a hoop truss of 600-inches deployed diameter at the tip of the shield. The hoop structure is maintained in its circular shape by a radial net of light Kevlar or Graphite strings that attach to a reinforced rim on the center cylinder. This radial net also supports and tensions the concentric cones. The hoop structure and radial net is in many ways very similar to the Astromesh structure used in large unfurlable MESH reflectors.
In its stowed condition the tubes are retracted back, the hoop truss is stowed in an elliptical annular space below the main mirror and the fabric is rolled or folded into the same annular space below the mirror. Figure 3.3-13 and Figure 3.3-14.depict the sunshade structure.

The deployment sequence would be to release the hoop truss from its stowage hard points and extend the telescopic legs to their full length. The opening of the hoop truss to tension the nets and cones would follow this. We need to do the following things next

- Establish a credible stowed configuration consistent with the available or a negotiated volume to establish hard points or tie down locations.
- Conceptually address the problems of fabricating, assembling, and handling these large areas of film material.
- Perform some conceptual finite element modeling trades to establish modes and frequencies in order to identify structure design parameters and strategies
- Generate a conceptual layout for the inner cylinder baffles to see how they interact with spacecraft structure and how they might be folded up for stowage.
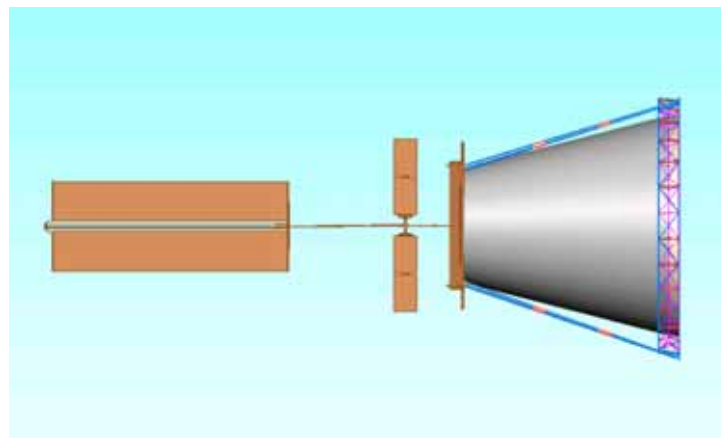
Figure 3.3-13. Deployed sunshade and deployment structure
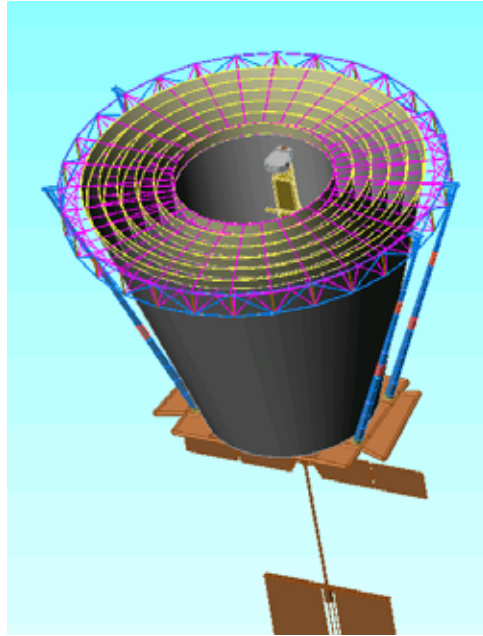
Figure 3.3-14. Sunshade Architecture Top View

3.3.1.3 Launch Vehicle

The baseline launch vehicle is Boeing's Delta-IVH, which provides the largest launch mass capability available within current NASA contracts (EELV). The large mass associate with the primary mirror and supporting the mirror in a vertical position during launch dictates the need for this maximum launch capacity

3.3.1.4 Mass

The mass estimates for the various FB-1 elements are shown schematically below in Figure 3.3-15 and summarized in Table 3.3-1.
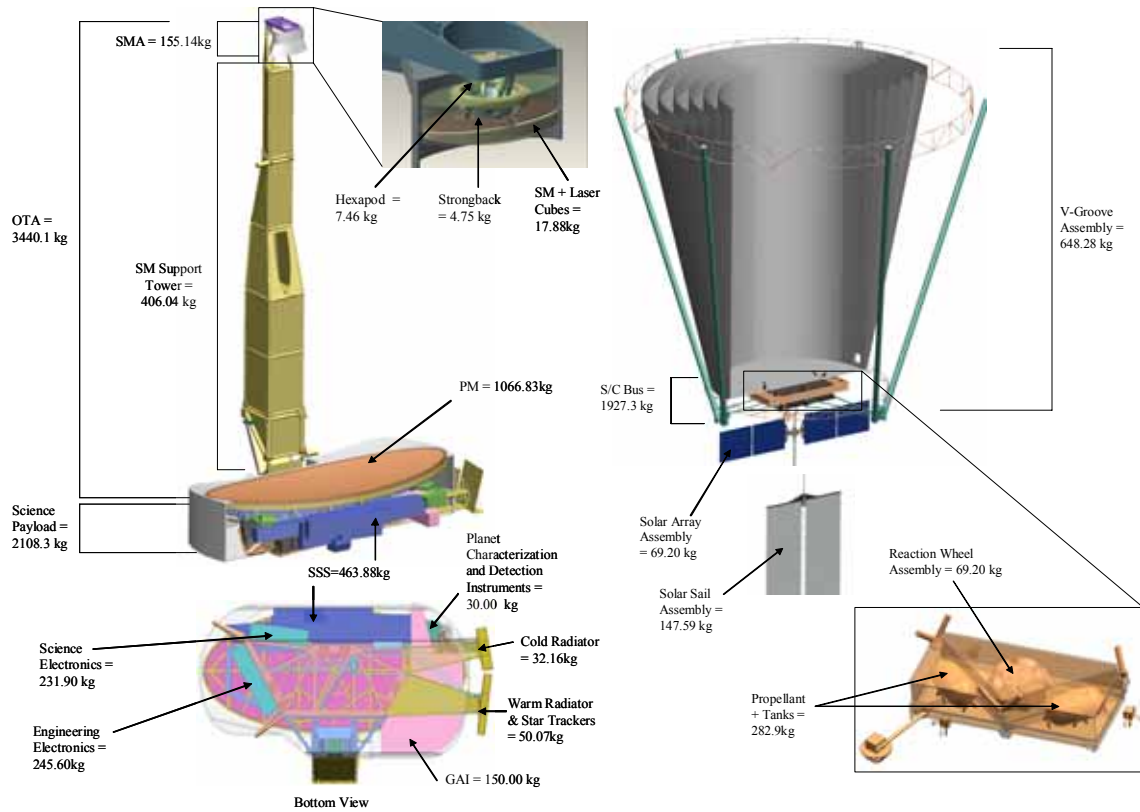
Figure 3.3-15. Schematic of the *TPF-C* Elements Mass Estimates

The mass estimates were determined both from analysis and from analogy to previous missions. The optical telescope assembly mass estimates were obtained from in-depth structural modeling. The listed mass of the science payload is based on the data available during the FB-1 analysis cycle, which was prior to the Instrument Concept Studies (ICS) studies. The Precision Sub-Structure (PSS) mass and Starlight Suppression (SSS) mass were also obtained from structural models. DC mass was based on a simple camera system estimate. The mass of the Planet Characterization Instrument was based on analysis performed at GSFC by R. Brown [ref]. The General Astrophysics Instrument (GAI) mass was modeled after the Hubble wide-field camera WIFPIC. Spacecraft masses were based on current best estimates for similar flight hardware components.

Table 3.3-1. Nominal Mass Estimates for FB-1 Design

Component	Mass (kg)	Mass Percentage
Optical Telescope Assembly	**3440**	**43%**
SMA	155	2%
SM Support Tower	406	5%
PM	1067	13%
AMS	1114	14%
Misc	698	9%
Science Payload	**2108**	**26%**
Starlight Suppression System	464	6%
Planet Detection Camera	10	0%
Planet Characterization Spectrometer	20	0%
General Astrophysics Instrument	150	2%
Radiators	82	1%
Structure	396	5%
Electronics	415	5%
Misc	571	7%
Spacecraft	**1993**	**25%**
V-Groove Sunshield	648	8%
Propellant	308	4%
Solar Sail	56	1%
Solar Arrays	69	1%
Structure	544	7%
Misc	367	5%
Total Observatory Wet Mass	**7541**	
Launch Support Structure	549	
Total Launch Mass	**8090**	
Launch Vehicle Capability	9250	
Launch Margin	13%	

*Defined as (LV Capability – Total Nominal Mass Estimate)/LV Capability.

The estimates for the FB-1 mass margin exceed the recommended limit of 30%. Therefore, several mass reduction options were explored including:

- Optimizing the AMS structure
- More efficient integration between the AMS and PSS
- Optimizing thermal enclosure structure
- Removing unnecessary primary mirror heaters
- Optimizing the SMA structure
- Optimizing the SM Support Tower structure
- Optimizing the weight of the optical bench
- Utilizing a lattice structure for the thermal cavity housing

- Changing to the Sugar-scoop Sunshield
- Changing to an actuated solar sail design to reduce ballast
- Changing to Ultra-Flex Solar Arrays
- Utilizing smaller reaction wheels
- Optimizing the launch support structure

After applying these options, we may obtain a new estimate of the observatory mass which meet the mass margin of 30% required for this phase of the program. This design is summarized in Table 3.3-2. The options proposed above will be implemented in next design cycle.

Table 3.3-2. Optimized Mass Estimate for *TPF-C*

Component	Mass (kg)	Mass Percentage
Optical Telescope Assembly	**2442**	**38%**
SMA	99	2%
SM Support Tower	266	4%
PM	1067	17%
AMS	696	11%
Misc	315	5%
Science Payload	**1691**	**26%**
SSS	269	4%
PDC	10	0%
PCS	20	0%
GAI	150	2%
Radiators	82	1%
Structure	317	5%
Electronics	415	6%
Misc	427	7%
Spacecraft	**1689**	**26%**
V-Groove Sunshield	522	8%
Propellant	249	4%
Solar Sail	56	1%
Solar Arrays	50	1%
Structure	509	8%
Misc	304	5%
Total Observatory Wet Mass	**5822**	
Launch Support Structure	602	
Total Launch Mass	**6424**	
Launch Vehicle Capability	9250	
Launch Margin	30.55%	

*Defined as (LV Capability – Total Nominal Mass Estimate)/LV Capability.

3.3.1.5 Power

TPF-C is powered by solar arrays, which for the FB-1 are sized to provide 3000 W of end of life power. This power capability was selected early in the design by analogy to similar space telescopes. Table 3.3-3 shows the power estimates with a 32% margin, which is consistent with the recommended margin of 30% prior to Phase B. Volume is available to increase the solar array size, if necessary, as discussed further in Section 3.3.4.5. All estimates are based on the FB-1 design, which does not reflect the Instrument Concept Study results.

Table 3.3-3. Nominal Power Estimated for FB-1 *TPF-C* Configuration

Component	Power (W)	Power Percentage
Telescope Electronics	**78**	**4%**
OTA Electronics	48	2.3%
Laser LD5 Electronics	30	1.5%
Science Payload	**385**	**19%**
Starlight Suppression System	87	4.3%
Planet Detection Camera	2	0.1%
Planet Characterization Spectrometer	40	1.9%
Payload Star Acquisition Camera	4	0.2%
General Astrophysics Instrument	100	4.9%
Electronics	152	7.4%
Thermal Control	**581**	**28%**
Telescope Assembly Heaters	274	13.4%
Payload Support Heaters	307	15.0%
Spacecraft	**1000**	**49%**
Total Observatory Power	**2044**	
Available EOL Power	3000	
Power Margin*	**32%**	

*Defined as (Available Power – Total Nominal Power Estimate)/Available Power.

The bases of estimates are summarized as follows: The telescope and science payload electronics power is estimated per a functional allocation of electronics boards and an estimate for each board. Thermal control heater power is estimated from the FB-1 analyses.

3.3.1.6 Trades

Identified trades leading to the adopted baseline design are summarized in the Table 3.3-4 below. Section 4 will define in more detail the status and disposition of these trades.

Table 3.3-4. List of Open Trades and Status
(Orange – done; Green – in progress; Blue – Deferred)

#	Description	Status
1.0	Mission - orbit detail, ΔV, Launch Vehicles, mission duration (may pad ΔV to be conservative)	Blue
2.0	Starlight Suppression System alternatives	
2.1	Consider alternates to dither maneuver for speckle removal (per NRA concepts)	Blue
2.2	Consider series DMs, remove beam-splitters, redundancy	Green
2.3	Consider increasing OWA for giant planets with larger DM, FOV for dust disk observations	Green
2.4	Consider longer wavelength observations (per NRA concepts) up to about 0.9μm	Green
2.5	Evaluate anamorphic optics compared to larger DM	Green
3	Instruments accommodations	Green
4	Pointing and Control - active vs passive dynamic isolation	Blue
4.1	Define frequency range and control loop bandwidths, assess compatibility with actuator capabilities	Orange
4.2	Evaluate necessity of secondary mirror steering, pending capability of payload vibration isolator	Orange
4.3	Evaluate mounting of payload Payload Acquisition Camera, evaluate changes to reaction wheels	Blue
5	Primary Mirror	
5.1	Consider shape changes - increased depth and 8x3m race-track vs elliptical PM shape	Orange
5.2	Open vs. Closed back PM structure evaluation	Orange
5.3	Evaluate PM actuators vs. Coarse DM	Orange
5.4	Resolve PM launch load issues - configuration change to reduce loads or add dampers/absorbers	Blue
6	Mass Management	
6.1	Redesign thermal enclosure/Secondary Tower/AMS/LD5 boxes - mass efficient stiffness, add 4 arcmin FOV	Blue
6.2	Add mass estimates for: launch constraints, dust covers, ballast, identify load bearing mass	Blue
6.3	Evaluate mass sensitivity to: PM frequency, vibration control, SM actuation, metrology, solar sail	Blue
7	Solar Array - Consider alternatives	Orange
8	Solar Sail - improve design for better torque balance	Orange
9	Sunshade - consider alternatives, add degradation features, trade performance against stowing/deploying issues	Orange
10	Stray Light - develop concept for telescope baffles, add vanes, deployment issues	Orange
11	Define viewing constraints from earth, moon, Jupiter, etc.- characterize vs. orbit size/position	Blue
11.1	Contamination: understand requirements, add covers on exposed optics as required	Orange
12	Thermal Control - incorporate active thermal control	Blue
12.1	Consider thermal configuration changes - electronics mounting, heat pipe dynamics, alternate approaches	Blue
13	I&T design issues	
13.1	Select OTA test configuration, incorporate features in flight design	Blue
13.2	Understand required flight jitter requirement - use to evaluate chamber availability and testing capability	Green
13.3	Understand required flight thermal gradient requirements - use to evaluate chamber availability and testing capability	Blue
13.4	Trade optical concepts for OTA tests - sub-aperture test requirements, model system, define requirements	Blue
14	Software Definition	Blue
15	Ground Segment Definition	Blue

3.3.2 Mission Operations

3.3.2.1 Mission Description

Table 3.3-5 below presents the choices for mission and spacecraft that create the framework of the Flight Baseline 1 (FB1) design configuration.

Table 3.3-5. *TPF-C* mission description summary

	Parameter	Value	Comments
Mission	Duration required/goal	5/10 years	Resources for 10 years
	Orbit	L2	Direct trajectory
	Field of Regard	Sun angles > 95°	Potential earth/moon/planet constraints
	Required ΔV	60 m/s	
	Launch Energy (C_3)	-0.69 km^2/s^2	
	Launch Vehicle	EELV	
	Launch Fairing	5 m diameter	limits primary mirror short axis to ~3.5 m
	Launch Mass	9200 kg	
	Time to reach operating orbit	109 days	
	Ground Station	34m DSN Ka-Band	
	Downlink Data Rate	64Mbps	
Spacecraft	EOL Power	3kW	provided by solar arrays
	Reaction Wheels	6 Ithaco- E	
	Propellant	350 kg Hydrazine	
	Thrusters	12 20N	
	Hi Rate Downlink Frequency	Ka-Band	avg duration 2.5 hours per day
	Engineering Downlink Frequency	X-Band	
	Uplink Frequency	X-Band	
	Transmitter Power	50W	
	Hi Gain Antenna	43dB	0.5m patch array

The primary mission duration is 5 years with consumables provided for a 5 year extended mission. A 6 month checkout phase is planned, followed by a 3 year search phase, nominally leaving 1.5 years for planet characterization. However, flexibility exists to conduct planet characterization during the search phase as well. Efforts to date have focused on defining the search phase for a set of 30 core stars. The operational concept is illustrated in section 3.3.2.3.

3.3.2.2 Observatory Field of Regard

The observatory is designed to examine stars in nearly the entire anti-sun semi hemisphere in order to keep sun light from entering the telescope sun-shade a 5° margin is included as shown schematically in Figure 3.3-15. The field of regard includes all stars located in the cone defined as greater than or equal to 95° away from the sun. As the observatory travels around the sun, this field-of-regard will sweep nearly the entire sphere of the universe, excluding the poles, allowing observation of all star targets of interest during nearly 5 months of the year.

3.3.2.3 Observational Scenario of Each Target Star

Achieving the desired level of planet search completeness requires about 4 repeat visits spread over 3 years (e.g., 1 visit in year 1, 2 in year 2 and 1 in year 3). Each visit requires taking multiple exposures of a star, for 2 different reasons. First, the elliptically shaped aperture requires taking exposures at 2 or 3 different roll positions to examine each star's habitable zone using the axis of smallest inner working angle (IWA). Second, at each roll position, 2 exposures are required with about 30° separation in roll angle; this difference of 2 images is called a "dither" and is described below. Very long exposures, beyond the time scales for system thermal stability, may need to be subdivided into multiple dithers.
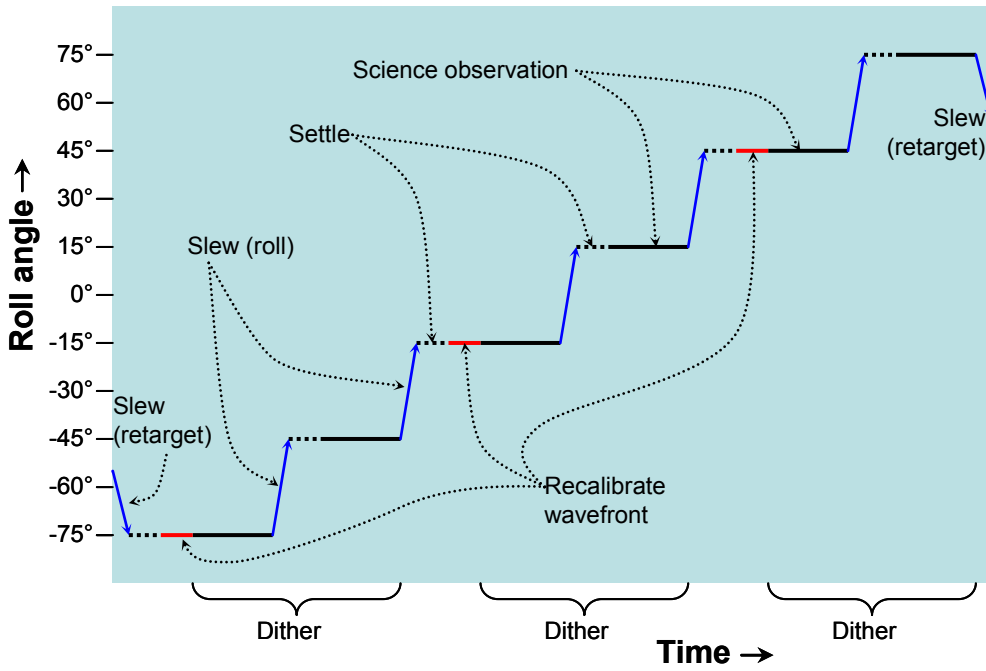
Figure 3.3-16 Timeline for a planet observation around one star. The observation includes 6 science integration periods separated by 5 roll slews. Each slew is followed by settling time. Each pair of science integrations constitutes a dither, and each dither is preceded by recalibration of the wavefront.

Figure 3.3-16 illustrates the timeline. During each star observation, the observatory will point at a star target. Once the dynamics are stabilized, the wavefront calibration begins. Using adaptive optics, the wavefront errors will be reduced until the starlight is suppressed adequately and a science image will be taken. Next the observatory will do a "dither" roll about its optical axis by 30 degrees. Once the dynamics are stabilized, but without recalibrating the wavefront control, the observatory will take a second science image in this new position. This image will be subtracted from the previous image to eliminate residual starlight scattered from the observatory optics. (The scattered starlight remains fixed on the detector while the planetary system rotates with the dither roll. Any planets present would then be detectable in this difference image.

The primary mirror is oblong, and its best IWA is aligned with its long axis. To study the habitable zone at all orientations around a star, the long axis has to be aligned at positions that are ±60º away from the starting point. This is accomplished by another "roll" around

the optical axis. At each new roll position, the adaptive optics are reset and then the two-image dither observation is repeated. With a ±15° dither around 60° roll positions, the total angular rotation around the target direction axis is ±75°.

The field of regard and target star observation scenario create the thermal environment constraints of FB1.
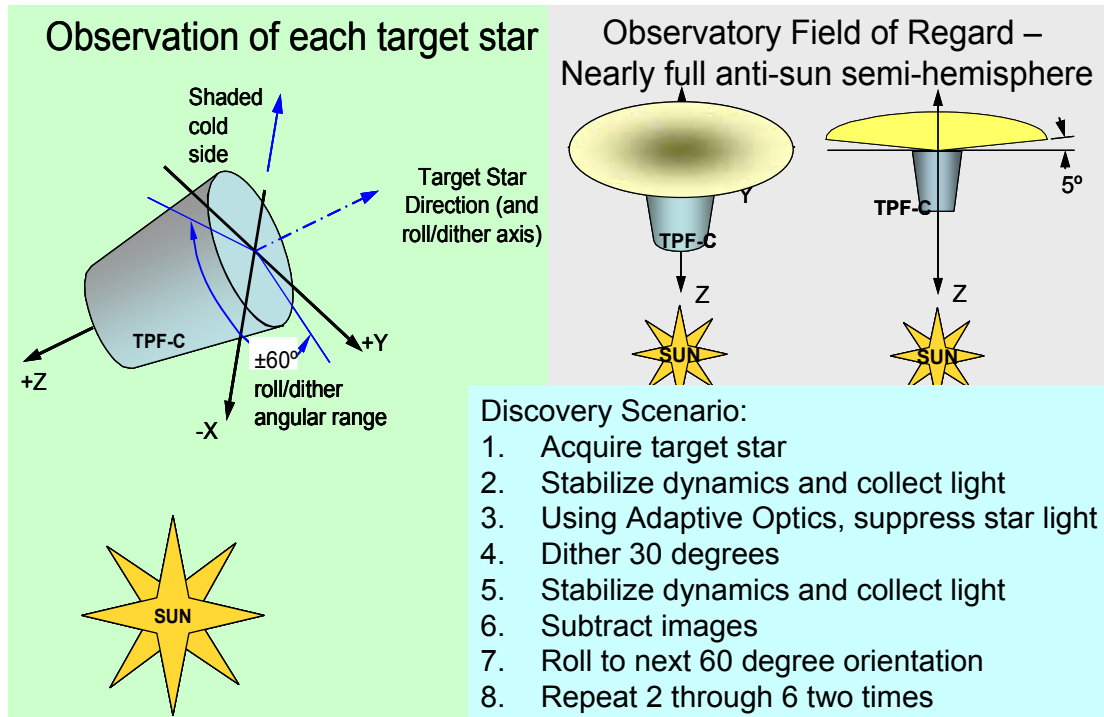
Figure 3.3-17. Schematic of the Observatory Field of Regard

3.3.2.4 Orbit Environmental Issues

The orbit environment is consistent with other missions flown in 1 AU heliocentric orbits that are not close to earth, such as Switzer and *JWST*. The space environments documents from these programs are available to us. To date the primary orbital environments issue has been the galactic cosmic ray environment, which drives strategy for reading out detectors. We have used an early *JWST* study to establish a 1,000s period between readouts as our baseline and are currently pursuing an update to this analysis.

3.3.3 Science Payload

3.3.3.1 Optical Telescope Assembly

3.3.3.1.1 Optical Telescope Assembly Requirements

We present the requirements on the Optical Telescope Assembly (OTA) as they are currently understood. Optical, mechanical, and thermal requirements are presented in turn.

3.3.3.1.1.1 Optical requirements

The need to avoid and/or control diffraction wherever possible in order to achieve the extreme contrast goals of *TPF-C* dictates that the PM have a monolithic surface. This is a departure from many recent ground and space-based systems including the James Webb Space Telescope. Studies indicate that a segmented design would need very small gaps (<100 μm) and extremely tight control of segment to segment piston, tilt, and curvature errors. Thus we view a monolithic facesheet as a key derived requirement. The secondary mirror (SM) and fold mirror (M3) are smaller and can readily be made as moderately lightweight monoliths from either Zerodur or ULE material

The optical design for the *TPF-C* OTA has been the subject of trade studies. In order to accommodate both excellent on-axis imaging plus good quality imaging over the wider General Astrophysics Instrument (GAI) field of view, as well as meet packaging requirements, a Ritchey-Chretien design was selected. The telescope is off-axis so as to not have any obscurations for secondary mirror supports, as required for the level of starlight suppression necessary. Table 3.3-6 presents the prescription for the *TPF-C* OTA.

Table 3.3-6 OTA Mirror Prescriptions

Name	Physical size (x by y), m	Off-axis distance	R, m	f#	k
PM	8.0 x 3.5	2.3	26.75	3.82	-1.00189
SM	0.89 x 0.425	0.237	3.041	4.13	-149
M3	0.29 x 0.31		-		-

Requirements for the primary mirror can be separated into static and dynamic terms. This is the basis of the organization of the error budget (Shaklan et al. (2005)). The static requirements have implications for fabrication, alignment, and ground testing. The dynamic terms enter not only into the primary mirror but also enter into observatory level analysis and design. As they enter into all of the requirements across the design, the emphasis has been on the dynamic requirements and they are perhaps the best understood.

The primary mirror static error can be corrected, in our baseline design, by a downstream coarse deformable mirror (DM) which has 10 μm total stroke. This has the ability to correct for some fabrication and launch induced errors as well as any aberrations from static thermal gradients on the primary mirror.

The static surface error allocation is based on the midfrequency requirement on the Technology Demonstration mirror. This midfrequency band, in the *TPF-C* context, refers to the band up to the limit of correctability by a high density deformable mirror placed downstream

at a pupil image of the primary mirror (for current work on demonstrations of Lyot corona-graphic contrast see, e.g. Trauger et al. (2005)). The specification is performed using a power spectral density specification on each optic, as they are used in the *TPF-C* error budget. Both the PM and SM have a total surface error allocation of 5.4nm over all spatial frequen-cies. M3 has an integrated rms over all bands which is tighter at approximately 1 nm total surface error allocation. We expect further analysis to show some relaxation within the low-est frequencies of the controllable bandwidth for the PM and SM.

The dynamic allocations come from studying the interaction of aberrations and jitter be-tween the primary mirror, subsequent mirrors, and the coronagraphic mask. As the mask is a linear mask, contrast is highly sensitive to the directionality and spatial frequency content of the errors. Work to date has indicated that the lowest ~12 Zernike terms (Noll-order ellipti-cal Zernikes) only are significant in the dynamic error budget and they are allocated individu-ally as can be seen in Table 3.3-7. The secondary mirror stability allocations are double those for the PM; those for M3 are 4 times those on the PM.

Table 3.3-7 Dynamic Wavefront Error Allocations for Primary Mirror Shape Change from *TPF-C* Error Budget.

Zernike terms	Zernike type	allocation (nm)
z4-z6, z8-z10	power, astigmatism, coma, trefoil	0.4
z7	coma	0.2
z11, z12	spherical, coma	0.005

Bulk motions within the OTA are referenced to the PM. Table 3.3-8 presents the long term and jitter (short term) allocations for bulk motions and tilts on the SM and M3.

Table 3.3-8 Dynamic Allocations for OTA Rigid Body Motions.

motion	lateral, nm	axial, nm	tilt, nrad
SM, thermal rigid body	65	26	30
SM jitter	~3	~1	~1.5
M3 thermal	100	100	10
M3 jitter	10	10	10

The primary mirror must not only have a highly reflective coating (protected silver), but the amplitude variations enter into the error budget just as much as phase (figure) errors do. Coating uniformity must be specified using a similar power spectral density form for ampli-tude errors; reflectance uniformity at the ~0.5% or better within the correctable band. Re-cent coating studies are discussed elsewhere (Balasubramanian et al. (2005)).

3.3.3.1.1.2 Mechanical requirements

Mechanical requirements are not yet well defined. The primary mirror must of course sur-vive launch, not deform under either mounting after polishing or under launch stresses. However, the vibration and jitter control architecture is still open (Blaurock et al. (2005), Liu et al. (2005)) and both active and passive reaction wheel disturbance mitigation schemes re-

main under consideration. Therefore it is difficult to assign a minimum first resonant frequency requirement; to date we have kept this value above ~10 Hz. Similarly, packaging is a strong constraint; the remainder of the observatory (secondary mirror and its support tower, instruments, thermal shroud, and spacecraft) all deploy outward after launch from the primary mirror assembly (PMA).

A three point bipod flexure mount was chosen (on each mirror in the OTA) to maximize on orbit stability by minimizing overconstraint on the mirror. A trade study considering the use of actuators on the primary for ground and/or flight to offload gravity and compensate for, e.g. gravity offload errors, launch effects, etc. was tabled when the optical stability requirements were much tighter than now, i.e. before the selection of the "8th order" coronagraph mask (Kuchner et al. (2005)). We plan to reassess this possibility and other possibilities to simplify ground testing and in flight correction in future configuration studies.

3.3.3.1.1.3 Thermal requirements

The thermal stability requirements are formidable if the optical stability requirements in Table 3.3-7 are to be met. The static gradient can (and will be) be fairly large (~4°C) but the dynamic gradients, during an observation and after a dither maneuver, must be held very low. Assuming a linear relationship, the FB1 integrated modeling showed a thermal stability of 0.08 mK worst case during the least stable dither maneuver solar orientation. This case still had substantial margin (40x) against the worst aberration. This suggests a thermal stability requirement of 3mK for the PM during an observation. Thermal gradients across and through the SM and M3 will be less as they only view room temperature surface

Such a lightweight structure does not conduct heat well, and trade studies have established that the usual ("textbook") thermal stability parameter, the ratio of thermal conductivity k to thermal expansion coefficient α, is not a good guide to thermal stability here. Rather, the thermal conductance overall is dominated by radiative, not by conductive coupling. This emphasizes the need for the lowest available thermal expansion and limits the materials choice to those specifically engineered for low expansion but available in large size, i.e. ULE fused silica and Zerodur.

3.3.3.1.1.4 Pointing Requirements

In the baseline design the secondary mirror is used as a component in the overall attitude control architecture, specifically as a fast steering mirror. We have recently reexamined the flowdown of requirements to this portion of the system, including the need for (slow) coarse alignment, large range of motion for SM-PM alignment as well as the pointing requirements; these are summarized in Table 3.3-9. Overall this two-stage mechanism is used in three control loops. The coarse stage is used whenever coarse telescope alignment (to 0.1 um tolerances) is required, such as on initial secondary mirror tower deployment. The fine stage is used to compensate very slow thermal drifts, with feedback from the laser truss. It is also used at a higher bandwidth for tip/tilt pointing control only, with feedback from the attitude control system.

Table 3.3-9. Secondary Mirror Actuator Requirements for Linear and Angular Resolution, Stroke, and Bandwidth.

	linear stroke (um)	linear resolution (nm)	angular stroke	angular resolution (nrad)	highest response frequency (Hz)	speed (nm/sec)
coarse/slow stage	±25000	100	0.4 mrad	400	DC, infrequent	8000
laser truss control loop	0.2	10	0.4 urad	10	0.01	300
pointing control loop	0.2	10	20 nrad	0.1	1	
high frequency stability	1		1 nrad		>1	

REFERENCES

S. B. Shaklan, L. F. Marchen, J. J. Green. "The Terrestrial Planet Finder Coronagraph Error Budget." *Proc. SPIE* **5905**, 2005.

J. T. Trauger, B. Gordon, J. J. Green, A. E. Lowman, D. Moody, A. F. Niessner, F. Shi, D. W. Wilson, C. J. Burrows, M. A. Ealey, and T. R. Price. "Laboratory demonstration of high-contrast imaging technologies and algorithms for space coronagraphy." *Proc. SPIE* **5905**, 2005.

K. Balasubramanian, P. Z. Mouroulis, L. F. Marchen and S. B. Shaklan. "Polarization-compensating protective coatings for *TPF-C*oronagraph optics to control contrast degrading cross-polarization leakage." *Proc. SPIE* **5905**, 2005.

M. D. Kuchner, J. Grepp, J. Ge. "Finding terrestrial planets using 8th order masks." *Astrophy. J.* (in press) 2005.

A. Kissil, G. J. Moore, J. E. Schiermeier, M. Chainyk. "Integrated modeling applied to the terrestrial planet finder mission." *Proc. SPIE* 5867 **2005**.

C. A. Blaurock, K. Liu, L. D. Dewell, J. W. Alexander, "Passive isolator design for jitter reduction in the Terrestrial Planet Finder Coronagraph *Proc. SPIE* **5867** 2005.

K. Liu, C. A. Blaurock, L. D. Dewell, J. W. Alexander, "*TPF* Coronagraph pointing control system design and evaluation." *Proc. SPIE* **5867**, 2005

3.3.3.1.2 OTA Design Description

The full system description has been given above. Here we describe the telescope, i.e. the system including the primary mirror assembly, secondary mirror tower and secondary mirror assembly, and the M3 fold mirror. These are all of the optics before the first image plane in the optical train.

The optical path enters the telescope baffle and reflects off an 8m x 3.5m elliptical-aperture, off-axis parabolic primary mirror. The light next reflects off the convex secondary mirror, towards a tertiary fold mirror that directs the beam into the coronagraph starlight suppres-

sion assembly. A pick-off mirror sends the outer portion of the beam to a general astrophysics instrument.

The mechanical interface between the OTA and the instruments and spacecraft interface is the payload support structure which is described elsewhere. Both the secondary mirror tower and the primary are mounted on the after metering structure (AMS), shown inFigure 3.3-18. The fold mirror also mounts directly to the AMS. We describe each of these assemblies in turn.
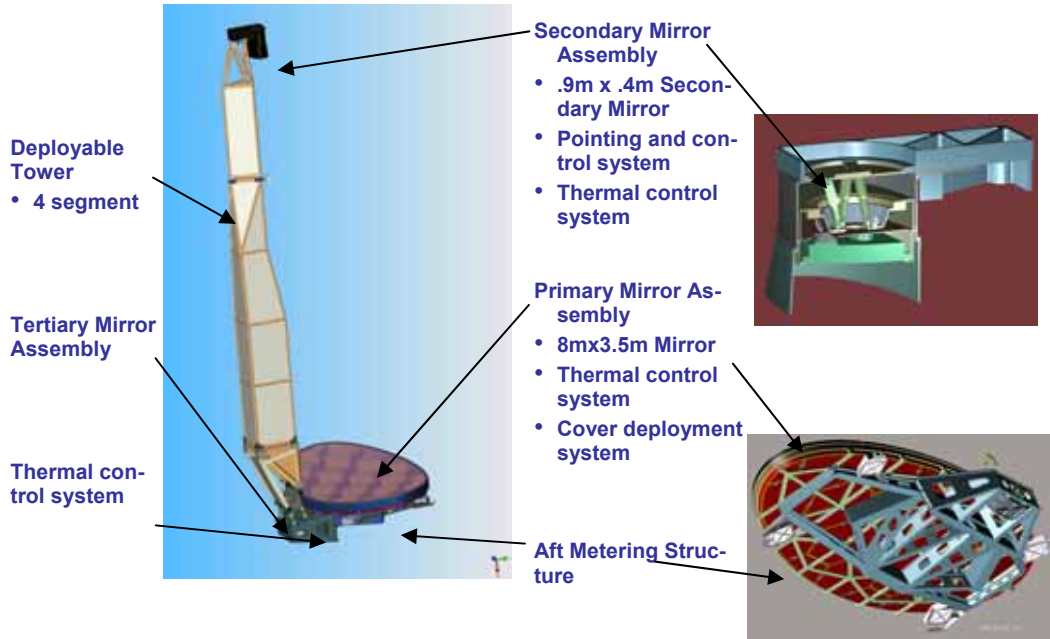
Figure 3.3-18. Optical Telescope Assembly Schematic

3.3.3.1.2.1 Telescope Design choices

Trade studies were performed among several telescope optical designs meeting requirements as well as packaging allocations. These include three-mirror anastigmats, Gregorian, Cassegrain, and the baseline Ritchey-Chretien design [Howard et al]. Considerations of aberration control and packaging led the final choice of the off-axis telescope whose optical prescription is given below (Table 3.3-10). The separation from PM to the secondary mirror (SM) is 12 meters.

Mechanical design was driven by packaging and stability as the foremost considerations.

Thermal design is driven by available power at L2 and the need for exceptional stability. Only the optical components are tightly controlled to room temperature; the secondary mirror tower, for example, is not tightly controlled nor heated to room temperature. It will have a substantial yet very stable axial gradient.

Table 3.3-10. OTA Prescription (mm units); the Separation from PM to SM is 12 Meters.

	Radius	Conic	Aperture	Off-axis decenter
Primary Mirror (PM)	26750.483 concave	-1.001939 hyperbola	8000 x 3500 ellipse	2300
Secondary Mirror (SM)	3041.014 convex	-1.470716 hyperbola	890 x 425 ellipse	237
Fold Mirror (M3)	Infinity	0.0	290 x 310 square	n/a
Effective Focal Length	140 m			
F/number, {x, y} axes	f/17.5	f/40.0		

The mirrors are lightweighted commensurate with their size to balance the need for observatory-level mass margin with exceptional stability. ULE fused silica or Zerodur would be used for the SM and fold; the primary would be ULE fused silica.

Primary to secondary mirror alignment is maintained during an observation by a laser truss [Shaklan, 2004]. Four corner cubes each on the edge of the primary and secondary are used; those on the primary have a partial hole to allow the beam to be reflected to the laser sensor from both mirrors. Eight beams overall are used which allows full six degree of freedom control as required for the off axis telescope.

3.3.3.1.2.2 Primary Mirror Assembly

The primary mirror is mounted semi-kinematically with 3 bipods to an aft metering structure (AMS). Behind the primary mirror, the AMS supports a set of heaters for maintaining the primary mirror at room temperature. Figure 3.3-19 shows an exploded view of the primary mirror assembly (PMA). From the front back, components are the stray light baffle, the primary mirror on a 3-point bipod mount (green), the thermal control system (red), the structure for the thermal system, MLI blanketing, and the AMS.

The 8 x 3.5m elliptical aperture primary mirror itself is made up of 20 individual segments of ULE fused silica joined into a monolithic mirror. Trade studies for the primary mirror that resulted in this design are described elsewhere [Content, et al.]. The segments are each a sandwich consisting of thin front and back plates with a lightweight core. The fabrication path for this mirror traces to established processes for on-axis mirrors with the technology extension to precision off-axis mirrors flowing through the Technology Demonstration Mirror (TDM). The mirror is a meniscus; i.e. it has constant 25cm thickness and a paraboloidal rear faceplate. This provides good stiffness at relatively low weight as well as uniform thermal conductivity across the mirror aperture. Table 3.3-11 lists the mass properties of the each of the telescope optics, and Figure 3.3-19 shows the exploded view of the primary mirror assembly (PMA).

Table 3.3-11. Areal Density, Light-Weighting Fraction, and Mass of each Telescope Optic. Light-Weighting Levels are a Compromise between Launch Weight Limits and Stability Requirements.

Name	Areal density (kg/m²)	Light-weighting (%)	Mass (kg)
PM	47	91 (~22 mm thick...)	1065.9
SM	60	70	17.7
M3	57	50	5
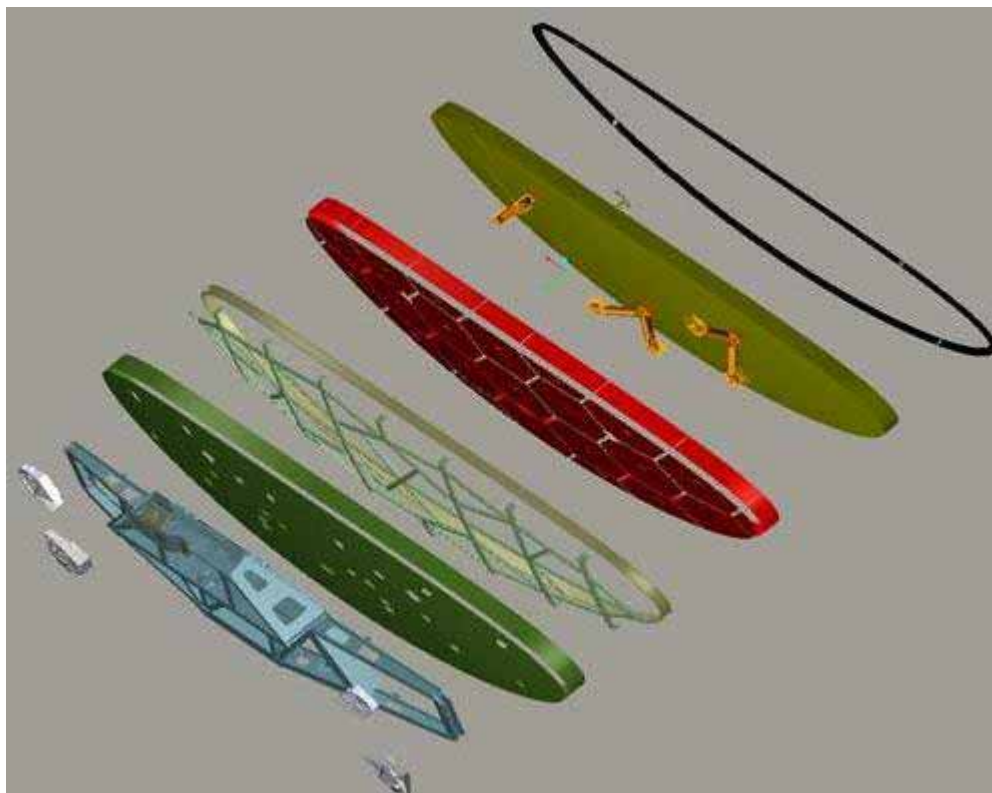
Figure 3.3-19. Exploded View of the Primary Mirror Assembly (PMA)

The primary mirror mounts are extensions of bipods previously used on other flight programs. They consist of a thin RTV compliant layer and an Invar mount pad held by Ti bipod flexures. These attach to strong points on the AMS which in turn are held in a semi-kinematic mount to the payload support structure (PSS) for a straight load path. The thermal structure has heater zones which can be separately controlled behind each segment that makes up the monolithic PM; this allows for compensation if there are slight CTE discontinuities from segment to segment. This structure (as do most of the thermal control components) is made from high thermal conductivity K1100 composite panels. The mechanical structures, including the structure supporting the PM thermal control assembly and the AMS are made from low thermal conductivity, high modulus M55J composite.

Modeling of the thermal performance of the PM shows high stability but significant front to back and edge to center gradients, as expected for a room temperature optic with a clear view of deep space. The slight static wavefront changes from these gradients are easily accommodated by the system design and the modeled thermal dynamic stability performance (§3.4.2.1) is excellent.

3.3.3.1.2.3 Secondary Mirror Tower
The tower provides deployable metering of the secondary mirror 12m in front and 2.3m laterally offset from the PM. The tower is hollow at the base with an opening through which the focusing beam from the SM is admitted to reach the fold mirror. The tower will also accommodate internal stray light baffles. It has hinges to allow unfolding from the launch configuration as shown below.

3.3.3.1.2.4 Secondary Mirror Assembly
The secondary mirror assembly is also designed for maximum stability; however it much also allow for both slow coarse and fast fine rigid body motions of the SM to account for deployment errors and pointing errors respectively. The mirror also does not have a view of space and so is held stable with minimal heater power. However it is still engineered with a complete thermal surround and a radiator to allow positive heater control to room temperature at all times. CAD views of the assembly are shown in Figure 3.3-21.

The mirror baseline design itself is a flat-back, 60% lightweighted mirror, of the same sandwich design as the PM but rather conservatively lightweighted to allow high stability (Figure 3.3-19). Weight details are shown above in Table 3.3-11.

The secondary mirror actuator is a hexapod so as to allow full six degree of freedom motion. The mirror must move to achieve good alignment against the primary; therefore it has (slow) coarse range of motion. In addition, it is part of both the laser truss control loop (keeping it aligned to the PM) and the pointing control loop (acting as a fast steering mirror). Therefore, at the ~10 nm motion level it must respond to at least a 1 Hz bandpass.
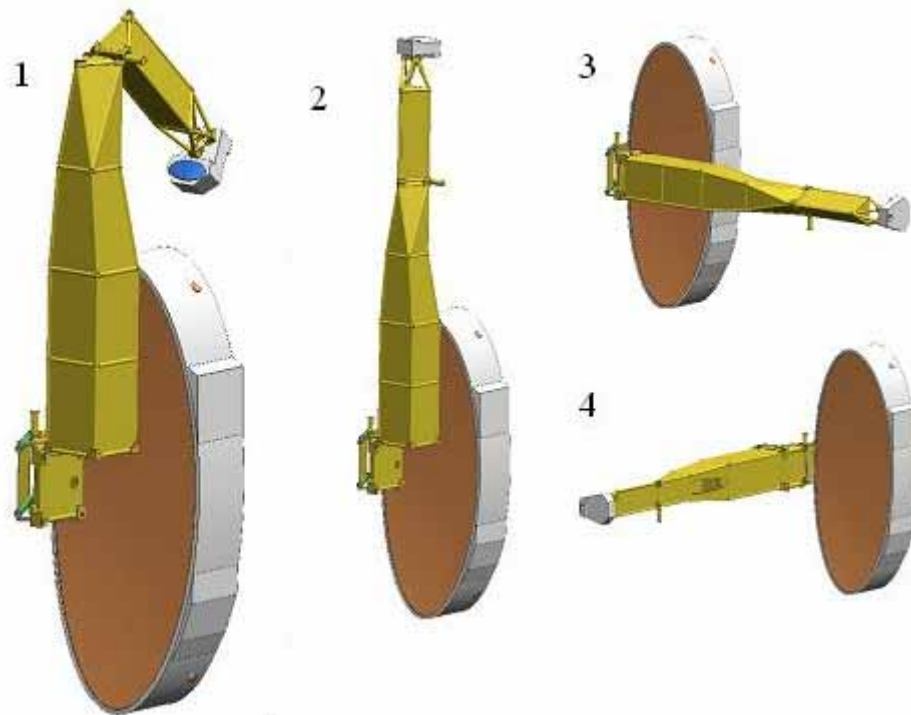
Figure 3.3-20. (1) Secondary mirror tower deployment sequence. (2) From the launch configuration, the top portion latches up to mate with the lower section (3) then the upper two sections rotate to mate with the base. 4) Finally the full tower is extended to its deployed position.
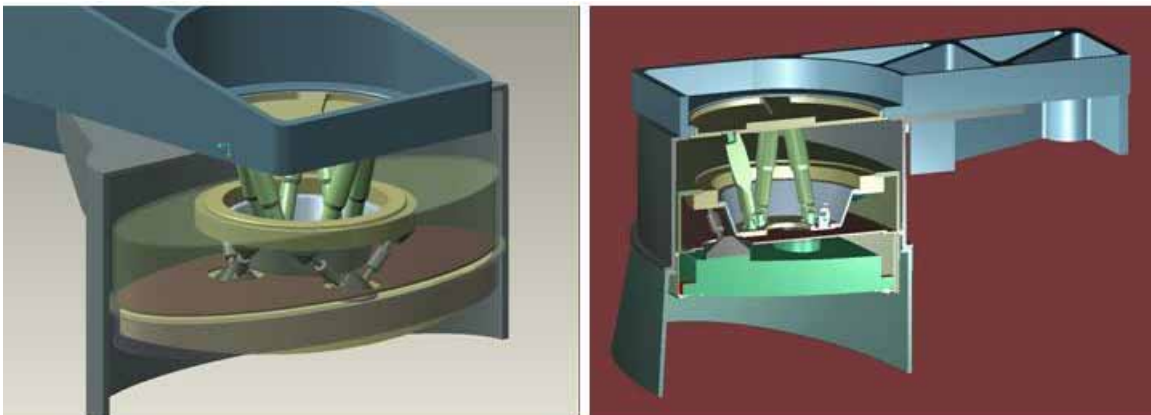
Figure 3.3-21. CAD Views of Secondary Mirror Assembly.
Left: cutaway through thermal shroud showing assembly mounting to the secondary mirror tower, with a hexapod actuator holding the secondary mirror mount, the mirror, its thermal control hardware, and its stray light baffle.
Right: cutaway through the assembly showing the reentrant interface from the hexapod to the mirror assembly, preserving stroke at minimum overall packaging volume.

Recent work on DM configuration [Shaklan & Green, 2005b] has shown that a serial DM layout significantly relaxes the static wavefront requirements on the SM and M3 optics (cf §4.1.2.1) such that their polishing and metrology requirements are not likely to be beyond the current state of the art.

3.3.3.1.2.5 Tertiary Fold Mirror (M3) Assembly

M3 is a moderately lightweighted ULE or Zerodur flat. It has a nearly square aperture, with rounded edges. It is tucked into the AMS behind the secondary mirror tower and folds the converging telescope beam under the primary mirror assembly towards the science instrument package. It has alignment actuation to position and steer the chief ray to align to the starlight suppression system (SSS). This system is used only on deployment and infrequently if the telescope alignment needs to be checked and is not used during observation.

The M3 is mounted using bipods similar in design to those used on the PM and SM to avoid mounting stress. Thermal control to room temperature is provided via small heaters and thermocouples with a MLI shroud on the sides and back of the assembly. The M# design
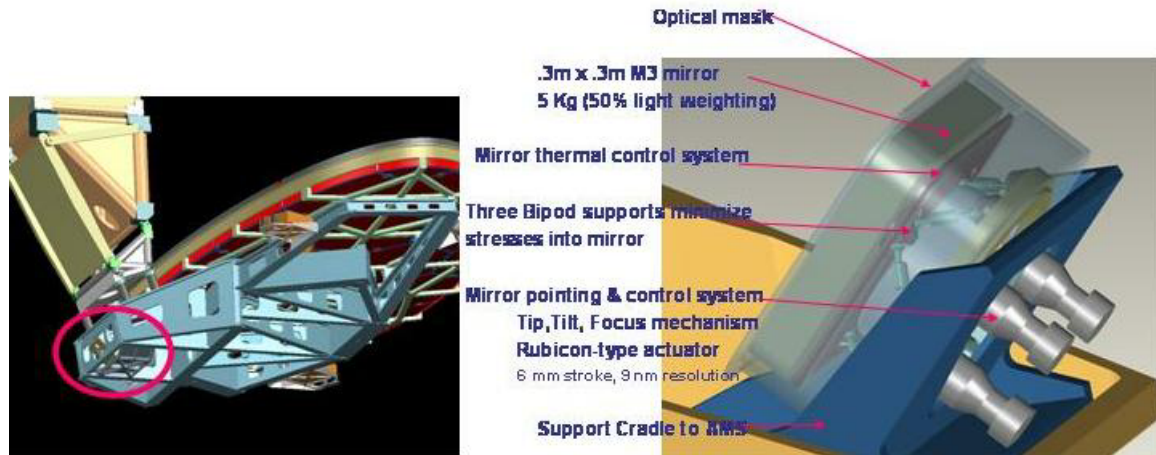
concept is illustrated in Figure 3.3-22.

Figure 3.3-22 M3 Assembly. Left: The M3 assembly (red circle) is in the AMS at the base of the secondary tower. Right: M3 view showing the components in the assembly including mirror, actuators, thermal control, and stray light mask.

REFERENCES

D. Content, R. Ohl, T. Cafferty, E. Cohen, R. Egerman, et al. "Engineering Trade Studies for the TFPc 8x3.5m primary mirror." *Proc. SPIE* **5867**-33 (2005).

Stuart B. Shaklan, Luis F. Marchen, Feng Zhao, Robert D. Peters, Timothy Ho, and Buck Holmes. "Metrology system for the Terrestrial Planet Finder Coronagraph." *Proc. SPIE* 5528, 22 (2004)

Shaklan & Green 2005b. "Reflectivity and Optical Surface Height Requirements in a Broadband Coronagraph I: Contrast Floor Due to Controllable Spatial Frequencies." submitted to Applied Optics

3.3.3.1.3 TPF-C Mirror Coatings
3.3.3.1.3.1 Introduction
The mirror coatings for *TPF-C* share some requirements with other, space borne observatories but also include some novel, high precision requirements. High reflectivity throughout the nominal bandpass (500–800 nm) and over the possible extended bandpass (– 1000 nm) is necessary considering the intrinsically faint targets and the potentially high number of reflective surfaces in the telescope and wavefront correction system. In addition, the effects of polarization can become significant, leading to the necessity to add multiple, polarized channels with the consequent increase in instrument complexity and mass. The magnitude of these polarization effects are closely related to the specific coronagraph design so that coating decisions have to be part of a much more integrated design than is usual. Finally, the ability to maintain and verify coating performance during the instrument integration and test period, likely to be several years, must be developed to assure the required in-flight performance.

We have considered a number of potential coatings for the nominal *TPF-C* optical design (23 reflecting surfaces in a single channel) which appeared as promising candidates. These include protected Ag, with a minimum polarization overcoat, protected Al, and bare Au. Initial coating samples have been obtained of the protected Ag coating to confirm the expected polarization behavior and some testing of these and other samples were performed. Analysis of the expected instrument performance with these coatings was also begun and illustrates the close coupling between coating performance and coronagraph design.

We will discuss each of these points and summarize the current status, conclusions and outstanding work regarding *TPF-C* coatings.

3.3.3.1.3.2 Requirements
The major *TPF-C* requirements are outlined in Table 3.3-12 where we have tried to indicate those requirements generally common with other space borne observatories and some requirements unique to *TPF-C*.

Table 3.3-12. *TPF-C* mirror coating requirements

Requirements generally common to spaceborne observatories		Notes
	High transmission over nominal bandpass (500-800nm)	Individual mirror R should be very high to keep R^{23} reasonable
	Lifetime of 5yrs (flight) + several years between original coating, through integration and launch	Lifetime requirement is to keep overall throughput high and maintain required uniformity properties
	Practical, simple, coating technology	
Requirements unique to *TPF-C*		
	Uniformity of phase & amplitude	- Must be within range necessary for wavefront correction - Specify both phase & amplitude PSD on coated optics - Phase non-uniformities due to non-uniform coating thickness (process control) and to intrinsic coating phase variation with angle of incidence for non-flat optics - Amplitude non-uniformities due to intrinsic variation with angle of incidence for non-flat optics & process control - Note that size of optics varies greatly between ~0.1 M to 8 M; high uniformity requirements are most difficult to achieve for large components
	Minimum polarization over band-pass	Polarization causes variable wavefront (phase and amplitude) to propagate through system while wavefront correction using deformable mirrors is a single, compromise setting. If instrument polarization can be kept small enough, and using aberration insensitive coronagraphic masks (eighth order mask for example) separate polarization channels may not be required. Eighth order mask throughput is lower than that with 4th order mask; therefore mirror coatings have to be less lossy.
	Verification of high performance properties throughout lifetime	Will need a means of verifying polarization properties by measurements, for example, on large, 8 M scale optics throughout the several years between coating and launch.

3.3.3.1.3.3 Reflectance and Bandpass

To meet the high, visible reflectance requirements we considered three designs: overcoated Ag, bare Au, and overcoated Al. Ag and Al require overcoats to protect from tarnish and oxidation respectively.

The expected single surface reflectance of these three coatings is illustrated in Figure 3.3-23 at the end of this section. It is seen that protected Ag has the highest reflectance throughout

the nominal (500–800 nm) *TPF-C* bandpass. Two different curves for protected Ag are shown in Figure 3.3-23 they both have minimum, polarization overcoats, but differ in the assumed optical constants of Ag. Of the other two coatings illustrated in Figure 3.3-23, bare Au has rapidly diminishing reflectance shortward of 600 nm, which will be greatly accentuated with multiple coated mirrors, while overcoated Al has a lower reflectance than either Ag or Au but does extend to much shorter wavelengths than either. This relatively low Al reflectance removes it from consideration for coating of as many as the 23 surfaces in the nominal *TPF-C* optical design, though configurations in which Al is used on only a few, key mirrors were further considered.

Figure 3.3-24 illustrates the effect of using either protected Ag or bare Au on the entire string of 23 mirrors. Illustrated in blue are models of the minimum polarization coating for Ag with SiO_2 overcoat thickness varying by 25 nm. The small differences in single mirror reflectance are magnified when applied to 23 mirrors as shown; illustrating that good process control over all coatings will be required to produce the optimum system throughput. Also shown is the near-normal incidence measured reflectivity of sample protected Ag coatings from two vendors, raised as R^{23} to simulate full observatory throughput. There are obvious differences throughout the *TPF-C* bandpass with neither having the optimum reflectance performance we would like. (These samples were only rough, initial attempts to produce the minimum polarization coatings for *TPF-C* and should not be taken as final products.) The model of bare Au shows that it would be expected to produce significantly lower total throughput shortward of 700 nm, and thus through most of the prime *TPF-C* bandpass, compared to any of the Ag models.

As previously noted, protected Al would produce prohibitively low observatory throughput if it were applied to a series of 23 mirrors. However, if only the first three, large mirrors were coated with protected Al (the *TPF-C* primary, secondary, and tertiary mirrors) there would be the possibility to pick off the field surrounding the *TPF-C* field after the tertiary and direct this outer field to a general astronomical instrument. Because protected Al can have high reflectivity into the ultraviolet (UV-Al), such a general instrument could potentially have high sensitivity down to about 120nm in the UV. We considered two configurations of overcoated Al mirrors: first a minimum polarization coating (using the same principle as the Ag design) to minimize visible polarization in the *TPF-C* bandpass, and secondly, a nominal, high efficiency, ultraviolet coating, such as those applied to the *HST* mirrors. Both coatings used MgF_2 as the protective overcoat in order to provide high UV reflectance. They differ in the overcoat thickness: 141 nm for the minimum polarization coating, and 25nm for the high reflectance UV coating. Figure 3.3-25 shows the expected single surface reflectance of the minimum polarization of both coatings. Models with various levels of the absorption parameter, k, of MgF_2 are illustrated (k reduced by ½ from the tabulated values provided a good fit to measured UV-Al coating reflectance, so is preferred). The different k values change the reflectivity below 300 nm only. The minimum polarization case has such a thick MgF_2 overcoat that the overall throughput, even if this coating were applied to only three mirrors, would be very non-uniform below 300 nm. In addition, the minimum polarization coating has the unfortunate coincidence of producing an interference minimum near 850 nm, enhancing the well known "Al dip" and would cause substantial throughput loss for the *TPF-C* observatory in the visible. Alternatively, we considered the application of a high UV reflectance coating (UV-Al), which would have less desirable polarization properties than the minimum polarization coating, but does have higher and more uniform reflectivity as shown

in Figure 3.3-25. The total throughput reduction of such a coating, assuming it was applied to only three of the *TPF-C* mirrors and that all other mirrors had protected Ag coatings, is illustrated in Figure 3.3-26. The throughput penalty would be about 25% over the *TPF-C* bandpass compared to a system with all protected Ag coatings. In spite of this penalty, such a system might be desirable either to increase the capability of *TPF-C* by enabling an ultra-violet capability for an auxiliary instrument, or to provide an alternative coating if technical difficulties were encountered in either the application or long term stability of the protected Ag coating.

3.3.3.1.3.4 Uniformity & Polarization

Both phase and amplitude variations and polarization will be present across the non-flat optics of *TPF-C* as rays strike these surfaces at non-normal incidence. Over the *TPF-C* range of incident angles ($\sim 1°- 11°$) the amount of non-uniformity for each mirror is small with either Au or protected Ag: < 0.01 wave (phase) and $< 5 \times 10^{-4}$ (relative amplitude). These levels are within the wavefront correction range and their expected power is dominantly in low order Zernike terms which have low sensitivity when using coronagraphic masks like the eighth order design (Shaklan and Green, 2005). More importantly, is the effect of coating polarization that could necessitate multiple optical paths and significant observatory complications for acceptable correction.

Figure 3.3-27 and Figure 3.3-28 show the single surface phase difference and amplitude ratio of the s and p polarizations for protected Ag with a minimum polarization coating of SiO_2. Each curve shows the results at a particular angle of incidence covering the range on the primary or secondary mirrors as functions of wavelength. Over the *TPF-C* range of 500–800 nn, Figure 3.3-27 shows the phase difference has been minimized with two wavelengths having 0 phase difference. The plot also shows the results outside the nominal bandpass where the phase difference is substantially greater. While minimization of phase difference was accomplished, the resulting amplitude ratio is also seen to be very small (Figure 3.3-28), including for wavelengths longward of the nominal bandpass.

Balasubrimanian et al. (2005) have also proposed a possible alternative design to produce polarization compensation by coating the *TPF-C* primary and secondary mirrors with protective Ag where the thickness of the protective layer is different on each substrate, causing a relative shift of the wavelength dependent polarization, and possible cancellation over a larger bandpass.

The polarization properties of bare Au are shown in Figure 3.3-29 and Figure 3.3-30 and the UV-Al coating in Figure 3.3-31 and Figure 3.3-32 . Through the 500-800 nm bandpass, the protected Ag coating polarization properties (Figure 3.3-27 and Figure 3.3-28) are clearly better than either Au or UV-Al. However, longward of 800 nm the minimum polarization Ag coating also has rapidly increasing polarization. The implications of these polarization properties for *TPF-C* must be assessed by determining the resulting contrast for a model observatory.

3.3.3.1.3.5 Initial Sample Performance

While these results demonstrate that protected Ag with a minimum polarization overcoat should be the most suitable coating for the defined *TPF-C* observatory we began to obtain

samples from two separate vendors to investigate the properties of real coated samples. Figure 3.3-33 compares some reflectance measurements of samples from two vendors with expectations based on available optical constant data.

Two different models of protected Ag are illustrated using Ag optical constants from a proprietary source and from Palik. For both models the same optical constants for SiO_2 were used. While both models produce high reflectivity, the Palik model is lower by about 2%; for single surface reflectance; this difference, while relatively small, would result in a significant difference if applied to all 23 surfaces. Also shown for comparison are the results from two initial coatings produced by different coating vendors for our testing. The reflectivity for a single surface is again high in both cases but the few percent differences in detail would lead to significant overall throughput differences if applied to all *TPF-C* mirrors (illustrated in Figure 3.3-25). We see as well that the differences between both samples and the models are also at the few percent level so that again, predictions for overall throughput based on such models are not highly reliable. The basic problem is that the optical constants of both Ag (subject to tarnishing) and the various materials used in the overcoats (more complicated than the simplest SiO2 layer modeled but these should not lead to significant differences) are not as well determined as we would like and are almost surely process dependent. Ellipsometric analysis of these coatings can better determine these optical constants and should be performed during the process of coating qualification in order to have highly reliable performance estimates. For comparison, we also show the modeled bare Au reflectance, using optical constants from Palik, and measurements of a sample in hand at Goddard. For this simple inert coating, the optical constants appear to produce good agreement with the measurements and predictions for bare Au using these optical constants should be more reliable than the protected Ag results.

Figure 3.3-34 shows some measurements of phase difference obtained by ellipsometry of the protected Ag sample provided by vendor #2 (see Figure 3.3-29 for reflectance measurements of this same piece). Instrumental restrictions allowed for measurements only as low as 16°, still larger than the ~11° largest angle of incidence for the nominal *TPF-C*. Nevertheless, the general minimum polarization behavior expected is verified: at two wavelengths in the bandpass, there is no phase difference between the s and p polarizations forcing the magnitude of polarization to be small throughout the visible. Also shown, in red, are models of the measured three angles of incidence where the nominal overcoat index of refraction was increased by 1.25 and the thickness set at 115 nm instead of the nominal 125 nm. These changes provide better agreement with this first attempt for a minimum polarization Ag coating.

3.3.3.1.3.6 Contrast Comparison of Various Coatings
In order to determine the effect of coating polarization on the overall constrast performance, several models to numerically simulate these effects have been constructed. Balasubramanian et al. analyzed the contrast from a model coronagraph employing both optimized protective Ag coatings as well as ½ wave coatings, an ideal, band limited $sinc^2$ mask and Lyot stop, and equipped with a Michelson wavefront corrector. All calculations were done at 600nm (the worst polarization wavelength for the protected Ag coatings over the 500-800nm bandpass). The Michelson corrector was set for various polarized wavefronts and the residual contrast computed from other selected wavefronts. In all cases of the pro-

tected Ag coatings, contrast was typically in the $10^{-14} - 10^{-11}$ range with the worst points not exceeding 1.2×10^{-10}. These initial results indicate that using protected Ag coatings, can enable the elimination of multiple polarization channels in *TPF-C*; use of eighth order masks, less sensitive to low order aberrations than the sinc^2 mask used in this study, should provide even better contrast results

Other contrast calculations have been recently performed. We used ZEMAX polarization tracing through the *TPF-C* optical design up to the pupil, just prior to the coronagraph (13 mirrors). Beyond that, Fourier transform coronagraph models were made using two different configurations: one using a sinc^2 mask (similar to the simulations of Balasubramanian et al.) and appropriate Lyot mask, and another using an eighth order coronagraphic mask and matching Lyot mask. Four different coatings were simulated as well:

1. The three coatings discussed so far (protected Ag coating applied to all 13 mirrors
2. The Al-UV high reflectivity ultraviolet coating using Al+MgF2 applied to the primary through tertiary mirrors with protective Ag coatings on subsequent mirrors
3. A bare Au coating applied to all 13 mirrors)
4. An ideal coating (R=1, no polarization) applied to all mirrors.

Runs through the coronagraph model with a perfectly uniform input pupil were also made to establish that the numerical limit of the model was significantly less than the coated model results.

We assumed an unpolarized source and simulated the resulting ensemble of wavefronts in two field directions at the exit pupil (Ex, Ey) which were propagated through the coronagraph model and intensities added at the image plane. A Michelson, conjugate pupil, wavefront correcting system was also simulated by determining an "average" wavefront to correct and applying this correction to the ensemble of wavefronts. This "average" wavefront was an intensity weighted mean of phase and relative amplitude variations; such a nominal correction may still not be optimal (no weighting for the coronagraph sensitivity to various spatial frequencies was employed, for example) but does make a significant contrast improvement as will be shown. Contrast at the image plane was calculated at the fiducial radius, $4\lambda/D_8$ (0.052 arcseconds at 500 nm, where D_8=8 meters, the longest extent of the elliptical primary mirror) and over the radial range 4-10λ/D_8. A central band, where planetary intensity is 30 % or less of its maximum throughout the field, due to the near-axis, coronagraphic mask transmission function, was excluded from consideration. All calculations performed to date were monochromatic; the coronagraph masks were sized for each particular wavelength. Broad band simulations also need to be performed to verify that the coatings do not produce any significant narrowing of the bandpass compared to that which is already present in the Michelson corrector (Bowers et al., 2003). Results for the case of a single corrector channel, as opposed to two separate polarization channels are shown here.

The main results from these simulations are illustrated in Figure 3.3-35 and Figure 3.3-36 showing the median contrast at $4\lambda/D_8$ for the sinc^2 and eighth order coronagraphs respectively and Figure 3.3-37 showing median contrast over the 4-10λ/D_8 region. All results are monochromatic – the coronagraph mask and Lyot stop were scaled appropriately for each wavelength shown.

The $4\lambda/D_8$ results for the $sinc^2$ mask show that all three coatings produce contrast greater than 10^{-10} without wavefront correction at nearly all wavelengths in the 500–1000 nm region. For comparison, the results substituting an ideal mirror show about an order of magnitude improvement, demonstrating that the coating polarization dominates the achievable contrast without wavefront correction. With wavefront correction applied, a clear distinction between coatings emerges. A substantial improvement in contrast is achieved, over the wavelengths < 800 nm, for the minimal polarization, protected Ag coating (as previously reported at 600 nm by Balasubrimanian). At ≥ 800 nm however little improvement is achieved; the other two coatings show much less improvement at all wavelengths. The low order aberrations due to changes in phase and amplitude from the coatings over the range of incident angles on the non-flat optics are too great for wavefront correction to improve greatly except for the case of the minimal polarization, protected Ag coating design.

The results for the eighth order mask are fundamentally different as illustrated in Figure 3.3-36 . In this case, without wavefront correction, the contrast for all three coatings is nearly identical to the ideal mirror case. This contrast level is set by the very small, residual phase error in the basic *TPF-C* design with essentially no contribution from any of the real coating models. When wavefront correction is applied, the contrast using any of the coatings improves about an order of magnitude, with median values typically about 2–3 x 10^{-12}, very close to the perfect case, that of a pupil with totally uniform phase and amplitude. The reason for this much improved coating contrast compared with the $sinc^2$ coronagraphic model is that the eighth order coronagraph is much less sensitive to the lower order pupil aberrations which the coatings add to the *TPF-C* design residual (see Shaklan and Green, 2005).

3.3.3.1.3.7 Summary and Recommendations

For the assumed *TPF-C* configuration (500–800 nm bandpass, 23 mirror system) we have concluded that protected Ag using a minimum polarization overcoat provides the best overall performance. The performance measurements we have made from our first two sample mirrors look very promising and confirm the minimum polarization properties we expected. This coating produces the highest overall system throughput and could be used with either a coronagraph of the sinc2 or eighth order type below 800 nm, without having to add separate polarization channels.

However if *TPF-C* is to operate with the same degree of contrast (< 10^{-10}) at wavelengths longward of 800 nm, and without separate polarization channels, none of the present coating designs will work with a $sinc^2$ coronagraph.

The eighth order coronagraph is greatly preferred from a coating and polarization perspective since it strongly suppresses the low order aberrations generated by the coatings studied. Use of this coronagraph allows the extension of observable wavelengths > 800 nm with all coatings studied. While protected Ag is still preferred for its higher total throughput, the contrast analysis suggests that the ultraviolet Al coating may be a viable alternative candidate coating (broad band calculations need to confirm this). This coating has been applied on numerous space missions (including the Hubble Space Telescope). Use of this coating could enable a general science instrument with ultraviolet capability or provide a possible alterna-

tive coating should technical difficulties with production or stability of protected Ag coatings on large optics appear. We note that even with the UV-Al option we assumed that all smaller optics would have a protected Ag coating applied. The major penalty of using the UV-Al option, would be an overall loss of throughput of about 25-30% compared to an all Ag configuration.

Further system modeling to establish the broad bandpass contrast performance of these coatings is required. Additional technological development of coatings, both Ag and possibly ultraviolet Al should also be undertaken to establish the long term performance to the high standards demanded by *TPF-C*. Protected Ag coatings originally suffered from inconsistent lifetime performance but in recent years have become more accepted and are used on the Gemini 8M telescope for example and are incorporated in the ACS instrument aboard *HST*. Process development and control to achieve this performance on mirrors as large as 8M will be challenging as well. If the science goals change so that the bandpass is shifted to longer wavelengths, bare Au coatings, or perhaps a protected or hardened Au coating may be another practical alternative. Finally, whichever coating is selected, a means of verifying performance during the probable several years between component coating and launch must be developed to assure flight qualification.

REFERENCES

Edward Palik. "Handbook of Optical Constants of Solids." *Academic Press*, 1998.

Kunjithapatham Balasubramanian, Daniel J. Hoppe, Pantazis Z. Mouroulis, Luis F. Marchen, and Stuart B. Shaklan. "Polarization compensating protective coatings for *TPF-Coronagraph* optics to control contrast degrading cross polarization leakage." *Proc. SPIE* Vol. 5905, 2005.

Bowers, Charles W., Woodgate, Bruce E., Lyon, Richard G. "Novel method of high-accuracy wavefront-phase and amplitude correction for coronagraphy." Instrumentation for Detection of Exoplanets. Edited by Coulter, Daniel R. *Proceedings of the SPIE*, Volume 5170, pp. 292-306 (2003).

Shaklan, Stuart B. and Green, Joseph J. "Low-Order Aberration Sensitivity of Eighth-Order Coronagraph Masks." *ApJ*, 628, 474.
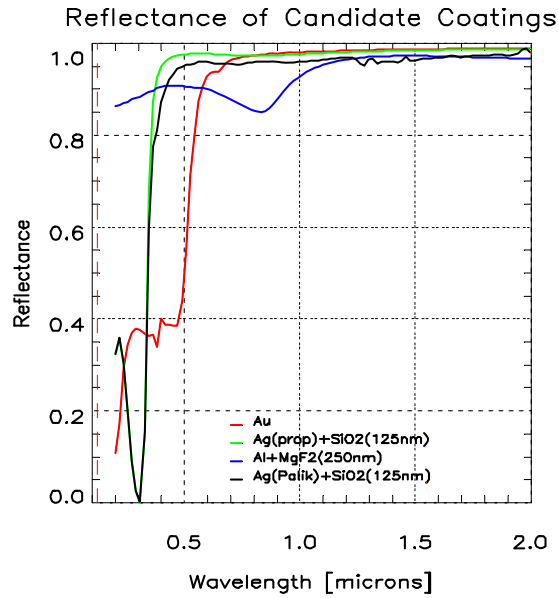
Figure 3.3-23. Single surface model reflectance of some candidate mirror coatings including Au (using indices from Palik), minimum polarization Ag (two models, one using proprietary indices and the other using indices from Palik), and Al+MgF2. The protected Ag coatings clearly have the highest reflectivity through the nominal *TPF-C* bandpass (500–800 nm) though even the small differences in these two models will result in significantly different predictions for the total system throughput (23 mirrors).
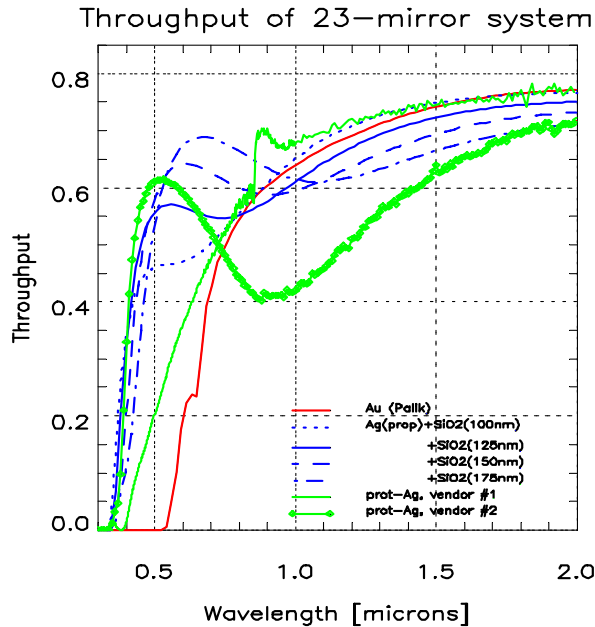
Figure 3.3-24. Predictions of the full *TPF-C* system throughput for the nominal, 23 mirror design shown are the results for modeled Au, three models of protected Ag using the indices from a proprietary source but for three different overcoat thicknesses (the minimum polarization is the solid blue curve with 125 nm thickness), and the extrapolated (R[23]) results from two preliminary test coatings from different vendors.
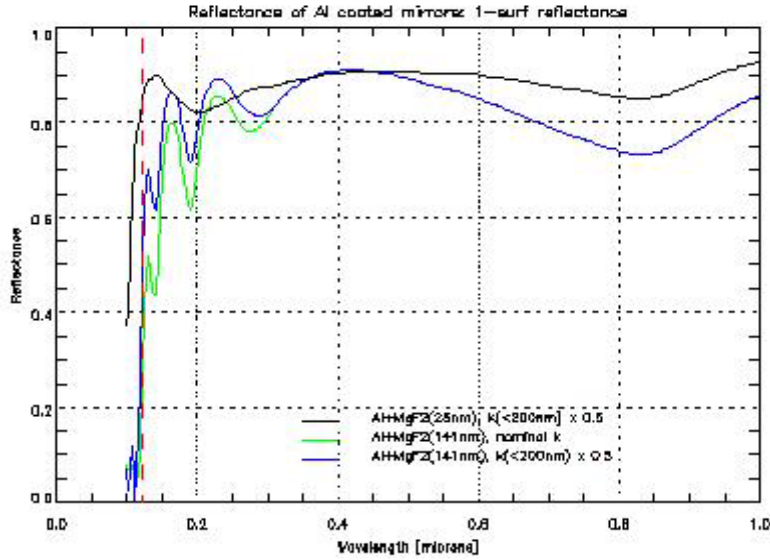
Figure 3.3-25. Predicted single surface reflectivity of Al+MgF$_2$ coatings for a high reflectance UV-Al coating (black curve with 25 nm MgF2 overcoat) and for a minimum polarization coating (visible) with 141 nm MgF2 overcoat. Several values of MgF2 absorption constant k were used to allow for the uncertainty in this value. Reflectance of the minimum polarization models is significantly reduced in the primary *TPF-C* bandpass and is very non-uniform below 300 nm. Coating three mirrors with such a coating will increase these deviations. The nominal UV-Al reflectance is much better, both in the visible and ultravio-

let.
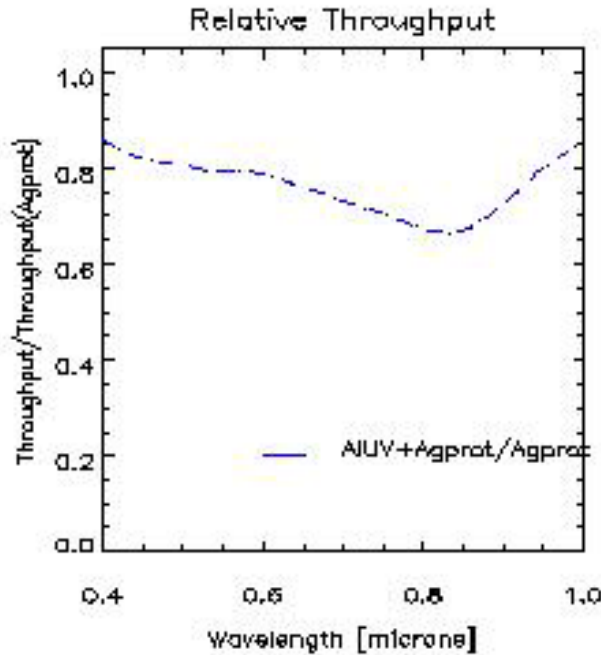
Figure 3.3-26. The relative throughput of a *TPF-C* design with three mirrors coated with UV-Al coatings and all others with protected Ag, compared to a design with all mirrors having protected Ag coatings.
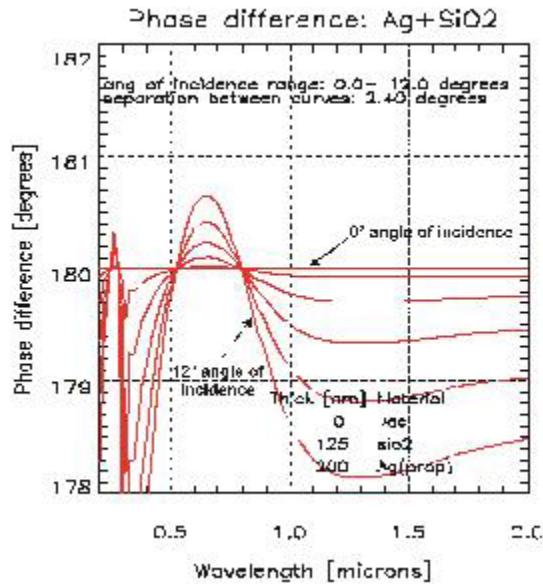
Figure 3.3-27. Models of the minimum polarization, protected Ag coatings (Balasubramanian) showing phase difference between polarizations for a single surface. Each solid curve represents a different angle of incidence from 0-12°, spanning the range (about 1-11°) incident on the non-flat optics of the nominal *TPF-C* design. Two wavelengths within the nominal bandpass (500–800 nm) have no phase difference and at other wavelengths within the bandpass, the polarization is minimal. Outside the bandpass, the polarization increases.
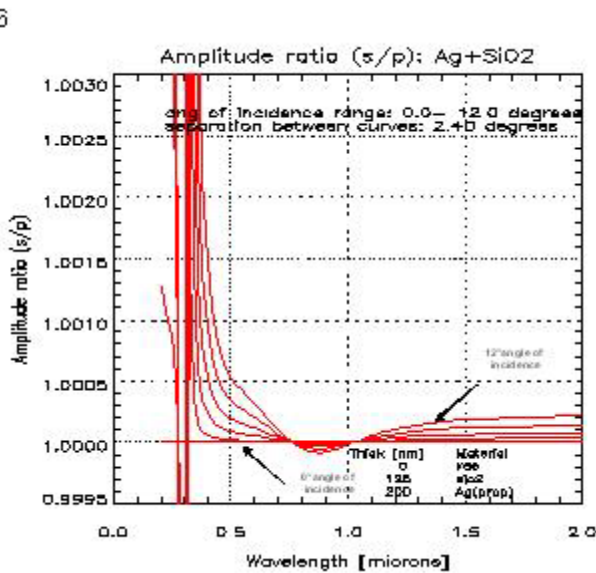
Figure 3.3-28. Models of the polarized amplitude ratio for a single surface using the minimum polarization, protected Ag coating. Each curve represents a different angle of incidence spanning the range encountered on the non-flat optics of the nominal *TPF-C* design. The minimal polarization coating, designed to minimize phase differences in the bandpass, also results in very low amplitude difference between polarizations including wavelengths longward of the nominal bandpass
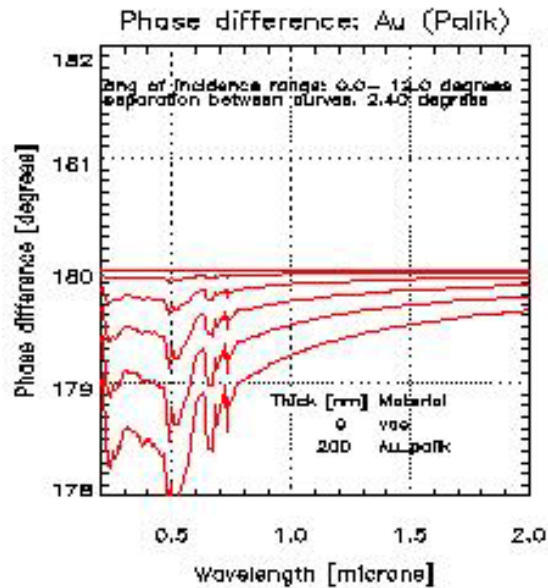
Figure 3.3-29. Models of the phase difference for bare Au coating using the indices of Palik. Each curve represents a different angle of incidence, spanning the range encountered on the non-flat optics in the nominal *TPF-C* design. The polarization is significantly greater than the models for protected Ag throughout (see Figure 3.3-27) the primary *TPF-C* bandpass (500–800 nm) but improving longward of this bandpass.
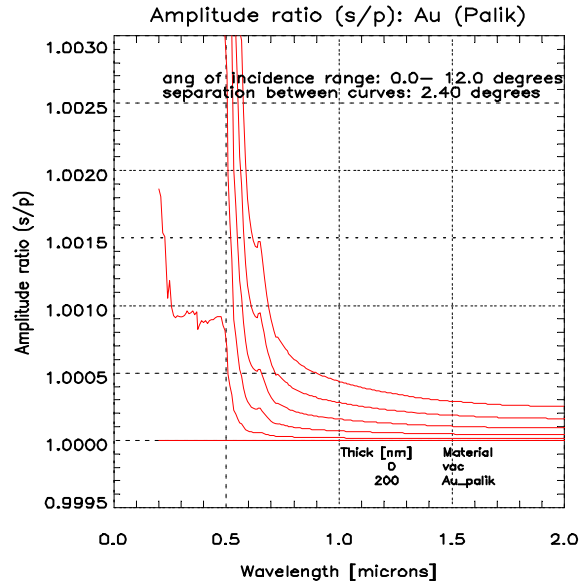
Figure 3.3-30 Models of the amplitude ratio for bare Au coating of a single surface using the indices of Palik. Each curve represents a different angle of incidence, spanning the range encountered on the non-flat optics in the nominal *TPF-C* design. The amplitude polarization is seen to be greater than the protected Ag results (see Figure 3.3-26) in the nominal *TPF-C* bandpass (500–800 nm).

Phase difference: Al+MgF2(25nm)

0° angle of incidence

12° angle of incidence
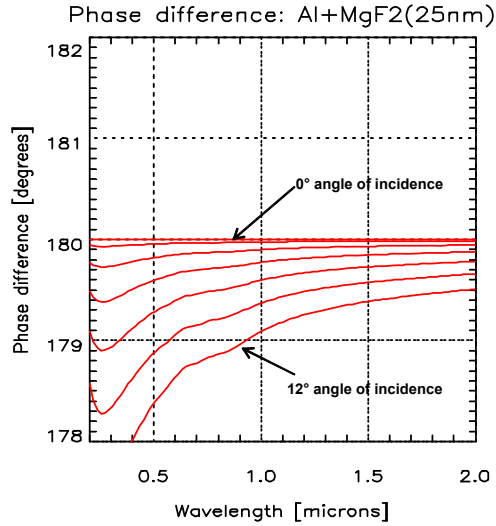
Figure 3.3-31. Models of the phase difference for UV-Al coating each curve represents a different angle of incidence, spanning the range encountered on the non-flat optics in the nominal *TPF-C* design. The polarization is significantly greater than the models for protected Ag throughout

Amplitude ratio (s/p): Al+MgF2(25nm)

ang of incidence range: 0.0– 12.0 degrees
separation between curves: 2.00 degrees

12° angle of incidence

0° angle of incidence

Thick [nm]	Material
0	vac
25	mgf2
5000	Al_hass&hadley
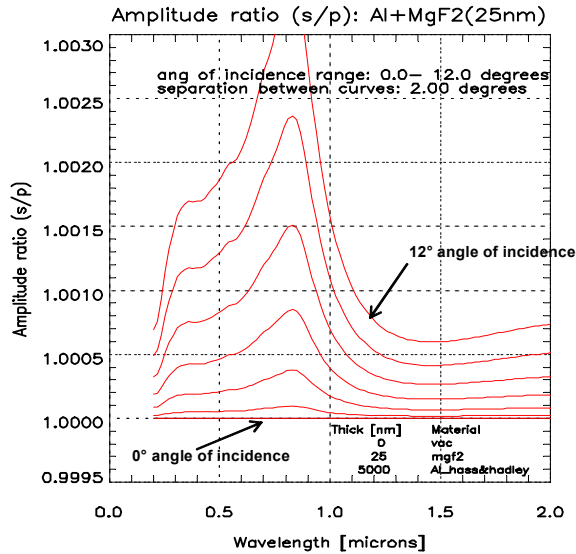
Figure 3.3-32. Models of the amplitude ratio for the UV-Al coating of a single surface. Each curve represents a different angle of incidence, spanning the range encountered on the non-flat optics in the nominal *TPF-C* design. The amplitude polarization is seen to be greater than the protected Ag results (see Figure 3.3-32) in the nominal *TPF-C* bandpass (500–800nm).

Reflectance (single surface)
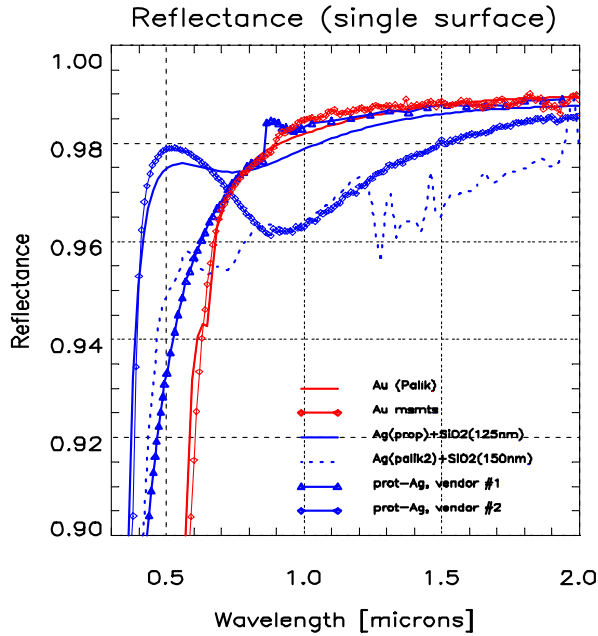
Figure 3.3-33. A comparison of single surface reflectance of measured and modeled mirror coatings shown are a model and measurements for a bare Au coating, two measurements of initial test coatings of protected Ag from two vendors, and two models using different Ag indices of refraction. Note that the small, jumps in measurements near 800 nm are due to instrumental causes when the configuration must be changed to span this wavelength. There is generally good agreement between the modeled and measured Au coating, but small differences between both the models and measured results for protected Ag. These small differences can cause significant differences when extrapolated to the total system throughput for the *TPF-C* design.

Phase difference: prot−Ag, vendor #2
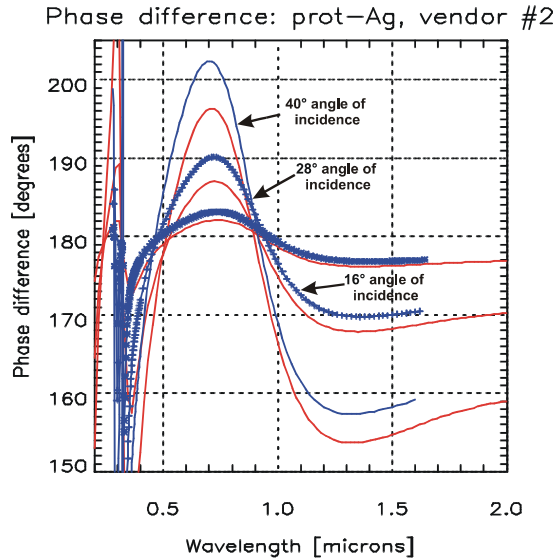
Figure 3.3-34. Results of measurements of phase difference for one of the initial test coatings of protected Ag compared with models of this coating. Shown are the phase differences between polarizations at three angles of incidence which could be determined using ellipsometric measurements. The limit of the particular ellipsometer prohibited measure-

ments below 16°, a little above the largest angle of incidence (about 11°) in the nominal *TPF-C* design. These measurements confirm the expected behavior of the minimum polarization design, namely, two wavelengths in the bandpass without polarization and minimal polarization between these wavelengths (compare with Figure 3.3-25). While this general behavior is confirmed, the polarization is greater than optimal; the red curves show models of the polarization at these angles after increasing the index of refraction of the SiO2 overcoat by 1.25 compared to the nominal values. Better determination of these indices and better process control is needed to produce polarization values closer to the models shown in Figure 3.3-27.
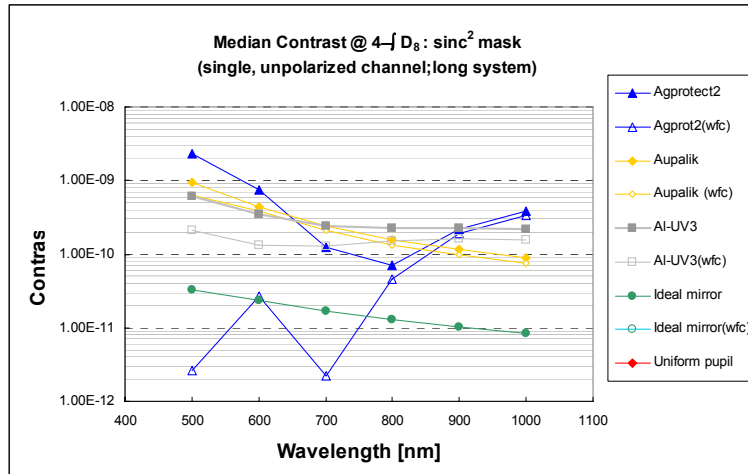
Figure 3.3-35. Median Contrast at $4\lambda/D_8$ for protected Ag, Au, and protected Al coated *TPF-C* models using a model sinc^2 coronagraph, without and with wavefront correction applied. Without wavefront correction, contrast is greater than the fiducial 10^{-10} at nearly all wavelengths. Application of wavefront correction produces much better contrast for the minimum polarization Ag coating but much less improvement for the more highly polarizing Au and Al coatings.
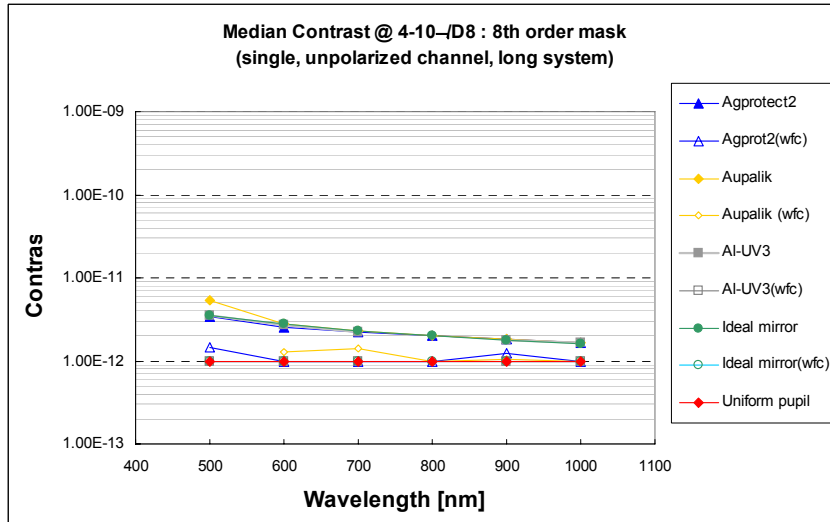
Figure 3.3-36. Median contrast at $4\lambda/D_8$ for protected Ag, Au, and protected Al coated *TPF-C* models using a model eighth order coronagraph, without and with wavefront correction applied. Without wavefront correction, the contrast is dominated by the intrinsic, very

small residual phase error of the *TPF-C* optical design. With wavefront correction applied, contrast improves for all coating models which are nearly identical with an ideal, uniform pupil. Also shown are the maximum contrast values with wavefront correction applied.
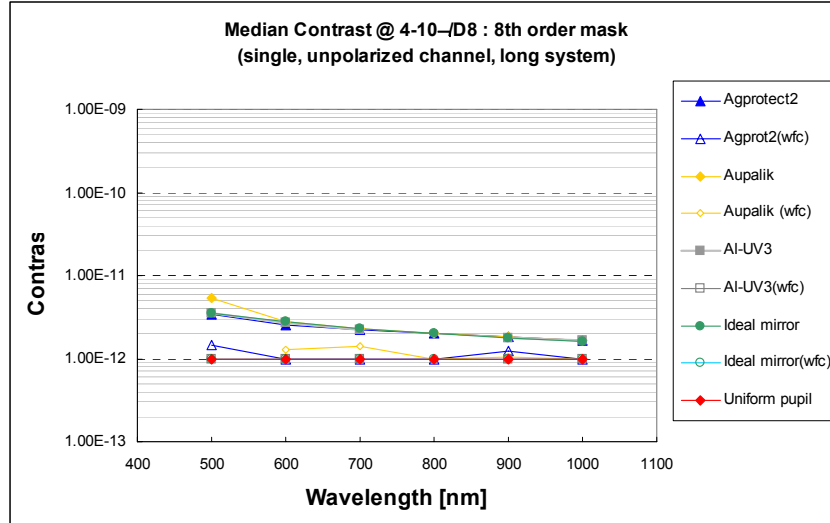
Figure 3.3-37. Median contrast at 4-10λ/D$_8$ for protected Ag, Au, and protected Al coated *TPF-C* models using a model eighth order coronagraph, without and with wavefront correction applied.

3.3.3.2 Starlight Suppression System

3.3.3.2.1 Architecture

<u>**Coronagraph**</u>

Several coronagraph forms have been considered, including band-limited Lyot coronagraphs (Kuchner & Traub, 2002), shaped pupils (Kasdin et al., 2003), remapped pupils (Guyon, 2005), a visible nulling instrument (Mennesson, 2003), and a vortex-mask coronagraph (Palacios, 2005). Four-quadrant phase masks are not considered because their 2nd-order dependence on wave front tilt does not sufficiently suppress starlight. Vortex masks appear to have good aberration rejection and high throughput but have not been modeled to the same level of detail as band-limited masks. The baseline design includes accommodation for Lyot coronagraphs and shaped-pupils. Both can be implemented using a filter wheel approach to select different masks for different purposes (e.g. improved discovery space vs. deeper contrast over a restricted space).

Table 3.3-13 outlines the trade-offs between the various concepts. PIAA (pupil remapping) is the most promising but least mature concept. PIAA offers a nearly 100% throughput (function of the coronagraph spectral bandwidth – see Section 4.1.2.2) and an increased discovery space for planets outside the 2nd Airy ring. However fabrication of components and potential diffraction limitations (Vanderbei, 2005) must be solved before this approach is deemed viable. Laboratory tests in a high-contrast range coronagraph are underway.

Table 3.3-13. Coronagraph trades

Property	Occulter / Lyot	Shaped Pupil	PIAA	Visible Nuller
Practical IWA	3.0-3.5 λ/D	3.5-4.5 λ/D	2.0-3.0 λ/D ?	3.0-3.5 λ/D
Stop Efficiency	40-60%	25%	~100%	40-60%
Immediate Discovery Space	>70% Constrained by occulter	>70% Constrained by limited diffraction shaping	> 90% Constrained by field dependent aberrations	<25% Constrained by fringe pattern and fiber attenuation
Minimum Primary Mirror Dimensions	8x3.5 m	8x3.5 m	< 6x3.5 m	8x3.5 m
SM Despace Stability	20 nm	20 nm	1 nm ?	1 nm
Implementation Complexity	Low	Low	Moderate	High
Critical Issue	Complex errors induced at a focal plane may limit broadband utility	Interaction between high-angle diffraction and high-frequency speckles	Fabrication of optical components. Diffraction?	Implementation complexity

The baseline Lyot coronagraph uses a linear 8th-order field occulter mask (Kuchner, Crepp, & Ge 2005, Shaklan & Green 2005). The 8th-order mask is effective at filtering low-order aberrations that will result when the primary mirror sees thermal gradients and when the secondary mirror moves relative to the primary. Compared to a 4th-order mask, the 8th-order mask is 10-100 times less sensitive to changes in aberrations for observations at the IWA. It also offers excellent discovery space – a planet can be detected with nearly equal efficiency beyond the IWA except for a central strip. The mask will likely be fabricated in HEBS glass (Trauger, 2005) as this continuous-tone approach is the least polarization sensitive. We are currently addressing chromaticity of the mask optical density. Binary mask implementations for the field mask, e.g. notch-filter masks (Kuchner & Spergel 2003), have severe polarization and chromaticity issues (Lay et al 2005).

The two-stage visible nuller is mathematically equivalent to a Lyot coronagraph with 4th-order mask. The disadvantages of 4th-order masks in wavefront sensitivity (discussed below) are to some degree overcome by an alternate method for measuring the wavefront errors; this method promises rapid measurement and correction of errors, a few minutes vs. the few-hours time scale assumed for the baseline concept. This means wavefront stability is only important for a few minutes or less. Further analysis and modeling are needed to compare the realistic performance of the visible nuller to the baseline concept. It may also be possible to implement an equivalent wavefront sensing method on the baseline concept, with similar benefits in shorter time scales for wavefront stability.

The bar-code variant of the shaped-pupil mask shares low aberration sensitivity and large discovery space with the 8th-order mask. It has comparable throughput at the IWA but lower throughput for planets beyond ~6λ/D. The polarization and chromaticity concerns of binary field masks (above) are less severe for pupil masks, because the mask features are much larger than the wavelength. It is the simplest form of coronagraph to implement.

Wave Front Control System

Wavefront sensing relies on the speckle nulling algorithm of Trauger et. al. (2004). Loosely analogous to Gerschberg-Saxton focus diversity methods, this algorithm uses images from the coronagraph science focal plane during series of "experiments" with the deformable mirror. A bright spot in the image is a direct measure of the magnitude of an error in the pupil at a certain spatial frequency; only the spatial phase (lateral position) of that error is unknown. By a series of trials, one can identify the best phase of a new sine-wave component on the DM to cancel the original bright spot. At the end, the DM profile has been optimized to produce a minimum intensity across the science focal plane.

Our WFC system employs two high-performance Xinetics DMs (Ealey & Trauger 2004) arranged in a Michelson interferometer configuration. This allows independent control of both phase and amplitude over the dark hole, but the wave front correction has wavelength dependence that does precludes full correction of reflectivity and phase-induced amplitude errors over a broad spectral band. We are also considering ways to implement sequential DMs to help conjugate far-from-pupil optics. This approach may also eliminate the need for the Michelson beamsplitter and wedges which are likely to introduce additional chromatic and polarization issues. The DM format is 96 x 96 actuators on a 1 mm pitch. Thermal stabilization of the DMs is crucial. Sub-Angstrom wave front stability is required during the extent of our 'set-and-forget' observing scenario (Shaklan et al., 2005)

Other Aspects

The optical design includes an afocal cylindrical telescope that reimages the short axis of the telescope across the full width of the DM (thus forming a square image of the primary aperture on the DM). This increase the outer working angle, significantly expanding the detection space of detection of Jovian planets.

The design also includes two orthogonal polarization channels. This was originally implemented for three reasons. First, the slightly different aberration content of each polarization leaked around the 4th order mask resulting in unacceptable static contrast. Second, binary masks are not simultaneously effective in both polarizations. These issues are remedied through the use of 8th order masks and by employing HEBS masks rather than binary ones. Third, the secondary channel offers full redundancy in case of DM or detector failure. We are currently considering eliminating the second channel and readdressing the redundancy issues.

Both the afocal system and the polarizing channels are described in detail below.

The arrangement of the SSS is shown in Figure 3.3-38 with only one polarization path for clarity, as well as a single path through the Michelson (one fine DM). The elements in Figure 3.3-38 are numbered in the order in which they are encountered by the light. See Mouroulis & Shaklan (2005) for the listing.

A discussion of the more interesting subsystems follows.
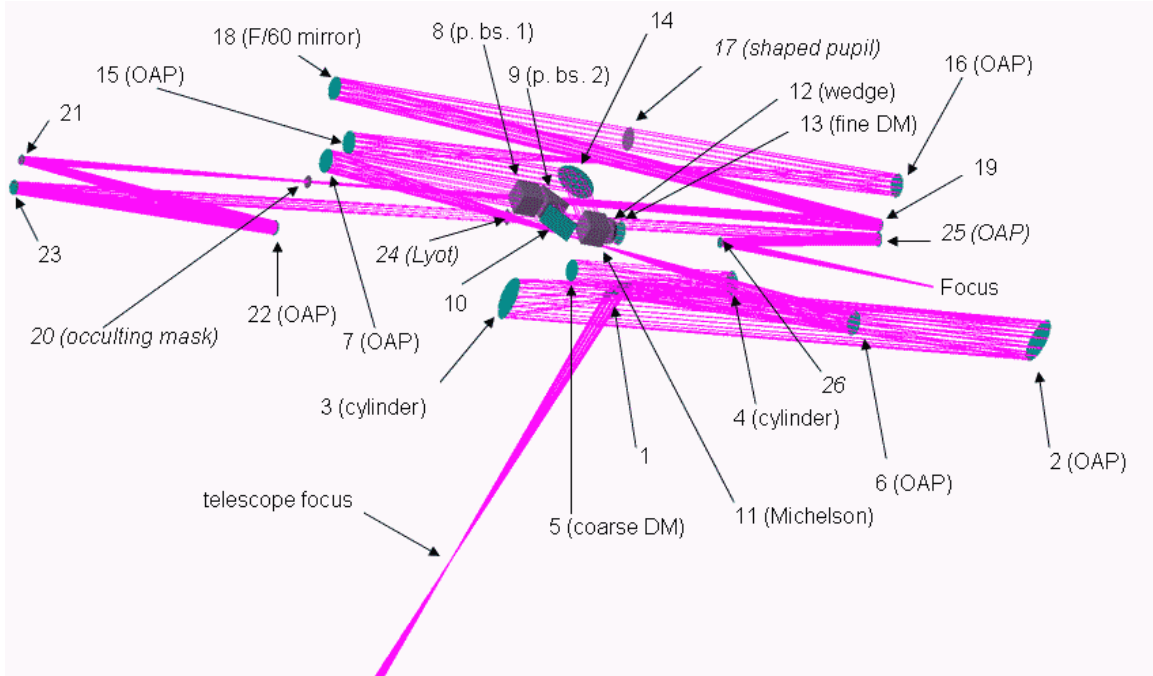
Figure 3.3-38. Ray trace of the starlight suppression system, one polarization path. Elements not otherwise labeled are flat fold mirrors.

The Anamorphic Reducer

This is placed before the first pupil image and immediately after the first (collimating) parabola. Its function is to produce a circular beam cross section by reducing the large axis of the beam. The need for this function arises from technological limitations in the fabrication of DMs. Specifically, the maximum DM size that can be envisioned at present is 10 cm square, with an element pitch of approximately 1 mm. If the large axis of the ellipse covers 10 cm, then the small axis is utilizing only a small fraction of the available elements. The result is a reduction in the outer working angle of the coronagraph, which is the limit of the zone within which a planet can be detected.

The anamorphic reducer comprises a cylindrical Keplerian telescope, used in reduction mode. Anamorphic optical systems normally do not produce a two-dimensional image. However, this can be achieved here by making use of the following property. In the direction of no power, insertion of the telescope in the path results in an image displacement along the z-axis equal to twice the separation between the two mirrors. All one has to do then is to arrange the conjugate positions and powers so that the powered direction also forms an image at the same location. It is to be noted that this property cannot be satisfied with an arbitrary anamorphic system and conjugate location, but it can be satisfied with a Keplerian telescope operating in reduction mode with a virtual object. A diagram of the configuration can be found in Mouroulis & Shaklan (2005).

The Polarizing Beamsplitter and Related Trades

The polarizing beamsplitter must operate over the minimum range of 500–800 nm, provide extinction of better than 10^{-4} for the cross polarization, and have an aperture slightly larger than the fine DMs (> 10 cm). Ghost reflections from the surfaces must also be suppressed.

This means that parallel surfaces must be avoided because they cannot be made parallel enough, nor can an antireflection coating suppress the ghost reflection sufficiently. Even a 10^{-4} ghost (from two reflections on   A/R coated surfaces) requires a parallelism tolerance of better than 1 arcsec. The solution is to introduce an intentional wedge in the design so that ghost reflections are directed outside the field of view, and then use additional compensating wedge elements as necessary to reduce or eliminate the resulting chromatic error. This trade is discussed in more detail in the next section.

Only two technologies have been identified that can support in principle the large aperture: thin film coatings and wire grid polarizers. The first one has been accepted as the baseline because it is the more mature of the two. This trade, however, is by no means closed; advances in wire grid fabrication technology may tip the balance in the future.

Although broadband thin-film polarizing beamsplitters are possible, they do not exhibit the necessary polarization purity (or extinction). It is necessary therefore to combine two in series with their axes crossed. By doing so, the second beamsplitter wedge can also be used to correct the chromatic error of the first one. This works sufficiently well with only two pieces of glass because the angle of incidence is very near normal. The beamsplitter quasi-cube sides are 11 cm. A preliminary, not fully optimized thin film design comprises ten alternating quarter-wave layers of MgF2 and ZnS or TiO2, sandwiched in a glass of the LaK or SK group. The performance estimate is given in
Figure 3.3-39.
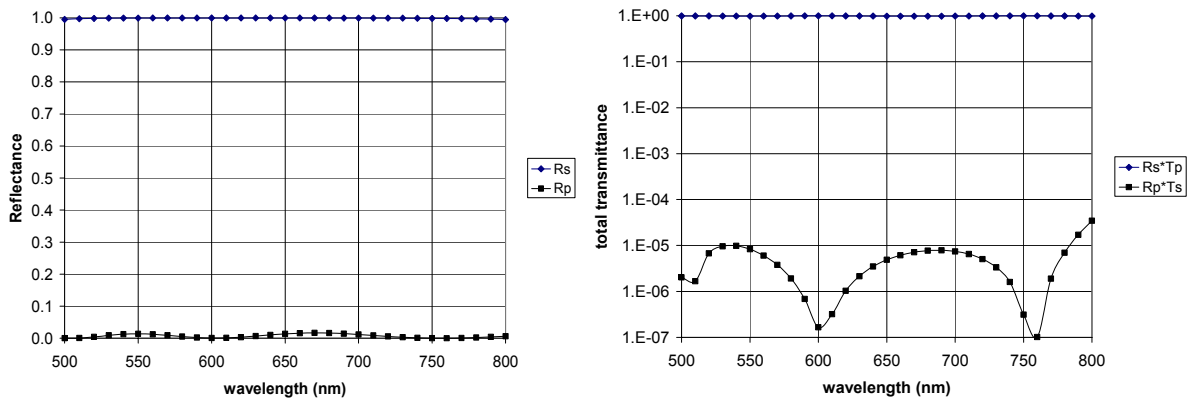
Figure 3.3-39 Left: p and s reflectance of beamsplitter design. Right: total transmittance of two crossed beamsplitters. The lowest value for the top curve (R_s*T_p) is 98.3%.

It can be seen that this design is satisfactory at least at this stage of maturity of the overall design. The extinction is below 10^{-4} and the transmittance is above 98%.

To avoid ghosts, the beamsplitters have a wedge angle of -0.2° and 0.4° respectively, while the gap between them has a wedge of 0.6°. In fabrication, there is a loose tolerance to these numbers since the air gap compensates for wedge errors. The red and blue rays exit this arrangement with an angular error of much less than 1 nrad and a linear displacement of only 0.1 μm. The difficulties introduced by these beamsplitters are mainly in maintaining refractive index uniformity across such a wide aperture and long path, as well as reducing stress birefringence to acceptable levels. There is evidence that stress birefringence can be reduced

with careful annealing (Ladison et al., 2001, Marker et al., 2000), but this will have to be confirmed for the specific glass type required by the beamsplitter design.

Optical Design Performance

A more complete analysis including additional descriptions of SSS components appears in Mouroulis & Shaklan (2005). The design is under continuous evaluation and its performance must ultimately be judged by its success in suppressing the starlight within the desired band.

This is a matter of detailed analysis that is outside the scope of this section and will be the subject of forthcoming publications. Here we show only the necessary minimum to demonstrate that the design itself has been put together properly.

Figure 3.3-40 shows spot diagrams at three positions: telescope focus, occulting mask, and final focus. The spots are shown inside the corresponding Airy disk size, and for two fields: center and 2 arcsec away (worst case among all orientations). At the telescope focus, the Airy "disk" is of course an ellipse, since it is located before the anamorphics. The corresponding Strehl ratio and RMS wave front aberration are shown in Table 3.3-13.

Figure 3.3-40. Spot diagrams at three positions inside the system. (a) telescope focus, (b) occulting mask, (c) final focus. The ellipse/circle represents the Airy disk size at the corresponding location. In each case, the middle of the field (left) and the worst-case 2 arcsec field (right) are shown.

Actually, Table 3.3-14 simply demonstrates that the system has been set up correctly in the software. The center of field error does not increase since neither the parabolic mirrors nor the flat surfaces add any wave front error at that location. And the edge of the field error increases gradually since no effort is made to correct it. In any case, the conclusion from Table 3.3-14 is that manufacturing and misalignment aberrations will overwhelm the design aberrations.

Table 3.3-14 Strehl Ratio and RMS Wave Front Error

	Field Position	Strehl Ratio	RMS Aberration (waves @ 500 nm)
Telescope focus	center	1.000	0.0001
	2"	1.000	0.0004
Occulting mask	center	1.000	0.0001
	2"	0.986	0.0145
Final focus	center	1.000	0.0001
	2"	0.974	0.0295

Of interest is also the polychromatic spot diagram, shown in Figure 3.3-41 for the final focus location. This demonstrates that the angular chromatic error introduced by the wedged transmissive elements is totally negligible at the design level.
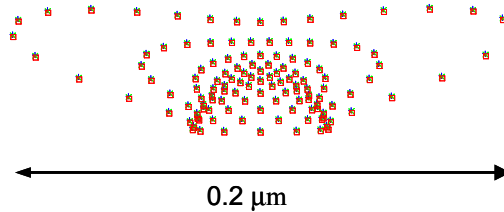
Figure 3.3-41. Polychromatic spot diagram at the center of the field and the final focus location It may be visible, if only barely, that each spot shown in fact comprises three different ones, corresponding to the different wavelengths, with a maximum separation of about 1.5 nm. Thus there is no residual chromatic aberration.

The system design has been guided by the principle of flexibility in providing for and facilitating alternative planet detection approaches as well as being consistent with the present state of the technology. Thus the design reflects to a great extent uncertainties in the limits of various key technologies. This ultimately makes it rather complicated in terms of the sheer number of optical elements that must be accommodated, and reduces the overall system throughput, though not to prohibitive levels. Future improvements in mask fabrication, DM fabrication, as well as advancements in analysis and understanding of all the parameters affecting the contrast, will hopefully permit the launching of a simplified and more efficient system.

REFERENCES

K. Balasubramanian, D. Hoppe, P. Z. Mouroulis, L. Marchen, and S. Shaklan: "Polarization compensating protective coatings for *TPF-C*oronagraph optics to control contrast degrading cross polarization leakage", to appear in Proc. SPIE **5905** (2005)

Ealey, M.A & Trauger, J.T. 2004 *Proc. SPIE* **5166**, 172

Guyon, O. et al. 2005 *ApJ* **622**, 744

Kuchner, M.J. & Traub, W.A. 2002 *ApJ* **570**, 900

Kuchner, M.J., Crepp, J., & Ge, J. 2005 *ApJ* **628**, 266

Kuchner, M.J. & Spergel, D.N. 2003 *ApJ* **594**, 617

J. L. Ladison et al. "Achieving low wave front specifications for DUV lithography; impact of residual stress in HPFS® fused silica." *Proc. SPIE* **4346**, 1416-1423 (2001)

Lay, O.P., et al. 2005 *Proc. SPIE* **5905** (in press)

A. J. Marker, III, B. Wang, and R. Klimek: "Effect of residual stress in optical glass on the transmitted wave front." *Proc. SPIE* **4102**, 211-218 (2000)

Mennesson, B. et al. 2003 *Proc. SPIE* **4860**, 32

Mouroulis, P.Z. and Shaklan, S.B. *SPIE* 2005 (in press).

Palacios, D. 2005 *SPIE* **5905** (in press)

Shaklan, S.B. & Green, J.J. 2005 *ApJ* **628**, 474

Shaklan, S.B. et al. 2005 *Proc. SPIE* **5905** (in press)

Trauger, J.T. 2005 *Proc. SPIE* **5905** (in press)

Vanderbei, R.J. 2005 *ApJ* (submitted)

3.3.3.2.2 Wavefront Sensing and Control

Wavefront sensing and control (WFSC) is the central enabling technology for a coronagraphic telescope. First and foremost, WFSC corrects the unavoidable amplitude and phase aberrations present in a telescope system. Second, WFSC has the potential to desensitize a coronagraph design to errors in manufacturing, modeling, and implementation. In many cases WFSC may relieve the requirements upon system modeling to demonstrate absolutely accuracy in its predictions. WFSC technologies present the unique opportunity to co-optimize a coronagraph, control system, and telescope design to best enable high contrast imaging for planet finding.

<u>Wavefront Sensing and Control Implementations</u>

A variety of methods are in use or have been proposed for controlling the wavefront in a coronagraphic telescope. By far the most experience with wavefront control has been for adaptive optics on ground-based telescope. All (or almost all) of these systems utilize a pupil plane sensor at the front end of the telescope (usually a Shack-Hartmann sensor) to reconstruct an estimate of the wavefront phase. This information is then used to adjust a deformable mirror, also at the front end, to correct the wavefront. While we can certainly benefit from the knowledge and experience of ground AO, it is generally agreed that such a front-end sensing system is inadequate for planet finding. Foremost among the problems is the existence of non-common path errors in the sensing leg of the instrument. These errors can produce speckles far larger than the sought after contrast of 10^{-10}.

All WFSC approaches for *TPF-C* must be common path; that is, sensing must occur in the same optical path as the science information (at least up until a light removal system). Nevertheless, there still remains quite a number of approaches to implementing wavefront sensing and control. In this section, we present several such systems, describe their salient characteristics, and highlight key limitations.

<u>Direct Speckle Nulling at the Science Focal Plane</u>

Speckle nulling refers to a closed loop system that removes speckle via a deformable mirror based only on measurements of the speckle in the image plane. By using a finite number of DM dithers, unambiguous information is acquired for speckle removal. No effort, however, is made to estimate the wavefront itself. If speckle is entirely due to phase errors in the wavefront, then a single DM can remove speckles in the focal plane to within the limitations

of the DM. These limitations come from the actuator density (within the pupil), accuracy, dynamic range and stability. For OPD errors that originate near pupil planes, the correction made by a DM is effective at any wavelength. However, if any speckle is produced by amplitude error or by any error near a focal plane, then there are optical bandwidth limitations imposed by the correction. If there are amplitude errors in the system, a single DM can only compensate by inducing a phase error that effectively cancels the amplitude speckle over half the controllable focal plane. A two DM system may be able to remove amplitude as well as phase everywhere in the search space, but will also impose an optical bandwidth limitation that scales with the magnitude of the amplitude errors.

Wavefront Sensing and Control Using Science Camera Imagery

This category of WFSC involves apply corrections that are based on estimates of the wavefront phase and amplitude. There are two approaches to wavefront correction marked by where the sensing and estimation is accomplished. We note that in all of these approaches, single measurements are inadequate for unambiguously determining phase and amplitude as measurements are made of only intensity. Thus, multiple measurements with some form of diversity are required.

In the first type of system, what we call *Lyot Plane Nulling*, the wavefront estimate is built up from measurements in the Lyot plane of the coronagraph (typically implemented by inserting a lens in front of the science camera while looking through the coronagraph). By dithering the DM and taking multiple measurements, estimates can be made of the wavefront phase and amplitude. In the second type, what we refer to as *Image Plane Nulling*, estimates of the wavefront phase and amplitude are made using only measurements in the final image plane. In this case, diversity is achieved through a variety of possible techniques, including focus, multiple pupils, multiple wavelengths, and DM dither.

In both of these approaches, a deformable mirror is used to make the final correction to the image plane. As before, a single DM can only correct phase achromatically in the entire search space or both phase and amplitude in a smaller area of the search space (but not over a infinite optical bandwidth). Two DMs can correct both phase and amplitude in the entire search space, but current methods only allow for narrow bandwidths of amplitude control.

We also point out that this category of correction method is model dependent as it relies on computational propagation of the wavefront to the image plane in order to compute the proper DM setting to achieve a high contrast dark hole. They also require an adequate model of the deformable mirror. This modeling requirement introduces a potential source of error not present in Speckle Nulling. However, these methods also potentially require less iteration than Speckle Nulling.

Interferometric Wavefront Sensing and Control

The light distribution a pupil downstream of the coronagraph, presents an opportunity for WFS. By splitting off some of this light and interfering it with a star-generated reference beam, the complex wavefront may be estimated. The reference itself originates from the pre-coronagraph light that has also been split from the optical train. This reference beam is spatialy filtered and delayed such as to produce decodable interferograms when combined with the post-coronagraph beam. This arrangement is referred to as a Mach-Zender interferometer (MZI).

Because the diversity needed to sense the complex wavefront errors is in the reference channel, this form of WFS can be conducted while integrating. As such the MZI has the potential to greatly reduce telescope and instrument stability timescales. Additionally, the MZI produces a sequence of complex pupil models, that represent not just the average WFE but a time history of dynamic wavefront variations. For a long integration time in the presence of thermal and mechanical disturbances, the MZI can produce a sequence of models that can drive the DM.

In addition to wavefront control, these same models can predict the distribution of speckles that should be seen in the science camera imagery. This speckle pattern prediction can serve the same purpose as the telescope roll-dither maneuver currently baselined as the planet detection strategy. Using a a MZI based estimate of the speckles, this speckle subtraction may be accomplished without the need of the telescope dither.

Performance Limitations

Each of these control approaches has certain categories of limitations. Foremost among the issues is *chromaticity*. Ideally, we like to see the WFSC system be able to correct both amplitude and phase at all wavelengths in the desired science band and in the entire coronagraph search space. Unfortunately, that has not yet been achieved. As currently conceived, the ultimate performance of many of the systems is determined by the capabilities of the deformable mirrors. These include dynamic range, accuracy, stability, and actuator density.

The temporal bandwidth of the systems also presents unique challenges. By temporal bandwidth we mean both the rate of response of the closed loop system and whether the controller can be used real time during an observation. All of the approaches above, save the MZI, are quasi-static. Corrections are made at one epoch, and stability is relied upon during an observation. The implicit requirement of the quasi-static assumptions is that need for a very stable telescope. Mechanical vibrations and thermal variations must be control to very strict tolerances. This is an area where accurate, predictive and validated models are being developed.

As alluded to above, for systems that rely on modeling of the DM or propagation, certain types of errors will be introduced. Only experiment will fully characterize the extent of these errors as well as give validity to models employed.

Finally, only certain categories of the errors described above may be addressable by any given wavefront control system. For instance, while sensitivity to finite stellar size is a critical characteristic of a coronagraph, the resulting error is uncontrollable by any of the wavefront control systems due to the incoherence of the arriving wavefronts.

3.3.3.3 Baseline Science Instruments

3.3.3.3.1 Detectors

<u>Introduction</u>
The current baseline for the *TPF-C* will require multiple high performance detectors operating in the visible portion of the spectrum. The four primary tasks supported by these detectors will include science, wavefront control, pointing control, and metrology. Table 3.3-15 Summary of Detector Applications on *TPF-C* identifies the tasks, functions, and current instrument/subsystems on *TPF-C* that require some form of detector.

<u>Science</u>
The key science task is the search for Earth-like planets around nearby stars, with the ability to determine the composition of the atmosphere for any detected planets.

Table 3.3-15 Summary of Detector Applications on *TPF-C*

Task	Function	Instrument/Subsystem
Science		
	Detection (Dark Hole)	Coronograph
	Composition/Characterization	Spectrograph, IFU/SS
	Imaging	Wide Field Imager
Wavefront Control		
	DM WFC	DM Pupil Imager
	DM WFC	Back end (Speckle Reduction)
Pointing Control		
	Acquisition (7")	Star Tracker
	Acquisition tracker (<1")	Acquisition Tracker
	Fine Guidance (<0.1 mas)	FGS
Metrology		
	Initial Alignment	Metrology

The performance driver for the planet detection detector is its required read noise of 2-3 electrons [rms]. This level of read noise has been achieved in ground based systems, and laboratories, but has not been demonstrated on flight instruments. The read noise performance for the characterization instrument, which will operate behind a spectrometer with R~70, is even more severe. Unless further refinement in the understanding of the limiting photometric backgrounds changes, the composition detector will require true sub-electron performance (per CorSpec ICS report).

The planet finding detector will be AR coated to obtain the maximum QE in the 500 nm to 800 nm band pass. An array of 1024 x 1024 pixels is more than enough to Nyquist sample the current science FOV. As with the composition detector, the planet detection detector will operate at a temperature which makes its dark current contribution to the noise negligible. For the current assessment, we have assumed a maximum single integration time of ~1000 sec. This implies that the dark current requirements for the planet detection detector can be met at or below ~ -105 C (perhaps as warm as – 95 C). Standard theoretical dark current curves are provided for a range of CCD's in Figure 3.3-42. As a goal the composition detector will operate out to 1050 nm. Operation in the 800– 1050 nm range is discussed below under "Further Study."

Standard dark current curves for a 12 micron pixel CCD

MPP Device – 0.1 nA/cm²

Typical Science CCD – 1.0 nA/cm²

Radiation Damaged CCD – 10.0 nA/cm²
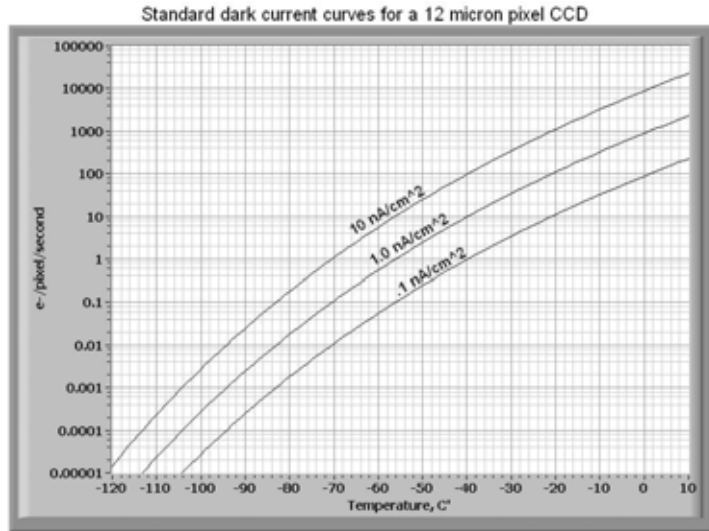
Figure 3.3-42. Standard Dark Current Curves for a 12 Micron Pixel CCED

The General Astrophysics (GA) task is not a primary mission requirement, and its guiding science requirements have yet to be defined. One concept for the GAI is a wide field imager. The most significant design aspect of the wide field imager for the *TPF-C* is the large size of its focal plane. One concept provides for a 4 arc-minute FOV (square), and requires a mosaic of 16 by 16, 2-mega-pixel detectors. Such a large focal plane would have significant impact upon the *TPF-C* architecture. Once again various assumptions about the size of the field and the spatial sampling strategy can be made to reduce the total number of detectors and the size of the focal plane.

Wave Front Control
In order to search for planets, stringent wavefront control is required. A wavefront sensor will provide the necessary measurements, either from a pupil image or through the direct image of the science field. This sensor will slightly over sample the spatial control frequencies of the DM. These detectors will be small, ~1024 square pixels, running at low (0.001Hz) frame rates with low read noise. If higher frame rates are required for the WFC detector, a sub-electron read noise detector might be required. Most of the requirements for WFC detector are similar to those of the planet detection detector.

Pointing Control
A pointing control system concept has been developed (Bower) which requires three separate camera systems, a commercial star tracker, an acquisition camera which feeds a moderate size CCD, and a FGS which uses a small, fast 100 Hz detector. Since the pointing concept relies on the signals from the target star, very low noise detector are not required, and additional signal attenuation might be required so as not to saturate the detectors. Frame rates of ~ 100 Hz would likely drive theses detectors to a frame transfer architecture, which would place limits on the size of the final mosaic for the acquisition camera.

Metrology

Finally, the metrology system will require detectors to sense the alignment lasers, which will be used to control the placement of the mirrors to the nm scale, upon deployment of the system. These detectors will likely be small area, single element or quad cell type detectors. Room temperature Si detectors should be sufficient for the primary mission.

A summary of some of the performance parameters for the detectors based upon the science requirement and the baseline mission are presented in the
Table 3.3-16.

Table 3.3-16. Detector Performance Parameter Summary

	Number of pixels	Pixel Size, m	Read Noise e-(rms)	Dark Current e-/sec	QE	Spect. Range, μm
SCIENCE						
Coronograph	>614 X 614	7.14E-06	< 3	<0.001 @ Tint=1000sec	>85%	.5-.8
Spectrograph, IFU/SS	100 x 100	TBD	< 0.3	<0.0003 @ Tint=1000sec	>85%	.5-.8 (1.1 goal)
Wide Field Imager	75529 X 75529	7.14E-06	> 20	TBD	>60%	TBD
WAVE FRONT CONTROL						
DM Pupil Imager	256x256	7.14E-06	> 20	TBD	>60%	.5-.8
Back end (Speckel Reduction)	256x256	7.14E-06	<3	<0.001 @ Tint=1000sec	>85%	.5-.8
POINTING CONTROL						
Star Tracker	8 degree field (480 arcmin)	TBD	TBD	TBD	> 50 %	Vis.
Acquisition Tracker	1800 arcsec	TBD	TBD	TBD	> 50 %	Vis.
FGS	>614 X 614	7.14E-06	TBD	TBD	> 50 %	Vis.
METROLOGY						
Metrology	TBD	TBD	TBD	TBD	> 50 %	TBD

3.3.3.3.2 Spectrometer

The science requirements document calls for an instrument with spectral resolution >= 70 over the bandpass from 0.5–1.1 microns, capable of seeing light from anywhere in the 'dark hole' region. The requirements do not state that the instrument must see the entire dark hole at once – it is possible to meet the requirements with 1) an instrument that selects and disperses the light from an observed planet; or 2) an instrument that selects and disperses the light from several regions within the dark hole; or 3) an instrument that observes and disperses into independent channels the full dark-hole region.

An instrument of the third type can serve as the primary planet detection instrument if it has comparable throughput and comparable overall noise compared to the planet detection camera (nominally a few arcsec square low-noise CCD or comparable detector in the coronagraph back focal plane).

Such an instrument could in principle be used to determine the wavelength-dependence of scattered light throughput the dark hole, and this information could be used to drive the wave front control system. This may prove to be a critical function as many of the requirements in the optical system are driven by wavelength-dependent effects.

The spectrometer is used at room temperature and is housed in the isothermal cavity region with the other science instruments. Some possible designs include: a fiber-fed spectrometer

with one or more fiber positioners spanning the dark hole region; an integral field unit; an image slicer; multiple instruments (several IFUs for example) each of which samples a portion of the full bandpass.

The FB1 design did not consider a specific spectrometer design. Signal-to-noise calculations were performed for the planet detection camera, and a multiplicative factor related to the spectral resolution (relative to the planet detection bandwidth) was assumed (see Section 2, Design Reference Mission).

3.3.3.3.3 Wide Angle Camera

The wide angle camera is envisioned to work in two modes: in the parallel mode, the camera observes a field surrounding a *TPF-C* program star. In the pointed mode, the telescope observes an astrophysical target.

Instrument line-of-sight (rigid body) control in the parallel mode may be derived from the starlight suppression system, and is required to be ~ 5 mas (1 sigma). In this mode, the light from a bright star is incident on pointing sensors tied to the coronagraph. The roll requirement is TBD arcseconds about the line-of-sight.

In pointed mode, when a bright point-source is not present, the Payload Acquisition Star camera, a high precision star tracker with a roughly 1–5 degree FOC, will be used and will deliver 100 mas 1-sigma jitter per axis This does not deliver diffraction-limited performance for the full aperture. It is thus important that the wide-angle camera generates a pointing signal adequate to meet its needs.

Like the other instruments, the camera is used at room temperature and resides in the isothermal cavity behind the primary mirror.

The FB1 design allocated power, space, and mass to the wide angle camera (see next section). The FB1 design does not make any allowance for field of regard or other considerations (e.g., mirror coatings) that may be driven by the wide angle camera.

3.3.3.3.4 Instrument Accommodation

Figure 3.3-43 shows the nominal accommodations for the science instruments. From the tertiary mirror of the telescope, a pickoff mirror sends the outer portion of the beam (red arrow) to the General Astrophysics Instrument (GAI) with an assumed 10 arcsec– 4 arcmin field of view. The inner portion of the beam goes to the Starlight Suppression System from where light is delivered to the detection and characterization instruments. Preliminary volume, mass and power have been allocated, as listed in

Table 3.3-17, Table 3.3-18, and Table 3.3-19 respectively; however, the layout will be refined in later design iterations once the instrument designs and requirements are better understood. The bases for the current allocations are discussed in Sections 3.3.1.4 and 3.3.1.5.
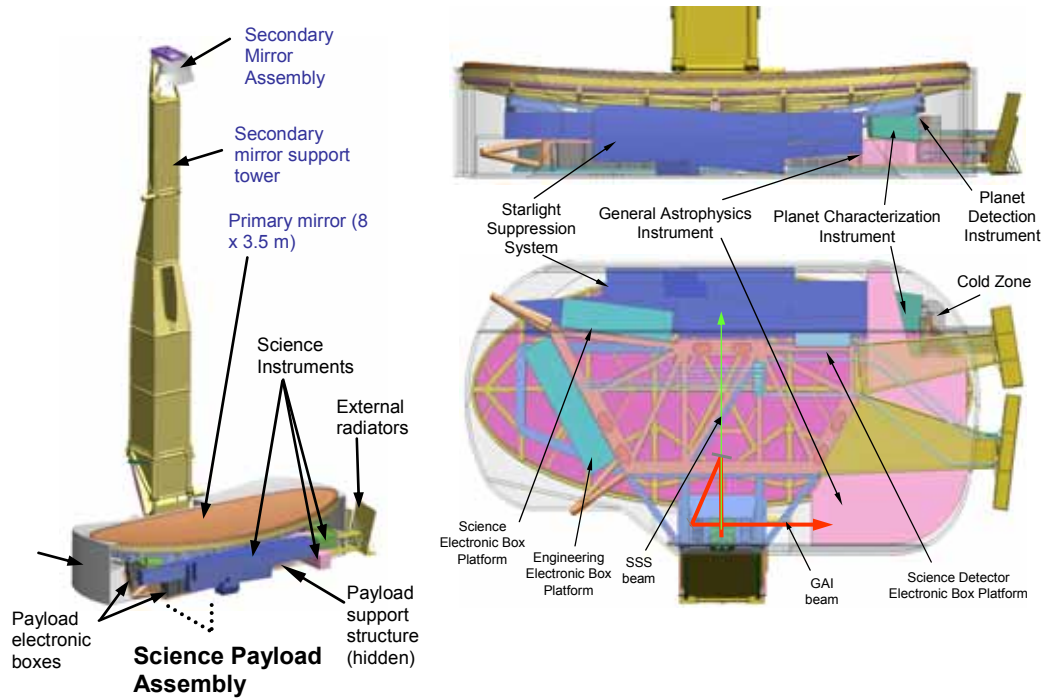
Figure 3.3-43. Instrument Accommodation Concept

Table 3.3-17. Instrument Volumes Assumed for FB1

Instrument	Placeholder Volume (millimeters)
General Astrophysics Instrument	2250 x 1400 x 400
Planet Detection Camera	325 x 400 x 300
Planet Characterization Instrument	750 x 400 x 300

Table 3.3-18. Instrument Mass Estimate Breakdown

Component	Mass Estimate (kg)	% of Total Launch Mass
Payload Support Subsystem	446	7.5
Starlight Suppression Subsystem	515	8.7
Planet Detection Camera	10	0.17
Planet Characterization Instrument	20	0.3
General Astrophysics Instrument	150	2.5

Table 3.3-19. Instrument Power Estimate Breakdown

Component	Power Estimate (W)	% of Total Power
Payload System Electronics	152	7.4
Starlight Suppression Subsystem	87	4.3
Planet Detection Camera	2	0.1
Planet Characterization Spectrometer	40	1.9
PSAC	4	0.2
General Astrophysics Instrument	100	4.9

Based on initial estimates of the placeholder instrument designs and the system capability, the observatory will have the capability to provide room temperature cooling that is tailored to the telescope temperature requirements of 290K – 305K. Stability is critical and precision thermal stability control will be developed for the telescope and the starlight suppression system. Instrument interfaces can be controlled as well, but the instruments should maintain a constant power profile during critical observations through the use of make-up heaters if needed.

The detectors that were included in the placeholder design were maintained within the temperature range -100C±5C and require 25 Watts of net cooling power (including detector electrical power and parasitics). For the placeholder instrument thermal assessment, the required power cooling allocation between instruments was selected as shown in Table 3.3-20.

Table 3.3-20. Placeholder Values for Instrument Detector Power Cooling Analysis

12 Watts	GAI detector
5 Watts	Detection camera
8 Watts	Characterization camera

The current thermal control design locates all the detectors within a cold zone shown in Figure 2 that has a dedicated cold radiator. The placeholder instrument detectors are structurally attached to their instruments with thermally isolating structure and thermal blanketing. A cold strap links each detector to a cold structure within the cold zone.

At the next design iteration the estimated instrument thermal requirements for cooling and interface stability will be updated to the specifications developed under the Instrument Concept Studies.

3.3.3.3.5 Instrument Concept Study Accommodations
The Instrument Concept Studies are now complete and their accommodations requests will be taken into consideration during the next design cycle. The following is the descriptions of the accommodations requested by the ICS.

CorSPec

The CorSpec team used Goddard's Instrument Synthesis and Analysis Lab (ISAL) to assess that the instrument concept is consistent with the requirements and objectives of the *TPF-C* project, and to identify needed technology development.

Estimates for resources (mass, power, and volume) were made and checked for consistency with the assumptions of the subsystem designs and the derived requirements.

Volume. Each of the four identical spectrographs has dimensions, 550 x 1000 x 250 mm. The four spectrographs are stacked in a 2 x 2 array with the instrument plate bisecting the four spectrographs (Figure 3.3-44). This is the simplest layout that fits the existing *TPF-C* structure, but may not be the lightest or smallest.

The instrument plate, designed as 3 inches thick, is the mechanical interface to the instrument bay. The instrument plate also provides mechanical support for two pairs or redundant electronics boxes as well as for heat pipes and thermal hardware. The "Stacked" configuration has an overall volume of 1.42 m^3.
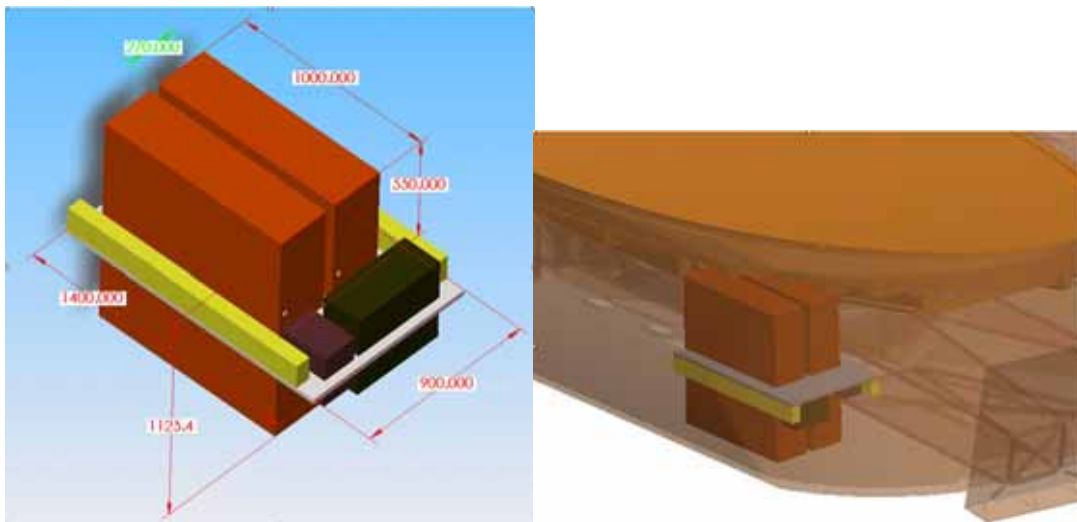
Figure 3.3-44. The Stacked Configuration Location within *TPF-C*

The CorSpec mass and power estimates are summarized in Table 3.3-21 and Table 3.3-22, respectively.

Table 3.3-21 CorSpec Mass Estimates

Mass Estimate	Mass (kg)	Contingency (%)	Mass with Contingency (kg)	
Optics	13.4	15	15.4	
Mechanisms	14.4	30	18.7	
Structure	63.4	30	82.5	
Thermal	39.7	30	51.7	
Electronics	71.4	30	92.8	
Total	202.3		261.0	kg

Table 3.3-22 CorSpec Power Estimates

Power Estimate	Qty	Power (Each) Watts	Average Power (Watts)	
Readout Electronics Boards			16.0	
WFSB Master FPGA/DSP	1	30.0	30.0	
WFSB FPGA/DSP	4	25.0	100.0	
WFSB Processor (Rad750)	1	8.0	8.0	
MEB Instrument Processor	1	8.0	8.0	
MEB Thermal Control	8	4.5	36.0	
MEB Housekeeping	2	3.0	6.0	
MEB Mechanism Control	2	2.0	4.0	
MEB Power Converter at 75% efficiency *	3	16.2	48.6	
MEB Power Converter for WFSB at 75% efficiency	2	23.0	46.0	
Heaters (62 prime precision controlled circuits)			75.7	
Solid State Recorder (0.5 Terabit)			100	
Total	24		478	Watts

DSP = Digital Signal Processor   * includes readout electronics boards, MEB boards, heaters
FPGA Field Programmable Gate Array   Qty = number of electronics boards
MEB = Main Electronics Box
WFSB = Wavefront Sensing Box

The mass and power estimates include elements of the starlight suppression system (components in the wavefront sensing box) and the solid state recorder, which are both observatory resources. When these elements are subtracted out, the CorSpec power estimate is 240 W.

3.3.3.4 Payload Support Structure (PSS)

As depicted in Figure 3.3-45, the Science Payload Assembly (orange box) is composed of two sub-assemblies – the Optical Telescope Assembly (OTA) (red box) and the Payload Support Assembly (blue box). The OTA consists of the primary, secondary, and tertiary mirrors, the structural and thermal support for those mirrors, and the laser metrology system. Details of the OTA design are presented in section 3.3.3.1.2. The Payload Support Assembly consists of the instruments and electronic boxes, the associated thermal control radiators/heat pipes and the thermal enclosure which are all attached to a main supporting structure called the Payload Support Structure (PSS). The details of the PSS sub-components are shown graphically in Figure 3.3-46.

OTA
(Optical Tele-
scope Assembly)
-Primary
-Secondary
-Tertiary
-Structural and
 thermal control
 support structure
 for mirrors
-Laser metrology

Payload
Support Assm
-Instruments
-Electronic boxes
-Thermal control for
 detectors & e-boxes
-OTA Support
-Spacecraft I/F

SCIENCE
PAYLOAD

SPACECRAFT
ASSEMBLY
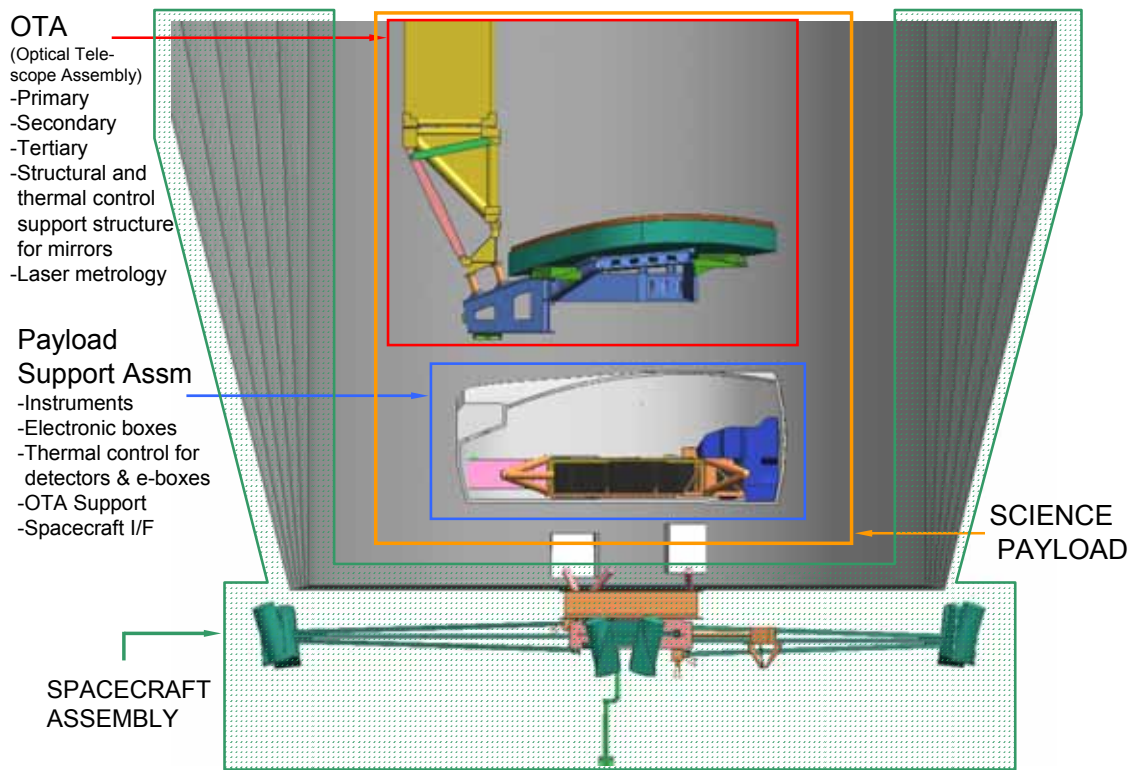
Figure 3.3-45. Science Payload Assembly Schematic

The Payload Support Structure (PSS) is also designed to provide a clean interface to the OTA and the spacecraft, and is the main load carrying interface for launch. The interfaces are as follows and are shown graphically in Figure 3.3-47:

- The Spacecraft interfaces to Payload Support Structure through 3 bipods. This interface also serves as isolation from the spacecraft.
- The Payload Support Structure interfaces to Optical Telescope Assembly (OTA) Aft Metering Structure (AMS) through 3 bipods.
- The primary mirror attaches to Aft Metering Structure (AMS) through 3 bipods.
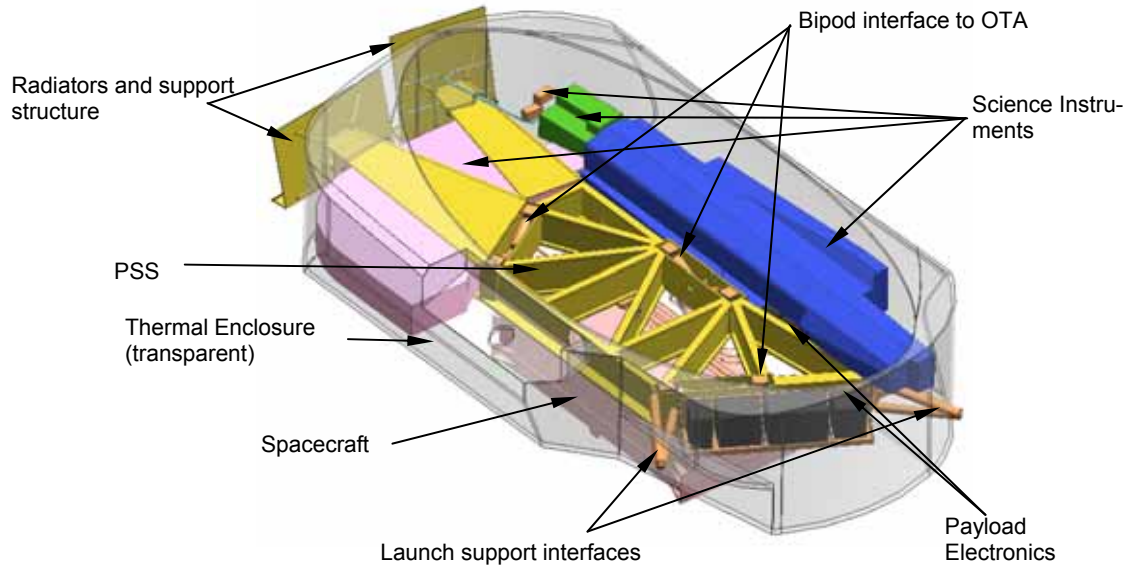
Figure 3.3-46 Details of the PSS Sub-components
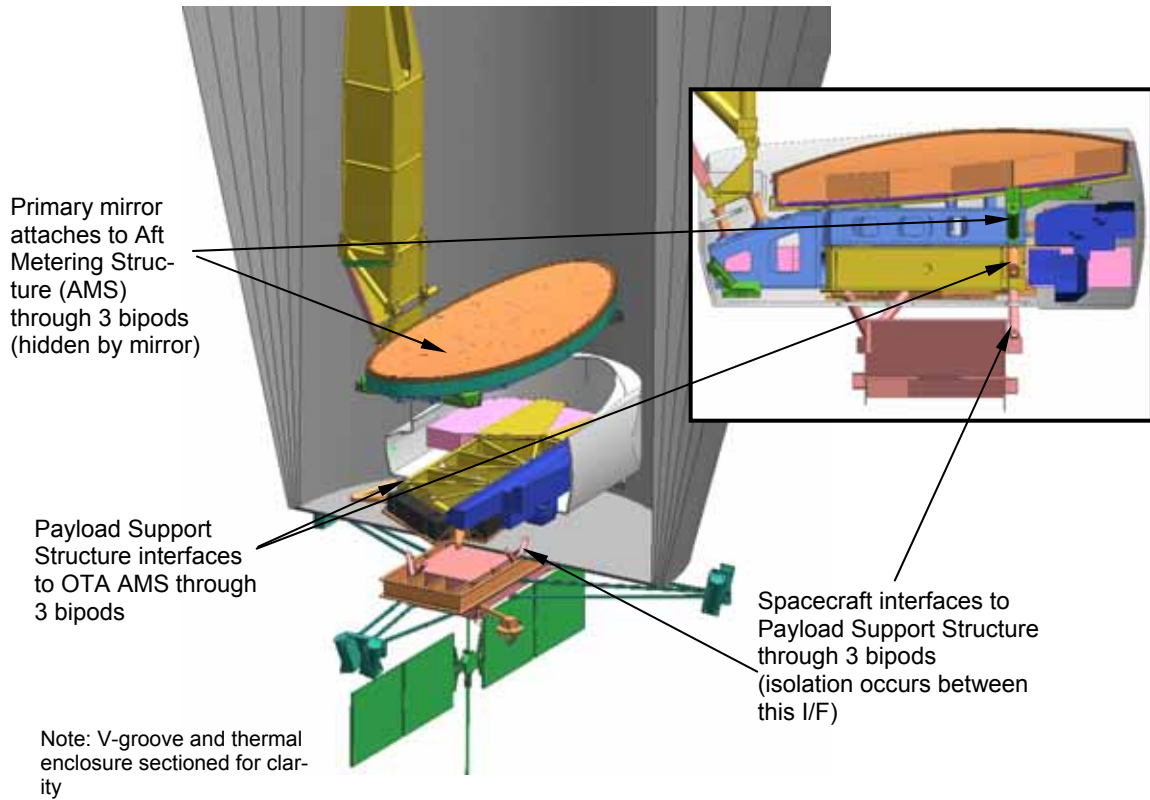
Figure 3.3-47 Interfaces Between the PSS, the Spacecraft and the Optical Telescope Assembly

3.3.4 Spacecraft

3.3.4.1 Attitude and Pointing Control System Design

The Pointing Control System (PCS) controls all aspects of pointing the *TPF* Coronagraph including the spacecraft attitude control system, the tip and tilt of the secondary mirror, and the rotation of the fine guiding mirror. The Payload Module (where the coronagraph and other science instruments reside) is isolated from the spacecraft by either an active (the current baseline) or passive isolation system. The two isolation systems have both been developed, analyzed and compared, and require different PCS architectures. The passive isolation system has no active control and is mature in development. The active approach is currently at TRL 5, meaning that it has been testing in the laboratory in an environment reasonably consistent (vacuum, temperature) with the flight environment. Hardware heritage has been considered in the selection of components for both architectures. All components are either fully mature, in an advanced state of development (TRL 5 or higher), or are a reasonable extrapolation from existing hardware. Photographs of existing PCS hardware components are shown in Figure 3.3-48.

Vibration is transmitted into the Payload Module from the spacecraft through the isolation system via isolation leakage and by transmission across cables connected between the Spacecraft and Payload Module. Vibrations in the Payload Module are also caused by movement of mechanisms on the payload side, thermal gradients, and external torques. The active isolation system provides a higher degree of isolation because positional control between the spacecraft and the Payload Module is induced through controllable magnetic coupling; there is no physical contact. Because of this, less vibration compensation is required for the active system. The active system has been analyzed based on a model that was developed at Lockheed Martin and tested on prototype hardware called Disturbance Free Payload (DFP).

Figure 3.3-49 shows schematics of both the active and passive PCS design options. Both systems receive light from the coronagraph target star and use the reaction wheel assembly in the spacecraft to point the observatory. The starlight is reflected off the surface of the coronagraph mask into a detector that senses starlight centering and provides feedback used to control observatory pointing. *TPF-C* performance has been evaluated for both the passive and active PCS design options and results are presented in this section. No decision has been made at this time as to which of the active or passive PCS designs is selected for the *TPF-C* baseline architecture as both appear to be viable in terms of system performance.

Reaction Wheel
Assembly

-

View of DFP Interface
DFP 3D Testbed

Actuator pair
&
Sensor pair

Payload

Spacecraft

DFP single
actuator
assembly

Actuator pair
&
Sensor pair
(1 of 3 pairs)

DFP Interface
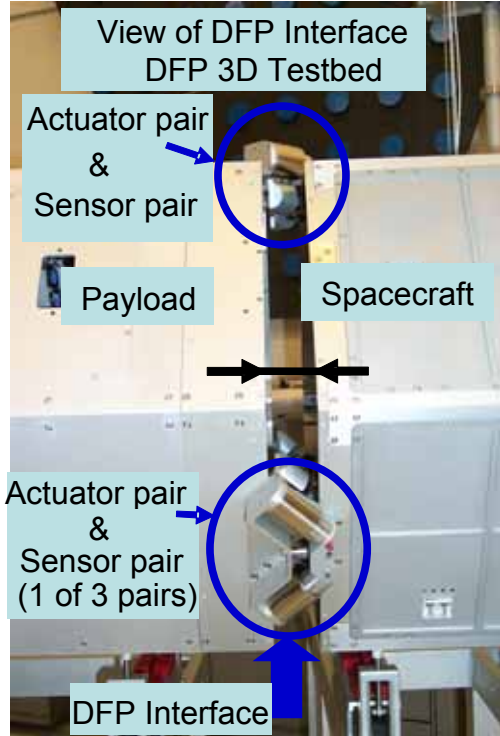
Laser Metrology System hardware,
based on *SIM* external metrology
design shown here
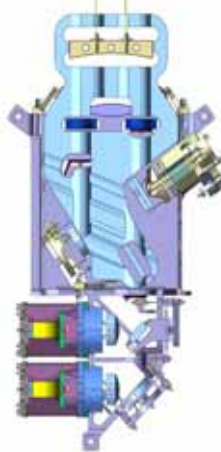
Figure 3.3-48 Attitude Pointing and Control Mechanisms
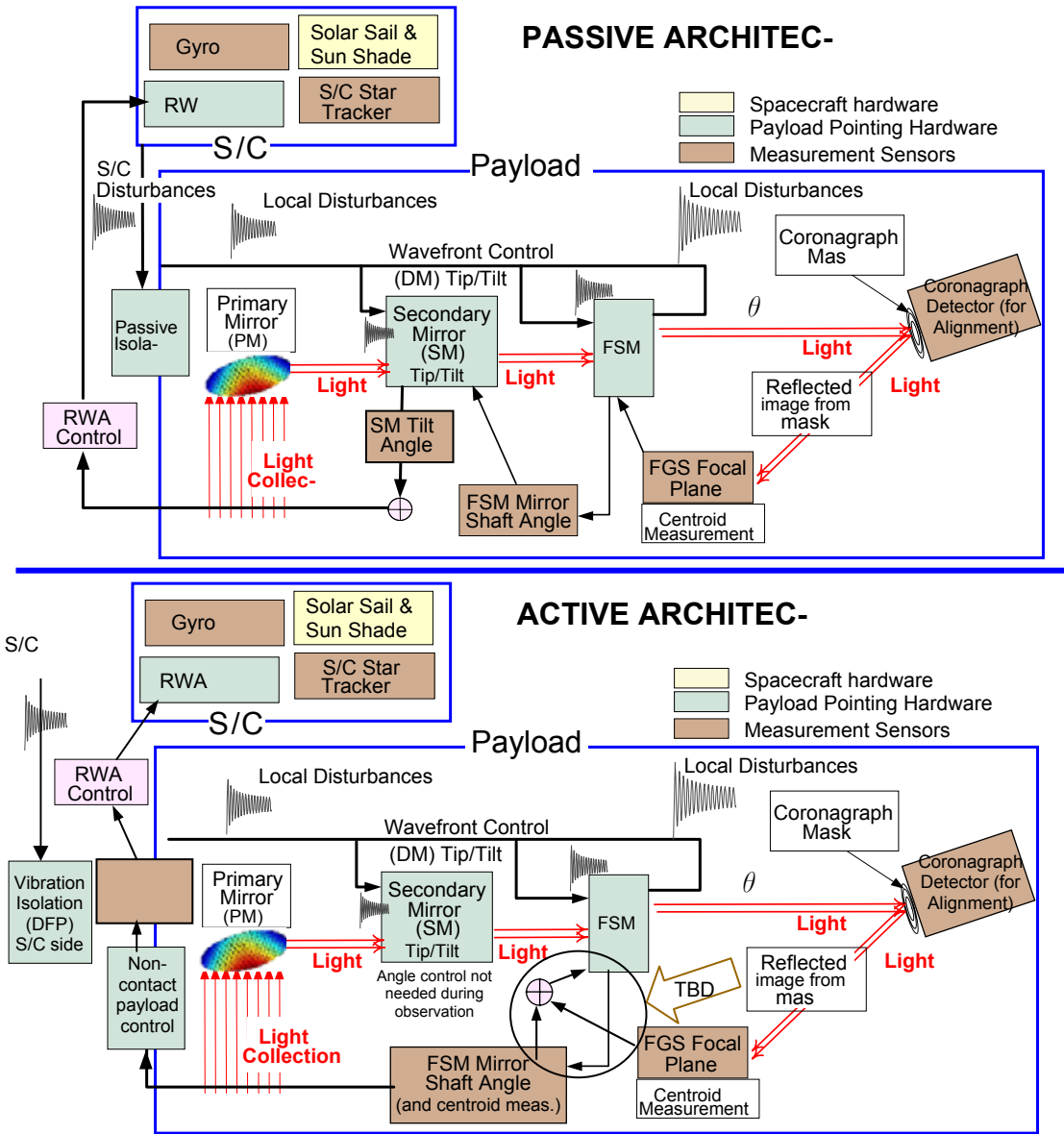
Figure 3.3-49. Schematics of Two Alternative Pointing Control Systems: Passive & Active

The passive system controls the secondary mirror tip and tilt to remove off-center beam walk in the telescope. The secondary mirror position is sensed using a laser metrology system that has been developed at JPL for *SIM*. The laser metrology system measures pointing angle of the secondary mirror and feeds that information to the Reaction Wheel Assembly to control the overall observatory position. The Fine Steering Mirror (FSM) is controlled using feedback from the starlight mask reflection and removes high frequency pointing errors.

The active system stabilizes the payload pointing using feedback directly from DFP position sensors. With this architecture, the secondary mirror does not need to be pointed for tip/tilt control. It is possible that the FSM control will also not be needed; however, the FSM loop is included in the architecture until all noise sources are evaluated.

The requirements for the Attitude and Pointing Control System derive from elements in the Observatory Error Budget and are allocated in terms of contrast degradation. The top level contrast requirements are listed in Table 3.3-23. These contrast allocations have been translated into angular errors and optical aberrations that are listed in the tables in Table 3.3-24 and Table 3.3-25 Table 3.3-26 shows derived rigid body motion requirements.

Table 3.3-23. Table of Top Level Contrast Requirements in Terms of Contrast

Beam Walk	LOS	LOS mask error	Structure Deformation	SD mask error	PM deformation	PM def. mask error	Total contrast
1.90E-12	9.04E-14	5.46E-13	2.75E-17	1.64E-17	8.55E-13	5.19E-15	**3.40E-12**

Table 3.3-24. Line-of-Sight and Beamwalk Error Allocations

Rigid-Body Error Allocations	
Image position (line of sight) errors	
- Image jitter (mas)	≤ 0.30 mas
- Image offset (mas)	≤ 0.30 mas
Beamwalk on each optic in error budget	
- Beamwalk due to pointing (mas)	≤ 0.04 mas

Table 3.3-25. Optical and Structural Deformation Error Allocations

Aberration Error Allocations (not Rigid Body)		
Zernike mode	Structural Deformation (nm)	Primary Mirror (nm)
4	4.78E-02	4.00E-01
5	6.21E-03	4.00E-01
6	4.58E-02	4.00E-01
7	2.50E-03	2.00E-01
8	6.00E-03	4.00E-01
9	3.48E-03	3.00E-01
10	4.41E-03	4.00E-01
11	1.29E-04	5.00E-03
12	1.44E-04	5.00E-03
13	3.77E-05	5.00E-03
14	7.95E-05	5.00E-03
15	4.56E-05	5.00E-03

Table 3.3-26. Physical Motion Requirements

	Rx (mas)	Ry (mas)	Rz (mas)	Tx (nm)	Ty (nm)	Tz (nm)
SM	0.377	0.251	1.078	2.6	5.5	1.1
Fold 1 (M3)	2.073	2.073	2.073	100.5	100.5	100.5
Fold 2 (M4)	2.073	2.073	2.073	100.5	100.5	100.5
Coronagraph Box	2.073	2.073	2.073	10.1	10.1	10.1
Observatory Rigid Body Pointing	4.000	4.000	1000.000	na	na	na

One additional requirement applies to the Attitude and Pointing Control System that derives from operational efficiency requirements. During a 30 degree slew of the observatory, the slew and settle time must be completed in 30 minutes.

The two Attitude and Pointing Control designs were modeled using an integrated approach which included observatory integrated structural and optical models. Disturbances flow through the structure, perturb the optical response, perturbations are measured by sensors and corrected by actuators that act on the structure. The integrated model captures all of these processes with associated errors and uncertainties. The model identified the disturbance sources with the largest impact on the performance of the coronagraph and was used to guide the observatory design choices. Engineering judgment identified the strongest design drivers, the reaction wheels. Error sources with lesser significance, such as sensor and actuator noise, were modeled with simple approximations unless analysis predicted performance impacts. If so, then more detail was added to the model. Model uncertainty factors were included in the error budget and consisted of model maturity– whether there was component, subsystem or system level testing, and frequency based inaccuracy. Materials uncertainties such as stiffness and damping were covered by a conservative knockdown factor.

Several integrated models were used to capture different performance aspects of the observatory dynamic response. A linear model was developed using DOCS Toolbox in MATLAB for high-bandwidth disturbances. A non-linear model was used for transient response. Several different levels of structural models, from high to low fidelity, were used to improve analysis efficiency and accuracy. Linear optical sensitivity matrices provided efficient computation of optical response. Optical performance from the error budget was used as the analysis metric. At this phase, only the primary mirror deformation was modeled. Optical deformation aberration for the secondary mirror and subsequent optics is anticipated for the next design cycle. Schematics of the passive and active Attitude and Pointing Control System models are shown in Figure 7.

Modeling results are shown in Figure 3.3-50 through Figure 3.3-53. Figure 3.3-50 shows the physical translations and rotations of the observatory optical elements, listed along the x-axis. The translations are in units of nanometers and the translations are in units of nanoradians. The direction of motion (X, Y, and Z in translation and around the X, Y, and Z axes in rotation) are indicated by the line color on the plots. The frequency which excites the highest response is indicated by the shape of the data point for each optical element. The requirements for each element are indicated by the pink, green and orange lines. Both systems meet requirements, with the passive system requiring secondary mirror steering.

Disturbance source: Reaction Wheel Vibrations and System Noise Simultaneously

Passive System – meets requirements – steering mirror is adjusted

Active System – meets requirements with margin
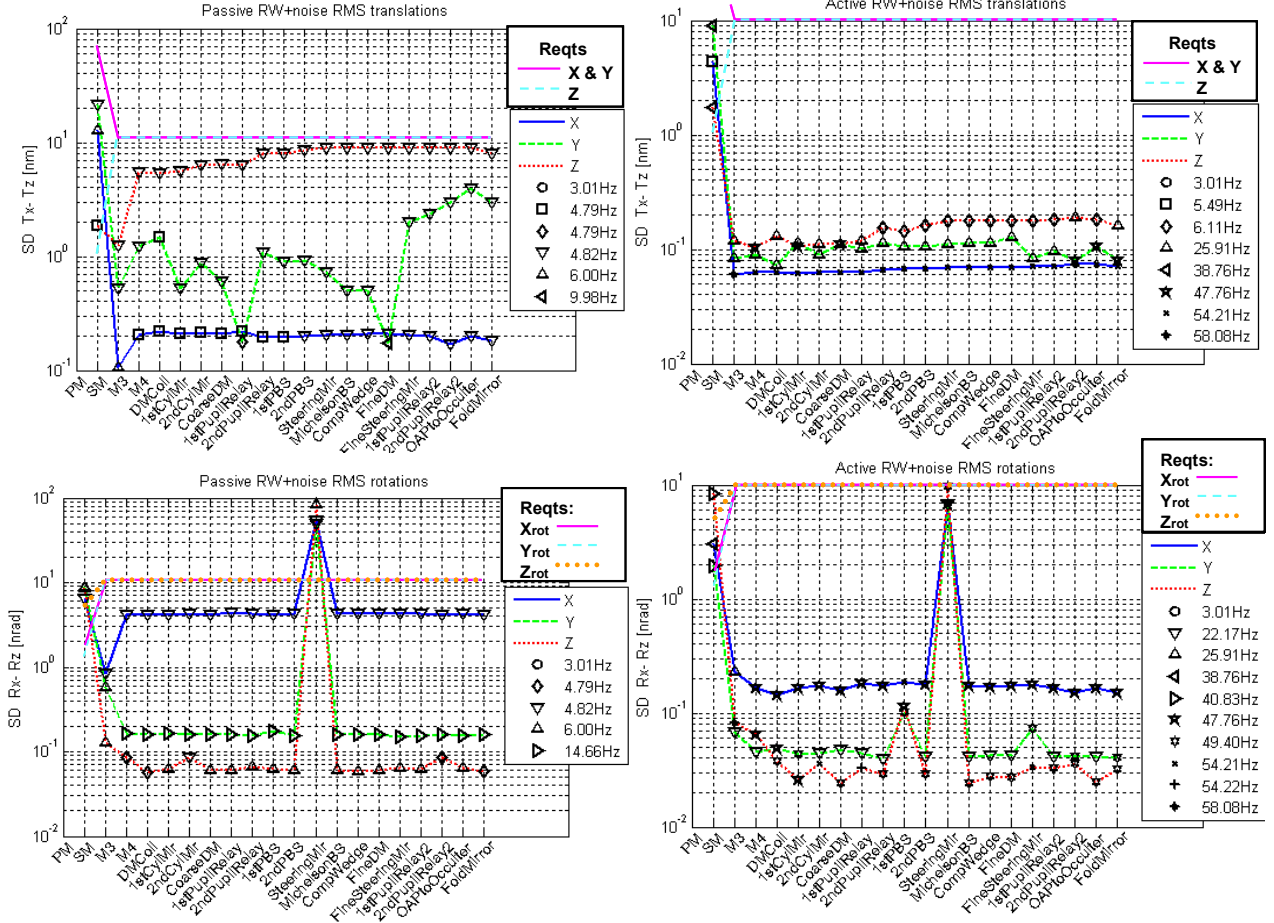
Figure 3.3-50. Rigid Body Disturbances, Both Passive and Active Systems

Figure 3.3-51 shows Line of Sight pointing variations and beam walk caused by jitter for both systems. The performance of the observatory is shown in green and blue and the requirements from the error budget allocation are shown in pink or red. The Line of Sight plots have reaction wheel speed in Hertz along the x-axis and the log of the Line of Sight deviation in milli-arcsecs along the y-axis. The beam walk plots have the magnitude of beam walk in nanometers along the y-axis and each optical element along the x-axis. The shape of the point symbols indicates which wheel speed frequency excites the larges beam walk response. The Primary Mirror Aberration plots have Zernike modes along the x-axis and the magnitude of the Zernike coefficient for the associated mode along the y-axis in units of nanometers. The data point symbol for each Zernike mode indicates the reaction wheel speed frequency that excites the largest response. Both systems meet the requirements for Line of Sight pointing and beam walk. The active system meets requirements for Primary Mirror aberration, but the passive system does not meet requirements at the higher order Zernike modes.
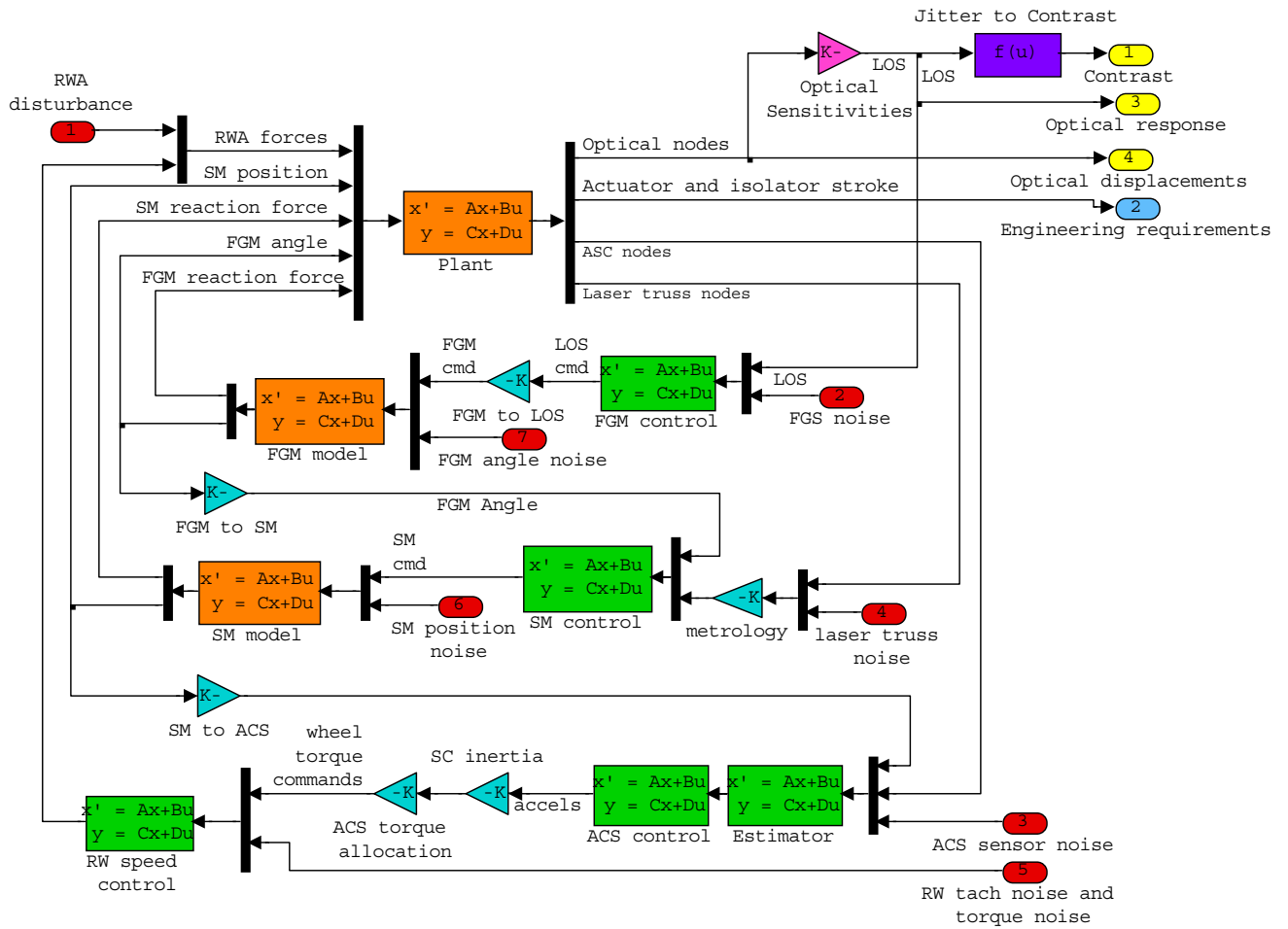
Figure 3.3-51. Attitude Control Schematic
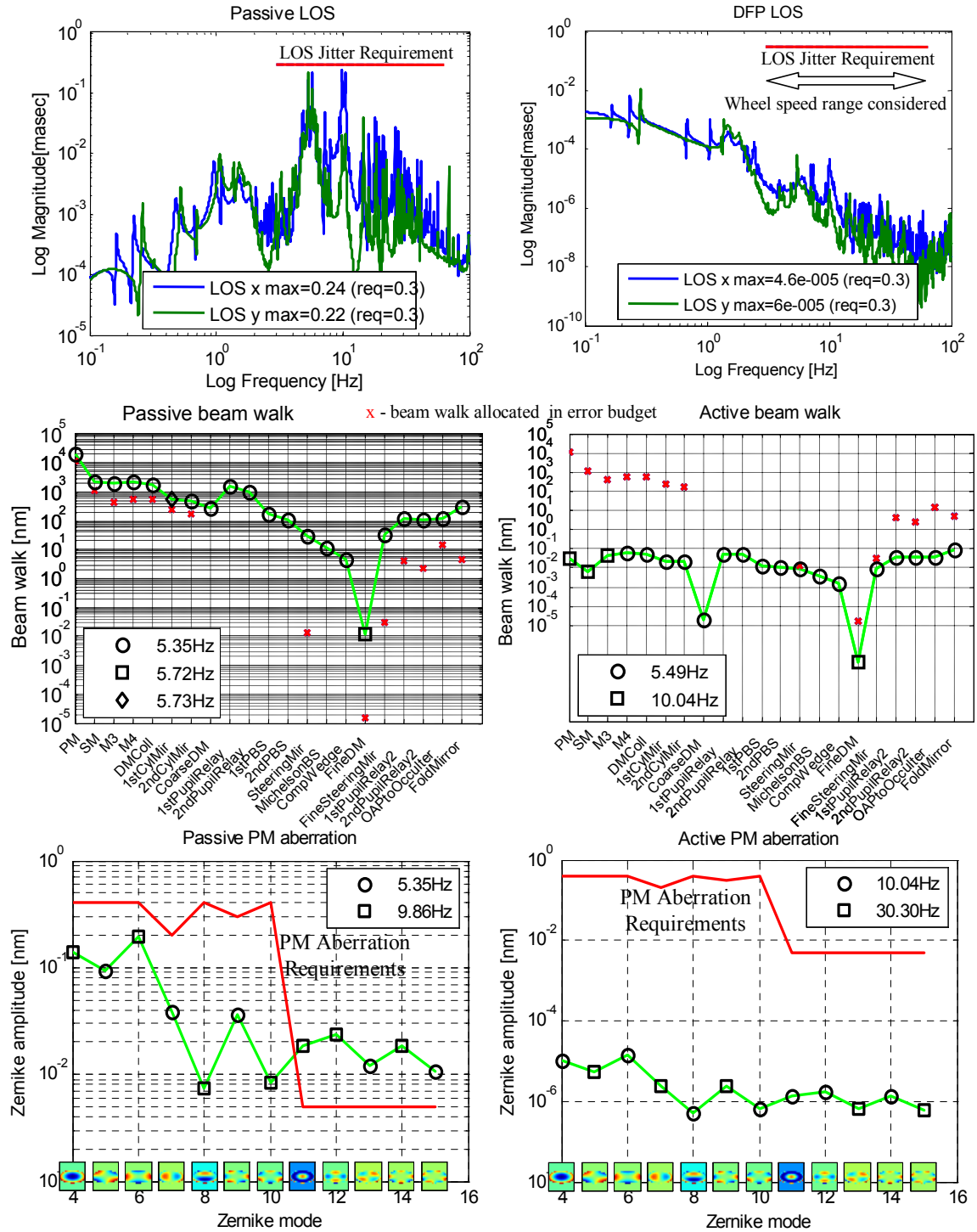
Figure 3.3-52. Optical Responses of both Passive and Active Systems Caused by Dynamics. Top: Line of sight; middle: Beam Walk; Bottom: Primary mirror aberrations

The final performance results are presented in Figure 3.3-53 showing the total contrast degradation caused by dynamic jitter. The contributors to the total contrast are shown in different colors. The left plot shows the contrast versus wheel speed for the passive design. The right plot shows the contrast versus wheel speed for the active design. For both plots, the requirement is shown by a solid red bar, the x-axis shows wheel speed frequency in Hertz and the y-axis shows the magnitude of the contrast. The passive system exceeds the contrast allocation around 5.35 Hz due to beam walk. The active system meets requirements.
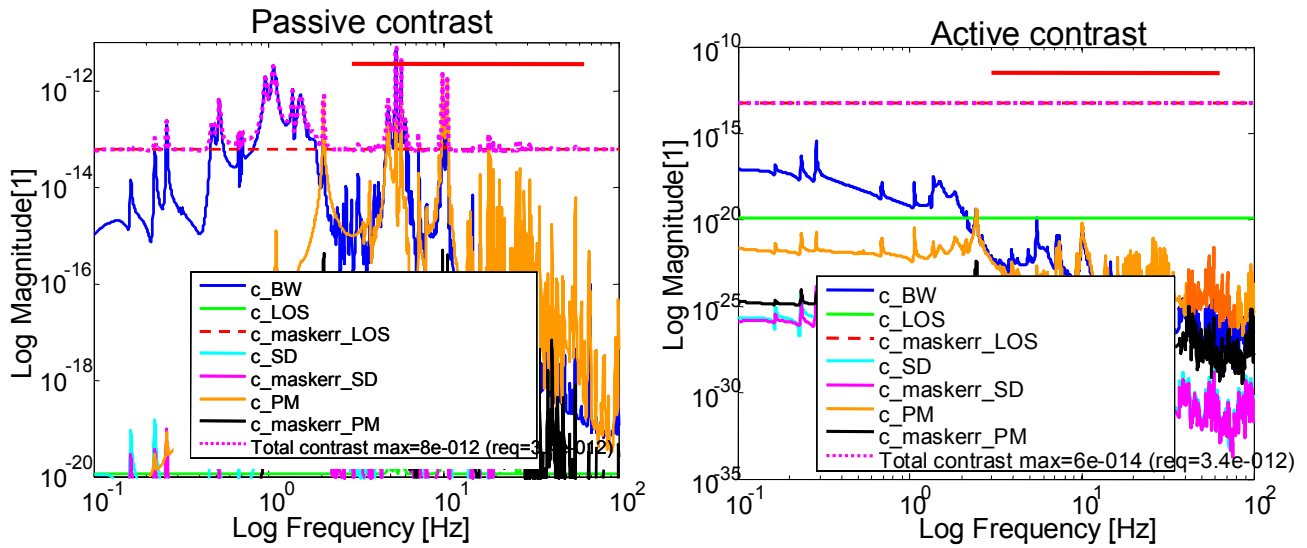
Figure 3.3-53. Contrast Comparison using Active Isolation and Passive Isolation.

3.3.4.2 Vibration Isolation

<u>**Overview:**</u> The Pointing Control System (PCS) must maintain the physical motions of the optical elements, and the position of the star image centroid on the coronagraph mask to prevent excess star leakage. To achieve the pointing accuracy and jitter suppression required to achieve the coronagraph requirements (0.04 mas jitter, better than 0.1 mas offset), both disturbances caused by spacecraft sources, such as reaction wheels and solar panels, and instrument sources are significant. The *TPF-C* design approach is to attempt to place the intrinsically noisy components, such as reaction wheels on a noisy platform on the spacecraft, and then limit the energy transmission into the optical payload, which will help to reduce excitation of the fine guidance mirror (FGM) and structural elements. The secondary mirror (SM) and FGM additionally produce local (payload mechanisms and structure being the source) disturbances when articulated to correct for pointing error or mechanical distortion (SM). If pointing of the payload was "perfect," jitter would be reduced by limiting motion of the SM and FGM, and the resulting disturbances. The payload and payload support module are connected to the spacecraft by cables for power and data, as well as the isolation system (which could be either passive or active), which becomes the path that disturbances are transmitted from the spacecraft to the payload.

TPF-C has studied two isolation systems. A passive system based on a "spring model" described below and an active system based on the Lockheed Disturbance Free Payload (DFP) model. Passive isolation systems have had previous flight heritage, whereas active isolation is relatively new, and the DFP approach analyzed by *TPF-C* is at the TRL-5 level of maturity, but shows great promise. In addition to the isolation implementation, a fundamental difference between the using the DFP active system and the passive system is that approach to correcting pointing errors uses a different set of hardware. Since the DFP is able to correct for small pointing errors, the spacecraft no longer needs to make "fine" pointing adjustments.

Comparison of the jitter and pointing errors due to the choice of isolation system is given in Section 3.3.4.1.

Reaction Wheels: Since the largest contributor of high frequency vibration is the reaction wheels, a brief summary is given. The current model of the reaction wheels is based on the following assumptions.

- The baseline design uses 6 Ithaco E wheels in a pyramid
- The reaction wheels are modeled as a sum of sinusoidal disturbances acting at harmonics of the wheel speed.

$$d(t) = \sum_{i=1}^{N_h} C_i f_{rw}^2 \sin(2\pi h_i f_{rw} t + \phi_i)$$

- Disturbance coefficients are derived from curve fits to force/torque vs RPM data
- Disturbance fundamental corresponds to static/dynamic imbalance
    - 0.273 g-cm, 21.4 g-cm²
- The response is scaled to approximate 2 of the 6 wheels spinning at the same speed provide a "real world" worst case scenario.
- The structural/optical response is computed by performing an RSS of the responses from each force/moment component from each wheel.
- Maximum wheel speed is 3850 RPM (64 RPS), minimum wheels peed 3RPS.

Image stabilization: Any vibration not removed by the isolation system is suppressed by an image control system. The image stabilization system uses nested control and the fine guidance sensor (FGS) loops to remove residual LOS error, due to residual disturbances that propagate through the isolators.

Control loop design parameters for the various pointing components are summarized in Table 3.3-27.

Table 3.3-27. Summary of Control and Sensing Loops and Passive Versus DFP Usage Comments

Control Loop	Parameter	Value	Sample Freq	Margins	Pointing Req.	Band-width
FGM (fine guidance mirror)	Break freq. Lead	1 Hz 45°	500Hz	7.01dB 25.6°	Passive and DFP high frequency	25.1 Hz
FGS (fine guidance sensor)			500Hz			
SM (secondary mirror)	Break freq. Lead	0.001 Hz 45°	1000Hz	49.11dB 45.7°	Passive system pointing SM. DFP does not	0.1Hz
ACS (attitude control subsystem)	Crossover Integral T.C. ratio Estimator freq. Elliptical order Elliptical ripple Elliptical atten. Elliptical freq.	0.016 Hz 0.075 10 Hz 3 1 dB 30 dB 0.56	2Hz	2.06dB 12.3°	S/C ACS points payload with passive system. DFP points payload, and SC ACS limits DFP range of motion.	0.043 Hz
RW speed control	Bandwidth Lead	1 Hz 60°	100Hz		looser control required for DFP/	1Hz

3.3.4.2.1 Passive Isolation

Passive isolation, analogous to using springs, is used to attenuate disturbance energy transmission from the reaction wheels to the telescope. The *TPF-C* passive isolation design effort focused on the need to apply realistic constraints to the performance of a passive isolator. Less description of the passive isolation implementation is given here, both because it is more commonly used in flight and that the description is simpler. However, the simple spring model has limitations that are discussed in the next paragraph.

Some comments on passive Isolation and Modeling, constraints: The general response of a passive isolator is that of a low-pass filter. simple models of passive isolators show a 40 dB/decade attenuation above the break frequency. Physical isolators exhibit an "isolation floor" where the transmissibility rolls from 40 dB/decade to (approximately) flat. There are four effects that drive isolator performance away from the nominal 40 dB/decade attenuation of the simplified isolator model:

1. Isolator damper "lockup": a pure damper acts as a rate feedback – which transmits force with + 20 dB/decade gain compared to a pure spring.

2. A non-ideal response of the payload and spacecraft structures: the simple damper model applies when the payload and structure roll off at 40 dB/decade. A structure will roll off between 10 and 30 dB/decade above its first mode. If the payload and spacecraft roll off at an average 20 dB/decade each, the transmissibility from disturbances, through both structures and the isolator, will be flat.

3. The isolator hexapod geometry: the typical isolator arrangement leads to coupling between isolators, leading to a high frequency floor

4. Cross-axis modes of the isolator: these modes can couple into the axial response, leading to localized high frequency amplification.

The *TPF-C* passive isolation design deals with these effects in the following manner. Damper lockup can be controlled by introducing a spring in series with the damper that effectively filters high frequency energy transmission. The other three effects are captured in the *TPF-C* analysis with a physical isolator model that couples the payload and spacecraft, and that includes the cross-axial modes of the isolator. The *TPF-C* passive isolation design and analysis deal with these effects in the following manner. Damper lockup can be controlled by introducing a spring in series with the damper that effectively filters high frequency energy transmission. *TPF-C* analysis captures the latter three effects with a physical isolator model that couples the payload and spacecraft, and that includes the cross-axial modes of the isolator.

Passive Isolation Placement
The *TPF-C* isolator stages are placed in two locations. The first is between the Reaction Wheel Assembly (RWA) and the spacecraft, and the second between the payload and the spacecraft. A possible additional stage of isolation would be to place individual isolators on each reaction wheel, in place of or in addition to the RWA isolator. The advantages of the single RWA assembly isolator are that it increases the suspended mass, enabling a lower break frequency, and that it requires fewer isolators. Analysis presented in [3.3.4.1], ACS, shows that the vibration suppression is sufficient.

Payload isolator. For the baseline design, the payload isolator is modeled as a set of 3-axis springs at each of the spacecraft/support module attachment locations. The springs are 30,000 N/m each.

The RWA isolator is a hexapod design using struts modeled on Honeywell D-struts (Davis et al. (1994)). The RWA mass is 61.4 kg, and the target frequency is 1.5 Hz. Each strut is modeled in NASTRAN with 3 nodes, two CBAR elements, two CONM2 elements, and 12 CELAS2 lumped stiffnesses. A 42,000 N/m flexure is assumed. The strut has a first bending (cross-axis) mode of 102 Hz.

3.3.4.2.2 Active Isolation
The model for the active isolation system is the Lockheed Disturbance Free Payload (DFP). In addition to the active isolator described below, passive isolation (see 3.3.4.2.1) is still used for the RWA isolation, although future studies may show that it is unnecessary.

The DFP concept is based on a strict mechanical separation of the payload from the spacecraft support module, so that no mechanical path exists for transmission of structural vibration through the isolator. Non-contact actuators at the payload-spacecraft interface allow the payload to react against the mass of the spacecraft to control inertial attitude and position. The position sensing is illustrated Figure 3.3-54.

The limited stroke and gap of the interface actuators is managed by control laws that command spacecraft reaction wheels based on non-contact interface sensors, essentially commanding the spacecraft to follow the payload in inertial space. Disturbances occurring through the isolation mechanical separation are eliminated, hence it is possible that only disturbances through other paths—cables, heat pipes, etc… are paths from the spacecraft

module to the payload. Moreover, the non-contact interface sensors do not participate in the derivation of payload inertial attitude control, since it is the payload Figure 2: DFP sensor. sensors that are controlling the pointing; thus, the payload attitude isolation is not limited by the noise characteristics of the DFP sensors.

Figure 3.3-54. Electrical Concept for DFP Sensor.
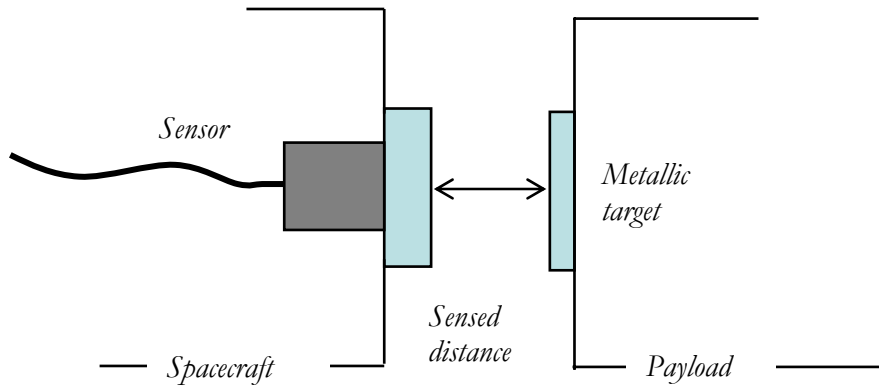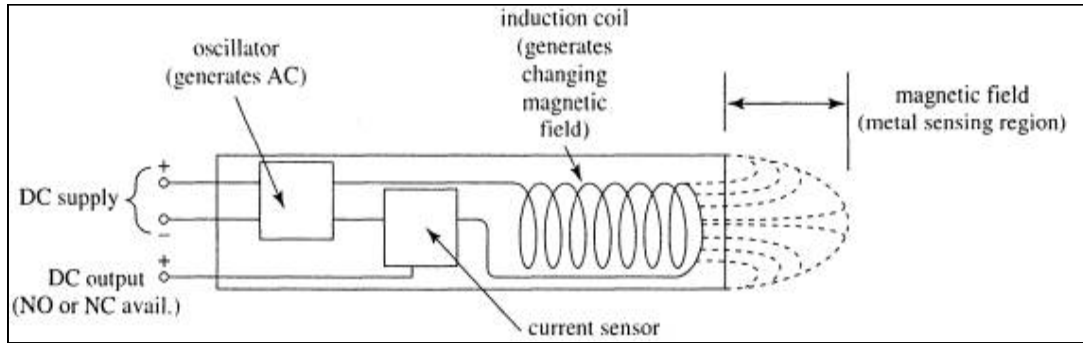
Figure 3.3-55. Sensors Based on Inductive (Eddy-Current) Sensor Technology

The DFP actuators have a range of roughly 1 degree of travel, allowing the DFP to "point" the payload, decreasing the range of travel for the secondary mirror, and allowing the SC to point the payload more coarsely without compromising the coronagraph pointing.

The differences between the passive and active vibration isolation design features are summarized in Table 3.3-28.

Table 3.3-28. Summary Differences Between Passive and Active Isolation

Control Loop	DFP	Passive Isolation
FGM (fine guidance mirror)	Required to take out high frequency disturbances to the coronagraph mask. Centers star image on coronagraph target point.	Required to take out high frequency disturbances to the coronagraph mask. Centers star image on coronagraph target point. Offloaded by SM.
FGS (fine guidance sensor)	Measures pointing error.	Measures pointing error.
SM (secondary mirror)	Metrology measurements used to maintain alignment.	Metrology measurements used to maintain alignment. Also used to offload FSM pointing range.
ACS (attitude control subsystem)	Takes out DFP pointing to keep DFP actuators within usable range.	Points Payload.
RW speed control	Somewhat loosely controlled since SM pointing is performed by DFP.	Very tightly control. Needed to point Payload.

REFERENCES

P. Davis, D. Cunningham, and J. Harrell, Advanced 1.5 Hz Passive Viscous Isolation System, 35th AIAA SDM Conference, Hilton Head, South Carolina, 1994.

3.3.4.3 Thermal Control and Sunshield

As has been made previously clear, a fundamental requirement driving the *TPF-C*oronagraph (*TPF-C*) system design is to control (or, perhaps more practically stated, effectively eliminate) thermally- and structurally-induced wave-front error (WFE).

The mission therefore presents the thermal system designer with major challenges to maintain unprecedented levels of thermal stability during very long imaging integration times. Further complicating the task is the requirement (at least in the FB1 approach) that, for speckle subtraction purposes, the initial image formation (following a slew to a new target and settling to a stable structural and thermal condition) must be followed by a 'dither' or roll maneuver about the boresight axis of about 30 degrees. This dither maneuver in effect 'moves' the Sun relative to the observatory, creating a powerful thermal destabilizing influence.

It is this 30° dither that drives the FB1 thermal control system design. Were there no need for such a dither, or a means of accomplishing speckle removal without moving the observatory relative to the Sun, thermal control would be significantly simplified.
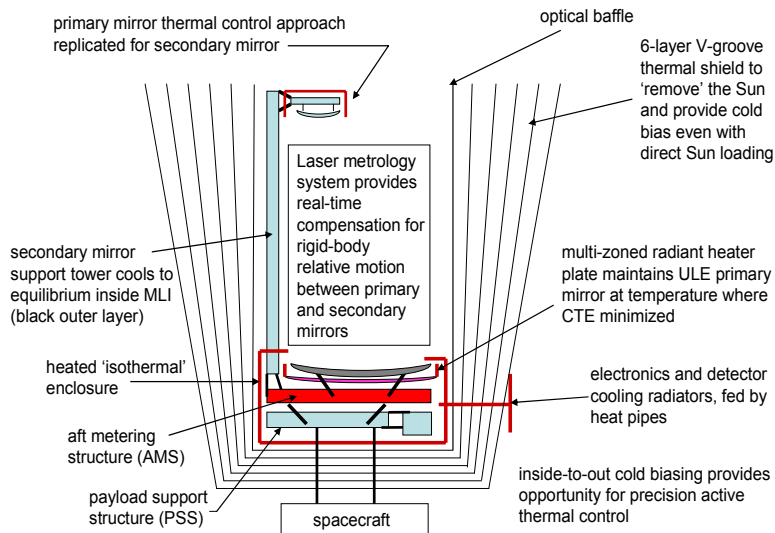
Figure 3.3-56. *TPF-C* **thermal control architecture**

The thermal control architecture adopted for *TPF-C* is shown schematically in Figure 3.3-56. There are two fundamental aspects of the FB1 thermal control system, both of which are critical to the achievement of success.

The first fundamental aspect of the thermal control system design is, to the greatest possible extent, to passively control of the effects of moving the relative position of the Sun midway through the imaging process. Especially since it is not possible to directly apply active thermal control to the reflective faces of the primary mirror (M1) and the secondary mirror (M2), passive control (in the form of highly effective thermal shielding) is essential for controlling environmentally induced spatial transient thermal distortions in the radiative background presented to the reflective face of the primary mirror by the large stray light baffle surrounding the incoming optical beam between M1 and M2. Controlling these gradients in the radiative background presented to the reflective faces of M1 and M2 is necessary because fluctuations in background result in fluctuations in the radiant flux rates from different parts of the mirror face, because such variations produce internal temperature gradients within the mirrors.

The most novel and important passive thermal control feature is a 6-layer conical V-groove shield, pictured in Figure 3.3-57. The reader is directed to Section 4.1.4.1 for a brief discussion of a design variant of this baseline conical sunshield that holds promises of improved thermal performance, improved compatibility with the detector cooling radiator, and improved feasibility with respect to packaging and deployment.).
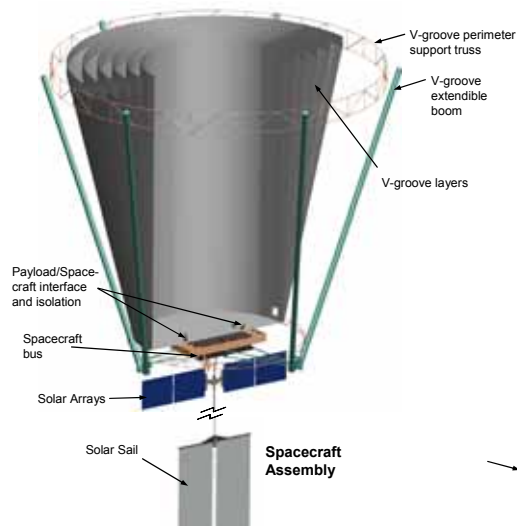
Figure 3.3-57. *TPF-C* **V-Groove Sunshield**

The second fundamental aspect of the thermal control system design is active thermal control, meaning the precise addition of resistive heating to the alignment-critical optical structure to maintain thermal stability during a full observational sequence of image, dither, re-image. The entire optically critical assembly (with little exception) is operated near room temperature, because the materials used for mirror and metering structure are biased in their fabrication processes to minimize their respective coefficients of thermal expansion (CTE) at 'room' temperature. This approach simplifies manufacturing and ground testing. (The reader is directed to Section 3.5 for a discussion of the thermal aspects of ground testing, including that of the Sun shield.) Since the combination of thermal control surface properties on the exterior of the sunshield, along with the fact that the telescope is pointed into the hemisphere away from the Sun, place a cold bias on the observatory, heating is required to maintain the optical system and instruments at room temperature. The exceptions are (1) the M1-M2 metering structure, which is thermally isolated at both ends and allowed to cool to 'equilibrium', since the alignment between M1 and M2 is maintained real-time, even during observations, by a laser metrology system driving an actively-controlled hexapod mount at M2; and (2) science instrument detector assemblies, which are cooled to the neighborhood of –100 C by a passive radiator and low-temperature heat pipes.

Those portions of the sunshield which are adjacent to and behind the edges of the primary mirror (PM) are less effective at rejecting post-dither thermal disturbances from the Sun than are those portions of the Sun shield which are in front of M1. Therefore, a highly thermally conductive enclosure, shown in Figure 3.3-58 surrounds the edges of M1, the aft metering structure and the instrument cavity. In addition, a highly thermally conductive, multi-zoned radiant heater plate is positioned directly behind M1, to provide a stable means of providing necessary heat to M1 without having to attach heaters directly to the back side of M1. Optical metering structure between the base of the secondary mirror (M2) support tower and the telescope aft metering structure (AMS), as well as between the payload support structure (PSS) and the AMS, and between these structures and the science instruments, is contained in the cavity defined by these two actively controlled, thermally isostatic structures.
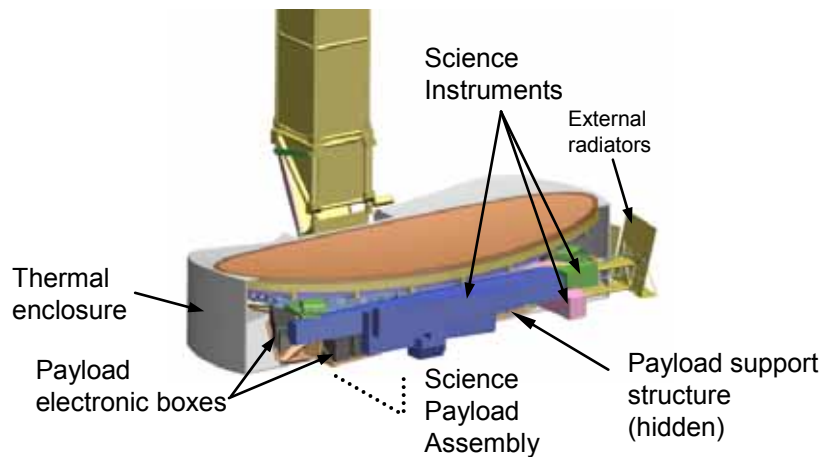
Figure 3.3-58. Thermal Enclosure

Prior to the FB-1 cycle, these structures were maintained at constant temperature in our models, to allow independent assessment of the performance of the passive Sun shield. At the end of the FB-11 design and analysis cycle, the thermal team was just beginning to explore the details of the heater control system. The reader is referred to Section 3.4.1.1 for further discussion of this topic.

Three other important aspects of the overall FB-1 thermal design approach are worthy of mention here:

First, the thermal control of M1 and its intimately associated equipment is analogous to the approach taken for M1.

Second, all payload-specific electronics (with the exception of those that dissipate very low and arguably stable power levels and that, for functional reasons are better located elsewhere in the cavity) are placed within the science instrument cavity, on thermally and structurally isolated 'pallets'. Their (during observations) 'constant' dissipative heat flows through heat pipes feeding a radiator sitting alongside the detector cooling radiator. We do this (as opposed to keeping some or all of these electronics on the spacecraft side) in order to minimize the thermal and vibration disturbance potential represented by the electrical cabling passing between the spacecraft bus and the science payload.

Third and finally, detectors and electronics are cooled passively. The alternative is active cooling, by placing a cooling source on the spacecraft side and circulating a fluid to remove heat. The passive approach was chosen to minimize the vibration potential represented by the active cooling conduits passing between the spacecraft and the payload, and to eliminate the reliability uncertainty associated with active cooling.

3.3.4.4 Solar Sail

The *TPF-C* design includes a solar sail to balance the torque induced by solar pressure on the sunshield. Without a solar sail, observation times would be limited by reaction wheel capacity, with a current estimate of only 4 hours. The FB-1 sail design is 14 ft. long with 2 separate 3 ft. wide panels deployed on opposing sides of a canister type, coilable longeron boom. A

single axis actuator feathers the sail for adjusting the torque balance (Figure 3.3-59). The sail material is silver coated Teflon chosen to provide the additional reactive torque from reflected photons.

FB-1 Design   **Proposed Design**
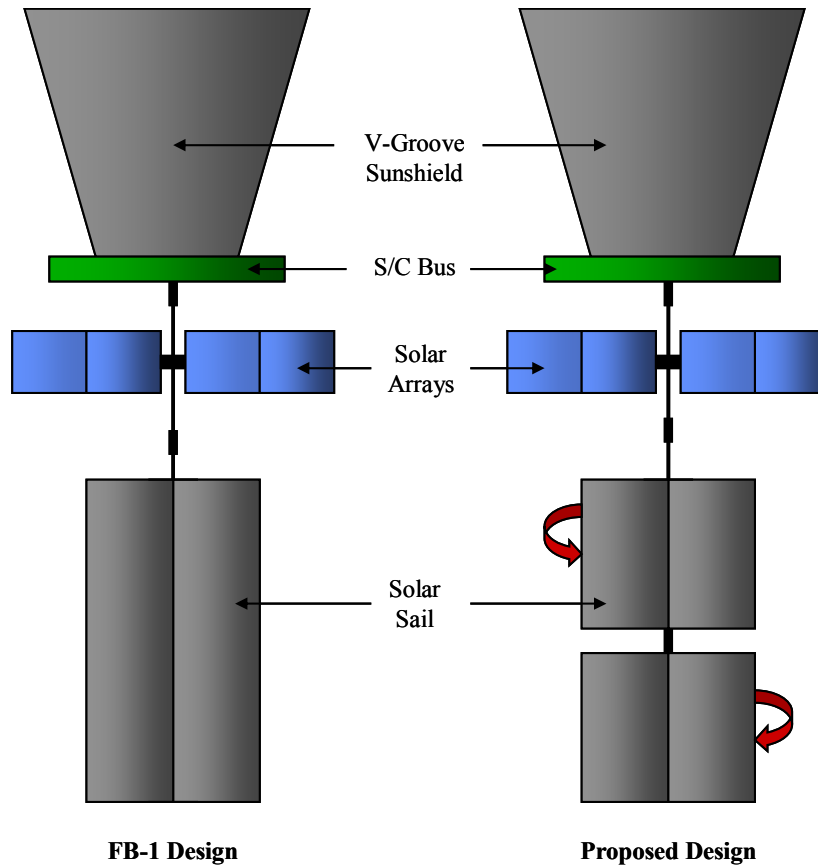
Figure 3.3-59. Comparison of Baseline and Proposed Solar Sail Designs.

Feathering the sail introduces a secondary torque about the sun line that would limit observation time to about 100 hours before saturating reaction wheels. Several options for a perfectly balanced system have been studied for future designs. The preferred method is to adjust the angle between the 2 sail panels, creating an X shape facing the sun (Figure 3.3-59). This can be achieved by adding an additional actuator between the two solar sail segments.

3.3.4.5 Solar Array

TPF-C is powered by solar arrays using triple junction cells with 27.4 % efficiency. The FB-1 array area is 12 m^2, sized to provide at least 3,000 W of end of life power for: maximum L2 sun range, a 85 % cell packing factor, and environmental degradations. Figure 3.3-60 shows the array configured as 2 wings each with 2 rectangular panels. The density by area is 5.77 kg/m^2. Array pointing is provided by single axis actuators on each of the 2 wings plus rotation of the combined array and sail mast.

Flat Panel Solar Array

Ultra-Flex Solar Array Panel
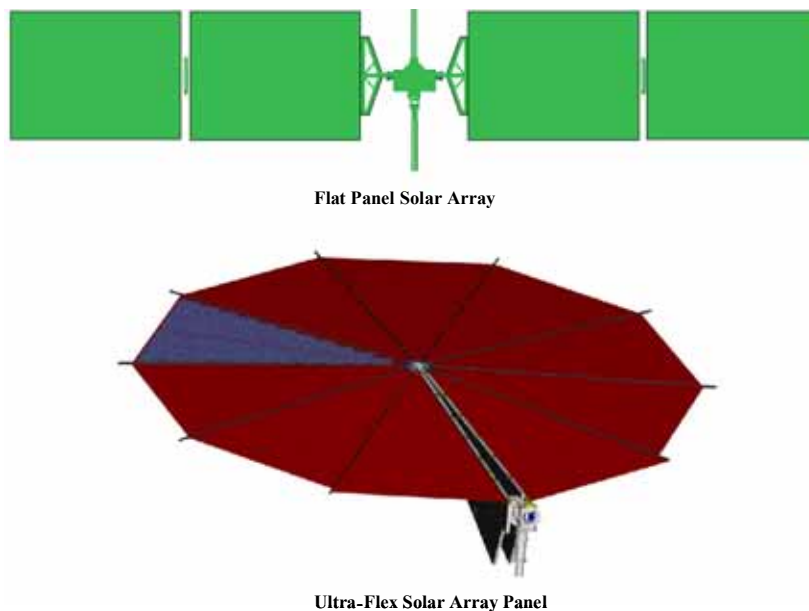
Figure 3.3-60. Comparison of Baseline and Proposed Solar Array Designs. Arrows Depict the Direction of Deployment.

Future *TPF-C* designs should consider use of ATK's Ultraflex style array as shown in Figure 3.3-60. This array, originally qualified for the Mars '01 Lander and now to fly on the Phoenix mission, provides dramatic reductions in both mass and stowed volume. The Ultraflex array, with its slight umbrella shape, can also provide greater stiffness than conventional arrays.

3.3.4.6 Electronics

The *TPF-C* spacecraft requires separate electronics for both science and engineering applications, which are mounted on two thermal control panels on the PSS. The only electronics on the OTA are the Laser Metrology Beam Launchers and actuators. In addition, electronics inside the optics box are minimized to provide thermal stability for the optics.

The two electronics thermal panels are placed at the current locations in the PSS (see Figure 3.3-61. and Figure 3.3-46) for several reasons. The thermal panels are placed away from the detector cold zone and stable optics assemblies to minimize thermal flux at these locations. However, the distance between the coronagraph and science electronics is constrained, necessitating placement of the electronics close to the science instruments. The engineering electronics are not constrained and are placed further away from the critical cold zones. Furthermore, the electronics are placed towards the exterior of the PSS to allow access to the electronics boxes during Integration and Test.

All electronics are redundant, except for the General Astrophysics Instrument (GAI) and Laser Metrology electronics. The box dimensions for the electronics are based on a 9U VME card format. The size of the box is based on a 3cm per card width (translates to length box dimension) and a 2 cm clearance in all dimensions. The mass of the boxes are estimated at 1 gm/cm^3 (consistent with CDS box on SeaWinds instrument that uses 6U VME cards).

The electronic hardware design concept is summarized in Figure 3.3-61
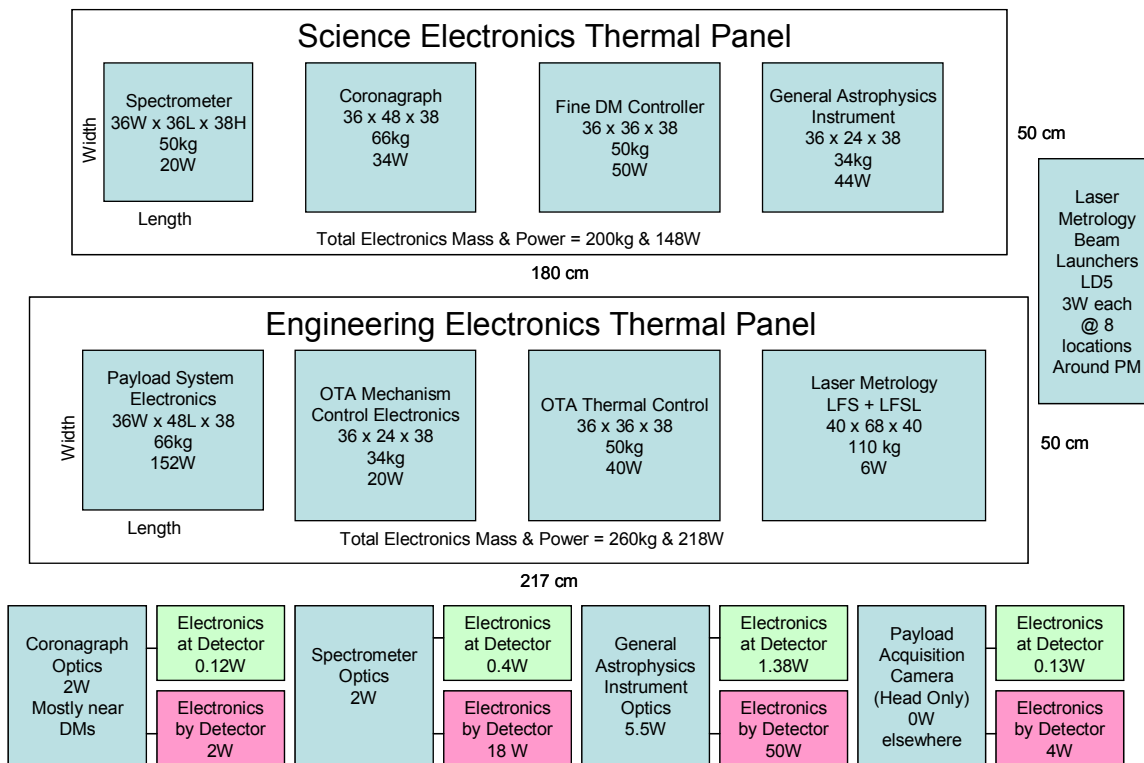
Figure 3.3-61. Strawman Allocation of Power
Denoting the Size of the Electronics Boxes, the Mass, and the Power Required for each Subsystem. Power Estimates do not Include Thermal Heaters.

3.3.4.7 Communications

The baseline telecom design provides a 1 Mbps downlink rate at a range of 0.5 AU (EDA orbit after 5 years), which supports the downlink of 2 days worth of coronagraph data in a single 6-hour pass. A single 6-hour pass would be planned each day, but the loss of one pass could be accommodated.

The baseline design is a conventional X-Band system. Two antenna panels on deployable booms with 2 axis of articulation are required to provide continuous coverage for the EDA orbit. A much simpler antenna configuration is possible for the L2 orbit, since earth is always oriented away from the star viewing direction.

A high rate spacecraft downlink is also provided which is capable of 64 Mbps, for a Ka-Band link to 34-m DSN stations. A daily downlink pass of 2.5 hour duration on average is assumed.

3.3.5 FB1 Performance Requirements

TPF-C performance is measured in terms of the level and stability of scattered light in the dark hole. The scattered light level is expressed in terms of instrument contrast, where contrast is defined as the integrated scattered light in a diffraction-limited resolution spot, normalized by the coronagraph mask throughput, and divided by the light from the star that would be present without a coronagraph mask. A rigorous definition is given in Green & Shaklan (2003). Table 3.3-29 gives the working requirements as of June, 2005.

Table 3.3-29. *TPF-C* **Contrast Error Budget Top Level Requirements**

Perturbation	Requirement	Comment
Static Contrast	6.00E-11	Coherent Terms
Contrast Stability	2.00E-11	Thermal + Jitter
Instrument Stray Light	1.50E-11	Incoherent light
Inner Working Angle	$4\,\lambda/D_{long}$	57 mas at λ=550 nm, D_{long} = 8 m
Outer Working Angle	$48\,\lambda/D_{short}$	1.5 arcsec at λ=550 nm, D_{short} = 3.5 m
Bandpass	500-1100 nm	Separate observ. in 100 nm bands.

The contrast level and stability are both functions of position in the image plane. We have found that the dynamic evolution of low-order aberrations and the predominance of low-order imperfections in the optics have their largest impact at the IWA, thus we evaluate the contrast at the IWA where we have the tightest engineering requirements, we evaluate the contrast error budget at the IWA. The dynamic (though not necessarily the static) contrast levels are smaller at larger working angles. We have not yet performed a detailed study of contrast stability at the OWA, though it is expected to be small compared to the IWA.

Over the last 3 years has led us to we have concluded that it is impractical to work within 3-4 λ/D (~ the third Airy ring) because as one removes diffraction at smaller working angles, the Lyot aperture is reduced while aberration sensitivity increases. Our work on aberration sensitivity (Green & Shaklan 2003, Shaklan & Green 2005) shows that for band-limited masks, the combination of reduced Lyot throughput and increased aberration sensitivity drives stability requirements (wave front shape change per unit time) up by ~ 1 order of magnitude when moving from 3 to 2 λ/D, and a factor of 4 between 4 and 3 λ/D. Our inner working angle of 4 λ/D represents a compromise between the required resolution (~ 60 mas), the largest aperture that can fit in an existing launch shroud, and the engineering requirements at the IWA.

The Contrast Error Budget (CEB) comprises the static terms (initial wavefront setting and stray light at the start of an observation) and dynamic terms (any changes to the wavefront during an observation) that contribute to image plane contrast. Static terms include wavefront sensing and control, stray light, coronagraph mask imperfections, and polarization leakage. Dynamic terms include motion of an optic or bending of an optic due to vibrations or thermal effects, and line-of-sight pointing fluctuations. Figure 3.3-62 shows the structure of the error budget including reserve factors, mean image plane contrast, and the standard deviation of contrast as detailed below.
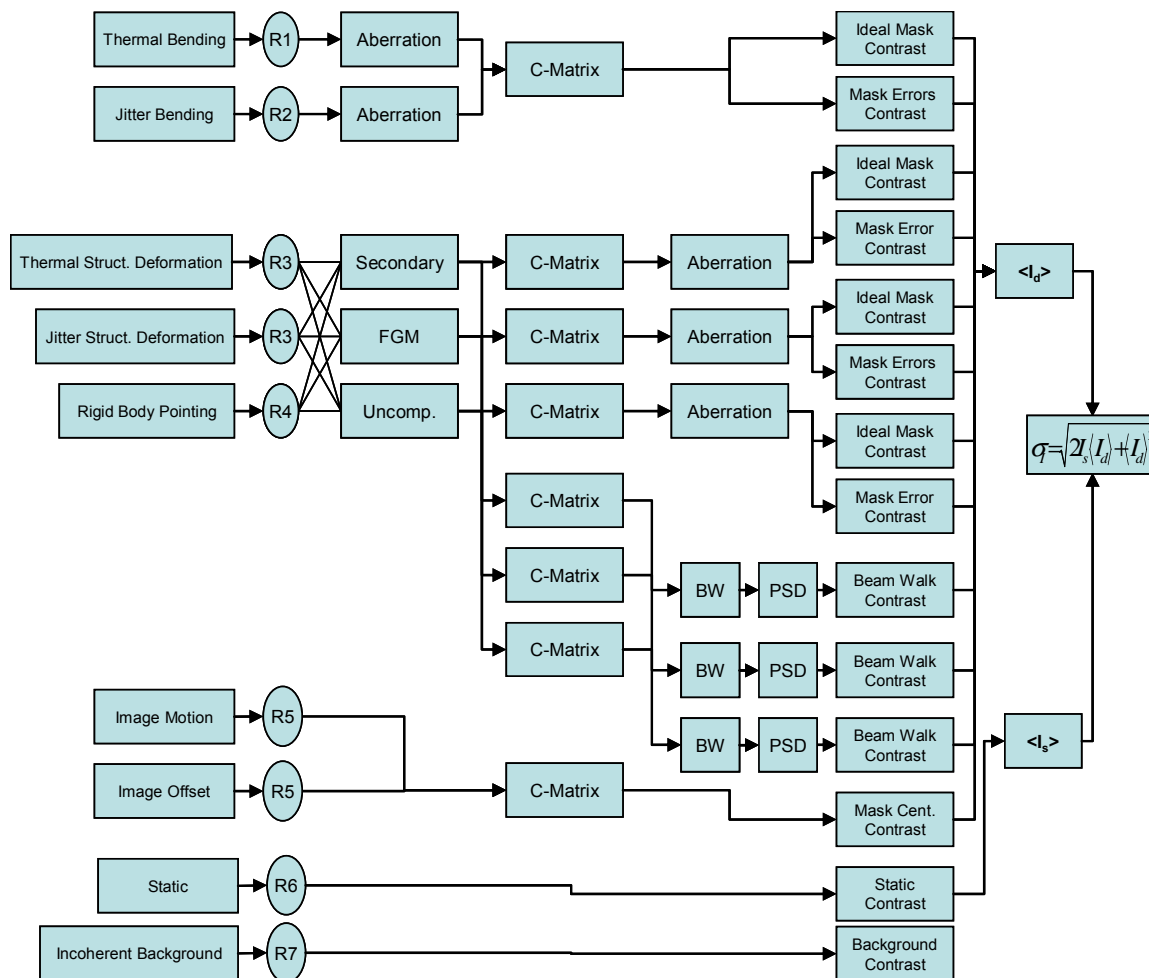
Figure 3.3-62. Error Budget Structure. 'C-matrix' is a Sensitivity Matrix or Equation. R1-R7 are Multiplicative Reserve Factors.

CEB rolls up the allocations for individual error contributions into an observatory system contrast. It is iterated regularly to reflect changing design baselines and system understanding. It is used to manage the allocation of challenging requirements between system components and to manage the reserve margins on each of those allocations. The CEB exists as a set of Excel spreadsheets utilizing data from several models described in Section 3.4.1.2.

Initial work has focused on the dynamic (thermal and jitter) part of the error budget for two reasons. First, dynamic terms are used to set requirements on telescope stability, from which design constraints follow, e.g. stiffness, thermal stability, and vibration isolation requirements. With dynamic requirements in hand, the *TPF-C* design team has been able to proceed with a design that can be modeled, compared to requirements, and iterated. Static requirements, on the other hand, drive technology, e.g. the approach to wavefront sensing and control, optical manufacturing, contamination control, and high-dynamic range baffling, among other things. Second, dynamic models are largely based on linear sensitivity matrices which are simple to develop and test. These are explained in detail in Section 3.4.1.1. In contrast, modeling of static wavefront contributors involves computer intensive diffraction propaga-

tions, electromagnetic modeling of mask transmission, and requires a broad-band wave front control algorithm to compensate for scattered light. This modeling is now underway and will be folded into the error budget studies.

Control Systems

Two control systems are represented in the CEB. The first is a multi-tiered pointing control system. We assume that the pointing errors are measured on a high-precision camera located in the coronagraph. This camera has yet to be designed, but might utilize light reflected from the coronagraph mask or measure the distribution of light diffracted around the Lyot stop. The high-frequency pointing is compensated by a fine-guiding mirror (FGM) at or near a pupil image in the coronagraph. This mirror is desaturated by tip-tilt motion of the secondary mirror, which in turn is desaturated by the spacecraft's reaction wheels or other pointing control mechanism. The CEB makes no assumptions about bandwidth but does assign a pointing residual to each subsystem. Our spreadsheet contains two switches allowing us to turn the secondary and FGM on and off while automatically redistributing residual pointing errors to the appropriate sensitivity matrices. The residuals will be reallocated to match the predicted subsystem bandwidths and disturbances once the dynamics modeling has been performed.

The second control system consists of a laser metrology truss between the primary and secondary mirrors, coupled to actuators attached to the secondary mirror. It maintains the relative positions (plus pointing offsets) between the primary and secondary. Position measurements are based on a *SIM*-like 6-beam laser metrology system (Shaklan et al, 2004). We assume that the metrology system has adequate bandwidth to compensate for thermal errors but is too noisy to compensate jitter. We note that the change from a 4th-order to an 8th order coronagraph mask has relaxed the secondary positional stability requirements (and laser metrology precision requirements) by 2 orders of magnitude compared to our earlier study (Shaklan et al 2004).

Allocations and Reserves

The error budget allocation process begins with a first order sensitivity analysis. Engineering judgment is used to partition allowable errors throughout the subsystems. In some cases, the allocations point directly to the difficult requirements, such as the primary mirror stability, while in others requirements are derived indirectly through engineering analysis, as is the case for temperature stability requirements on the primary mirror. Reserve factors are allocated for each source and account for the performance reserve, the modeling uncertainty factor and the error in the modeling. The modeling uncertainty relates to aspects of the model which do not accurately reflect physical behavior while the modeling error refers to inaccuracies in the as-built model or physical properties. These reserve allocations are initially chosen based on engineering judgment and over time modified to reflect bounding of model calculations via testbed results. Presently, the reserve factors R1 – R7 (fig. 3.3.5-1) are all set to 2. In practice, the modeling activity carries additional model uncertainty factors of 3 and 10 for low- and high-order modal amplitudes, respectively.

Combining Static and Dynamic Contrast

The error budget tracks contrast (energy) contributions from many sources. Here we briefly summarize how the contrast terms are combined, and how the contrast variance is determined. Assuming a set of random, uncorrelated complex field amplitudes in the Lyot plane of a stellar coronagraph, the summed variance of the contributions at a point in the image plane is equivalent to the sum of the intensity (contrast) contributions from each field component weighted by the component variances. That is, given an aberration $\phi(\vec{x},t)$ defined as the sum of time-varying orthogonal modes $a_i(t)\phi_i(\vec{x})$,

$$\phi(\vec{x},t) = \sum_{i=1}^{N} a_i(t)\phi_i(\vec{x}) \tag{1}$$

where the variance of the amplitudes is $\sigma_i^2 = \langle a_i^2 \rangle$, it can be shown that the mean intensity in the image plane is given by

$$\langle I(\vec{n}) \rangle = \sum_{i=1}^{N} \sigma_i^2 I_i(\vec{n}) \tag{2}$$

where $I_i(\vec{n})$ is the intensity at an image point $\vec{n}$ for the ith aberration. In other words, *contrast terms sum linearly; they are not combined as the root-sum-square of contrast values.* (Although from eq. 2 it can be shown that the wavefront errors do combine in a root-sum-square sense.) Further, it is shown that in the presence of both static contrast I_s and dynamic contrast I_d , the mean contrast level (ignoring incoherent scatter) is the sum of these terms,

$$\langle I \rangle = I_s + \langle I_d \rangle \tag{3}$$

while the variance of the contrast includes static and dynamic cross-terms and is given by

$$\sigma_I^2 = 2I_s \langle I_d \rangle + \langle I_d \rangle^2 \tag{4}$$

Eq. 4 was first published by Soummer & Aime (2004).

The *TPF-C* science requirements are tied to the engineering requirements by both $\langle I \rangle$ and σ_I. The mean intensity level, $\langle I \rangle$, determines the instrument contrast and the standard deviation, σ_I, determines the stability of the contrast.

REFERENCES

Green, J.J., & Shaklan, S.B., "Optimizing Coronagraph Performance Designs to Minimize Their Contrast Sensitivity to Low-Order Optical Aberrations," Proc. SPIE Vol. 5170, pp. 25-37 (2003).

Kuchner, M.J., Crepp, J., & Ge, J., "Eighth-order Image Masks for Terrestrial Planet Finding," ApJ 628, pp. 466-473 (2005).

Shaklan, S.B., et al, "Metrology System for the Terrestrial Planet Finder Coronagraph," Proc. SPIE Vol 5528, pp. 22-31 (2004).

Shaklan, S.B., & Green, J.J., "Low-Order Aberration Sensitiity of Eigth-Order Coronagraph Masks," ApJ 628, pp. 474-477 (2005)

Noecker, M.C., "*TPF* Coronagraph Wavefront Changes Due to Beam Walk," Proc. SPIE Vol. 5905 (2005).

Soummer, R. & Aime, C., "Statistics of Pinned Speckles in Direct and Coronagraphic High Contrast Imaging," Proc. SPIE Vol. 5490, pp. 495-503 (2004).

3.3.5.1 Static Error Budget

The portion of the CEB addressing the dark-hole light level that is present when the system is perfectly stable is called the static error budget. The static error budget considers both incoherent scattered light (e.g., from multiple reflections, particulate contamination, polarization cross-coupling, or off-axis sources) as well as coherent light (e.g., wave front and reflectivity imperfections on real optical surfaces). Thermal and jitter effects are carried in the dynamic error budget (Section 3.3.5.2.).

3.3.5.1.1 Incoherent Scattter

TPF-C has a significant optical bandwidth, thus a short (micron-scale) optical coherence length. Light arriving in the focal plane that has not followed a direct path, but instead has scattered two or more times, will combine incoherently with the directly imaged starlight. Light reflecting off of (and to an extent diffracting around) particulates also contributes to incoherent scatter, as does light from off-axis sources.

Polarization cross-coupling is another form of incoherent scatter. When light from one polarization is rotated by aperture-dependent off-normal reflections into the orthogonal component, the two components have no mutual coherence and different aberration content. The wave front control system corrects the weighted mean of these, resulting in light leakage especially near the inner working angle.

The light leakage is required to be below the level of the solar system zodiacal light and the exo-zodiacal light around the target star. These sources lead to a background level of 10^{-10} – 10^{-11} relative to the target star. We carry a requirement of 1.5×10^{-11} contrast for incoherently scattered light so that it does not contribute significant shot noise during planet detection.

The incoherent light is treated as static for the duration of an observation; there is no change in this light level during the sequence of line-of-sight rolls to build up an image.

Particulate Scatter

Particulate scatter is the main source of incoherent single-scatter light. For a given surface contamination density, the scatter grows worse as the beam diameter shrinks. Thus the primary mirror has the most relaxed particulate contamination requirement while the small optics where the beam is 10 cm in diameter have the tightest requirement. Since the *TPF-C* field of regard is only ~ 2 arcsec across, we specify the particulate contribution in terms of the BRDF at zero angle (the value is indistinguishable from 1 arcsec). Table 3.3-30 shows the required BRDF at zero angle, the approximate surface cleanliness class (not to be confused with clean room classification), and the fractional obscured surface (after Dittman, 2002).

Table 3.3-30. Required Optical Surface Cleanliness

	BRDF (0 deg)	Approx Surf. Clean Class	Obscuration Ratio
Primary Mirror	40	500	3.E-03
Secondary Mirror	5	300	3.E-04
Fold Mirrors	0.1	200	4.E-05
SSS mirrors	0.02	<100	3.E-06

We note that the calculations performed to generate the table assume that both the forward and backward scattered light are incoherent with the unscattered beam. In fact, the forward component (which is much larger than the backscattered one) is simple light loss and can be represented as a half-wave shift that follows a $1/\lambda$ wavelength amplitude dependence. It is partially correctable by the wave front control system. This is an area of ongoing research that may result in relaxed cleanliness requirements.

Polarization Cross Talk

Polarization cross-terms leak directly through the two independent polarization channels. The cross-polarization amplitude and phase follow the incidence angle across the optics, forming tilt, focus, coma, astigmatism, etc. This is a rather serious problem for 4th-order coronagraphs and the visible nuller instrument (Sect. 4.1.3.5) at $4 \lambda/D$ because they do not sufficiently attenuate low-order aberrations. At smaller inner working angles, the problem grows rapidly and becomes the dominant source of scattered light. Eighth-order coronagraphs (Shaklan & Green, 2005) and shaped pupil coronagraphs (Green et al., 2004) are relatively insensitive to this effect and we find that there is no significant polarization leakage if these kinds of coronagraphs can be realized (Balasubramanian et al., 2005).

Multiple Scatter

Multiple scatter has several sources, including particulates, molecular contamination, and baffling. Multiple scatter from particulates and molecular contamination is expected to be well below the single-scatter level. Some preliminary baffle design has been completed under the assumptions that we do not look within 95 degrees of the Sun, Earth, or Moon; there

can be no direct illumination of the inside of the main telescope baffle from these sources. We do not yet have a specification for proximity of bright stars and planets.

3.3.5.1.2 Coherent Scatter
Coherent scatter refers to the speckles that appear because the wave front is not an ideal, uniformly illuminated plane wave. The deviations from ideal are caused by imperfect optics and optical misalignments.

Phase Errors

Optical surfaces are specified by their Power Spectral Density (PSD). The PSD has low, medium, and high spatial frequency branches that contribute to the static error in different ways. The low frequencies may be very large – several microns or more – because some fraction of gravity release and the thermal equilibrium temperature are unpredictable on-orbit. This level of deformation requires a large-stroke DM (we refer to it as a coarse DM) or active primary mirror control. We assume in FB1 that the large scale error is compensated by a coarse DM and that the residual wave front error is compensated by the fine DM. Thus the static low-spatial frequencies do not contribute to the static contrast.

Mid-spatial frequencies, covering 4 to ~ 48 λ/D, are compensated by the high-precision DM. The optical bandwidth of the compensation and the configuration of the compensation scheme (Michelson or sequential DMs) dictate the maximum PSD for optics not conjugate to the pupil plane.

Shaklan & Green (2006) have shown that the propagation of phase errors from non-pupil optics into the pupil plane leads to wavelength-independent amplitude errors. The sequential configuration generates wavelength-independent amplitude compensation, so this effect does not limit the PSD or the bandwidth. The Michelson configuration has $1/\lambda^2$ compensation, so it controls contrast over a finite bandwidth. Figure 3.3-63 shows the required PSD for mid-spatial frequencies for several key *TPF-C* optics in the Michelson configuration assuming a 100 nm bandpass centered at 630 nm, for a contrast level of 10^{-12} at any spatial frequency.

Figure 3.3-63 also shows the required PSD in the sequential configuration. The first order propagation terms are fully compensated broad-band (as with the Michelson), but the second order terms are not. This leads to a relaxed requirement in mid-spatial frequencies but the 4th-order slope makes the requirements for the two configurations comparable at about 20 cycles/aperture.

High spatial frequencies by definition scatter their light outside the dark hole. The mixing of high-spatial frequencies (e.g. 50 cycles per aperture beats with 55 cycles/aperture) creates low and mid-spatial frequency amplitude speckles (5 cycles/aperture in this example) that scatter into the dark hole (Give'on et al, 2006). The wavelength dependence of the amplitude varies as $1/\lambda^2$. This is perfectly compensated by the Michelson configuration. We are presently analyzing the required high-spatial frequency PSD in the sequential configuration.

The dashed curves in Figure 3.3-63 show the PSD of state-of-the-art optics manufactured for extreme-ultraviolet lithography systems. The optics are coated, mounted aspheres with 0.3 nm wave front errors. The curves show that for the Michelson and sequential configurations, there is substantial performance margin up to 10 (Michelson) and 20 (sequential) cycles/aperture. To operate beyond 20 cycles/aperture, *TPF* requires either 1) optics superior to the SOA, or 2) reconfiguration of optics to move them closer to pupil images, to operate in 100 nm bandpasses beyond 20 cycles/aperture.
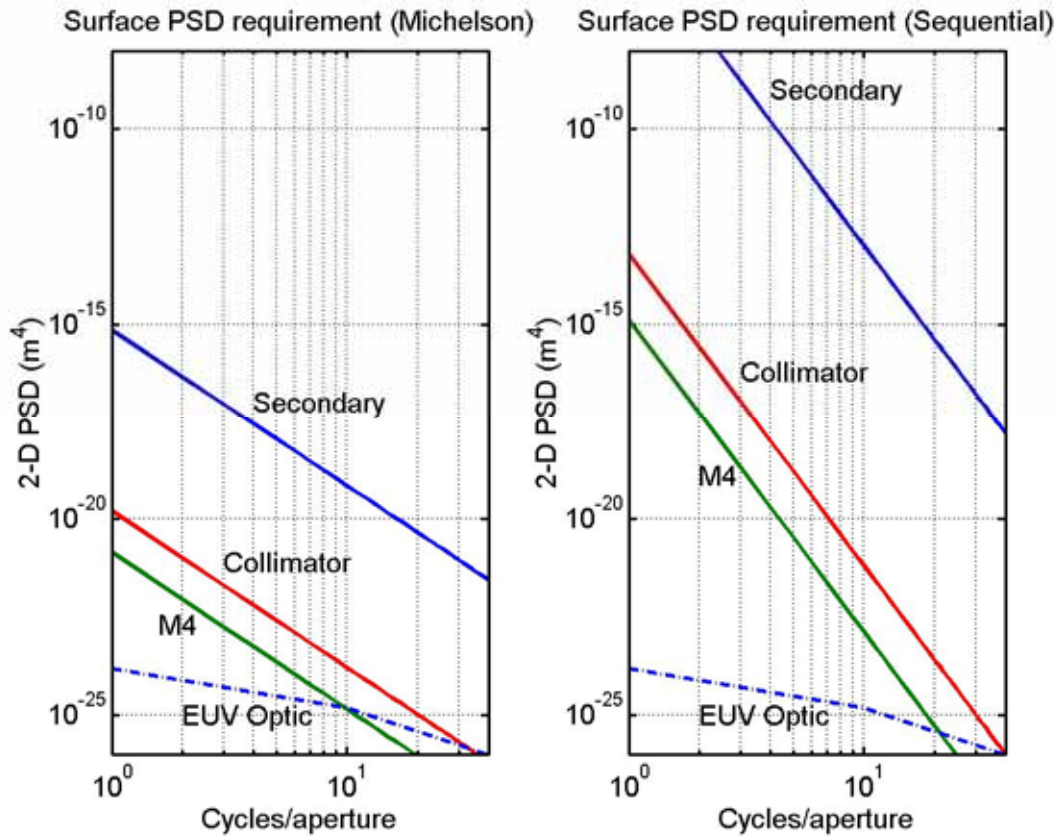
Figure 3.3-63. Required 2-D PSD of Optical Surface Height in the Michelson and Sequential Configurations Assuming A 100 nm Bandpass. We also Show the Surface PSD Achieved for EUV Optics. The EUV Curve is a Fit to Data Provided by Lawrence Livermore National Laboratory of Interferometric Measurements of Two Aspherical Optics Produced for EUV Lithography By Tinsley. The R.M.S. WFE of the EUV Optic for the Spatial Frequencies Shown is 0.30 nm.

Amplitude Errors

Reflectivity non-uniformities, like phase errors, lead to speckles in the dark hole. We use the same methodologies described for phase errors to specify the reflectivity uniformity assuming different wave front control schemes. We assume the reflectivity variations are grey; they have uniform fractional losses across the optical spectrum of interest.

As noted above, the Michelson wave front control system exhibits $1/\lambda^2$ wavelength dependence. This does not compensate the wavelength-independent reflectivity variations over a

broad band. Figure 3.3-64 shows the required reflectivity uniformity requirement for the Michelson configuration (horizontal line) assuming a 100 nm bandpass and contrast $= 10^{-12}$ at any spatial frequency.

The sequential DM configuration has greatly reduced reflectivity uniformity requirements compared to the Michelson because the propagation of light reflected from the DM (λ-dependent) cancels the wavelength dependence of the DM phase ($1/\lambda$) creating a wave-length-independent amplitude. The amplitude uniformity for the optics comes from the propagation of amplitude ripples to phase ripples, which has λ-dependence and is not can-celled broad-band by the $1/\lambda$ DM surface phase. Figure 3.3.5.1-2 shows the reflectivity re-quirements on key optics in the system assuming the sequential DM configuration. It also shows the control authority (green dashed curve) of the DM assuming it pistons only 30 nm at any spatial frequency. The mirror surfaces amplitude variations must be below the solid and dashed diagonal lines.
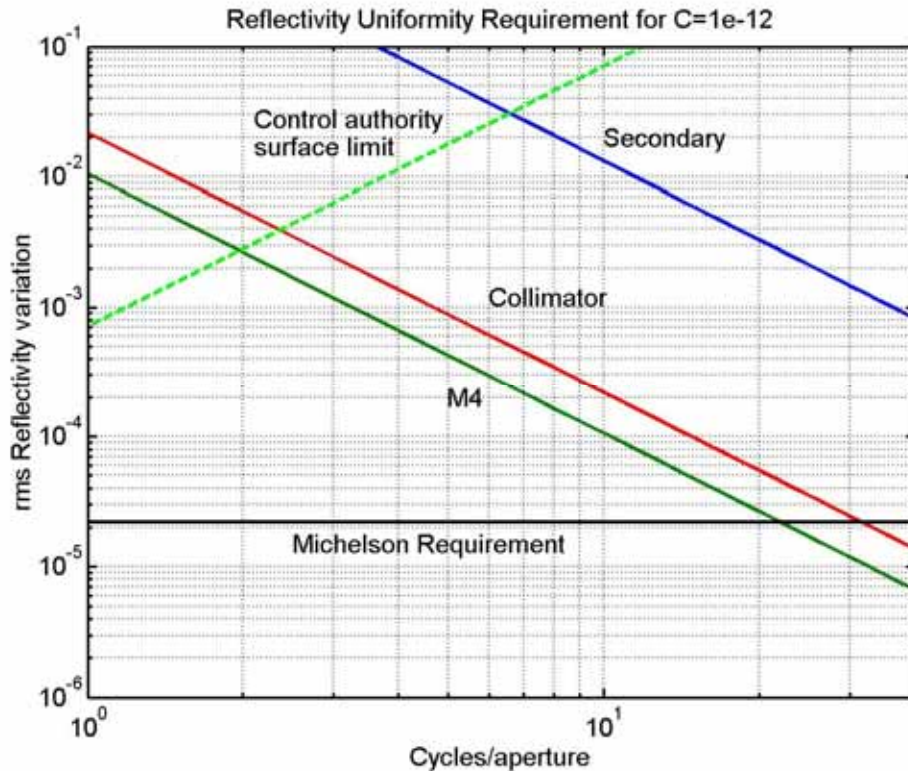
Figure 3.3-64. The Solid Diagonal Lines Show the Allowed RMS Reflectivity Variation vs. Spatial Frequency in the Sequential Configuration for a Periodic Deformation Resulting in a Contrast Floor oOf 10-12 per Optic. The Requirement for the Michelson Configuration is the Horizontal Line at 2.2e-5. The Dashed Line Shows the Allowed Reflectivity Variation Assuming that the DM is Limited to 30 nm Piston and is at a Distance of 3m from the Pupil.

Note that there is no requirement on the primary mirror (PM) except for the green dashed line. This is because the PM is located at a pupil conjugate so there are no propagation ef-fects to the exit pupil. This analysis indicates that reflectivity variations of 1% at 4 cy-cles/aperture (in a 1 cycle/aperture bandwidth) are allowed. Thus the sequential DM con-

figuration relaxes the reflectivity uniformity requirements by several orders of magnitude compared to the Michelson. We also point out that at 1-3 cycles/aperture, the requirement is significantly relaxed compared to the green-dashed line in fig. 3.3.5.1-2 because most of this light is blocked by the coronagraph and it scatters inside the dark hole.

3.3.5.1.3 Drivers of Mirror Figure

The PM surface figure at low and mid-spatial frequencies is compensated in broad-band light by the DMs, and the amplitude uniformity requirement is likely achievable with current technology. The high-end spatial frequency requirements are TBD. Other than the high-end frequencies, what drives the PM figure?

The only hard requirement known as of this writing is the need to deliver a diffraction-limited image to the General Astrophysics Instrument (GAI). This instrument does not, in its present configuration (Sect. 4.1.3.4), have an adaptive optics system, so it relies on the telescope to be diffraction limited, i.e. r.m.s. surface errors ~ 50 nm and negligible align-ment errors. We assume the secondary mirror is significantly better than the primary. This assumes that a sequential DM configuration is in place. Using the Michelson DM configura-tion (as well as the Visible Nuller instrument, Sect. 4.1.3.5), the requirements are substantially tighter. We are still evaluating the high-spatial frequency requirements for frequencies be-yond the control bandwidth of the DM. We must be sure not to violate the requirements of the GAI over its field of regard (up to 10 arcmin from the target star).

3.3.5.1.4 Summary

We find that the static wave front allocation of 5×10^{-11} is met assuming:

1. Particulate contamination meets the requirements of Table 3.3-30.
2. Optical surface PSDs are at or below the curves of Figure 3.3-63 (assume a sequen-tial DM configuration).
3. Reflectivity uniformity is better than the curves in Figure 3.3-64.
4. The telescope (not including the wave front control system) produces a diffraction-limited image
5. We do not yet have a specification for high-spatial frequencies (light falling outside the dark hole).

REFERENCES

K. Balasubramanian, D. Hoppe, P. Z. Mouroulis, L. Marchen, and S. Shaklan: "Polarization compensating protective coatings for *TPF-C*oronagraph optics to control contrast degrading cross polarization leakage", to appear in Proc. SPIE **5905** (2005).

M.Dittman, "Contamination Scatter Functions for Stray-Light Analysis," Proc. SPIE vol. 4774, pp.99-110 (2002).

Give'on, A., Kasdin, N.J., Vanderbei, R.J., and Avitzour, Y., "On Representing and Correct-ing Wave Front Errors in High-Contrast Imaging Systems," accepted for publ. in JOSA-A (2006).

Green, J.J., Shaklan S.B., Vanderbei, R.J., and Kasdin, N.J., "The Sensitivity of Shaped-Pupil Coronagraphs to Optical Aberrations," Proc. SPIE 5487, pp. 1358-1367 (2004).

Shaklan, S.B., & Green, J.J., "Low-Order Aberration Sensitivity of Eighth-Order Coronagraph Masks," ApJ 628, pp. 474-477 (2005)

Shaklan, S.B., & Green, J.J., "Reflectivity and Optical Surface Height Requirements in a Broad Band Coronagraph I: Contrast Floor Due to Controllable Spatial Frequencies," submitted to Appl. Opt. (2006).

3.3.5.2 Contrast Stability Error Budget

Time-variable errors include optical aberrations, beam walk and image motion. Aberrations arise as the system is perturbed from its ideal design, independent of the quality of the optics. Aberrations result from bending of optics (the primary mirror is of greatest concern), as well as from structural deformation. When the structure deforms, the secondary mirror moves relative to the primary mirror, as do downstream optics. This introduces low-order aberrations that scatter light near the inner edge of the dark hole. Aberrations contribute to contrast in two ways: first, in the case of the ideal mask and Lyot stop, the mask and stop act as a spatial filter that passes a fraction of the light to the image plane. Second, mask transmission and phase errors allow aberrated light through the system, as if there were a light source located at the position of the mask error.

Beam walk is the motion of the beam across the optics. Both rigid body pointing errors and structural deformation cause the beam to deflect from its initial state at the beginning of an observation. When the beam reaches the deformable mirror (DM), it contains wave front corrugations that are shifted with respect to the compensating corrugations on the DM. The resulting wavefront adds to the scattered light level. The phase deviation of the wavefront varies linearly with displacement and spatial frequency, while the scattered energy varies as the square of the uncompensated wavefront error (Noecker, 2005).

In addition to aberrations and beam walk, one other dynamic term contributes to image plane contrast. This term is labeled 'image motion' and is the energy that leaks around the mask when the beam is not perfectly centered on it. For the 8th-order Lyot coronagraph (Kuchner, Crebb, and Ge, 2005, Shaklan and Green, 2005) that we have baselined, the mask intensity leakage is proportional to the 8th power of wavefront tilt.

Eq. 4 of Sect. 3.3.5 demands a balance between the static and time-variable contributions. As the static contribution I_s grows larger, the time variable contribution I_d is more tightly constrained. For example for $I_s = 6 \times 10^{-11}$ (our self imposed limit to keep contrast well below scattered exo-zodiacal light), we require $I_d = 3 \times 10^{-12}$ to maintain $\sigma_I = 2 \times 10^{-11}$. At present our best estimate of I_s is 3.6×10^{-11}, allowing $I_d = 5.14 \times 10^{-12}$. This is the requirement for time-variable contrast contributions.

Table 3.3-31 is a roll-up of time-variable contrast contributors, including bending of the optics, beam walk across all optics, and pointing errors. The roll-up is based on allocations of

engineering requirements (e.g., allowed motion of a given optic, allowed bending of an optic) applied throughout the system. Allocations were derived from extensive modeling efforts on a previous 6-meter version of *TPF-C.*

Perturbation	Contributor	Nature	Contrast	Fraction
Structural Defomation	Beam Walk	Thermal	8.29E-13	16.12%
		Jitter	6.33E-13	12.31%
	Aberrations	Thermal	3.28E-14	0.64%
		Jitter	4.43E-17	0.00%
Bending of Optics	Aberrations	Thermal	8.60E-13	16.72%
		Jitter	8.60E-13	16.72%
Pointing	Beam Walk		1.29E-12	25.10%
	Image Motion		9.04E-14	1.76%
	Mask Error		5.46E-13	10.63%
SUM			5.14E-12	

Table 3.3-31. Rolled Up Time-Variable Error Budget Contributors

The largest grouped contributor to image plane contrast is beam walk caused by pointing errors. The majority of this occurs on the first five mirrors following the secondary mirror, near the Cassegrain focus. The walk is due to 0.4 mas of pointing error that remains uncompensated by the secondary mirror. (Recall that the secondary corrects up to 4 mas of rigid body pointing, but 0.4 mas is at frequencies beyond the secondary mirror control bandwidth.) The first two folds and the first off-axis parabola have 'Super Fold' and 'Super OAP' PSDs, while the cylindrical optics are about 2.5 times worse. To reduce the beam walk, we must adopt a combination of better pointing and better optical surfaces. Note that if the secondary mirror is not used in the pointing control loop, and if rigid body pointing stability is $\sigma = 4$ mas, there is 10x more beam walk on these optics, resulting in contrast of 1.3×10^{-10} (and the overall time-variable contrast going to 1.67×10^{-10}).

The single largest contrast term in the error budget is the 'Mask Error' term at the bottom of Table 3.3-31. As noted above, this term is the leakage of light that is offset by 0.3 mas with 0.3 mas random pointing error, through a mask with a 5×10^{-4} transmission error at 4 λ/D. We expect that it will be challenging to build a mask to this level of precision. The leakage falls off as the square of the pointing error, so a reduction in pointing error will relax the mask requirement.
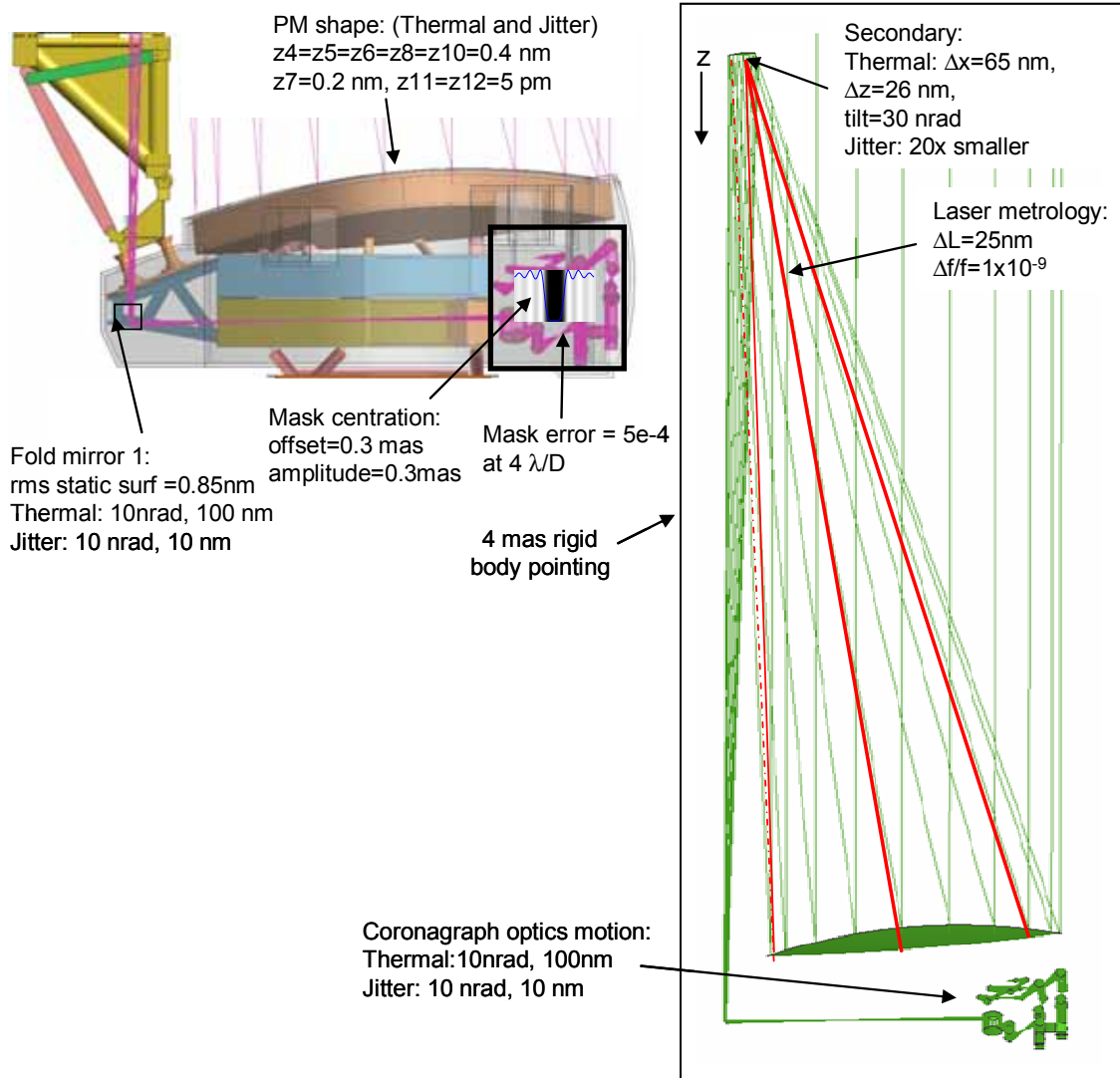
Figure 3.3-65 Summary of Major Engineering Requirements to Meet the Time-Variable Error Budget. Thermally Induced Translations Lead to Beam Walk that is Partially Ccompensated by the Secondary Mirror. Jitter is Partially Compensated by the Fine Guiding Mirror.

Bending of optics is mainly bending of the primary mirror. The 8th-order mask filters out low-order bending up through Z10 (trefoil), but higher order modes (Z11, spherical aberration and above) scatter light at much lower aberrations levels. Figure 3.3-65 [shows the requirements on the primary mirror wave front bending modes (surface deformation is 2x smaller). The major contributors are 0.2 nm RMS. of coma (contrast = 2.7×10^{-13}), and 0.005 nm of Z11 and Z12 (3.7×10^{-13} combined). We assume that bending of the secondary is 4x smaller than the primary, and all other optics bend 8x less than the primary. As aberration leakage scales as the 4th (Z3-Z10) or 2nd (Z11 and higher) power of aberration amplitude, the downstream optics play only a small role in the overall contrast. Mask errors combined with

the small primary mirror aberrations do not significantly increase the contrast. Presently we have placed identical requirements on thermal- and jitter-induced bending but will adjust this as our model fidelity improves.

Finally, structural deformation (the motion of optics relative to one another, with the PM fixed) contributes both beam walk and aberrations. The beam walk is a far worse effect, again dominated by optics M3-M7. Thermal motions of the secondary mirror are corrected to the precision of the laser metrology truss (25 nm per beam RMS); this results in ~ 20 nm of motion along the line-of-sight, and 65 nm of lateral motion. With the system stop placed at the DM, most of the beam motion occurs on the secondary mirror but it is only a small contrast contributor because the PSD has not scaled with the optic diameter relative to the downstream optics. Optics between the secondary and coronagraph mask are restricted to thermally-induced motions of 10 nrad and 100 nm in tilt and translation, respectively. These motions are partially compensated by the secondary mirror. Within the bandwidth of the fine steering mirror, the motions are 10 nrad and 10 nm. Higher frequency (uncompensated) motions are restricted to 1 nrad and 1 nm.

3.4 Baseline Observatory Performance

3.4.1 Modeling Approach

Because of physical, financial, and infrastructure constraints, *TPF-C*—more so than any previous mission of its class—will have to rely on modeling and simulation to demonstrate its performance prior to launch. The requirements for the larger, more flexible and more precise system will not be able to overcome excessive perturbations from the ground environment such as gravity, jitter and temperature. These challenges preclude the end-to-end ("e2e") system, encompassing the coupled thermal, structural, optical, control and science instrument components, to be tested on the ground as a system. The project will have to rely heavily on the use of engineering and science simulations to predict on-orbit performance requirements from the lowest level of assembly on up. For full verification of the on-orbit performance, analyses will have to incorporate all the sub-system features leading to an end-to-end simulation as depicted in Figure 3.4-1. Analyses will not be limited to predicting the end-to-end *TPF-C* system, but will be extended to simulate the full planetary signal extraction process, incorporating planetary system models as well as the complete on-orbit observational maneuvers.

At the core of this modeling approach is the need to effectively and accurately integrate the thermal, structural, and optical simulations that are inter-related by multi-physics control. This is depicted graphically in Figure 3.4-2.
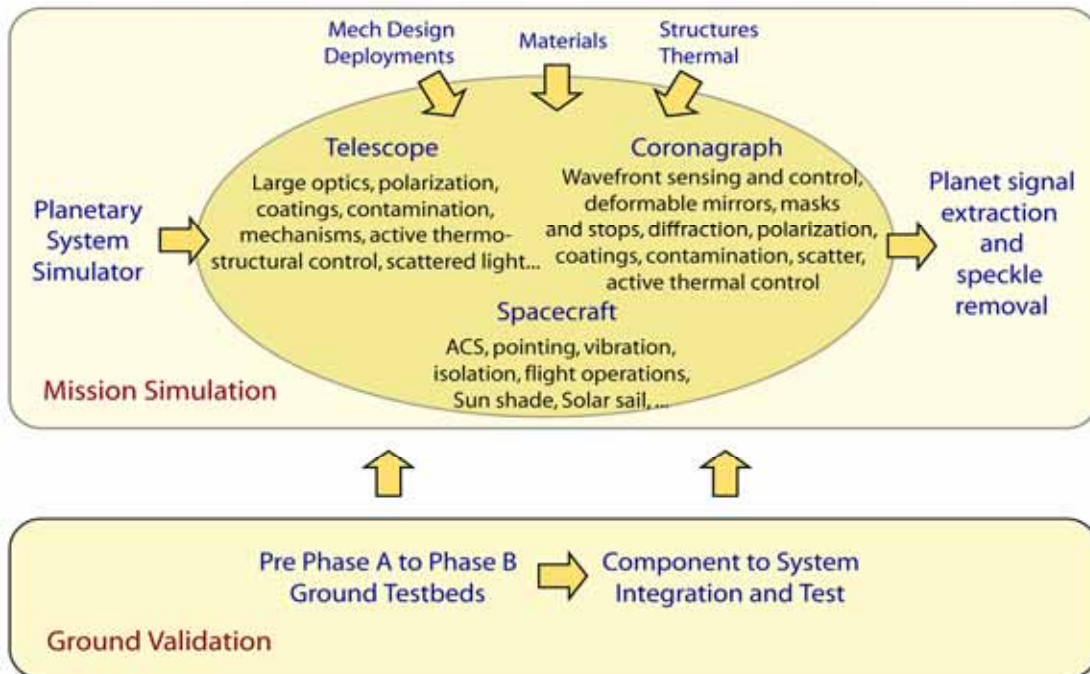
Figure 3.4-1. *TPF-C* **Modeling and Simulation Roadmap**
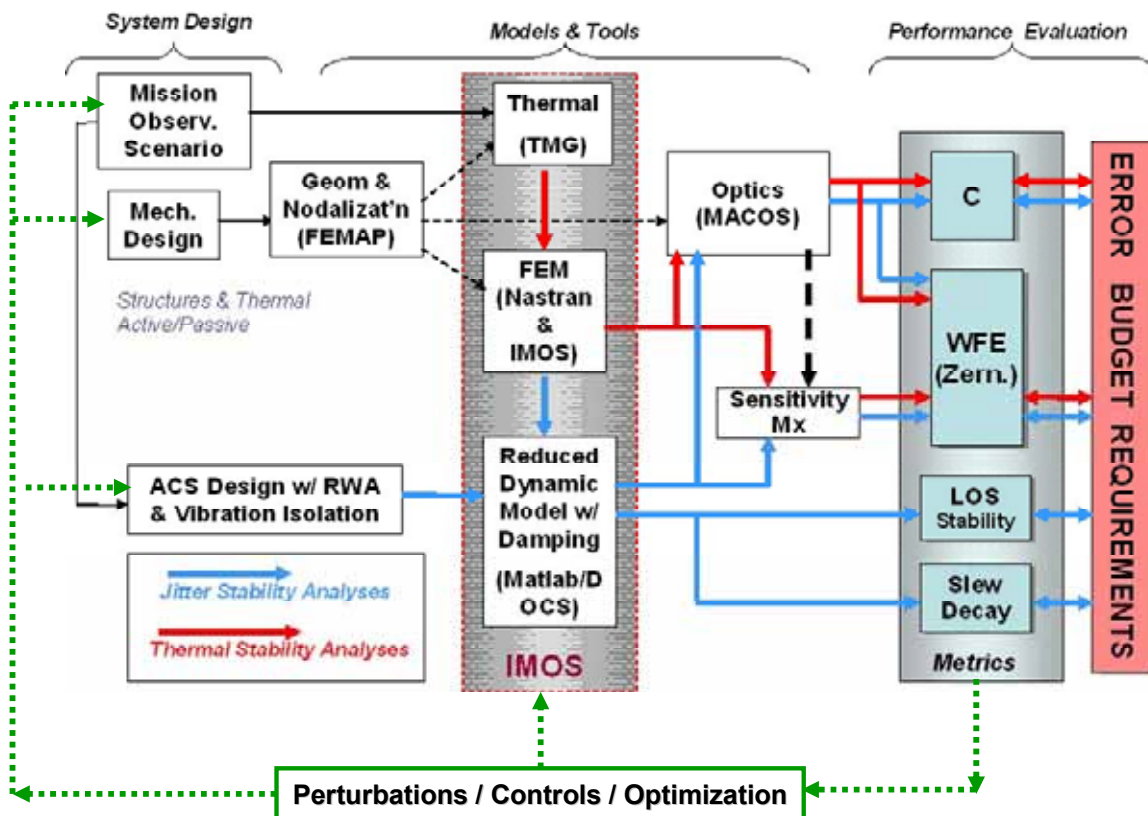
Figure 3.4-2 Integrated Simulation Process for *TPF-C*

The ability to do such analyses is pushing existing commercially available analysis tools beyond their limits of applicability in terms of precision, physics, process turn-around time, and shear physical size of the problems. Current understanding of the system indicates that the 8m class optical system needs to be as stable as picometers in wavefront and sub-milli arcsec in pointing, pushing the simulations into the realm of multi-scale physics. These extremely small requirements impose on the models a level of predictive accuracy heretofore never achieved, especially in the area of microgravity effects, material property accuracy, thermal solution convergence, optical diffraction and polarization effects, disturbance environment models and all other second order physics typically ignored. This further imposes extreme challenges on the approach to experimental validation of models, since ground testing conditions and sensor accuracy will often exceed performance levels expected on orbit. Hence to support *TPF* modeling needs, new modeling tools and analysis paradigms are proposed which emphasize computational accuracy and fully integrated simulations.

TPF has developed a technology plan that addresses the means by which models and analyses will be validated to meet the mission needs. The goal is to develop and validate on a suite of testbeds, a modeling methodology which authenticates the processes and models that will eventually be implemented for predicting the *TPF* flight performances. This will involve modeling the testbeds to the best of our ability by comparing measured and predicted performances, quantifying Modeling Uncertainty Factors (MUFs) to reflect where the agreement between the model predictions and measurements breakdown, incorporating the MUFs within the testbed requirements to validate the error budget allocation process, then incrementally implementing the same procedure to build up the flight system models starting with the flight materials characterization through to model validation of progressively higher levels of flight hardware assembly. The goal of the model validation activity will be first to identify and then to improve those aspects of the integrated models, such as thermo-mechanical physical parameters and model forms, which contribute the most to reducing errors in our final optical metrics: contrast, null depth, OPD, and WFE.

By the end of the project, the primary questions asked to the analysts will be "why do you believe the prediction?" To help achieve this challenge, a novel modeling strategy will be implemented. It is standard practice to include hardware fabrication tolerances as margins within the error budget. For *TPF* it is proposed to treat models as "software fabrication" by including additional margin in the error budget to account for modeling tolerances, *a.k.a.* modeling uncertainties. This implies that the accuracy of the prediction will be quantified by tracking contributions to the modeling errors during the project lifecycle.

Because the system performance objective now takes into account the predictability variances of the analysis, the design goal is no longer to select the design which meets the best nominal performance, but one that meets the best bounded performance including the modeling uncertainty. This means for instance that, from the view point of predicting performance and meeting the error budget, a low CTE (coefficient of thermal expansion) material having high variability and high uncertainty may not be as good a design choice as a higher CTE material with low variability and low uncertainty. Additional examples of modeling uncertainties include the nonlinear mechanics of hinges/latches, damping, etc.

Another mean of reducing modeling uncertainty is to allow on-orbit adjustments through control strategies, either active or passive. Current design features include the active deformable mirror for wavefront correction, active thermal control of the secondary mirror assembly and the aft-metering structure, active position alignment of the secondary mirror tower, and active vibration isolation of the reaction wheel disturbances. In these instances, the control errors will define the performance uncertainties. *TPF* will continue exploring, when necessary, other mitigating design solutions which implement control strategies for on-orbit adjustments. Other features that could be considered, but are not yet part of the baseline design of *TPF*, are active or passive structural damping, active wavefront control of the primary through mechanical actuators or distributed thermal control, or active wavefront control through a two-stage deformable mirror.

In effect, the *TPF* modeling challenge is now turned into validation of analysis bounds, whereby the uncertainty needs to be quantified and managed in the error budget by propagating error contributions from the lowest level of assembly on up. Another implication of this new modeling paradigm is that modeling margin allocations will be used to derive levels of accuracy required from the model validation, as well as the measurement accuracy of the test facility itself. Questions regarding what constitutes a validated model have plagued projects in the past. Through the use of the modeling error margins, we will now be able to derive rational and consistent acceptance criteria for the validation and delivery of models.

In summary, *TPF-C* has developed a modeling approach which spans the lifecycle of the project, from mission formulation and optimization, technology, design and performance verification through launch, and is later carried into the operational phases of the project once on orbit.

3.4.1.1 Engineering Models and Sensitivity Analysis

The engineering models and analyses described herein follow the process depicted previously in Figure 3.4.1-2. Based the CAD descriptions of the design, thermal, structural, optical and control models are built. The flow of the analysis starts with the definition of thermal observational environment applied to the thermal model to generate temperatures. These temperatures, either steady-state or transient, are mapped onto the structural model to generate thermal distortions. In turn these are mapped into the optical model from which Contrast and wave-front error (WFE) are predicted. similarly for jitter, reaction wheel disturbances and slew motions are applied the structural model to generate dynamic structural responses which are in turn applied to the optical model. The metrics of interest for dynamic simulations are not only Contrast and WFE, but also line of sight stability and slew settling times. As a means to rapidly assess optical performance, linear sensitivity matrices are defined which map structural motions at the optical degrees of freedom of interest to WFE and Contrast. The following describes in detail the models and analysis results.

It should be noted that for FB1 this process employed commercial off the shelf tools, which proved to be used at the limits of their capability in terms of problem size, model turnaround time and precision and accuracy. It is recognized that in the future *TPF-C* will need to deploy improved modeling tools and capabilities. These are described in the Technology Section 5.

3.4.1.1.1 Optical Performance Models

TPF-C optical performance modeling employs several models, as shown in Figure 3.4-3. Static models describe the optical performance of various algorithms and optical effects (e.g. stray light) that are independent of dynamic effects. Dynamic models describe the change in wavefront and contrast leakage that occur when the state of the system changes. Dynamic models used to compute the error budget include:

- A Fraunhofer pupil-to-image plane model is used for calculating image plane contrast as a function of wavefront components for ideal coronagraph designs as well as coronagraphs with mask transmission errors. The wavefront components are decomposed into Zernike polynomials that are orthogonal over circular and elliptical apertures. This is called the 'diffraction aberration sensitivity' model.

- A MACOS-based aberration sensitivity model determines the Zernike mode amplitudes when any optical component is moved over 6 degrees of freedom (DOF). This model is the 'Zernike sensitivity matrix.' MACOS stands for Modeling and Analysis of Controlled Optical Systems and is the JPL optical sensitivity and diffraction code.

- The Diffraction Aberration Sensitivity model computes the scattered light level throughout the image plane resulting from Zernike aberrations in the system. The model utilizes Fourier Transforms to represent Fraunhofer diffraction between the entrance aperture, the coronagraph mask, the Lyot stop, and the final image plane.

- The calculation of wave front errors and loss of contrast due to beam walk is described in detail by Noecker (2005). The beam walk δx at each surface is determined by a 'beam walk sensitivity matrix' from MACOS. The error budget is based on one location in the image plane, $4\lambda/D$ away from the star image; thus we are interested in one spatial frequency, k_x, at each mirror, the one that has 4 cycles across the beam diameter. Both k_x and the power spectral density (PSD) are computed accordingly for each mirror. The PSD function we use is flat below a turnoff spatial frequency and decreases as f^{-3} above that frequency. The PSD amplitude and turnoff frequencies are selected for the primary, secondary, small flat, and small powered optics (Table 3.4-1). The PSD of the DM is the summed PSD of the other optics in the system in front of the mask (for the critical spatial frequencies comprising the 'dark hole') since its wavefront is set to be equal and opposite to the summed wavefronts of the other optics. Its roll-off parameter of 320 cycles/m is scaled by the ratio 10 cm / 8 m from the primary mirror value of 4 cycles/m.

- The model of the laser metrology system between the primary and secondary mirrors is based on a simple linear point-to-point analysis of the metrology beams to determine beam length sensitivity to the 6 degree-of-freedom (6-DOF) motion of the secondary. We use ray tracing of the *TPF-C* telescope to determine aberration sensitivity versus motion of the secondary mirror. These two models are combined to yield the aberration sensitivity versus metrology beam lengths. The coronagraph model determines image plane contrast as a function of aberrations. We can thus de-

termine by combining the linear ray trace and coronagraph models, the image plane contrast versus metrology beam length deviations (Shaklan et al, 2004).

Static error models, as noted above, are based on Fresnel diffraction analysis and include broad-band multi-DM wave front control systems. Coronagraph mask errors include phase and amplitude transmission errors measured in the laboratory (Halverson et al., 2005), and theoretical models based on detailed electromagnetic calculations of mask transmission (for binary masks) (Lay et al, 2005). We have also modeled the expected distribution of micrometeoroid damage to the primary mirror. We are currently studying scatter from particle contamination to determine what fraction of the forward and backward scattered light can be compensated by the DMs. Standard polarization ray-tracing is used to determine polarization amplitude and phase non-uniformity in the off-axis system (Balasubramanian et al., 2005) but we have not yet performed modeling of polarization effects arising from coating non-uniformities (Breckinridge & Oppenheimer, 2004). The full scope of these models and the details of the static error budget will be the subject of future work.
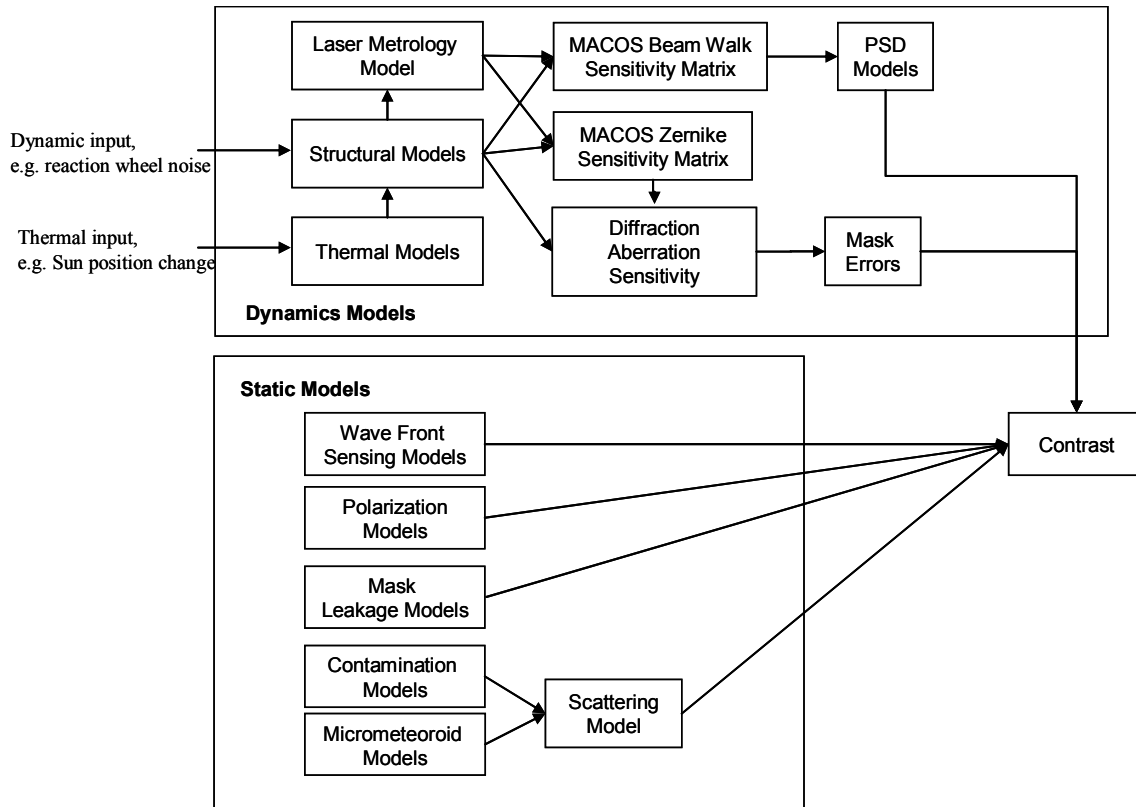
Figure 3.4-3. Models Used to Calculate Static and Dynamic Contrast.

Table 3.4-1. PSD Specifications for Optics Modeled in the Contrast Error Budget

	Primary	Secondary	Fold	Super Fold	OAP	Super OAP	Anamorphic 1	Anamorphic 2	DM
D (m)	8.02	0.83	0.1	0.1	0.1	0.1	0.23	0.10	0.10
k0 (cy/m)	4	4	10	10	10	10	10	10	320
A (m^4)	9.60E-19	9.60E-19	1.25E-20	7.58E-21	1.25E-20	1.09E-20	5E-20	7.5E-20	8.52E-22
n	3	3	3	3	3	3	3	3	3
RMS WF	8.51E-09	9.55E-09	2.15E-09	1.67E-09	2.15E-09	2.00E-09	5.24E-09	5.27E-09	1.62E-08

3.4.1.1.2 Structural Models

Because the wavefront stability requirements during long integrations are severe, careful structural analysis of the system is needed to quantify the expected physical distortions and the associated reductions in contrast performance.

Structural finite element models of FB1 were generated for the purposes of design feasibility studies. Model size and fidelity was made detailed enough to capture the first order structural effects, within an expected accuracy of generally 10 to 20 %.

The models included many idealizations: small displacement, material linearity, ideal flexures, fittings, hinges and latches. We used the small displacement assumption and modal superposition for computing displacements induced by dynamic and thermal disturbances. Material properties were assumed to remain constant during the analyses; however, coefficient of thermal expansion spatial variability within the primary mirror was accounted for in a separate study. Conservative, bounding material property values were used when possible. Flexures were not modeled in detail, but were assumed to behave in an ideal fashion. Member fittings were also not modeled in detail; however, associated masses were smeared onto the parent members. Hinges and latches were assumed to behave ideally, such that mating surfaces are rigidly locked together after deployment. Hinge and latch non-linearity will be addressed in a separate study.

We developed both a stowed (launch) configuration, and a deployed (in-orbit) configuration. The stowed configuration structural model is used for evaluating the structural vibration modal frequencies, to ensure compliance with launch vehicle requirements. The stowed model is also used to demonstrate design feasibility with respect to member stress levels, and project mass margin.

The deployed configuration model is used for characterizing the system dynamic behavior (modal frequencies and eigenvectors), which is needed for pointing and attitude control analysis: including reaction wheel jitter and slew-settle analyses. We also use the deployed configuration model for evaluating the effects of thermal disturbances on system performance. System performance is evaluated either directly, using end-to-end modeling, or indirectly, using wave-front error budget requirements, derived from contrast.

Stowed (Launch) Configuration Model

The launch configuration model (Mv4a-S) consists of the stowed observatory, as well as launch-dedicated hardware. There are launch support struts and a launch vehicle/payload interface adaptor that provide structural support during the launch phase only, and are ejected thereafter.

Deployed (In-Orbit) Configuration Model

The deployed configuration model (Mv4a-D) consists of a science payload, as well as a spacecraft with isolation system. The science payload is composed of the deployed telescope, having a 12 m separation between primary and secondary mirrors, and science instruments. Currently, we have only modeled the coronagraph instrument, but additional instruments can be added as needed.

The spacecraft sub-system is composed of the bus, propulsion tanks & thrusters, reaction wheels, sunshield & baffle, solar array, solar sail, antennae, and dynamic isolation system. The bus hardware also provides a primary load path for launch support.

Primary Mirror Model

The primary mirror, being the most critical component of the telescope, was modeled using three different levels of fidelity, based on the requirements for a particular mode of analysis. The baseline primary mirror design has an Ultra-Low-Expansion (ULE) glass substrate, using a light-weighted honeycomb sandwich type of design: having two face-sheets separated by a honeycomb core. The core structure is composed of multiple glass segments that are jointed into a monolithic structure via fusion to the face-sheets. This construction design is consistent with the current state of the art manufacturing techniques being used for large ULE mirrors. Our baseline primary mirror design has 21 segments joined together as shown in Figure 3.4-4.
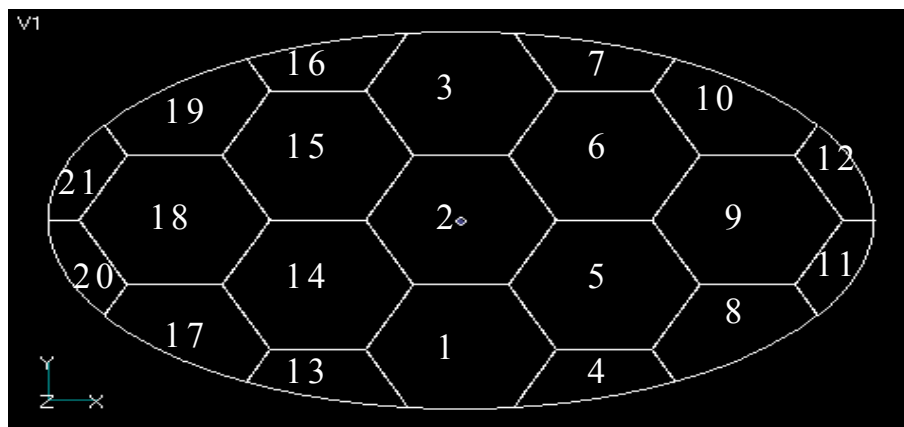
Figure 3.4-4. Primary Mirror Core Segmentation

The basic mirror segment is hexagonal in shape, measuring 1.2 meters flat-to-flat, based on what can be accommodated with standard ULE glass boules, which are approximately 1.5 meters in diameter and 0.15 m (6 inches) thick. However, there are six segments that are only partial hexagons, due the accommodation of the overall elliptical shape of the mirror. Each of the core segments has an edge wall around its perimeter.

The mirror design parameters are as follows:
- Major axis dimension = 8 m
- Minor axis dimension = 3.5 m
- Overall thickness = 0.25 m
- Front face-sheet thickness = 6 mm
- Back face-sheet thickness = 5 mm
- Honeycomb core wall & edge thickness = 1.4 mm
- Core hex-cell size (flat to flat) = 80 mm

The Low-Fidelity primary mirror model is composed of a single layer of plate elements, having the equivalent overall in-plane and bending properties of the light-weighted mirror construction. This model does not capture core cell print-through, or through-thickness com-

pliance, but it has the fewest degrees of freedom, and is used for most of the dynamic response analyses.

The Mid-Fidelity mirror model is composed of two layers of plate elements, representing the front and back face-sheets, and solid elements representing the honeycomb core structure. This model does capture through thickness compliance, and is used primarily for the thermal distortion analysis. However, this model doesn't capture core cell print-through or core segment separation effects. Comparison of Mid-Fidelity with High-Fidelity model results allows us to verify the applicability of our simplifying assumptions.

The High-Fidelity mirror model is similar to the Mid-Fidelity model, except that the honeycomb core structure of three critical segments was also modeled using plate elements. The core structure of the other segments is modeled using solid elements. Having the detailed core model for the three critical segments allows us to evaluate the extent of print-through effects, and quantify the effects of neglecting these.

Secondary Mirror Model
The secondary mirror was modeled as a simple lumped mass, because we expect design feasibility to be realistically limited by the primary mirror. Our baseline assumption is that the secondary mirror rigid-body motion can be controlled with feedback provided by a metrology system (laser truss), for response frequencies less than approximately 1Hz. The secondary mirror is mounted on a hexapod-type actuator (probably two-stage), which can control all six degrees of freedom. We expect to use the active control to compensate for thermal-induced distortions, which are generally very slow, but cannot use this system to compensate for disturbances caused by the reaction wheels, which operate above 1 Hz.

Tensioned Membranes
The sunshield and solar-sail use pre-loaded (tensioned) membranes to provide adequate stiffness to keep their shapes during operation. The stiffening effects of these tensioned membranes were incorporated directly into the models, using effective finite element properties. In particular, it was important to adequately capture the low frequency modes which might influence the attitude control performance, as well as modes which might couple with the dynamics of critical optical elements. See Section 6.1.1.2 of the Minimum Mission Report for further details.

Launch Analysis
For launch analysis, we analyzed the response to quasi-static loading using launch vehicle limit load factors, combined with equivalent acoustic pressure. We also performed a normal modes analysis to verify that our fundamental axial and lateral modes were greater than the minimum allowable frequencies specified in the launch vehicle payload planner's guide.

In-Orbit Thermal Distortion Analysis
For in-orbit thermal distortion analysis, we looked at the system performance for a 20 degree dithering observational scenario. Dithering involves the rotation of the telescope about the line-of-sight (LOS) by approximately 20 degrees, without adjustment or compensation with the deformable mirror, and is performed in an effort to reduce the effects of diffraction speckles. Ideally, the telescope diffraction speckles should remain stationary in the target im-

age, and the planet image should move with respect to the speckles. See Section 6.5.1 of the Minimum Mission Report for analysis results and further details.

CTE Variability Study

We performed a Monte-Carlo type study of the effects of primary mirror coefficient of thermal expansion (CTE) spatial variability on system performance. We assumed that the mirror would be made of high quality ULE glass, having CTE spatial variation tolerances consistent with the TDM specifications. The results of this study showed that the uniform cte assumption (30 ppb/K) is overly conservative for the focus response, but under-predicts some of the higher Zernike terms such as astigmatism and coma. Additionally, we found that having a capability of optimally placing the mirror segments, based on measured spatial maps of CTE distributions, before final mirror blank assembly, has the potential of greatly reducing the response magnitudes, allowing much enhanced system contrast performance. See Section 6.5.1.3 of the Minimum Mission Report for further details.

ULE vs. SiC Primary Mirror Trade Study

We performed a trade study comparing the performance of ULE and Silicon Carbide primary mirrors for a typical 20 degree dithering scenario, using the existing minimum-mission configuration. This simplified study assumed uniform material properties and geometry for both mirror materials. We found that the ULE mirror outperformed the Silicon Carbide mirror by a factor of approximately 400 to 600, based on wave-front error.

3.4.1.1.3 Thermal Models

In order to reveal thermally induced optical system distortions to the necessary level, *TPF* Coronagraph thermal models were built to predict transient temperature response (at high spatial resolution) at the µK level. Early in the program and focused primarily in the Minimum Mission phase, our chief thermal analyst deeply investigated a number of thermal analysis codes, including radiation packages and temperature solvers, from steady-state and transient points of view. Only after carefully studying and comparing output from these various packages did he begin to generate results.

In order to translate thermal output into WFE, it was necessary for our analyst and the structural analysts to develop efficient and accurate means of transferring thermal output into structural software, so that distortions could be mapped and resulting WFE determined.

Over a period of about a year, this process was improved to the degree that the team began to see clearly the effects of design options on transient thermo-optical performance.

By the time the FB-1 phase was concluding, the total system (TMG I-DEAS) thermal model comprised over 18,000 nodes and nearly 40,000 elements. Figure 3.4-5 shows a view of the total system model, as well as the science payload portion of that same system model.
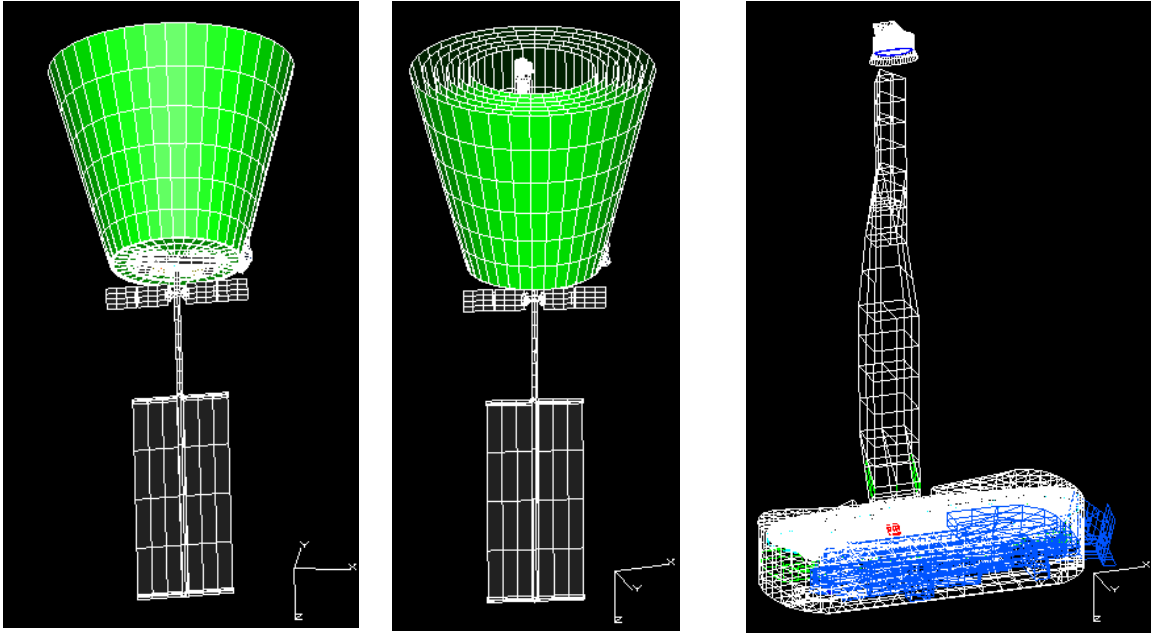
Figure 3.4-5. *TPF-C* **Thermal Model**

Because the Sun shield performance is critical to the transient response prediction domi-
nated by radiation, and because the 6-layer Sun shield is made up of mostly highly reflective
and highly specular material, a very time-consuming Monte Carlo analysis was required to
generate the Sun shield internal radiative conductances to a sufficient level of accuracy. So
these radiative couplings were generated separately and then transported into the system
transient response model.

To generate a thermal transient response, the 'Sun' is 'positioned' corresponding to its loca-
tion during the steady-state or pre-dither imaging period, and a steady-state temperature so-
lution is generated. Then, using that steady-state temperature field as initial conditions, the
'Sun' is 'moved' to the post-dither position and a transient temperature response is gener-
ated. (The reader is directed to section 3.4.2.1.2a for a discussion of a typical result from this
modeling process.)

Transient dither analyses conducted during the FB-1 design and analysis phase were limited
to cases where the mean solar flux vector is normal to the telescope line of sight, because
distortions of M1 dominate the total WFE and these cases are believed to produce the
worst-case M1 distortions. As mentioned in section 3.3.4.3, these M1 distortions arise as a
result of solar induced changes in the spatial temperature field presented to the M1 face by
the interior surfaces of the main telescope baffle. Future work will include post-dither tran-
sient system response for cases where the mean solar flux vector is pointed at the aft end of
the observatory, where changes are most likely to effect the aft metering structure and per-
haps place more stringent demands on the active portions of the thermal control system.

REFERENCES

Balasubramanian, K., et al, "Polarization compensating protective coatings for *TPF-Coronagraph* optics to control contrast degrading cross polarization leakage," Proc. SPIE Vol. 5905 (2005).

Breckinridge, J.B., & Oppenheimer, B.R., "Polarization Effects in Reflecting Coronagraphs for White-Light Applications in Astronomy," ApJ 600, pp. 1091-1098 (2004)

Halverson, P.G., et al, "Measurement of Wavefront Phase Delay and Optical Density in Apodized Coronagraphic Mask Materials," Proc. SPIE Vol. 5905 (2005).

Lay, O.P., et al, "Coronagraph Mask Tolerances for Exo-Earth Detection," Proc. SPIE Vol. 5905 (2005).

Noecker, M.C., "*TPF* Coronagraph Wavefront Changes Due to Beam Walk," Proc. SPIE Vol. 5905 (2005).

3.4.1.2 Throughput Models

The current baseline *TPF-Coronagraph* design is based on a Ritchey-Chrétien telescope with a 8mx3.5m elliptical shaped primary mirror and a 0.89x0.425m secondary mirror separated by 12m. Anamorphic beam shaping optics are employed for circularizing the beam at the 100mm diameter pupil in the back end. The coronagraph is implemented with a gray scale 8th order occulting mask at an intermediate focal plane followed by an appropriate size Lyot stop. For a detailed description of the optical system, see [sections 3.3.3.1 and 3.3.3.2].

For the baseline system bandwidth spanning 500 to 800nm, protected silver coatings are employed for all the mirrors in the system. Silver was chosen over aluminum primarily to improve the throughput and to mitigate polarization induced contrast degrading effects of aluminum [Balasubramanian *et al*, Proc. SPIE 5905-17, 2005]. Aluminum suffers from a reflectivity dip at around 800nm and consequently the throughput drops significantly when a number of surfaces are considered. Figure 3.4-7 shows the throughput losses from one to four aluminum surfaces in comparison with those of silver surfaces in Figure 3.4-6. With silver as the choice, the key components that cause throughput reduction besides the 23 front surface reflectors are the Lyot stop (34%) and occulting mask (56% at $4\lambda/D$) followed by the cube beam splitter (94.8%) for the Michelson configuration and the polarizing beam splitter (95%) that splits the two orthogonal polarizations into two separate coronagraph paths. These four components alone cause a throughput efficiency of about 17%; together with the reflection losses at the 23 reflecting surfaces and losses at other transmissive optics, the system total efficiency becomes about 9% at the inner working angle (IWA) of $4\lambda/D$. Beyond $5\lambda/D$, the average throughput ranges from about 12.3% to 13.6% for different wavelengths.

Table 3.4-2 shows the efficiencies of various components and net system throughput for 500 and 700nm wavelengths. Extending the bandwidth to either end of this spectrum presents

challenges in coating designs and transmissive optical elements. However, one may consider aluminum only for the first 3 mirrors to enable extended blue end (i.e., below ~ 450nm) for science instruments at the front end, taking a small additional loss in throughput for the coronagraph; this is a subject for further investigation taking into account all the phase and polarization effects potentially induced by aluminum in the front end curved mirrors
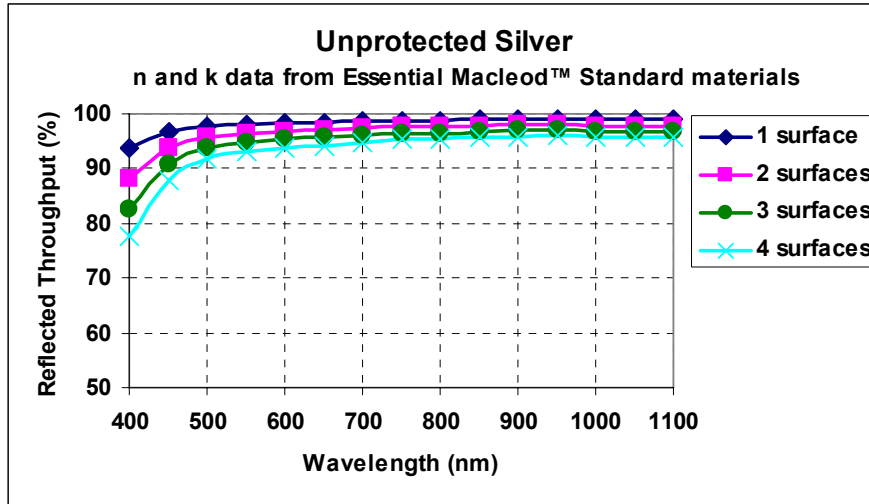
Figure 3.4-6. Reflected throughput after 1, 2, 3 and 4 <u>silver</u> surfaces at normal incidence

.
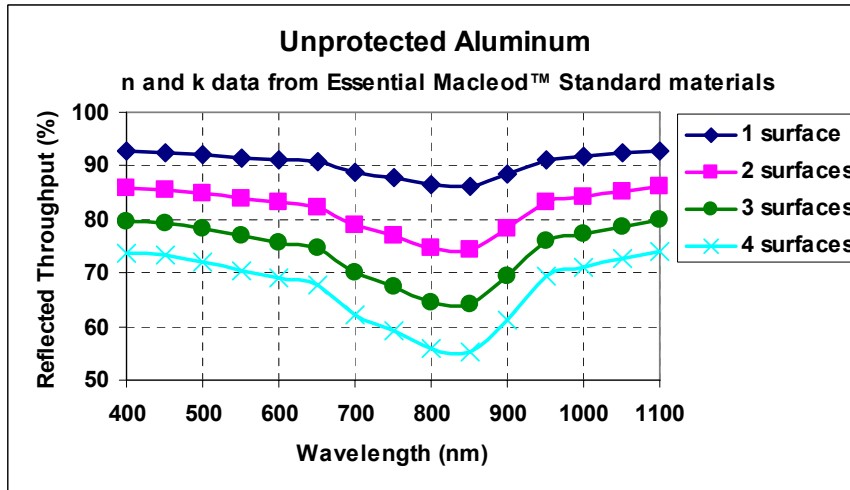
Figure 3.4-7. Reflected throughput after 1, 2, 3 and 4 <u>aluminum</u> surfaces at normal incidence

Table 3.4-2. Throughput estimate for 500nm and 700nm wavelengths at the Inner Working Angle (4λ/D) and for the region from 5λ/Δ το 40λ/D.

Equipment	Qty	Times light sees optic	500nm @ IWA		500nm (average 5λ/D to 40λ/D)		700 nm @ IWA		700 nm (average 5λ/D to 40λ/D)	
			Efficiency	Total optical efficiency	Efficiency	Total optical efficiency	Efficiency	Total optical efficiency	Efficiency	Total optical efficiency
Primary Mirror	1	1.0	0.978	0.978	0.978	0.978	0.975	0.975	0.975	0.975
Secondary Mirror	1	1.0	0.978	0.978	0.978	0.978	0.975	0.975	0.975	0.975
Super Fold Mirror 1 (Optic 3 / M 3)	1	1.0	0.978	0.978	0.978	0.978	0.975	0.975	0.975	0.975
Fold Mirror 2	1	1.0	0.978	0.978	0.978	0.978	0.975	0.975	0.975	0.975
Super OAP 1	1	1.0	0.978	0.978	0.978	0.978	0.975	0.975	0.975	0.975
Anamorphic Optic 1	1	1.0	0.978	0.978	0.978	0.978	0.975	0.975	0.975	0.975
Anamorphic Optic 2	1	1.0	0.978	0.978	0.978	0.978	0.975	0.975	0.975	0.975
Coarse DM	1	1.0	0.978	0.978	0.978	0.978	0.975	0.975	0.975	0.975
Pupil Relay 1	1	1.0	0.978	0.978	0.978	0.978	0.975	0.975	0.975	0.975
Pupil Relay 2	1	1.0	0.978	0.978	0.978	0.978	0.975	0.975	0.975	0.975
Polarizing BS[2]	2	1.0	0.950	0.903	0.950	0.903	0.950	0.903	0.950	0.903
Pol BS Anti-Ref Coating	2	2.0	0.994	0.977	0.994	0.977	0.995	0.979	0.995	0.979
Optic 13 Fold Path 1	1	1.0	0.978	0.978	0.978	0.978	0.975	0.975	0.975	0.975
Optic 13 Fold Path 2	1	1.0	0.978	0.978	0.978	0.978	0.975	0.975	0.975	0.975
Michelson BS[2]	1	1.0	0.948	0.948	0.948	0.948	0.981	0.981	0.981	0.981
Mich BS Anti-Ref Coating	1	4.0	0.994	0.977	0.994	0.977	0.995	0.979	0.995	0.979
Fine DM	1	1.0	0.978	0.978	0.978	0.978	0.975	0.975	0.975	0.975
Compensating Wedge	1	2.0	0.999	0.998	0.999	0.998	0.999	0.998	0.999	0.998
Comp Wdg Anti-Ref Coating	1	4.0	0.994	0.977	0.994	0.977	0.995	0.979	0.995	0.979
Fold/FSM	1	1.0	0.978	0.978	0.978	0.978	0.975	0.975	0.975	0.975
Pupil Relay 3	1	1.0	0.978	0.978	0.978	0.978	0.975	0.975	0.975	0.975
Pupil Relay 4	1	1.0	0.978	0.978	0.978	0.978	0.975	0.975	0.975	0.975
OAP	1	1.0	0.978	0.978	0.978	0.978	0.975	0.975	0.975	0.975
Fold	1	1.0	0.978	0.978	0.978	0.978	0.975	0.975	0.975	0.975
Occulting Mask[1,3]	1	1.0	0.560	0.560	0.790	0.790	0.560	0.560	0.790	0.790
Mask Anti-Ref Coating	1	2.0	0.994	0.989	0.994	0.989	0.995	0.990	0.995	0.990
Fold	1	1.0	0.978	0.978	0.978	0.978	0.975	0.975	0.975	0.975
Collimator	1	1.0	0.978	0.978	0.978	0.978	0.975	0.975	0.975	0.975
Fold	1	1.0	0.978	0.978	0.978	0.978	0.975	0.975	0.975	0.975
Lyot Stop	1	1.0	0.340	0.340	0.340	0.340	0.340	0.340	0.340	0.340
OAP	1	1.0	0.978	0.978	0.978	0.978	0.975	0.975	0.975	0.975
Fold	1	1.0	0.978	0.978	0.978	0.978	0.975	0.975	0.975	0.975
Total System				**0.090**		**0.127**		**0.087**		**0.123**
Total System (w/o) Lyot				**0.265**		**0.373**		**0.257**		**0.362**
Total System (w/o) Lyot and Mask				**0.473**		**0.473**		**0.459**		**0.459**

[1] Occulting mask transmission is the same over all bands due to necessary implementation of different masks for different wavelengths

[2] Optical cement not included in throughput calculations

[3] Occulting mask throughput is 0.79 over most of the dark hole. At 4 lambda/D, the throughput is approximately 56%.

Therefore a value of 0.675 was chosen as a compromise between the value at 4 lambda/D and the value over the remainder of the dark hole.

REFERENCE

Kunjithapatham Balasubramanian, Daniel J. Hoppe, Pantazis Z. Mouroulis, Luis F. Marchen, and Stuart B. Shaklan, Polarization compensating protective coatings for *TPF-Coronagraph* optics to control contrast degrading cross polarization leakage, in Techniques and Instrumentation for Detection of Exoplanets II, edited by Daniel R. Coulter, Proc. SPIE Vol 5905, PP 5905H-1 to 5905H-11, (2005).

3.4.1.3 Instrument Models

We use an idealized instrument model for our Design Reference Mission (DRM) studies and a detailed instrument model, described in Section 3.4.1.1, for engineering analysis. Here we describe the idealized DRM model. The two models have the same characteristic systematic noise floor and inner working angle (IWA).

The instrument is modeled as a coronagraph with the following characteristics: it has a systematic noise floor; it has a well-defined IWA with circular symmetry, and it has a detector with pixels that Nyquist sample the incident image and add read noise and dark current noise. The assumed throughput was described in Section 3.4.1.2.

The systematic noise floor is assumed to be $\Delta mag_o = 25$, as described in the DRM section of this report. The floor applies to the level of residual speckles in the difference image formed from two images observed at different rotation angles about the line-of-sight (the 'LOS dither'). The speckle variations are driven by thermal and vibrational changes in the state of the telescope at the two orientations. We have not modeled multiple dithers but note that multiple dithers do not necessarily reduce the noise floor because the same speckle patterns might simply reappear at the (very low) dither frequency. For the next iteration of modeling, we will set the noise floor to $\Delta mag_o = 25.5$ based on the program completeness studies described in the DRM.

The effective IWA is assumed to be an azimuthally independent radius of 65.5 mas. The instantaneous IWA using a linear 8th-order band-limited mask with IWA = 4 λ/D approaches 57 mas (along the telescope's high-resolution axis) from the star. When the pattern is dithered in 30 deg steps, and the dither pattern is rotated in 60 degree steps, the effective IWA is 65.5 mas, with more complete coverage at larger angles and worse coverage at smaller ones. For simplicity in modeling, we assume it is a step function with a hard-edge circular IWA = 65.5 mas.

The detector model comes from the published work of Brown (2005). We adopt his assumptions, summarized here. The detector quantum efficiency is 0.8. The pixels critically sample the point spread function at λ=550 nm, leading to a sharpness factor of 0.07. The dark current rate is 0.001 counts/s/pixel and the read noise is 2 counts/pixel. The detection signal-to-noise ratio calculations account for the factor of 2 increase in background variance when two images are differenced.

Our DRM studies include a simple planet characterization instrument model that scales the detection integration time by 4.5 (Heap, private communication), e.g. it takes 4.5 times as long to characterize the planet to the required spectral resolution as it takes to detect the planet in a 100 nm bandpass using 3 rotations about the line-of-sight. (The characterization time is 13.5 times longer than the single-rotation, two-dither detection time.) More advanced models have recently been provided from the instrument concept studies but have not yet been integrated to the *TPF-C* project DRM studies.

REFERENCES

Brown, R.A., "Single-Visit Photometric and Obscurational Completeness", ApJ **624**, 1010-1024 (2005).

3.4.2 FB1 Design Performance Assessment

3.4.2.1 Contrast Performance

The major result of our FB1 modeling work is that the environmental perturbations during operation appear to be controlled adequately—both thermally and dynamically—to ensure that the image plane contrast remains stable to the required levels. The current sunshade isolates the telescope and payload adequately. Active vibration control easily isolated the payload from reaction wheel vibrations. Passive vibration isolation control could be effective but with less margin and with more tuning necessary. Vibrations from mechanisms in the instruments and starlight suppression system have yet to be included, but selective damping seems feasible and promising. The next cycle will include these.

An important feature of this area is that the commercial thermal and dynamic analysis software have limitations that are becoming well understood, and the team has implemented patches where appropriate to produce believable results. For longer term production mode use, better integrated modeling tools are being developed which will provide parallel code architectures for much improved analysis cycle time, efficient inter-operability between the multi-physics analyses (thermal, structural, dynamics, controls and optics) and numerical algorithms required for high accuracy solutions.

Our analysis and modeling have shown that the combination of the baseline wave front control system and baseline optical specifications are not compatible with broad-band contrast suppression. We have learned how to modify the dual-deformable mirror wave front controller to perform over a broad band while relaxing wave front and reflectivity uniformity requirements. The new design also reduces the number of optical components in the system. These changes will be incorporated in the next design cycle.

The primary mirror assembly meets all operational requirements, but needs more consideration of fabrication, ground handling and testing accommodations. In the baseline design, launch loads are too severe around the mounting points. This complex assembly will need more development to address the full range of difficulties it will encounter. Furthermore, the FB1 observatory mass margin is too low for the capability of the chosen EELV launch vehicle. FB1 was not focused on mass optimization but significant improvements have already been identified and will be applied to the next cycle.

Within FB1, the active thermal control system was simplified to include only heaters as locally applied power within the thermal enclosure. FB1 purposely strove to only derive requirements on the active control system rather than include detailed features which were not yet well understood. The goal was to use FB1 to understand how difficult and challenging the active control system will be before addressing how it should be implemented. FB1 sensitivity analyses defined the heater location, power levels and cycles required for maintaining the observatory thermally stable. This information will be used in the next cycle to design a higher fidelity representation of the active thermal control system.

Conclusions from the FB1 design and analysis cycle, along with open trades for possible design alternatives, will guide the next design cycle toward better performance and deeper detail. The team and community have gained significant knowledge through this exercise and will continue to do so as it waits for the start of the next design iteration, FB2.

3.4.2.1.1 Contrast Stability Performance

Our overall contrast stability requirement for changes in contrast relative to a perfectly black 'dark hole' is 3.4×10^{-12}. When mixed with a static contrast floor of 5×10^{-11}, the contrast is stable to 2×10^{-11}, our requirement for SNR =5 at a contrast of 10^{-10}. Our models predict that dynamic and thermal performance meet the contrast stability requirement with margin.

3.4.2.1.1.1 Dynamics

The performance of both the active (Dewell et al., 2005) and passive isolation systems is given in Table 3.4-3. Results are shown for structural damping of 0.1% and 0.5% (see Blaurock et al, 2005). The highlighted boxes show performance categories that do not meet requirements. The bottom line of Table 3.4-3 shows that the total contrast stability performance easily meets the requirement for the active isolation system, but requires 0.5% structural damping to meet the overall requirement for the passive damping system. The active system contrast is dominated by the Line-of-Sight (LOS) offset term (which enters via assumed mask errors), thus it is not a function of damping.

Table 3.4-3. Dynamic Contrast Stability Results

	Passive 0.1%	Passive 0.5%	Active 0.1%	Active 0.5%	Contrast Req
Beam walk	7.7e-12	2.6e-12	1.2e-20	1.1e-22	1.9e-12
LOS	8.1e-17	5.7e-18	1.2e-20	1.2e-20	9e-14
LOS mask error	9.7e-14	7.4e-14	6e-14	6e-14	5.5e-13
Structural deformation	1.6e-16	3.4e-17	3.3e-26	1.8e-27	2.8e-17
SD mask error	7.9e-17	2.7e-17	5.3e-26	6e-28	1.7e-17
PM deformation	1.8e-12	6.6e-13	5.9e-21	8.9e-21	8.5e-13
PM deform. mask error	4.9e-16	1.8e-16	2.6e-24	1.3e-23	5.2e-15
Total contrast	9.5e-12	3.3e-12	6e-14	6e-14	3.4e-12

Note that many of the contrast requirements are well below 3×10^{-12}; this is related to the ability of the eighth-order coronagraph mask to reject low-order aberrations. For example, the 'Structural deformation' error is the contrast related to the appearance of low-order aberrations in the optical train as the secondary mirror and other optics jitter. The contrast would be substantially more severe if a 4th-order mask or the Visible Nuller was used because they are much less efficient at rejecting low-order aberrations. The deviations of the 8th-order mask from its ideal design lead to the 'mask error' boxes on the left side of the table. The most severe error for the active control system is the leakage of an imperfectly centered star image through a mask imperfection of a part in a thousand appearing at $4 \lambda/D$.

Table 3.4-3 shows the contrast after applying reserve factors to both the engineering parameters (e.g. motion of an optic) and the models. The FB1 error budget carries a factor of 2 reserve on all dynamic engineering terms as well as the mask leakage term, and the dynamics models carry an uncertainty factor of 3 for low order structural modes (0–20 Hz), ramping up to a 8.8 for modes above 40 Hz. Thus, if the error budget requirements are met and the models are accurate, the structural deformations will be 6–20 times smaller than the values used to calculate the contrast values in the table. For beam walk effects and mask errors, this will lead to a factor of 6–20 reduction in contrast from the values in the table. For aberrations, the effect is squared so we would see factors of 36–400 reduction in contrast.

3.4.2.1.1.2 Thermal

Changes in thermal gradients through the primary mirror and through the structure lead to both low-order deformations and beam walk that scatter light near the inner portions of the dark hole. Figure 3.4-8 shows the predicted bending modes of the primary mirror after a 30 degree roll of the telescope about the line of sight. The sun is assumed to be normally incident to the line-of-sight at angles of 195 and 225 deg (where 180 deg is along the short axis of the telescope opposite the secondary tower). This combination of angles is the most thermally sensitive roll studied to date. The simulation includes the passive isolation of the V-groove sun shield but it assumes that the temperature of the back-plane of the PM is held constant. The figure shows the requirements and two different PM cases; one is a uniform CTE ULE mirror; the other is a mirror in which each of the 23 boules has 4 layers of CTE variation, with each layer having bias, side-to-side, radial, and axial CTE variations of ~10 ppb. (See Kissil (2004) for more detail). As seen in the figure, the uniform CTE assumption is not conservative as it generally underestimates the wave front error relative to realistic variations in the CTE.

The thermal requirements are depicted by circles for each of the elliptical Zernike modes shown on the bottom of the figure. The 8th-order mask is effective at rejecting the first 10 Zernikes, but it begins to leak Z11 (spherical aberration) and higher order astigmatism and coma. As with jitter, each of the requirements carries a factor of 2 reserve; the maximum allowed contrast per aberration would still be met a factor of 2 above the requirement curve.

The thermal control system meets all the requirements including the higher-order modes. This was not the case with a 4th-order mask. With substantial margin in the lowest modes, we will rebalance the requirements in the next round of analysis to improve margin at the higher modes. We have not yet looked at sun angles incident from behind the telescope, and we have not yet analyzed the CTE variation with temperature. If needed, we can significantly improve performance with segment positioning based on CTE measurements of the actual boules.

Steady-State Dither Results
30 deg Dither (195-225)
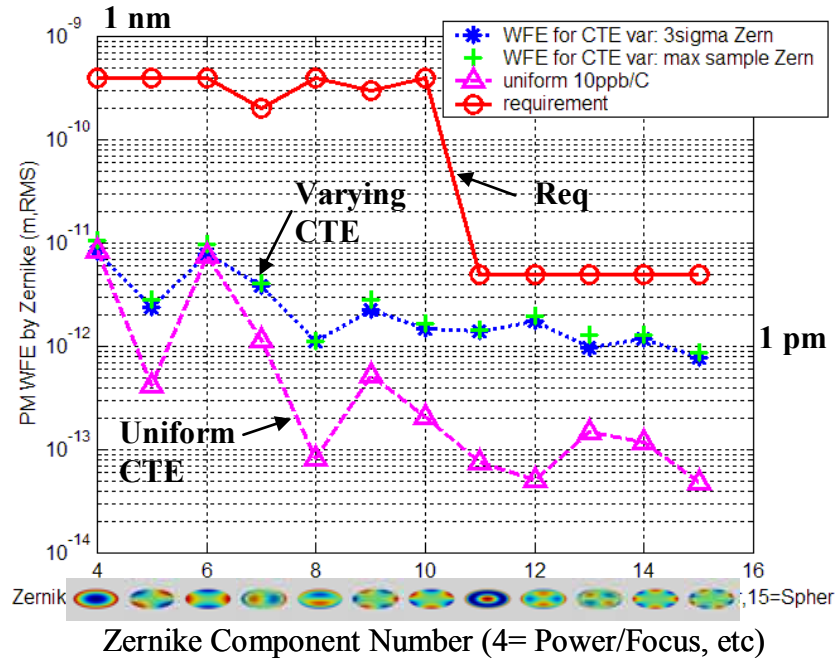
Figure 3.4-8. Thermal deformation of the Primary Mirror

We also show that, for the simple secondary tower model considered, thermal deformation of the structure (carrying optics modeled as rigid bodies except for the PM) leads to motions that do not exceed the error budget allocations. Figure 3.4-9 shows the motion of the secondary mirror and other key optics in the train after the same 30 deg dither described above. The secondary mirror moves laterally by less than 60 pm and axially less than 10 nm. In this model, we have assumed the tower holding the secondary is made entirely of graphite epoxy with CTE = 10-7. In reality, the tower has hinges, joints, and multiple materials and interfaces that will be modeled. For thermally induced motions, a 6-point metrology system measuring 6-DOF motion between the secondary and primary mirrors is in place. The metrology has a precision of < 25 nm and it is used closed-loop with the secondary-mirror active position control system.

Figure 3.4-9 shows the motions of M3, M4, and the (modeled as) rigid coronagraph box containing the SSS optics. The motions are relative to the vertex of the primary mirror. Several optics move almost as much as the allocated requirement of 10 nm; in the next round of error budgeting we will reallocate to provide margin against motion of these optics.

In conclusion, we find that the jitter requirements are met with orders of magnitude of margin using the magnetically isolated active isolation system. We have some overall margin with a passive system but require 0.5% structural damping and have only low fidelity with respect to mounting structures, hinges, and joints. The thermal requirements are also met with similar caveats. We are still early in the design phase, and there are

many possibilities to improve performance as our models grow in fidelity and present new challenges.

All Optics Motions are Relative to Primary Mirror

Motion Budget Values Derived from Beam-Walk Effects

Secondary Mirror   **M3, M4 & Coronagraph Box**
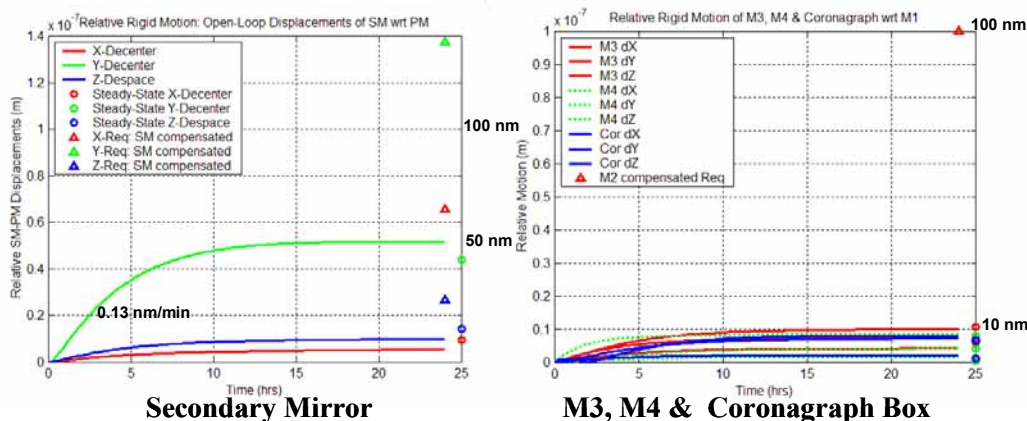
Figure 3.4-9. Motion of Optics after a 30 Deg LOS Slew

3.4.2.1.2 Static Contrast Performance

The static contrast is the residual light level in the dark hole once the wave front has been set. We require this level to be better than 10^{-10} of the incident star light for two reasons: 1) it then does not contribute significant shot noise, and 2) it reduces sensitivity to changes in the state of the system (e.g. bending of optics, jitter). Section 3.3.5 gives the relationship between static contrast and contrast stability.

Assuming a 100 nm bandwidth, it has been shown Sect. 3.3.5.1 that state-of-the-art optics provide static contrast margin up to ~ 20 cycles/aperture for the SSS and fold optics. This result is based on the sequential wave front control system and it does not account for the PSD of the optics outside the controllable spatial bandpass. Spatial frequencies beyond the control range of the DM may require a Michelson controller for broad-band compensation.

The secondary mirror requirements are relaxed compared to the smaller optics. The secondary mirror surface requirements can be relaxed relative to the assumed 4.5 nm r.m.s. surface error without reducing the useful bandpass or significantly increasing system beam walk sensitivity.

We do not yet know the low, mid, and high spatial frequency requirements on the primary mirror because the work to date has focused on compensation of phase at planes conjugate to the PM, and compensation of amplitude using sequential DMs. The sequential configuration provides wavelength-independent amplitude control. We believe (but have not proven conclusively) that the requirement on mid-spatial frequencies of the PM is set only by the dynamic range of the deformable mirrors (DMs). The low-spatial frequency requirement is set only by the range of the coarse DM, and the high-spatial frequency requirement awaits analysis of broad-band frequency mixing and compensation. We can conclude, however, that

the PM requirements are significantly relaxed compared to the current FB1 baseline (4.5 nm r.m.s. surface).

We have determined the requirements on particulate contamination but have not modeled contamination in the system. We do not know the limiting static contrast due to particles on the PM.

We have not implemented a wave front control scheme that provides timely, broadband performance. Our laboratory work has demonstrated repeatability to lambda/10000 (Green et al 2003) in monochromatic light. Many ideas for wave front sensing and control have been proposed, but none adequately address the broadband sensing requirement. This is a high priority for future work.

REFERENCES

Blaurock, C., Liu, K-C., Dewell, L., and Alexander, J., "Passive Isolator Design For Jitter Reduction in the Terrestrial Planet Finder Coronagraph", Proc. SPIE vol. 5867. (2005).

Dewell, L., Pedreiro, N., Blaurock, C., Liu, K-C., Alexander, J., Levine, M., "Precision Telescope Pointing and Spacecraft Vibration Isolation for the Terrestrial Planet Finder Coronagraph," Proc. SPIE vol. 5899 (2005).

Kissil, A. et al, "Integrated Modeling Applied to the Terrestrial Planet Finder Mission", Proc. SPIE vol. 5867, 306-317 (2005).

Kissel, A. et al, "Structural Modeling for the Terrestrial Planet Finder Mission", Proc. SPIE vol. 5528, 10-21 (2004).

Liu, K-C., Blaurock, C., Alexander, J., and Dewell, L, "Terrestrial Planet Finder Coronagraph Pointing Control System Design and Ealuation for Flight Baseline 1", Proc. SPIE vol. 5867 (2005).

Shaklan, S. B. et al, "Metrology System for the Terrestrial Planet Finder Coronagraph", Proc. SPIE vol 5528, 22-31 (2004).

3.4.2.2 System Thermal Performance

As was explained in Section 3.4.1.1, by the conclusion of the FB-1 phase of the project, the total thermal system model had been developed to the point that it became possible to predict the transient thermal response of the total system to a 30-degree dither, with the initial condition being the steady-state total system temperature field under the influence of a stable pre-dither Sun position.

The right-hand side of Figure 3.4-9 shows the total change in the primary mirror (M1) temperatures resulting from such a 30-degree dither, from 195° to 225°. This dither was found to have a significantly greater impact in comparison with the dither from 255° to 285°, because the former induces (at least for constant control heater power) a bulk temperature drop in M1. The latter move, being symmetrical about the long dimension of M1, induces no such bulk temperature drop.

Figure 3.4-10 orients the reader to the relative movement of the Sun with respect to the observatory during the dither for which the total transient response is shown. The dither is assumed to occur instantaneously, which is effectively true given the very long system response thermal time constant. In this case, all throughout the post-dither response period, the control heater nodes in the system model were supplied with a fixed power level (approximately 14 kW total, spread among various parts of the system, but concentrated mainly on heating the isostatic structures surrounding the science payload and the M1 heater plate). These heater power levels were determined during a series of initializing steady-state runs.
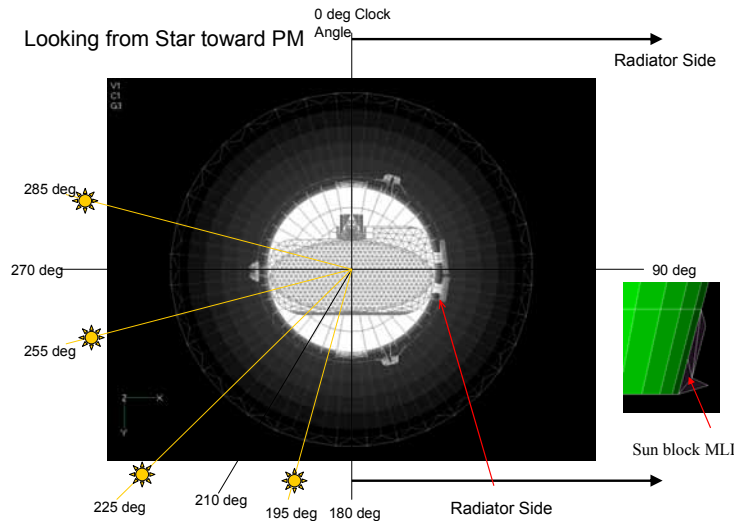
Figure 3.4-10. Clock Angle Definition for Thermal Analyses

The maximum (steady-state) change in the primary mirror (M1) temperature field from pre- to post-dither is approximately 0.23 mK (Figure 3.4-11).
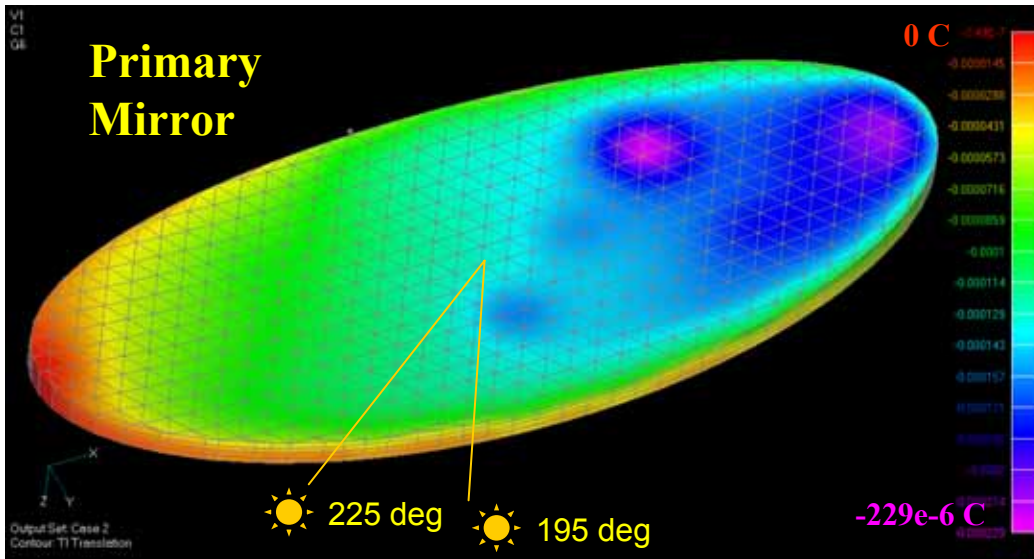
Figure 3.4-11. Delta Steady-State Temperatures on the Primary Mirror from a 30° Dither

Other parts of the system underwent more or less temperature excursions, the maximum of approximately 10 mK being the peak of a generalized overall cooling due to a decrease in the cross-sectional area presented by the isostatic thermal enclosure to the warm part of the interior of the Sun shield following the dither (Figure 3.4-12). The secondary mirror (M2) support tower saw some changes on the order of a few mK, but this change is well-within the compensatory capture range of the active M1-M2 laser metrology system.
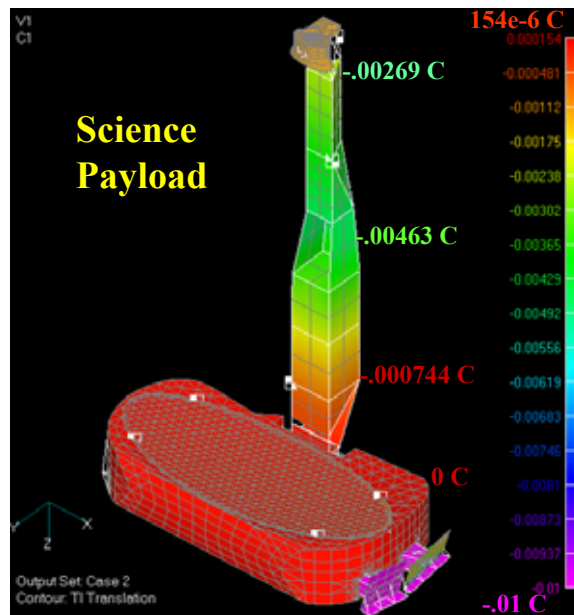
Figure 3.4-12. Delta Steady-State Temperatures on the Observatory from a 30° Dither

The corresponding time constant is approximately 6 hours, but even at the steady state condition following the dither, the resultant WFE falls within the thermal distortion contribution to the overall error budget (Figure 3.4-13).
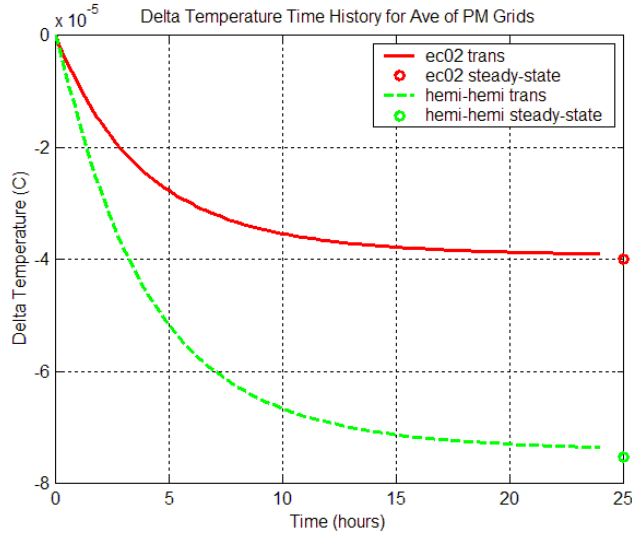
Figure 3.4-13. Delta-Temperature Time-History of Averaged Temperature of PM 30 deg Dither (195 to 225 deg)

3.4.2.3 Gravity Sag

Analysis was performed to assess the amount of deflection on the primary mirror due to gravity. The analysis was performed on the high fidelity model of the primary mirror which represents in detail each cell of the hexagonal core, the front facesheet and back facesheet of the PM, as well as the mirror mount assemblies. The high fidelity finite element model of the mirror contains over 300,000 elements and over 189,000 node points. The model is shown graphically in Figure 3.4-14.

Core model detail

Mount model detail
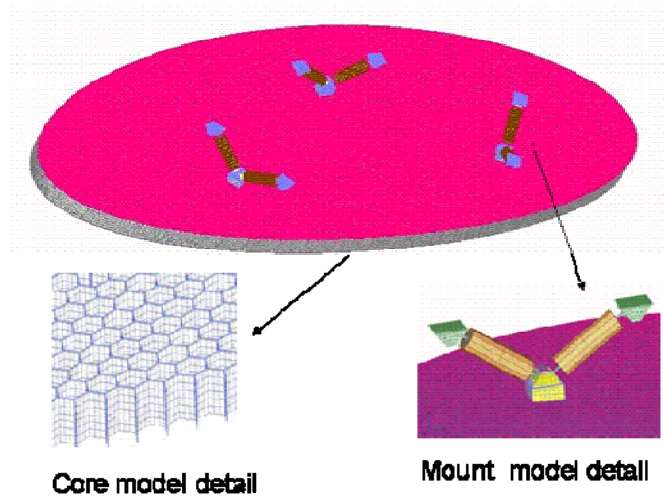
Figure 3.4-14. High Fidelity Finite Element Model of the Primary Mirror used for the Gravity Sag Analysis

The analysis applies a 1-g field onto the primary mirror assembly perpendicular to the mirror surface and predicts the resulting deflections. Although the mirror is made of ULE glass and

is 90% lightweighted, it still weighs 1065.9 kg. All dimensions chosen for this baseline design are such that it can be manufacturd by currently available processes.

The analysis shows that for the flight baseline 1 design, the maximum deflection due to 1-G load applied is 0.473 mm in the direction perpendicular to the surface of the mirror. This is the estimated deformation that will need to be off-loaded on the ground in order to perform optical measurements during ground testing. Figure 3.4-15 graphically shows the 1-G sag on the mirror where the red area is the largest deformation.
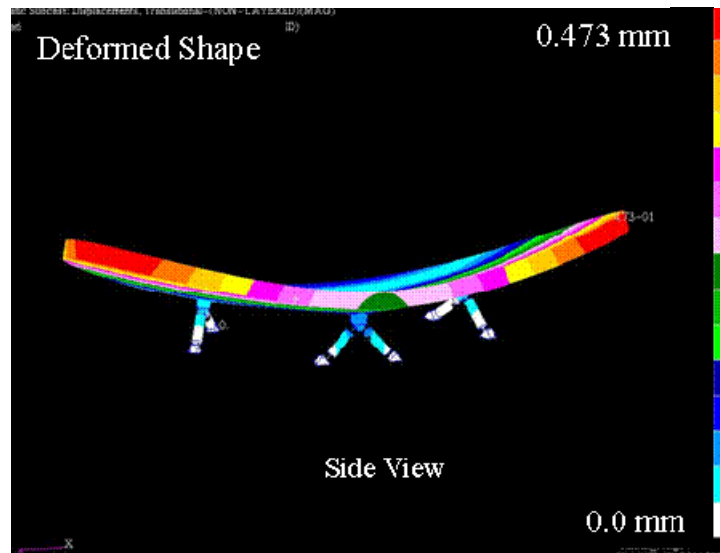
Figure 3.4-15. Gravity Sag of Primary Mirror Assembly

The optical performance due to a 1 G gravity loading was then estimated, after rigid body motion and tilt were removed from the deflections. Figure 3.4-16 shows the results graphically where the RMS OPD error is 62 μm, P-V error is 229 μm, and the errors are then decomposed into the first 15 Zernicke coefficients.
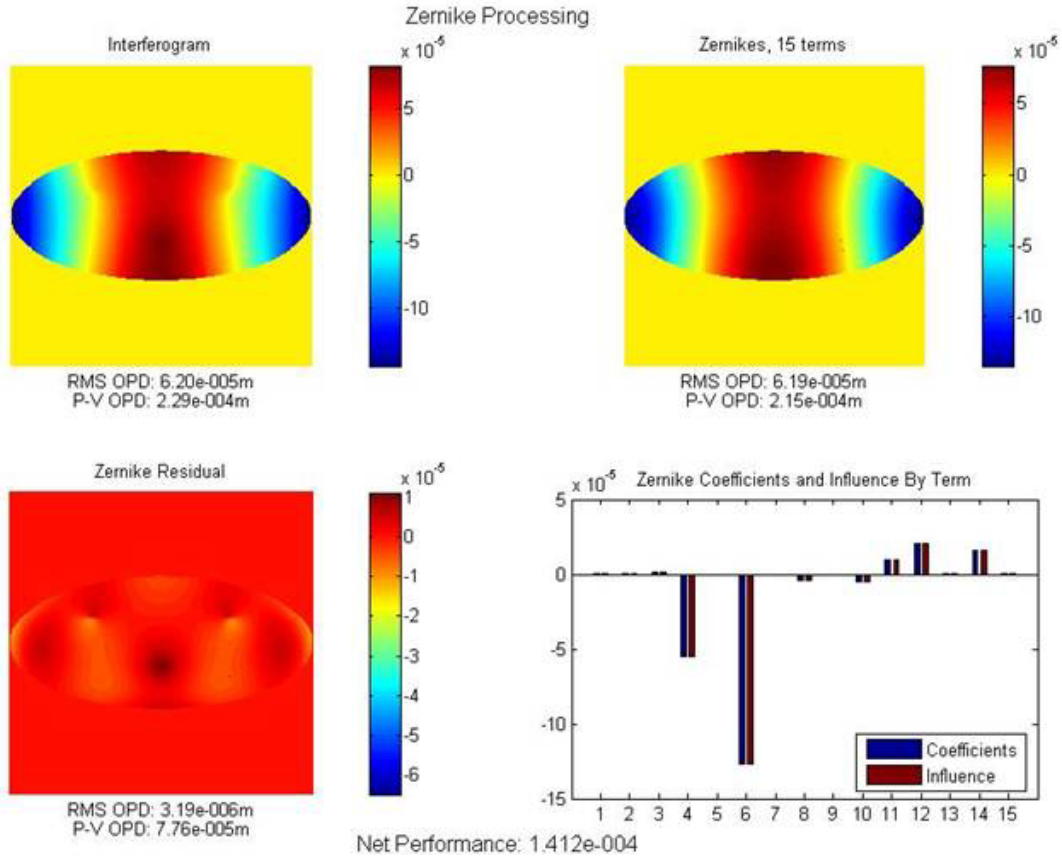
Figure 3.4-16. Optical Performance Due to 1-G Sag on the Primary Mirror

3.4.2.4 Launch Loads

The same high fidelity primary mirror model described in previously in [section 3.4.2.3] for gravity sag, was used to estimate the mirror stress due to launch. Table 3.4-4 summarized the launch loads, allowable strengths of materials and safety factors currently being used for the PM stress analysis. The quasi-static loads applied to the mirror assembly are 6 G in the X, and 5 G in the Y and Z directions. The acoustic load is 10 G in the Z direction. Recall that the mirror is folded vertically in the shroud in its launch configuration. The loads are based on the Delta IV loads manual and on acoustics analysis. The allowable strengths of the ULE and RTV bonding material are the same that are being used for the Technology Demonstration Mirror (TDM) program. All factors of safety are based on the recommendations listed in NASA-STD-5001.

The results summarized in Table 3.4-5 show that FB1 PM assembly has negative launch margin in the PM and RTV bond material, while the margin is positive in the mount hardware. The high stresses are concentrated around back facesheet and mirror core where the mounts are bonded.

Since the flight baseline 1 design for the PM showed a negative margin of safety, modifications to the design were considered. These modifications included adding stiffness to the areas behind and around the mount locations. Although the margins of safety improved they were unfortunately still negative. It was concluded that for FB2 the mounts would have to

be completely redesigned as to not apply excessive loads onto mirror during launch. Preliminary analyses looked at the advantage of using launch locks as shown in Figure 3.4-17. With 8 launch locks and an additional 414 kg of weight, this design shows positive margin of safety in the PM and the stresses in the PM were found to be less than 5.0 Mpa. This is just one option that would allow the PM to pass the launch load requirement. Other options are being evaluated.

Table 3.4-4. Allowable Strengths and Factors of Safety used for the PM Launch Loads Analysis

Component	Peak Stress (Mpa/ksi) Quasi-static Load (6 G in X, .5 G Z) Acoustic Load (10 G in Z)	Margins of Safety
PM ULE	151.8 / 22.02 66.71 / 9.68	**-.97** **-.92**
RTV	20.64 / 2.99 (tensile) 6.16/.89 (tensile)	**-.95** **-.83**
Ti bar	403.5 / 58.5 469.4 / 68.08	.59 (ultimate) / .64 (yield) .36 (ultimate) / .41 (yield)
Invar Mount	50.52 / 7.33 70.47 / 10.22	5.53 (ultimate) / 3.15 (yield) 3.68 (ultimate) / 1.97 (yield)

Table 3.4-5. Launch Stress on the FB1 PM Mirror Assembly

Materials	ULE	RTV	Invar	Titanium (Ti-6Al-4V)
Allowable	15.2 Mpa/2200 psi (tensile)	2.1 Mpa/300 psi (tensile) 1.2 Mpa/173 psi (shear)	461.9 Mpa/67 ksi (ultimate) 262.0 Mpa/38 ksi (yield) 96.5 Mpa/14 ksi (microyield, 1ppm plastic deformation)	896.3 Mpa/130 ksi (ultimate) 827.4 Mpa/120 ksi (yield)
Source for Allowable	ITT TDM baseline	ITT TDM baseline	Daniel Polis NASA code 541	MIL-HBK-5H
Factor of Safety (FS)	3.0 5.0 (analysis only)	2.0	1.4 (ultimate) 1.25 (yield)	1.4 (ultimate) 1.25 (yield)
Source for FS	NASA-STD-5001	NASA-STD-5001	NASA-STD-5001	NASA-STD-5001

Mod 5-8 includes 414 kg of additional weight and 8 launch locks.

479 x 277mm (18.8" x 10.9"). Wall thickness is 42mm (include both side facesheet)

870 x 583mm (34.2" x 22.9") (exclude 479 x 277 mm area). Core thickness is 6 mm. Both side facesheet thickness is 7.3mm.

867 x 582mm (34.1" x 22.9"). Core thickness is 4 mm. Back facesheet thickness is 5 mm. Front facesheet is 7.3 mm.
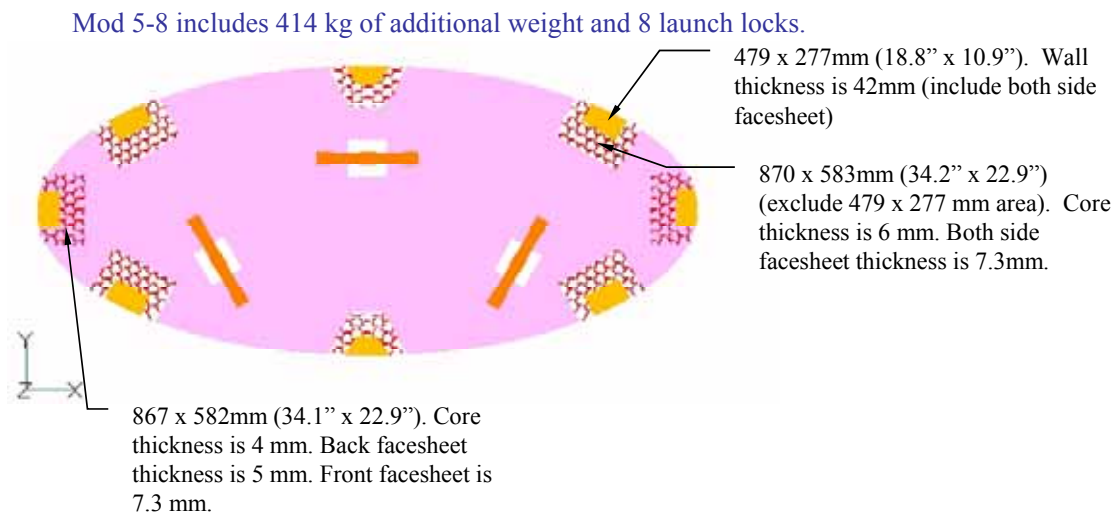
Figure 3.4-17. Modified PM Assembly with 8 Launch Locks

3.4.2.5 Stray Light

Understanding and controlling stray light due to in-field and out-of-field sources will be critical to the success of *TPF-C*. This section summarizes preliminary stray light analysis results incorporating the effects of surface imperfections and contamination of the primary and secondary mirrors of the pre-Phase-A baseline *TPF-C* architecture. The results from additional stray light analyses incorporating scatter off the interior of the baseline primary mirror baffle that is part of the larger sunshield are also discussed.

The baseline optical design for *TPF-C* incorporates an off-axis reflecting Cassegrain telescope followed by a Lyot type coronagraph. For these analyses, only the telescope front end was modeled. The telescope front end consists of an 8 meter x 3.5 meter elliptical off-axis parabola (OAP) primary mirror followed by a secondary mirror OAP 12 meters away. The focal length of the telescope is 120 meters and covers a square sensed field of view (FOV) of 3.6 arc-sec. The secondary OAP is followed by a 45 degree fold mirror, a pair of OAPs (with an aperture STOP between them), and a second fold mirror. This back end simulates how the light from the telescope would be coupled into the coronagraph, and the 3.6 arc-sec FOV is modeled at this simulated coronagraph focus. The optical model originally developed in ZEMAX was imported into TracePro for stray light analysis. TracePro was used for all stray light calculations, and some calculations were verified using Optical Surface Analysis Code (OSAC).

The following Table 3.4-6 summarizes the various cases analyzed in TracePro, including the details of the surface properties (BRDFs) applied in the various cases. The results of the analyses are summarized in a detailed report to be published separately.

Table 3.4-6. Summarization of Cases Analyzed in TracePro

ID	Tel. Type	Baffles, Field Stops	PM	SM	Inputs	Outputs
: Preliminary Runs						
1	8m Cass w/ 12m PM/SM separation	no external baffles; two back end parabolas simulate the coronagraph field stops after the telescope focus.	Perfect surface	Perfect Surface	Shoot rays IN from point sources within a few arc-sec of the target star (LOS)	Measure the Point Source Transmittance from the external point sources to the active detector area of the back end simulator.
2	same	same	TDM BRDF	TDM BRDF	same	same, but subtract out all non-scatter reflections
3	same	same	TDM BRDF + low/high Contamination	TDM BRDF + low/high Contamination	same	same; provide one set of data for low contamination, and one for high contamination
Runs with external scattering surfaces, but no specially-designed baffles						
4	same	Scattering surfaces: Inside of sunshade; outside/inside of cylindrical tower simulator; sides of PM; closeout behind PM; all "typical" black; same back end simulator	Perfect surface	Perfect Surface	Shoot rays OUT from selected points representative of the active detector area of the back end simulator	Measure the Point Source Transmittance from the active detector area of the back end simulator to the hemisphere centered on the target star (LOS)
5	same	same	TDM BRDF	TDM BRDF	same	same, but subtract out all non-scatter reflections
6	same	same	TDM BRDF + low/high Contamination	TDM BRDF + low/high Contamination	same	same; provide one set of data for low contamination, and one for high contamination
Runs with TBD external specially-designed baffles						
7	same	TBD	same	same	same	same
8	same	TBD	same	same	same	same
9	same	TBD	same	same	same	same
10	same	TBD	same	same	same	same

To simulate the surface imperfections, the Power Spectral Density (PSD) specification of the Technology Demonstration Mirror (TDM) was converted into a BRDF, which was then used as input to the TracePro optical model. Scattering calculations in TracePro are consistent with the well-known Harvey-Shack formulation of surface scatter, which is based on Kirchoff's scalar diffraction theory. Based on the PSD of the TDM mirror, a preliminary PSD specification was derived for the secondary mirror, which when converted into a BRDF is used as input for the secondary mirror surface property in the TracePro model. Once the scattered light distribution (BRDF) is specified in TracePro, it is treated as a statistical rather than a deterministic phenomenon. Generally, a brute-force scattering analysis would require tracing many millions of rays to get just a handful onto the collecting surface. TracePro allows the user to define an "important area", known as "importance sampling" when generating random scattered rays. The direction and solid angle subtended by the detector is specified as the "important area" and only rays scattered towards the "important area" are created, though their flux is scaled as if power had been scattered into the entire hemisphere. This eliminates the need for generating millions of rays and thereby controls computer run times.

For contamination, we followed the exhaustive study performed by Spyak and Wolfe and published as a series of four articles in Optical Engineering. Part 1 of the series compares measurements of scattered light due to spherical particles on mirror surfaces with predictions by Mie Theory at 0.632microns. His data demonstrated that the Mie model fit the spherical particle data quite well for both visible and infrared radiation out to 10 microns. Part II of the series showed that the same Mie-modeled data compared well against observed scatter by dust in spite of the spherical-particle assumption. These measured BDRFs served as input for various cleanliness levels in predicting in and out-of-field scatter.

From this preliminary analysis, we conclude that scattering due to contamination is comparable to scattering due to surface imperfections at reasonably achievable cleanliness level of 300.

3.4.2.6 Trades

Cassegrain Telescope vs Gregorian Telescope

A trade between a Cassegrain and Gregorian design for the telescope was investigated and is summarized in Table 3.4-7. A fixed distance of 12 m between the primary and secondary mirrors was enforced, which necessitated the Gregorian design to have a faster primary mirror surface. The resulting greater incident angles lead to higher sensitivities to alignment and polarization for the Gregorian design. On the other hand, the concave secondary mirror for the Gregorian design is generally considered easier to fabricate than the convex version for the Cassegrain design, and the internal image for the Gregorian design allows the opportunity for a field stop to help control stray light.

Table 3.4-7. Summary of Cassegrain vs. Gregorian Telescope Design Trade Study

Subject	Cassegrain	Gregorian
Alignment Sensitivity	+	
Polarization Sensitivity	+	
Fabrication Issues		+
Stray Light Rejection		+

Although the effect of stray light rejection has yet to be quantified, the team decided to continue with the Cassegrain telescope as the baseline design for *TPF*, and to continue the stray light investigations in parallel.

Primary Mirror Material Trade Study

ULE vs Sic

To gain insight into the possibility of using silicon carbide (SiC) for the PM, we simply changed material properties in the PM model, which was coded for ULE. Realizing that a SiC mirror would not look like a ULE mirror, we elected to run the comparison to quickly ascertain whether there is a significant advantage from one material to the next. ULE was shown to be the best candidate, mostly because of the difference in the dominant heat transfer mode. For SiC, internal radiation is insignificant compared with conduction, whereas for ULE internal radiation is the dominant mode of heat transfer working to equilibrate internal thermal gradients.

The mirror deformations for a typical 20 degree dithering scenario were compared for ULE and SiC. This simplified study assumed uniform material properties and geometry for both mirror materials. Because of the different heat transfer mechanism, found that the ULE mirror outperformed the Silicon Carbide mirror by a factor of approximately 400 to 600, based on wave-front error.

3.5 Verification Approach

This section addresses the formulation completed to date of an approach to *TPF-C* verification readiness for launch. Consistent with this early phase of design, we address herein not only a notional baseline verification approach but a number of options and alternatives that are within the scope of project formulation, such as for balancing system risks, working within assumed cost constraints, attempting to make use of existing test facilities, or enhancing verification fidelity. Because the pre-Phase A formulation of *TPF-C* has been halted midstream in the process, trades and analyses supporting refinement of the baseline that evaluate these options and alternatives suggested from across the *TPF-C* design team, STDT and review panels have not been completed. Similarly, many critical aspects of this notional approach to verification, such as implementation costs and verification effectiveness, have not yet been fully assessed. As addressed in Section 5.1.3, completion and refinement of this formulation of our approach to *TPF-C* verification is one aspect of further work rated amongst the highest in importance and priority at this time by the design team and STDT.

This section puts forth our strawman baseline approach to integration and test of the *TPF-C* observatory system (Section 3.5.1), drawing heavily from work conducted by the *TPF-C* verification working group as documented in Smith et al 2005 (Section 3.5.4 and attached in the appendices). Within this strawman verification approach we include our list of key assumptions, including a subset of those observatory level requirements that drive, or are driven by, the observatory verification approach. Because we assume at the outset that *TPF-C* observatory verification requires testing supported by rigorous analyses at each major level of assembly, we describe next in Section 3.5.2 our approach to validation and verification of *TPF-C* modeling and analyses, drawing heavily from the work conducted by the *TPF-C* integrated modeling working group as documented in Levine et al 2004 plus many ensuing *TPF-C* project library documents. Open issues, trades and analyses supporting continued formulation of this *TPF-C* verification strawman are identified in Section 3.5.3. Finally, key References related to the verification of *TPF-C* are listed in Section 3.5.4.

Note also that the approach to *TPF-C* verification documented herein relies heavily on many aspects of supporting *TPF-C* technology development plans now in place and in work, as documented in the *TPF-C Technology Plan*, Dooley et al 2005. Examples of this interdependence are the significant NASA investments made in fabrication of the Technology Demonstration Mirror (TDM), infusion of state of the art vibration isolation technology, as well as in nanometer precision observatory modeling and analysis techniques validation

3.5.1 Baseline System Integration and Test

We follow the verification process shown conceptually in Figure 3.5-1. This process starts with top level requirements and constraints developed and specified prior to Phase A by NASA, and controlled thereafter. Those top level considerations include science observations, mission profiles, cost and schedule, as listed in the figure examples. During the Phase A formulation timeframe, these top level considerations are flown into a baseline observatory design, error budgets with allocations, and a strawman verification flow. During this *TPF-C* pre-Phase A study we have initiated those aspects of the verification process because of the many unique and challenging aspects of *TPF-C* development and implementation. During Phase B/C/D implementation an iterative set of design cycles with corresponding test-verifiable design parameters are derived and specified, to enable the verification test and analysis flow. Examples of aspects of these activities in the process are listed in the figure. Again because of uniqueness of the *TPF-C* challenges, we have made inroads into defining critical aspects of these implementation phase activities of the verification process.
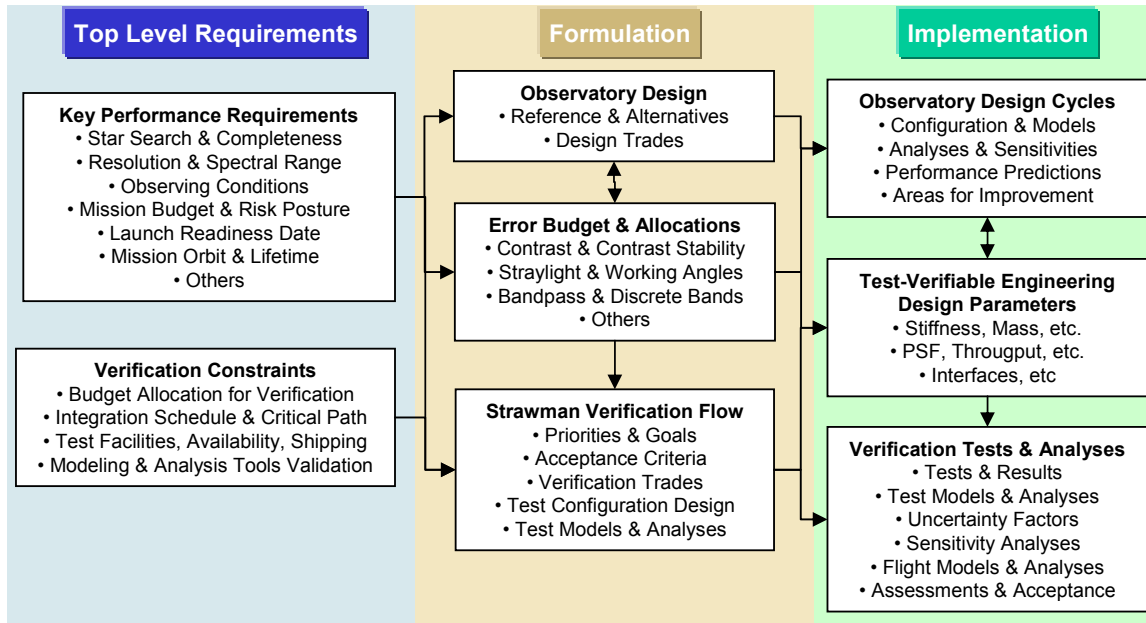
Figure 3.5-1 *TPF-C* **Verification Process, with Examples of Key Considerations**

3.5.1.1 Key Assumptions

In developing this strawman, we assumed the following observatory performance levels (Shaklan et al 2005, Ford 2004) as guidance for verification needs and approaches:

- Static contrast of $6e^{-11}$ for coherent light
- Contrast stability of $2e^{-11}$, accounting for thermal and jitter disturbances
- Instrument stray light of $1.5e^{-11}$ for incoherent light
- Inner & outer working angles of 4 and 48 times λ/D, respectively
- Bandpass of 500-800nm, with an upper end stretch goal of 1050nm
- Bandpass observed in at least three 100nm bands
- Spectral resolution of 70, with a goal of 140
- Mission lifetime of 5 yrs (10 yr goal) at L2

From these we derive measurable engineering test parameters (Smith et al 2005) as guidance for strawman test configurations, such as:

- PMA figure stability of 0.2 to 0.4 nm RMS, and <0.05 for spherical aberration
- PMA temperature stability to within about 0.001K
- Position stability of the SMA relative to the PMA of about 25nm
- Occulter mask lateral position stability of about 0.5 microns

Our general approach to flowing these key driving requirements down into engineering terms that are test verifiable at the component, subsystem and element levels of planned testing and analyses is shown in Figure 3.5-2 TPF-C Requirements Flowdown Approach (Smith et al 2005)

This starts with high level science performance requirements, and flows those down into elements, subsystems and components, as shown notionally in the figure.
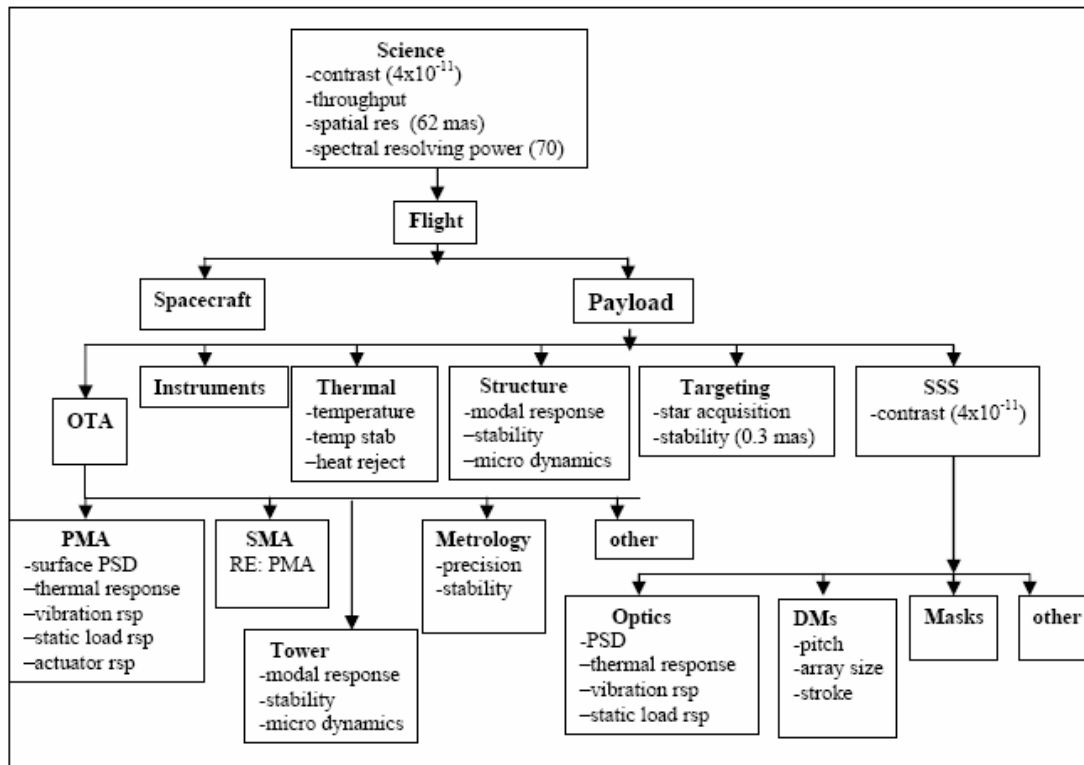
Figure 3.5-2 *TPF-C* Requirements Flowdown Approach (Smith et al 2005)

3.5.1.2 Strawman Observatory I&T Flow

Our approach uses the strawman integration and test flow shown in , developed in 2005 by the *TPF-C* verification working group, as a basis for formulating a workable approach to *TPF-C* observatory verification planning. The rationale and basis for this overall observatory I&T flow is further described in Smith et al 2005. We summarize below this overall observatory flow, and summarize in subsequent sections the most critical aspects of lower levels of assembly verification supporting this flow.

As seen from the figure, we plan an initial set of subscale experiments, used as a logical extension for supplementing existing testbed technology development work, representing planned early risk reduction activities. These subscale tests primarily validate modeling and analysis methods, enabling refinement in analytical approaches driven by comparing test results to pre- and post-test analytical predictions. We plan to iterate such subscale hardware behavior comparisons, with the goal of characterizing all significant sources of modeling uncertainty, enabling us to drive the *TPF-C* flight design such that it minimizes the effects of model uncertainties on system level performance predictions and margins. These subscale hardware tests are shown in the upper half of this figure, and include a subscale Primary Mirror Assembly (PMA), Secondary Mirror Assembly (SMA), and Optical Telescope Assembly (OTA) assemblies of the payload element, and the sunshield and the Pointing Control System (PCS) assemblies of the spacecraft element. Sizes of these subscale articles may vary

and are the subject of trades, but are roughly ¼ scale, with a goal of using full scale mechanisms in those subscale assemblies whenever possible.

Flight hardware verification is shown in the bottom half of the figure. Assuming a successful subscale methods validation program is completed early in the *TPF-C* development program to infuse all its results into the flight design in a timely fashion, then the flight hardware verification plans focus on the largest risk item, the integrated OTA, and critical aspects of its supporting lower levels of assembly. Our strawman approach relies on extensive optical testing of the standalone PMA and SMA separately, each under a variety of diagnostic test conditions. This then evolves to a combined PMA and SMA intermediate level assembly testing to ensure compatible optical performance in their closed-loop control mode, using either full aperture or sub-aperture testing (a key verification trade). Parallel tests characterize the OTA flight structure assembly, initially without any optical assemblies, primarily driven by the contrast stability requirements imposed on relative position of SMA and PMA as well as on PMA figure stability for about 2 weeks of continuous observation. These three major assemblies of the OTA (the PMA, SMA and OTA Structure) are then integrated and tested in a large vacuum chamber such as JSC Chamber A. At each of these sequential steps of assembly, models are built and analyses are conducted of the test article in its test configuration for comparison to test results, as a means to drive down uncertainties applicable to final verification of analytically predicted flight performance.

For the two critical spacecraft elements, the sunshield and PCS subsystem, we rely on advances made by other programs (such as *JWST* for their sunshield) to infuse their lessons learned, facilities and approach to ground test verification. We assume that the majority of *TPF-C* verification for these two subsystems can be accomplished by subscale article testing correlated to analyses, and by only analyses of the full scale flight hardware, using analytical modeling and analyses methods validated previously on the subscale hardware. We note that dropping or deferring for too late into the *TPF-C* program these sunshield and PCS subscale hardware test articles adds significant cost, risk and uncertainty to later verification of the flight hardware.

Major trades and supporting analyses yet to be completed, aimed at advancing this strawman formulation and anchoring its assumptions, include: full versus sub-aperture collimator testing; use of existing versus new test facilities; the scope, timing and fidelity of the subscale test articles; and completion near term of a collection of defining ground test configuration analyses, as described in Smith et al 2005 and identified in Section 3.5.3.

TPF-C Verification Plan Summary

Smith/Krim/Pitman/Ohl/Lisman/Martino

Updated 5/14/05

Methods Validation

- **Validates Methodology**
  - **Modeling, Analyses, Testing**
- **Reduces Risks**
  - **Design, Performance**
- **Quantifies Uncertainties**
  - **Persistent High-Contrast Images**

Testbeds
- TCS Testbed
- HCIT
- PCS Testbed
- TDM
- WFSC Testbed
- Metrology
- Others

Subscale PMA
- Metrology
- CTE/Thermal
- Mounts
- Thermal
- Structural
- Dynamics

Mirror Coupon

TDM-2's ?
- Reference Technology
- Alternate Technology

Material Coupons

Full Scale
Hinges & Latches

Subscale OTA Structure
- Dynamics
- Thermal
- Deployment
- Nonlinearities

S/C Vibration Isolation

SI Simulator

Subscale OTA
- Optical Tests
  - With & Without HCIT
  - TDM-1 Pathfinder
  - Subscale PMA
- Model Correlation
  - Contrast
  - Stability
    - Thermal
    - Structural
    - Dynamics
  - Straylight
- Unknown-Unknowns

Little Chamber X

Subscale Sunshield
- Model Correlation
  - Thermal
  - Dynamics
  - Structural
- Deployments
- Packing
  - Effects on Layers
  - Efficiency

Subscale PCS Simulator
- Model Correlation
  - Control Dynamics
  - Active/Passive
- Closed-loop Optical Control with SMA

Flight Hardware

- **Verifies Design**
- **Estimates Performance**
- **Quantifies Uncertainties**

8g Static in Long Axis Direction

Acoustic Loads

8g Static in Long Axis Direction

PMA
- Metrology
- CTE
- Mounts
- Thermal
- Structural
- Dynamics

SMA
- Metrology
- CTE
- Mounts
- Thermal
- Structural
- Dynamics
- Hexapod

PMA & SMA
Collimator

3m

- Collimator Size Trade
  - Full vs Partial
- Optical Train Truth Test
- Correlate with Metrology Signals
- PMA Surface Check
  - CoC Interferometer
- Prescribed PMA Disturbances
- Instrument Simulator Interface Checks

Instrument Simulator (s)

OTA Structure
- Flight (and ETU?)
- Sensitivity
  - Vertical vs Horizontal
  - Joints, Linearity
- Model Verification
  - Dynamics
  - Thermal

8m Collimator ?

S/C Simulator

S/C Vibration Isolation

OTA
JSC Chamber A

TPF-C MSF

- Model Correlation
  - Thermal
  - Structural
  - Dynamics
  - Straylight
- Sensitivities

Large Chamber Y

LEGEND

PMA = Primary Mirror Assembly	HCIT = High Contrasting Imaging Testbed	WFSC = WaveFront Sensing & Control	S/C = SpaceCraft
SMA = Secondary Mirror Assembly	TDM = Technology Demonstration Mirror	TCS = Thermal Control Subsystem	SI = Science Instrument
OTA = Optical Telescope Assembly	ETU = Engineering Test Unit	PCS = Pointing & Control Subsystem	CTE = Coefficient of Thermal Expansion

Figure 3.5-3. Strawman *TPF-C* Observatory Integration & Test Flow

3.5.1.3 Strawman OTA Element I&T Flow

We assume that the PMA will be tested and then delivered attached to the flight Aft Metering Structure (AMS) complete with any required actuators. We also assume all relevant subsystems will have been qualified and integrated into one complete SMA, including the secondary mirror (SM), the SM hexapod support mechanism, the SM thermal enclosure, the SM support tower and the laser truss. Our verification approach for the OTA starts with verifying the PMA, using the strawman approach shown in Figure 3.5-4. We consider a series of incremental steps to PMA verification, in each case repeating prior measurements after making a configuration change (such as adding flight mounts) to ensure understandable changes to PMA figure and response to prescribed and finely controlled applied loads (mechanical and thermal). The particulars in approach are subject to considerable trades, such as the key trade of whether or not to use actuators to control PM shape during ground testing, also during flight, or not at all. Regardless of this and other trades, the PMA verification test flow, requirements and assessment are guided by an iterative process of refining math models, analysis techniques and test configuration details that collectively demonstrate the maximum achievable correlation between analytical prediction of test results, thus reducing uncertainty factors imposed on flight PMA performance analytical predictions (refer to Section 3.5.2.2.).
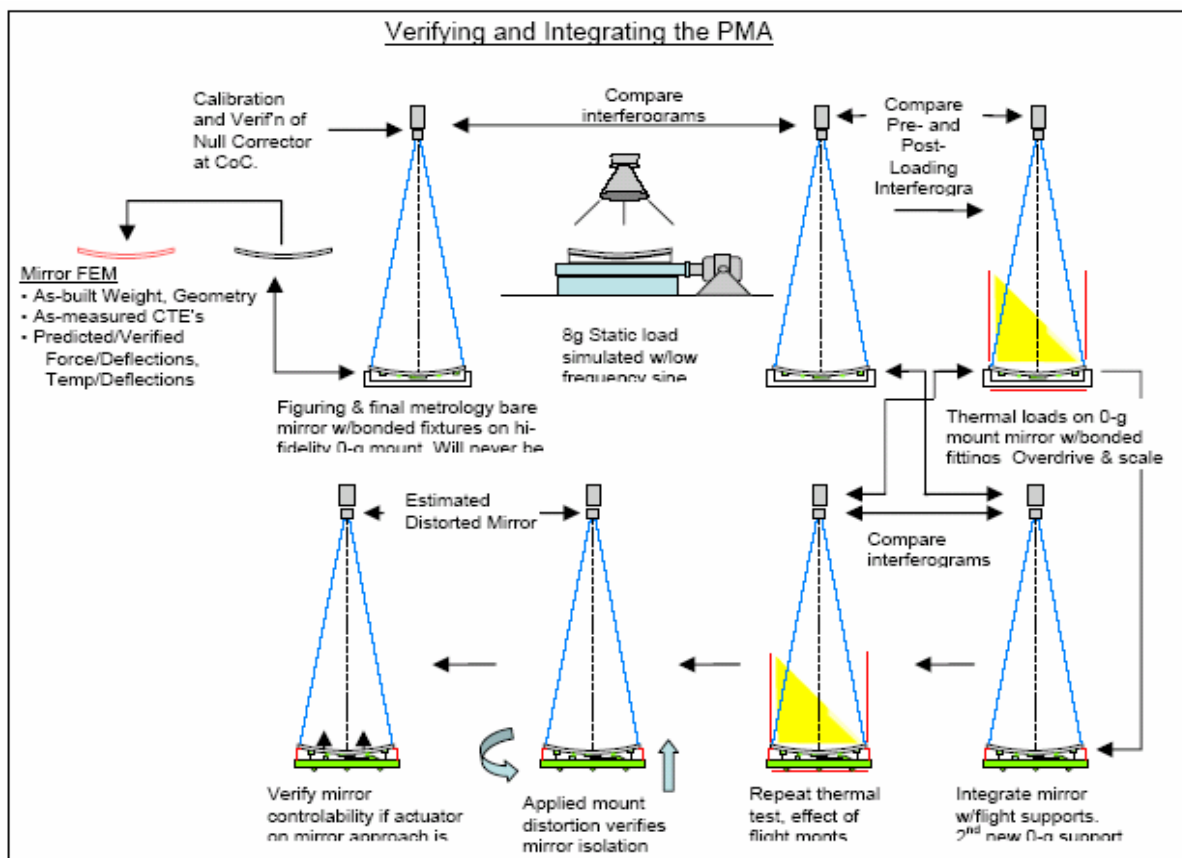
Figure 3.5-4. Strawman *TPF-C* PMA Integration & Test Flow (Smith et al 2005)

This PMA verification is complemented with parallel verification of the SMA, using the strawman approach shown in Figure 3.5-5. Similarly, these SMA verification steps incrementally change configuration and subject the SMA to know loads, evaluating change in figure and response, compared to SMA level model predictions.
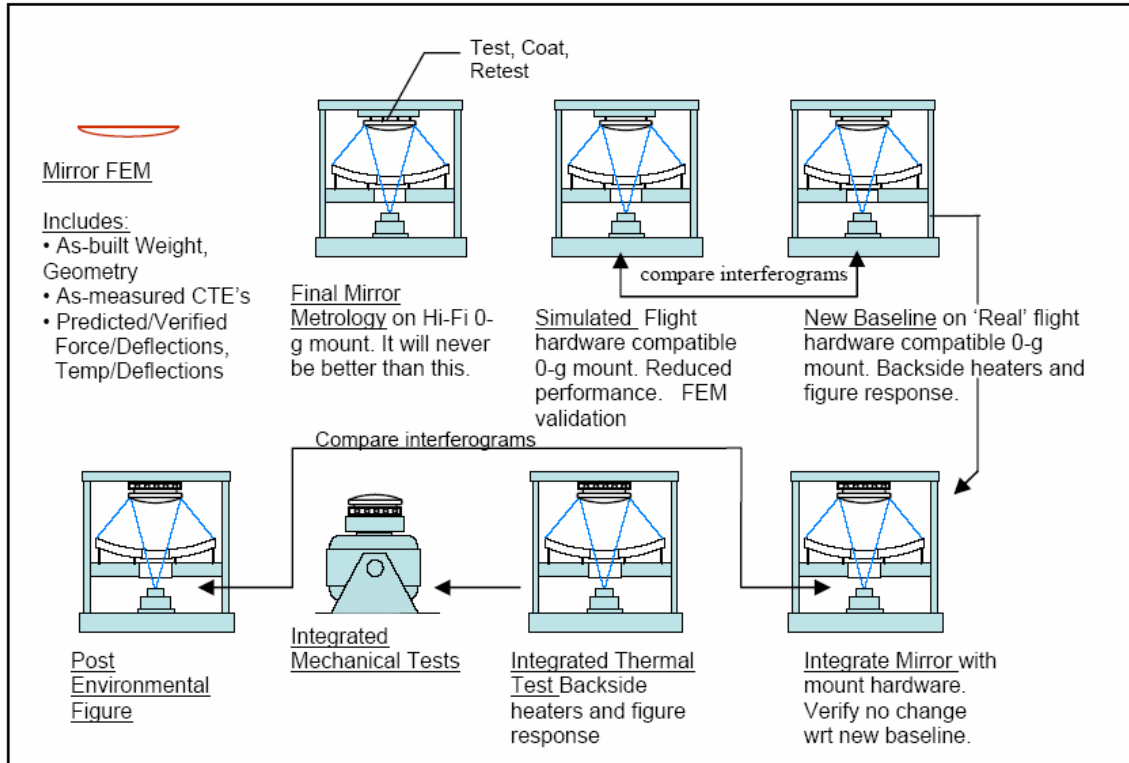
Figure 3.5-5. Strawman *TPF-C* SMA Integration & Test Flow (Smith et al 2005)

OTA level verification follows these lower level PMA and SMA levels, using the strawman approach of testing of only the OTA optics and only the OTA structure, as two separate and parallel activities, followed by testing of the same OTA flight structure with flight optics integrated. Each of these tests are summarized below and described more fully in Smith et al 2005.

The flight OTA optics are integrated by means of test fixtures and tested at first interferometrically for combined optical prescription, as shown in the left side of Figure 3.5-6, and then with a surrogate Starlight Suppression System (SSS) as shown in the right side of Figure 3.5-6. The former tests are done either full aperture or by sub-aperture stitching, a significant verification trade involving cost, risk and verification fidelity. The latter tests are done primarily to verify the critical interface of the SSS to the OTA, and could readily be repeated in a similar fashion to verify the somewhat less critical interfaces between the OTA and each science instrument. In both cases, a similar set of tests proceeded these during the OTA subscale methods validation efforts, providing a strong basis for flight OTA model and analysis correlation with test results, and an important set of critical verification milestones that would need to be satisfied prior to subsequent levels of testing.
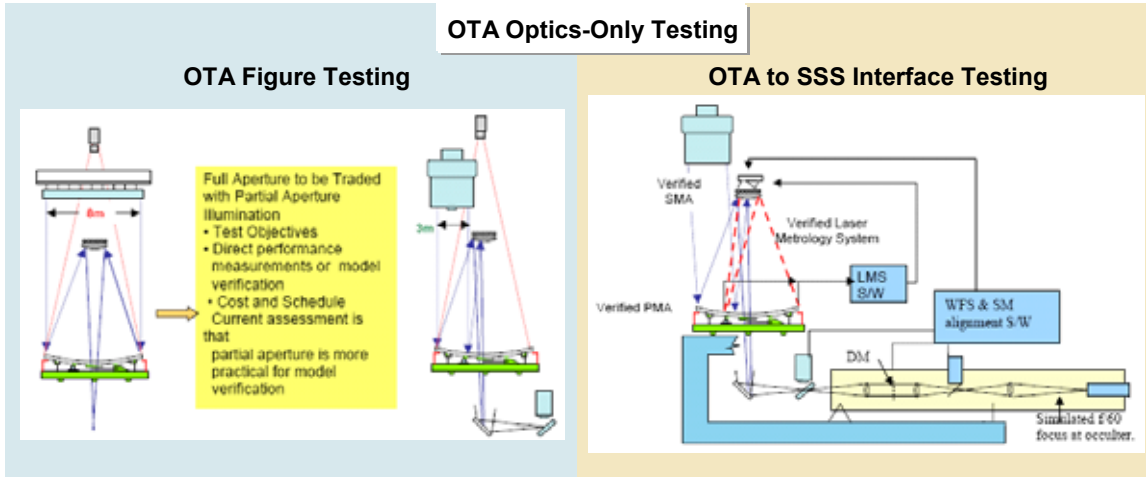
Figure 3.5-6. Strawman *TPF-C* OTA Optics-Only Testing (Smith et al 2005)

The flight OTA structure, at first without any mounted optics as shown at the left of Figure 3.5-7, is tested in parallel to the aforementioned OTA optics-only tests. This OTA structure-only assembly is tested rigorously under a variety of static and then dynamic load conditions, and most likely in both a vertical and horizontal orientation, under room temperature (RT) and thermal vacuum chamber environmental conditions. Goals include assessing response linearity at magnitudes and regimes of interest to the flight article, obtaining the maximum practical degree of predictability from models and analyses, and flagging all aspects of nonlinearity, performance sensitivity to operating conditions, and other sources of uncertainties. Upon completing these tests the OTA optics are integrated and a subset of OTA optics and structure testing is repeated, as described in Smith et al 2005.
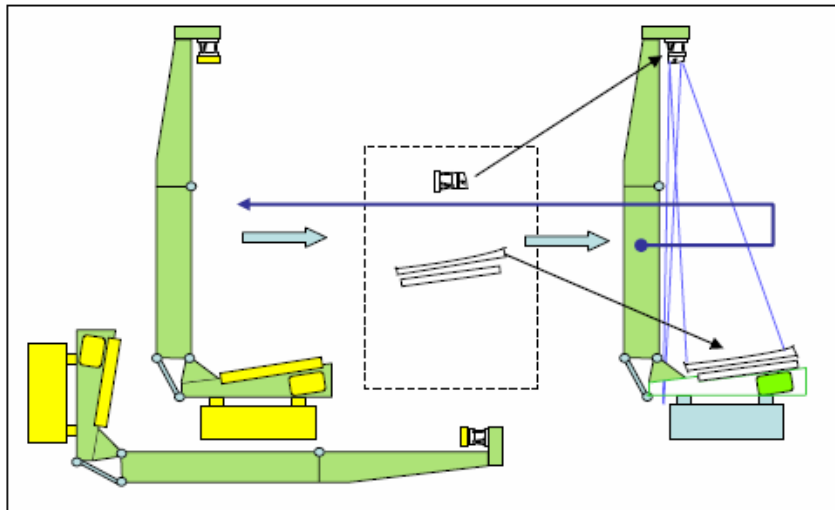
Figure 3.5-7. Strawman *TPF-C* OTA Testing (Smith et al 2005)

Our strawman approach to the final step of contemplated optical tests of the flight OTA consists of payload level performance checks under simulated on-orbit conditions and environments, to the maximum extent practical, as shown in Figure 3.5-8. This uses an optical test package to enhance

our ability to measure with sufficient fidelity the payload performance parameters needed to complete analytical verification of the flight payload (see Smith el al 2005).
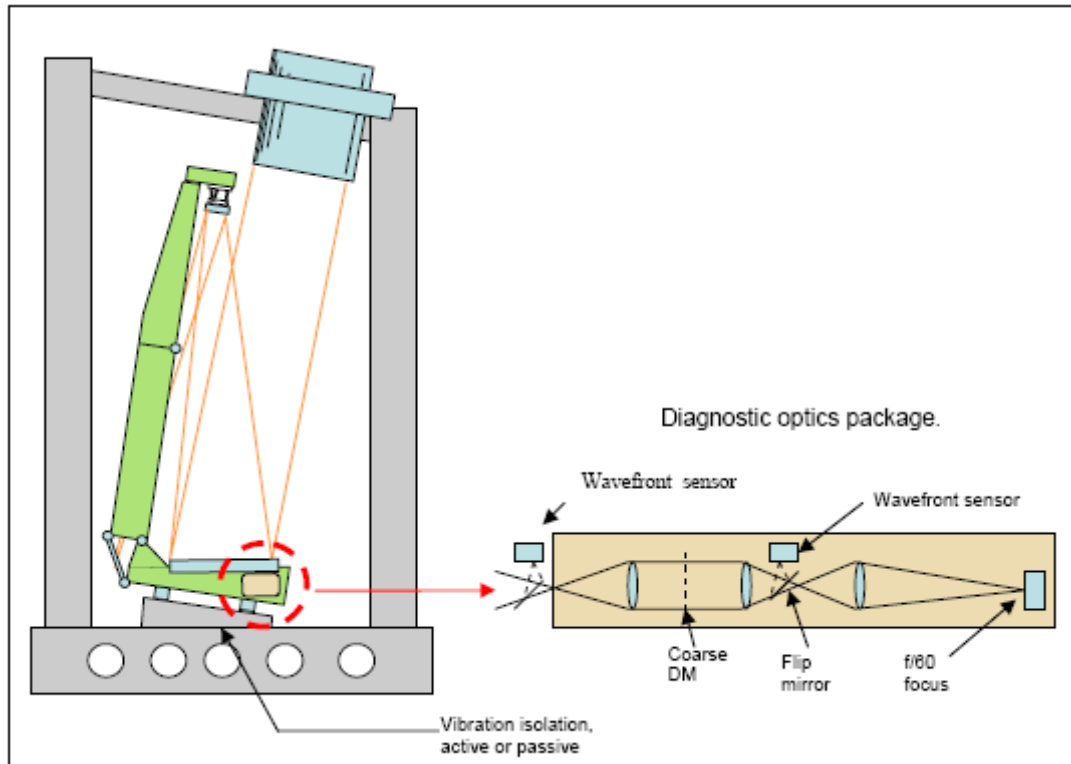
Figure 3.5-8. Strawman *TPF-C* Final Payload Optical Testing

Next, a series of confirmation tests will be completed on the integrated OTA flight assemblies. The initial of these tests will be a repeat of PMA figure testing, carried out at the PM center of curvature, with the PMA now integrated into the OTA. Initially, compensation for gravity forces will be accomplished by actuation of the primary mirror on the basis of previous measurements at the vendor. (Note: Actuation of the primary mirror is not currently part of the baseline design. However, since the maximum deformation of the PM due to gravity in the present design will exceed 600 microns, some form of gravity compensation will be required to make any useful optical measurements of telescope performance.) Interferometric measurements at the center of curvature will enable the surface errors to be minimized in the presence of gravity. The SM alignment will then be initiated with traditional metrology techniques and will be refined in a double pass interferometric measurement also illustrated in the TIM report. This measurement requires an accurately flat mirror. It is assumed that at this level of assembly, a flat of approximately 2 m in diameter will be used for sub-aperture sampling of the 8 m PM with "wavefront stitching" to evaluate the entire wavefront. Since gravity compensation procedures will not completely remove the effects of gravity on the telescope wavefront, the predicted on-orbit performance will use modeling and analysis methods validated from the subscale and full scale OTA testing. These optical measurements may require activation of the laser truss to compensate for thermal induced fluctuations in addition to vibration isolation. The clean room facility is kept at a constant temperature, with heat lamps or equivalent sources provid-

ing the desired thermal gradients indicative of OTA flight element on-orbit performance environments (such as the significant thermal gradients along the SMA tower).

The test facility will provide class 1000 conditions, at least in the neighborhood of the telescope optics, and will incorporate vibration and vibro-acoustic isolation from the chamber background. We envision leveraging to the extent practical test facilities and approaches developed for the *JWST*, modified as needed to accommodate *TPF-C*. The interferometric tests will be made in air with simultaneous phase sensing interferometers that utilize high speed data acquisition and bright sources to mitigate the effects of thermally induced turbulence. Alignment, stability, wavefront error, throughput, polarization, straylight, and other characteristics of the OTA will be tested.

3.5.1.4 Instrument Integration and Test

After the telescope has been aligned and its performance established the instruments are attached to the AMS and test verified. At the present level of maturity of *TPF-C*, these instruments include the coronagraph/spectrograph and the General Astronomical Instrument (GAI). For preliminary and perhaps continuous in-orbit alignment of the telescope we project the need for a wavefront measuring device independent of the coronagraph, such as a phase retrieval system. This can be a physically separate system sampling the image space close to but outside of the 4 arcsecond field of the coronagraph, or can be included in the WFC. Another option is to make the external surface of the coronagraph entrance aperture a mirror, flat or powered, and use it to reflect out of field stellar images to the wavefront analyzer. (This capability can also help with in-orbit alignment of the telescope-coronagraph system and with target acquisition.) The integrated components now constitute the science payload and the principal task at this point is alignment. (Note: In the present science payload configuration no optical measurements can be performed because the gravity off-loading actuators will have been removed in order to make room for the instruments. This leaves the telescope image unusable.) There will be additional measurements to be made unique to the instruments such as throughput, flat-fielding and scattered light tests. Alignment tests can be performed using a collimator with an aperture smaller than the primary mirror, say 2 m., and for these purposes can be an on-axis system.

Since radiative cooling of the instruments will not be effective in ambient conditions, suitable alternative cooling methods will have to be found that will allow the PMA/AMS to remain thermally stable. At this stage of integration detector exposure times can be short (tens of seconds) and long term temperature variations will not be important. After the ambient tests are completed the thermal enclosure surrounding the AMS and instruments will be installed. The science payload will be folded into its launch configuration and shipped to a facility in which thermal-vacuum (T/V) tests will be performed. At present, these tests are planned to be conducted in the same JSC Chamber A facility now planned for *JWST*, though that is a trade for *TPF-C*.

The primary added value of the T/V test is to evaluate the performance of the thermal control system including its capacity to handle heat generated by the instruments, and to correlate the test results with math models. The absolute temperatures attained and in particular the stabilities of those temperatures are critical to the effective performance of the science payload. The spacecraft including the sunshield is not included in these tests. The tests will require test stands providing isolation from the ambient vibration background and shrouds cooled to at least LN2 temperatures, and perhaps LHe temperatures, simulating cold space and its stability. In the absence of the sunshield an aluminized kapton sheet is substituted and configured to approximate the temperature profile com-

puted for the interior surface of the actual sunshield. Solar driven flux can be simulated by heaters. It is anticipated that thermal noise will mask variations in the PM figure arising from the simulated dither-produced variations in solar heating. Changes in the solar heating will be "overdriven" and the results correlated with math models, which have been validated by measurements on subscale optics. The effects of simulated variations in the solar heating will be measured optically using the telescope wavefront sensor and/or the coronagraph imaging detector. A collimator will provide the optical stimulus through an opening, or openings in the thermal shroud that closes out the telescope aperture. It is planned that the ambient vibration background seen by the science payload due to the T/V facility will be attenuated to levels below those introduced on-orbit by the reaction wheels. This will permit the input of disturbances simulating the dynamic effects of wheel noise such that its effect on the coronagraph performance can be evaluated.

Presently no optical end-to-end tests of the telescope-coronagraph system have been baselined. Its performance is to be inferred through use of validated models supported by rigorous testing of both the subscale test articles and lower levels of assembly. As an example, vibration isolation system between the science payload and the spacecraft will have been demonstrated in both a testbed (see Section 3.3.4.2) and the subscale PCS simulator. Analytical methods with appropriately derived uncertainty factors are then use to verify the flight system vibration isolation. Similarly, a "reduced" coronagraph test involving a small collimator or phased collimated beam array, a specially designed occulter and if needed a specially designed Lyot stop could provide data to allow correlation to previously validated sub-scale models. Considerations of coronagraph testing will be moot; however, if as noted previously, the absence of PM gravity off-loading mechanisms prevents optical testing of the science payload. The remaining value of the T/V test is to correlate thermal models such that the resulting on-orbit thermal predicts are shown to be in acceptable ranges.

3.5.1.5 System Integration and Test - Description and Requirements

After thermal vacuum testing the spacecraft will be integrated with the science payload to form the observatory, which is then subjected to EMI and EMC tests in its folded configuration. Then, the observatory is integrated to the launch support structure and subjected to environmental tests, e.g. vibration, acoustics, low level sine sweep, sine-burst and shock. The specifics of these tests and test levels will be determined during implementation. The unique character of the primary mirror will have a strong effect on the decision. Post environmental/pre-ship functional tests will be made, and pending favorable results the observatory will be shipped to the launch site.

3.5.2 Model Verification and Validation

3.5.2.1 Philosophy

Because *TPF-C* cannot be fully tested on the ground, successful implementation of the mission requires that models accurately predict sub-nanometer level performance prior to launch. This poses a major challenge on the modeling technologies which will need to demonstrate predictive accuracy to levels heretofore never achieved, representing about 2 orders of magnitude improvements over the current state-of-the-art (e.g., *SIM* is ~100pm for rigid body motions of 35cm optics, *JWST* requires ~150nm WF stability of its telescope with 6m segmented/active optics). By the end of the project, the primary questions asked to the analysts will be "why do you believe the prediction?"

To help achieve this challenge, a novel modeling strategy will be implemented on *TPF-C*. It is standard practice to include hardware fabrication tolerances as margins within the error budget. For *TPF-C* it is proposed to treat models as "soft ware fabrication" by including additional margin in the error budget to account for modeling tolerances, a.k.a modeling uncertainties. This implies that the accuracy of the prediction will be quantified by tracking contributions to the modeling errors during the project lifecycle. In effect, the *TPF-C* modeling challenge is now turned into validation of analysis bounds where the uncertainty needs to quantified and managed by the error budget.

3.5.2.2 Approach
Definitions
The NASA System Engineering Handbook SP-610S (June 1995) is clear about the distinction between verification and validation: "The purpose of verification is to ensure that the subsystems conform to what was designed and interface with each other as expected in all respects that are important: mechanical connections, effects on center of mass and products of inertia, and so on. Validation consists of ensuring that the interfaced subsystems achieve their intended results… While validation is even more important than verification, it is usually much more difficult to accomplish… Strictly speaking, validation can be accomplished only at the system level, while verification must be accomplished throughout the entire system architectural hierarchy."

When applied to models, model verification checks that the various sub-component models and discipline models are properly built and integrated, while model validation assesses how well the integrated models correlate to the measured data. This also is not to be confused with error budget validation which demonstrates that the as-built system meets the requirement goals through a combination of both analysis and tests.

Verification Plan
On *TPF-C*, model verification will be enforced by strict management of the model configuration and of the integrated modeling process. The model management approach will be described in the "Model Delivery Guideline Document" which will dictate for all disciplines the requirements for the delivery of each system and sub-system model. Examples of the issues addressed in this project document include:
- System level definitions of coordinate systems and units
- Modeling design cycles will be defined for several project maturation phases which will have prescribed levels of detail and configuration fidelity.
  - For each modeling cycle, descriptors of the sub-component models used to assemble the system models will be recorded as to keep historical information on the fidelity of the results.
  - At each modeling cycle, a review board will verify that the delivered models are consistent with the "Model Delivery Guideline" requirements.
- A *TPF-C* Material Database will maintain the project approved material properties to be used for all analyses. Among other things, the database will track the measurement uncertainty of the various properties so as to propagate these uncertainties up to system modeling tolerances.
- At each model cycle delivery, it will be required to perform baseline analyses to verify the sanity of the results. For structural analyses, examples include performing unit gravity analy-

sis checks, rigid body characteristics for stiffness matrix checks, isothermal expansion checks, etc…

- Subsystems will be pre-allocated node numbering schemes such as not to experience overlap at the time of system model integration

Validation Plan

A systematic approach will be used to identify which error budget terms, starting from Level 2 requirement levels on down. A Project "Verification and Validation matrix" will document which requirement will be validated by analysis and which will be directly validated by tests. Each of the terms validated by analysis will be linked to a metric, such as Contrast, wave-front error (WFE), line-of-sight (LOS) jitter, etc … In turn each of these metrics will be associated with a type of analysis (e.g., static errors, thermal distortion analysis, and dynamic jitter analysis), each of which requires a set of parameters and assumptions for the development of the models. Each of the models, parameters and assumptions used for validating the error budget terms, will then need to be validated themselves through a series of tests or testbed results, starting from the lowest level of assembly on up.

For now, the most critical issues for *TPF-C* models include 1) precision material property measurements, 2) validation of the physics described in the models such as mechanism frictional stability, scattered light behavior, thermal performance prediction of the sunshade and polarization propagation, and 3) validation of scaling laws used to extrapolate the results from the ground to flight environment especially for thermal gradients and jitter. Testbeds and breadboards needed to validate these most critical modeling risks are in the process of being defined, and will be described in the upcoming release of the *TPF-C* Technology Plan. As the design of *TPF-C* matures test-analysis validation of the actual hardware and instruments will be defined in more detail, culminating with the final I&T at the highest system assembly possible.

Validation of *TPF-C* models will fall in one of two categories: 1) validation of absolute predictive accuracy, such as that needed for removing 1-g sag effects from ground test data to predict on orbit performance. Initial estimates require that predictive models need to be better than 0.5%, or 1 micron, of the total 1-g sag estimate; 2) validation of relative predictive accuracy, such as that needed to predict the stability of the system between the beginning and end of 2 observational states. Although stability requirements represent some of the tightest requirements on *TPF-C*, the validation goal for relative predictive accuracy will rely mostly on understanding the sensitivities of the parameters driving the change at each state, providing relaxed expectation from the modeling capability.

In either case, the approach implemented on *TPF-C* will require that validated accuracy be bound by the modeling uncertainties. An implication of this new modeling paradigm is that modeling margin allocations will be used to derive levels of accuracy required from the model validation, as well as the measurement accuracy of the test facility itself. Questions regarding what constitutes a validated model have plagued projects in the past. Through the use of the modeling error margins, we will now be able to derive rational and consistent acceptance criteria for the validation and delivery of models.

A corollary goal for the *TPF-C* project is to develop design concepts which reduce the amount of modeling uncertainty. Examples include previous work done for *SIM* whereby Microdynamics Design Guidelines were developed for improved linearity in hinge/latch mechanisms, development of

passive/active damping devices to increase nominal structural damping levels in critical modes to deterministic values, use of materials with minimal variability in physical properties, and development of opto-thermo-mechanical architecture strategies that minimize uncertainty in component interfaces such as those found in joining/bonding of CFRP parts. Because the system performance objective now takes into account the predictability of the analysis, the design goal is no longer to select the design which meets the best nominal performance, but one that meets the best bounded performance including the modeling uncertainty. This means for instance that, from the view point of predicting performance and meeting the error budget, a low CTE material having high variability and high uncertainty may not be as good a design choice as a more uniform material having higher CTE, or that an active 1-g sag figure control approach may be favored over a passive one to reduce the modeling uncertainty margins.

3.5.3 *TPF-C* Verification Open Issues

The strawman baseline verification approach put forth herein requires further formulation and refinement, primarily by means of completing verification related trades, analyses of ground test configurations, and observatory design refinement decisions. The highest priority work items currently identified for future *TPF-C* verification risk reduction work are listed below:

- Scope, timing and fidelity of the planned subscale test articles, test configurations and supporting analytical model analyses
- Analyses of the PMA ground test configuration to estimate the effectiveness of its zero-G metrology mount
- Trade of full aperture versus sub-aperture collimator testing at the OTA level
- Analyses of the combined PMA and SMA level of assembly ground test configuration thermo-mechanical stability under achievable levels of ground test vibration isolation and planned flight assembly thermal control
- Trade of the extent of combined OTA, SSS and Instruments optical level testing
- Trade of OTA level and Observatory level test facilities, ranging widely from use of existing facilities to creation of a new dedicated facility at a launch site
- Analyses of the SSS effectiveness and stability achievable during ground testing

3.5.4 *TPF-C* Verification References

Below we list citations related to the subject of *TPF-C* verification, alphabetically ascending by primary author name.

Dooley, J. A. and P. R. Lawson, *TPF-C* Technology Plan, Version 1.1 dated 2 March 2005, JPL Publication 05-8, *TPF-C* Library File ID 14310

Ford, V. G. (2004) The Terrestrial Planet Finder Coronagraph: Technology and Mission Design Studies, *Proceedings of SPIE - Astronomical Telescope and Instrumentation 2004*, Glasgow Scotland, June 2004. Paper [5487 182]

Levine, M, G. Moore, S. A. Bassinger, A. Kissil, E. Bloemhof, S. Gunter (2004) Integrated Modeling Approach For The Terrestrial Planet Finder Mission, *Proceedings of SPIE - Astronomical Telescope and Instrumentation 2004*, Glasgow Scotland, June 2004. Paper [5497-18].

Levine, M. et al. (2004) *Terrestrial Planet Finder Coronagraph – Minimum Mission Baseline Design and Analysis*, Jet Propulsion Laboratory, Pasadena CA, Report JPL D-28535, April 28, 2004.

Shaklan, S. B., L. Marchen, J. J. Green O. P. Lay (2005) The Terrestrial Planet Finder Coronagraph Dynamics Error Budget, *Proceedings of SPIE*, 2005.

Smith, A. M., C. Blaurock, M. Krim, M. Levine, A. Liu, A. J Martino, R. Ohl, J Pitman (2005) Integration and Verification of the Terrestrial Planet Finder Coronagraphic Observatory, *Techniques and Instrumentation for Detection of Exoplanets II, D. Coulter editor, Proceedings of SPIE Vol. 5905*, pp. 59051C1-12, 2005.

4.0 Alternate Concepts and Trades

There are many alternate approaches that must be studied to further optimize the performance of TPF-C. These approaches span the entire observatory, from the nature of the primary mirror, to the type of coronagraph used, to the type of data processing required to extract the planet image. Some of these studies have been carried out to one degree or another, and are summarized in this section.

A major issue affecting the primary mirror is gravity sag during ground testing. A way must be found to support the mirror to provide a figure sufficient for testing (e.g. ~ 1 wave error). In FB1, the mirror is not actuated – it is supported kinematically and must release on-orbit into a shape that falls within range of a coarse deformable mirror located in the optical train. Alternatively, we can use a few actuators to bend the primary mirror to within the capture range of the fine DM, eliminating the need for the coarse DM. Another possibility is to provide ~1000 actuators behind the primary, eliminating the need for a fine DM as well (although at least one other fine DM is needed for control of amplitude-induced speckles). Actuating the primary has the added advantage of providing a diffraction-limited wave front to the general astrophysics instrument (GAI) – in the current design (sect 4.1.3.4) the GAI does not have a deformable mirror.

The GAI could also perform more science if the ultraviolet spectrum were available. We thus consider using Aluminum coatings on the primary mirror, secondary mirror, and fold mirror that precede the coronagraph; however we must look at the resulting impact to the coronagraph throughput in the visible and near infrared.

We also consider different primary mirror designs. Because we have baselined a linear (as opposed to elliptical) band limited coronagraph mask, the Lyot stop throughput is significantly higher if a rectangular aperture is used instead of the baselined ellipse. We consider a rectangle with rounded corners, called a 'racetrack' design and show how it impacts performance.

The baseline coronagraph includes polarizing beamsplitters, as well as non-polarizing beamsplitters in the Michelson wave front control system. It also has accommodations for band limited masks as well as shaped-pupil masks. Analysis during the FB1 cycle showed that many of the optics in the train are not required, and that superior wave front control could be accomplished with a different deformable mirror configuration.

Another important aspect of the design that is being reconsidered is the V-groove sun shield configuration. The FB1 shield has a circular cross section and allows the telescope to spin 360 degrees around its line of sight. But the shield presents several difficulties, including interference with radiator views to space and deployment challenges. We consider an approach dubbed the 'sugar scoop' because it contains incomplete conical layers leaving an opening to space for radiators and providing additional exit paths for heat as well as an improved deployment scheme.

In parallel with the FB1 project work, NASA funded industry and university Instrument Concept Study (ICS) teams to conduct studies of alternative coronagraph designs (the visible nuller interferometer, and pupil remapping combined with anti-halo apodization). They also funded the study of a candidate for the primary planet detector (CorECam), the spectrometer (CorSpec), and the general astrophysics wide-field camera. These are described below.

4.1 Science Payload

4.1.1 Alternative Concepts and Trades, with impact on Aperture size

4.1.1.1 Three-Mirror Anastigmat Telescope Design Option

4.1.1.1.1 Motivation

As discussed in other sections of this report, a wide-field survey camera (WFC) that could observe in parallel with the planet detection system could be a valuable addition to the *TPF-C* mission. The instrument concept study of this camera developed a scientific case for a diffraction limited field of view of up to 10 arcmin radius from the optical axis, where the coronagraph field of view is located. However, the current baseline telescope design is a two-mirror system that was designed to satisfy the requirements of the planet detection instrument alone. The diffraction-limited field of view of the two-mirror system is less than 95 arcsec.

An attempt to design WFCs that work with the current two-mirror design was not completely satisfactory. A field corrector was needed to control the aberrations from the two-mirror telescope; an all-reflective corrector system was prohibitively large, so glass corrector plates were used instead. The WFC system performance was adequate at longer wavelengths but was significantly degraded in the 400–700 nm wavelength range. Concerns remain about the manufacturability of the corrector plates and about the difficulty of aligning the system.

The fold mirrors needed after the secondary were quite large, approaching a one meter major diameter. This is driven mainly by the distance from the preceding pupil and the large field of view desired for the WFC. Previous coronagraph optical designs had a smaller fold mirror mainly because they did not aim for such a large field of view.

There would be significant benefits to the WFCs if the baseline telescope design could be changed to a three-mirror system. Preliminary analysis shows that it could be done with only minor detriment to the planet-detection system. Table 4.1-1 summarizes the requirements for a telescope that could support both instruments.

**Table 4.1-1. System Requirements for a Telescope
That Would Support both the Coronagraph and the Wide-Field Camera**

Parameter	Value
Primary Diameter	8×3.5 m
System F/#	17.3
Diffraction-limited FOV at $\lambda = 500$ nm	6×20 arcmin
On-axis RMS wavefront error (used by coronagraph)	< 2 nm
Coronagraph pupil diameter[a,b]	25 cm
WFC pupil diameter[a,c]	< 15 cm
Minimum primary mirror f/#	> F/1.5
Maximum number of reflections in the coronagraph beam path (telescope only)	4

[a] at an accessible location
[b] coronagraph path without wide-field pickoff mirror
[c] wide-field camera path, with wide-field pickoff mirror

4.1.1.1.2 A Preliminary Three Mirror Design

We investigated a few preliminary designs to determine if a three mirror anastigmat (TMA) could give adequate performance for the proposed wavefront control's (WFC) fields of view. We did not try to satisfy all the requirements in Table 4.1-1 due to funding and time limitations. We found that the TMA design shown in Figure 4.1-1 achieved adequate performance to support the WFC. Figure 4.1-2 shows a plot of RMS wavefront error versus field of view. The field of view in Figure 4.1-1 is 6×20 arcmin; wavefront error is 3.5 to 57nm. The primary is F/1.1 for the TMA. If this were re-turned to f/1.67, the tolerances on the secondary position would be about the same as the two-mirror system or slightly better. It is unlikely that we can loosen the secondary tolerances in the TMA design without some negative effect on the coronagraph, such as an increase in the secondary mirror size, perhaps with a partial obscuration. The prescription for the proposed TMA is defined in Table 4.1-2.
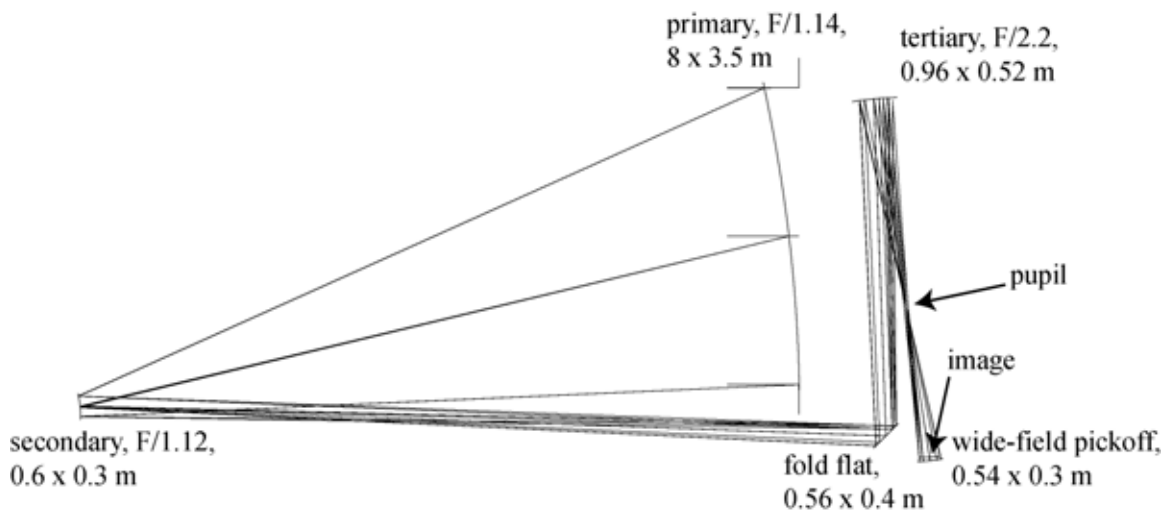
Figure 4.1-1 A TMA Design that has Adequate Performance to Support the Wide-Field Camera
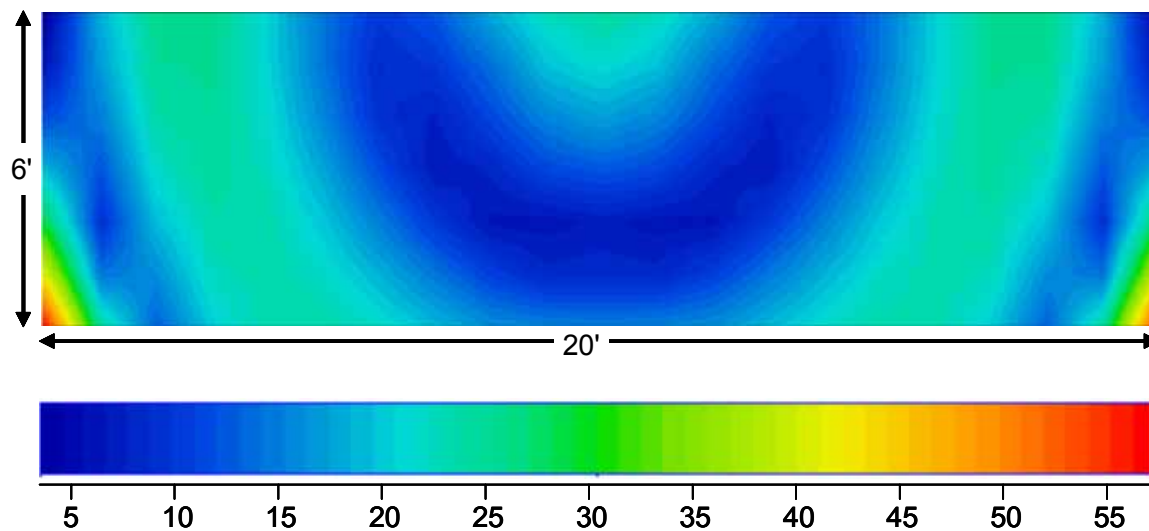
Figure 4.1-2. RMS Wavefront Error versus Field of View
(Top) for the TMA Shown in Figure 4.1-1; with Color Legend (Bottom)

This particular design example was tailored purely for the WFC, and needs some modification to accommodate the coronagraph system well. This unusually fast primary (f/1.14) is not necessary, and probably can be restored to the f/# in the coronagraph FB1 design, without sacrificing the field of view of the WFC. Ideally we would like to match the TMA output beam to the input of the existing coronagraph design with few if any additional mirrors in the coronagraph beam path. It appears feasible to add one mirror and adjust mirror curvatures and positions to prepare the beam this way.

The WFC pickoff mirror is located very near an internal image; naturally, it should be exactly at the image plane. The WFC pickoff mirror is then curved, to correct some of the field curvature and control the pupil location in the WFC. The WFC detectors would be positioned to minimize any remaining field curvature.

Table 4.1-2. Prescription of the TMA shown in Figure 4.1-1

	ROC (mm)	Thickness[a]	Conic	Off-Axis Distance
Primary	-18217.930	8481.5317	-0.9987	-2150.0
Secondary	-1342.823	9500	-1.2808	-0.0332
Fold flat	infinity	4000	–	–
Tertiary	4195.874	4300	-0.5955	265.379
WFC pickoff	-1858.880	50	–	
Image	-5533.0609	–	–	
[a] distance to the next optical surface				

Figure 4.1-1 [FB1] is a point design that serves as the existence proof of a successful design that is traceable to the science requirements. While Figure 4.1-1[FB1] has not been tested against all the science requirements, it does appear to have the sensitivity, stability, and throughput required to carry out a significant science program. It can detect Earth-like planets in other solar systems.

4.1.1.1.3 Comparison to the Baseline Two-Mirror Design

Mirror dimensions are also shown in Table 4.1-3. The total glass area did not increase significantly for the TMA, but this is mainly because the addition of the tertiary mirror was offset by the smaller secondary and fold mirror needed for the faster primary. With an f/1.67 primary, the TMA would need about the same size secondary and fold as for the two-mirror, but the TMA's additional tertiary would still be about 1 m as shown here.

Table 4.1-3. Comparison of Two-Mirror and Three-Mirror System Parameters

	Two-Mirror	TMA
Effective focal length	140.0 m	138.6 m
System F/#	17.5	17.3
Primary F/#	1.67	1.14
Distance from primary to secondary	12 m	8.48 m
Secondary decenter to reach 100 nm of on-axis wavefront error	0.25 mm	0.1 mm
Total glass area	22.7 m^2	22.9 m2
Primary size	8 × 3.5 m	8 × 3.5 m
Secondary size	0.88 × 0.38 m	0.6 × 0.3 m
Fold mirror size	0.77 × 0.61 m	0.56 × 0.4 m
Tertiary size	(N.A.)	0.96 × 0.52 m

4.1.1.1.4 Conclusions and Future Work

We hope to continue development of a three-mirror design that would satisfy all the requirements in Table 4.1-1. The TMA design above shows that requirements for the WFCs can be met with a three-mirror system. A solution that can satisfy all the requirements seems possible.

Future Work:
- Continue development of a TMA design.
- Design Offner-style reflective relays for the proposed WFCs.
- Further assess the impacts on the coronagraph instrument design.
- Outline packaging, alignment, and manufacturing strategies.

4.1.1.2 Existing Coronagraph Designs and Potential Alternatives to the Baseline Coronagraph

Table 4.1-4 lists all coronagraphs known to us to theoretically achieve a 10^{10} PSF contrast within 5 λ/D of the central source. Although several of these designs are clearly unsuitable for TPF, this table shows that 5 new coronagraph designs were proposed in 2005 alone. In the last few years there has been a strong interest in the scientific community to directly image exoplanets and therefore to develop efficient coronagraphs.

The coronagraph adopted for TPF-C baseline is shown in Table 4.1-4 in yellow. Many of the coronagraphs listed in this table are unable to maintain high contrast on a partially resolved star, which is typically 0.01 λ/D in radius for TPF-C observations. At least three coronagraphs however appear to be theoretically superior to the TPF-C baseline coronagraph, in terms of their ability to achieve smaller inner working angle:

Table 4.1-4. Existing Coronagraph Designs as of April 2006

Coronagraph	Reference
"Interferometric" coronagraphs	
Achromatic Interferometric Coronagraph (AIC)	Baudoz et al. (2000)
Common-Path Achromatic Interferometer-Coronagraph	Tavrov et al. (2005)
Visible Nulling Interferometer (VNI)	Mennesson et al. (2003)
Pupil Swapping Coronagraph (PSC)	Guyon & Shao (2006)
Pupil apodization	
Amplitude Pupil Apodization (CPA)	Kasdin et al. (2003)
Achromatic Pupil Phase Apodization	Yang & Jostinski (2004)
Phase Induced Amplitude Apodization Coronagraph (PIAA)	Guyon (2003)
Phase Induced Zonal Zernike Apodization	Martinache (2004)
Improvement on the Lyot concept with amplitude masks	
Apodized Pupil Lyot Coronagraph (APLC)	Soummer et al. (2003)
Multistep Apodized Pupil Lyot Coronagraph, n steps (APLCn)	Aime & Soummer (2004)
Band limited, 4th order (BL4)	Kuchner & Traub (2002)
Band limited, 8th order (BL8)	Kuchner et al. (2005)
Improvement on the Lyot concept with phase masks	
Phase Mask (PM)	Roddier & Roddier (1997)
4 quadrants (4QPM)	Rouan et al. (2000)
Achromatic Phase Knife Coronagraph	Abe et al. (2001)
Optical Vortex Coronagraph, topological charge m (OVCm)	Palacios (2005)
Angular Groove Phase Mask Coronagraph	Mawet et al. (2005)
Optical Differentiation (ODC)	Oti et al. (2005)

- The 4th order Band-limited Lyot coronagraph (BL4), the Visible Nulling Interferometer (described in Section 4.1.3.5), and its "cousin" the Pupil Swapping Coronagraph, all offer ~2 λ/D IWA. The BL4 and VNI coronagraphs are two implementations of the same 4rth order pupil shear null, and are therefore equivalent. Their average throughput is similar to the baseline TPF-C, but the peak throughput (reached if the telescope is properly oriented to place the planet in a transmission peak) is significantly better: exposure time for spectroscopy can be reduced. For these coronagraphs, there is a trade-off between IWA and throughput. Two versions of these coronagraphs are shown in Figure 4.1-3: a small IWA version noted VNI/BL4(1), and a larger IWA version noted VNI/BL4(2). These corona-

graphs are highly sensitive to low order aberrations and therefore require exquisite control of tip-tilt and focus (see discussion in below).

- The Phase-Induced Amplitude Apodization Coronagraph (PIAA, also referred to as pupil remapping) offers a ~2 λ/D IWA and a nearly 100% throughput (function of the coronagraph spectral bandwidth – see Section 4.1.2.2). This technique is described is section 4.1.3.3.
- The Optical Vortex Coronagraph (OVC) can be designed to offer ~2 λ/D IWA and a nearly 100% throughput.

In what follows, we analyze preliminary models of ideal coronagraph systems operating in the presence of finite-size stars. Final results are pending review and publication. The ability to probe the 2 to 4λ/D region is primarily measured by the amount of planet light available for detection in the focal plane. This excludes planet light which is mixed with much brighter starlight on a pixel of the detector. This amount, when normalized to the amount of planet light entering the coronagraph, is the useful throughput of the coronagraph. It is plotted in Figure 4.1-3 as a function of angular separation for many of the coronagraphs in Table 4.1-4, for a 1e^{-10} contrast level. The stellar angular diameter is taken into account in this figure, which explains the poor performance of several coronagraphs (AIC, PM, 4QPM, ODC) for which the useful throughput curves stay close to zero.
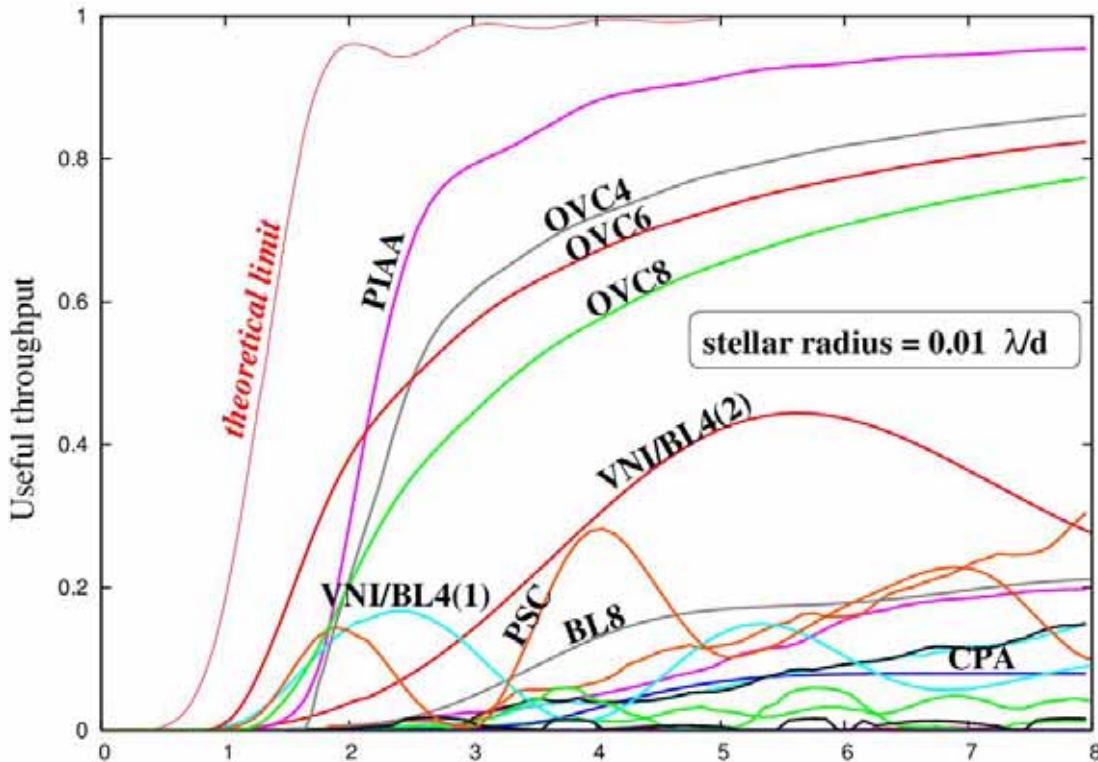
Figure 4.1-3. Useful Throughput of Several Existing Coronagraph Designs

In Figure 4.1-3, the TPF-C baseline coronagraph is BL8 (grey) in this plot. The useful throughput shown here is radially averaged, and is for some coronagraphs significantly higher if the telescope is properly oriented. The theoretical limit shown in red is explained below. The x-axis scale is in λ/D.

The PIAA and OVC6 coronagraphs appear to be the most powerful alternatives to the TPF-C baseline, as they combine small IWA (half of the TPF-C baseline) and a nearly 100% throughput (function of the coronagraph spectral bandwidth – see Section 4.1.2.2). The BL4/VNI (and PSC) also offers a small IWA, but its radially averaged throughput is lower because many rotations are needed to sample the full image plane.

What is the Theoretical Limit of Coronagraphic Performance?
Optical systems are (usually) linear in complex amplitude: the complex amplitude anywhere in the system can be written as a linear combination of complex amplitudes in the entrance pupil. This property can be used to derive the theoretical performance limits of coronagraphy, utilizing linear algebra to place limits on the coronagraph throughput as a function of angular separation. This theoretical limit, shown in Figure 4.1-3, is highly dependent upon the stellar angular diameter, and has been computed here for a 0.01 λ/D stellar radius (typical for TPF-C observations).

This "basic physics" tells us that a coronagraph with ~1.5 λ/D IWA and a nearly 100% throughput (function of the coronagraph spectral bandwidth – see Section 4.1.2.2) is theoretically possible. This coronagraph can theoretically be built with a large number of beam splitters and phase shifters (all achromatic): this solution not realistically feasible, and it remains unknown if such a coronagraph can be practically built.

Our preliminary modeling shows that out of the many high contrast coronagraph designs which have recently been proposed, several appear in theory to approach this fundamental limit, offering ~2 λ/D IWA and a nearly 100% throughput (function of the coronagraph spectral bandwidth – see Section 4.1.2.2).

Number of Stars Sampled as a Function of Coronagraph Design and Telescope Diameter
In the previous sections, coronagraph performance has been quantified by the useful throughput. This single metric is not sufficient to accurately quantify coronagraph performance. A probabilistic approach is needed to take into account the planet's orbit and phase angle (Brown 2004, Brown 2005):

- Exozodiacal and zodiacal backgrounds are an important contribution to the noise. Broader PSFs tend to mix more background with the planet's image
- Exozodiacal light is not a smooth background (it is significantly brighter closer to the star and in a high inclination system, the exozodi disk can be a narrow linear feature): its effect cannot be accurately modeled by the background amplification factor. Planets are brighter when in nearly full phase, but are then closer to the star and therefore over brighter portions of the exozodi cloud.
- In the presence of background light (zodiacal + exozodiacal light), faint parts of the PSFs that contribute to the useful throughput can have a negligible contribution to the detection SNR: the spatial distribution of the planet light affects the SNR.

In this section, the performance of five representative coronagraphs is quantified for the direct detection of Earth-type planets: CPA, PIAAC, BL8, OVC6, and BL4, plus the "theoretically ideal" coronagraph named here ICC6. The simulation model used explicitly computes coronagraphic images and only takes into account fundamental effects such as stellar angular diameter, zodi and exo-zodi, and photon noise. Chromaticity, wavefront errors and calibration errors are not included. Exposure

times given in this section are therefore highly optimistic, but can still serve the purpose of quantifying the relative efficiencies of several coronagraph design/telescope diameter combinations. Key parameters adopted for the simulation are given in Table 4.1-5.

Examples of frames obtained with this simulation tool are shown in Figure 4.1-4. These images nicely illustrate coronagraphic characteristics quantified in the previous section:

Useful throughput at large separation: The CPA, BL8, and to a lesser extent BL4 suffer from low coronagraphic throughput. As a result, the planet's image, even if well outside the coronagraph mask's influence, appears noisy (few photons detected). The PIAAC, OVC6 and ICC6, on the other hand, enjoy nearly 100% throughput (function of the coronagraph spectral bandwidth – see Section 4.1.2.2): the planet image is brighter and less noisy.

Angular resolution: The CPA, BL8, and to a lesser extent BL4 have poorer angular resolution: the planet image is larger and more zodi/exozodi light is mixed with it.

Ability to work at small angular separation: None of the coronagraph tested can detect the planet on a 2m telescope with the exposure time, wavelength, and throughput used in Figure 4.1-3. Detection appears feasible on a 4m telescope with the BL4, PIAAC, OVC6 and ICC6, but requires a 6m telescope with the BL8. Finally, an 8m telescope is needed for detection with the selected CPA.

Table 4.1-5. Key Simulation Parameters

	Value	Unit	Notes
Optics throughput	0.25		
Wavefront quality	perfect		
Detector	perfect		No readout noise or dark current
Wavelength	0.5 – 0.6	micron	0.1 micron bandwidth
Zodiacal background	23.28–22.24	mV	Function of target ecliptic latitude
1 zodi brightness	22.53	mV	At the habitable zone, for a face-on system
Exozodi inner edge	0.02 sqrt(L)	AU	L = star bolometric luminosity
Exozodi inner edge	5.0 sqrt(L)	AU	L = star bolometric luminosity
Exozodi thickness	0		Cloud thickness unresolved by telescope
Exozodi optical depth	Cst*r^-0.34		
Planet radius	6400	km	
Planet albedo	0.33		
Semi-major axis	sqrt(L)	AU	L = star bolometric luminosity
Eccentricity	0		
Orbit inclination	pi/3	rad	Statistical median for random orientation

Sensitivity to stellar angular size: The CPA and BL8 are extremely robust to stellar angular size: starlight leaks are virtually nonexistent even on the 12m telescope. With the BL4, PIAAC, OVC6 and

ICC6, starlight is visible on the 12m telescope (equivalent to a 6m telescope observing the same system at 5pc), although it is still fainter that the exozodiacal contribution.

Images similar to the ones shown in Figure 4.1-4 have been generated for each possible position of the planet along its orbit, and for all nearby (<100 pc) main sequence stars of spectral types F, G and K. For the BL4 and BL8 coronagraph, it was assumed that the coronagraph was properly orientated along the planet's orbit major axis. Figure 4.1-5 compiles the results obtained for a 3 zodi exozodiacal cloud.
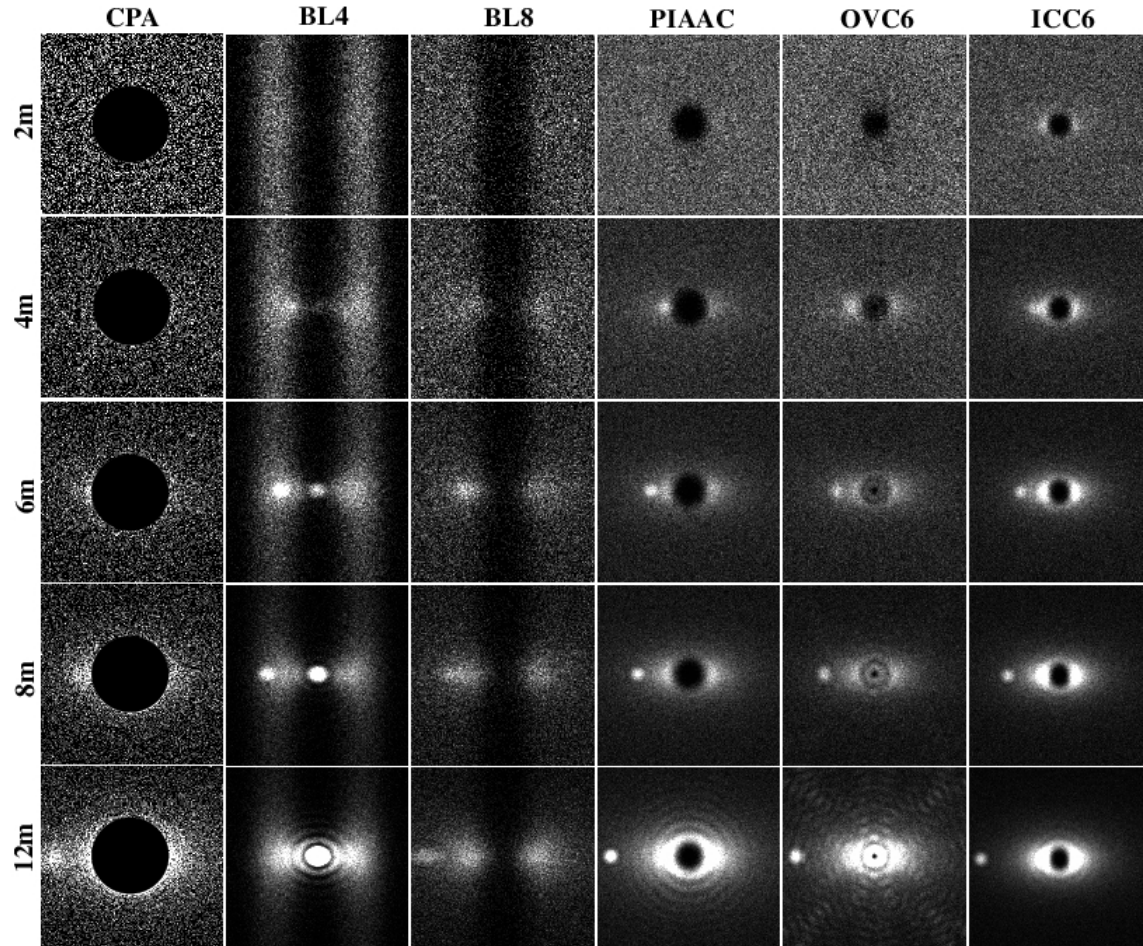
Figure 4.1-4. Simulated 4-hour Exposures of HIP 56997 and a Hypothetical Earth-Type Planet at Maximum Elongation for Telescope Sizes Ranging from 2m to 12m

In Figure 4.1-4, HIP 56997 is a G8 type main sequence star at 9.54 pc. Each image assumes a perfect detector, minimum zodiacal background (mV = 22.95 zodiacal background for this 29 deg ecliptic latitude source), a 1 zodi exozodi cloud, a 25% telescope + camera throughput, and a 0.1 micron bandpass centered at 0.55 micron. The system inclination for this particular simulation was arbitrily set at i = 59 deg. Each image is 20 × 20 lambda/d, and the planet-star separation is 80 mas.

In Figure 4.1-5 for all simulations, a 25% throughput in the 0.5–0.6 micron band is adopted, and targets are ordered with increasing exposure time. Each curve terminates when the required exposure time per target reaches 1 day. Results are shown for a 4 m telescope (left) and an 8 m telescope

(right). The number of accessible targets for which the required exposure times are less than 1 hour, 10 hour and 1 day are listed for each case in the grey boxes. In the 8 m telescope plots, the horizontal line corresponds to a 2 month "shutter open" cumulative exposure time, and may be considered as a practical limit on the number of targets that can be visited.
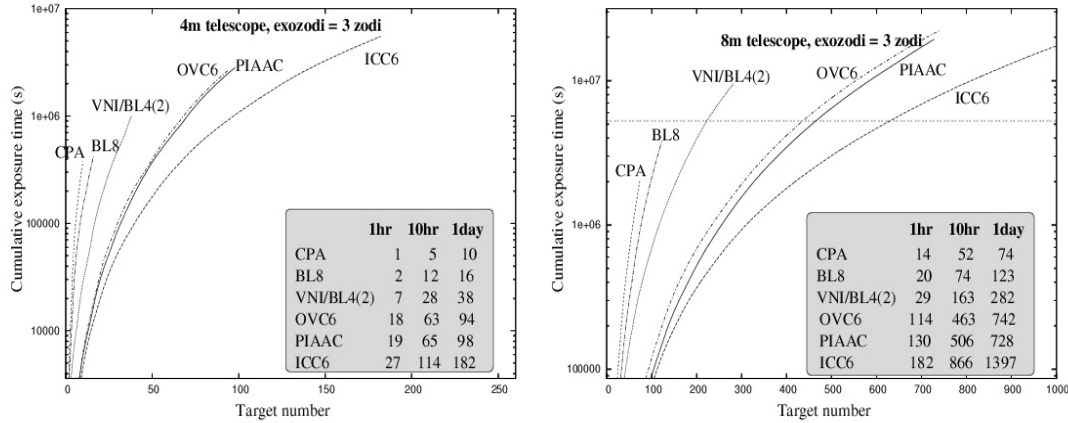
Figure 4.1-5. Total Cumulative Exposure Times Required to Reach a 50% Planet Detection (SNR = 7) Probability for a Single Observation as a Function of Number of Targets

Figure 4.1-5 accurately quantifies the gain offered by a coronagraph more efficient than the TPF-C baseline:

- Adopting an efficient coronagraph (PIAA or OVC6) multiplies by approximately 10 the number of accessible targets for a given telescope diameter and a fixed exposure time per target. For a fixed mission duration, this gain is smaller, and approximately equal to a factor 5.
- The performances of a 4m telescope equipped with an efficient coronagraph and an 8 m telescope with a conventional coronagraph (similar to the TPF-C baseline) are equivalent. More efficient coronagraphs therefore have the potential of allowing a TPF-C mission with a 4m diameter telescope.

Wavefront Control Requirements with High Performance Coronagraphs

Coronagraphs with smaller IWAs are more sensitive to low order aberrations (tip, tilt, focus, etc) which also tend to diffract light in the 2 to 4 lambda/D region (Shaklan & Green 2005). Requirements for the control of these low order aberrations are much tighter than for the TPF-C baseline. Among low-IWA coronagraphs, the BL4 and VNI coronagraphs are the most sensitive to low order aberrations; the PIAA and OVC are somewhat less sensitive (but still significantly more than CPA and BL8 used for FB1).

Adopting a high performance coronagraph therefore requires exquisite control of low-order aberrations, to a level much below what is envisioned for FB1. Low order aberrations need to be actively controlled. While this may require some modification of the optical design (e.g. a low-order wave front sensor such as the one employed by the ground-based LYOT adaptive optics coronagraph project), there appears to be no fundamental obstacle to doing so:

(1) PIAA and OVC coronagraphs transmit more photons than FB1, leading to shorter sampling time for measuring low order aberrations.

(2) In a small-IWA coronagraph, the edges of the pupil, where the light most valuable for sensing of low order modes is, are not blocked by coronagraphic masks, resulting in increased sensing efficiency.

(3) The strong starlight rejected by the coronagraph can be used to accurately measure low-order aberrations.

Field of View / Number of Actuators

When a high efficiency and small IWA coronagraph is used, most planet detections are expected to occur at separations below 4 λ/D. These coronagraphs can therefore operate with a reduced field of view and therefore a smaller number of DM actuators.

In summary, our preliminary modeling of specific coronagraph mask configurations shows the potential advantages of PIAA and OVC over the baseline and other approaches. Our models are not comprehensive and do not, for example, include aberrations, details of the optical train, or bandwidth limitations associated with wave front control.

REFERENCES

Abe, L., Vakili, F., Boccaletti, A. 2001, A&A, **374**, 1161

Aime, C., Soummer, R. 2004 Proc. SPIE, **5490**, 456

Baudoz, P., Rabbia, Y., & Gay, J. 2000, A&A Suppl., **141**, 319

Brown, R.A. 2004, ApJ, **607**, 1003

Brown, R.A. 2005, ApJ, **624**, 1010

Guyon, O. 2003, A&A, **404**, 379

Guyon, O., Shao, M. 2006, submitted to PASP

Kasdin, N.J., Vanderbei, R.J., Spergel, D.N., & Littman, M.G. 2003, ApJ, **58**2, 1147

Kuchner, M.J., Traub, W.A. 2002, ApJ, **570**, 900

Kuchner, M.J., Crepp, J., Ge, J. 2005, ApJ, **628**, 466

Martinache, F. 2004, J. of Opt. A, **6**, 809

Mawet, D., Riaud, P., Absil, O., Surdej, J. 2005, ApJ, **63**3, 1191

Mennesson, B.P., Shao, M., Levine, B.M., Wallace, J.K., Liu, D.T., Serabyn, E., Unwin, S.C., Beichman, C.A. 2003, Proc. SPIE, **4860**, 32

Oti, J.E., Canales, V.F., & Cagigal, M.P. 2005, ApJ, **630**, 631

Palacios, D.M. 2005, Proc SPIE, **5905**, 196

Roddier, F., & Roddier, C. 1997, PASP, 109, 815

Rouan, D., Riaud, P., Boccaletti, A., Clenet, Y., & Labeyrie, A. 2000, PASP, **112**, 1479

Shaklan, S.B., & Green, J.J. 2005, ApJ, **628**, 474

Soummer, R., Aime, C., & Falloon, P.E. 2003, A&A, **397**, 1161

Tavrov, A.V., Kobayashi, Y., Tanaka, Y., Shioda, T., Otani, Y., & Kurokawa, T. 2005, Optics letters, **30**, 2224

Yang, W., & Kostinski, A.B. 2004, ApJ, **605**, 892

4.1.1.3 Actuated Primary Mirror Alternative

4.1.1.3.1 Justification and Motivation

The viability of *TPF-C* on the scale currently envisaged by will depend to a large extent on the affordability and performance of its 3.5 × 8 m primary mirror which must be monolithic. The optical system must yield star images of a completely unprecedented quality. Issues for any primary mirror concept are:

1) Can it be figured to the required accuracy?
2) What optical metrology method will be used to measure wavefront from the mirror to the required accuracy?

The above two issues are serious, but are largely independent from the structural and control concept. However, the next three are concept dependent:

3) How can we be sure from lab metrology that the primary will take on a good enough figure in the zero g and thermal environment of space?
4) If an additional optical relay with deformable optics is required to correct primary mirror errors, what will be its cost and reliability, and what will be the performance penalty in terms of chromatic amplitude variations?
5) Is the primary mirror compatible with a full closed-loop system test in zero g before launch?

The baseline design calls for the primary to be constructed as a single honeycomb sandwich of 3.5 × 8 m, supported in flight on three points. Its passive design means it is likely to be by far the largest source of wavefront phase and amplitude errors in the optical system. This is because the difficulties of figuring, metrology, uniformly coating and predicting the gravity free shape from lab measurements all increase strongly with size.

With regard to the above issues, (3) its shape in space will have to be computed, based on analysis and indirect measurements of thermal and mechanical response. (4) The FB1 uses the additional active relay with a small conjugated dm with small stroke and likely still more active correction for larger amplitude gravitational sag. The performance penalty must be quantified. (5) For the passive monolith, there will be no opportunity for a full system test prior to launch, unless a flotation system independent of the space requirements is included in the full system test.

4.1.1.3.2 Description of Alternative

The alternative to the passive primary of FB1 is an active one. An important consideration is the number of modes to be controlled and the requirement for extreme mechanical and thermal stability. Gravity release will involve mostly low order modes, though higher modes that were imprinted by the distributed supports of the flotation system will also be apparent at lower amplitude. The actuator system will be used to control to exquisite accuracy those Fourier components that diffract light into the search zone. If a search is to be made to 10 λ/D, then Fourier components up to 10 waves across the aperture will be controlled to an amplitude of a few picometers, requiring at least 30 actuators across the diameter. These actuators will be chosen to add no additional thermal sensitivity of their own.

Active mirrors of around 1 m dimension are now being used or developed for astronomical systems, and fall into two types. In type 1, the reflecting surface is deposited on a thin deformable substrate referenced by many position actuators to a much more rigid substrate. The 1-m class deformable secondary mirrors for the MMT and LBT mirrors built by Steward and Arcetri Observatories are of this type, with 336 or 672 actuators. These are similar in principle to the small deformable mirrors envisaged for FB1. However, because of their larger scale, they are able to incorporate additional features such as internal metrology with capacitive sensors between the reference body and face-sheet, and more reliable actuators which cannot fail in a stuck position because there is no physical contact. In type 2, the mirror remains a single structure, but actuators are incorporated into the structure to cause localized strains that induce shape changes. Meter scale mirrors of silicon with integrated PMN actuators are being developed for defense space optics. These can be considered as a scaled up version of bimorph adaptive mirrors in which strain is introduced by making the small mirror as a piezo bimorph.

A type 1 active mirror for *TPF-C* would use highly stable, zero-expansion material for both the rigid lightweight reference structure and the faceplate. The actuators should have the stroke to compensate for gravity release and stability to picometer level of the timescale of minutes between updates from the focal plane sensor, either intrinsically or by operation in closed loop about sensors which have the required resolution and stability. An example would be a ~ 1 cm thick meniscus connected via ~ 104 position actuators to a lightweight welded ULE structural support. Suitable piezo actuators could be developed from the current DM concepts or from existing commercial actuators which with internal capacitive sensors achieve 50 pm resolution and 10 micron stroke. Further study is required to understand and develop solutions for athermalizing and reducing the mass of the actuators, and for the transition from the launch to operational environment. In addition, concepts are needed to control the mass of the cables across the 8 m aperture.

A type 2 system might be built with thermal actuators. The mirror would be a figured lightweight honeycomb mirror of glass with small but finite expansion coefficients, so that shape changes could be introduced by introducing thermal gradients. It will likely be necessary already for the passive FB1 solution to use active thermal control to millikelvin level. The active thermal control system would work on a balance between radiative cooling to a sink slightly below the operating temperature (e.g., with a cold finger into each honeycomb cell) and resistive heaters on the ribs and face-sheets. The expansion coefficient of the gas used to make the ribs and facesheets would be chosen separately for optimum control. For example, if 30 cm deep ribs were made with fused silica of thermal expansion coefficient of 5×10^{-7}, 100mK heating would cause local expansion of 15 nm. At the same time, if the facesheets were made with lower coefficient glass, for example titania doped silica like ULE but with coefficient 5×10^{-8}, a 10 mK difference on average induced between the front a back facesheet temperatures would cause curvature of 40 nm sagittal depth across the 8 m dimension, and ~ 1 nm across 1 m. Thus by active thermal controls to tens of **microkelvins**, the figure could be both controlled and stabilized (Angel, 2006).

4.1.1.3.3 Improvement/Impact

The potential for improvement for an active primary is in several areas:

- *Improved performance on orbit.* Direct correction of the primary removes the limits set to starlight nulling set by chromatic amplitude errors arising in the propagation from the primary or from relay mirrors.

- *Improved reliability.* Whether thermal or piezo/PMN, actuators built on the large scale of the primary can incorporate redundancy. This is not possible for a small scale deformable mirror conjugated to the primary, where a non-redundant stuck actuator could become a single point failure.

- *Improved testing.* With the active primary, system test to final performance level becomes possible. The primary actuators would be given enough stroke to compensate for residual bending under 1 g load, allowing for full system test in a 1 g environment. The FB1 baseline conjugated mirror does not allow for this.

- *Cost impact.* The system with either alternative type is not likely to cost more that the FB1 concept, which already involves thermal controls, and has the additional costs of a relay of extremely high quality and a second actuated mirror.

4.1.1.3.4 Alternative I&T test

It is highly desirable to have a ground test of the fully configured *TPF* that accurately reproduces the operation in space. Not just the optics but the control systems and the control software should ideally all be operated together just as they will in space. The ultimate proof would be to recover the image of a star and faint planet from a full aperture collimator input, using all the internal wavefront control and star suppression systems working as on orbit (Angel, Burge and Worden, 2005). While there will be a significant initial cost of building the test facility, ultimately the overall costs may be lowered, and the system reliability and confidence will be greatly increased. However, such a test will not be possible or optimal if it is not allowed for from the start in the telescope design. Thus we examine first the constraints of a valid test.

To test the *TPF-C* spacecraft system prior to launch, an off-axis collimator must be used to illuminate the full aperture with a scene of a star and planet at 10^{-10} contrast.

4.1.1.3.5 Low Authority Actuated Primary Mirror

The baseline concept has no actuators on the PM. The SM is actuated to align to the PM, and PM stability is enhanced through a near-kinematic mount. As has been discussed, this mirror has large gravity sag in the ground testing environment, complicating telescope and system end to end verification. A strong desire in the next design phase is to examine the two likely alternative technologies, which are high authority control on the primary (discussed above in 4.1.1.3.2) and low authority.

A low authority mirror actuation scheme could obviate the need for the type of coarse deformable mirror included in the baseline. The idea would be to engineer a few (6-20) high-load, high stability actuators into the PM assembly. The requirements would be to remove uncertainties in ground testing to within a budget based on the range of the fine deformable mirror and to control actual figure error in operation to the same range. This scheme is more consistent with actuator densities used for *JWST* and large ground based telescopes than are either the passive PM baseline or the high authority meniscus alternate. The key would be demonstrating mechanical and thermal stability at the required levels for this application.

TDM is planned to be tested on an air bag after polishing and before mounting. This test is consistent with the baseline concept for the PM; however, final TDM testing will include actuation to off-load gravity in a manner consistent with the low authority concept for the flight PM.

Recent work has allowed us to optimize mount locations for the baseline PM design as the beginnings of exploring this concept. Sigmadyne has developed a genetic algorithm approach for optimization of mount and actuator locations. Figure 4.1-6 shows the baseline and μm to μm optimized mount locations; the peak gravity deflection is reduced from 483 to 82 μm.
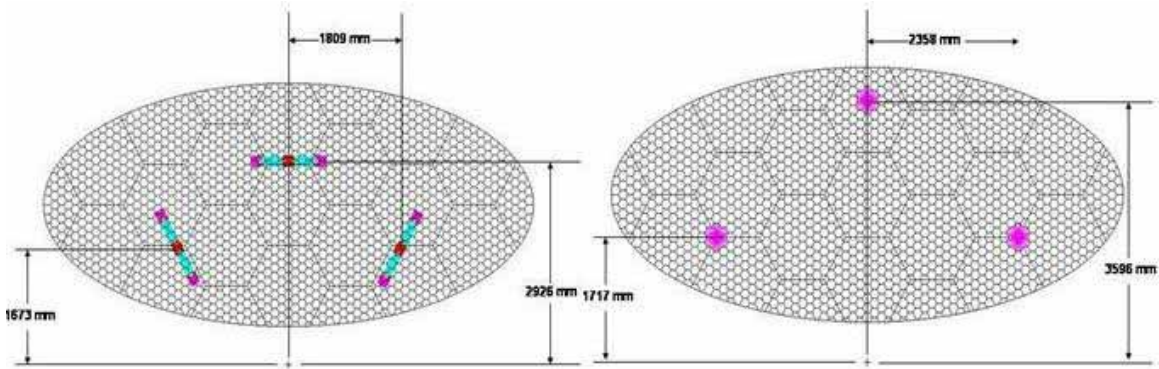
Figure 4.1-6. Optimization of the Mount Point Locations Reduces the Peak Gravity Self Deflection of the PM from 483 μm to 82 μm; the Optimized Mounting Points were then Studied for Optimal Actuator Location and Gravity Offloading Performance vs. Actuator Count.

Two levels of actuator correction were studied; one would be enough actuators to remove the need for a coarse PM error correction even during ground testing. We assumed that this would require < 0.5 μm total error in order to fit within the stroke range of current high density deformable mirrors. The second level would aim to get the 1g gravity load uncertainty less than this range; if one could engineer a static 1g correction into the ground testing environment, then the coarse DM again would be unnecessary. Both alternatives allow removal of the coarse DM in flight, which reduces

overall errors (particularly beam walk) and simplifies the optical train. While absolute uncertainties in 1g models can be difficult to quantify, we use an estimate of 5% of the peak gravity deflection. Krim reported a 2% value for the HST PM after calibration of its mounting and actuation system. This would require correction to < 10 μm total error. Figure 4.1-7 shows the results for these two requirements, while Figure 4.1-18 shows example actuator layouts for the limiting cases of the lower count, i.e. 6 and 20 actuators. Mounts are the large red shaded areas and mounting points are the smaller locations. In practice, the mirror segmentation and the mounting locations would be optimized together; for this exercise the mirror segmentation was held fixed.
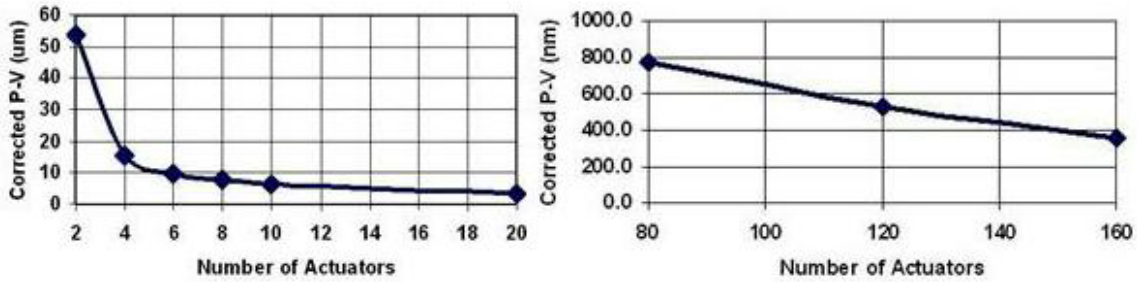
Figure 4.1-7. Left: Low Authority can Easily Achieve Correction of Self Gravity Deflection to the 10 μm level with a low actuator count; Right: In order to correct to within the stroke of the fine DM a significant number of actuators is required.
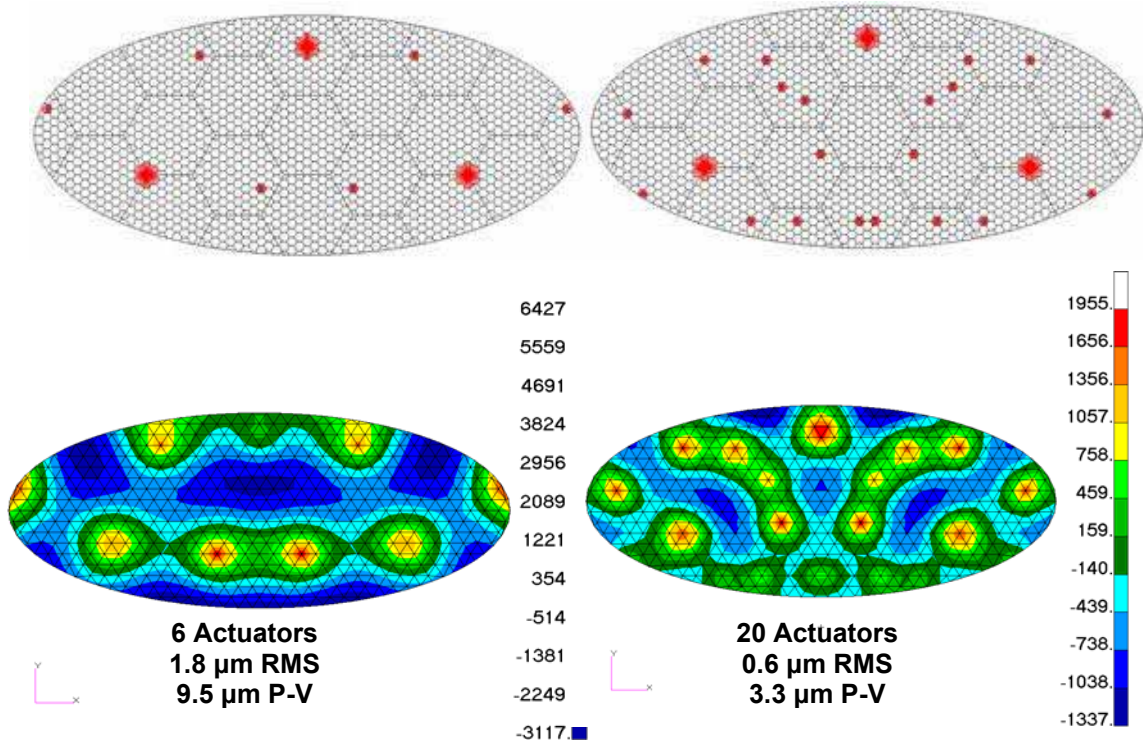
Figure 4.1-8. Actuator Locations as Optimized for 6 (left) and 20 (right) Actuators. Mounts are the large red shaded areas and mounting points are the smaller locations. In practice, the mirror segmentation and the mounting locations would be optimized together; for this exercise the mirror segmentation was held fixed. With 6 actuators, 1g deflection is reduced to 1.8 µm RMS, 9.5 um P-V; with 20 Actuators Deflection is reduced to 0.6 µm RMS, 3.3 um P-V.

4.1.1.4 Coatings: Aluminum vs. Silver for the Coronagraph PM, SM, and M3

The basic differences between the two mirror materials are in their reflectivity and polarization behavior at oblique incidence besides protection requirements for environmental stability and handling. Both materials have been applied to astronomical telescope optics in the past. While silver mirrors, without any special enhancements, give >98% reflectance over much of the visible spectrum, the sharp cut off around 400nm makes them unsuitable for UV applications, though some recent laboratory techniques have demonstrated application of UV enhancing coatings for silver mirrors. For *TPF*, the very large mirror sizes present major challenges for adopting such techniques readily. On the other hand, Aluminum mirrors have better UV performance though with lower reflectance (typically ~ 92% with a dip to ~ 86% around 800nm) than silver in the visible spectrum. Hence, choice of aluminum for *TPF-C* primary (PM), secondary (SM) and tertiary (M3) mirrors alone will result in a throughput reduction of about 25 to 30% as seen in
Figure 4.1-9 and Figure 4.1-10. While enhancement of Al reflectance may be achieved by employing more complex protective coatings, manufacturing will be more challenging due to the large size and consequent uniformity issues. Note that the calculations behind Figure 4.1-9 and Figure 4.1-10 are based on known optical constants of materials from the literature while the actual optical constants of these materials depend critically on the process conditions. Therefore, these estimates have to be taken as a guide only.

The Hubble telescope primary mirror employs aluminum protected by a thin (25nm) layer of MgF2. This ensures >70% reflectance over the UV spectrum particularly at the Lyman Alpha wavelength (121.6nm). A similar coating may be chosen for the *TPF-C* primary mirror. Such a thin layer provides less reflectance variation over the spectrum while a thicker layer of about 140nm provides less phase difference between p and s polarizations at oblique incidence. Therefore, the Al mirror performance for *TPF-C* in the visible spectrum needs to be evaluated with a full system Fresnel propagation analysis including the mask and Lyot stop to assess the effects of polarization splitting, particularly if two independent polarization paths are not chosen.

In summary, to make the final choice of Al vs. Ag, the following considerations are necessary:

1. **Bandwidth and Throughput comparison:** Theoretical models based on optical properties of materials from the literature and employing simple single layer dielectric protective coatings show a throughput loss of about 25 to 30% in the visible spectrum if aluminum is employed for the PM, SM and M3 mirrors only, leaving the rest of the mirrors as silver based. However, UV coverage becomes feasible with Aluminum.

2. **Polarization splitting, cross polarization leakage and consequent contrast degradation, if any:** The throughput loss depends on the protective layer/s and their thicknesses which also affect polarization splitting and leakage. Optimizing the protective coatings considering the polarization behavior (both amplitude and phase) is a necessary study yet to be done for Aluminum when propagation past all mirrors is considered. Fortunately, the 8th order occulting mask provides more margins than the 4th order mask and hence the polarization leakage errors introduced by Al mirrors may not be issue. A detailed study with Fresnel propagation and final contrast estimate is needed for Al as has been done for Ag.

3. **Uniformity, durability, cleaning and handling requirements:** *TPF-C* error budgets require stringent wavefront quality beyond those of other instruments in the past. Coating uniformity has to be assured to better than 0.1% in thickness and reflectance, which is a challenge for either material. While the experience gained with the Hubble mirrors on the coating, and the care and handling, may be extended to *TPF* mirrors, scaling up to the 8 × 3.5m *TPF* primary mirror will require significant experiments and process technology development because conventional thermal evaporation processes are unlikely to guarantee the uniformity and durability over such a large area; measurement techniques to the required accuracy must also be developed. Durability, handling and cleaning requirements have yet to be compared for the two materials taking into consideration the manufacturing constraints and size.

4. **Manufacturing constraints / needed technology development in comparison to current state of the art:** Typically mirror coatings have been done with thermal evaporation processes; *TPF-C* mirrors will require more advanced techniques such as ion assisted e-beam evaporation or sputtering with carefully designed masks appropriate to the particular chamber geometries to ensure uniformity and process controls. Similarly, new measurement techniques and instruments have to be developed to the accuracy levels demanded of *TPF-C* mirrors. Technology developments have to happen in both these areas, independent of the material choice, i.e. Al or Ag.
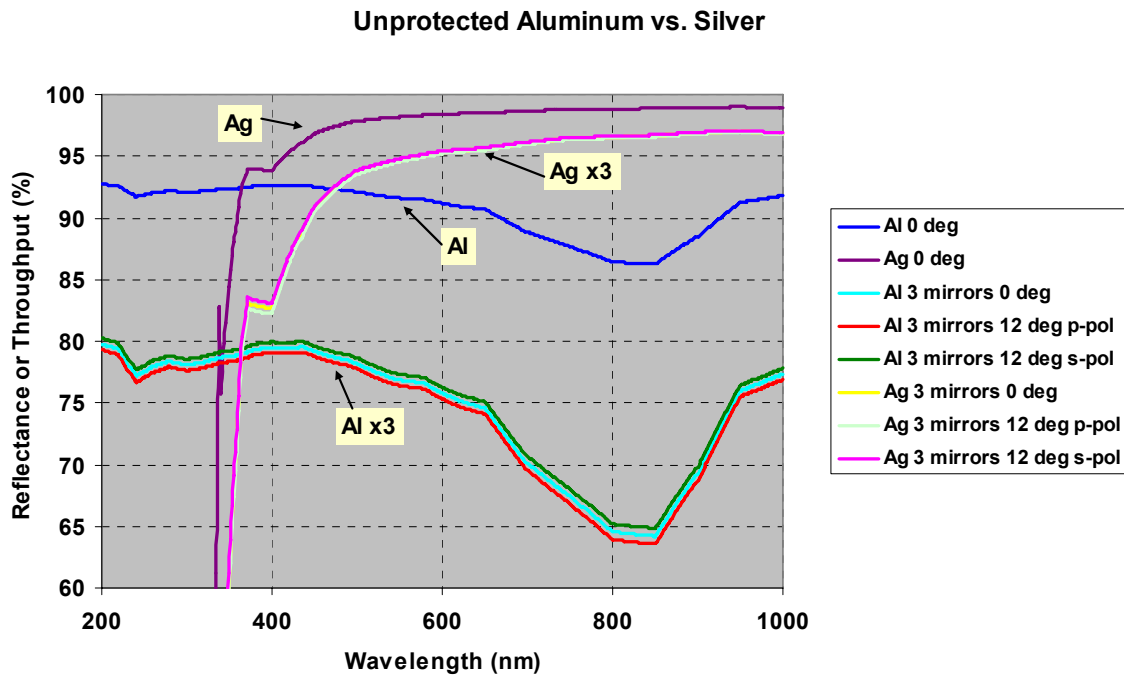
Figure 4.1-9. Unprotected Al vs. Ag: Reflectivity and Throughput after 3 Mirrors.
***TPF-C* primary mirror presents up to 12 deg angle of incidence for the incident rays causing polarization splitting in both amplitude and phase.**
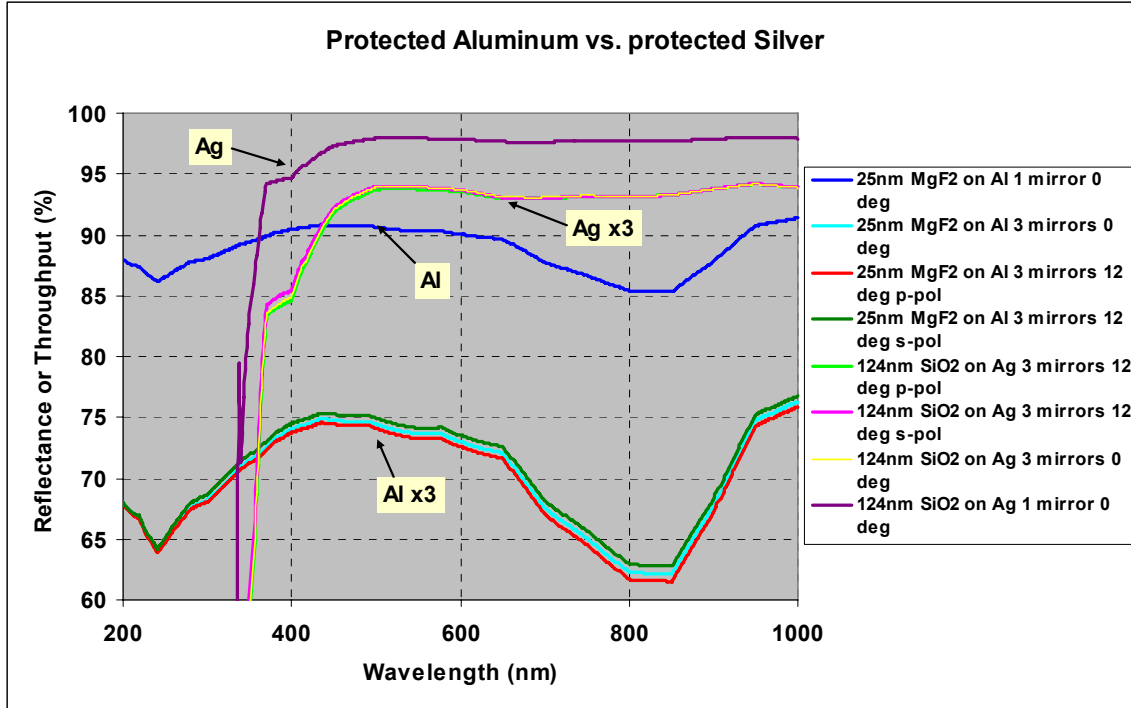
Figure 4.1-10. Protected Aluminum vs. Silver with Typical Single Layer Overcoats

4.1.1.5 Racetrack/Bandaid Mirror Configurations

After FB1 was frozen significant analyses were performed to increase the performance of the *TPF-C* observatory. One analysis consisted of examining different mirror shapes (see Figure 4.1-11). Two shapes in particular were explored: the racetrack mirror (rectangle with rounded corners) and the bandaid mirror (rectangle bounded by a circle) (Figure 4.1-11 b and c, respectively). The analysis investigated the aberration sensitivity, throughput, integration time, and completeness permitted by the new shape. Variations on mirror length and width were also investigated to maximize performance and minimize system impacts.
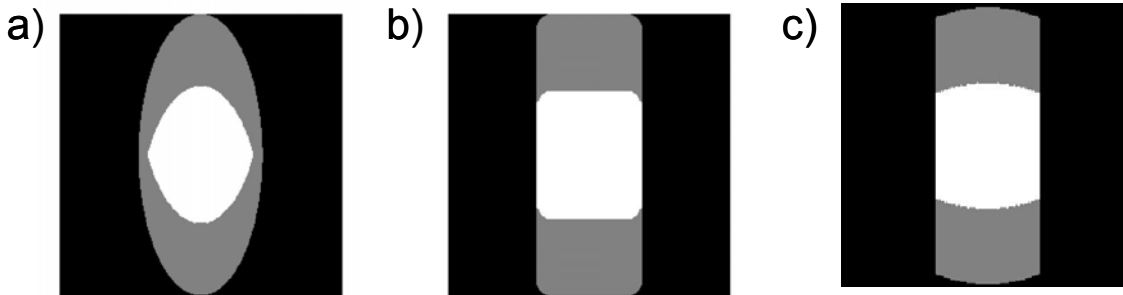
Figure 4.1-11. Mirror Shapes Corresponding to a) Current FB-1, b) Racetrack, and c) Bandaid. (The grey area represents the actual shape of the mirror and the white area corresponds to the Lyot spot size.)

Changing the shape of the mirror necessitates decreasing the minor dimension of the mirror to decrease mass and shift the center of mass of the telescope. However, with this decrease, the major dimension may be increased. Several mirror shape cases are outlined in Table 4.1-6.

Table 4.1-6. Comparison of Several Different Mirror Shapes

Primary Mirror Shape	PM Area (m²)	Lyot Efficiency	Net Area (m²)	FWHM PSF Core Area	4 λ/D IWA (mas)
8x3.5 Elliptical	21.991	0.340	7.479	1118.6	56.7
8x3.0 Racetrack (r_c =0.5m)	23.837	0.449	10.696	741.5	56.7
8x3.0 Bandaid (D=8.0)	23.410	0.440	10.307	766.7	56.7
8x3.0 Bandaid (D=8.1)	23.703	0.440	10.436	757.2	56.0
8x3.0 Bandaid (D=8.2)	23.995	0.440	10.565	748.0	55.3
8x3.0 Bandaid (D=8.3)	24.288	0.440	10.694	739.0	54.7
8x3.0 Rectangle	24.000	0.453	10.875	741.5	56.7

Even with the minor axis decrease, both bandaid and racetrack mirror shapes allow for a larger physical aperture and larger Lyot stop size than the baseline elliptical primary shape. These features allow greater throughput with a smaller PSF, thereby reducing the integration time necessary to observe to the limiting Δmag. Figure 4.1-12 depicts the integration time benefit obtained by using a band-aid mirror shape.
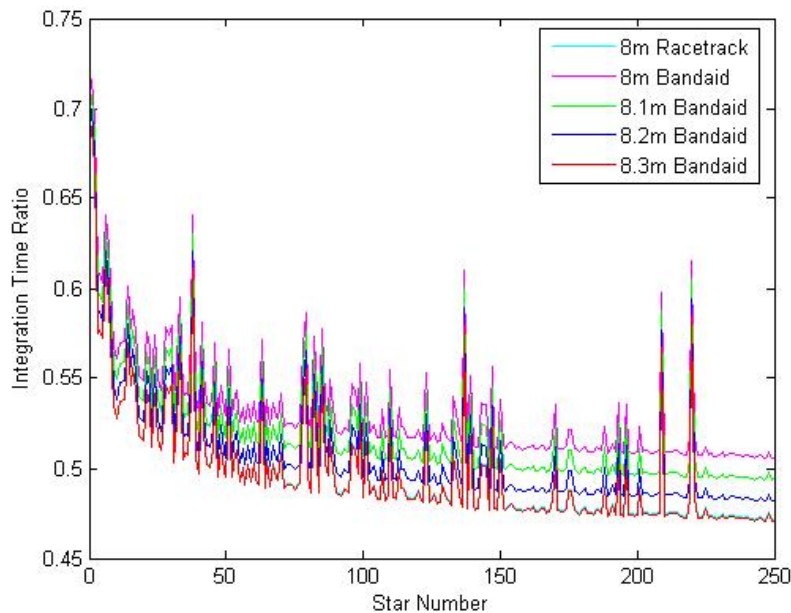
Figure 4.1-12. Comparison of Integration Times for Different Mirror Configurations (The Integration Time Values are depicted as a Ratio to that of the Baseline Values. Stars are Sorted by Angle to the Habitable Zone.)

By also increasing the major dimension of the mirror, we may decrease the IWA. This permits viewing of the habitable zone (HZ) closer to the star and greater scientific benefit. Figure 4.1-13 shows the increase in completeness for different choices of mirror shape.
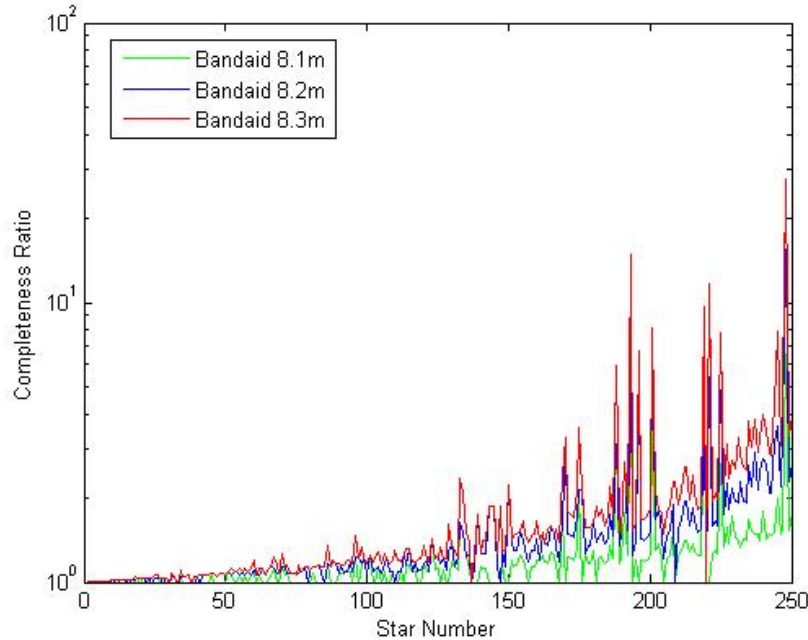
Figure 4.1-13. Comparison of Completeness for Different Band-Aid Shape Mirrors (The Complete-ness Values are depicted as a Ratio to that of the Baseline Values. Stars are Sorted by Angle to the Habitable Zone.)

Although the efficiency of the mirror increases dramatically, changing the mirror shape has a nega-tive impact on the aberration sensitivity. Figure 4.1-14 depicts the increase in aberration sensitivity for one case of the mirror shape change.
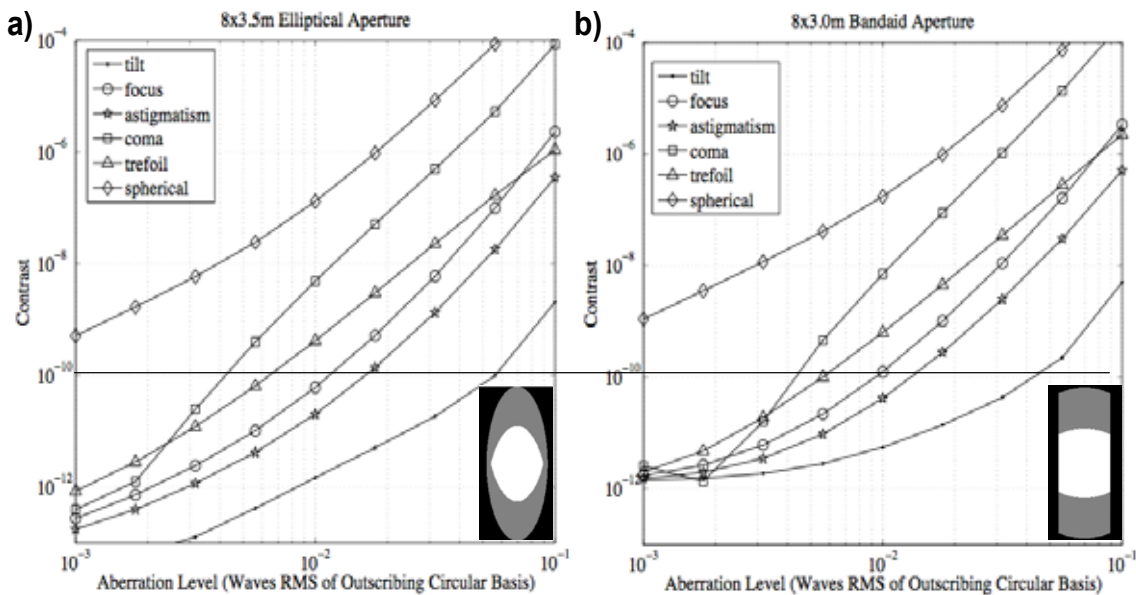
Figure 4.1-14. Comparison of Aberration Sensitivity of the Baseline Mirror and the 8 x 3.0m Bandaid Mirror (The Horizontal Line Represents the Contrast Limit for FB1.)

The 8 × 3 m bandaid is 2–4 times (for different aberrations) more sensitive to aberrations than the baseline design. This sensitivity would increase slightly for mirrors with a larger major dimension. However, the sensitivity increase can be accommodated via error budged reallocations. Because of the significant positive impact on scientific gain, new mirror shapes, in combination with other beneficial alternative designs, should be employed for future design iterations.

4.1.2 Starlight Suppression System Alternatives

The telescope diameter required to reach the TPF-C science goals is largely driven by the coronagraph performance, especially its throughput and IWA. The coronagraph design adopted for the TPF-C baseline has a 4 λ/D IWA and ~20% throughput.

In the last years, many new high contrast coronagraph designs have emerged, and several appear to theoretically offer ~2 λ/D IWA and a nearly 100% throughput (function of the coronagraph spectral bandwidth – see Section 4.1.2.2). If adopted for TPF-C, such coronagraphs could halve the telescope diameter or, for the same telescope diameter, greatly increase scientific return. Although these coronagraphs have lower TRL than the TPF-C baseline coronagraph, the huge potential gain in performance/cost they could bring justifies further investigation, as they could enable a significantly simpler/smaller TPF-C.

4.1.2.1 FB1 Simplification

Analyses performed during and subsequent to the FB1 study have led to several simplifications of the SSS that will improve throughput and bandwidth, relax fabrication tolerances, improve redundancy, and simplify design. These improvements, discussed below, are:

- Eliminate polarizers, controlling all the light in one optical train.
- Eliminate the Michelson dual-DM configuration and replace it with a 3-DM sequential arrangement.
- Use superior (but within the existing state-of-the-art) optics in critical parts of the beam train.

4.1.2.1.1 Elimination of Polarizing Beam Splitters and Second Polarization Channel

The present SSS design has two orthogonal polarization channels, each with it own coronagraph, wave front control system, and detectors. The system was designed this way because the band-limited 4th-order coronagraph masks in the Lyot coronagraph do not sufficiently filter the low-order aberrations resulting from non-normal angles of incidence across the primary, secondary, M3, and M4. Other optics are used at low-angles of incidence or in collimated beam space and do not significantly affect polarization performance. If the two polarizations are not separated, the wave front control system can only control one, or the mean of the two, but not both simultaneously to the required levels (Balasubramanian et al, 2005).

The polarizations are split before the wave front control system using two sequential polarizing beamsplitters (PBS). The PBS's are challenging optics for several reasons, including optical coating bandwidth, multiple-reflection control, and strict birefringence requirements.

In FB1, the 4th order masks have been replaced by 8th-order masks (Kuchner, Crepp & Ge 2005, Shaklan & Green, 2005a). The 8th-order masks have greatly reduced sensitivity to low-order aberrations (at the expense of throughput in the Lyot aperture). With 8th-order masks, the polarization-induced tilt, focus, astigmatism, coma, trefoil, and spherical aberrations are filtered to better than 10-12 contrast. This is sufficient to warrant **eliminating the polarizing beamsplitters and the duplicate optical train that follows.**

One drawback of this approach is that the coronagraph mask must be polarization-insensitive. Our analysis and experimental work on HCIT have shown that binary mask forms (e.g. so called 'notch-filter' masks (Kuchner 2003)) won't work; they limit image plane contrast to ~ 1e-8 when one polarization is controlled to 1e-10.

4.1.2.1.2 Alternative to Michelson DM configuration

Deformable mirrors control the shape of the wave front surface. When they are arranged in a Michelson interferometer configuration, the surfaces interfere and can control both the amplitude and phase of the wave front (Littman et al 2002). The amplitude control is wavelength-dependent (the field amplitude varies as the square of the wavelength). This limits the useful optical bandwidth and places tight requirements on any reflectivity non-uniformity across the aperture that does not have quadratic wavelength dependence.

Shaklan & Green (2005b) have shown that a sequential DM configuration presents wavelength-independent amplitude control. This **relaxes both the amplitude uniformity requirement and the surface uniformity requirement** for optics located at non-pupil plane locations. In the latter case, the propagation of the wave front to the pupil introduces a wavelength-dependent amplitude term that is perfectly cancelled by propagation from the non-pupil DM.

Figure 4.1-15 shows a proposed configuration (from Shaklan & Green 2005b). The system has 3 DMs in series. Two of them are in non-pupil locations, while the third is at a pupil. In this arrangement, broad-band amplitude and phase control is achieved with any two of the three DMs. Thus the system is robust against DM failure.

The arrangement also has the advantage of eliminating the Michelson beamsplitter and associated compensation wedges. The beamsplitters, like the PBS, has limited optical bandwidth and tight birefringence specifications.
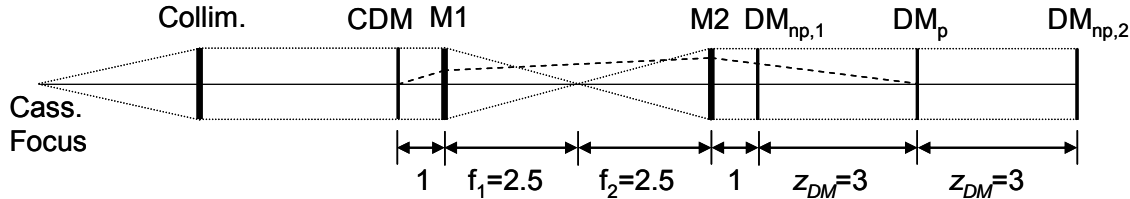
Figure 4.1-15. 3-DM Sequential Arrangement. The DMs are the 3 surfaces on the right side of the figure. DM_p is at a pupil image.

4.1.2.1.3 Use of State-of-the-Art Optics at Critical Locations in the Optical Train

Throughout the FB1 study, the optical train from M3 (the first fold after the secondary mirror) to the coronagraph mask were assumed to have 2–6 nm rms. wavefront quality. The best performance was reserved for the M3 and M4 where the lateral beam walk is most severe. These are also the locations where the largest phase-to-amplitude coupling via wave front propagation occurs.

We have shown that through the use of SoA optics of quality comparable to those manufactured for extreme-ultraviolet applications, the phase-to-amplitude coupling is reduced to tolerable levels (assuming the sequential DM configuration) (Shaklan & Green, 2005b). This change also **reduces beam-walk effects** and may allow the rigid-body pointing and structural stiffness requirements to relax by a factor of a few. The optics have RMS wave fronts of ~ 0.3 nm and are ~10 cm in diameter. For *TPF-C*, there is performance margin for low spatial frequencies up to about 20 cycles per aperture. For larger spatial frequencies, it is desirable to improve the PSD compared to the state-of-the-art.

REFERENCES

K. Balasubramanian, D. Hoppe, P. Z. Mouroulis, L. Marchen, and S. Shaklan. "Polarization compensating protective coatings for *TPF-C*oronagraph optics to control contrast degrading cross polarization leakage." to appear in *Proc. SPIE* **5905** (2005)

Kuchner, M.J., Crepp, J., & Ge, J., 2005, ApJ **628**, 266

Kuchner, M.J. & Spergel, D.N., 2003, ApJ **594**, 617

M.G. Littman, M. Carr, J. Leighton, E. Burke, D. N. Spergel, and N. J. Kasdin, "Phase and amplitude control ability using spatial light modulation and zero path length difference Michelson interferometer," in *Future EUV/UV and Visible Space Missions and Instrumentation*, J. C. Blades and O. H. W. Siegmund, eds., *Proc. SPIE* **4854**, 405-412 (2003).

Shaklan, S.B. & Green, J.J. 2005a *ApJ* **628**, 474

Shaklan & Green 2005b. "Reflectivity and Optical Surface Height Requirements in a Broad-band Coronagraph I: Contrast Floor Due to Controllable Spatial Frequencies." To be published in *Applied Optics* July 20, 2006.

4.1.2.2 Pupil Remapping

In pupil re-mapping (also referred to as Phase-Induced Amplitude Apodization, PIAA), an apodized beam suitable for high contrast imaging is produced by geometrical redistribution of light in the pupil plane rather than selective absorption (Guyon 2003, Traub & Vanderbei 2003, Guyon et al. 2005, Vanderbei & Traub 2005). The apodization is performed by reflection on two aspheric mirrors, as shown in Figure 4.1-16. The system is designed to deliver a beam with a prolate radial surface brightness profile, therefore allowing high contrast (better than 10^{-10}) in the focal plane. In Figure 4.1-16, the two-pupil remapping mirrors are shown in red, and the gray scale corresponds to light intensity. Light from the telescope's unapodized beam enters the system in the top left. After reflection on the two mirrors, a collimated apodized beam is produced and shown here exiting the figure in the lower right.
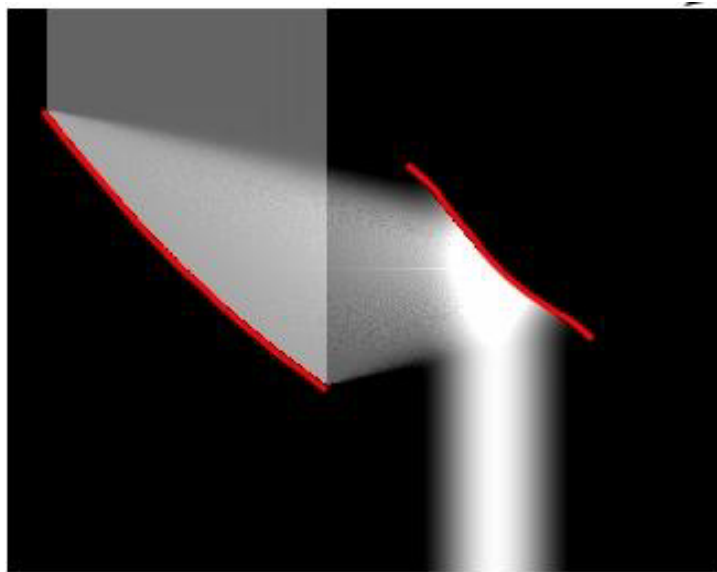
Figure 4.1-16. Cut Through a Pupil Remapping System

A coronagraph utilizing pupil re-mapping offers the following advantages:

- Achieves **high contrast (10^{-11}) at small IWA (**50% max throughput at 1.88 λ/D**).** Allowing for the fact that the planet image needs to be unaffected by the coronagraphic mask for a significant fraction of its orbit and for the finite stellar size as described in Section 4.1.1.2, we therefore expect to be able to detect planets on orbits as small as 2 λ /d. The ability to search for planet at this angular separation (0.1" in the visible) is key to accessing the habitable zone of nearby stars.

- **High throughput (~90%) and 360 degree search area.** The low intrinsic luminosity of planets within the HZ imposes strong requirements on the throughput and efficiency of the coronagraph. The PIAA system throughput is a function of the "instantaneous" bandpass, and ranges from 60% for a system designed to perform $1e^{-10}$ contrast across the whole visible band in one shot to ~90% for a system with independent wavefront correction in

smaller (~0.1 micron wide) bands.

- **Preserves the telescope's angular resolution.** Thanks to the absence of an undersized Lyot pupil plane stop, the planet light is confined into a single λ /d – wide diffraction core. This is critical to minimize the amount of zodiacal and exozodiacal light mixed with the planet light, and provides additional robustness against confusion with exozodiacal features, coronagraphic leaks, background sources and other planets.

- **Can be designed with high level of achromaticity.** Pupil apodization is performed by geometric reflection of mirrors, which is a very achromatic process. When diffraction propagation effects are taken into account, the aspheric shape of the mirrors is a source of chromatic diffraction effects (Vanderbei 2006). The recently developed "hybrid" PIAA design (Pluzhnik et al. 2006), which relies on both PIAA apodization and classical apodization and can be designed to maintain high contrast simultaneously in a broad spectral band, at the cost of a mild loss of light in the classical apodizer(s).

- **Provides appropriate level of robustness to stellar angular size.**

Thanks to the combined effect of small IWA, high throughput and full search area, a pupil re-mapping-based coronagraph can theoretically perform as well as a classical apodization-based coronagraph on a telescope ~3 times smaller in diameter (Martinache 2006). Compared with a Band-limited Lyot type coronagraph, the gain offered is equivalent to a factor ~2 in telescope diameter.

A preliminary laboratory experiment with lenses has demonstrated the principle of lossless apodization of a collimated beam (Galicher et al. 2005). A high contrast imaging coronagraph utilizing pupil re-mapping and wavefront control is currently being assembled at Subaru Telescope (project co-funded by JPL and Japan/Subaru Telescope).

Current theoretical work on this coronagraph include algorithms for wavefront control in a close loop correction and sensitivity to low order aberrations.

REFERENCES

Galicher, R., Guyon, O., Otsubo, M., Suto, H., Ridgway, S.T., 2005, PASP, **117**, 411
Guyon, 2003 A&A, **404**, 379
Guyon, O., Pluzhnik, E.A., Galicher, R., Martinache, F., Ridgway, S.T., & Woodruff, R.A., 2005, ApJ, **622**, 744
Martinache, Guyon, Pluzhnik & Galicher, 2006, ApJ, **639**, 1129
Pluzhnik, E.A., Guyon, O., Ridgway, S.T., Martinache, F., Woodruff, R.A., Blain, C., Galicher, R. 2006, accepted to ApJ
Traub & Vanderbei, 2003, ApJ, **599**, 695
Vanderbei & Traub, 2005, ApJ, **626**, 1079
Vanderbei, 2005, ApJ, **636**, 528

4.1.2.3 Optical Vortex Coronagraph

Conventional coronagraphs utilize an opaque amplitude mask to obstruct starlight, allowing imaging of faint, nearby objects. Unfortunately, the performance of a conventional coronagraph rapidly degrades with increased spectral bandwidth and increased wave-front aberrations. The optical vortex coronagraph (OVC) is a unique and innovative solution to these problems.

Unlike the conventional coronagraph, an OVC makes use of a transparent optical vortex mask (OVM). The layout is similar to a conventional Lyot coronagraph (Figure 4.1-17). The OVM is created by etching a helical relief pattern into an optical surface as depicted in Figure 4.1-18(a). The azimuthally varying surface of the mask transforms the impinging wavefront into a helix. Total destructive interference occurs along the axis of the helix attenuating an on-axis source without significantly affecting the images of other nearby objects (i.e. planets or dust disks). An OVC may be designed to null over a significant portion of the exit pupil, increasing the planet light throughput and decreasing the inner working angle of the coronagraph [Foo et al. (2005) and Mawet et al. (2005)]. Previous work illustrated that compared to an 8th-order Lyot coronagraph, an OVC exhibits less sensitivity to aberrations, obtains higher planet light throughput, and yields a higher planet/star contrast than a conventional coronagraph (Palacios (2005)). Additionally, simulations demonstrate than an achromatic OVM may be designed for broadband operation (Swartzlander (2005)).
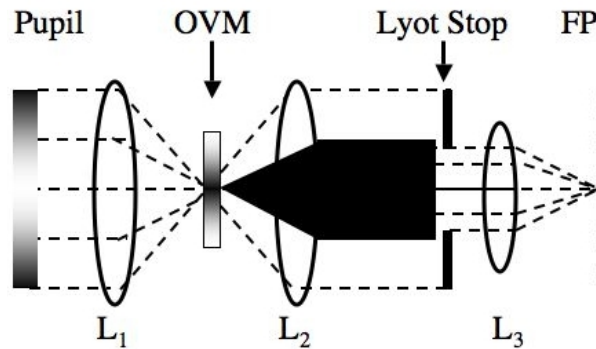
Figure 4.1-17 An Unfolded Model of an Optical Vortex Coronagraph. Lens (L1) Represents the Telescope Optics, which Focus the Light from the Entrance Pupil onto an Optical Vortex Mask (OVM). Lens (L2) Collimates the Light forming an Exit Pupil where we Place a Lyot Stop. A Third Lens (L3) Re-Images the Light to the Final Focal Plane at (FP).

A key performance criterion used to compare various coronagraph architectures is the sensitivity of the system to low-order aberrations (Green and Shaklan (2005)). The OVC demonstrates an aberration sensitivity that is proportional to the OVM's topological charge (m), which is equal to the phase increase in a single revolution about the axis of its helical surface divided by 2π radians (Figure 4.1-18). Previous work quantified this proportionality, giving a 2mth order sensitivity to tip/tilt aberrations (Foo et al. (2005)). Therefore, an m=4 OVM will obtain an 8th order sensitivity to tip/tilt aberrations, rivaling that of the 8th order amplitude occulting masks presently under investigation for high contrast imaging. The contrast obtained from an m=5 OVC (Lyot stop = 0.52 x pupil diameter) at 4 λ/D is plotted in Figure 4.1-19 for several low-order Zernike polynomials. In this configuration, the throughput at 4 λ/D is equal to that of an 8th-order mask but the OVC aberration sensi-

tivity is substantially relaxed. The OVC allows one to trade throughput with aberration sensitivity by applying a smaller or larger topological charge.
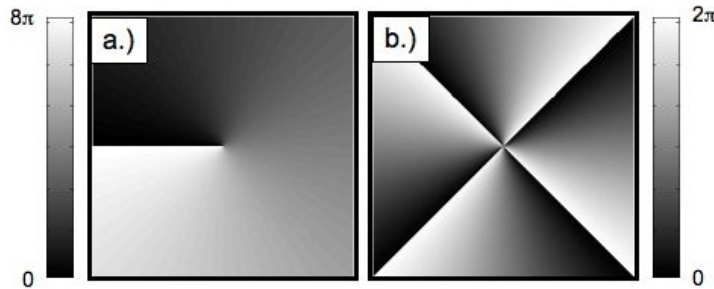
Figure 4.1-18 A Comparison of the Relief Patterns of Two Types of m=4 Vortex Phase Masks. a.) The Helical Relief Pattern of an m=4 Single Spiral Vortex Mask. b.) The Multi-Ramp Relief Pattern of an m=4 Propeller Vortex Mask. The Topological Charge of the Mask is the Total Phase Change around the Center of the Spiral/Propeller Divided by 2p.

Since the aberration sensitivity decreases with increasing values of m, OVMs with higher topological charge are desirable. However, construction of a single-spiral OVM with a topological charge m>4 is difficult with current technologies. One way to alleviate this concern is by clustering several helical phase ramps in a propeller shape, creating a propeller OVM. This configuration produces the same effect as a single spiral OVM (Figure 4.1-17) while decreasing the etching difficulties. It is also possible to combine several vortex masks of low topological charge to obtain the same result as a single spiral OVM. For example, placing two m=2 vortex masks together will have the same effect on starlight as a single m=4 vortex mask. Alternative architectures that make use of this characteristic include stacked masks, re-imaged vortex masks, and multiple vortex beam recombination.
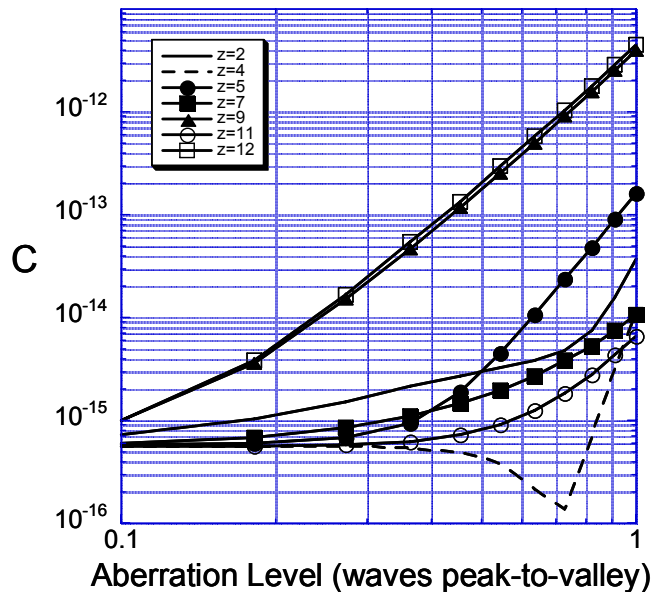
Figure 4.1-19 Plots of Contrast vs. Aberration Level (Waves Peak-to-Valley) Depicting the Aberration Sensitivity of an M=5 Vortex Coronagraph to Low-Order Zernike Modes (Z=2-12). Only one of each of Tip/Tilt, Astigmatism, Coma, and Trefoil, are Shown Since their Curves were Nearly Identical.

Additionally, the operating spectral bandwidth of an OVM may be significantly increased by depositing a glass layer on top of the spiral substrate layer (Swartzlander (2005)). By choosing glasses with complimentary dispersion properties, the induced helical phase shift of the mask may be equalized over a wide spectral bandwidth ($\Delta\lambda$ ~100nm). This allows for a vortex of equal topological charge (i.e. equal nulling) to form for each wavelength within the spectral range of interest. Simulations of an OVM composed of an F5 Schott glass spiral substrate and a deposited layer of N-SK15 Schott glass demonstrate less than $\pm$ 2.5% change in the topological charge over an operating bandwidth of ~140nm (central wavelength = 550nm). This small variation in topological charge doesn't degrade the on-axis nulling of the OVM.

REFERENCES

G. Foo, D.M. Palacios, G.A. Swartzlander Jr. **30**, 3308 (2005).
D. Mawet, P. Riaud, O.Absil, and J. Surdej, APJ **633**, 1191 (2005).
D.M. Palacios, Proc. SPIE **5905**, Article # 5905-25 (2005).
G.A. Swartzlander Jr., Opt.Lett. **30**, 2876 (2005).
J.J. Green and S.B. Shaklan, Proc. SPIE **5170**, 25 (2003).
P.G. Halverson, M.Z. Ftaclas, K. Balasubramanian, Proc. SPIE **5905**, Article # 59051I (2005).
G.A. Swartzlander Jr., Opt. Lett. **26**, 497 (2001).

4.1.3 Instrument Concept Studies

4.1.3.1 CorSpec Instrument Description

The coronagraphic spectrograph (CorSpec) team explored an instrument concept that would fulfill all four scientific objectives of *TPF-C* by:

- Spectrally characterizing the atmospheres of detected planets;
- Directly detecting terrestrial planets in the habitable zone around nearby stars;
- Studying all constituents of a planetary system including terrestrial and giant planets, gas and dust around sun-like stars of different ages and metallicities;
- Enabling simultaneous, high-spatial-resolution, coronagraphic spectroscopy of AGNs, supernovae, and other objects requiring high-contrast spectroscopy.

The instrument concept consists of a set of four integral field spectrographs (IFS), each covering a spectral band $\Delta\lambda/\lambda$~22% wide, and together covering the full spectral range of *TPF-C*. Each IFS has a 134 × 134 microlens array to obtain an R~70 spectrum of each Nyquist-sampled image element in the coronagraphic field, and each uses a photon-counting charge-multiplication CCD to record the ~18,000 spectra. Figure 4.1-20 shows the layout of one of the four spectrographs including calibration hardware. Figure 4.1-21 shows a simulated spectrogram of the 18,000 spectra.
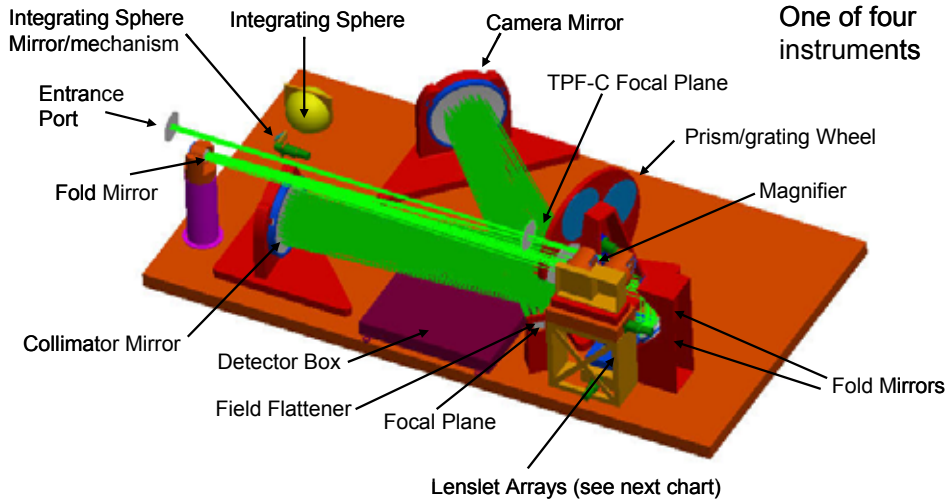
Figure 4.1-20. Layout of One of Four IFS Units
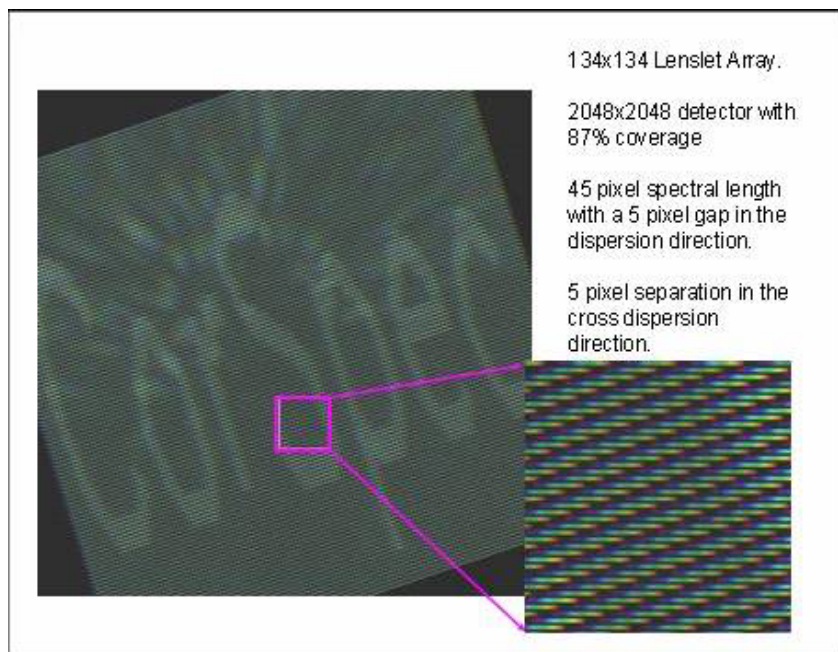
Figure 4.1-21. Simulation of a CorSpec Observation of a Fanciful Source

Each of the 18,000 spectra will be extracted and inserted into a data-cube like the one shown in Figure 4.1-22 . The dimensions of the data-cube are $134 \times 134 \times 45$. The data-cube can then be sliced and/or collapsed to form:

- Monochromatic images at a selected wavelength;
- Spectra of planets or unresolved disk structures;
- Pictures of wavefront sensing performance.
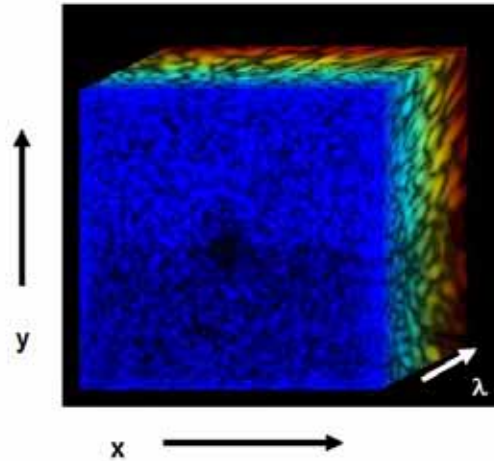
Figure 4.1-22. IFS Data Cube

While the CorSpec concept is compatible with all types of masks in *TPF-C*'s starlight suppression system (SSS), it assumes that the facility SSS is composed of four independent units, each optimized for a given spectral band, and that each unit is capable of suppressing the starlight to an acceptable level over a passband 22% wide. Members of the CorSpec team have developed a preliminary concept design of the starlight suppression system.

4.1.3.2 CorECam

The CorECam instrument concept study addressed the requirements and science program for *TPF-C*'s primary camera. The CorECam concept has been evaluated on the basis of the *TPF-C* and Starlight Suppression System (SSS) architecture presented in the PIP and FB1 documents.

CorECam provides a simple interface to the Starlight Suppression System (SSS) provided by the *TPF-C* Project, and comprises two camera modules (one per SSS polarization channel), each providing a visible, and near-infrared (NIR) camera focal plane camera (Figure 4.1-23). In its primary operating mode, CorECam will conduct the core science program of *TPF-C*, detecting terrestrial planets at visible wavelengths. CorECam additionally provides the imaging capabilities to characterize terrestrial planets, and con-duct an extended science program focused on investigating the nature of the exosolar systems in which terrestrial planets are detected. An alternative to this architecture would be three visible and one infrared channel, fed by a dichroic chain.

The CorECam science program focuses on detecting terrestrial planets, with an extended program to characterize these terrestrial planets and the exosolar systems in which they are found. One additional goal, however, has further motivated the design of our instrument. We believe that understanding how these exosolar systems are populated by planets and dust is fundamental in addressing the larger question regarding the origins or life. Indeed, addressing this question may actually help focus the search for systems with terrestrial planets. The CorECam strawman filters (Figure 4.1-24) have been chosen to optimize the detection and characterization of terrestrial planets, while providing flexibility to photometrically characterize planets with un-expected spectral characteristics, as well as gas giant planets.
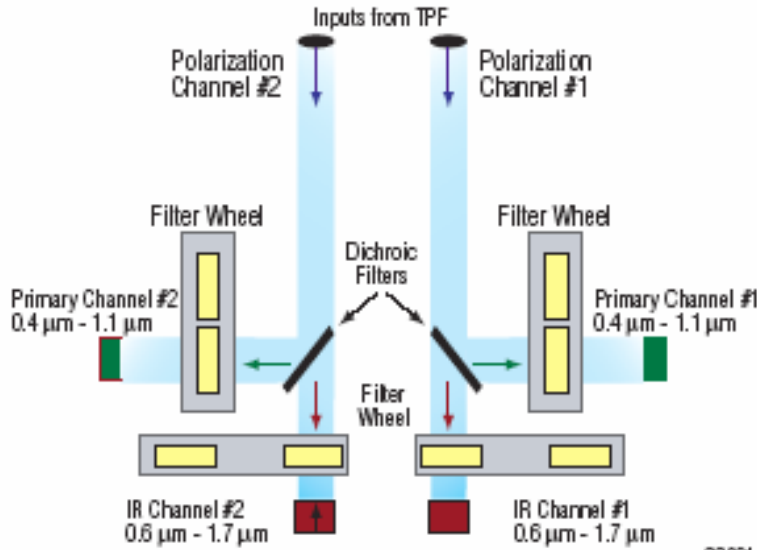
Figure 4.1-23. Schematic of the Baseline CorECam Design
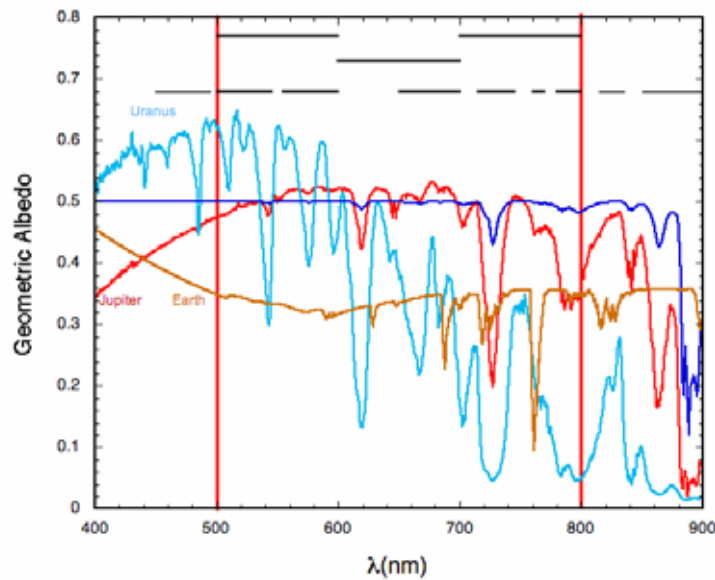
Figure 4.1-24. CorECam Filter Complement, Shown with Spectra of Earth, Jupiter, and Uranus

CorECam provides additional capabilities to *TPF-C* beyond the core science requirement by going to longer wave-lengths. The CorECam's near-infrared capabilities can be used to characterize a subset of terrestrial planets detected at wider angular separations. CorECam's expanded wavelength coverage allows more flexibility to study all types of terrestrial planets, including those not known in the Solar system. CorECam's images of terrestrial planets in the habitable zone of nearby stars could simultaneously reveal extrasolar giant planets (EGPs) and super-Earth planets (SEPs), i.e. predominantly rocky planets substantially more massive than Earth. CorECam will also observe the interplay between planets and planetesimal reservoirs, observed as disks, and trace their planetary system architectures.

In order to evaluate the performance of CorECam we have developed a comprehensive, end to end model using OSCAR (Figure 4.1-25). Design parameters from the *TPF-C* flight baseline-1 (FB1) were collected and input to OSCAR along with the set of defined science filters for CorECam. The output of the OSCAR consisted of star/planet images as "seen" through *TPF-C* with wave-front/amplitude control and with residual speckle and detector effects. For each planet to star angular separation, an ensemble of images were generated and averaged to obtain the contrast and error bars. Image post-processing was also incorporated via rotation and averaging and by matched filtering (sharpness), the contrast was calculated and the results parameterized. The CorECam model provides an independent assessment of focal plane contrast as a function of wavefront error. A number of key conclusions can be made based on our model results:

- Contrast is not uniform as a function of IWA, as shown in Figure 4.1-26.

- Broadband imaging will degrade the inner working angle.

- Image processing is required to detect extrasolar terrestrial planets, as shown in Figure 4.1-27. Any relaxation of *TPF-C*'s wavefront error requirements results, due to sub-allocation of requirements, could result in more demanding raw data processing requirements

- A significant fraction of targets can be imaged in the near-infrared providing improved photometric characterization.
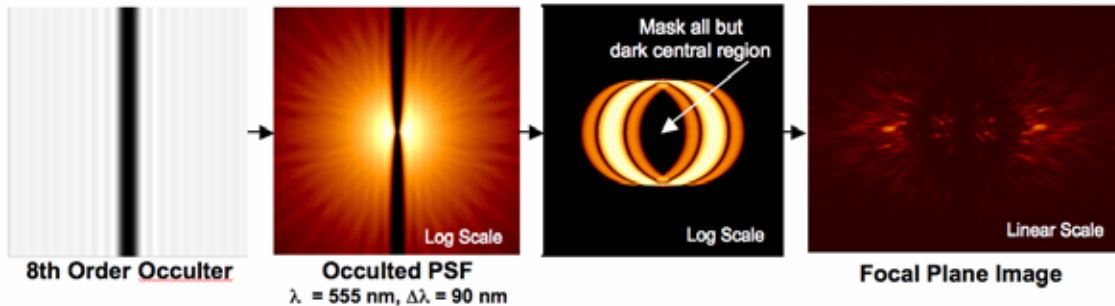
Figure 4.1-25. Propagation through Starlight Suppression System

OSCAR modeling of *TPF-C* and CorECam is also being employed to address issues related to Wavefront sensing and control. In particular we propose several alternative approaches for CorE-Cam which might significantly enhance the performance of *TPF-C* by relaxation of stability requirements.

Phase retrieval is performed simultaneously from the occulter bright image and coronagraphic image. One way to mitigate the low photon counts is to deliberately introduce a known error into the system, such as focus, or partially mispointing, or wave-length changes a technique we call Speckle Straddling. We also recommend the study of speckle nulling in combination with phase retrieval to increase focal plane coverage. The use of parallel versus serial DMs also provides possible benefits

in the form of chromatic correction of both amplitude and wavefront errors that occur at both pupil and focal planes.
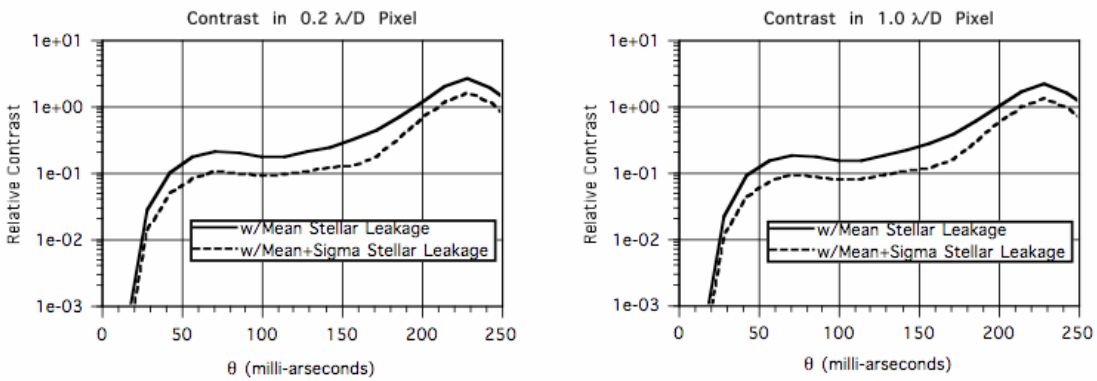
Figure 4.1-26. Planet-to-Star Mean Contrast with Error Bars
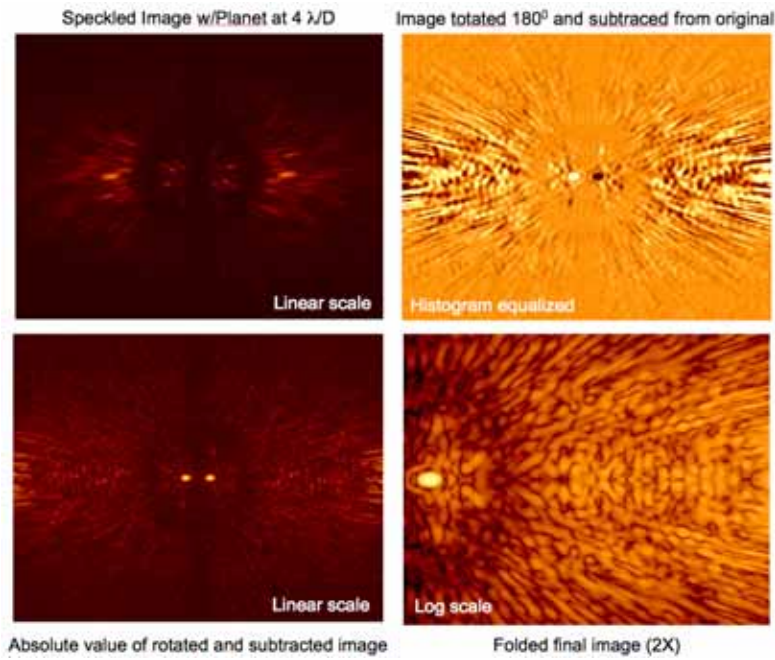
Figure 4.1-27. Raw and Processed Focal Plane Image

4.1.3.3 Broadband Camera/Spectrometer for Terrestrial Planets

Angel and Guyon have led development of an instrument with integrated star suppression system for imaging and spectroscopy of terrestrial exoplanets with 0.5-1.5 μm cover. It combines the suppression methods of pupil mapping or 'phase induced aperture apodization method' (PIAA) and anti-halo apodization (AHA). The two methods in conjunction promise not only close inner working distance, but high sensitivity over a full 360° field without the losses in resolution and flux inherent in the baseline Lyot system. The instrument incorporates dichroic mirrors to allow simultaneous full spectral cover from 0.5–1.5 μm. The combination of increased throughput, resolution, field cover and bandwidth yields more than an order of magnitude reduction in integration time compared to the baseline design. This combined with closer inner working angle allows for a much richer observing program.

In the PIAA method apodization is made with two mirrors figured so that uniform-amplitude light incident at the first mirror is reshaped to illuminate the second mirror with higher density in the middle and a tapered (apodized) profile toward the edge. The second mirror is shaped to compensate the wave front and form diffraction limited images with a sharp core and low wings at the image plane. Because there is no Lyot stop, no pupil shear, and no masking of the pupil, this approach has very high throughput and also avoids the image broadening of the other methods. It focuses the starlight into a sharp spot enabling detection of planets perhaps as close as 2 λ/D radius from the star. Since these apodizers only do a small part of the beam shaping work, they do not have the same challenging requirements or light losses as a classic pupil apodizer.

AHA is a new interferometric technique to sense and suppress the weak residual starlight halo that becomes apparent after the diffraction halo is removed by PIAA and the stellar core blocked by focal plane field stop. The suppression is accomplished by destructive interference with an explicitly created anti-halo which has the same amplitude but opposite phase to that measured for the residual halo. Like PIAA, AHA loses almost no light from the planet and works over the full angular field. The anti-halo is created explicitly from the coherent core starlight removed at the focal plane, with the aid of two deformable mirrors in the Michelson configuration conjugated to the final image plane. The two opposing halos are combined at a semitransparent beamsplitters where only the starlight halo is cancelled. The planet light itself is incoherent and cannot be suppressed by interference. The measurement of the complex amplitude of the halo is made within the same interferometer. Halo images are recorded to show the effects of interference with starlight reference beams of uniform amplitude and different phases, and from these the phase and amplitude of the halo speckles is derived by standard phase shifting metrology method. The photon noise of the zodiacal background does not interfere with this measurement provided the reference beam intensity is made brighter. In operation the interferometer will cycle between these measurement and nulling modes, with the same photon counting detector array serving to both measure the halo complex amplitude and as the science detector. In this way common path errors are completely eliminated.

Both the PIAA and AHA methods work best over a limited bandwidth, and so our implementation calls for division of the incoming light into multiple wavelength channels by cascaded dichroic mirrors, before the focal plane stops. In this way the planet can be observed over spectral channels covering simultaneously 0.5–1.5 microns. Photon counting detectors with negligible dark count will be used, so signals from the different spectral bands can be co-added with no noise penalty. Spectro-

scopic measurements at resolution higher than the channel bandwidth will be made within the individual channels.

We note that if this instrument were adopted for *TPF-C*, the *HST-JWST* paradigm in which instrument teams are selected independent of the telescope would break down. This is because the science imaging and spectroscopy and the star suppression and wavefront correction systems are of necessity completely integrated, with the same imaging arrays providing the science data as well as the wavefront and speckle nulling data. At the start of this award, *TPF-C* was working on the premise that there would not be time to develop revolutionary technologies such as PIAA and AHA to the TRL needed for a Phase A in 2006. Now that *TPF* is delayed, there is time.

The funding provided by this award has allowed us to complete more extensive analysis of PIAA and AHA. At the same time advances have been made under separate funding toward lab tests to be made during the coming year. The key activities are Guyon's lab test of PIAA, funded by the *TPF* project, and Codona's test of AHA funded by NASA HQ. Optics to test PIAA at the diffraction limit are now nearing completion, and the components for the first AHA system have been ordered.
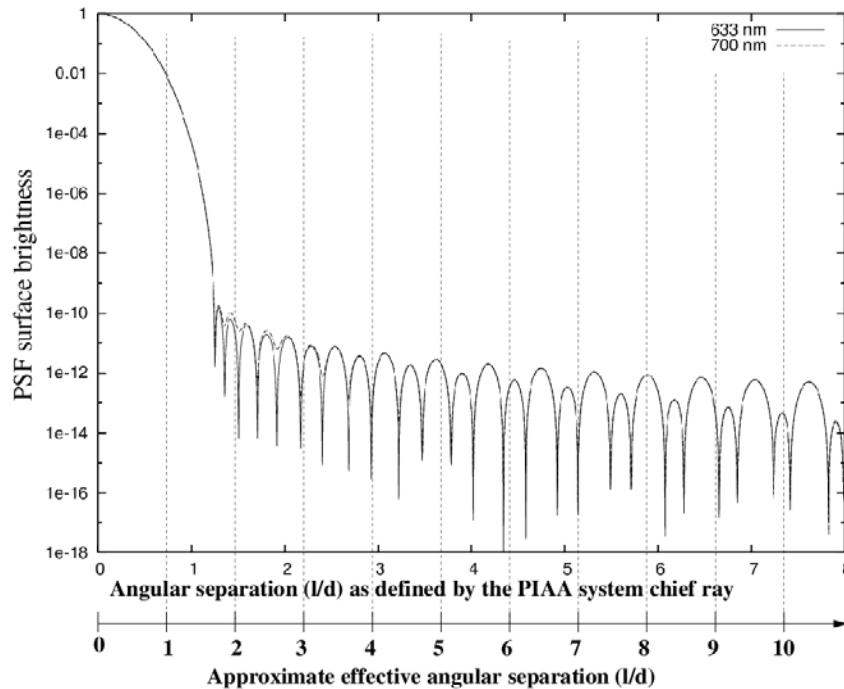
Figure 4.1-28. On-axis PSFs for an Advanced Hybrid PIAA Design optimized for robustness against chromatic diffraction propagation effects at 633nm. This particular design can maintain better than 1e^{-10} contrast in a 60% bandwidth with a 76% throughput. The PSFs are shown here in the intermediate focal plane of the PIAA, where a focal plane occulter is placed to block starlight. Plate scale in this intermediate focal plane is difficult to define, as off-axis sources exhibit strong aberrations due to the remapping effect. Two plate scale units are therefore shown: the "chief ray" plate scale, a well-defined unit obtained geometrically by the central ray of the PIAA system, and the more approximate "effective" plate scale. The "effective" plate scale indicates approximately where most of the light of an off-axis source falls in this highly distorted intermediate focal plane. Plate scale is easier to measure in the final focal plane of the PIAA, which is free of such distor-

tions. For a full PIAA system designed as shown in this figure, the IWA (where the planet light throughput is 76% x 0.5 = 38%) is approximately 1.9 λ/d.

Assuming these first demonstrations are very successful, it will be highly desirable to prove the PIAA-AHA concept with a smaller space mission. Indeed, because PIAA achieves closer inner working distance for given aperture, even the smaller apertures that might now be affordable could have a valuable science program, including exploration of the nearest stars for Earthlike planets.

The progress made during this study in developing the concept and different optical elements of the system is summarized in Table 4.1-7.

Table 4.1-7. Design Progress

Element	Purpose	Progress	By
1. PIAA	Remove diffraction rings from star	Improved performance by a hybrid design in which the extreme edge shading is obtained by classical intensity apodization of 5–25% of the total flux (Figure 4.1-28). Sensitivity to pointing errors studied.	Guyon, Pluzhnik, Vanderbei
2. Dichroic mirror tree	Wavelength channel separation	Preliminary design and tolerance analysis shows that many bands separable while maintaining high throughput and good wavefront quality.	Macleod
3. AHA	Suppression boost	Specific optical design developed for the AHA interferometer, incorporating relatively low precision segmented MEMS mirrors to create the anti-halo	Codona, Angel, Peng
4. 0.5–2 λ/D guider	Tip/tilt and low order sensor < 2λ/D	New concept introduced for phase diversity sensor fed by reflecting annulus, provides picometer level measurement of tip/tilt and low order errors	Guyon
5. Photon counting imagers	Sense exoplanets and complex amplitude of star halo in search field	Single photon imaging array detectors covering 0.5–1.5 μm range studies (CCDs with gain, image tubes with IR photocathodes and transition edge superconductor sensor arrays (TES)	Woodgate, Angel

4.1.3.4 Wide-Field Camera

One Instrument Concept Study (ICS) focused on a program of general astronomy for *TPF-C* and found a promising fit for imaging with a wide-field camera (WFC). Within the guideline that general astronomy should not affect the number or nature of planetary observations, the WFC has unique and truly astonishing scientific potential. It would be an instrument unrivaled by any other currently planned, on the ground or in space.

Operating in parallel mode, taking no time from the coronagraph, the WFC would obtain the deepest and widest survey of the cosmos ever (Figure 4.1-29). The survey would address multiple problems in the high-redshift universe, notably galaxy evolution, which is poorly understood at the current time and will not be resolved by Webb's small sample size. In order to understand which early galaxies evolve into which modern ones, we need excellent resolution, broad wavelength coverage, high sensitivity—and a huge sample. Good statistics are required to key galaxies to their clustering properties, in order to follow populations of galaxies in time. No currently envisioned observing program besides *TPF-C*'s deep parallel survey can perform this epochal research.

In a five-year mission, parallel observations with the WFC could produce a survey of 10 $\deg^2$ of sky to beyond 30th magnitude. Such a survey would comprise 1000 times more cosmic volume than the various Hubble deep fields and greater sensitivity than any of them.
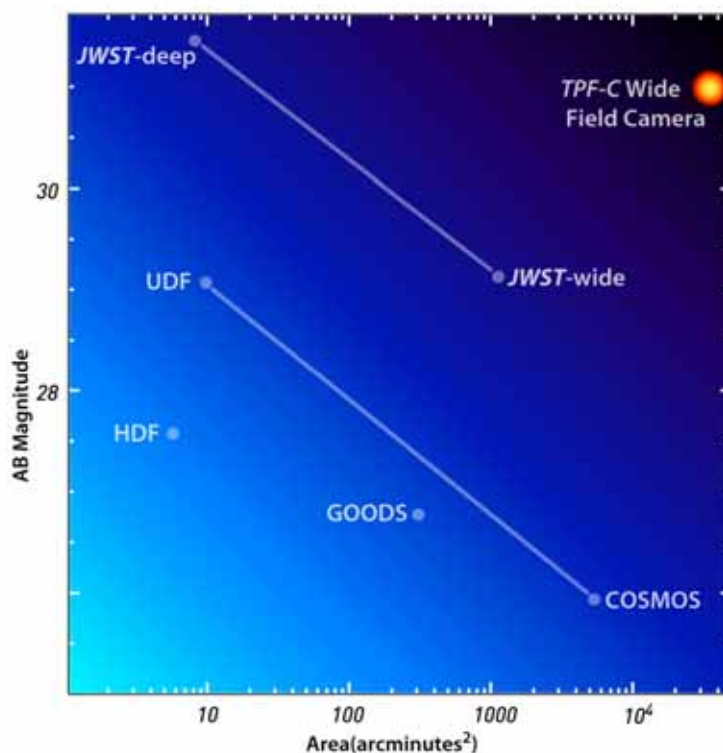
Figure 4.1-29. The Deep Parallel Survey of the *TPF-C* Wide-Field Camera (WFC) will surpass current and future space-based surveys by order of magnitude in both depth and area. (Shown for 800 nm.)

The powerful features of *TPF-C* for general astronomy are its great aperture for collecting light, and its sharp and stable point-spread function, useful for precision photometry, astrometry, and morphology. The limiting magnitudes for the coronagraph and WFC will be similar: the typical coronagraphic exposure time of 50 hours (to detect a 32nd magnitude terrestrial planet located 0.1 arcsec from a 6th magnitude target star) will permit the WFC to record starbursts in an L^* galaxy at $z = 4$, reach a 12 Gyr main-sequence turnoff for stellar populations in galaxies at 2 Mpc, and measure the proper motion of any solar-type star in our galaxy (except for extinction).

In pointed mode, the WFC could extend Hubble-type imaging to 10× greater sensitivity and 3× better resolution for physical studies of faint and distant galaxies and clusters of galaxies, records of star-formation in nearby galaxies, and star-forming regions in our own galaxy (see Figure 4.1-30). Only the WFC can fully investigate objects and phenomena found by Spitzer, Chandra, or Webb. In the next decade, no other instrument but the WFC is planned to replace Hubble's sharp and stable point-spread function over a wide field of view, which have proven invaluable across the frontiers of modern astrophysics.

Figure 4.1-30. The Improved Resolution and Sensitivity of *TPF-C*'s WFC Compared with Webb and Hubble. The Simulated Object is an L* galaxy at *z* = 4 Observed in a Broadband Filter Centered at ~900 nm.

Such powers would not be surprising for so large telescope optimized for general astronomy. However, it is unexpected and remarkable that these powers may be available at the same time the coronagraph is searching for planets around bright stars.
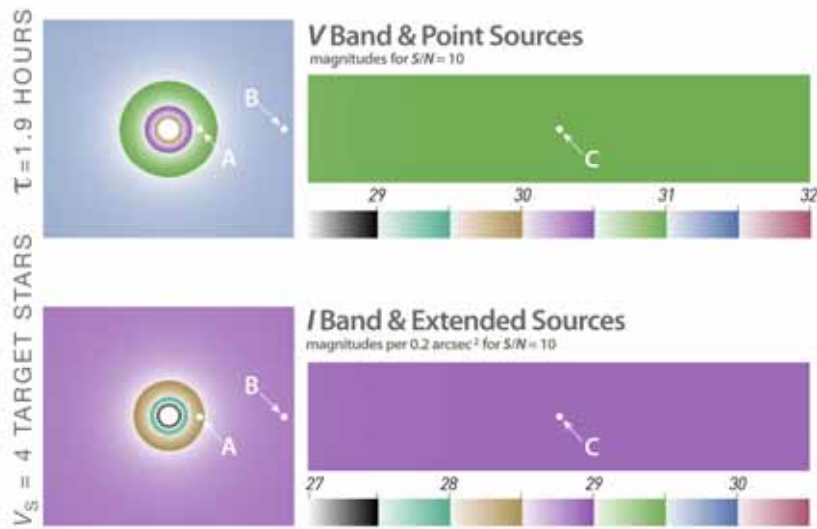
Figure 4.1-31. The Parallel-Mode Limiting Magnitudes—Approaching or Exceeding 30th Magnitude—For the two fields of View (FOVs) in the ICS. The Exposure Time is Dictated by the Coronagraph Searching A V = 4, I = 3.31 Target Star to its Sensitivity Limit (Δmag_0 = 25). The Degradation Of WFC Limiting Magnitudes is Greater than One Magnitude only within about 20" of the Coronagraphic Aperture.
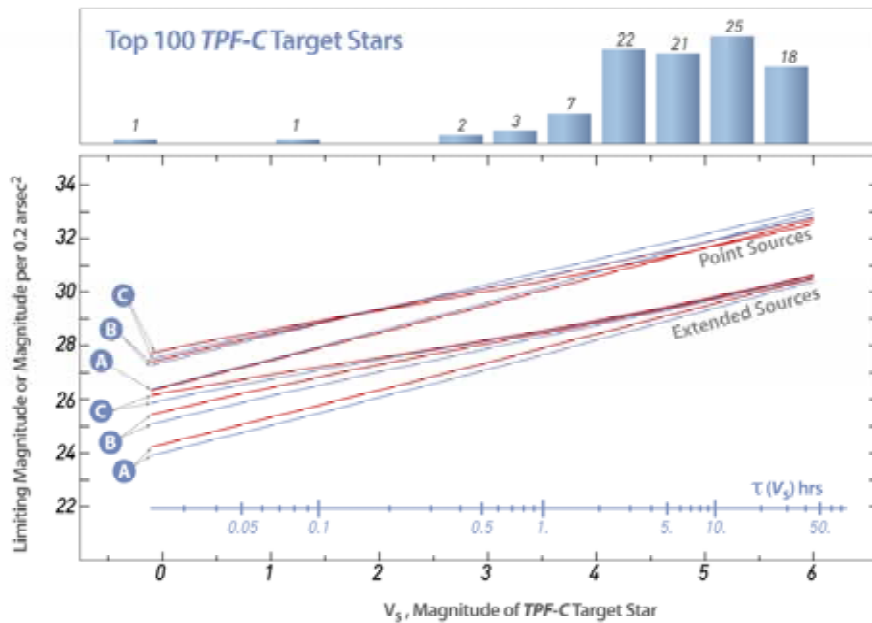
Figure 4.1-32. The Limiting Magnitude for Point Sources will be fainter than 30th magnitude for WFC observations in parallel with planet searches of target stars fainter then 4th magnitude, which includes 86 of the 100 top-ranked *TPF-C* target stars. Letters refer to positions in Figure 4.1-31. Red for I band, blue for V band.

For purposes of its investigation, the ICS considered the parallel and pointed modes of the WFC to be instrumentally and operationally distinct. The nominal 16 arcmin² square FOV for pointed observations is located on-axis. Outside this, the wedge-shaped FOV for parallel observations extends nominally to 10 arcmin off axis. The focal-plane design for the on-axis/square/pointed FOV offers six pass-band filters covering 400–900 nm and detectors with half-critical sampling compensated operationally by half-pixel dithering. The design uses a dichroic beam-splitter to divide the off-axis/wedge/parallel FOV into two focal planes, covering 425–850 nm and 850–1700 nm. Each focal plane has three filters and a grism, and the detectors offer third-critical sampling compensated by third-pixel dithering. These two octaves of wavelength will permit the parallel survey to fully characterize the spectral energy distributions of objects in the parallel survey at a single epoch.

The genius of the off-axis FOV is the advantage of the roll maneuvers for the coronagraphic observations. As the telescope rolls around a coronagraphic target star, the cumulative survey area in parallel mode increases as the square of the off-axis extent. The ICS team feels that an off-axis extent three times smaller than nominal, or 3 arcmin (equivalent to the on-axis FOV), would result in an inadequate survey, of only 1 deg². An extent three times larger than nominal, or 30 arcmin, would produce a survey of 100 deg², which would, for example, put the instrument in the range of the supernova projects for the Joint Dark Energy Mission.

While NASA included space for the on-axis FOV in the call for ICS proposals, it did not foresee the strong interest in an off-axis FOV, which was consequently not accommodated in the guidelines.

Therefore, the compatibility of the off-axis FOV with the baseline telescope and spacecraft designs is a top issue. To address it, the ICS team developed new tools and metrics.

To address the question of acceptable off-axis performance, the WFC ICS team developed and optimized an instrument design, from which the optical designer generated aberrations for each filter and selected wavelengths as a function of field position. The degradation in signal-to-noise ratio (SNR), expressed as a delta limiting magnitude for point sources, was evaluated for sampling and aberrations separately—a new approach to camera design. The ICS team adopted as a working criterion that the delta magnitude in SNR due to aberrations alone should not exceed that due to the choice of sampling alone. It is possible that alternative telescope designs could improve off-axis aberrations without compromising the quality or stability of the wavefront in the coronagraph.

Packaging constraints led the ICS team to a camera design with all refractive optics. CCD and HgCdTe technology were selected for the short and long wavelengths, respectively. Problems from cosmic rays seem acceptable.

The ICS team addressed scattered light due to dust and micro-roughness on the *TPF-C* telescope mirrors. Their performance model for the WFC is valid if dust contamination is less than 4% coverage for 10 micron equivalent dust particles, and if scattering due to micro-roughness is $\leq 10\%$ of the Hubble level. These are reasonable specifications.

The ICS team studied the question whether the WFC observing program could rely on the pointing control system developed for the coronagraphic observations. For pointed observations, this means being able to guide the telescope accurately with ~20th magnitude field stars. The project affirmed that this performance is available, assuming the option to pick off the star image in the coronagraphic FOV with a mirror, to feed light to the guidance sensor.

After investigating the opportunity of a WFC for six months, the ICS team is excited about the scientific and technical possibilities. The WFC—instrument and operations—appears technically feasible, with low or no impact on the coronagraphic program. The team believes that community reviewers will rank the scientific program of the WFC on *TPF-C* highly. They recommend that NASA include a WFC in the plans for this mission, including awarding it some fraction of mission time for pointed observations.

A WFC is a low-risk option for *TPF-C*. It would add greatly to the science return by effectively doubling the mission at only a marginal increase in cost and with a loss in mission time for exoplanets that could be as low as zero if NASA assigned no pointed time to the WFC. The ICS team for this study strongly endorses the WFC as beneficial and feasible, and recommends that it be accorded the stature of a full scientific partner in the *TPF-C* program and project.

4.1.3.5 Visible and Infrared Nulling Coronagraph Spectrometer

4.1.3.5.1 Executive Summary

This report outlines a concept study for a high contrast instrument for the Terrestrial Planet Finder Coronagraph (*TPF-C*) mission. The objectives are to develop a nulling coronagraph based imager and spectrometer concept that will increase the number of planets *TPF-C* detects, and will expand the wavelength range of the spectrometer into the near-IR to enable detection of additional unique visible biomarkers. This instrument utilizes an alternative starlight suppression system (SSS) based on the principles of nulling interferometry, which allows inner working angles (IWA) within 2–3 λ/D to be obtained, and also to measure low resolution (R = 80) spectra. Equally important, this concept contains a post starlight suppression wavefront sensor (or calibration wavefront sensor) to increase the achievable contrast level, and to substantially decrease stability requirements during integration.

Like band-limited Lyot Coronagraphs, the nulling coronagraph can, in theory, achieve the required 10^{-10} suppression of starlight within an IWD of 2 λ/D. Coverage of the 0.5 ~1.7 μm wavelength range is done in intervals of 25% bandwidth. The search for planets will be conducted at short wavelengths, where the IWA is smaller. Extending spectroscopy to 1.7 μm, the visible and near infra-red signatures of likely atmospheric constituents include oxygen, ozone, water, methane, and carbon dioxide, some combinations of which are considered to be bio-signatures.
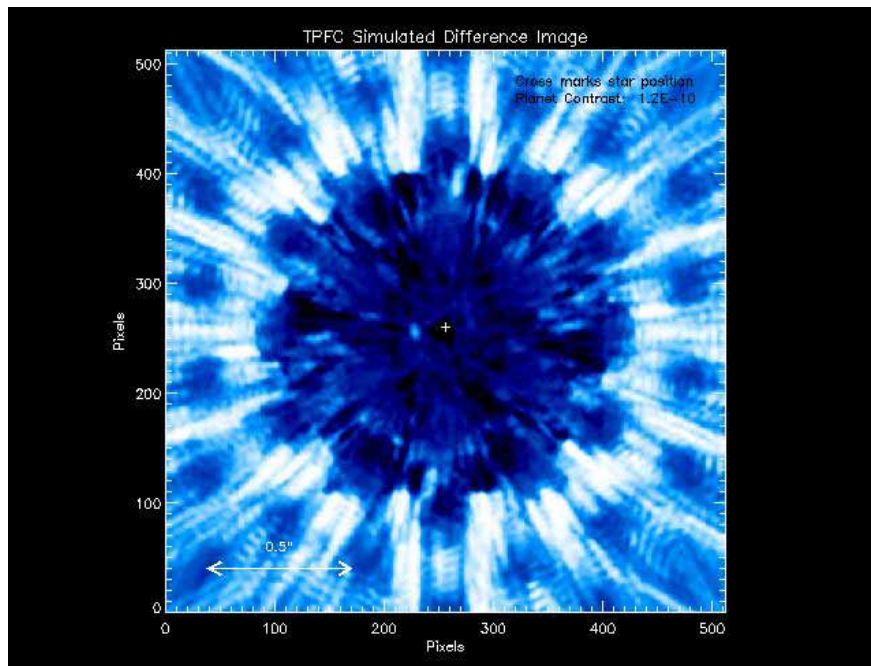
Figure 4.1-33. Simulated Image from *TPF-C* of an Earth-Like Planet Orbiting Around a G2V-Type Star at 10 pc.

4.1.3.5.2 Science Drivers: How Many Stars Can Be Surveyed by the Nuller?

Like 4th-order Lyot coronagraphs, the nulling coronagraph, or simply the nuller, has a couple of advantages over the baseline 8th order mask Lyot coronagraph. One is higher photon throughput, and

the second (more important) is the ability to work at 2 λ/D rather than 4λ/D. This comes at the expense of greatly increased sensitivity to low-order instabilities in the system (e.g., thermal warping of the primary mirror). Starting with *TPF-C* project code, using comparable detection sensitivities, we have found that on an equal signal to noise basis, that if *TPF-C* were to repeatedly visit a moderate number of stars, 30~50, the 4th-order nuller would be able to visit those objects between 2~3 times as often for a fixed integration time, increasing the geometric completeness (and the number planets found) by roughly a factor of ~2.5. (Figure 4.1-34). On the other hand, the nuller has substantially more optical surfaces than the coronagraph, which is not accounted for in Figure 4.1-34.
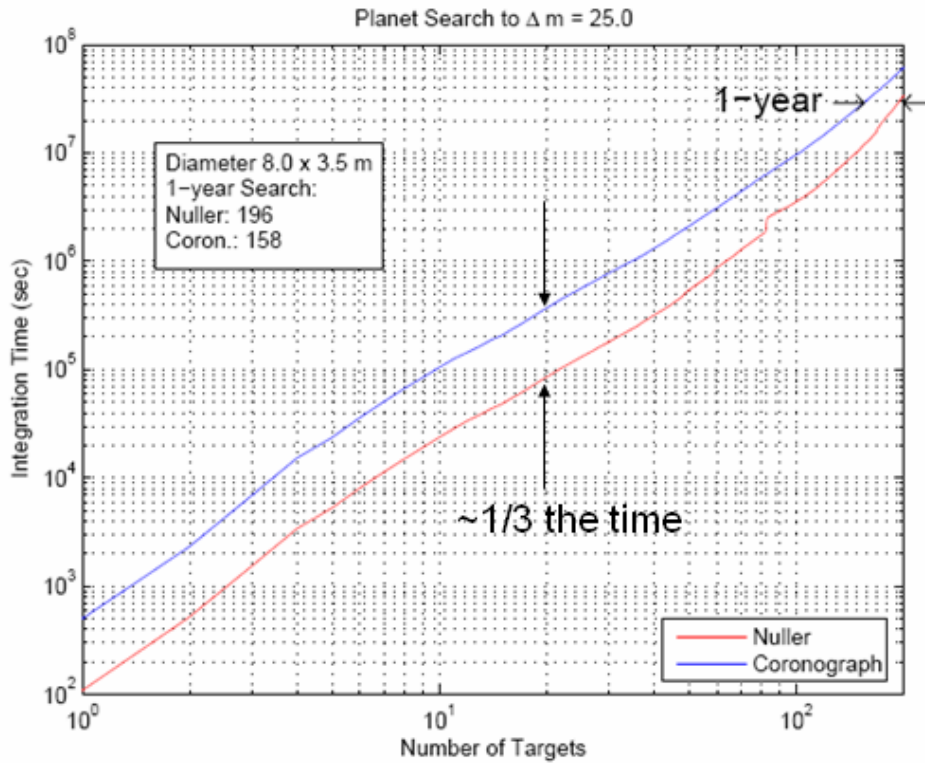
Figure 4.1-34. Throughput Advantage of Nulling Coronagraph to See More Targets in a Fixed Observation Period

In assessing the number of potential targets for the nulling coronagraph, we search through the list of Hipparcos stars < 30 pc from the Sun brighter than 7 mag. We can calculate the number potential targets at 2 λ/D and 4 λ/D for several scenarios. The scenarios are 1) discovery at 0.5 ~ 0.6 μm, 2) detection of oxygen at 0.78 μm, and 3) detection of near IR molecular signatures at 1.6 μm. Table 4.1-8 below lists the number of potential target stars around which an Earth can be detected at various wavelengths for a nuller (2 λ/D) and the baseline coronagraph (4 λ/D).

Table 4.1-8. Number of Potential Targets vs. Wavelength

Wavelength	Detect Earth (0.5~0.6 μm)	Det Oxygen 0.78 μm	NIR 1.6um
2 λ/D	276	131	20
4 λD	59	19	3

4.1.3.5.3 Nulling Architecture Concept for *TPF-C*

Our conceptual instrument for *TPF-C* is called the 'Boomerang' configuration and is shown in Figure 4.1-35. It chief benefit is that the shear which controls the IWD and the control for phase can be adjusted independently: And at the same time the deformable mirror is only tilted slightly (15 degrees) so that it can be sharply imaged to an intermediate pupil. The candidate *TPF* configuration uses 2 of these 'Boomerangs' stacked atop the other. The nulled output of the first interferometer is directed to a second identical nuller via a vertical rooftop mirror. The second nuller works in reverse, consequently the output of the second interferometer is located near the input position at the first beamsplitter.
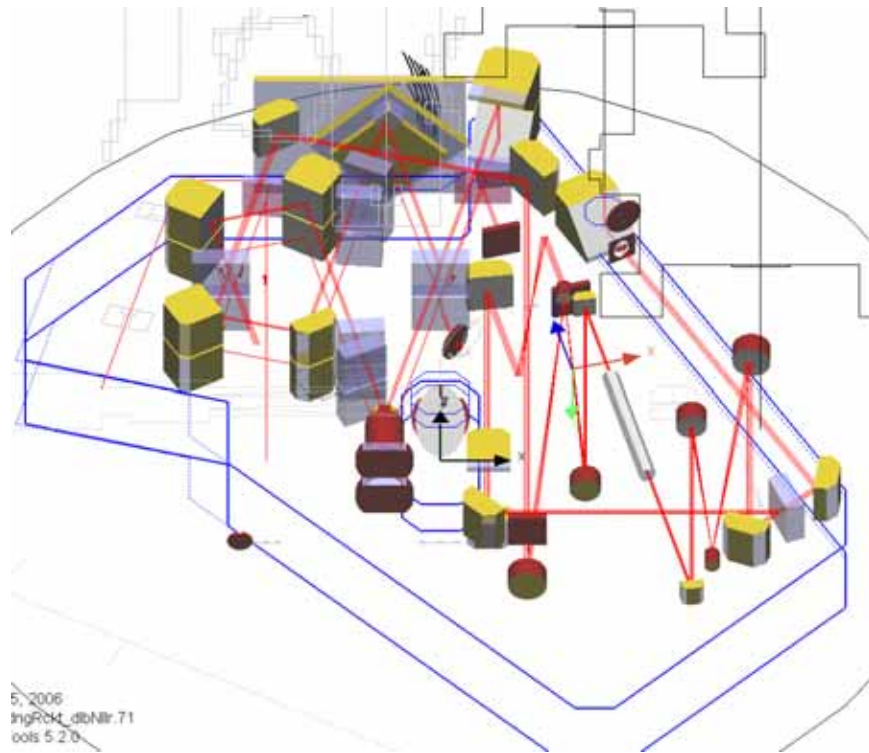
Figure 4.1-35. Three Dimensional View of Double 'Boomerang' Nulling Coronagraph SSS for *TPF-C*

The top down view shown in the next figure (Figure 4.1-36) shows the optics from the top and bottom layers showing the science leg and the leg to the calibration camera which is on the lower level interferometer. Light from the science leg is split and directed to the lower nuller by a turning mirror and a vertical roof mirror (needed to maintain the same spatial orientation as the bright output) to a pair of off axis parabolic (OAP) mirrors. This OAP mirror pair is identical to the one (just below) that focuses the bright output of the interferometer, spatially filters the light through a pinhole,

and then recollimates the reference light. Both beams are then recombined at a beam splitter which lies below the fiber array. Both outputs are redirected through a triangular mirror to a calibration camera which simultaneously images both interference patterns. By modulating the phase delay in these beams, one needs two images to capture 4 phases (0 $\pi/2$, π, $3\pi/2$) in the calibration camera from which the amplitude and phase of the stellar leakage is computed.

The wave front control system configuration is not yet defined. It will likely consist of a pair of segmented deformable mirrors (DMs) located in the first nuller. The configuration shown includes one DM.
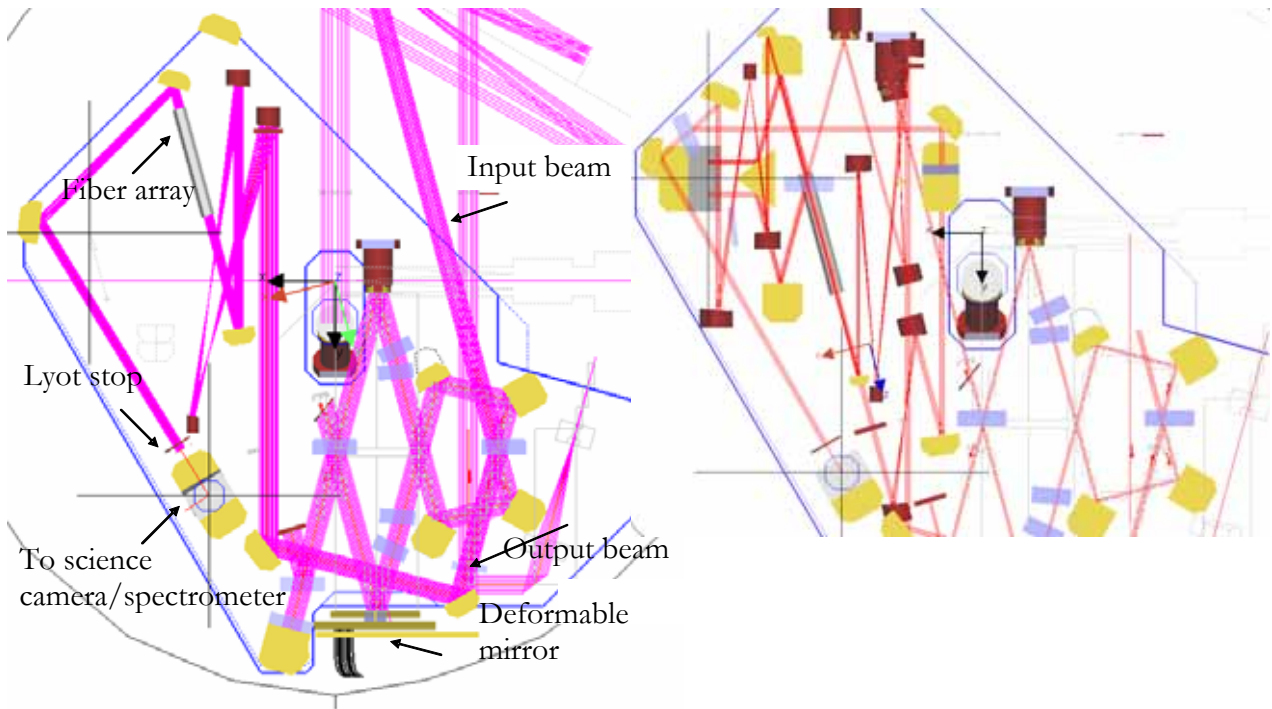
Figure 4.1-36. Two Top-Down Views of a Boomerang-Configuration Double-Nulling Interferometer (Our Configuration for the *TPF-C* Starlight Suppression System): Left–Overall View and Right– View Revealing Lower Calibration Leg.

4.1.4 Spacecraft

4.1.4.1 An Alternate Sunshield Configuration

While thermal modeling showed that the baseline conical V-groove sunshield is adequate to its required shielding task, as the team considered more deeply the practical ramifications of the conical shield, a number of difficulties surfaced having to do primarily with deployment of the shield assembly in the area of the electronics and detector cooling radiators.

It is preferable that the heat pipes feeding these radiators are of the rigid type, and that the radiators be in a fixed position relative to their heat sources from assembly on. The alternative involves deploying the radiators and using flexible heat transport sections to make this possible, and this was felt to be unwise from a reliability point of view.

A continuous conical Sun shield would occlude the view from the detector and electronics radiators to cold space; therefore, it would be necessary to leave a 6-layer "window" in the Sun shield and somehow "miss the radiators" during shield deployment. This seemed risky at best, and disastrous at worst. Northrop Grumman Astro Aerospace, specialists in space deployable structures, agreed that the problem was a sticky one, and the entered into a consideration of alternatives.

The primary alternative Sun shield design that came from Northrup Grumman Astro Aerospace's deliberations, aptly dubbed the "sugar scoop" by reason of its shape, is depicted in Figure 4.1-37.
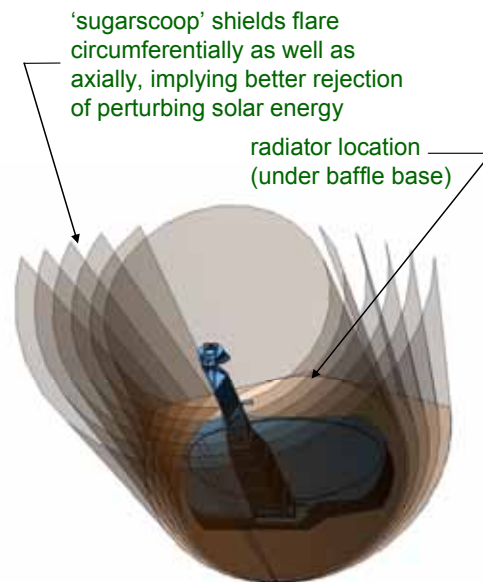
Figure 4.1-37. Sugar-Scoop Sunshield Concept

Since the sugar scoop is wide open in an area where the electronics and detector cooling radiators might reside, there is no interference to shield deployment.

The sugar scoop Sun shield effectively eliminated the deployment conflict with the fixed radiators. An intuitive thermal examination of the concept by the team concluded that the new design could represent improved shielding efficiency in comparison with the conical shield, because the sugar scoop has two ways to reject potentially disturbing radiant heat: axially and circumferentially.

Therefore, a thermal model of the sugar scoop configuration was built and subjected to the post-dither distortion test.

Preliminary analytical results suggest that the sugar scoop is as good as, if not better than the conical design. Further study is needed to reach a firm conclusion.

4.2 Alternative I&T Test

It is highly desirable to have a ground test of the fully configured *TPF* that accurately reproduces the operation in space. Not just the optics but the control systems and the control software should ideally all be operated together just as they will in space. The ultimate proof would be to recover the image of a star and faint planet from a full aperture collimator input, using all the internal wavefront control and star suppression systems working as on orbit (Angel, Burge and Worden, 2005). While there will be a significant initial cost of building the test facility, ultimately the overall costs may be lowered, and the system reliability and confidence will be greatly increased. However, such a test will not be possible or optimal if it is not allowed for from the start in the telescope design. Thus we examine first the constraints of a valid test.

To test the *TPF-C* spacecraft system prior to launch, an off-axis collimator must be used to illuminate the full aperture with a scene of a star and planet at 10^{-10} contrast.

The general layout of a full system test is shown in Figure 4.2-1. The off-axis collimator at the top of the vacuum chamber produces an 8-m beam pointing directly down. This orientation is chosen so that the beam quality can be verified by retro-reflection against a liquid flat, removing the need for any other metrology elements. For test purpose the liquid does not have to be highly reflective, the few percent reflection of a transparent liquid surface is adequate. The liquid should be chosen to have very low vapor pressure and optimum viscosity. Diffusion pump oil is a good candidate. The collimator could be made following the prototype 8.4 m off-axis mirror at this size now fully funded and in optical fabrication at the Steward Observatory Mirror Lab for the Giant Magellan Telescope. The Lab is currently completing the current largest vacuum collimator, an on-axis 6.5 m system for Lockheed Martin.

The important requirement set by such a liquid-validated collimator system is that the spacecraft under test must be oriented zenith-pointing. The spacecraft optical system should therefore be able to accommodate operation with or without an axial load of 1g.

A test like this of the FB1 design would not be possible, because of uncorrectable gravity bending of the primary in the spacecraft configuration. But it would in principle be possible for the alternative actuated primary described above, given actuators of sufficient authority. The stroke of the actuators would be matched to the bending of the integrated reference structure, so the primary figure could be corrected under 1 g load as well as in space. The residual local quilting of the facesheet would be moved to high enough frequency ≥10 cycles across the aperture, so it would not spoil a test of the critical search region near the star. The optical quality of the collimator need not be significantly better than that of the primary. The spacecraft star suppression system would take care of the residual collimator wavefront errors along with those of the primary.
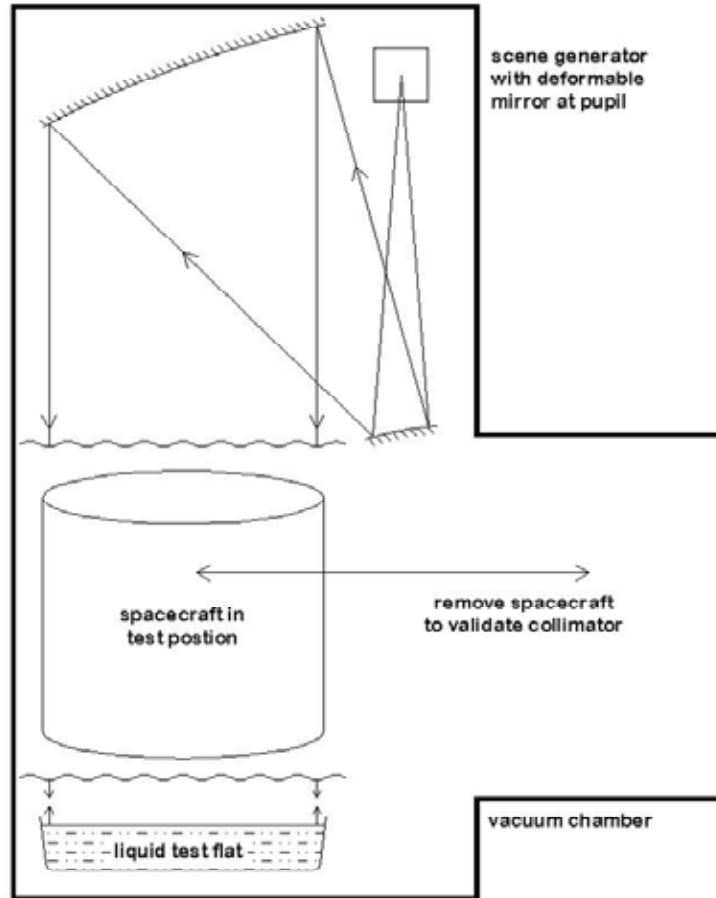
Figure 4.2-1. Test Configuration
(The test beam is produced by an off-axis collimator. By moving the spacecraft to one side, the beam is validated against a liquid flat.)

The test would be successful only if the vibration and thermal environment were adequately controlled. The test facility would have to be designed from the ground up with these requirements in mind. We recommend that a feasibility study for the complete test facility be included when *TPF* funding again becomes available.

5.0 Key Technologies, TRL Assessment, Development Plans & Progress to Date

The *TPF-C* telescope represents a large step between current or near-future heritage and what is required for a successful mission. This step spans spatial scales from sub-atomic (the wave front stability scale is sub-Angstrom) to building-size (the deployed dimension including the sun shield is 16 × 37 m).

Driven by mission scale, a central theme in the *TPF-C* technology plan is that of verification. It will likely be impossible to test the entire observatory under flight-like conditions prior to launch. Predictability of success and minimization of risk are therefore paramount. Verification of *TPF-C* flight hardware will be accomplished by subsystem and component testing at the most detailed level. The results of these tests will be used to confirm analytic models, and these models will then be linked together to estimate the overall performance of *TPF-C.* By comparing the interaction of individually tested elements (represented by verified independent models), confidence in the overall systems model will be obtained. The fidelity of the models and their analytic interfaces will be verified. Proof that the required tolerances can be achieved in a repeatable and robust manner will be completed prior to the start of Phase C/D. Such proof will be obtained by measurements of appropriately scaled testbeds and components and correlating these results with models whose scalability and linearity can be verified. The approach to verification will be an integral part of the architecting and design process to ensure that what is ultimately designed will be testable.

The overall *TPF-C* technology plan is introduced in Section 5.1.4 and described in detail in "*TPF-C* Technology Plan," JPL Publication 05-8 available through JPL The following sections address the current status of *TPF-C* technology development activities, the technology drivers identified by the recently-completed Instrument Concept Studies, and the modeling verification and validation approach.

The TPF-C technology plan identified 4 major technology milestones required to demonstrate sufficient technology maturation to move forward into Phase-A. These milestones are not intended to be all inclusive but serve only as benchmarks of progress. The first of these technology milestones is the achievement of better than 1e-9 contrast in laser light over a dark hole spanning the 4th–10th Airy rings. This was achieved in the JPL High Contrast Imaging Testbed. This exciting result was achieved using a Xinetics deformable mirror to control the wave front incident on a continuous-tone band-limited image plane mask in a Lyot coronagraph configuration. The ultimate goal of 1e-10 contrast in broad-band light is still several years away, but many of the major hurdles to the *TPF-C* requirement have been identified, modeled, and overcome in the last year.

5.1 TPF-C Mission Risks

This section addresses the key risks of the *TPF-C* mission, as currently defined. We first describe our approach to identifying and mitigating *TPF-C* risks, then list our current identification of key *TPF-C* risks, and then put forth a *TPF-C* team consensus view of priority near-term investments needed for further mitigation of key *TPF-C* risks. We conclude by summarizing existing plans that have been mitigating *TPF-C* risks.

5.1.1 Approach to *TPF-C* Mission Risk Mitigation

The *TPF-C* team adopts an approach to risk mitigation that enables NASA management to identify early potential risks, including cost, technical and schedule problems, as well as to determine how to best allocate resources to balance and mitigate those risks. Plans that manage risks early in the *TPF-C* development cycle are key to maintaining estimated program schedule and budget. Managing a crisis late in a program is extremely expensive – a gram of prevention is worth a kilo of cure.

Our risk mitigation approach on *TPF-C* generally consists of:
- Generating, constantly revisiting and maintaining a list of program risks
- Determining the relative ranking of risks based on estimated probability of occurrence and potential severity of the consequence should that risk be realized
- Developing and implementing means for balancing and mitigating the highest ranked risks by means of design changes, technology investments, and programmatic means.

The technical risk mitigation approach had previously been reviewed by the *TPF*-Technology Advisory Committee (*TPF*-TAC), the *TPF*-Science and Technology Definition Team (*TPF*-STDT), and NASA HQ. Heretofore it will be reviewed by internal and external stakeholders. A work plan that outlines this risk mitigation approach and includes measurable quantitative technical targets for functionality and performance was developed and implemented by the project. The risk mitigation strategy and priorities are informed by technology heritage from *JWST*, *SIM*, *HST*, LBTI, Starlight and Keck-I for individual technologies as well as for integration and test approaches which include validation through analytical modeling. We recognize that the transfer of technology to the system implementers is a critical component of a successful development program, and we plan for doing such, as part of NASA's acquisition strategy plans.

5.1.2 Current List of *TPF-C* Mission Risks

The *TPF-C* team has continually identified, assessed, and revisited *TPF-C* risks, guided primarily by impacts to the system error budget. Table 5.1-1 lists our current key *TPF-C* mission risks. Additional risks are expected to be identified as the design and the corresponding error budget continue to evolve. The error budget is continuously updated to reflect the current estimated system performance. This allows the *TPF-C* development team, led by the system architect, to balance risks by relaxing derived performance requirements in one area while more tightly constraining those in another area.

The *TPF-C* team recognizes that the scientific observing modes imposing the most stringent performance requirements go hand-in-hand with the prioritized technology development plans. As an example, stability of the system is likely to be driven by the planet detection objective, while the

planet characterization objective is likely to drive the bandwidth requirements. Because science requirements and estimated design performance evolve, the operational modes and their derived implementation requirements are expected to continuously be evaluated and updated.

Table 5.1-1. Current List of *TPF-C* Mission Risks

Risk	Concern
Optical Design and Fabrication Risks	
Wavefront amplitude & phase control	DM performance and optical bandwidth
Large primary mirror fabrication	CTE uniformity, handling risk, long-lead schedule, etc.
Broadband mask physics	May need restricted bandpass & longer integration times
Mirror coating performance	Uniformity, reflectivity, polarization, stability, wavelength
Mask and coating characterization	Facilities not available at this spatial resolution
Dynamics and Thermal Stability Risks	
Primary surface figure stability	Behavior not understood at pico-m level
Secondary tower deployment precision and stability	Behavior of hinges, latches, joints not understood down to sub-nano-m level
Secondary position control	Requires laser metrology and hexapod to 25 nm level
V-groove sun-shade	Extreme isolation from sun, including roll maneuvers, packaging & large deployment, and thermal / mechanical stability affect on stray light
Primary/secondary thermal control	Thermal control to sub-milli-K level; isothermal cavity
Verification and Validation Risks	
Verification and validation approach	Best mix of integrated observatory performance test and analysis required & flow, limited by ground test capability (chamber size, environment, metrology, cost, schedule), at the highest level of assembly (functional vs. performance).
System level mission performance	Test facility environment disturbances and cleanliness preclude flight level contrast or wavefront stability tests
OTA optical testing	Complexity of illuminated full aperture test compared to short-comings of subaperture interferogram stitching.
Ground testing not representative of flight environment	Removing ground testing condition artifacts (gravity, jitter, drift, thermal, etc) from results used to accurately predict flight environment system performance margins. Overdriving tests as a means for validating performance models in flight regime.
Test facility	Existence and availability when needed
Primary mirror actuation	Impact on performance (ground & on-orbit), if needed
Transportation	Shipping environment, container height restrictions. Post-shipment optical verification test versus only testing at the manufacturing and integration sites. Optimize the number of "pack & ship" cycles which drive the cost and risk.
Instrument Risks	
Integral Field Spectrometer	New mask designs for high throughput in multiple channels
Visible Nuller/Spectrometer	Overall complexity, throughput, number and type of DMs
Broadband Camera/Spectrometer	Optical fabrication, number of DMs, number of detectors
Planet Detection Camera	Yet to be identified
General Astrophysics Instrument	Requires diffraction limited telescope, may be driving requirement on Primary Mirror

Risk	Concern
Other Risks	
Planet characterization completeness	Ability to completely characterize planets with current state of development of the design
Contamination	Partial coherence issues. Current specs are tight.
Launch mass margin	May not achieve desired margins
Pointing control	Challenging pointing requirements not yet demonstrated. FGS not designed yet. I&T, modeling, and RWA minimum impulse.
Stray light	May not be able to design and/or test at low levels required
Detectors	Photon counting for spectroscopy & planet detection
On-orbit check-out & calibration	On-orbit capability to determine performance and adjustability
Analytical modeling fidelity & uncertainty	Methodology for validating model results at all levels. Includes methods to bound model predictions for unknown unknowns.
On-orbit deployment	Reliable deployment sequence & damage vulnerability
Spectral characterization requirements	Variability of bio-signatures over orbit may require many repeat visits and/or better spectral resolution than specified

5.1.3 Near-Term Priorities for Key *TPF-C* Risk Mitigation

The set of highest priority *TPF-C* near-term mission risk reduction activities, as guidance to NASA/HQ in their deliberations and planning of near term technology maturation investments related to the *TPF-C* science payload, are listed below in no particular order of priority amongst themselves. Relevant existing technology development plans are cited where appropriate.

- Demonstration of broadband starlight suppression and model validation (Tech Plan Sect 3.1, 3.2 & 7.4)
- Demonstrations of large mirror fabrication techniques and coating methods (Tech Plan 3.1.2, 3.1.6, 7.4.3, 7.4.7)
- Updated design and performance margins for latest updated SRD
- Formulation of a baseline verification and validation strategy
- Maturation of key technologies in instrument concept designs

5.1.4 Existing Plans for Mitigating Key *TPF-C* Risks

In 2002, a comprehensive technology plan for *TPF* was developed by JPL (*Technology Plan for the Terrestrial Planet Finder*, JPL Publication 03-007, March 2003). It put forth the strategies and initial plans for NASA's investments in *TPF* risk reductions, as summarized by its roadmap. The driving need for these planned efforts was to support the *TPF* architecture decision (coronagraph or interferometer) needed to programmatically focus and establish priorities for mission development. Over the ensuing four years, much progress has been made in advancing technologies and mitigating driving risks for *TPF*.

The *TPF-C Technology Plan* (JPL Publication 05-8) was then developed and updated, most recently in March 2005, to refine the *TPF* Coronagraph team's assessment of risks and plan detailed mitigation plans addressing *TPF-C* technology and engineering risks. A summary of the risk mitigation plans copied here from this *TPF-C* Technology Plan is included as Table 5.1-2. These plans include clear paths to mitigate each risk, with corresponding technology roadmaps with milestones, options and

off-ramps. Although cut short by NASA's FY06 and FY07 budget decisions, much progress has been made towards accomplishing the established 2005 *TPF-C* Technology Plan as reported later in this Section.

Table 5.1-2. Technology and Engineering Risks Addressed by the *TPF-C* Technology Plan

Subject Area	Error Budget Allocations	Development Task Where Addressed
Optics and Starlight Suppression Technology		
Technology Risks		
Broadband mask physics	Masks consistent with 10^{-10} contrast requirement	Apodizing Masks and Stops High Contrast Imaging Testbed
Amplitude and phase wave-front control	Demonstrate sensing and control to 10^{-5} wave in mid-spatial frequencies in a flight-like system	High Contrast Imaging Testbed Wavefront Sensing and Control Deformable Mirror Planet Detection Simulator
Optical coating performance and characterization	10^{-3} reflectivity uniformity	Coatings Technology Demonstration Mirror
Straylight	10^{-11} background	Scatterometer
Transmissive Optics	Sub-Angstrom wavelength transmission uniformity	Transmissive Optics Characterization
Engineering Risks		
Large primary mirror fabrication	<25 kg/m^2, <7 nm rms surface error at 4–100 cycles\aperture, 8 m class	Technology Demonstration Mirror
Contamination	Small optics better than class 100	Scatterometer High Contrast Imaging Testbed
Structural, Thermal and Spacecraft Technology		
Technology Risks		
Primary mirror surface figure stability	Sub-nm for up to 24 hours	Technology Demonstration Mirror Sub-scale EM Primary Assembly Testbed
Stability of structures	10–30 nm stability*	Precision Structural Stability Testbed Secondary Mirror Tower Partial Structure Testbed Vibration Isolation Testbed
Secondary mirror position control system	25 nm multi-axis control	Metrology Components, Precision Hexapod Closed-loop Secondary Mirror Position Control
Material property characterization		Precision Structural Stability Testbed
Engineering Risks		
Thermal control system	mK-class thermal control of primary mirror and instrument	Sub-scale EM Primary Assembly Testbed Sub-scale EM Sunshield and Isothermal Enclosure
Sunshade deployment		Sunshade deployment testing
Pointing control	5 mas rigid body pointing	Pointing Control Testbed

Subject Area	Error Budget Allocations	Development Task Where Addressed
Integrated Modeling and Model Validation		
Technology Risks		
Thermo-mechanical analytical modeling fidelity	Validation of the tools at a contrast level of 10^{-10}	Sub-scale EM Primary Assembly Testbed Sub-scale Em Sunshield and Isothermal Enclosure Integrated Modeling Tools
End-to-end system testbed modeling and simulation	Contrast better than 10-10 at <4 λ/D; 0.5–0.8 microns	High Contrast Imaging Testbed, Planet Detection simulator, Sub-scale EM Primary Assembly Testbed Sub-scale EM Sunshield and Isothermal Enclosure Closed-loop Secondary Mirror Position Control

For purposes of guiding *TPF-C* Technology Plan implementation, risks are considered primarily technology maturation risks if they represent performance requirements and goals that are beyond those readily achieved within NASA's state-of-the-art, or are considered as primarily engineering risks if they represent engineering design implementation challenges. To date, more emphasis has been placed on technology maturation risks compared to engineering risks, consistent with the early phase of *TPF-C* design development.

As the project moves into formulation, the technology development must be balanced within the funding and programmatic constraints. As the technical risks are better understood, and the details of the formulation phase technology plan evolve, some risks may have to be accepted without complete mitigation. Technology risks will need to be retired on the schedule described above, while certain engineering (or design) risks may be accepted. The project will engage the internal and external stakeholders to gain agreement on the risk assessment and the details of the mitigation approach. In parallel, the *TPF-C* Integration & Test plan will be evolving along with the baseline system technical design. By the end of pre-Phase A, a preliminary description of essential tasks and tests will be developed based on the project technical risk mitigation strategy, consistent with the project acquisition strategy. By the end of formulation, the integration and test plan will be fully defined describing a risk mitigation driven technical approach.

In pre-Phase A, the TPF-C Technology Plan defines 4 high level technology milestones as technology maturation gates to proceed into Phase-A. These technology milestones are not meant to be all inclusive, but serve only as benchmarks of progress. These 4 high level Technology Milestones are defined as follows:

Milestone #1: Starlight Suppression

Demonstrate that the High Contrast Imaging Testbed (HCIT) is capable of achieving a baseline contrast of 1×10^{-9} (goal 1×10^{-10}) at a 4 λ/D inner working angle, at λ=785 nm and stable for at least one hour.

Milestone #2: Broadband Starlight Suppression

Demonstrate that the HCIT is capable of achieving a baseline contrast of $1x10^{-9}$ (goal $1x10^{-10}$) at a 4 λ/D inner working angle over a 60 nm bandpass (goal 100 nm) with the center wavelength in the range of 0.5 μm to 0.8 μm.

Milestone #3: Model Validation and Performance Feasibility

3A: Demonstrate that starlight suppression performance predictions from high-fidelity optical models of the HCIT, utilizing measured data on specific testbed components, are consistent with actual measured results on the testbed. Correlation of model predictions with experimental testbed results validates models at a baseline contrast ratio of better than $1x10^{-9}$ (goal $1x10^{-10}$) over a 60 nm bandwidth.

3B: Demonstrate, using the modeling approach validated against the HCIT performance combined with appropriate telescope models and the current mission error budget, that TPF-C could achieve a baseline contrast of $1x10^{-10}$ over the required optical bandwidth necessary for detecting Earth-like planets, characterizing their properties and assessing habitability.

Milestone Development

To date Milestone 1 is complete and work is proceeding towards demonstrating Milestone 2. Schedules for Milestone completion are not available at this time due to mission deferrement. The intent is to update the Technology Plan in regular intervals to document progress and to define further technology milestones in later Project phases. Quantitative milestones for entry into Phase B and C will be developed by the project based on the design, the error budget and the technical risk mitigation strategy; reviewed by the TPF-TAC, TPF-STDT, and HQ; and approved by HQ. Approval of the milestones from HQ is required before the project enters Phase A.

5.2 Telescope Technology

5.2.1 Overview

Many aspects of the *TPF-C* telescope will require some technology investment before they will be mature enough to proceed into a flight phase. As is clear from the discussion of requirements (§3.2.) and the telescope baseline design (§3.3), both the size and stability are significantly more challenging than prior space observatories. Aspects of technology development we have begun are covered in subsequent sections.

The technology path towards an 8m × ~3m monolithic, lightweight, off-axis, ultrastable primary mirror was considered early in the *TPF-C* program. The result was a set of four studies and a subsequent contract award to Kodak Commercial & Government systems division (now ITT Space Systems) for the Technology Demonstration Mirror [Cohen and Hull]. Most of the technology aspects for the primary mirror were specifically part of the charter for this mirror and its role in the technology development is included as appropriate.

5.2.2 PM Blank Technology

While many 8m-class mirrors have been built and are in operation around the world, none have within a decade of the lightweighting necessary for launch and deployment in deep space. Hence there is a need to demonstrate a clear path to an 8m lightweight blank that is consistent with all of the requirements. The TDM study contracts made it clear that glass (including glass ceramics such as Zerodur) is the only material with a clear path to the required size.

5.2.2.1 Mirror material

Thermal stability studies also showed that with this degree of lightweighting, the usual thermal stability parameters do not apply and thermal stability directly requires very low coefficient of thermal expansion; thus there are only two candidate materials (for operation at room temperature); ULE fused silica (Corning) and Zerodur (Schott).

We performed a trade study between these two materials (Content, Ohl, Cafferty, et al.) which concluded that while both are likely to be viable candidates, current work would be based only on a ULE fused silica mirror. A summary of the conclusions from this trade study appears in Table 5.2-1.

One drawback to ULE is the size limit of a single boule (~1.3m diameter by ~0.15m thick before any flowing out).

Table 5.2-1. Factors Considered in the Primary Mirror Material Trade Study

note - # of + or - relates to importance in overall preference			
factor	Zerodur VLT	ULE	comments
CTE predictability	-	+	Zerodur needs dilatometer testing; VLT blank samples gone
CTE uniformity across 8m	+	-	ULE may improve over historical variability
Young's modulus	+	-	Zerodur slightly higher
Nonlinear effects	--	-	Zerodur testing harder
risk of LTB on central hole	-		1m diameter hole to fill in
ability to create 2nd or spare blank	--	+	8m furnace disassembled
maturity of lightweighting to ~47kg/m2	--	++	
thermal stability	+	+	differences directly related to CTE
traceability to TDM	-	+	
risk of woodgrain enhanced roughness	+	-	

5.2.2.2 Blank fabrication

To achieve the maximum stiffness per weight, it is well established that the closed-back sandwich design is preferred. The baseline design and the TDM are both sandwich mirror blanks with hex cores comprising ~2% of the overall weight. Both are meniscus mirrors with the back taking (to mechanical accuracy) the same shape as the front surface.

TDM uses single piece faceplates because they can still be fabricated from single boules of ULE; however for the baseline design, more than one boule (even if flowed out to the final thickness of 7.3mm) is required. Also a working assumption is that the flight PM must be made from many boules as handling a 8m by 7mm facesheet would be too risky.

Therefore some technique for building up a monolithic mirror from sections is required. The TDM intentionally was planned to demonstrate build up of core segments. However, additional demonstrations would be necessary to show a complete manufacturing compatability so as to include joining of faceplate sections.

The TDM uses established technologies of water-jet cutting, and low temperature fusion, to fabricate the lightweight ULE cores, and fuse them along with the faceplate into a complete plano mirror blank. The next step, low temperature slumping, has been done only for smaller and on-axis mirror shapes and so requires demonstration for *TPF-C.* TDM is a circular aperture, off-axis parabola to achieve this goal.

ITT and Corning are fabricating this mirror. Figure 5.2-1 shows the mirror concept with the front face sheet removed. Figure 5.2-2 shows some core segments during fabrication. Currently all segments are complete, substantial review work is complete, but hardware work has been deferred pending resumption of program funding.
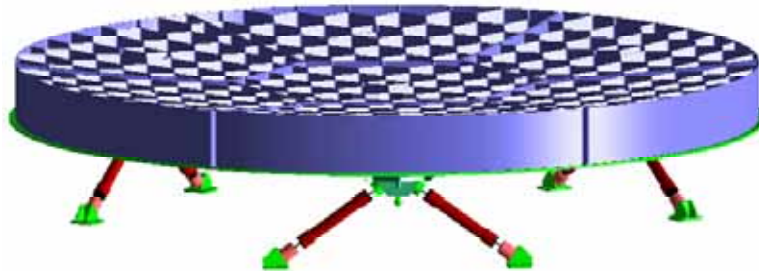

Mounts, Bipods, Glass with front facesheet removed

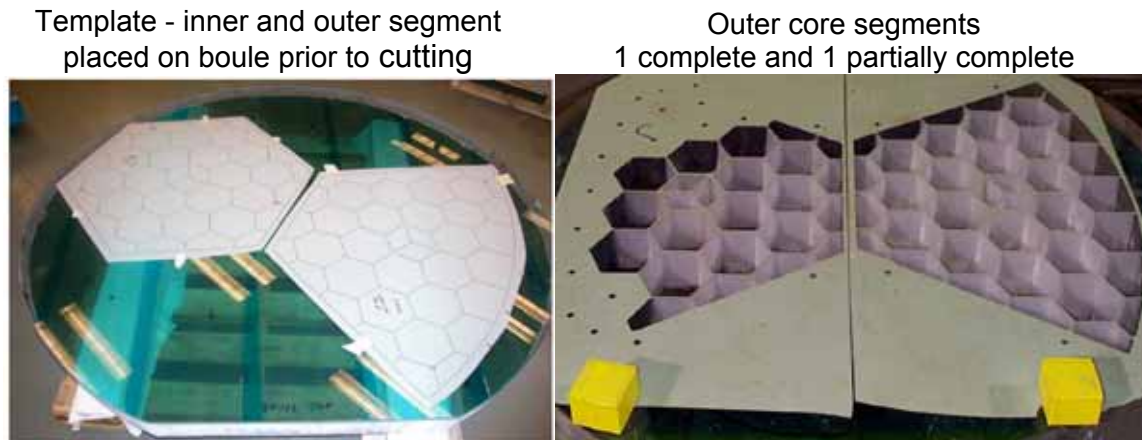**Figure 5.2-1. Technology Demonstration Mirror Design Concept (ITT)**

Template - inner and outer segment placed on boule prior to cutting

Outer core segments 1 complete and 1 partially complete

Figure 5.2-2. Technology Demonstration Mirror Core Is Made from Six Outer and One Inner Segment (Cohen, ITT)

5.2.3 PM Polishing and Metrology Technology

Polishing an off-axis 8-m class mirror is a recent goal. For ground based work, R. Angel has worked to demonstrate this for the Giant Magellan telescope [Johns, Angel et al.]. For *TPF-C* the polishing process must also be compatible with the lightweighting and very tight surface requirements, particularly in the critical spatial frequency range down to ~2cm error periods that map to the edge of the coronagraph high contrast field of view. In addition, trade studies have shown that an excellent polish (e.g., 0.5nm microroughness) is strongly recommended to enable the wide field instrument to surpass *HST* performance in spite of the scatter off of the primary from the very bright coronagraph target.

TDM uses an actively controlled aspheric lap [Strafford and Charles] to achieve good smoothness with small edge rolloff on aspheres. Zero pressure fine tools (ion milling) are well established for figure control. Conventional small tool polishing is also available if necessary.

5.2.4 PM Coating Technology

In addition to the coating design (cf. §3.3.3.1.3. and §4.1.1.4), the coating must be highly uniform in reflectance and must conform to the figure requirements. The TDM contract tasked ITT to examine feasibility of protected silver coatings for high uniformity in reflectance with encouraging results. Over a 2.5 m aperture, measured reflectance uniformity in the *TPF-C* passband varied from ~ 0.2 to 0.4 % and was dominated by reflectometer measurement scatter [Cohen and Hull]. This compares well to the 0.3 % RMS reflectance uniformity requirement. In addition, if a high stress coating such as protected Ag is used, the stress should be minimized and kept uniform. Kodak reported reductions in coating strain as well.

5.2.5 SM Polishing and Metrology Technology

The baseline secondary mirror is a 0.9×0.4 m convex hyperboloid. Experience from *JWST* and other programs has demonstrated that the difficulty in testing large convex aspheres is often underestimated. A program plan to alleviate this risk was formulated, including multiple new technologies

for convex aspheric testing. We planned to complete the baseline approach for *JWST* (which would require an improvement in precision by a factor of several) with the QED subaperture stitching interferometry approach [Murphy, Flieg et al.].

The polishing of this optic is expected to be similar to previous space flight precision optics and does not require substantial new technologies beyond the metrology development.

5.2.6 Laser Truss and Secondary Mirror Rigid Body Actuation

The laser truss uses retroreflectors at the periphery of the PM and SM to register changes in their relative position. Eight beams in total are used; the differential path lengths are processed into controls for a hexapod controlling the SM. Overall this sensing and positioning system must have a (very low bandwidth, primary used on deployment) long stroke capability as well as a ~1 Hz bandwidth, ~10 nm resolution actuation system.

Flight actuators combining the relevant load limits, long stroke, high resolution, and very good stability require significant development and testing. Examining the types of actuators in use for various applications, it is clear that new technologies may not be needed, rather combining existing designs and materials with a robust test program is likely sufficient to demonstrate the required capabilities. We have funded a SBIR contract with NightSky Systems to being this examination as well as a compilation of requirements for this application.

The laser sensing portion of this has been funded in the context of *SIM* and LISA. The primary technology extension here is the long time between rephasings of the system, implying small drift requirements. This flows down to a frequency stability requirement on the laser system compatible with existing demonstrations of stability over shorter time periods. Demonstration of stability over the full range of relevant timescales may require some extensions to current technology.

5.2.7 Mechanical Configuration

The telescope mechanical structure must be compatible with the very high stability needed for long term observation of very dim targets. Some technology development in the area of hinge and latch stability and stable structural materials (e.g., very low mass-loss composites, and super-low structural material CTE verification) will be needed to ensure the requisite stability during observations.

Static requirements on the structure are not dramatically different from other large telescope structures such as *JWST* or *SIM*.

5.2.8 Thermal Stabilization

Very high thermal stability is essential for the OTA operation, as discussed in §3.3.4.3. The developments in this area require careful engineering but not new technologies.

REFERENCES

Eri Cohen and Tony Hull, "Selection of a mirror technology for the 1.8m Terrestrial Planet Finder Demonstrator Mission," SPIE **5494** 350-365 (2004).

D. Content, R. Ohl, T. Cafferty, E. Cohen, R. Egerman, et al., "Engineering Trade Studies for the TFPc 8x3.5m primary mirror," Proc. SPIE 5867-33 (2005).

Matt Johns, J. Roger P. Angel, Stephen Shectman, Rebecca Bernstein, Daniel G. Fabricant, et al., "Status of the Giant Magellan Telescope (GMT) project," Proc. SPIE **5489** 441-453 (2004).

D. Strafford and B. Charles, "Advances in rapid fabrication of aspheric optics – post AMSD," presentation #05 to 2004 "NASA MSFC mirror technology days" conference, available at http://optics.nasa.gov/tech_days/tech_days_2004/index.html

Stuart B. Shaklan, Luis F. Marchen, Feng Zhao, Robert D. Peters, Timothy Ho, and Buck Holmes, "Metrology system for the Terrestrial Planet Finder Coronagraph," Proc. SPIE **5528**, 22 (2004)

Paul E. Murphy, Jon Fleig, Greg Forbes, and Marc Tricard, "High precision metrology of domes and aspheric optics, Proc. SPIE 5786, 112 (2005)

5.3 Starlight Suppression System Technology

As a program matures, technology groupings grow to increasingly higher levels of integration. What began as individually identifiable component technologies naturally lead to subsystems and with them, testbeds that are used to validate them. The development of *TPF-C* critical technologies can be understood in this framework. The bulk of the technology development effort has taken place at JPL. Unless otherwise noted, the component technologies and testbeds described below are JPL products.

5.3.1 Apodizing Masks and Stops

Objective: The *TPF* coronagraph must suppress on-axis starlight, while passing light from off-axis planets that are many orders of magnitude dimmer. In order to meet the required contrast over the full bandwidth, the masks must be fabricated with extremely high optical density and controlled diffraction characteristics. This activity is aimed at developing the technology necessary to produce and test several types of high precision masks.

Approach: Several candidate technologies are being explored to demonstrate the feasibility of manufacturing various kinds of masks that would achieve the end goals for star light suppression. The two basic classes of masks are focal plane and pupil plane.

Focal plane masks: Apodizing occulting masks to be placed at a focal plane require a very high dynamic range in optical density (OD from 0 to 8) and smooth variations within that range. There are two fundamental approaches to designing such masks: analog (i.e., gray scale) and binary (opaque and transparent). We have shown that binary focal plane masks have large polarization and wavelength-dependent phase effects that make the problematic to employ in a broad band coronagraph. Several manufacturing techniques will be examined for the apodizing approach. JPL is leading the effort in developing the technology for occulting masks in association with industry resources for materials development, fabrication and characterization. Final performance of the masks will be evaluated in the High Contrast Imaging Testbed (HCIT) at JPL. This activity will demonstrate that hardware can be manufactured to meet optical requirements of the coronagraph in space environment.

Pupil plane masks: A second approach for coronagraphy is to employ masks at a pupil plane that apodize the pupil in such a way to suppress and diffract away unwanted star light thereby providing the required contrast between star and planet lights at the image. Several theoretical designs have been proposed for such masks with varying throughput efficiencies and system complexities, primarily at universities under JPL subcontract. Experimental demonstrations are aimed at discriminating between technologies to allow selection of those with best system performance. To support and complement experimental work, teams at JPL (Hoppe et al.), Princeton (Kasdin et al.), UC Berkeley (Neureuther et al.) Ball Aerospace (Lieber et al.) and GSFC (Lyon) focus on incorporation of experimental results into the optical system model and validation of those models. The goal is to develop an understanding of the limits of the scalar diffraction theory for this application and determine whether any design modifications are necessary to achieve the desired coronagraph performance.

Significant progress has been made in the past two years in fabricating and testing focal plane masks at JPL. The first approach uses a high energy electron beam sensitive glass (HEBS). HEBS glass is manufactured by Canyon Materials, Inc., San Diego, CA, and further modified for JPL to meet *TPF-C* requirements. HEBS glass will darken to different levels of absorption of visible light when exposed to different electron beam levels. This makes it possible to create controlled optical density profiles in the glass with each mask design. Masks with linear 1-sinc2 patterns and eighth-order attenuation profiles have been written in such glass with a state-of-the-art electron beam exposure system at the Micro Devices Laboratory (MDL) at JPL. Tests with such masks during the past year in the HCIT have shown average contrast of 0.9 x10-9 in the dark field with 784 nm laser light[4] and more recently in the 5x10-9 level with about 40 nm bandwidth around 785 nm.

Figure 5.3-1 shows a mask and a picture showing the dark region in the image plane when such a mask is employed. Further experiments are in progress with continuous improvements in the mask material, fabrication progress, algorithms and testbed optics. Initial radiation tests show minimal HEBS mask performance degradation for the expected environmental exposure over mission lifetime.
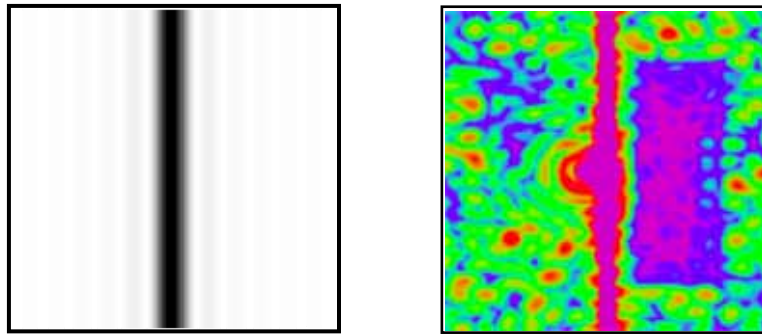

Figure 5.3-1. Mask (Left) and Picture (Right) Showing Dark Region When Mask Is Employed. (The mask is included in the optical train of the High Contrast Imaging Testbed (HCIT) where the corresponding image is recorded.)

In addition to the HCIT implemented for evaluating mask performance and perfecting methodologies for star light suppression, an interferometer system has been developed at JPL to characterize HEBS mask material. This system, shown in Figure 5.3-2 [5.3-2] incorporates 830, 785, 635 and 532 nm wavelength laser sources and a cooled CCD camera to capture interference fringe images. Algorithms have been developed to extract phase retardation/advance from such fringes from the various regions of different optical densities in the HEBS mask. This information is fed into models to validate experimental results. Reduction of error bars in measurement is an ongoing activity. Additionally, precision spectrophotometry and spectroscopic ellipsometry are employed to measure optical density and optical constants of the material as a function of wavelength.

---

[4] Trauger et al., Coronagraph contrast demonstrations with the High Contrast Imaging Testbed, Proc. SPIE V.2 5487-65, 2004
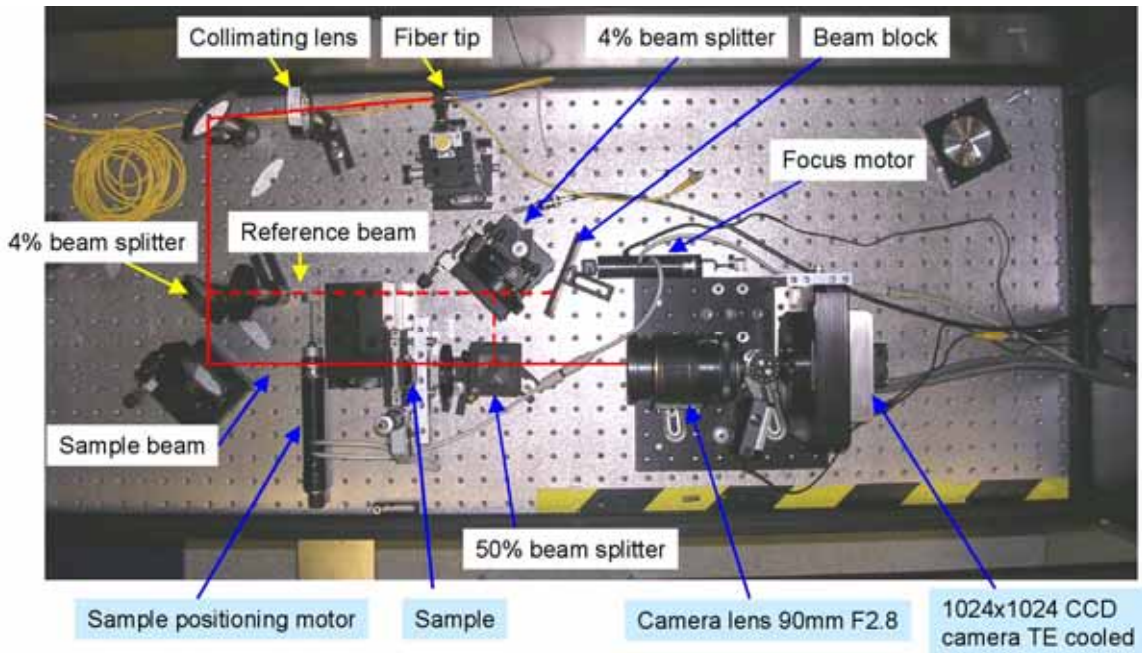
Figure 5.3-2. Interferometric Characterization of Mask Phase Retardance

Pupil plane masks: Pupil masks of various designs are being studied theoretically and experimentally primarily at Princeton University by a group headed by Professor Jeremy Kasdin under JPL subcontract. A parallel effort is also undertaken for accurate vector diffraction modeling of the system by a group headed by Professor Andy Neureuther at UC Berkeley [5] and in association with Ball Aerospace. A few examples of such pupil plane masks are shown in Figure 5.3-3.

Initial experiments using Princeton-designed, JPL-manufactured silicon masks in HCIT have yielded contrast of 4x10-8 in the near IR. Further experiments with improved masks are expected to provide pathways to reach the final goals.

Figure 5.3-3 Bar Code Masks and Shaped Elliptical Masks.
From left to right: 1-D bar code mask; 2-D bar code mask; four-aperture mask elliptical mask; multi-aperture elliptical mask.

---

[5] D. Ceperley et al, Vector Scattering Analysis of *TPF* Coronagraph Pupil Masks, Proc. SPIE 5526B pp. 228-239, SPIE Denver Annual Meeting 2004.

5.3.2 Wave Front Sensing and Control

Objective: Imperfections in the optical surfaces and coatings create starlight speckles over the field of view. To enable the planet detection and characterization objectives of *TPF*, these speckles must be sensed and controlled to the 10-10 level as compared to the brightness of the parent star. For the planet detection objective this speckle suppression must be achieved over the entire controllable field of view as defined by the actuator geometry of the deformable mirrors and this suppression must be achieved over an optical bandwidth of up to 25%.   For planet characterization, the speckle suppression need only be achieved over a smaller range of field angles about the planet but maintain a suppression that enables the planet spectral reflectivity to be measured over a substantial portion of the overall *TPF* sensitivity range.

Approach: Deformable mirrors are an integral part of the speckle control methodology. The density and geometry of the DM actuators define the ultimate extent and shape of the "dark hole" where the speckles are suppressed and planets can be detected and characterized.   The resolution at which the actuators are controllable (and remain stable) together with the actuator density define the ultimate suppression level that can be achieved. In fact there is an inverse relationship to the actuator density and actuation resolution that can be traded-off to specify the level of achievable speckle suppression. A higher density of actuator reduces the level of actuator command resolution required as well as reduces the surface figure requirements of the optical elements in the telescope.

The optimal arrangement of multiple DMs is a major consideration for wavefront control system architecture.   A single DM at pupil (such as on the High Contrast Imaging Testbed) is capable of controlling conventional phase errors over the entire controllable field of view, however amplitude errors are only controllable over half the FOV and the wavelength dependence of the amplitude terms is a limiting factor. More complex schemes that involve interferometric [6,7] or multi-conjugate [8] DM arrangements are currently being evaluated for their ability to enable full control of speckles over the entire FOV in the presence of broadband illumination.   Having a full-field discovery space is vital for the overall survey completeness required for *TPF-C.*

In addition to the deformable mirror technologies described previously, wavefront sensing and control algorithm development is key to achieving the required contrast. The primary function of wavefront sensing on *TPF-C* is to establish optimal settings for the DM surfaces such that the intensity level of the stellar speckles is reduced to the 10^{-10} contrast level over a suitable field of view and optical bandwidth. This process of determining beneficial updates to the optical degrees of freedom must take place in short time spans as compared to the stability of the system and in general it must enable a substantial portion of the operation time for science observations. The time it takes to sense and null the speckles must take no longer than the time it takes to detect a planet.

Typically a sequence of images is taken with a camera to observe residual light from the on-axis source in the presence of a known induced diversity. For example, on HCIT the DM actuators are

---

[6] M. G. Littman, M. Carr, J. Leighton, E. Burke, D. N. Spergel, and N. J. Kasdin, "Phase and Amplitude Control Ability using Spatial Light Modulators and Zero Path Length Difference Michelson Interferometer," Proc. SPIE Int. Soc. Opt. Eng. 4854, 405 (2003).

[7] C. W. Bowers, B. E. Woodgate, and R. G. Lyon, "Novel method of high-accuracy wavefront-phase and amplitude correction for coronagraphy." Proc. SPIE Int. Soc. Opt. Eng. 5170, 292 (2003).

[8] S. B. Shaklan and J. J. Green, "Reflectivity and Optical Surface Height Requirements in a Broad Band Coronagraph I: Contrast Floor Due to Controllable Spatial Frequencies," accepted for publication in Applied Optics, 2006.

moved in a predetermined way while a series of images is collected at either the post-coronagraph pupil [9] or post-coronagraph focal plane. [10] Other approaches have considered using phase-retrieval using imagery collected about the occulter focal plane, [11,12] by inducing diversity through the optical element alignments or by the introduction of a coherent reference beam to conduct direct interferometry on the speckles.[13]

Ultimately the wavefront sensing schemes must be well matched to the wavefront control and coronagraph architectures in a way that enables efficient and reliable high contrast imaging.

Progress to Date: Experiments on the HCIT have to date demonstrated a single-DM-based wavefront sensing and control architecture. Aside from having a single DM at a pupil, the HCIT employs a Lyot coronagraph that has a HEBS glass occulting spot. The camera at the final focal plane represents the science camera. Using a phase-retrieval approach at the HCIT occulter focus, it has been demonstrated that the testbed is stable to the l/10000 level. [12] Using a focal-plane speckle nulling approach [10] the residual light from the on-axis source has been suppressed to levels approaching 10^{-9} over a portion of the controllable field of view.

5.3.3 Deformable Mirrors

Objective: Unlike adaptive optics systems designed for correction of atmospheric seeing in ground based observatories, the active optical system for a space telescope needs only to correct for wavefront errors created in the telescope itself. The magnitude of wavefront errors is reduced to the magnitude of errors expected in a diffraction-limited optical system, and the bandwidth required to follow significant wavefront drift is reduced from kHz rates to the time scales associated with mechanical and thermal stability of spacecraft systems. The accuracy with which the wavefront can be corrected is fundamentally limited to the accuracy of wavefront error information that can be collected on time scales short compared to the stability of the optical system. The stability of a space environment provides the opportunity for extremely high-order wavefront correction.

Deformable mirrors are a critical component of speckle control methodologies for all wavefront control architectures under consideration. The deformable mirror must have sufficient control authority to correct the wavefront phase as commanded to ~1 Angstrom accuracy. The objective is to develop deformable mirrors (DMs) that are reliable and robust to support the *TPF-C*/High Contrast Imaging Testbed with the goal of demonstrating contrast performance of $1x10^{-10}$ or better at angular separations of $4 \lambda/D$ or greater from the central point source.

---

[9] S. B. Shaklan, D. Moody, and J. J. Green, "Residual wave front phase estimation in the reimaged Lyot plane for the Eclipse coronagraphic telescope," Proc. SPIE Int. Soc. Opt. Eng. 4860, 229 (2003).

[10] J. T. Trauger, C. Burrows, B. Gordon, J. J. Green, A. E. Lowman, D. Moody, A. F. Niessner, F. Shi, and D. Wilson, "Coronagraph contrast demonstrations with the high-contrast imaging testbed," Proc. SPIE Int. Soc. Opt. Eng. 5487, 1330 (2004).

[11] J. J. Green, D. C. Redding, S. B. Shaklan, and S. A. Basinger, "Extreme wave front sensing accuracy for the Eclipse coronagraphic space telescope," Proc. SPIE Int. Soc. Opt. Eng. 4860, 266 (2003).

[12] J. J. Green, S. A. Basinger, D. Cohen, A. F. Niessner, D. C. Redding, S. B. Shaklan, and J. T. Trauger, "Demonstration of extreme wavefront sensing performance on the *TPF* high-contrast imaging testbed," Proc. SPIE Int. Soc. Opt. Eng. 5170, 38 (2003)

[13] R. Angel, "Imaging Extrasolar Planet From the Ground", ASP Conference Series, Vol. 294, (2003).

Approach: Two current technologies are viable for the DM, one made by Xinetics the other a MEMs device by Boston Micromachines. The MEMs device capabilities are a lower TRL than Xinetics as seen in Table 5.3-1. The Xinetics mirrors are being developed for use in the HCIT and they compose the bulk of this discussion.

Ongoing development at Xinetics will provide the next generation modular mirror technology, including refinements in material processing, larger module dimensions, larger actuator count per module, and more efficient and compact low-power actuator driver systems. The procured components from Xinetics will be integrated on the testbed in order to continue an establishing path of technology advancement for *TPF-C* High Contrast Imaging Testbed.

The DMs are built up from 32x32 mm electroceramic blocks, each delineated with 1024 actuators arrayed on a 1 mm pitch. Single-module 1024-actuator mirrors, and a four-module assembly with 4096 actuators driving a single 64x64 mm mirror facesheet, as shown in Figure 5.3-4, are currently available for HCIT experiments. These are an outgrowth of seven years of development of modular PMN actuator technology at Xinetics Inc., a research effort initiated in 1997 within NASA's small business innovative research (SBIR) program. The DM actuators are driven by a multiplexed voltage supply with 100 volt range and 16-bit voltage resolution. A vacuum-compatible, low-power 64-channel multiplex switch ASIC has been developed at JPL to distribute the voltage settings while minimizing the number of control wires that must pass through the vacuum chamber wall.
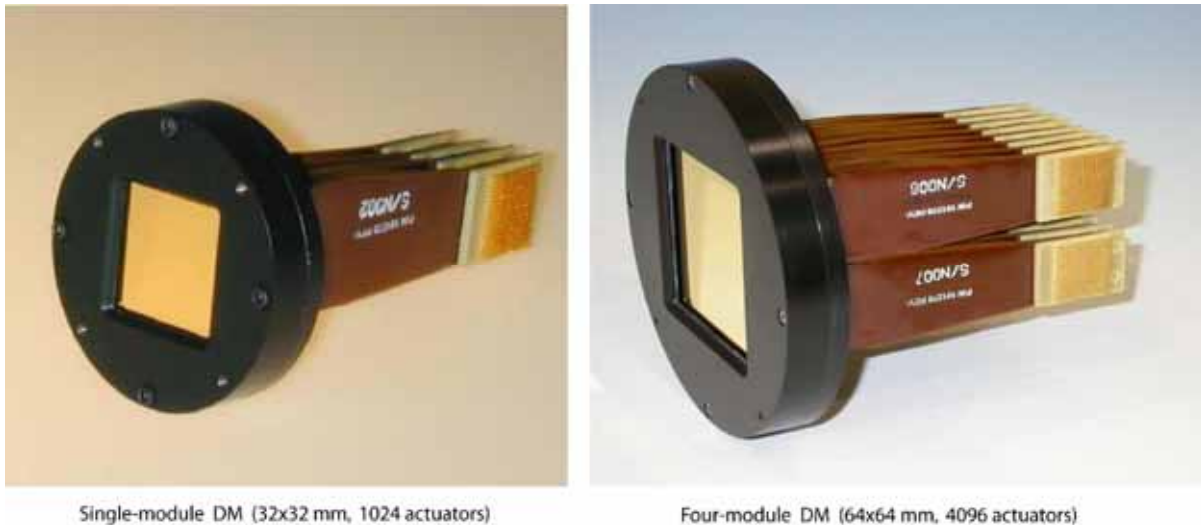

Single-module DM (32x32 mm, 1024 actuators)   Four-module DM (64x64 mm, 4096 actuators)

Figure 5.3-4. Xinetics Deformable Mirrors, 32x32 and 64x64

Table 5.3-1. Deformable Mirror Specifications

Deformable Mirror Property	State of the Art - MEMS[*]	State of the Art - Xinetics	TPF-C Flight Baseline
Actuators across aperture	32 actuators/pupil	64 actuators/pupil	96 actuators/pupil
Actuator spacing	3.3 actuator/mm	1 actuator/mm	$\geq$ 1 actuator/mm
Command resolution	~5 Å surface/step [†]	< 0.10 Å surface/step	< 0.05 Å surface/step
Actuator stroke	~20000 Å surface [‡]	> 2000 Å surface	> 2000 Å surface
Actuator position stability	TBD	< 0.20 Å surface/hour (includes effects of 10 mK thermal stability)	< 0.02 Å surface/hour
Actuator thermal stability	TBD	~ 3.5 % of stroke / K	TBD
Mirror surface quality at uncontrollable spatial scales	~10 nm surface [§]	< 10 Å surface	TBD

* Based on Boston MicroMachines Devices
† Command resolution is currently limited by the precision of the high voltage drivers with an average step size of ~10 nm/V; with custom 16-bit electronics, an average 0.3 Å/step is expected. Current devices on order are expected to achieve up to 12-13 bit resolution or 4.9-2.4 Å/step.
‡ Nominal actuator stroke is ~20,000 Å (2 ? m), however usable stroke over full aperture is limited by unpowered, surface curvature to somewhat less than this.
§ Small area, periodic deviations at actuator frequencies (2x outer working angle frequency) in unpolished devices. Devices on order are being polished to reduce this level.

The products to be developed are 32x32, 48x48, 64x64, and 96x96 deformable mirrors leading toward technical hardware that are reliable, large enough and robust to support flight performance levels required by Sept. 2008. Module development and combinations will enable best understanding of last path for flight hardware development.

In addition, Boston Micromachines is providing DMs for the GSFC Michaelson testbed, Princeton pupil plane testbed, and NOAO PIAA testbed with a similar architecture to the DMs required by HCIT. Boston Micromachines also provides the Visible Nuller (VN) with segmented DMs. The alternative approach and supplier represented by these MEMS DMs provide risk mitigation.

Progress to Date: Xinetics has delivered five 32x32 actuator DMs and two of four 64x64 actuator DM. The 32x32 DMs have been used in HCIT to achieve suppression approaching 10-9 with speckle nulling. Work is currently progressing on the 48 × 48 DM 2,304 channel single module manufacturing pathfinders, which includes module development, actuator machining and delineation pathfinder, interconnect evolution pathfinders, and facesheet development.

5.3.4 High Contrast Imaging Testbed

The High Contrast Imaging Testbed (HCIT) is an adaptable testbed located at JPL, established to validate the high-contrast coronagraphic technology fundamental to direct detection of extrasolar planets from a spaceborne observatory. The optical layout of HCIT is shown in Figure 5.3-5. This facility is modular, allowing for integration of modules from a variety of sources and designed for remote observing, so that users from many institutions can be supported. JPL has begun to support guest users.

Empirical investigation/validation of core coronagraph technology is practical with HCIT. This testbed represents two essential subsystems of a high contrast instrument: wavefront retrieval and correction, and coronagraphic control of diffracted light. The testbed will validate that an instrument can achieve and maintain contrast beyond 10^{-10} (10^{-9} in pre-Phase A) at the required inner working angle of the *TPF* coronagraph telescope. This constitutes a fundamental confirmation that phase and amplitude errors can be sensed, corrected, and held for the time period of extrasolar planet detection. Furthermore, it will validate software, diffraction models, and an error budget necessary to construct and operate a flight instrument.
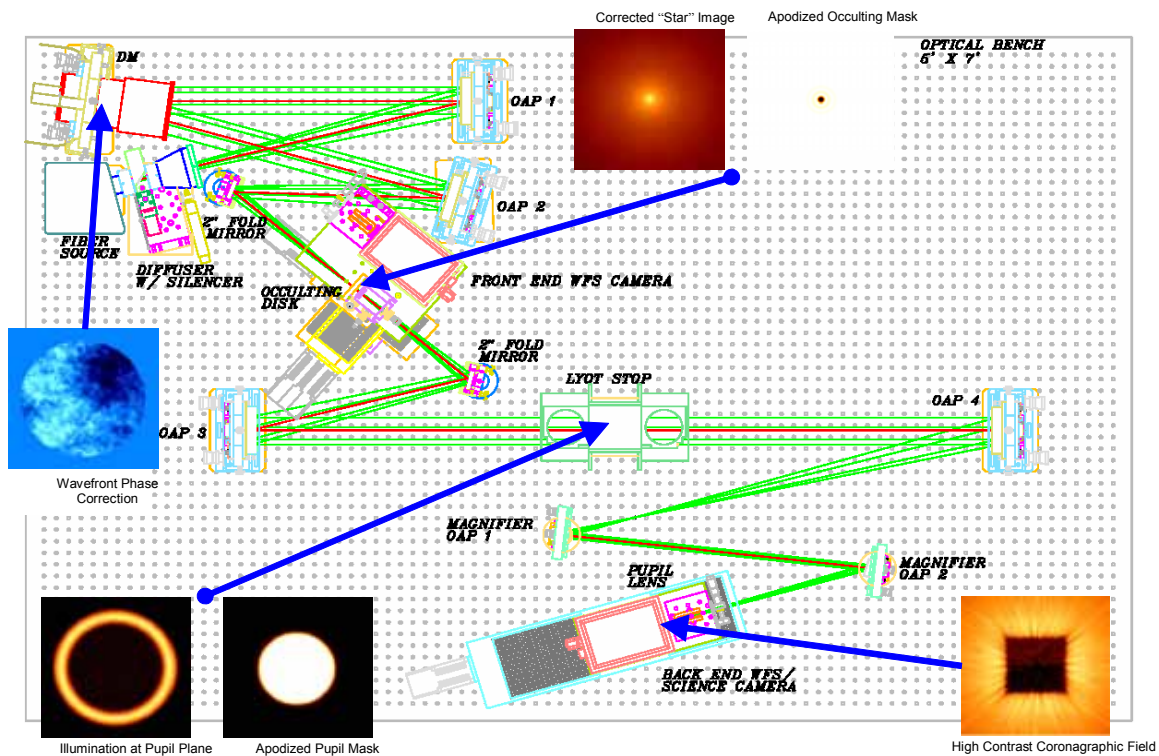

Figure 5.3-5. Layout of the HCIT with Insets of Focal and Pupil Planes

The HCIT development will consist of the following hardware thrusts: continued improvement in the deformable mirror and its performance; continued demonstration of wavefront sensing and control; and testing of apodizing masks and Lyot stops provided by government, industry, and academic sources. The testbed has been designed to accommodate a suitable subscale telescope and associated

masks/stops such as are planned to be developed as part of the Industry Coronagraph Technology thrust. In addition, the HCIT can be used to correlate analyses provided by outside sources and can accommodate possible additional back-end subsystems. The testbed is in operation and has achieved contrasts in a half dark hole of better than 10^{-9}.

Progress to Date: The testbed was aligned in a clean tent and became operational in ambient conditions in October 2002. Experiments with a 1764-actuator deformable mirror yielded contrast on the order of 10^{-5}. Modeling suggested that better contrast was not attainable given the imperfections in this DM. In April 2003 the testbed was moved to a vacuum chamber. Wavefront sensing experiments commenced in June 2003 using a flat mirror as a surrogate for the DM. The first fully-functional 1024-actuator DM was installed in October 2003. Initial experiments using phase retrieval, a phase-only method, to sense and correct the wavefront, immediately yielded contrast of 2×10^{-6}.

Speckle nulling experiments commenced in December 2003. This technique, which uses science camera images to calculate the DM control, has the ability to compensate for amplitude errors over half the field. These experiments quickly drove the contrast to 7×10^{-9}. In addition to the speckle nulling technique, two Lyot plane algorithms have been developed and tested. These algorithms have limitations in achievable contrast, but they provide useful tools for diagnostic and error modeling experiments. Combining speckle nulling with one of these approaches has yielded improved control of the DM and better contrast. Other algorithms under development in the *TPF* community will eventually be tested on the HCIT.

The HCIT has achieved a contrast of 0.9×10^{-9} for laser light ($\lambda = 785$ nm).[14] This contrast is an average measured in the half dark hole over a range of angles from 4 to 10 λ/D. Experiments in white light (40 nm bandpass) have yielded an average contrast over the half dark hole of 5×10-9.

5.4 Science Instrument Technologies

5.4.1 CorSpec Key Technologies

5.4.1.1 Detectors

CorSpec requires sensitive, photon-counting detectors to fulfill its scientific promise. In consultation with the CorSpec science team, we have developed a set of baseline detector requirements for Cor-Spec to inform our evaluation of existing technology candidates, e.g. e2v's L3 series of charge-multiplying CCDs (CMCCDs); and our development of new technologies capable of individual photon-counting in the λ=800-1050 nm wavelength range.

Operation of CMCCDs on-orbit will be very different to a normal CCD. In particular, because readout noise referred to the pixel is negligible (σread~0 e-), there is no penalty for taking many short exposures. We therefore envision that each observation will be built up from many very short, t~1-10 seconds, integrations. A thresholding algorithm will be used to differentiate photon events

---

[14] J. T. Trauger, C. Burrows, B. Gordon, J. J. Green, A. E. Lowman, D. Moody, A. F. Niessner, F. Shi, and D. Wilson, "Coronagraph contrast demonstrations with the high-contrast imaging testbed," in *Optical, Infrared, and Millimeter Space Telescopes*, J. C. Mather, ed., Proc SPIE **5487**, 1330-1336 (2004).

from non-events, and cosmic rays will be discriminated based on the statistics of pulse height and spatial proximity of "hit" pixels.

The CorSpec team has been evaluating e2v L3 CCDs under flight-representative background in the DCL since late-summer, 2005. Some authors have reported seeing Clock Induced Charge (CIC) in e2v's L3 CCDs. CIC is an effect whereby the act of reading out the CCD induces charges that appear in the photo-sensitive area. We have also observed CIC, and also some other effects that can masquerade as CIC and make CIC appear worse than it actually is. We have been able to develop mitigations that exploit our ability to vary the readout speed and phasing of clocks. At present, and when these mitigation strategies are used, we have found no show-stoppers with regard to using e2v L3 CMCCDs for the λ=500-800 nm wavelength range, although there are some areas where the performance could be improved.

The present generation of L3 CCDs cannot meet our long wavelength requirements, so we are working with vendors to ensure that detectors will be available that meet all requirements over the full $\lambda = 400\text{-}1050$ nm wavelength range. These efforts are comparatively low TRL at the time of writing, and we estimate that the most promising technologies are at TRL-3 today. With our current level of development effort, we believe that we will achieve TRL-5 in late 2006. Achieving TRL-6 will require more extensive radiation testing than is in our current plan. However, this could easily be done as part of the flight program or a separately funded technology development program.

5.4.1.2 Dichroics

Dividing the total CorSpec spectral range (450–1000nm) into multiple bandpasses will allow Cor-Spec to have much higher observational efficiency provided that the dichroic filters used to separate the bandpasses have high efficiency, minimal scattering, and a sharp cutoff in wavelength.

5.4.2 CorECam Technology Assessment

CorECam will be required to operate in the radiation environment of an L2 orbit where solar events over the lifetime of a mission can result in significant degradation of CCD detector performance. While the TRL level 5 for L3 CCDs is relatively high, we believe that further work is required. Specifically, p-type CCD architectures are indicated for the L2 environment and this will require significant development. The Wavefront sensing and control approaches proposed are currently at low TRL levels, having been evaluated using OSCAR models. Future investment is required by *TPF-C* to evaluate these techniques and mature them to appropriate levels for flight.

5.4.3 Broadband Camera/Spectrometer

Technology development needed for the PIAA/AHA concept includes optical fabrication, detectors, wave front control, apodizing masks, and optical systems integration.

5.4.4 Wide Field Camera

Technology development needed for the Wide Field Camera includes large format detectors.

5.4.5 Visible and Infrared Nulling Coronagraph Spectrometer

5.4.5.1 Technology Summary

This is a broad survey of the state of technology needed to build the components of a visible nulling coronagraph. Progress toward achieving deep achromatic nulls is addressed as well as progress updates on efforts to fabricate coherent fiber optic array assemblies, to build segmented deformable mirrors, and to fabricate its associated electronics. Also, the technology of detecting radiation in the 0.5–1.7 µm bandpass by using a substrate removed Mercury Cadmium Telluride (HgCdTe) array detector is discussed.

5.4.5.2 Status of Deep Nulling

We used laser and filtered white light (broadband) sources. The laser sources was laser diode module at 638nm terminate with a single mode fiber pigtail. The white light source used was incandescent (filament) type and installed on a mini bench, equipped with a filter wheel with choice of filters with central wavelength 650nm, then a lens focused the beam on the core of the single mode fiber leading to the nuller. For bandpass verification we injected the light into a spectrometer module from Ocean optics. Note that our 650nm and 638nm laser diodes showed a linewidth of about 1nm (i.e., 0.15% bandpass). Laser nulling results are shown in Figure 5.4-1.
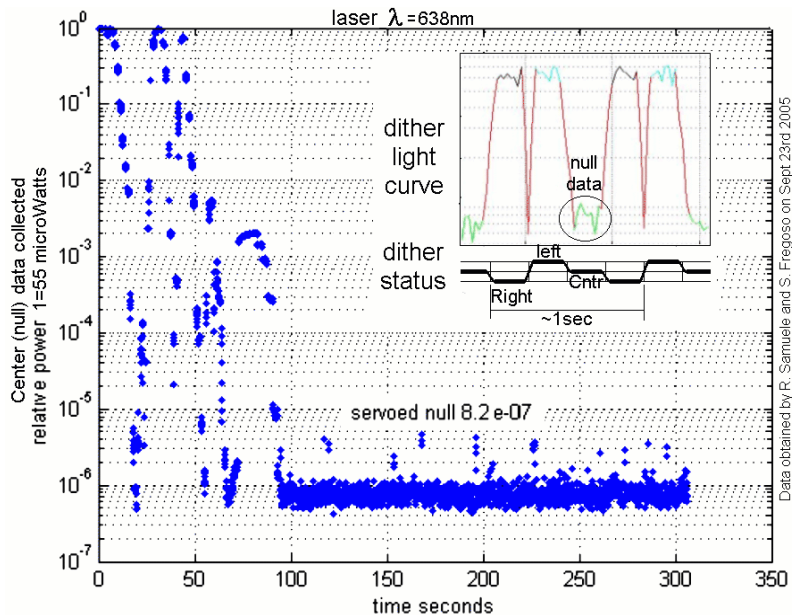

Figure 5.4-1. A 1.2 Million-to-One Servo Null Using a Laser Source

For white light nulling (Figure 5.4-2), the nuller was equipped with tilted glass plates (dispersion plates) to create varying glass effective thickness between the right and the left arm. We have experimented with only one glass type per arm, but have plans for 2006 to install two glasses (two plates) per arm to augment bandwidth.
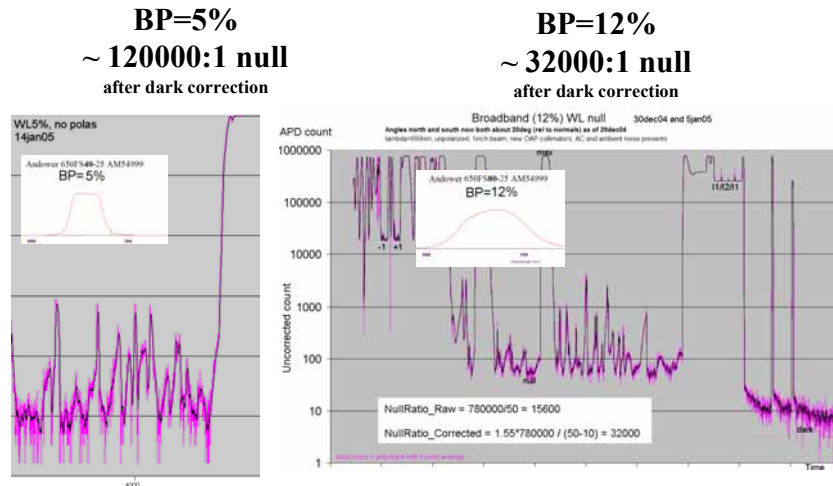

Figure 5.4-2. Experimental White Light Nulling Results

5.4.6 Spatial Filter Arrays

A single mode spatial filter array consists of a coherent fixed-length fiber array sandwiched by two lenslet arrays as shown in Figure 5.4-3. Approximately 1000 fibers are needed in the array for implementing nulling imaging of planets.
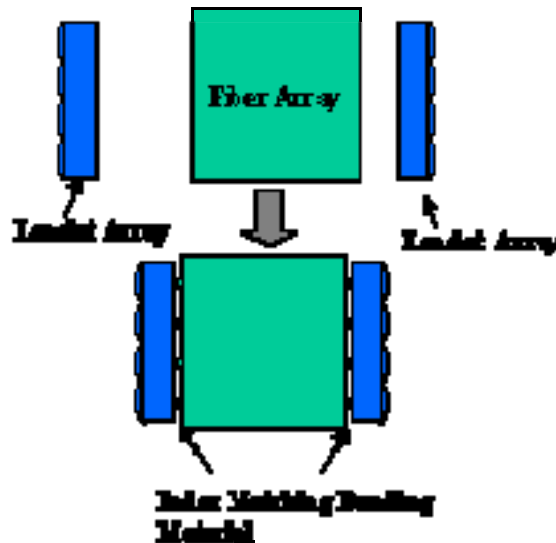

Figure 5.4-3. Assembly of a Fiber Bundle with Two Lenslet Arrays to Make a Coherent Fiber Array

JPL has developed a visible wavelength single mode fiber array using precision prisms to confine the fibers in a hexagonal pattern (Figure 5.4-4), and a method to align the fiber array to a custom lenslet array using a Zygo interferometer and a PI F206 Hexalign 6-axis stage. To reduce the alignment sensitivity in future arrays, we will use a custom large mode field diameter (~9µm) single mode fiber. A fiber position mapping method is also developed for the lens array design. The RMS fiber position error for the 496 fiber (331 in a hexagon) fiber array was measured to be < 3 µm (see Figure 5.4-5). The result is comparable to that of previously produced smaller arrays. In the future, we plan to build another 496/331 (triangle/hexagon) fiber array using a 300 µm cladding diameter and 12 µm mode field diameter single mode fiber with a cutoff wavelength of 500 nm. The 300 µm cladding diameter is chosen to match half of the spacing of the deformable mirror to be used in a future system demonstration.
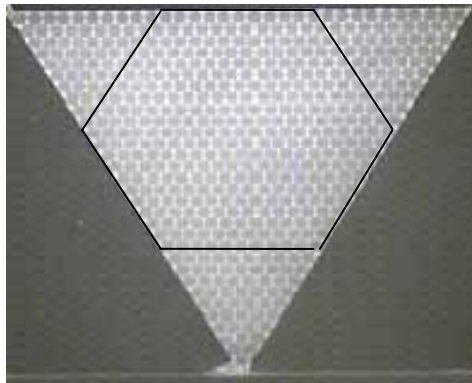

Figure 5.4-4. Polished End of the Large Core 496/331 (Triangle/Hexagon) Fiber Array
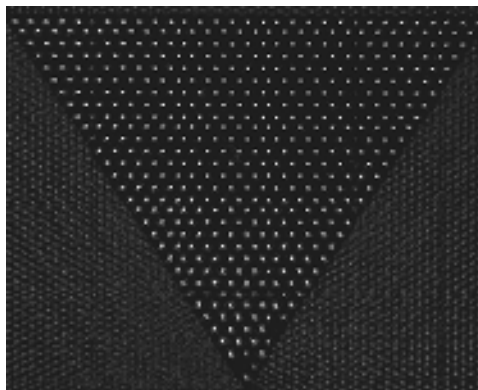

Figure 5.4-5. Light Output of the Large Core 496/331 Fiber Array When a Collimated HeNe Laser Beam Is Coupled into the Array via a Lens Array

The University of Florida uses V-grooves etched in silicon to hold fibers with large mode field diameters (MFD) fibers in precise alignment to one another and stack layers of V-grooves with fibers to form a 2-D fiber array shown in Figure 5.4-6. The silicon serves as a support to the fibers, not pressing down on them but merely holding them into position. The bundle is made from a single silicon wafer, whose thickness matches the dimensions of the existing lenslet array, eliminating any error due to thickness variations caused by using multiple wafers. The desired sub-micron precision is maintained by using nanometer accurate E-Beam generated masks to transfer a pattern onto the

silicon substrates. A strong base then preferentially etches the pattern along the silicon's crystal planes to form precise V-grooves, maintaining the required precision. A 10 x 10 bundle has been fabricated and is shown in Figure 5.4-7.
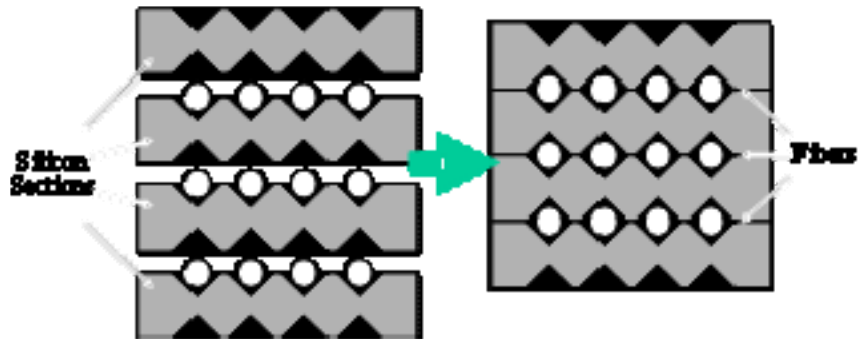

Figure 5.4-6. Schematic Drawing for Constructing a Fiber Bundle in the U Florida Approach
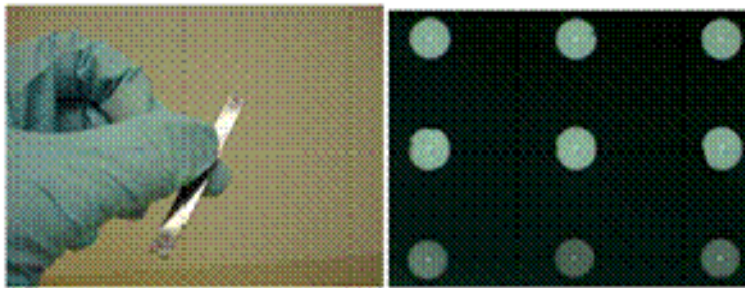

Figure 5.4-7. (Left) a newly completed 10x10 fiber bundle (6.8mm width, 2.8mm height, and 63.5mm length). (Right) Part of the fiber end illuminated by a microscope.

After the fiber bundle is developed with either method, it is assembled with two lenslet arrays to make a complete coherent single mode fiber array (Figure 5.4-3).

5.4.6.1 Deformable Mirrors

A schematic and summary for a Boston University DM design can be seen in Figure 5.4-8 and Figure 5.4-9. It consists of 331 hexagonal mirror segments, each supported by three independent electrostatic actuators from two different actuator rows.

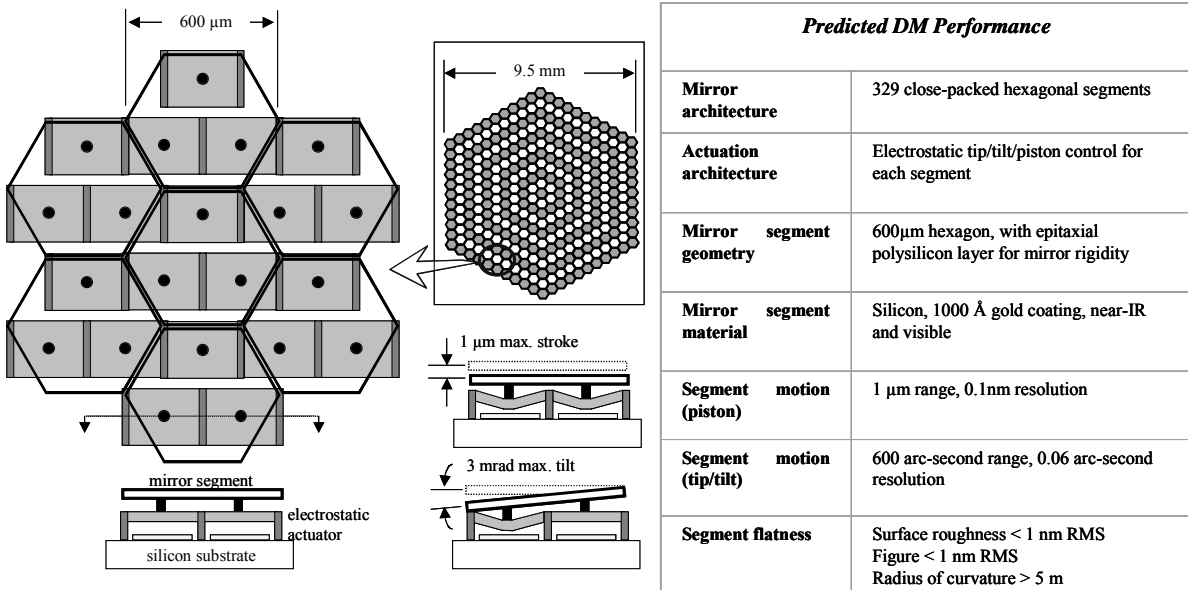| Predicted DM Performance	
Mirror architecture	329 close-packed hexagonal segments
Actuation architecture	Electrostatic tip/tilt/piston control for each segment
Mirror segment geometry	600μm hexagon, with epitaxial polysilicon layer for mirror rigidity
Mirror segment material	Silicon, 1000 Å gold coating, near-IR and visible
Segment motion (piston)	1 μm range, 0.1nm resolution
Segment motion (tip/tilt)	600 arc-second range, 0.06 arc-second resolution
Segment flatness	Surface roughness < 1 nm RMS Figure < 1 nm RMS Radius of curvature > 5 m

Figure 5.4-8. Top and side view of the Boston University MEMS *TPF* DM architecture for tip/tilt and piston motion (left). Table summarizing predicted DM performance (right).

The three actuators are connected to the hexagonal mirror segment via posts that resemble vertices of an equilateral triangle. These actuators are identical to those exhibited in a 'conventional' MEMS deformable mirror, but every other row is now offset by a length equal to half the actuator span. This actuator geometry provides the mirror with unlimited degrees of tip/tilt motion, and when the actuators are deflected by equal amounts, the mirror segment can be moved in a piston motion. The mirror segments are designed to have 1μm of piston stroke when they are tilted to 3mrad. In other words, if the mirror elements remained flat, the mirror could experience 2μm of piston motion before reaching the actuator limit. However, 1μm of this motion is reserved for tip/tilt behavior. Lastly, the mirror segments are 600μm in their longest dimension, creating a DM aperture of 9.5mm by 12mm. In addition JPL is following technology development efforts from other DM companies, IrisAO and Umachines.
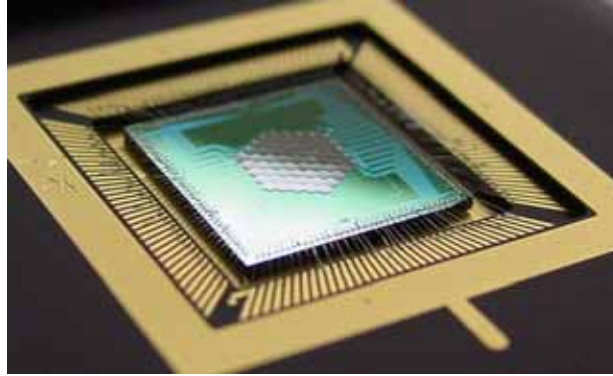
Figure 5.4-9. Early Prototype 61 Hexagonal Segmented BU Eformable Mirror

5.4.6.2 DM Electronics

Working with Analog Devices Inc., JPL has developed a set of electronics for driving deformable mirrors that will be suitable to many applications. Based on the new AD5535 chip, a modular deformable mirror controller board has 128 independent high voltage, 14 bit digital-to-analog converters, each driving a single deformable mirror pixel. These electronics have been demonstrated with a MEMS deformable mirror from Boston University and from Boston Micromachines, using automated procedures for characterizing and calibrating each individual mirror actuator. For a square-law DM with a range of 2 microns, the high resolution of the AD5535 chip gives a displacement resolution better than 3A.
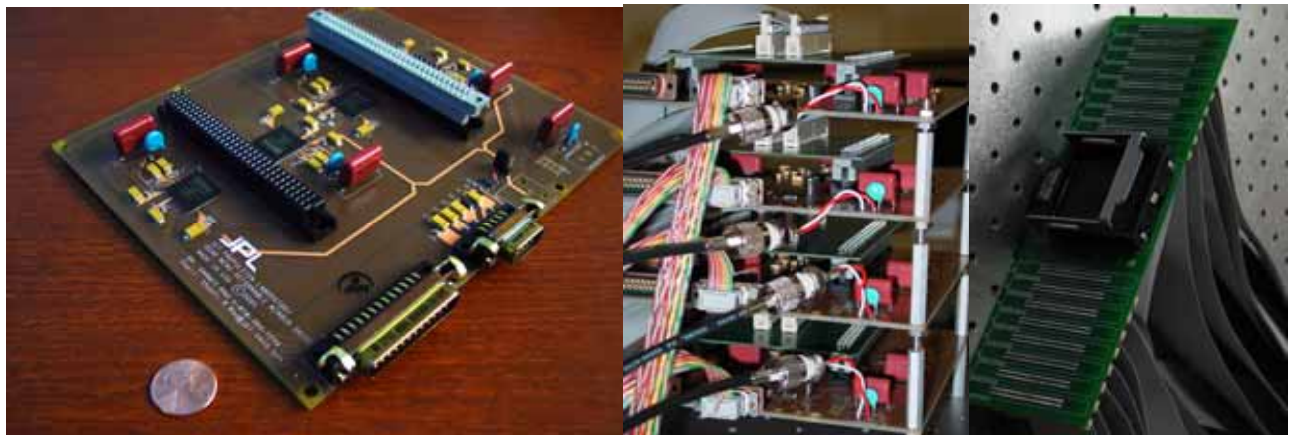

Figure 5.4-10. Left, A circuit board with 128 channels of voltage output. Center, An assembly of 4 of 8 boards set up for a laboratory demonstration. Right, ZIF socket for 1000 actuator deformable mirror (331 segments)

5.4.6.3 Status of Detector Arrays

According to our co-insvestigator, Dr. James Beletic of the Rockwell Science Center (RSC), the family of substrate removed HgCdTe Focal Plane Array (FPA) technology for *TPF-C* is mature. A single sensor of 64x64 pixels can now cover the entire bandpass (0.5–1.7 µm) with a high QE of 80% or better, low noise: (2-3 e- rms after multiple sampling), and negligible dark count with cooling. These are current capabilities and they will be improved with future development. This technology is already in hand and is being used for a number of government sponsored programs including, *HST* WFC-3, WISE, JDEM, and *JWST*. The technology is a developed by depositing HgCdTe detector layer on a ZnCdTe detector substrate. Since ZnCdTe is opaque to visible light, it is removed in the last processing step, after it has been hybridized to the silicon readout circuits. The other big advantage of substrate removal is it enhanced quantum efficiency. This process has been under development at RSC for over 6 years.
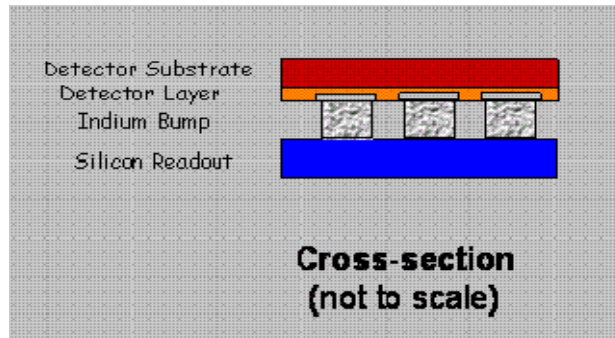

Figure 5.4-11. Schematic method for produce a substrate removed HgCdTe array
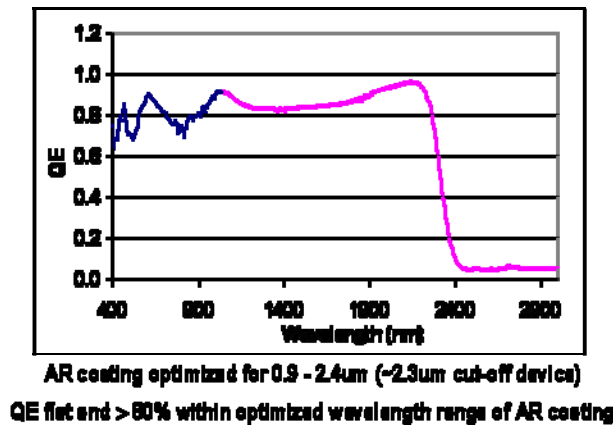
Figure 5.4-12. Quantum efficiency for a substrate-removed 2.3 µm cutoff array produced for a government customer. The cutoff and the AR coating for *TPF-C* will be optimized for 0.5-1.7 µm.

5.4.6.4 Wavefront Sensing

The wave front sensing approach is still in the conceptual stage. Detailed optical propagation models have shown that a separate DM is likely to be needed in each arm of the first nuller, and the DMs do not help improve performance of the second nuller. Broad band approaches are still conceptual in nature.

5.5 Integrated Modeling Tool Development

Accurately predicting optical performance for any of the near-term concepts proposed under NASA's Origins missions is a uniquely challenging task, and one that has served to highlight a number of areas of necessary advancement in the field of computer-aided engineering analysis. The unique combination of multidisciplinary thermal and structural analyses, to unprecedented levels of required optical precision, demand a solution approach that is itself fundamentally integrated if accurate, efficient analyses, capable of pointing the way towards improved designs are to be achieved. Since it is unlikely that any of the large aperture systems currently envisioned for *TPF* will be able to be fully ground-tested, at anything approaching operational conditions, prior to launch, analytical capabilities that can be used to support what testing is possible, explore performance envelopes, and suggest ways in which the design robustness may be improved become all the more critical.

Current technology development efforts have laid the foundation for an entirely new finite element-based analytical capability; one that is open, highly extensible, is Matlab-hosted, and which utilizes NASTRAN syntax to describe common-model multidisciplinary analysis tasks. It stands in contrast to other "integrated modeling" efforts in that it does not rely on existing commercial, closed-source components, but rather implements native finite element-based thermal, structural, and optical aberration computational capabilities in an environment intended to facilitate continuing research and development efforts. In addition to providing a much-needed independent verification and validation capability, these new technologies are also intended to address the error accumulation issues that arise from the sequential use of disparate, closed-source components and meshing (discretization) schemas. Although small and perhaps perfectly acceptable under most circumstances, such errors are simply not acceptable in systems where we seek to characterize nanometer, or even smaller, deformations due to milli-Kelvin degree temperature changes as functions of time.

5.5.1 Status

Though development efforts have been strongly *TPF* technology-driven the resulting technologies are nonetheless entirely general, and have focused on delivering a large problem-capable, common-mesh approach to coupled nonlinear transient heat transfer and resulting linear structural deformations. Development of appropriate analytical methods combined with a strong emphasis on nonlinear convergence strategies, adaptive time-stepping schema and accurate integration strategies are intended to result in time-dependent deformations which can then be used as a basis for direct computation of optical aberrations to extremely high accuracy. This section will briefly outline the development effort's status, with discussion of future development plans and other longer-term goals provided in the following section.

5.5.2 Program Architecture

Starting with the self-imposed requirement that this new code provide a readily extensible platform for methods development both within JPL and perhaps one day to a wider NASA community, the program architecture as implemented combines a large-problem capable, object-based design with core computational modules written in C and high-level hosting in Matlab which, combined, facilitate extensibility at virtually all code levels. The approach is a highly modular one, based on industry-standard practices for large code development, and also borrows heavily from the primary devel-

opers' experience in NASTRAN development. From a user's perspective, the code can also be entirely data-driven, meaning all discretized model data as well as state (boundary and load condition selection, time dependency, etc.) information can be specified in a single input file; an improvement not only over current processes but also a fundamental requirement for future goals such as automated design sensitivity and optimization. Program interaction is not limited to purely data-driven formats, however, as hosting within the MATLAB environment allows for an even greater degree of interaction and the freedom to change solution procedures, interact with intermediately-computed data, interface with other MATLAB-based solutions, and so on.

Figure 5.5-1 is a highly simplified schematic of this new code framework, many components of which are still under construction. Though all multidisciplinary input data can be localized within a single input file, this is not to imply a single analyst will, in practice, be responsible for all attributes. Rather, such a common-model approach provides a framework within which to capture the contributions of all discipline-specific contributors. NASTRAN syntax has been chosen (though the front-end data structures are readily extensible to other formats such as STEP), since virtually all pre- and postprocessors "speak" NASTRAN, providing a fairly robust method of interacting with geometry-based model building applications. Additional data formats have been invented, where necessary, to support analysis types not found in any of the commercial NASTRAN-based offerings (vehicle orbit positioning, optical "element" definition, specular surface behavior to name but a few.)
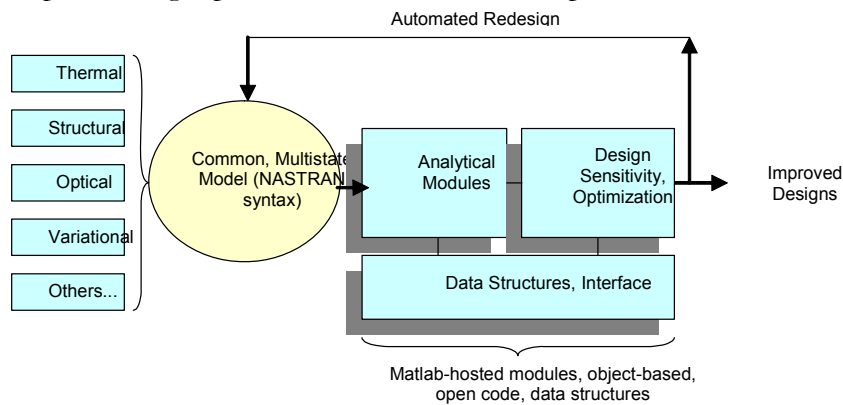

Figure 5.5-1. Code framework schematic

The code's object-based framework is also a key factor in enabling the solution of extremely large problems on either local, or remote, parallel architectures (planned future development.) Since the finite element method of thermal and structural analysis can be about as data- as it is computationally-intensive, especially given the trend towards ever-larger problem sizes, conservation of heap memory is as critical today as it was in the days of small problems and severely memory-constrained systems. To accommodate finite element bookkeeping and results data for huge systems (matrix storage is a separate and well-defined issue), this new code has implemented a generalized DataSet container class for storage of non-homogeneous arrays of objects. DataSets manage object lists, can dynamically allocate and de-allocate themselves, can reinstate themselves in memory from disk or remote locations, and are capable of providing basic object-level polymorphic function capabilities. Though such operations greatly increase the code sophistication at levels usually not apparent to the casual user, this heap/disk data duality is absolutely essential in providing solutions which can scale to very large sizes.

5.5.3 Structural and Thermal Finite Element Technologies:

The set of general purpose 2-D (plate and shell) and 1-D (bar and beam) elements that have so far been developed have both structural and thermal attributes, and modularly interact with the program architecture just described. In keeping with the project's larger development goals, providing an environment into which new elements can easily be added has been as important a consideration as the end-user functionality itself.

2-D shell elements for both thermal and structural analysis are fully hierarchical, with linear, quadratic and cubic interpolation functions available for both triangular and quadratic element geometries. Linear structural elements include shear corrections to avoid shear locking phenomena (element stiffnesses which are excessive), and thermal gradients through the element thicknesses are available for all element types as well. Point, edge, and face loads may be applied in both structural and thermal senses. Elements, of course, have both flexible as well as inertial properties (conductance and capacitance in the case of thermal analysis), thus providing a basis for static as well as modal analysis types (dynamic analyses are a scheduled future development task), and isotropic, anisotropic and orthotropic material types are all supported.

Figure 5.5-2 is an example of a common-mesh thermal/structural solution for a simple elliptical mirror geometry of the type considered for the *TPF* Coronagraph. Thermal loads in the form of through-thickness temperature gradients were applied to, in this case, a flat mirror (for theoretical validation purposes), and the resulting out-of-plane structural deformations computed. Higher order elements, if used, correlate exactly with the known theoretical solution as do the low-order elements (used here) with their shear correction terms.
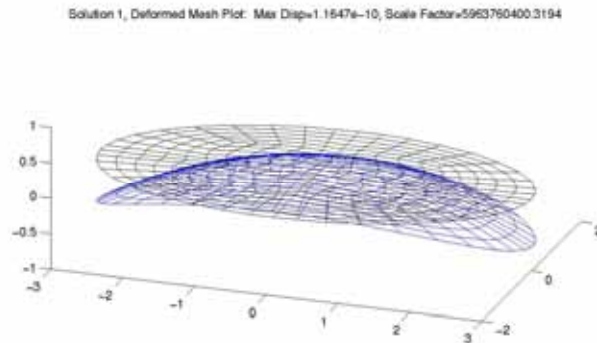

Solution 1, Deformed Mesh Plot: Max Disp=1.1647e-10, Scale Factor=5963760400.3194

Figure 5.5-2. Simple elliptical mirror deformation due to uniform Fthrough-thickness temperature gradient.

5.5.4 Nonlinear Transient Thermal Solution Procedures

Though finite element-based methods have gained wide acceptance in structural analysis, thermal engineering has not been quite so quick to adopt the same solution strategy, remaining entrenched in resistive network codes of one form or another. These disparate solution methods tend to collide when high resolution potentially coupled thermal structural analyses are deemed necessary, and fail

miserably when attempting seamless thermal, structural, and optical optimization and control. Thermal analyses are generally performed using a less refined model, necessitating the use of ad-hoc mapping schemas when attempting to use resulting temperatures as a basis for computing structural deformations. It is precisely the use of such disparate models, and the inherent introduction of un-necessary interpolation errors that development of this code intends to address.

Given that thermal stability due to on-orbit re-pointing maneuvers is a prime consideration for *TPF*, analytical capabilities developed to date have focused on general, comprehensive solutions to the nonlinear transient radiation exchange-dominate heat transfer problem including, of course, conduc-tion and capacitance effects. Computational modules developed so far include time-dependent rela-tive vehicle sun/earth positioning, area-weighted view factor calculation, and radiation exchange ma-trix generation with time-dependent solar flux and earth albedo loading (in progress.) Grey body diffuse effects are assumed for now, though specular exchange and adaptation of the tools to handle stray light issues are planned tasks currently in the design phase.

These numerically intensive computational phases, handled at the module level, are scheduled from the higher-level Matlab-hosted solution sequence which is where other logic such as tangent matrix update strategies, nonlinear convergence detection, time integration, adaptive time stepping schemas and so on has been implemented. The benefit to both users and developers is that much of the code normally locked up in proprietary closed-source codes is available directly, and at a high level, for verification and, if necessary, customization and extension.

Figure 5.5-3 is a simple example of radiant exchange between two thin foil elements that serves to illustrate some of the more salient features of this new code. The back side of the first foil is mod-eled as perfectly insulated, while the back side of the second is exposed to a convection environment with a heat transfer coefficient of 10.W/sq-cm/deg-K and an ambient boundary condition main-tained at 300.0deg-K. (Alternatively, either element could have been subjected to thermal fluxes due to radiation loads, etc.) Radiation heat transfer takes place between the active sides of the foils and an infinite absolute zero temperature environment. Foil-1 has an emissivity equal to .5 and a total heat capacitance equal to 1.0E-05J/sec. Foil-2 has an emissivity equal to .2 and a total heat capaci-tance equal to 1.0J/sec. Surface to surface radiation exchange is assumed to be diffuse.
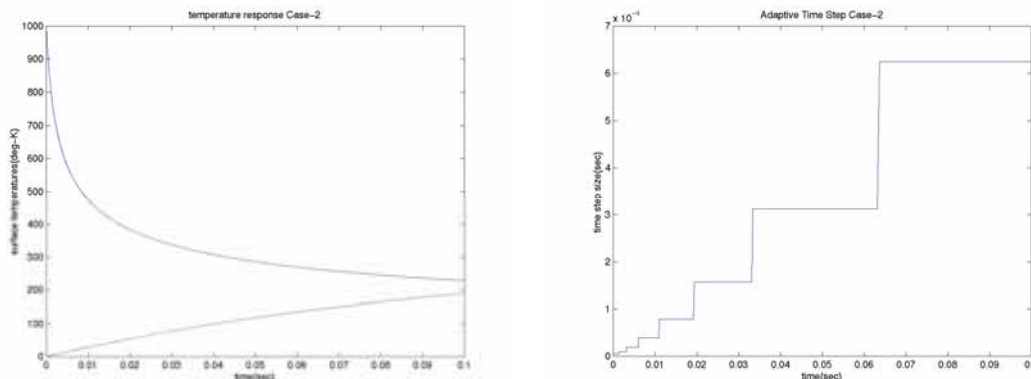

Figure 5.5-3. Test 2 Temperatures and Time Steps

Foil initial conditions were 0.0deg-K and 1000.0deg-K, respectively. For testing purposes fairly stringent solution control delimiters were specified which resulted in automatic step size bisection before obtaining an acceptable starting solution, followed by automatic step size increases as a function of grid point temperature rates of change. A final analysis occurs at the user requested final time.

5.5.5 Planned Technology Development

Though this new code will include a number of features developed specifically for *TPF* classes of problems, it will nonetheless contain quite a bit of functionality that may be found in a number of other commercial codes. Though at first glance it may seem somewhat redundant to implement technology available elsewhere, it is absolutely essential in order to provide the fundamentally integrated analytical capabilities already outlined, as well as the design sensitivity and optimization technologies planned. And, in order to capture *TPF*-specific multidisciplinary effects, the lower-level building blocks need to be on hand in such a fashion that they may be accessed directly rather than being run, in an ad-hoc fasion, and remotely, from other codes offering little to no chance of fundamental methods investigation and/or modification.

In the area of heat transfer, for example, *TPF* Coronagraph will require solutions to radiation exchange for surfaces having specular properties, and may also benefit from an analytical stray light capability that can be run at the high discretization levels likely for heat transfer and structural analysis. Such methods, of course, need to be available in a computational environment that can also immediately yield accurate optical aberration information in a form required by optical engineers, placing additional requirements on integrated thermal/structural analytical capabilities and data visibility. In the area of structural analysis the previously-mentioned thermal gradients through the thickness of shell elements is one such example, and additional enhancements in the area of composite material deformations to applied temperatures are also envisioned.

Finally, and though probably not under focused development until well into FY'05, the overarching design sensitivity and optimization goals of the project have already heavily influenced all aspects of code design to date. An automated analytic capability is the first step in any automated redesign strategy, and the underlying analyses must be efficient and accurate if the optimization procedure is to be robust. Hundreds, or even thousands of design variables will render conventional approaches such as Monte Carlo techniques impractical, and will place an added emphasis on advanced numerical techniques, most likely including exploitation of parallel architectures, and will require efficient approximate design space construction, with updates, for efficient coupling with numerical optimizers.